



## ATLAS Note

ANA-TOPQ-2018-01-INT1

31st October 2019



Draft version 1.3

# Observation of the associated production of a top quark and a Z boson at 13 TeV with ATLAS

Brad Abbott<sup>d</sup>, Muhammad Alhroob<sup>d</sup>, Marius Blaut<sup>a</sup>, Chris Boever<sup>a</sup>, Ian Brock<sup>a</sup>, Irina Cioară<sup>c</sup>, Lidia Dell'Asta<sup>e</sup>, Dylan Frizzell<sup>d</sup>, Phillip Gutierrez<sup>d</sup>, Tanja Holm<sup>a</sup>, Joseph Lambert<sup>d</sup>, Alex Sherman<sup>b</sup>

<sup>a</sup>*Universität Bonn*, <sup>b</sup>*Boston University*, <sup>c</sup>*IFIN-HH Bucharest*, <sup>d</sup>*University of Oklahoma*, <sup>e</sup>*Università di Roma Tor Vergata*

The production of a top quark in association with a Z boson is measured in the trilepton channel. The data collected by the ATLAS experiment in 2015 to 2018 at a centre-of-mass energy of  $\sqrt{s} = 13$  TeV are used, corresponding to an integrated luminosity of  $139 \text{ fb}^{-1}$ . Events containing three identified light leptons ( $e$  and/or  $\mu$ ) and two or three jets, one of which is identified as a  $b$ -quark jet are selected. The major backgrounds are from diboson,  $t\bar{t}V$  and  $t\bar{t}$  production. A neural network is used to improve the background rejection. The measured  $pp \rightarrow t\ell^+\ell^-q$  cross-section with  $m_{\ell\ell} > 30 \text{ GeV}$  is  $97^{+13}_{-12}$  (stat.)  $\pm 7$  (syst.)  $\text{fb} = 97^{+14}_{-13} \text{ fb}$ , which has a relative uncertainty of 14 %, to be compared with the Standard Model expectation of  $101.7 \text{ fb}^{+5.2}_{-1.3} \text{ (scale)} \pm 1.0\% \text{ (PDF)}$ .

# 20 **Contents**

21	<b>1</b>	<b>Introduction</b>	<b>9</b>
22	<b>2</b>	<b>Analysis strategy</b>	<b>11</b>
23	2.1	Overall plan of the analysis	11
24	2.2	Blinding strategy	12
25	<b>3</b>	<b>Data and Monte Carlo samples</b>	<b>13</b>
26	3.1	Data sample	13
27	3.2	Monte Carlo simulated samples	14
28	3.2.1	Signal sample	14
29	3.2.2	Background samples	15
30	<b>4</b>	<b>Object definition</b>	<b>18</b>
31	4.1	Electrons	18
32	4.2	Muons	18
33	4.3	Jets	19
34	4.4	$b$ -jets	19
35	4.5	Missing transverse momentum	19
36	4.6	Overlap removal	19
37	<b>5</b>	<b>Event selection</b>	<b>20</b>
38	5.1	Final-state reconstruction	20
39	5.2	Signal regions	21
40	5.3	Signal-region yields	22
41	5.4	Signal-region yields with pure Monte Carlo samples	24
42	5.5	Signal-region plots	27
43	<b>6</b>	<b>Non-prompt leptons</b>	<b>33</b>
44	6.1	Non-prompt lepton origin	33
45	6.2	$b$ -jet replacement method	33
46	6.3	$b$ -jet replacement sample normalisation	38
47	6.4	$b$ -jet replacement validation	38
48	6.4.1	Shape comparison between $b$ -jet replacement and MC for the $O_{NN}$ discriminant	38
49	6.4.2	Shape comparison between various fake sources	41
50	6.4.3	Lepton flavour plots	42
51	6.5	Contribution of signal with a fake lepton	43
52	<b>7</b>	<b>Background modelling</b>	<b>44</b>
53	7.1	Background sources	44
54	7.2	Validation and control regions	44
55	7.2.1	Diboson validation and control regions	44
56	7.2.2	$t\bar{t}V$ and $t\bar{t}$ validation and control regions	45
57	7.3	Modeling of diboson	46
58	7.3.1	Validation-region yields	46
59	7.3.2	Validation-region yields with pure Monte Carlo samples	47
60	7.3.3	Validation-region plots	49

61	7.3.4	Control-region yields	55
62	7.3.5	Control-region yields with pure Monte Carlo samples	56
63	7.4	Modeling of $t\bar{t}$ and $t\bar{t}Z$	58
64	7.4.1	Validation-region yields	58
65	7.4.2	Validation-region yields with pure Monte Carlo samples	59
66	7.4.3	Validation-region plots	61
67	7.4.4	Control-region yields	67
68	7.4.5	Control-region yields with pure Monte Carlo samples	69
69	<b>8</b>	<b>Multivariate analysis</b>	<b>72</b>
70	8.1	Implementation and input variables	72
71	8.1.1	Signal purity as a function of the NN output	75
72	8.2	Input variable distributions	76
73	8.2.1	Input variable normalised distributions in the SRs	76
74	8.2.2	Input variable distributions in the SRs	81
75	8.2.3	Input variable distributions for the diboson VRs	86
76	8.2.4	Input variable distributions for the $t\bar{t}V + t\bar{t}$ VRs	91
77	8.3	Neural-network output distributions	96
78	8.3.1	Neural-network output distributions in the SRs	96
79	8.3.2	Neural-network output distributions in the VRs	100
80	<b>9</b>	<b>Systematic uncertainties</b>	<b>102</b>
81	9.1	Sources of systematic uncertainties	102
82	9.2	Acceptance and shape uncertainties	106
83	<b>10</b>	<b>Profiled likelihood fit</b>	<b>108</b>
84	10.1	Introduction	108
85	10.2	Asimov fit	110
86	10.3	Unblinded fit	118
87	10.3.1	Correlation matrix	119
88	10.3.2	Nuisance parameters pulls and constraints	120
89	10.3.3	Nuisance parameters pruning	124
90	10.3.4	Nuisance parameters ranking	126
91	10.3.5	Red and blue plots	127
92	10.3.6	Fractional uncertainties	131
93	10.3.7	Pre- and post-fit plots of fitted variables in fit regions	134
94	10.3.8	Pre- and post-fit distributions of the 4 highest ranked NN input variables in the SRs	142
95	10.3.9	Pre- and post-fit distributions of the 4 highest ranked NN input variables in the VRs	146
96	10.3.10	NN output variable distributions in VRs pre- and post-fit	154
97	10.3.11	Checks - Diboson HF rescaling	157
98	10.3.12	Checks - Pruning	158
99	10.3.13	Checks - Split into years	159
100	<b>11</b>	<b>Conclusion</b>	<b>162</b>

101	<b>Appendices</b>	<b>168</b>
102	<b>A List of Monte Carlo datasets</b>	<b>169</b>
103	<b>B Grouping of background sources</b>	<b>176</b>
104	B.1 $tWZ, t\bar{t}Z, t\bar{t}W$ and $t\bar{t}H$	176
105	B.2 $t\bar{t}$ and $tW$	183
106	B.3 Diboson flavours	184
107	<b>C More plots in SRs and VRs</b>	<b>187</b>
108	C.1 Signal regions	187
109	C.2 Validation regions	193
110	C.2.1 Diboson VRs	193
111	C.2.2 $t\bar{t}V + t\bar{t}$ VRs	194
112	<b>D Plots in CRs</b>	<b>205</b>
113	D.1 Basic kinematic plots	205
114	D.1.1 Diboson CRs	205
115	D.1.2 $t\bar{t}$ CRs	217
116	D.1.3 $t\bar{t}Z$ CRs	229
117	D.2 NN input variable plots	239
118	D.2.1 Diboson CRs	239
119	D.2.2 $t\bar{t}$ CRs	244
120	D.2.3 $t\bar{t}Z$ CRs	249
121	<b>E Additional BJR validation plots</b>	<b>254</b>
122	E.1 Plots in SR-LTT regions	254
123	E.1.1 SR LTTs with electron fake	254
124	E.1.2 SR LTTs with muon fake	270
125	E.2 BJR vs MC shape comparisons	286
126	E.2.1 Shape comparison between $b$ -jet replacement and MC for $t\bar{t}$	286
127	E.2.2 Shape comparison between $b$ -jet replacement and MC for $Z + \text{jets}$	291
128	<b>F Z + jets background estimation using the fake factor method</b>	<b>296</b>
129	F.1 Introduction	296
130	F.2 Fake-factor estimation in the 2j1b SR	298
131	F.2.1 Electron channel	298
132	F.2.2 Muon channel	298
133	F.2.3 Z + jets estimation in the SR	300
134	F.2.4 Check in the diboson VR	300
135	F.3 Fake-factor estimation in the 3j1b SR	302
136	F.3.1 Electron channel	302
137	F.3.2 Muon channel	302
138	F.3.3 Z + jets estimation in the SR	302
139	F.3.4 Check in the diboson VR	302
140	<b>G Additional fit studies</b>	<b>306</b>
141	G.1 Diboson CR fitted variable	306

142	G.2	Asimov fit - Additional material	308
143	G.2.1	Pre- and post-fit plots of fitted variables in fit regions	308
144	G.3	Unblinded fit - Red and blue plots for pulled NPs	312
145	G.3.1	Normalization uncertainties	312
146	G.3.2	Modeling uncertainties	315
147	G.3.3	Detector uncertainties	318
148	G.4	Fit in signal-depleted regions	329
149	G.4.1	NN input variable distributions in VRs pre- and post-fit	340
150	G.4.2	NN input variable distributions in unblinded part of the SRs pre- and post-fit	348
151	G.5	Unblinded fit checks - Diboson falavour split	352
152	G.5.1	Pre- and post-fit plots of fitted variables in fit regions	352
153	G.5.2	NN input variable distributions in SRs pre- and post-fit	364
154	G.5.3	NN input variable distributions in VRs pre- and post-fit	368
155	G.5.4	NN output variable distributions in VRs pre- and post-fit	376
156	G.6	Unblinded fit checks - Split into years	379
157	G.7	Fits in signal-depleted regions with $\mu_{\text{SIG}} = 1, 0$ and floating	391
158	G.8	Floating backgrounds - Fits in signal-depleted regions	395
159	G.8.1	Introduction	395
160	G.8.2	Fit in signal-depleted regions with $\mu_{\text{SIG}} = 1$	398
161	G.9	Floating backgrounds - Asimov fit	413
162	<b>H</b>	<b>Comparison with CMS</b>	<b>426</b>

## 163 List of contributions

---

Brad Abbott	Supervisor.
Muhammad Alhroob	Main analyser.
Marius Blaut	Background estimation.
Chris Boever	Background estimation and differential cross-section.
Ian Brock	Supervisor.
Irina Cioară	Background estimation and supervisor.
164 Lidia Dell'Asta	Supervisor.
Dylan Frizzell	Main analyser.
Phillip Gutierrez	Supervisor.
Tanja Holm	Alternative MVA studies and $Z \rightarrow \tau\tau$
Joseph Lambert	Signal generator and initial $\bar{t}/t$ cross-section ratio studies.
Alex Sherman	Main analyser.

---

## 166 Notes for the readers

167 This section summarises changes between versions of the supporting note. We summarise what we have  
 168 changed and/or added.

169 **Version 0.2, 2018-07-25** This is the very first version of the INT note for the  $t\bar{Z}q$  trilepton analysis. For  
 170 this version:

- 171 • v23 SgTop ntuples are used;
- 172 • the analysis is blinded;
- 173 • for the fake background, the fake-factor method is used;
- 174 • the NN is used;
- 175 • the fit is performed on the two SRs.

176 **Version 0.21, 2018-07-26** Some missing plots are fixed in this version. No other change.

177 **Version 0.3, 2018-09-29** In this version:

- 178 • the multivariate analysis is changed and now GBDT is used;
- 179 • the NN based analysis is moved to the appendix.

180 **Version 0.4, 2019-03-22** In this version:

- 181 • v28 SgTop ntuples are used;
- 182 • the signal sample is changed to a new dataset; this has a showering bug fixed;
- 183 • the full Run 2 luminosity is used;
- 184 • the integrated luminosity is updated to the latest value of  $139 \text{ fb}^{-1}$ ;
- 185 • the lepton  $p_T$  cuts are changed from 28, 25 and 15 GeV to 28, 20 and 20 GeV, since this reduces  
 186 the contribution of  $Z + \text{jets}$  substantially;
- 187 • the jet  $p_T$  cut is increased from 30 GeV to 35 GeV, to reduce the impact of the mismodelling in  
 188 the calorimeter crack region;
- 189 • for the non-prompt lepton background estimation, the  $b$ -jet-replacement method is used;
- 190 • new diboson validation regions are included (with 1 ‘Loose’  $b$ -jet);
- 191 • new  $t\bar{t}Z$  control regions are included (with 2  $b$ -jets);
- 192 • NN is chosen as the default MVA technique;
- 193 • the fit is performed on both SRs and diboson,  $t\bar{t}$  and  $t\bar{t}Z$  CRs.

194 **Version 0.41, 2019-03-26** In this version a simpler version of the Asimov fit has been included.

195 **Version 0.5, 2019-05-07** In this version:

- 196 • new fits (both in signal-depleted regions and Asimov) with priors for the  $t\bar{t}Z$  and diboson  
 197 backgrounds are added in Appendix G.4 and Section 10.2;
- 198 • the integrated luminosity is updated to the latest value of  $139 \text{ fb}^{-1}$ ;
- 199 • ROC curves have been added;
- 200 • the grouping of the  $t\bar{t}V + t\bar{t}H + tWZ$  samples was split into  $t\bar{t}Z + tWZ$  and *small backgrounds*,  
 201 which include  $t\bar{t}W$  and  $t\bar{t}H$ ;
- 202 • studies about the treatment of the  $t\bar{t}Z$  and  $tWZ$  samples are added in Appendix B;
- 203 • studies about the variable to be fitted in the diboson CRs are presented in Appendix G.1;
- 204 • studies about the CMS analysis acceptance are reported in Appendix H.

205 **Version 0.51, 2019-05-08** In this version:

- 206 • information about the modeling systematic samples (for both signal and backgrounds) are  
207 added;
- 208 • all MC sample descriptions are now taken from the official PMG document;
- 209 • kinematic distributions in fake-enriched regions are added in ??.

210 **Version 0.6, 2019-06-10** In this version:

- 211 • all comments from the EB on v0.51 have been implemented;
- 212 • results of the unblinded fit (with blinded  $\mu_{\text{SIG}}$  and highest bins of  $O_{\text{NN}}$  blinded) has been  
213 included in Section 10.3;
- 214 • studies about unblinded fits (with blinded  $\mu_{\text{SIG}}$  and highest bins of  $O_{\text{NN}}$  blinded) done separately  
215 on the 2015+2016, 2017 and 2018 datasets have been added in Section 10.3.13;
- 216 • the fit results (both in signal-depleted regions and Asimov) with floating backgrounds, as this  
217 is not the default fit, are moved to Appendix G;
- 218 • the  $O_{\text{NN}}$  distributions for  $t\bar{t}Z$ ,  $tWZ$  and small backgrounds have been added in Appendix B.1;
- 219 • the  $O_{\text{NN}}$  distributions for  $t\bar{t}$  and  $tW$  has been added in Appendix B.2;
- 220 • the Appendix about GBDT results has been removed, as no more updated with respect to the  
221 rest of the analysis.

222 **Version 0.7, 2019-06-17** In this version:

- 223 • the  $m_{\text{T}}(W)$  cut is removed;
- 224 • the SRs are fully unblinded;
- 225 • event yields in CRs have been added in ???;
- 226 • concerning the  $Z + \text{jets}$  background treatment:
  - 227 – the pre-normalization of the BJR sample for the  $Z + \text{jets}$  background estimation has been  
228 changed;
  - 229 – an additional systematic uncertainty for the  $Z + \text{jets}$  background has been added (more  
230 details in Section 9);
- 231 • concerning the diboson background treatment:
  - 232 – plots showing the diboson components shapes have been added to Appendix B.3;
  - 233 – results of an unblinded fit (with blinded  $\mu_{\text{SIG}}$ ) done splitting the three diboson components  
234 are reported in Appendix G.5;
- 235 • concerning the BJR method:
  - 236 – event yields tables with and without BJR are added for all regions;
  - 237 – more BJR validation plots have been added;
- 238 • the  $t\bar{t}Z$  sample used for the systematic uncertainty has been updated to the latest one available  
239 (changes are not reflected in the sample description yet).

240 **Version 0.71, 2019-06-18** In this version:

- 241 • the measured cross section has been added to the abstract.

242 **Version 0.8, 2019-08-20** In this version:

- 243 • results of the fit are updated with the following changes:
  - 244 – the signal is now scaled to the 5FS NLO cross-section, instead of the 4FS NLO cross-  
245 section,

- 246     – the signal radiation systematic is fixed (the normalization was also taken into account),  
247     – the diboson uncertainty is 20 % for LF (as it used to be) and is 30 % for HF, as suggested  
248     during Top Approval,  
249     – the systematic uncertainty for  $tWZ$ , comparing DR1 and DR2 schemes, has been included;  
250     • all comments from Top Approval have been implemented.

251 **Version 0.9, 2019-09-04** In this version:

- 252     • results of the fit are updated with the following changes:  
253         – the signal PDF uncertainties are also applied in the  $t\bar{t}Z$  CRs (they were applied only in the  
254         SRs),  
255         – the Flavour Composition NP has been split into 4 uncorrelated components: diboson LF,  
256         diboson HF,  $t\bar{t}Z$  and a fourth NP which is correlated among all other samples,  
257         –  $t\bar{t}Z$  scale and shower uncertainty has been split into two components;  
258     • all changes from the second iteration of Top Approval comments have been implemented.

259 **Version 1.0, 2019-09-06** In this version:

- 260     • the pruning has been changed from 1 % to 0.5 %;  
261     • all plots and tables for both the Asimov and unblinded fit have been updated;  
262     • the measured cross section and the observed and expected significance have been updated.

263 **Version 1.1, 2019-09-06** In this version:

- 264     • minor fixes.

265 **Version 1.2, 2019-10-21** In this version:

- 266     • updated signal PDF uncertainty and results.

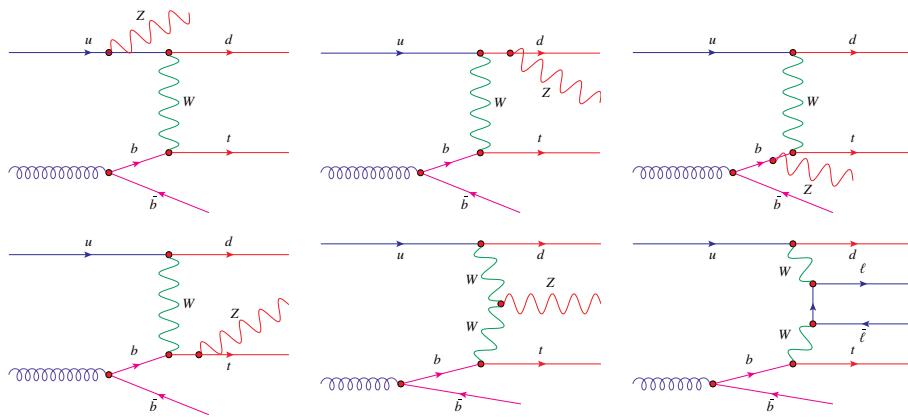
267 **Version 1.3, 2019-10-31** In this version:

- 268     • fix some typos;  
269     • add plots for  $t$ -quark reconstructed mass separated by year (See Section 10.3.13).

## 270 1 Introduction

271 The production of a single top quark in association with a  $Z$  boson ( $tZq$ ) is an interesting process that is  
 272 predicted by the Standard Model (SM). The ATLAS and CMS collaborations separately reported the first  
 273 evidence for a  $tZq$  signal using proton–proton collision data collected at the LHC in 2015 and 2016 at a  
 274 centre-of-mass energy of  $\sqrt{s}=13$  TeV [1, 2]. ATLAS used a dataset corresponding to an integrated luminosity  
 275 of  $36.1\text{ fb}^{-1}$  and reported a result with significance of  $4.2\sigma$  in the data and an expected significance of  
 276  $5.4\sigma$ , with a measured cross-section for  $tZq$  production of  $600 \pm 170$  (stat.)  $\pm 140$  (syst.)  $\text{fb}$ . CMS recently  
 277 published a cross-section measurement of  $\sigma(pp \rightarrow tZq \rightarrow t\ell^+\ell^-q) = 111 \pm 13$  (stat.)  $^{+11}_{-9}$  (syst.)  $\text{fb}$  using  
 278 data collected in 2016 and 2017 [3]. The difference between the two cross-sections measured by ATLAS  
 279 and CMS comes from various reasons, being mainly that ATLAS measured  $tZq$  production while CMS  
 280 measured the  $t\ell^+\ell^-q$  production, meaning that CMS included the BR of the  $Z$ -boson into leptons. Moreover,  
 281 CMS signal included off-shell contributions. More details can be found in [4]. The signal definition has  
 282 been harmonized in this analysis.

283 The dominant process is the  $t$ -channel production of a top quark and a real  $Z$  boson. Hence, the process is  
 284 designated  $tZq$  in the following. For illustration, Fig. 1 shows the lowest-order Feynman diagrams used in  
 285 the leading-order (LO) cross section calculation [5].



286 Figure 1: Feynman graphs to calculate the lowest order amplitudes.

287 The measurement of the  $tZq$  process can significantly improve the limits on EFT couplings [6].  
 288 Standard Model  $tZq$  production is a background in the search for  $tZ$  production via flavour-changing neutral  
 289 currents (FCNC). At lowest order, the SM  $tZ$  production contains one extra jet compared to the FCNC  
 process, as this is not dominated by  $t$ -channel diagrams.  
 290 For the SM  $tZq$  process, different topologies can be defined experimentally:  
 291 **All hadronic** In this channel both the  $Z$  boson and the top quark decay hadronically. The backgrounds in  
 292 such all-hadronic processes are huge and so it has not been investigated further.  
 293 **Single lepton** In this channel the  $Z$  boson decays hadronically or into two neutrinos and the top quark  
 294 decays semileptonically. This is one of the main backgrounds in the search for  $tH$  production, when  
 295 the Higgs boson decays to  $b\bar{b}$ . A measurement of  $tH$  production with  $H \rightarrow b\bar{b}$  certainly requires  
 296 that  $tZq$  production has already been measured in this channel, so that the analysis procedure can be

297 verified. While this channel has a large branching fraction ( $\mathcal{B}Z \rightarrow b\bar{b} \approx 15\%$ ), it suffers from very  
298 large backgrounds, e.g.  $t\bar{t}$ .

299 **Dilepton** In this channel the  $Z$  boson decays into charged leptons ( $e$  and  $\mu$ ), while the top quark decays  
300 hadronically. The main background is  $Z + \text{jets}$ . Suppression of the background relies on good  
301 resolution for the hadronic decays of the  $W$  boson and the top quark.

302 **Trilepton** In this channel the  $Z$  boson decays leptonically and the top quark decays semileptonically. It  
303 has the smallest branching ratio, but the presence of three charged leptons reduces the background  
304 dramatically.

## 305 2 Analysis strategy

306 This section describes the analysis strategy, along with the blinding strategy.

### 307 2.1 Overall plan of the analysis

308 The general strategy of the analysis is the following:

- 309 • only the trilepton channel is considered;
- 310 • the non-prompt lepton contribution from  $Z + \text{jets}$ ,  $t\bar{t}$  and  $tW$  are evaluated using the  $b$ -jet-replacement
- 311 method;
- 312 • all other background sources (mainly diboson and  $t\bar{t}Z$  processes) are estimated using Monte Carlo;
- 313 • a neural network (NN) is used to improve the discrimination of signal to background events providing
- 314 a region with increased  $S/\sqrt{B}$ ;
- 315 • evaluation of the cross-section and significance is done using the **TRExFitter** package; the fit is
- 316 done using a binned maximum likelihood method in the signal regions and in various control regions
- 317 (listed in Table 34).

318 This analysis differs from the one published in TOPQ-2016-14 [1] in the following aspects.

#### 319 Dataset and samples

- 320 • samples produced with release 21 instead of 20.7 are used;
- 321 • 2017 and 2018 data are added;
- 322 • the signal MC is generated as  $t\ell^+\ell^-q$  instead of  $tZq$  and at NLO instead of LO;
- 323 • for the samples where **PYTHIA** is used, **PYTHIA** 8 is used instead of **PYTHIA** 6.

#### 324 Event selection

- 325 • the event selection has been re-optimised;
- 326 • an additional signal region is added, where events with three jets are selected.

#### 327 Background treatment

- 328 • the normalisation of the diboson background is no longer corrected by a scale factor;
- 329 • the non-prompt lepton contribution from  $Z + \text{jets}$  and  $t\bar{t}$  are evaluated using the  $b$ -jet-replacement
- 330 method, instead of the previously used fake-factor method and Monte Carlo, respectively.

331 **Fit**

- 332 • several control regions, to control the diboson,  $t\bar{t}Z$  and  $t\bar{t}$  backgrounds, are included in the fit;  
333 • the  $Z + \text{jets}$  and  $t\bar{t}$  backgrounds are free floating in the fit;  
334 • for the diboson and  $t\bar{t}Z$  backgrounds, pre-fit normalization uncertainties are used;  
335 • the fitting package used is now **TRExFitter** instead of **HistFitter**.

336 **2.2 Blinding strategy**

337 A blinding strategy is set to reduce any possible bias in the measurement. The prescriptions of the Top WG  
338 are followed [7]. To make sure that the background sources are correctly described, data is only looked at  
339 in regions where the signal contribution is expected to be small.

340 The blinding strategy is the following:

- 341 • NN input variables are shown in the validation regions (VR), including data, to make sure the input  
342 to the NN training is sound;  
343 • as an additional check, the NN output score,  $O_{\text{NN}}$ , is unblinded for those bins, where  $S/B$  is expected  
344 to be less than 5 %, (i.e. the bins with  $O_{\text{NN}} > -0.4$  are blinded).

### 3 Data and Monte Carlo samples

- This section describes the samples used in this analysis. The detailed lists of data and Monte Carlo (MC) samples can be found in Appendix A, while a description is presented below.
- The starting point for the analysis is the single-top ntuples [8], version 28 [9] (which uses AnalysisTop-21.2.58). These ntuples are produced from TOPQ1 derivations [10]. The derivations contain a filter that requires at least one lepton (an LH loose electron or a good combined muon) with a  $p_T$  above 20 GeV and  $|\eta| \leq 2.5$ .

#### 3.1 Data sample

- The analysis described in this paper uses data collected from 2015 to 2018 by the ATLAS detector at a centre-of-mass energy of 13 TeV. The complete sample includes all 25 ns data periods from 2015, as well as the whole 2016, 2017 and 2018 datasets. The total integrated luminosity is of  $139 \text{ fb}^{-1}$ . The selected data periods were collected during stable beam LHC operations and with the ATLAS detector fully functioning.

The partial integrated luminosities and the Good Run Lists used are reported in Table 1.

Table 1: Integrated luminosity per year.

Year	Int. lumi. ( $\text{fb}^{-1}$ )	GRL
2015	3.2	data15_13TeV/20170619/physics_25ns_21.0.19.xml
2016	33.0	data16_13TeV/20170605/physics_25ns_21.0.19.xml
2017	44.3	data17_13TeV/20180619/physics_25ns_Triggerno17e33prim.xml
2018	58.5	data18_13TeV/20181111/physics_25ns_Triggerno17e33prim.xml

- Starting from the Main stream, events are considered only if they are accepted by at least one of the single-muon or single-electron triggers described in Refs. [11–13] and listed in Table 2.

Table 2: Trigger selections.

Year	Single $e$	Single $\mu$
2015	HLT_e24_lhmedium_L1EM20VH HLT_e60_lhmedium HLT_e120_lhloose	HLT_mu20_iloose_L1MU15 HLT_mu50
2016–2018	HLT_e26_lhtight_nod0_ivarloose HLT_e60_lhmedium_nod0 HLT_e140_lhloose_nod0	HLT_mu26_ivarmedium HLT_mu50

- The electron triggers select a calorimeter cluster matched to a track. Electrons must then satisfy identification criteria based on a multivariate technique using a likelihood (LH) discriminant. In 2015, electrons had to satisfy a medium identification and have  $E_T > 24 \text{ GeV}$ . In 2016, 2017 and 2018, electrons had to satisfy a tight identification together with an isolation criteria and have  $E_T > 26 \text{ GeV}$ . During the four years, to avoid efficiency losses due to identification and isolation at high  $p_T$ , two other triggers were also available, selecting medium electrons with  $E_T > 60 \text{ GeV}$  and selecting loose electrons with  $E_T > 120 \text{ GeV}$  (140 GeV in 2016 and 2017).

366 Muons are triggered on by matching tracks reconstructed in the muon spectrometer and in the inner detector.  
 367 In 2015, muons had to satisfy a loose isolation requirement and have  $p_T > 20$  GeV. In 2016, 2017 and  
 368 2018, the isolation criterion was tightened and the threshold increased to  $p_T > 26$  GeV. During the four  
 369 years, to avoid efficiency losses due to isolation at high  $p_T$ , another muon trigger without any isolation  
 370 requirement was available, selecting muons with  $p_T > 50$  GeV.

### 371 **3.2 Monte Carlo simulated samples**

372 ATLAS MC samples for analyses on the 2015–2018 dataset are split into three subsets: mc16a reflects  
 373 the pile-up conditions of the years 2015 and 2016, mc16d reflects the pile-up conditions of 2017 data  
 374 and mc16e reflects the pile-up conditions of 2018 data. Therefore, mc16a samples need to be scaled to  
 375 2015+2016 integrated luminosity, mc16d samples need to be scaled to 2017 integrated luminosity and  
 376 mc16e samples need to be scaled to the 2018 integrated luminosity.

377 The generated MC samples containing top-quarks are produced with the top-quark mass,  $m_t$ , parameter set  
 378 to 172.5 GeV and a branching fraction of the top-quark decay to a  $W$  boson and a  $b$  quark of 1.

379 In all samples, decays into  $\tau$  leptons are included and if the  $\tau$  decays leptonically such events are taken into  
 380 account in the analysis.

381 In the following, samples used in the analysis are explained in detail, both for the signal and for the  
 382 background sources.

383 Background contribution from  $t\bar{t}\gamma$  events was investigated and the contribution was found to be less  
 384 than 0.5% in both signal regions, therefore estimated contributions from this background is not further  
 385 considered.

#### 386 **3.2.1 Signal sample**

387 The  $tZq$  sample is simulated using the `MADGRAPH5_AMC@NLO` v2.3.3 [14] generator at NLO  
 388 with the NNPDF3.0NLO [15] parton distribution function (PDF). The generator is interfaced with  
 389 `PYTHIA8.230` [16] using the A14 tune [17] and the NNPDF30\_NLO\_AS\_0118\_NF\_4 [15] PDF set. Off-  
 390 resonant events away from the  $Z$  mass peak are included. An invariant mass cut is applied, requiring  
 391  $m_{ll} > 30$  GeV. Top quark is decayed at LO using `MADSPIN` [18, 19] to preserve spin correlations. The  
 392 four-flavour scheme is used where all the quark masses are set to zero, except for the top and bottom quarks.  
 393 Following the discussion in Reference [20], the functional form of the renormalization and factorization  
 394 scale is set to the  $4\sqrt{m_b^2 + p_{T,b}^2}$ , where the  $b$ -quark is the external one produced from gluon splitting in the  
 395 event. The decays of bottom and charm hadrons are simulated using the `EvtGEN` program [21].

396 The SM  $t\ell^+\ell^-q$  MC sample used in the analysis (DSID: 412063) contains a trilepton filter, so the  $W$  boson  
 397 from the top-quark decay is forced to decay leptonically.

398 Following the recommendations from theorists during an LHC Top Working Group [22], the cross-section  
 399 is calculated using the five-flavour scheme with the renormalisation,  $\mu_R$ , and the factorisation scales,  $\mu_F$ ,  
 400 set to  $\mu_R = \mu_F = (m_t + m_Z)/4$ . The total SM  $t\ell^+\ell^-q$  cross-section at NLO is 101.7 fb, with  $m_{ll} > 30$  GeV.  
 401 The renormalisation and factorisation scale uncertainties are  $^{+5.2}_{-1.3}\%$  and the PDF uncertainty is  $^{+1.0}_{-1.0}\%$ . The  
 402 PDF uncertainty is calculated following a PDF reweighting procedure using the NNPDF30\_NLO\_AS\_0118  
 403 PDF error sets. The simulated sample is normalized to the 5FS cross-section.

404 The uncertainty due to initial-state-radiation (ISR) is estimated by comparing the nominal  $tZq$  sample with  
 405 two additional samples, which have the same setting as the nominal one, but with the Var3 up or down  
 406 variation of the A14 tune (DSID: 412064-412065). The Var3c A14 tune variation corresponds to the  
 407 variation of  $\alpha_s$  for initial state radiation (ISR) in the A14 tune.

408 To evaluate the renormalization and factorization scale uncertainties, the two scales are varied simultaneously  
 409 by factors 2.0 and 0.5. To evaluate the PDF uncertainties for the nominal PDF, the 100 variations for  
 410 NNPDF2.3LO are taken into account.

411 **3.2.2 Background samples**

412 Simulated samples are included in the analysis in order to account for all the SM predicted background  
 413 channels. The samples are normalised to the cross-sections given in Appendix A multiplied by the  $k$   
 414 factors given in the same tables.

415  **$t\bar{t}$  production** The production of  $t\bar{t}$  events is modelled using the PowHEGBox [23–26] v2 generator  
 416 at NLO with the NNPDF3.0NLO [15] parton distribution function (PDF) and the  $h_{\text{damp}}$  parameter<sup>1</sup> set  
 417 to  $1.5 m_t$  [27]. The generator is interfaced with PYTHIA8.230 [16] using the A14 tune [17] and the  
 418 NNPDF23LO PDF set. In the sample used (DSID: 410472), it is required that both the  $W$  bosons from the  
 419  $t$  quarks decay leptonically.

420 The uncertainty due to initial-state-radiation (ISR) is estimated by comparing the nominal  $t\bar{t}$  sample  
 421 with two additional samples [28] (DSID: 410472 and 410482). To simulate higher parton radiation, the  
 422 factorisation and renormalisation scales are varied by a factor of 0.5 while simultaneously increasing the  
 423  $h_{\text{damp}}$  value to  $3.0 m_t$  and using the Var3c up variation from the A14 tune. For lower parton radiation,  $\mu_r$ ,  
 424 and  $\mu_f$  are varied by a factor of 2.0 while keeping the  $h_{\text{damp}}$  value to  $1.5 m_t$  and using the Var3c down  
 425 variation in the parton shower. The impact of final-state-radiation (FSR) is evaluated using PS weights  
 426 which vary the renormalisation scale for QCD emission in the FSR by a factor of 0.5 and 2.0, respectively.

427 The impact of the parton shower and hadronisation model is evaluated by comparing the nominal generator  
 428 setup with a sample (DSID: 410558) produced with the NLO PowHEGBox [23–26] v2 generator using the  
 429 NNPDF3.0NLO [15] parton distribution function (PDF). The generator is interfaced with HERWIG7.04 [29,  
 430 30], using the H7UE set of tuned parameters [30] and the MMHT2014LO PDF set [31].

431 To assess the uncertainty due to the choice of the matching scheme, the PowHEG sample is compared  
 432 to a generator setup of MADGRAPH5\_AMC@NLO +PYTHIA8 (DSID: 410465). For the calculation of  
 433 the hard-scattering, MADGRAPH5\_AMC@NLO v2.6.0 with the NNPDF3.0NLO [15] PDF set is used.  
 434 The generator is interfaced with PYTHIA8.230 [16], using the A14 set of tuned parameters [17] and the  
 435 NNPDF23LO PDF.

<sup>1</sup> The  $h_{\text{damp}}$  parameter controls the transverse momentum  $p_T$  of the first additional emission beyond the leading-order Feynman diagram in the parton shower and therefore regulates the high- $p_T$  emission against which the  $t\bar{t}$  system recoils.

436 **Single top-quark production** Although having a very low contribution, single top-quark production is  
 437 also considered. The  $s$ - and  $t$ -channels have no overlap with the  $tZq$  final state, so only the  $tW$  sample  
 438 is evaluated. Single-top  $tW$  associated production is modelled using the PowHEGBox [24–26, 32] v2  
 439 generator at NLO in QCD in the five flavour scheme with the NNPDF3.0NLO [15] parton distribution  
 440 function (PDF) set. The diagram removal (DR) scheme [33] was employed to handle the interference with  
 441  $t\bar{t}$  production [27]. The generator is interfaced with PYTHIA8.230 [16] using the A14 tune [17] and the  
 442 NNPDF23LO PDF set. In the samples used (DSIDs: 410648 and 410649), it is required that both  $W$   
 443 bosons in the event decay leptonically.

444  **$t\bar{t}H$  production** The production of  $t\bar{t}H$  events is modelled using the PowHEGBox [23–26] generator at  
 445 NLO with the NNPDF3.0NLO [15] PDF set. The generator is interfaced with PYTHIA8.230 [16] using  
 446 the A14 tune [17] and the NNPDF2.3LO [15] PDF set. In the samples used (DSID: 346343, 346344  
 447 and 346345), it is required that none, just one or both  $W$  bosons from the  $t$  quarks decay leptonically,  
 448 respectively.

449  **$t\bar{t}V$  production** The production of  $t\bar{t}V$  events (DSID: 410155-410157 and 410218-410220) is modelled  
 450 using the MADGRAPH5\_AMC@NLO v2.3.3 [14] generator at NLO with the NNPDF3.0NLO [15] parton  
 451 distribution function (PDF). The generator is interfaced with PYTHIA8.210 [16] using the A14 tune [17]  
 452 and the NNPDF2.3LO [15] PDF set.

453 The uncertainty due to initial-state-radiation (ISR) is estimated by comparing the nominal  $t\bar{t}V$  sample with  
 454 additional samples (DSID: 410370-410375), which have the same setting as the nominal one, but with the  
 455 Var3 up or down variation of the A14 tune.

456 An additional  $t\bar{t}Z$  samples (DSID: 413023) are produced with the SHERPA 2.2.1 [34] generator at NLO  
 457 accuracy. A dynamic renormalization scale is used that is defined very similarly to that of the nominal  $t\bar{t}Z$   
 458 samples. The CKKW matching scale of the additional emissions is set to 30 GeV. The default SHERPA 2.2.1  
 459 parton shower is used along with the NNPDF3.0NNLO [15] PDF set.

460  **$tWZ$  production** The production of  $tWZ$  events is modelled using the MADGRAPH5\_AMC@NLO v2.3.3 [14]  
 461 generator at NLO with the NNPDF3.0NLO [15] parton distribution function (PDF). The generator is  
 462 interfaced with PYTHIA8.212 [16] using the A14 tune [17] and the NNPDF2.3LO [15] PDF set. In the  
 463 sample used (DSID: 410408), it is required that the  $Z$  boson decays leptonically.

464 An additional  $tWZ$  sample is used to estimate the uncertainty connected with the description of the  
 465 interference between  $t\bar{t}Z$  and  $tWZ$ . The nominal samples is generated with the DR1 scheme, while the  
 466 alternative sample is generated using the DR2 scheme (DSID: 412119).

467 **Diboson production** The samples simulating  $WW$ ,  $WZ$  and  $ZZ$  events with at least two charged leptons  
 468 are all considered. In the trilepton topology,  $WZ$  events are the ones that significantly contribute to the  
 469 background. Fully leptonically and semileptonically decaying diboson samples are simulated with the  
 470 SHERPA v2.2 [34] generator. In this setup multiple matrix elements are matched and merged with the SHERPA  
 471 parton shower based on Catani-Seymour dipole [35, 36] using the MEPS@NLO prescription [37–40]. The  
 472 virtual QCD correction for matrix elements at NLO accuracy are provided by the OPENLOOPS library [41],

473    42]. library [42]. Samples are generated using the `NNPDF3.0nnlo` set [15], along with the dedicated set of  
 474    tuned parton-shower parameters developed by the `SHERPA` authors.

475    The diboson background is split into  $VV + HF$  (heavy flavour) and  $VV + LF$  (light flavour) based on the  
 476    types of jets associated: if one of the associated jets originated from  $b$ -quark or  $c$ -quark then it is considered  
 477    as  $VV + HF$ , otherwise it is considered as  $VV + LF$ . The jet type is determined using the `jet_truthflav`  
 478    variable. This variable, provided by the flavour tagging group, defines a cone of  $\Delta R < 0.3$  associated with  
 479    each jet. If a  $b$ -hadron with ( $p_T > 5 \text{ GeV}$ ) is found within this cone the jet is identified as a  $b$ -jet. If no  
 480     $b$ -hadrons are found, the algorithm searches for  $c$ -hadrons, then  $\tau$  leptons. If none of these identifiers are  
 481    found the jet is labeled as a light jet.

482    **Z + jets production**    QCD  $V +$  jets production is simulated with the `SHERPA` v2.2 [34] generator. In  
 483    this setup multiple matrix elements are matched and merged with the `SHERPA` parton shower based on  
 484    Catani-Seymour dipole [35, 36] using the `MEPS@NLO` prescription [37–40]. The virtual QCD correction  
 485    for matrix elements at NLO accuracy are provided by the `OPENLOOPS` library [41, 42]. Samples are  
 486    generated using the `NNPDF3.0nnlo` set [15], along with the dedicated set of tuned parton-shower parameters  
 487    developed by the `SHERPA` authors. A generator-level cut requiring the invariant mass of the two leptons to  
 488    be  $\geq 40 \text{ GeV}$  is applied. While  $Z +$  jets production contains events where the two leptons come from a  $Z$   
 489    boson, the third lepton must be a fake lepton (or from a semileptonic  $b$ - or  $c$ -hadron decay). Two additional  
 490    jets must also be produced in order to fake the signal signature. The tight selection criteria on the third  
 491    lepton, as shown in the following, allows to suppress this background almost completely.

## 492 4 Object definition

493 In general, the object identification follows the standard recommendations of the ATLAS CP groups for  
 494 data collected by ATLAS in 2015–2018 [43]. The CP recommendations available in AnalysisTop-21.2.58  
 495 are implemented.

496 **4.1 Electrons**

497 Electron candidates are reconstructed from energy deposits in the EM calorimeter associated with ID  
 498 tracks [44–46]. The clusters are required to be in the pseudorapidity  $|\eta| < 2.47$  region, excluding the  
 499 transition region between the barrel and end-cap EM calorimeters,  $1.37 < |\eta| < 1.52$ . The candidate  
 500 electrons are required to have transverse energy  $E_T > 15$  GeV. Further requirements on the electromagnetic  
 501 shower shape, calorimeter energy to tracker momentum ratio, and other discriminating variables are  
 502 combined into a likelihood-based object quality cut, optimised for strong background rejection. Specifically,  
 503 three categories are available: `LooseLH`, `MediumLH`, and `TightLH`, in order of increasing background  
 504 rejection power.

505 All electron candidates in this analysis must pass the `TightLH` selection to reject electrons from photon  
 506 conversion, hadronic particle decays, and fake electrons.

507 Electrons are further required to be isolated, using the `Gradient` working point. This working point varies  
 508 the electron selection efficiency depending on the electron  $p_T$ , i.e. lower efficiency at low  $p_T$  and higher  
 509 efficiency as the  $p_T$  rises. For example, the isolation is 90 % efficient for electrons with  $p_T = 25$  GeV and  
 510 99 % efficient for electrons with  $p_T = 60$  GeV.

511 Electron tracks are also required to be consistent with the beam line applying the requirements:  
 512  $|d_0^{\text{BL}} \text{ significance}| < 5$  and  $|\Delta z_0^{\text{BL}} \sin \theta| < 0.5$  mm.

513 **4.2 Muons**

514 Muon candidates can be reconstructed both using only the Muon Spectrometer (MS) information (standalone  
 515 muons) or combining the MS reconstruction with Inner Detector (ID) tracks (combined muons) [47]. To  
 516 increase the background rejection, some additional requirements are applied on track-parameter quality.  
 517 Various working point are provided: `Loose`, `Medium`, and `Tight`.

518 The muon candidates in this analysis must pass the `Medium` identification definition, based, for muons  
 519 with  $|\eta| < 2.5$ , on requirements of hits in MS subsystems, and on the compatibility between ID and  
 520 MS momentum measurements to remove fake muons. Furthermore, they must have  $|\eta| < 2.5$  and  
 521  $p_T > 15$  GeV.

522 The isolation requirement is the same as that of electrons, the `Gradient` working point, which results in a  
 523 similar  $p_T$ -dependent efficiency.

524 Muon tracks are also required to be consistent with the beam line applying the requirements:  $|d_0^{\text{BL}} \text{ significance}| <$   
 525 3 and  $|\Delta z_0^{\text{BL}} \sin \theta| < 0.5$  mm.

### 526 4.3 Jets

527 Jets are reconstructed from topological calorimeter clusters [48] at the EM scale using the anti- $k_t$  algorithm  
 528 with radius parameter of 0.4. They are required to have  $p_T > 35$  GeV and  $|\eta| < 4.5$ .

529 In order to reject forward jets originating from additional proton-proton interactions, a forward jet vertex  
 530 tagger (fJVT) requirement is applied. This combines information about jet shapes and topological jet  
 531 correlations in pile-up interactions, in order to maximise the number of selected jets coming from the  
 532 hard scattering and reduce pileup jets contamination. All jets with  $|\eta| > 2.5$  are required to pass the  
 533 requirements of the fJVT Medium working point. This has an efficiency of selecting hard scattered jets of  
 534 up to 97 % and a pileup-jet efficiency of 53.4 % for jets with  $p_T$  between 40 GeV and 50 GeV [49].

### 535 4.4 $b$ -jets

536 Jet containing a  $b$  hadron are identified using the MV2c algorithm. The MV2c10 variant is used, corresponding  
 537 to the current recommendations [50]. It is based on a neural network using the output weights of the  
 538 JetFitter, IP3D and SV1 algorithms as input, which are described in [51]. Pseudo-continuous  $b$ -tagging [52]  
 539 working points are used with a default working point near 70 % and some validation regions use a working  
 540 point near 85 %.

### 541 4.5 Missing transverse momentum

542 The missing transverse momentum,  $E_T^{\text{miss}}$ , is a measure of the transverse momentum imbalance due to  
 543 escaping neutrinos. The  $E_T^{\text{miss}}$  is calculated as the magnitude of the negative vector sum of the transverse  
 544 momenta of all identified jets (with  $p_T > 20$  GeV), electrons and muons (with  $p_T > 25$  GeV) in the event,  
 545 as well as a soft term built from tracks that are associated to the hard-scatter vertex but are not associated to  
 546 any of the reconstructed objects. The soft term is included in order to account for low-momentum particles  
 547 that are not identified among the final state objects [53–55].

### 548 4.6 Overlap removal

549 Overlap removal is performed during the production of the single-top ntuples. It follows the usual strategy  
 550 of the top group. First, an electron sharing a track with a muon is removed to avoid cases where a muon  
 551 mimics an electron through radiation of a hard photon. Next, the closest jet to each electron within an  $\eta$ – $\phi$   
 552 cone of size  $\Delta R = 0.2$  is removed to reduce the proportion of electrons being reconstructed as jets. Next,  
 553 electrons with a distance  $\Delta R < 0.4$  from any of the remaining jets are removed to reduce backgrounds from  
 554 non-prompt, non-isolated electrons coming from heavy-flavour hadron decays. Jets with fewer than three  
 555 tracks and distance  $\Delta R < 0.4$  from a muon are then removed to reduce fake jets from muons depositing  
 556 energy in the calorimeters. Finally, muons with a distance  $\Delta R < 0.4$  from any of the surviving jets are  
 557 removed to avoid contamination of non-prompt muons from heavy-flavour hadron decays.

## 558 5 Event selection

559 In the following the final state reconstruction and the definition of the signal regions are described.

### 560 5.1 Final-state reconstruction

561 At lowest order, the final state of the trilepton channel of the SM  $tZq$  process consists of three charged  
562 leptons (two coming from the  $Z$  decay and one from the leptonic  $W$  decay), one neutrino, one  $b$  quark, as  
563 well as one light quark (expected to go preferentially in the forward direction).

564 Reconstructing the mother particles ( $Z$  boson and  $t$  quark) is important in order to identify specific features  
565 that help to separate signal from background. For example, the  $Z$ -boson mass distribution can contribute  
566 to the reduction of top-quark backgrounds, as these do not include a  $Z$  boson in the final state, while the  
567 untagged jet pseudorapidity distribution has a very different shape in  $tZq$  events than in  $t\bar{t}Z$  events, which  
568 constitute one of the largest backgrounds.

569 In order to reconstruct the  $Z$  boson, an opposite-sign, same-flavour (OSSF) lepton pair is needed. In the  
570  $\mu ee$  and  $e\mu\mu$  channels, this is uniquely identified. For the  $eee$  and  $\mu\mu\mu$  events, both possible combinations  
571 are considered and the pair that has the invariant mass closest to the  $Z$ -boson mass is chosen.

572 The  $W$  boson, that is expected to decay leptonically, is reconstructed from the remaining lepton and the  
573 missing transverse momentum. The missing part of the neutrino four-vector is the longitudinal component  
574 along the  $z$ -axis ( $E_Z^{\text{miss}}$ ), which can be obtained by using the mass constraint of the  $W$  boson

$$(P^W)^2 = (P^\ell + P^{\text{miss}})^2 = M_W^2, \quad (1)$$

575 where the  $M_W$  is the  $W$  boson mass, 80.4 GeV.

576 The solution of the quadratic equation given in Equation 1 in terms of the  $E_Z^{\text{miss}}$  can be expressed as follows  
577

$$E_Z^{\text{miss}} = \frac{\alpha \cdot P_Z^\ell \pm \sqrt{(P_Z^\ell)^2 \cdot [\alpha^2 - p_T^\ell \cdot E_T^{\text{miss}}]}}{(p_T^\ell)^2}, \quad (2)$$

578 where  $\alpha$  is given by

$$\alpha = \frac{M_W^2}{2} + \vec{p}_T^\ell \cdot \overrightarrow{E_T^{\text{miss}}}. \quad (3)$$

579 When the quantity under the square root is positive ( $\alpha^2 \geq p_T^\ell \cdot E_T^{\text{miss}}$ ), then there are two real solutions, and  
580 the smallest one in magnitude is taken, since the  $W$  boson is expected to be produced with small rapidity.  
581 For some of the events, Equation 2 has imaginary solutions ( $\alpha^2 < p_T^\ell \cdot E_T^{\text{miss}}$ ), which is interpreted as a  
582 mis-measurement of  $E_T^{\text{miss}}$ . In this case,  $m_T(W) > M_W$ . Ignoring the square root in Equation 2 violates  
583 Equation 1, and the measured values of  $E_T^{\text{miss}}$ ,  $E_X^{\text{miss}}$  and  $E_Y^{\text{miss}}$  cannot be taken as the components of the  
584 neutrino momentum. If  $m_T(W)$  is fixed to be equal to  $M_W$ , which corresponds to a vanishing of the square  
585 root in Equation 2, a quadratic dependence of  $E_X^{\text{miss}}$  on  $E_Y^{\text{miss}}$  appears. Technically this is resolved by  
586 introducing a new scale factor  $\beta$ , which is defined by

$$\beta = \frac{M_W^2}{2 \cdot p_T^\ell} \cdot E_T^{\text{miss}} - \vec{p}_T^\ell \cdot \overrightarrow{E_T^{\text{miss}}}. \quad (4)$$

- 587  $\beta$  is used to scale  $E_X^{\text{miss}}$ ,  $E_Y^{\text{miss}}$  and  $E_T^{\text{miss}}$ , and then  $\alpha$  is recalculated as shown in Equation 3. Following that,  
 588  $E_Z^{\text{miss}}$  is found by considering only the offset part of the Equation 2.
- 589 For the  $t$ -quark reconstruction, the previously reconstructed  $W$  boson, together with the  $b$ -tagged jet are  
 590 used.
- 591 A summary of the symbols representing the reconstructed objects is presented in Table 3. These symbols  
 592 are used in the plots.

Table 3: Object reconstruction. More details about the reconstruction process can be found in the text.

Symbol	Description
$\ell_1^Z$	Highest $p_T$ lepton from the reconstructed $Z$ boson
$\ell_2^Z$	Lowest $p_T$ lepton from the reconstructed $Z$ boson
$Z$	Reconstructed $Z$ boson
$\ell^W$	Lepton from the reconstructed $W$ boson from the $t$ -quark decay
$W$	Reconstructed $W$ boson from the $t$ -quark decay
$b_1$	$b$ -tagged jet
$t$	Reconstructed $t$ quark
$j_f$	Forward jet (see Section 5.2 for more details)
$j_r$ or $j_{\text{Rad}}$	Radiation jet (see Section 5.2 for more details)
$\ell_{1/2/3}$	$p_T$ ordered leptons
$j_{1/2/3}$	$p_T$ ordered jets

## 593 5.2 Signal regions

- 594 Two orthogonal signal regions (SR) are defined. In one region events with three leptons, one  $b$ -tagged  
 595 jet (using the 70 % working point) and one untagged jet<sup>2</sup> are selected. This region will be referred to as  
 596  $2j1b$  in the following. In the second signal region, events are selected identically to the first except for the  
 597 inclusion of a second untagged jet. This region will be referred to as  $3j1b$  in the following. Of the two  
 598 untagged jets, the one that gives, with the  $b$ -jet, the highest value of  $m_{bj_f}$  is selected to be the *forward* jet.  
 599 The remaining jet is called *radiation* jet. In the  $2j1b$  SR, the forward jet is uniquely defined. The same  
 600 nomenclature is used for the jets in the validation and control regions.
- 601 The three leptons are sorted by their  $p_T$ , irrespective of flavour, and required to have transverse momenta  
 602 of at least 28, 20 and 20 GeV, respectively. At least one of the leptons needs to be trigger matched. All  
 603 leptons must be reconstructed in the central detector region ( $|\eta| < 2.5$ ).
- 604 Jets are required to have  $p_T > 35$  GeV. Since the untagged jet (or one of the two untagged jets in the  $3j1b$   
 605 SR) tends to be in the forward direction, the cut on  $|\eta|$  is set to 4.5, compared to  $|\eta| < 2.5$ , which is the cut  
 606 applied to the  $b$ -tagged jet.
- 607 Additionally, in order to suppress backgrounds that do not contain a  $Z$  boson, a cut is applied on the invariant  
 608 mass of the two OSSF leptons associated to the  $Z$ . This is required to be between 81 and 101 GeV.

<sup>2</sup> An “untagged” jet is a jet that fails the  $b$ -jet selection. Given that the requirement is to have exactly one  $b$ -tagged jet with 70 % WP, the other jet is untagged in the sense that it fails the 70 % WP selection.

Not reviewed, for internal circulation only

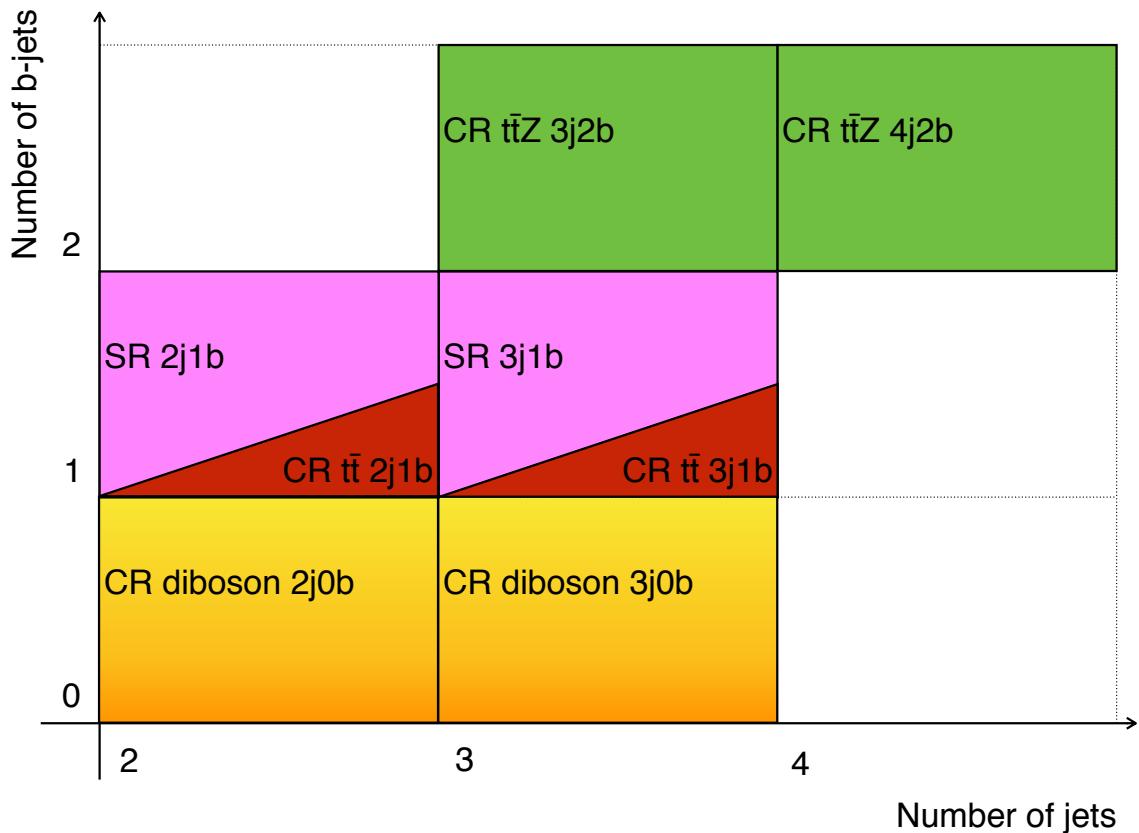


Figure 2: Summary of the analysis regions.

609 The selection cuts applied in the signal regions are listed in Table 4. In this table, also the selection  
 610 cuts for the definition of validation and control regions are reported. These regions are constructed such  
 611 that they are enriched in three of the main sources of background, diboson,  $t\bar{t}Z$  and  $t\bar{t}$  production. Their  
 612 definition is very close but still orthogonal to the signal region one. Figure 2 visualize the signal and  
 613 control regions, in terms of jet and  $b$ -jet multiplicities. The validation and control regions are described in  
 614 detail in Section 7.2.

### 615 5.3 Signal-region yields

616 The two signal regions show similar signal to background ratios when studying simulated events. The  
 617 event yields in the SRs after the full selection can be found in Tables 5 and 6. For the remainder of this  
 618 note some samples will be treated together as a single background groups, namely  $t\bar{t} + tW$ ,  $t\bar{t}Z + tWZ$ , and  
 619  $t\bar{t}W + t\bar{t}H$  (referred to as small backgrounds). Justification of these background groupings can be found  
 620 in Appendix B.

621 A variety of background sources are considered. These include SM processes with similar final states as  
 622  $tZq$  (such as diboson or the associated production of  $t\bar{t}$  with a  $W$ ,  $Z$  or  $H$  boson), as well as events in which  
 623 at least one of the leptons in the final state is ‘fake’ (either a jet misidentified as a lepton or a non-prompt

Table 4: Overview of the requirements applied for selecting events in the signal, validation and control regions. The ‘Loose’  $b$ -jet requirement means that one jet passes the 85 % efficient  $b$ -tagging working point requirement but does not pass the 70 % efficient working point.

Common selections			
Exactly 3 leptons with $ \eta  < 2.5$ $p_T(\ell_1) > 28 \text{ GeV}$ , $p_T(\ell_2) > 20 \text{ GeV}$ , $p_T(\ell_3) > 20 \text{ GeV}$ $p_T(\text{jet}) > 35 \text{ GeV}$			
SR 2j1b	Diboson 2j0b CR	$t\bar{t}Z$ 3j2b CR	$t\bar{t}$ 2j1b CR
$\geq 1$ OSSF pair $ m_{\ell\ell} - m_Z  < 10 \text{ GeV}$ 2 jets, $ \eta  < 4.5$ 1 $b$ -jet, $ \eta  < 2.5$	$\geq 1$ OSSF pair $ m_{\ell\ell} - m_Z  < 10 \text{ GeV}$ 2 jets, $ \eta  < 4.5$ 0 $b$ -jets	$\geq 1$ OSSF pair $ m_{\ell\ell} - m_Z  < 10 \text{ GeV}$ 3 jets, $ \eta  < 4.5$ 2 $b$ -jets, $ \eta  < 2.5$	$\geq 1$ OSDF pair No OSSF pair 2 jets, $ \eta  < 4.5$ 1 $b$ -jet, $ \eta  < 2.5$
Diboson 2j1Lb VR		$t\bar{t}V + t\bar{t}$ 2j1b VR	
$\geq 1$ OSSF pair $ m_{\ell\ell} - m_Z  < 10 \text{ GeV}$ 2 jets, $ \eta  < 4.5$ 1 ‘Loose’ $b$ -jet, $ \eta  < 2.5$		$\geq 1$ OSSF pair $ m_{\ell\ell} - m_Z  > 10 \text{ GeV}$ 2 jets, $ \eta  < 4.5$ 1 $b$ -jet, $ \eta  < 2.5$	
SR 3j1b	Diboson 3j0b CR	$t\bar{t}Z$ 4j2b CR	$t\bar{t}$ 3j1b CR
$\geq 1$ OSSF pair $ m_{\ell\ell} - m_Z  < 10 \text{ GeV}$ 3 jets, $ \eta  < 4.5$ 1 $b$ -jet, $ \eta  < 2.5$	$\geq 1$ OSSF pair $ m_{\ell\ell} - m_Z  < 10 \text{ GeV}$ 3 jets, $ \eta  < 4.5$ 0 $b$ -jets	$\geq 1$ OSSF pair $ m_{\ell\ell} - m_Z  < 10 \text{ GeV}$ 4 jets, $ \eta  < 4.5$ 2 $b$ -jets, $ \eta  < 2.5$	$\geq 1$ OSDF pair No OSSF pair 3 jets, $ \eta  < 4.5$ 1 $b$ -jet, $ \eta  < 2.5$
Diboson 3j1Lb VR		$t\bar{t}V + t\bar{t}$ 3j1b VR	
$\geq 1$ OSSF pair $ m_{\ell\ell} - m_Z  < 10 \text{ GeV}$ 3 jets, $ \eta  < 4.5$ 1 ‘Loose’ $b$ -jet, $ \eta  < 2.5$		$\geq 1$ OSSF pair $ m_{\ell\ell} - m_Z  > 10 \text{ GeV}$ 3 jets, $ \eta  < 4.5$ 1 $b$ -jet, $ \eta  < 2.5$	

624 lepton). The estimation for the first type of background relies on MC simulations, while for the fake-lepton  
 625 backgrounds a special procedure is used, which will be described in detail in Section 6.

Table 5: Numbers of expected events in the 2j1b SR broken down by process. The left table shows the number of events after luminosity weighting, while the right table shows the raw number of simulated events available. The uncertainties include only statistical uncertainties. The  $t\bar{t}$  and  $Z + \text{jets}$  backgrounds are estimated using the technique explained in Section 6.

Process	Number of events	Process	Number of raw events
$t\bar{t}Z$	$62.7 \pm 1.4$	$t\bar{t}Z$	45 837
$t\bar{t}W$	$4.3 \pm 0.3$	$t\bar{t}W$	1513
$t\bar{t}H$	$2.1 \pm 0.1$	$t\bar{t}H$	4487
$tWZ$	$17.9 \pm 1.0$	$tWZ$	2992
$VV + \text{HF}$	$101.3 \pm 1.0$	$VV + \text{HF}$	39 010
$VV + \text{LF}$	$22.7 \pm 0.6$	$VV + \text{LF}$	5137
$Z + \text{jets}$	$10.2 \pm 0.0$	$Z + \text{jets}$	173 703
$t\bar{t}$	$23.7 \pm 0.1$	$t\bar{t}$	172 074
$tW$	$1.1 \pm 0.0$	$tW$	1969
$tZq$	$81.1 \pm 0.7$	$tZq$	307 562
Total expected	$327.0 \pm 2.3$	Total expected	754 284
Data	359		

## 626 5.4 Signal-region yields with pure Monte Carlo samples

627 As it will be explained in the following, a special treatment is used on the MC samples for  $Z + \text{jets}$  and  
 628  $t\bar{t}$  to increase the statistics of the samples. To show the impact of this, the event yields tables shown in  
 629 the previous section are here repeated using the out-of-the-box MC samples for  $Z + \text{jets}$  and  $t\bar{t}$ . The event  
 630 yields in the SRs after the full selection can be found in Tables 7 and 8.

Table 6: Numbers of expected events in the 3j1b SR broken down by process. The left table shows the number of events after luminosity weighting, while the right table shows the raw number of simulated events available. The uncertainties include only statistical uncertainties. The  $t\bar{t}$  and  $Z + \text{jets}$  backgrounds are estimated using the technique explained in Section 6.

Process	Number of events		Process	Number of raw events	
$t\bar{t}Z$	96.6	$\pm 1.9$	$t\bar{t}Z$	77 643	
$t\bar{t}W$	2.2	$\pm 0.2$	$t\bar{t}W$	765	
$t\bar{t}H$	2.4	$\pm 0.1$	$t\bar{t}H$	4442	
$tWZ$	20.2	$\pm 1.1$	$tWZ$	3601	
$VV + \text{HF}$	59.4	$\pm 0.6$	$VV + \text{HF}$	24 821	
$VV + \text{LF}$	12.3	$\pm 0.4$	$VV + \text{LF}$	3164	
$Z + \text{jets}$	4.8	$\pm 0.0$	$Z + \text{jets}$	77 167	
$t\bar{t}$	11.1	$\pm 0.0$	$t\bar{t}$	73 697	
$tW$	0.4	$\pm 0.0$	$tW$	736	
$tZq$	46.1	$\pm 0.5$	$tZq$	208 092	
Total expected	255.3	$\pm 2.4$	Total expected	474 128	
Data	259				

Table 7: Numbers of expected events in the 2j1b SR broken down by process. The left table shows the number of events after luminosity weighting, while the right table shows the raw number of simulated events available. **For the  $Z + \text{jets}$  and  $t\bar{t}$  samples, the BJR method is not applied, in order to show the available statistics in the MC samples.** The uncertainties include only statistical uncertainties.

Process	Number of events		Process	Number of raw events	
$t\bar{t}Z$	62.7	$\pm 1.4$	$t\bar{t}Z$	45 837	
$t\bar{t}W$	4.3	$\pm 0.3$	$t\bar{t}W$	1513	
$t\bar{t}H$	2.1	$\pm 0.1$	$t\bar{t}H$	4487	
$tWZ$	17.9	$\pm 1.0$	$tWZ$	2992	
$VV + \text{HF}$	101.3	$\pm 1.0$	$VV + \text{HF}$	39 010	
$VV + \text{LF}$	22.7	$\pm 0.6$	$VV + \text{LF}$	5137	
$Z + \text{jets}$	10.2	$\pm 1.4$	$Z + \text{jets}$	368	
$t\bar{t}$	23.7	$\pm 1.2$	$t\bar{t}$	485	
$tW$	1.1	$\pm 0.4$	$tW$	9	
$tZq$	81.1	$\pm 0.7$	$tZq$	307 562	
Total expected	327.0	$\pm 3.0$	Total expected	407 400	
Data	359				

Table 8: Numbers of expected events in the 3j1b SR broken down by process. The left table shows the number of events after luminosity weighting, while the right table shows the raw number of simulated events available. **For the  $Z + \text{jets}$  and  $t\bar{t}$  samples, the BJR method is not applied, in order to show the available statistics in the MC samples.** The uncertainties include only statistical uncertainties.

Process	Number of events		Process	Number of raw events
$t\bar{t}Z$	96.6	$\pm 1.9$	$t\bar{t}Z$	77 643
$t\bar{t}W$	2.2	$\pm 0.2$	$t\bar{t}W$	765
$t\bar{t}H$	2.4	$\pm 0.1$	$t\bar{t}H$	4442
$tWZ$	20.2	$\pm 1.1$	$tWZ$	3601
$VV + \text{HF}$	59.4	$\pm 0.6$	$VV + \text{HF}$	24 821
$VV + \text{LF}$	12.3	$\pm 0.4$	$VV + \text{LF}$	3164
$Z + \text{jets}$	4.8	$\pm 0.6$	$Z + \text{jets}$	180
$t\bar{t}$	11.1	$\pm 0.8$	$t\bar{t}$	217
$tW$	0.4	$\pm 0.2$	$tW$	3
$tZq$	46.1	$\pm 0.5$	$tZq$	208 092
Total expected	255.3	$\pm 2.6$	Total expected	322 928
Data	259			

## 631 5.5 Signal-region plots

632 Distributions of lepton, jet and event variables in the two signal regions are shown in Figs. 3 to 5 for the  
 633 2j1b SR and in Figs. 6 to 8 for the 3j1b SR.

634 More plots, showing  $p_T$ -ordered objects, are reported in Appendix C.

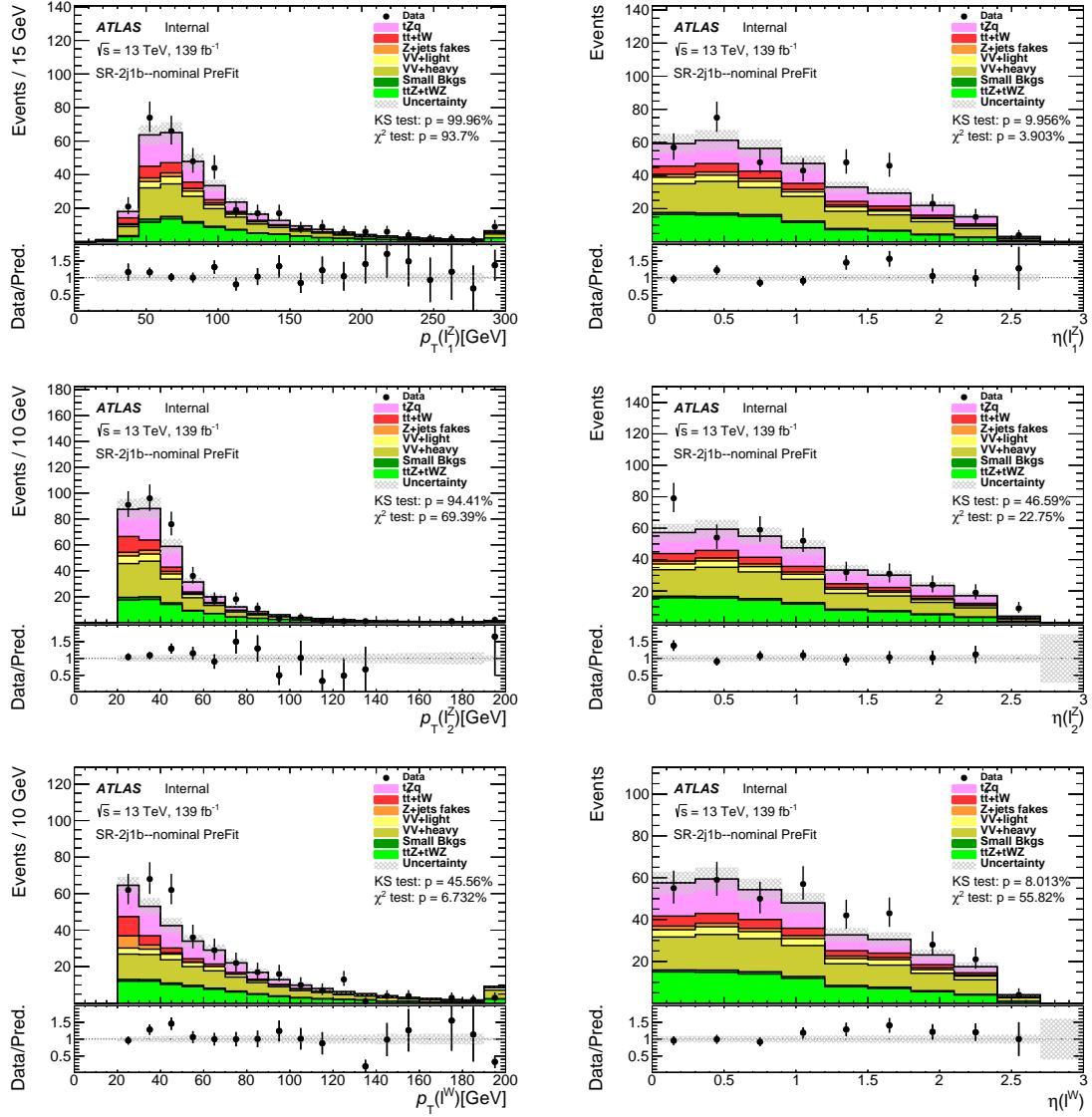


Figure 3: Comparison of data and MC predictions for reconstructed lepton-related quantities for events in the 2j1b SR. Both signal and backgrounds are normalised to the expected number of events before the fit. The uncertainty band includes statistical uncertainties for signal and backgrounds and background normalization uncertainties due to the prior assumptions and the modeling systematics, with the exception of  $t\bar{t}$  and  $Z + \text{jets}$ , where only the statistical uncertainties are shown. The  $t\bar{t}$  and  $Z + \text{jets}$  backgrounds are estimated using the technique explained in Section 6.

Not reviewed, for internal circulation only

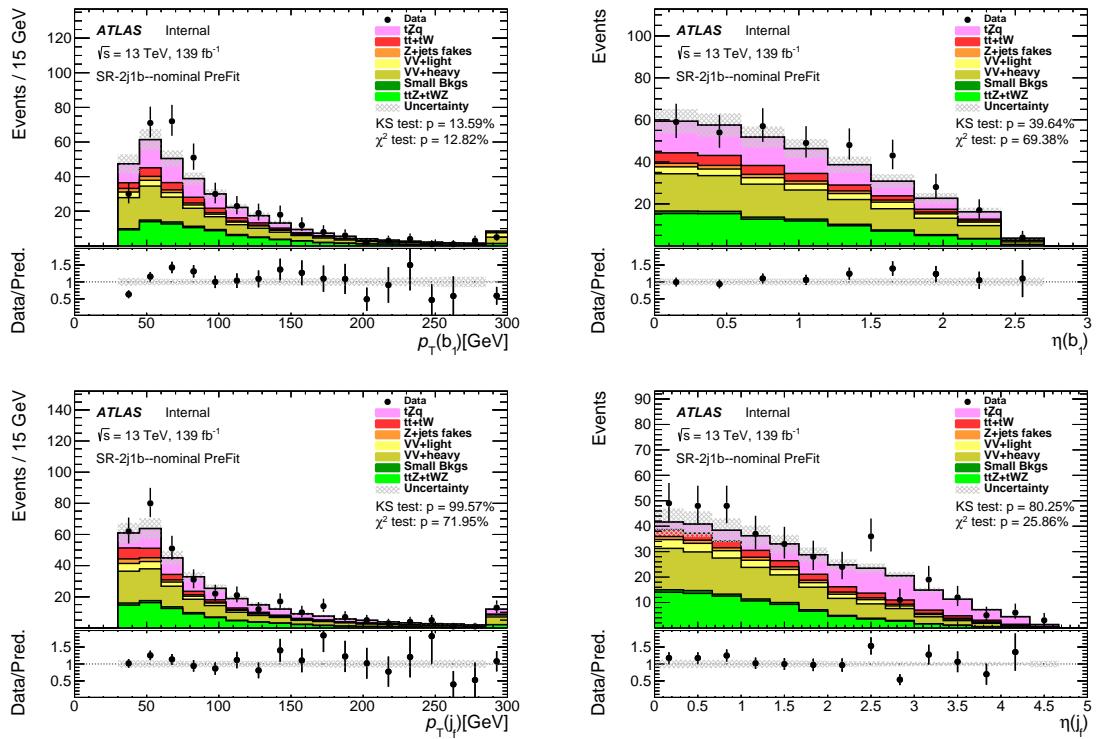


Figure 4: Comparison of data and MC predictions for reconstructed jet-related quantities for events in the 2j1b SR. Both signal and backgrounds are normalised to the expected number of events before the fit. The uncertainty band includes statistical uncertainties for signal and backgrounds and background normalization uncertainties due to the prior assumptions and the modeling systematics, with the exception of  $t\bar{t}$  and  $Z + \text{jets}$ , where only the statistical uncertainties are shown. The  $t\bar{t}$  and  $Z + \text{jets}$  backgrounds are estimated using the technique explained in Section 6.

Not reviewed, for internal circulation only

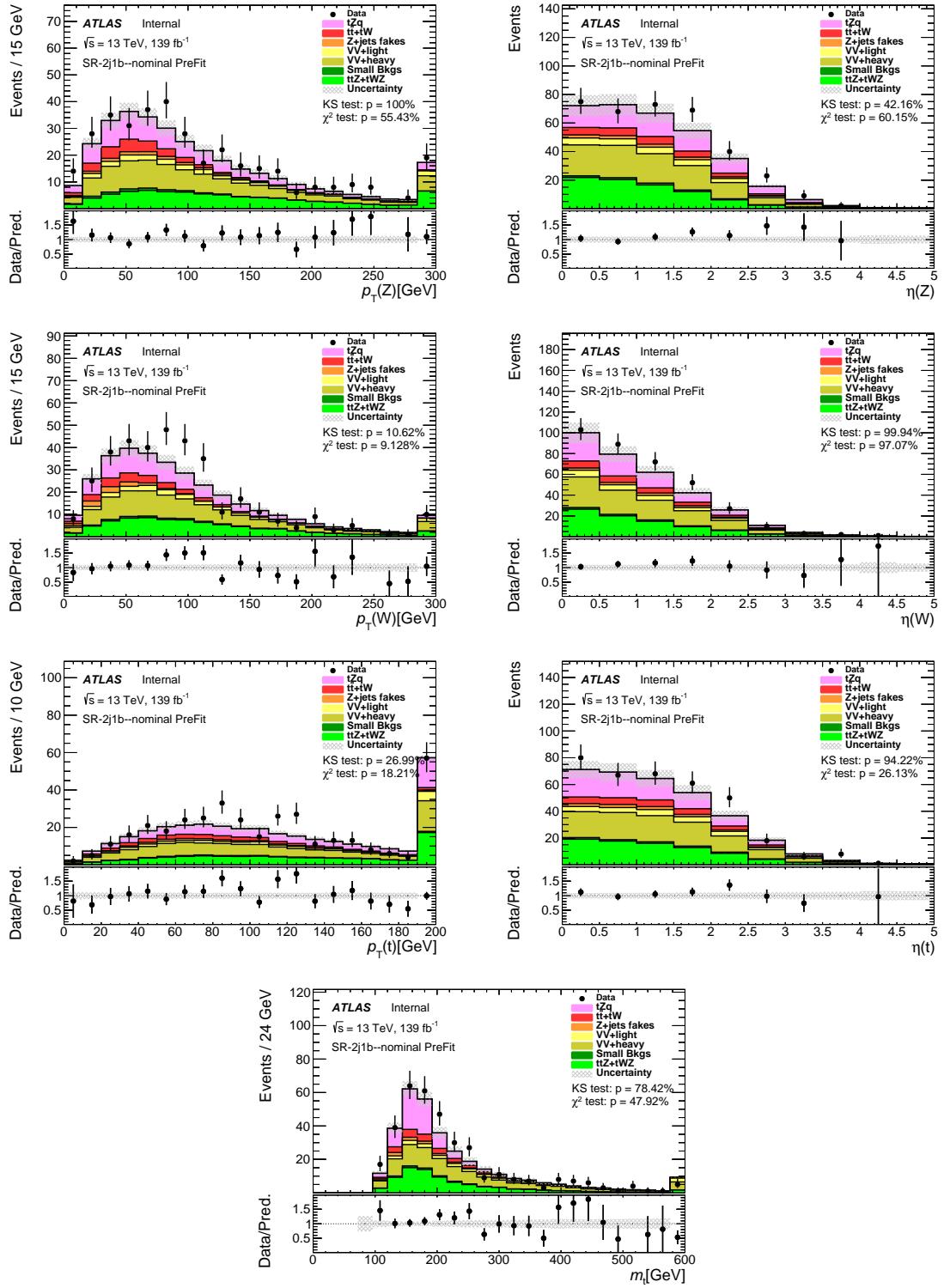


Figure 5: Comparison of data and MC predictions for reconstructed event-related quantities for events in the 2j1b SR. Both signal and backgrounds are normalised to the expected number of events before the fit. The uncertainty band includes statistical uncertainties for signal and backgrounds and background normalization uncertainties due to the prior assumptions and the modeling systematics, with the exception of  $t\bar{t}$  and  $Z + \text{jets}$ , where only the statistical uncertainties are shown. The  $t\bar{t}$  and  $Z + \text{jets}$  backgrounds are estimated using the technique explained in Section 6.

Not reviewed, for internal circulation only

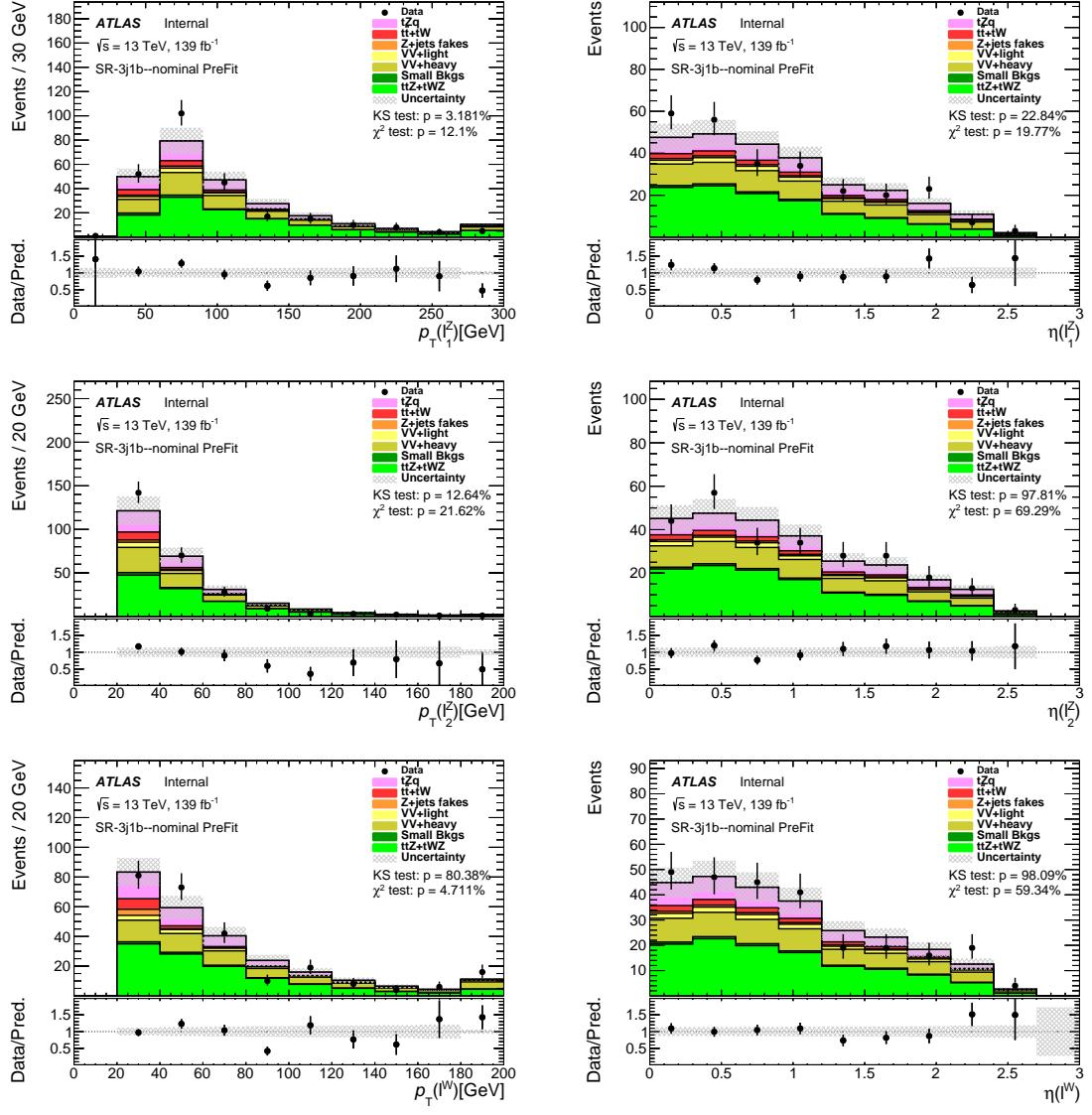


Figure 6: Comparison of data and MC predictions for reconstructed lepton-related quantities for events in the 3j1b SR. Both signal and backgrounds are normalised to the expected number of events before the fit. The uncertainty band includes statistical uncertainties for signal and backgrounds and background normalization uncertainties due to the prior assumptions and the modeling systematics, with the exception of  $t\bar{t}$  and  $Z + \text{jets}$ , where only the statistical uncertainties are shown. The  $t\bar{t}$  and  $Z + \text{jets}$  backgrounds are estimated using the technique explained in Section 6.

Not reviewed, for internal circulation only

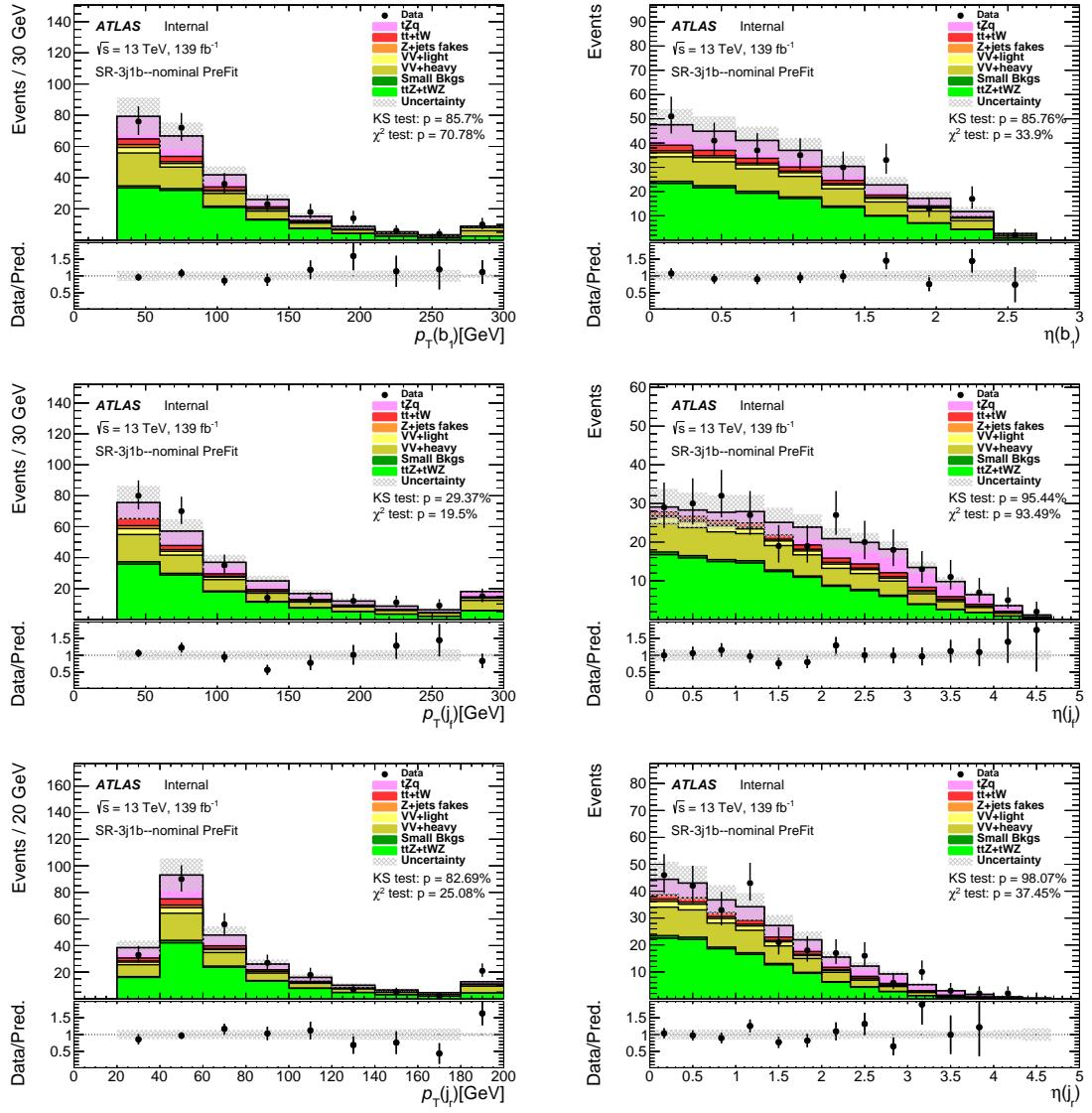


Figure 7: Comparison of data and MC predictions for reconstructed jet-related quantities for events in the 3j1b SR. Both signal and backgrounds are normalised to the expected number of events before the fit. The uncertainty band includes statistical uncertainties for signal and backgrounds and background normalization uncertainties due to the prior assumptions and the modeling systematics, with the exception of  $t\bar{t}$  and  $Z + \text{jets}$ , where only the statistical uncertainties are shown. The  $t\bar{t}$  and  $Z + \text{jets}$  backgrounds are estimated using the technique explained in Section 6.

Not reviewed, for internal circulation only

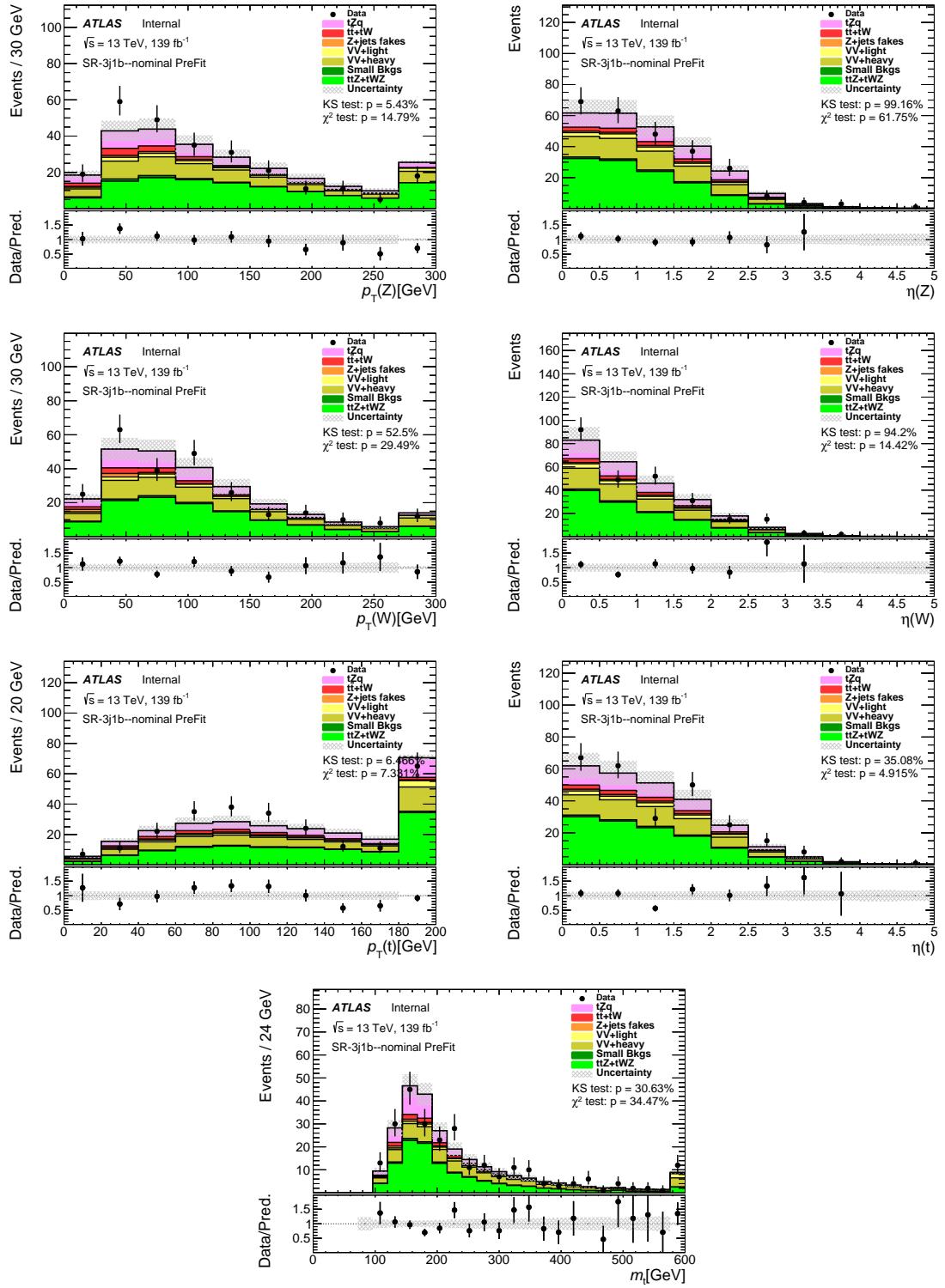


Figure 8: Comparison of data and MC predictions for reconstructed event-related quantities for events in the 3j1b SR. Both signal and backgrounds are normalised to the expected number of events before the fit. The uncertainty band includes statistical uncertainties for signal and backgrounds and background normalization uncertainties due to the prior assumptions and the modeling systematics, with the exception of  $t\bar{t}$  and  $Z + \text{jets}$ , where only the statistical uncertainties are shown. The  $t\bar{t}$  and  $Z + \text{jets}$  backgrounds are estimated using the technique explained in Section 6.

## 6 Non-prompt leptons

635 The  $tZq$  final state includes three ‘prompt’ (or ‘real’) leptons (electrons or muons), coming from a  $W$  or  $Z$  boson or a  $\tau$  lepton decay. However, it is possible that certain events pass the trilepton selection even if one of the leptons is not real. Such ‘non-prompt’ (or ‘fake’) leptons can originate from decays of bottom or charm hadrons, a jet that is misidentified as an electron, leptons from kaon or pion decays or even electrons coming from photon conversions.

641 The two sources of fake-lepton background for this analysis are  $t\bar{t}$  and  $Z + \text{jets}$  events. Truth level studies 642 investigating the origin of the non-prompt leptons were performed for both processes. These are included 643 in Section 6.1. The cuts applied for the signal region selection are designed to reduce that as much as 644 possible. These two contributions are estimated using a MC-based method called the  $b$ -jet replacement 645 (BJR) method. This is described in Section 6.2.

646 For  $Z + \text{jets}$  events, a purely data-driven technique (namely the fake-factor method) was also tested and 647 details about it are included in Appendix F. In the 2j1b SR, the two methods yield consistent results 648 within their associated uncertainties. Using the fake-factor method for the 3j1b region yields unreliable 649 results due to very low statistics, thus further motivating the need for an alternative background estimation 650 technique.

### 651 6.1 Non-prompt lepton origin

652 In order to better understand the non-prompt lepton background composition, the origin of the non-prompt 653 leptons in the trilepton final state is investigated. This is done using the `MCTruthClassifier` [56] and 654 is checked for the 2j1b and 3j1b SR, as well as the  $t\bar{t}$  validation and control regions, keeping the event 655 selection cuts described in the previous sections.

656 For  $t\bar{t}$  and  $Z + \text{jets}$ , the origins of the non-prompt or fake selected leptons can be seen in Figs. 9 to 12, 657 respectively. The plots indicate that, in the case that the fake lepton is a muon, the dominant source are 658 heavy-hadron decays. In the case, instead, that the fake lepton is an electron, the dominant source are 659 still heavy-hadron decays but with a non negligible fraction (ranging between 40 and 50 %) from photon 660 conversions. The fake background composition is similar between the different regions for each source 661 ( $Z + \text{jets}$  and  $t\bar{t}$ ) and for each lepton (electrons or muons) separately.

662 ‘Not defined’ leptons are leptons coming from internal conversions that are not correctly classified by the 663 `MCTruthClassifier` (this is a feature seen in `PYTHIA` 8 samples).

664 In Figs. 9 to 12, the fake lepton composition is shown also in the ‘LTT’ (loose-tight-tight) regions. These 665 regions have the same selection as the SRs, with the request that one of the leptons satisfies a loose selection. 666 The loose selection requirements are reported in Table 9. The LTT regions are dominated by fakes and are 667 used to further validate the fake estimation described in the following.

### 668 6.2 $b$ -jet replacement method

669 The  $b$ -jet replacement method was developed by the  $tZ$  production via FCNC analysis team [57]. This 670 method can be applied for processes in which the main source of non-prompt leptons is  $b$ -hadron decays. 671 In a nutshell, it uses dilepton events with an extra reconstructed  $b$ -jet compared to the standard SR selection

Not reviewed, for internal circulation only

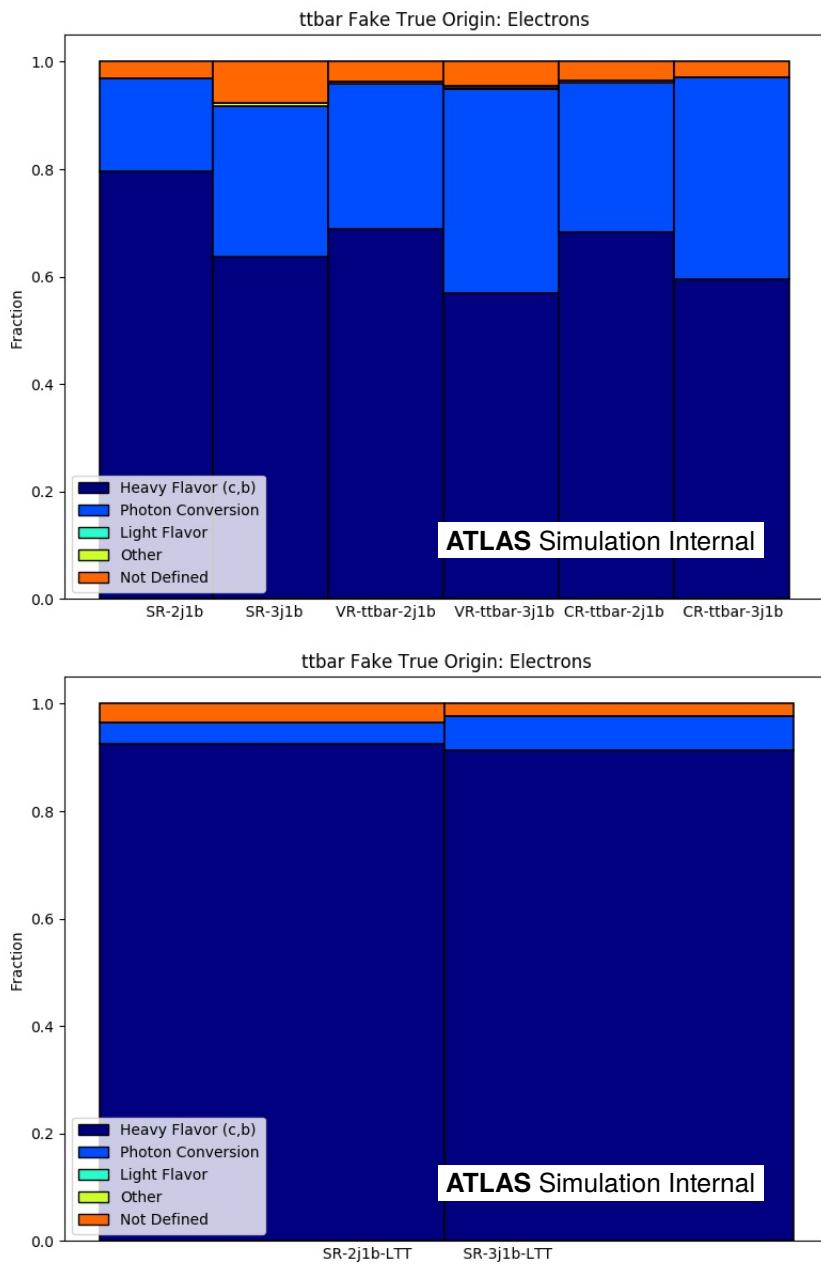


Figure 9: Origin of the fake electrons in the  $t\bar{t}$  sample. The fraction of the different sources is shown on the y-axis. The different signal, validation and control regions are shown on the x-axis. The top plot includes all  $t\bar{t}$  analysis regions and the bottom LTT regions (defined in the text).

Not reviewed, for internal circulation only

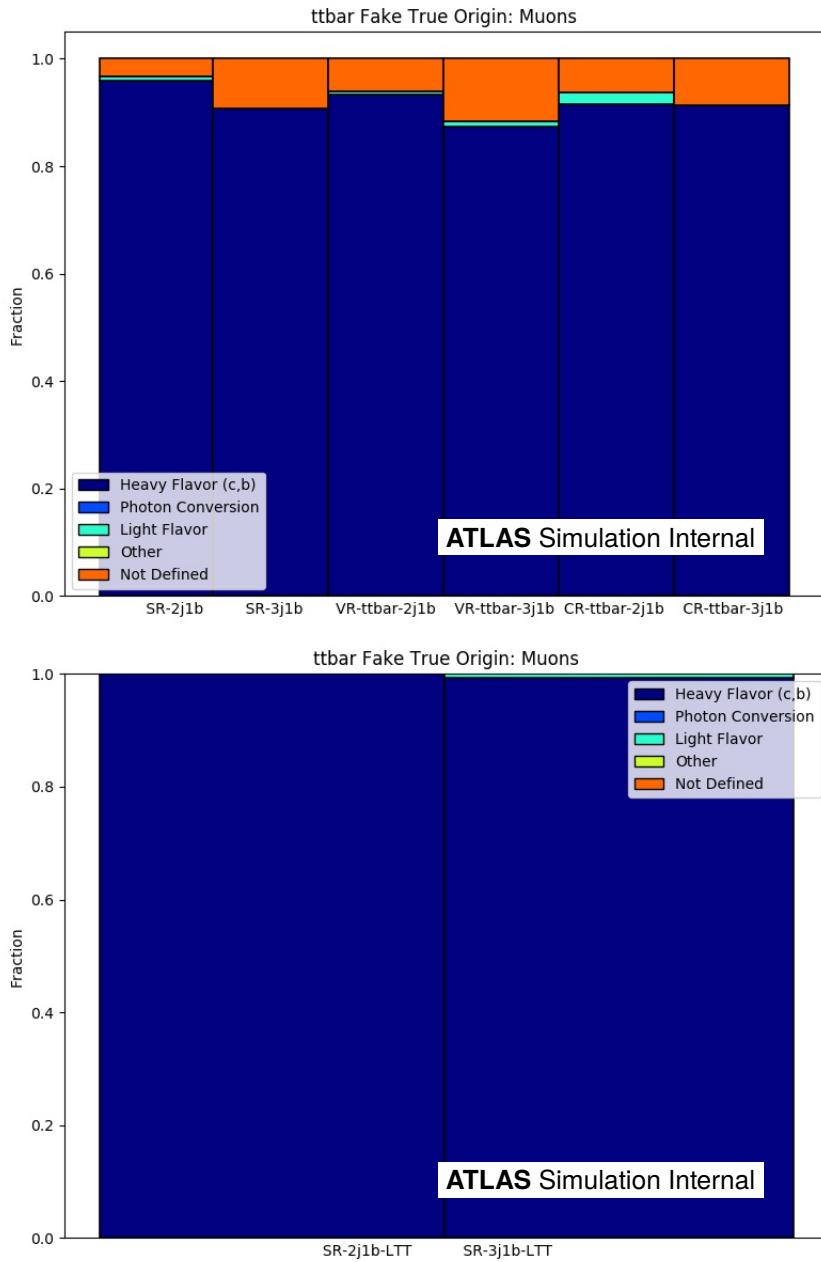


Figure 10: Origin of the fake muons in the  $t\bar{t}$  sample. The fraction of the different sources is shown on the y-axis. The different signal, validation and control regions are shown on the x-axis. The top plot includes all  $t\bar{t}$  analysis regions and the bottom LTT regions (defined in the text).

Not reviewed, for internal circulation only

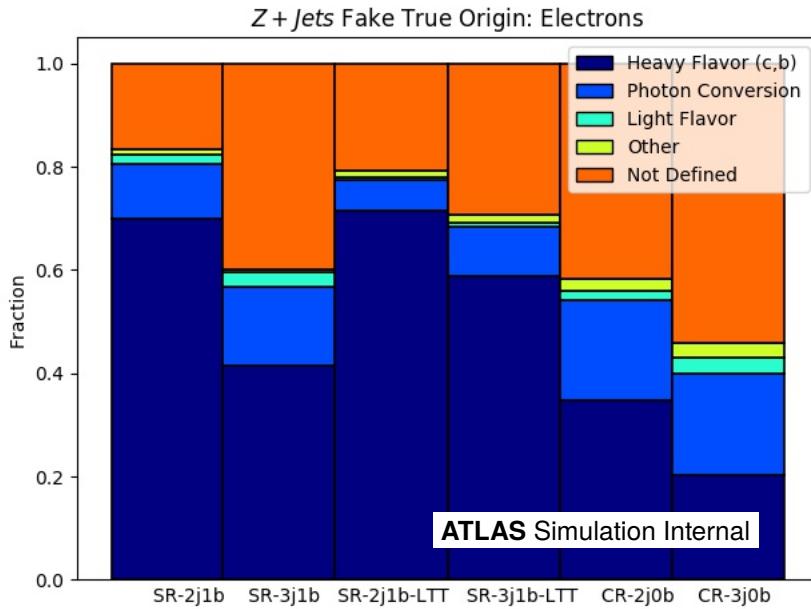


Figure 11: Origin of the fake electrons in the  $Z + \text{jets}$  sample. The fraction of the different sources is shown on the  $y$ -axis. The different signal, validation and control regions are shown on the  $x$ -axis.

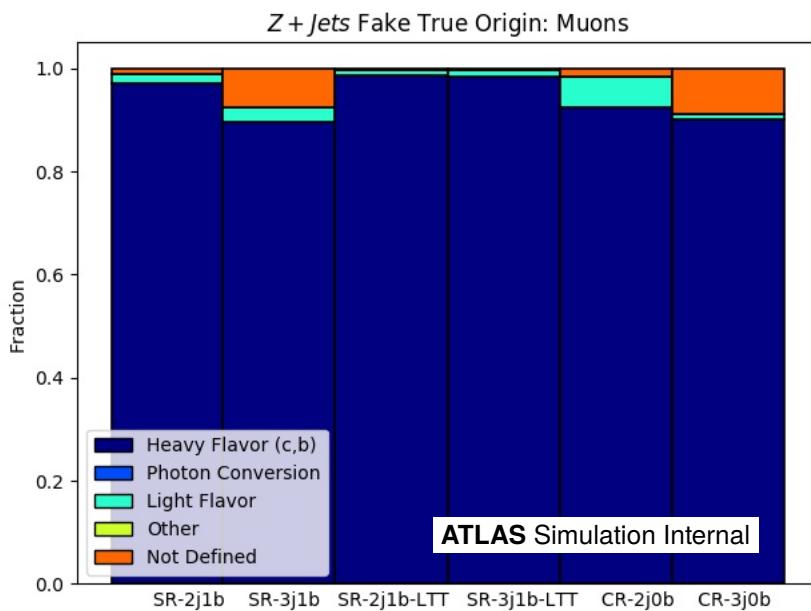


Figure 12: Origin of the fake muons in the  $Z + \text{jets}$  sample. The fraction of the different sources is shown on the  $y$ -axis. The different signal, validation and control regions are shown on the  $x$ -axis.

Table 9: Definition of electron and muon selection criteria for ‘loose’ and ‘tight’.

Loose		Tight	
	Definition	Isolation	Definition
Electrons	MediumLH	None	TightLH
Muons	Medium	None	Medium
			Gradient
			Gradient

672 and replaces one of the  $b$ -jets with an artificially generated non-prompt lepton. The advantage of this  
 673 method is that it greatly increases statistics in the non-prompt lepton samples.

674 The method is applied for both  $Z + \text{jets}$  and the  $t\bar{t}$  backgrounds. In order to estimate the backgrounds in the  
 675 2j1b and 3j1b SR, a preselection step is applied. Events are selected by requiring 2 instead of 1  $b$ -jet and 2  
 676 leptons instead of 3.

677 Of the two reconstructed  $b$ -jets in the event, one of them is selected randomly to be replaced by a lepton. A  
 678 branching ratio of 100 % is assumed for the  $b$  hadron decay to an electron or a muon, meaning that for all  
 679 the preselected events, the extra  $b$ -jet will be replaced by a generated non-prompt lepton. This serves the  
 680 purpose of increasing the statistics of the sample and does not affect the number of estimated non-prompt  
 681 lepton decays since the normalisation factor will be determined by the fit.

682 The properties of non-prompt leptons coming from  $b$ -hadron decays are studied in order to determine  
 683 properties of such leptons that can be used in the generation step. In order to do that, a  $t\bar{t}$  MC sample is  
 684 used. Using truth-level information, events in which a non-prompt lepton coming from a  $b$ -hadron decay is  
 685 present are selected.

686 The momentum of the identified lepton is then boosted in the rest-frame of its parent  $b$  quark<sup>3</sup>. Using  
 687 this transformed four-momentum, the energy of the lepton in the  $b$  rest-frame and its decay angle,  $\alpha$ , are  
 688 determined. The decay angle is defined as the angle between the lepton three-momentum in the  $b$  rest-frame  
 689 and the  $b$  three-momentum in the laboratory frame. The distribution obtained is shown in Fig. 13.

690 The generation step follows the preselection discussed above. The non-prompt leptons are generated in the  
 691  $b$ -hadron rest frame. In each selected dilepton event in the  $t\bar{t}$  and  $Z + \text{jets}$  samples, a lepton is generated for  
 692 a randomly chosen jet in the event, according to the presented energy vs.  $\alpha$  distribution. Positively and  
 693 negatively electrically charged electrons and muons are generated with equal probabilities. Because the  
 694 decay is isotropic in the  $b$  rest-frame, the azimuth of the lepton is generated randomly between 0 and  $2\pi$ .  
 695 Once the lepton is generated in the  $b$  rest-frame, this has to be boosted along the jet axis into the laboratory  
 696 frame. This is done using the  $b$ -jet four-momentum.

697 Once the lepton is generated, the  $b$ -jet is removed if it is within a angular distance of  $\Delta R = 0.4$  from the  
 698 lepton, similar to standard overlap removal. In over 95 % of events, this results in the  $b$ -jet being removed  
 699 from the event record. If this is not the case and both the  $b$ -jet and the generated lepton are kept, the event  
 700 will fail the standard jet multiplicity selection criteria.

<sup>3</sup> The method assumes, that the  $b$ -quark and the  $B$  meson have the same four-momentum.

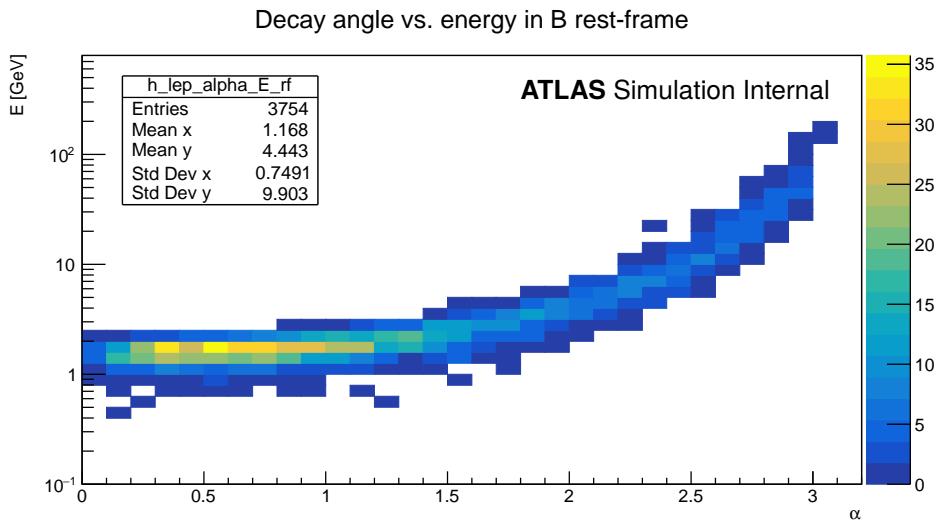


Figure 13: Distribution of the energy vs. the the decay angle of leptons coming from  $b$ -hadron decays, in the rest frame of the  $b$ -hadron.

### 701 **6.3 $b$ -jet replacement sample normalisation**

- 702 The BJR method gives the shape of the fake lepton kinematics, but not its normalisation.
- 703 The initial yield for the BJR samples is taken from nominal MC passing trilepton requirements. An  
704 uncertainty for each region is added to account for relative statistical fluctuations between regions of this  
705 initial estimate. A normalization uncertainty of 15 % for  $Z + \text{jets}$  and 7 % for  $t\bar{t}$  de-correlated for each  
706 region is added to the signal and relevant control regions.
- 707 The final number of non-prompt lepton background events is determined in the fits to the  $O_{\text{NN}}$  distributions.

### 708 **6.4 $b$ -jet replacement validation**

- 709 In the following, various validation studies of the  $b$ -jet replacement method are shown. More checks are  
710 available in Appendix E.

#### 711 **6.4.1 Shape comparison between $b$ -jet replacement and MC for the $O_{\text{NN}}$ discriminant**

- 712 A shape comparison of the neural network discriminant for  $Z + \text{jets}$  and  $t\bar{t}$  MC and the BJR samples is  
713 shown in Figs. 14 and 15 for the two signal regions. Reasonable agreement between is observed.
- 714 A shape comparison of the neural network discriminant for  $Z + \text{jets}$  and  $t\bar{t}$  BJR samples is shown in Fig. 16  
715 for the two signal regions.

Not reviewed, for internal circulation only

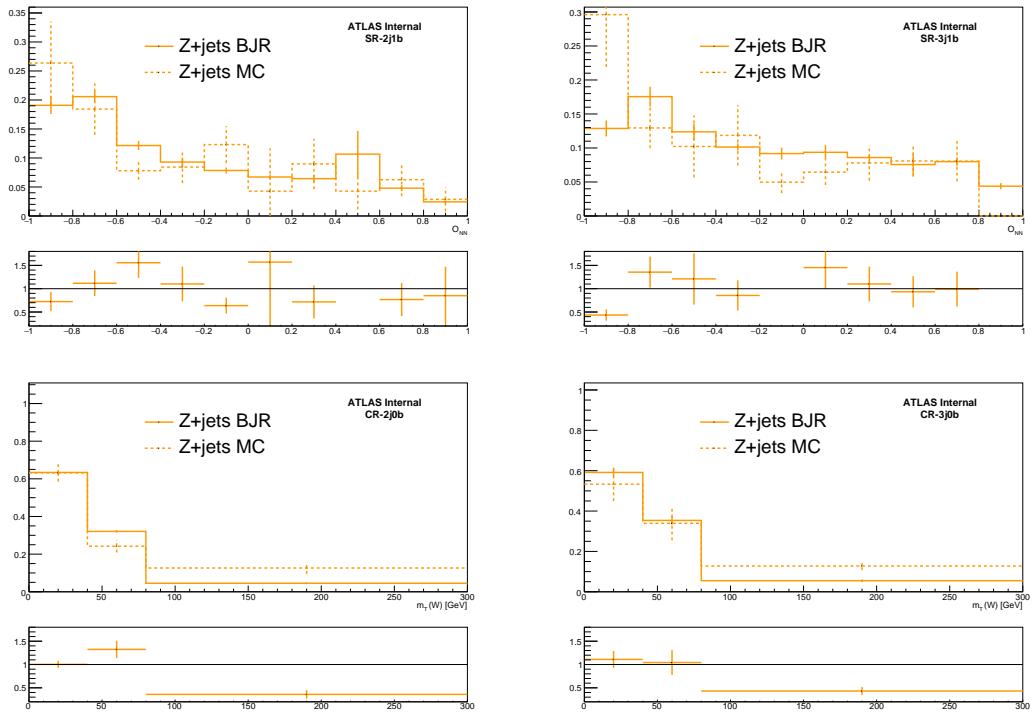


Figure 14: Top: comparison of  $O_{NN}$  shape for  $Z + \text{jets}$  MC and the corresponding BJR samples in the 2j1b SR (left) and 3j1b SR (right). Bottom: comparison of  $m_T(W)$  shape for  $Z + \text{jets}$  MC and the corresponding BJR samples in the 2j0b diboson CR (left) and 3j0b diboson CR (right).

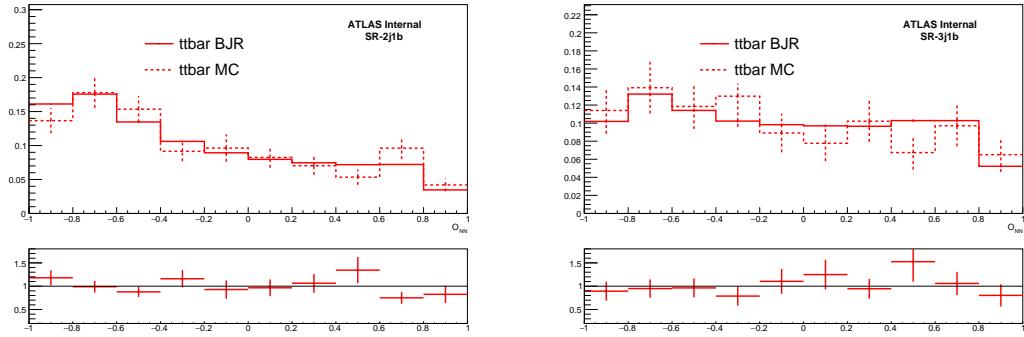


Figure 15: Comparison of  $O_{NN}$  shape for  $t\bar{t}$  MC and the corresponding BJR samples in the 2j1b SR (left) and 3j1b SR (right).

Not reviewed, for internal circulation only

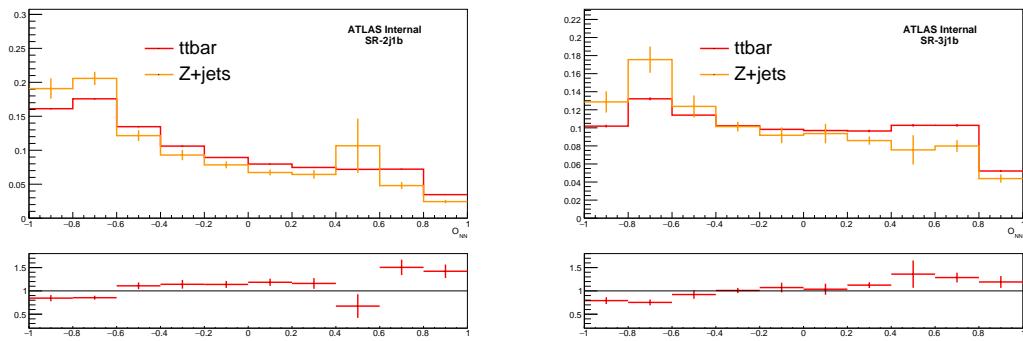


Figure 16: Comparison of  $O_{NN}$  shape for  $t\bar{t}$  and  $Z + \text{jets}$  BJR samples in the 2j1b SR (left) and 3j1b SR (right).

### 716 6.4.2 Shape comparison between various fake sources

717 In the following, plots comparing the shapes of different fake sources for  $t\bar{t}$  and  $Z + \text{jets}$  events in 2jXb and  
 718 3jXb regions are shown. All events in 2j regions, meaning in 2j1b SR and all 2j control regions, are used in  
 719 the same plot, and the same is done for 3j regions.

720 As shown in Fig. 17, different fake sources from  $t\bar{t}$  have comparable shapes, while differences are visible  
 721 for  $Z + \text{jets}$ . For this reason for  $Z + \text{jets}$  an additional uncertainty is added to cover the differences. This is  
 722 described in Section 9.1 (paragraph starting with “BJR shape uncertainty”).

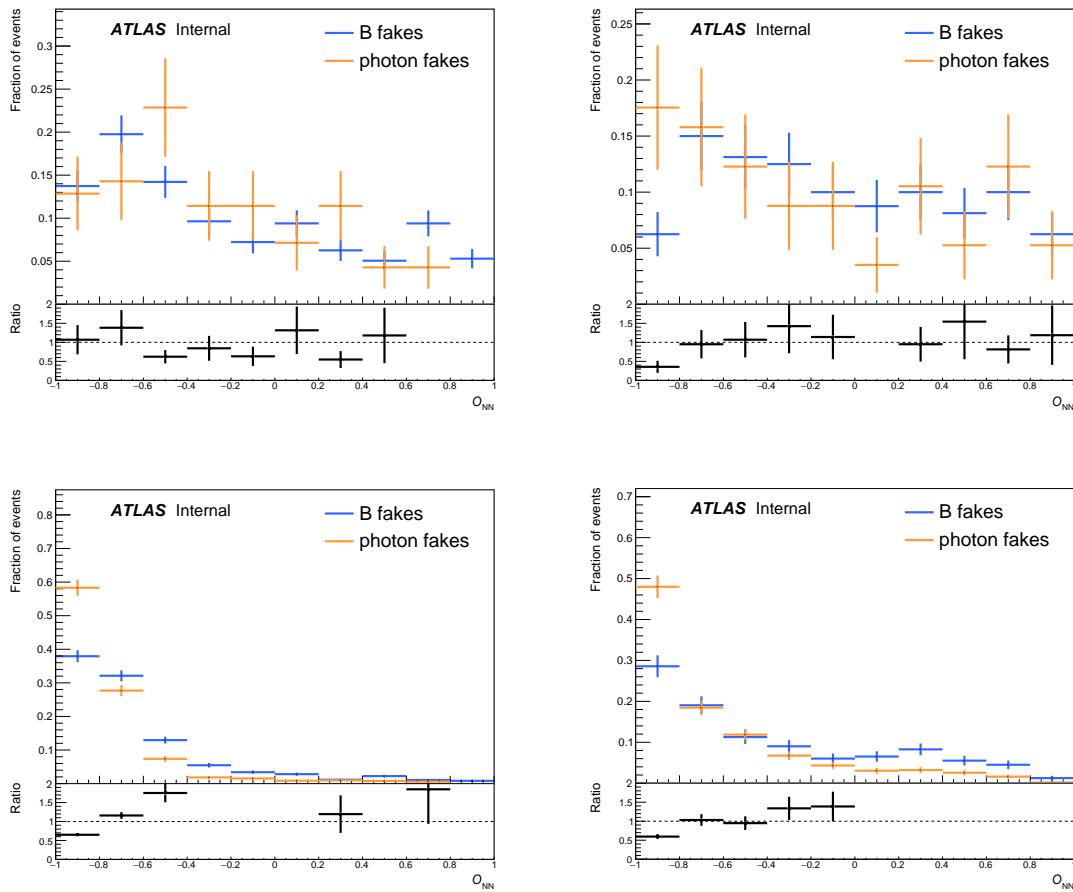


Figure 17: Comparison of shapes of different fake sources for  $t\bar{t}$  (top) and  $Z + \text{jets}$  (bottom) events in 2jXb and 3jXb regions with three tight leptons.

723 **6.4.3 Lepton flavour plots**

724 In the following, plots showing the number of electrons in the various regions with  $t\bar{t}$  and  $Z + \text{jets}$  fakes are  
 725 shown. The number of muons can be deduced from these plots too, as there are just three leptons (and  
 726 therefore the number of muons is just 3 minus the number of electrons).

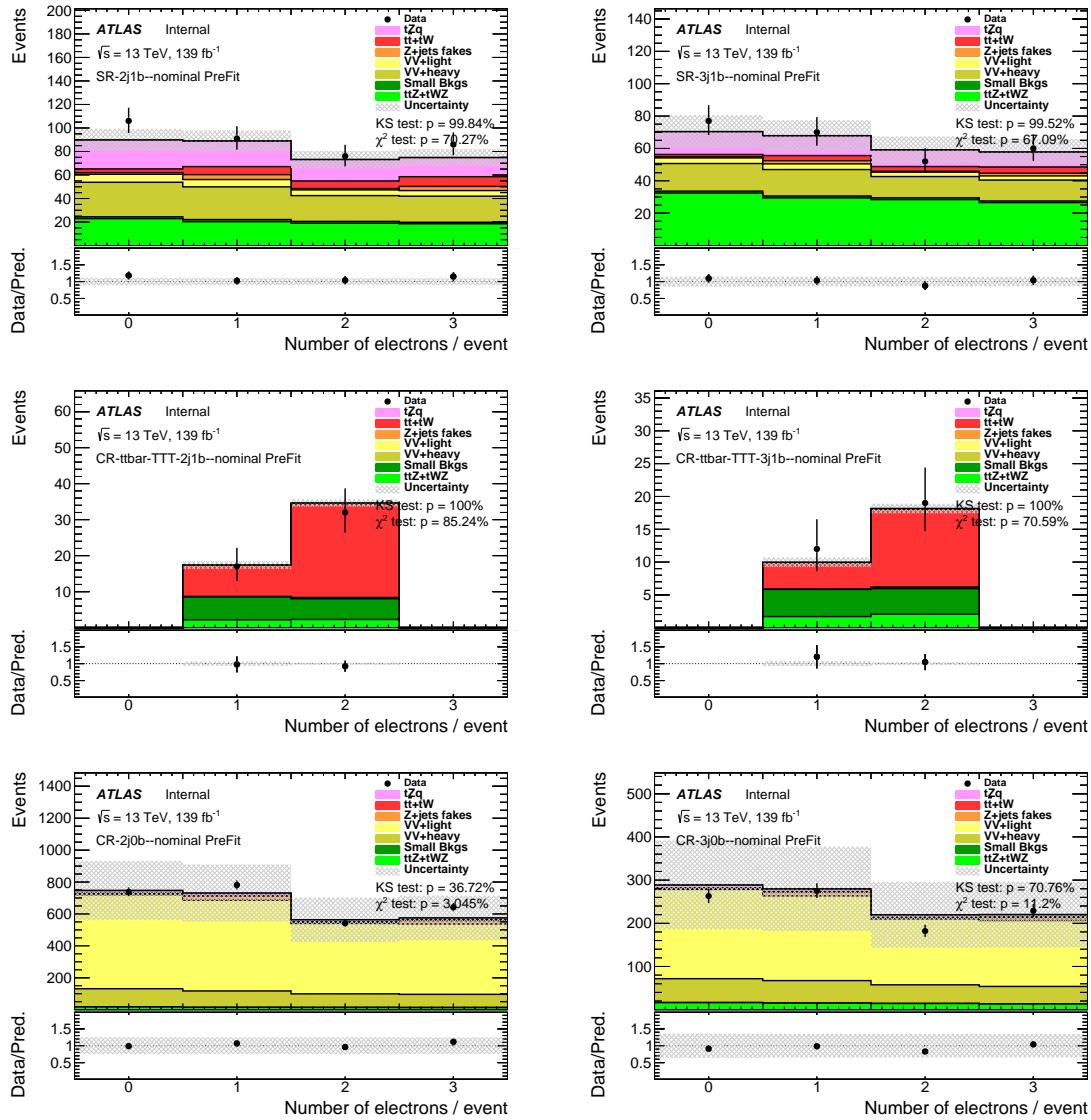


Figure 18: Number of electrons in the events in various regions. Both signal and backgrounds are normalised to the expected number of events before the fit. The uncertainty band includes statistical uncertainties for signal and backgrounds and background normalization uncertainties due to the prior assumptions and the modeling systematics, with the exception of  $t\bar{t}$  and  $Z + \text{jets}$ , where only the statistical uncertainties are shown.

## 727 6.5 Contribution of signal with a fake lepton

728 The signal sample used in the analysis was produced with a 3-lepton filter. However the  $tZq$  process with  
729 the Z-boson decaying leptonically and the  $t$ -quark decaying hadronically could also enter the signal regions  
730 if a jet fakes a lepton. This type of contribution has been evaluated as follows.

731 In the case where the fake lepton comes from the hadronic decay of the  $W$ -boson from the  $t$ -quark, the  
732 expected number of events is: Luminosity  $\times$  cross-section  $\times W \rightarrow qq$  BR  $\times 2 \times$  trilepton selection  
733 efficiency  $\times$  fake probability  $= 139 \times 101.7 \times 67\% \times 2 \times 1.8\% \times 0.1\% = 0.34$  events.

734 In the case where the fake lepton comes from the  $b$ -quark, we need to know the probability that neither  
735 the lepton coming from the  $b$  decay chain nor the reconstructed  $b$ -jet are removed by overlap removal,  
736 otherwise the event would not pass the selection (because either the  $b$ -jet or the third lepton would be  
737 missing). To do this, we have applied to our tri-lepton signal, a four-lepton selection (meaning that the  
738 fourth lepton comes from the  $b$ ) and we have seen how many events survive the selection w.r.t. a trilepton  
739 selection. In this case the expected number of events is: Luminosity  $\times$  cross-section  $\times W \rightarrow qq$  BR  $\times$   
740 dilepton selection efficiency  $\times b/\text{lepton}$  overlap survival probability  $= 139 \times 101.7 \times 67\% \times 14\% \times 0.02\%$   
741  $= 0.27$  events.

742 This last computation was also done extracting the  $b/\text{lepton}$  overlap removal survival probability from  $t\bar{t}$   
743 dilepton events and it yields to the same conclusion.

744 Overall, both contributions are negligible.

## 745 7 Background modelling

### 746 7.1 Background sources

747 A variety of background sources are considered. These include SM processes with similar final states as  
 748  $tZq$  (such as diboson or the associated production of  $t\bar{t}$  with a  $W$ ,  $Z$  or  $H$  boson), as well as events in which  
 749 at least one of the leptons in the final state is ‘fake’ (either a jet misidentified as a lepton or a non-prompt  
 750 lepton). The estimation for the first type of background relies on MC simulations, while for the fake-lepton  
 751 backgrounds a special procedure is used, which has been described in detail in Section 6.

752 After applying the event selection cuts, diboson,  $t\bar{t}Z$  and  $t\bar{t}$  production constitute the major backgrounds, as  
 753 shown in Tables 5 and 6. In the 2j1b SR, diboson events are the dominant background source, while in the  
 754 3j1b SR  $t\bar{t}Z$  and diboson events are the dominant background source.

### 755 7.2 Validation and control regions

756 In order to study the modelling of the main background samples, several validation and control regions are  
 757 defined as described in Table 4.

758 Validation regions (VRs) are used to check the modelling of background sources. The data and MC  
 759 agreement is shown both using the normalisation of the background before the fit (in ?? and Appendix C)  
 760 and after the fit (in Appendix G.4.1).

761 Control regions (CRs) are used in the fit to extract the normalisation of several background sources.

#### 762 7.2.1 Diboson validation and control regions

763 In order to keep the selection as close to the SR as possible, the validation and control diboson regions are  
 764 selected with the same cuts as the SR definitions, but with the following differences:

765 **diboson Xj1Lb VRs** (with X being either 2 or 3) accepting events that have exactly one jet passing an  
 766 85% efficient  $b$ -tagging working point requirement but not passing a 70% efficient working point.  
 767 This is referred to as a ‘Loose’  $b$ -jet in Table 4. Note that these events are a (small) subset of the  
 768 Xj0b CR regions, but are enhanced in  $VV + HF$  events.

769 **diboson Xj0b CRs** (with X being either 2 or 3) rejecting events that have a  $b$ -jet passing the 70% efficient  
 770  $b$ -tagging working point requirement.

771 These regions are orthogonal to the signal region.

772 The SRs and the diboson VRs and CRs have different heavy- and light-flavour compositions, as shown in  
 773 Tables 5, 6, 10 and 11. The  $VV + LF$  and  $VV + HF$  components are treated separately in the fit.

### 7.2.2 $t\bar{t}V$ and $t\bar{t}$ validation and control regions

774 The  $t\bar{t}V$  and  $t\bar{t}$  control and validation regions are defined such that they enrich the contribution of  $t\bar{t}V$  and  
775  $t\bar{t}$  events. The regions are defined as follows:

776  **$t\bar{t}V + t\bar{t}$  Xj1b VRs** (with X being either 2 or 3) all the cuts are kept identical to the signal regions'  
777 definitions, with the only exception being the cut on the invariant mass of the two leptons. The  
778 events required to be outside of the  $Z$  mass window ( $m_{\ell\ell} < 81$  GeV or  $m_{\ell\ell} > 101$  GeV).

779  **$t\bar{t}$  Xj1b CRs** (with X being either 2 or 3) an opposite-sign different-flavour (OSDF) lepton pair is requested,  
780 instead of an opposite-sign same-flavour (OSSF) lepton pair, and an explicit veto for an OSSF pair is  
781 included. This veto implicitly removes the cut on the  $Z$  mass window.

782  **$t\bar{t}Z$  Xj2b CRs** (with X being either 3 or 4) all the cuts are kept identical to the signal regions' definitions,  
783 with the only exception being the request of the presence of an additional  $b$ -jet in the event.

785 **7.3 Modeling of diboson**786 **7.3.1 Validation-region yields**

787 The number of observed data events in the diboson validation regions and expected numbers of signal  
 788 and background events for the luminosity of  $139 \text{ fb}^{-1}$  are listed in Tables 10 and 11 for the diboson Xj1Lb  
 789 VRs.

Table 10: Number of observed and expected events in the diboson 2j1Lb VR. The left table shows the number of events after luminosity weighting, while the right table shows the raw number of events available. The uncertainties include only statistical uncertainties.

Process	Number of events		Process	Number of raw events
$t\bar{t}Z$	16.2	$\pm 0.7$	$t\bar{t}Z$	11 395
$t\bar{t}W$	1.2	$\pm 0.2$	$t\bar{t}W$	360
$t\bar{t}H$	0.5	$\pm 0.0$	$t\bar{t}H$	1068
$tWZ$	5.3	$\pm 0.5$	$tWZ$	741
$VV + \text{HF}$	87.0	$\pm 0.9$	$VV + \text{HF}$	28 586
$VV + \text{LF}$	172.7	$\pm 1.5$	$VV + \text{LF}$	43 227
$Z + \text{jets}$	7.5	$\pm 0.1$	$Z + \text{jets}$	33 306
$t\bar{t}$	2.8	$\pm 0.1$	$t\bar{t}$	3648
$tW$	0.3	$\pm 0.0$	$tW$	58
$tZq$	13.5	$\pm 0.3$	$tZq$	50 224
Total expected	307.0	$\pm 2.0$	Total expected	172 613
Data	275			

Table 11: Number of observed and expected events in the diboson 3j1Lb VR. The left table shows the number of events after luminosity weighting, while the right table shows the raw number of events available. The uncertainties include only statistical uncertainties.

Process	Number of events		Process	Number of raw events	
$t\bar{t}Z$	$33.1 \pm$	1.1	$t\bar{t}Z$	25 897	
$t\bar{t}W$	$0.7 \pm$	0.1	$t\bar{t}W$	249	
$t\bar{t}H$	$0.8 \pm$	0.1	$t\bar{t}H$	1513	
$tWZ$	$6.4 \pm$	0.6	$tWZ$	1029	
$VV + HF$	$53.6 \pm$	0.6	$VV + HF$	18 904	
$VV + LF$	$88.4 \pm$	0.9	$VV + LF$	25 448	
$Z + \text{jets}$	$2.5 \pm$	0.0	$Z + \text{jets}$	25 780	
$t\bar{t}$	$2.6 \pm$	0.1	$t\bar{t}$	2398	
$tW$	$0.2 \pm$	0.0	$tW$	24	
$tZq$	$11.1 \pm$	0.3	$tZq$	46 506	
Total expected	$199.3 \pm$	1.7	Total expected	147 748	
Data	172				

Not reviewed, for internal circulation only

<sup>790</sup> **7.3.2 Validation-region yields with pure Monte Carlo samples**

<sup>791</sup> As done in Section 5.4, event yields tables not using the BJR method are shown in the following. Event  
<sup>792</sup> yields are shown in Tables 12 and 13 for the diboson Xj1Lb VRs.

Table 12: Number of observed and expected events in the diboson 2j1Lb VR. The left table shows the number of events after luminosity weighting, while the right table shows the raw number of events available. **For the  $Z + \text{jets}$  and  $t\bar{t}$  samples, the BJR method is not applied, in order to show the available statistics in the MC samples.** The uncertainties include only statistical uncertainties.

Process	Number of events		Process	Number of raw events	
$t\bar{t}Z$	$16.2 \pm$	0.7	$t\bar{t}Z$	11 395	
$t\bar{t}W$	$1.2 \pm$	0.2	$t\bar{t}W$	360	
$t\bar{t}H$	$0.5 \pm$	0.0	$t\bar{t}H$	1068	
$tWZ$	$5.3 \pm$	0.5	$tWZ$	741	
$VV + \text{HF}$	$87.0 \pm$	0.9	$VV + \text{HF}$	28 586	
$VV + \text{LF}$	$172.7 \pm$	1.5	$VV + \text{LF}$	43 227	
$Z + \text{jets}$	$7.5 \pm$	1.2	$Z + \text{jets}$	186	
$t\bar{t}$	$2.8 \pm$	0.4	$t\bar{t}$	56	
$tW$	$0.3 \pm$	0.2	$tW$	2	
$tZq$	$0.0 \pm$	0.0	$tZq$	0	
Total expected	$293.5 \pm$	2.4	Total expected	85 621	
Data	275				

Table 13: Number of observed and expected events in the diboson 3j1Lb VR. The left table shows the number of events after luminosity weighting, while the right table shows the raw number of events available. **For the  $Z + \text{jets}$  and  $t\bar{t}$  samples, the BJR method is not applied, in order to show the available statistics in the MC samples.** The uncertainties include only statistical uncertainties.

Process	Number of events		Process	Number of raw events	
$t\bar{t}Z$	$33.1 \pm$	1.1	$t\bar{t}Z$	25 897	
$t\bar{t}W$	$0.7 \pm$	0.1	$t\bar{t}W$	249	
$t\bar{t}H$	$0.8 \pm$	0.1	$t\bar{t}H$	1513	
$tWZ$	$6.4 \pm$	0.6	$tWZ$	1029	
$VV + \text{HF}$	$53.6 \pm$	0.6	$VV + \text{HF}$	18 904	
$VV + \text{LF}$	$88.4 \pm$	0.9	$VV + \text{LF}$	25 448	
$Z + \text{jets}$	$2.5 \pm$	0.5	$Z + \text{jets}$	118	
$t\bar{t}$	$2.6 \pm$	0.4	$t\bar{t}$	50	
$tW$	$0.2 \pm$	0.2	$tW$	1	
$tZq$	$0.0 \pm$	0.0	$tZq$	0	
Total expected	$188.2 \pm$	1.8	Total expected	73 209	
Data	172				

793 **7.3.3 Validation-region plots**

794 Distributions of lepton, jet and event variables in the diboson VRs are shown in Figs. 19 to 21 for the 2j1Lb  
 795 VR and in Figs. 22 to 24 for the 3j1Lb VR.

Not reviewed, for internal circulation only

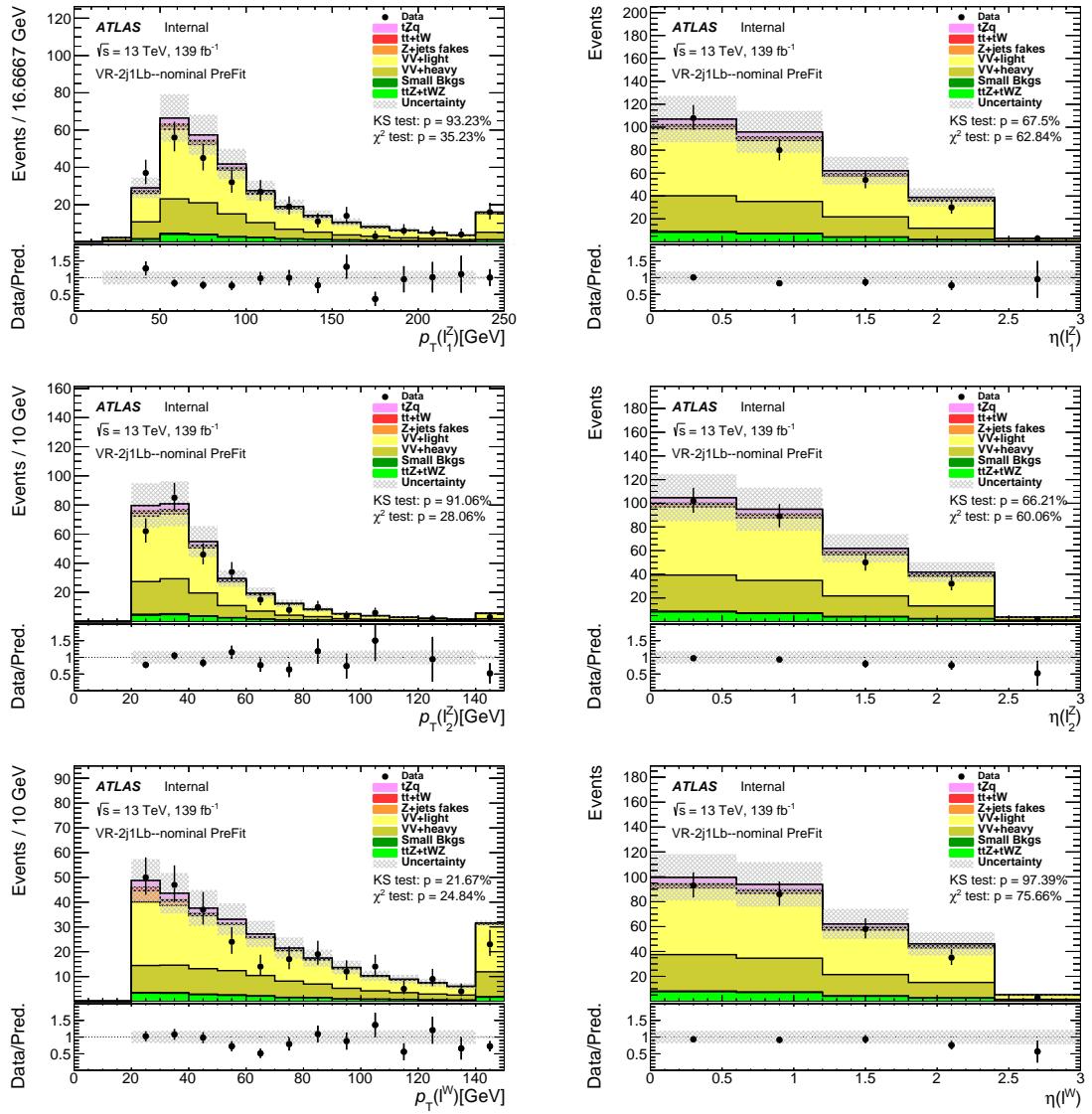


Figure 19: Comparison of data and MC predictions for reconstructed lepton-related quantities for events in the diboson 2j1Lb VR. Both signal and backgrounds are normalised to the expected number of events before the fit. The uncertainty band includes statistical uncertainties for signal and backgrounds and background normalization uncertainties due to the prior assumptions and the modeling systematics, with the exception of  $t\bar{t}$  and  $Z + \text{jets}$ , where only the statistical uncertainties are shown.

Not reviewed, for internal circulation only

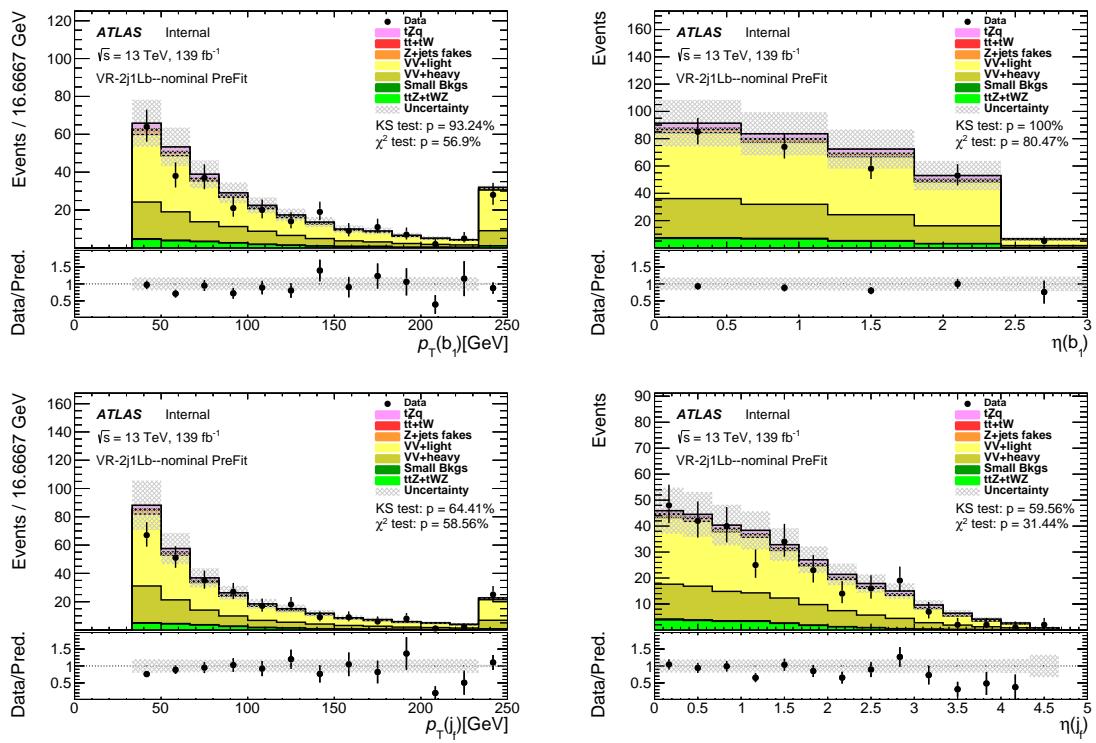


Figure 20: Comparison of data and MC predictions for reconstructed jet-related quantities for events in the diboson 2j1Lb VR. Both signal and backgrounds are normalised to the expected number of events before the fit. The uncertainty band includes statistical uncertainties for signal and backgrounds and background normalization uncertainties due to the prior assumptions and the modeling systematics, with the exception of  $t\bar{t}$  and  $Z + \text{jets}$ , where only the statistical uncertainties are shown.

Not reviewed, for internal circulation only

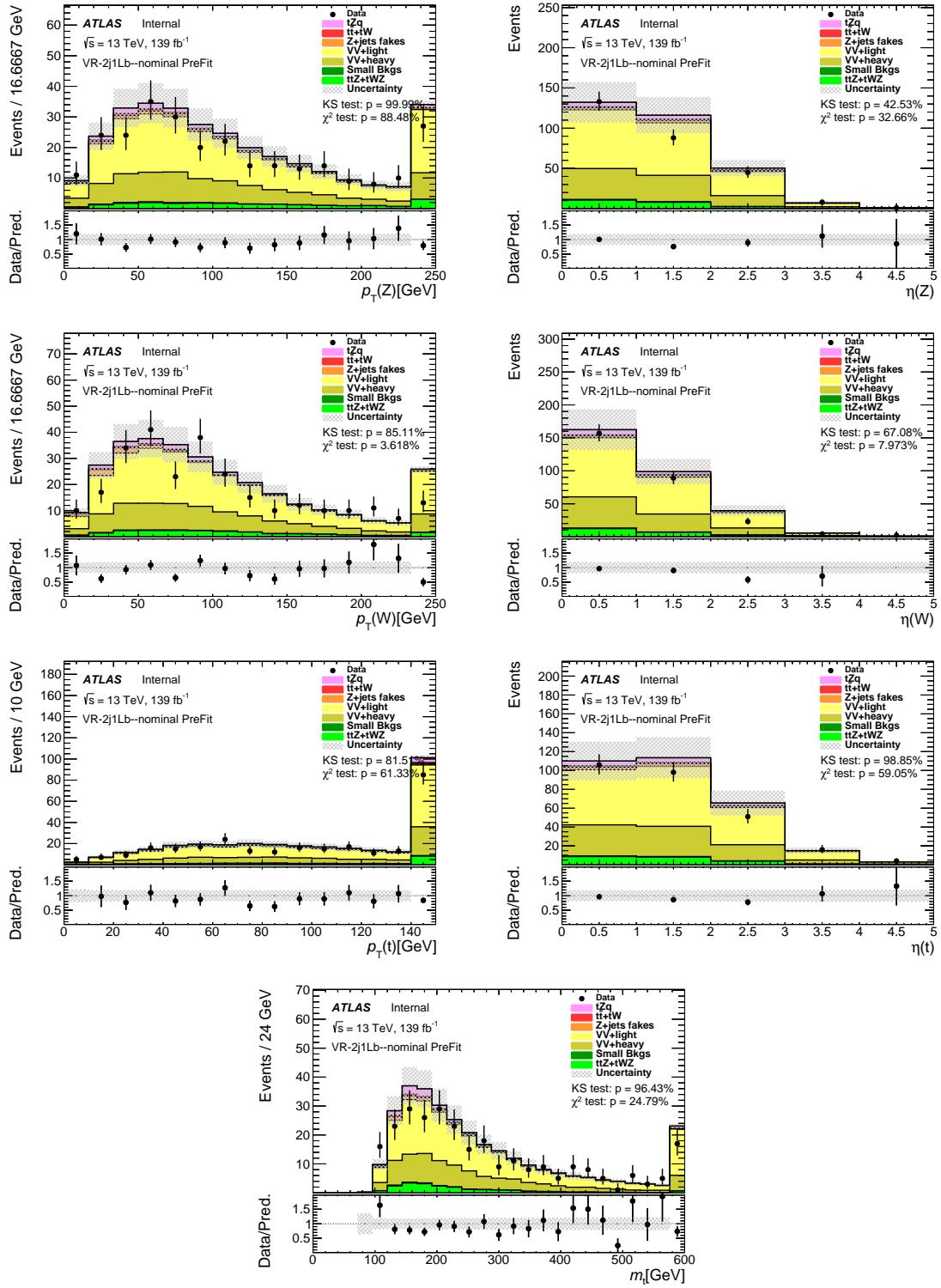


Figure 21: Comparison of data and MC predictions for reconstructed event-related quantities for events in the diboson 2j1Lb VR. Both signal and backgrounds are normalised to the expected number of events before the fit. The uncertainty band includes statistical uncertainties for signal and backgrounds and background normalization uncertainties due to the prior assumptions and the modeling systematics, with the exception of  $t\bar{t}$  and  $Z + \text{jets}$ , where only the statistical uncertainties are shown.

Not reviewed, for internal circulation only

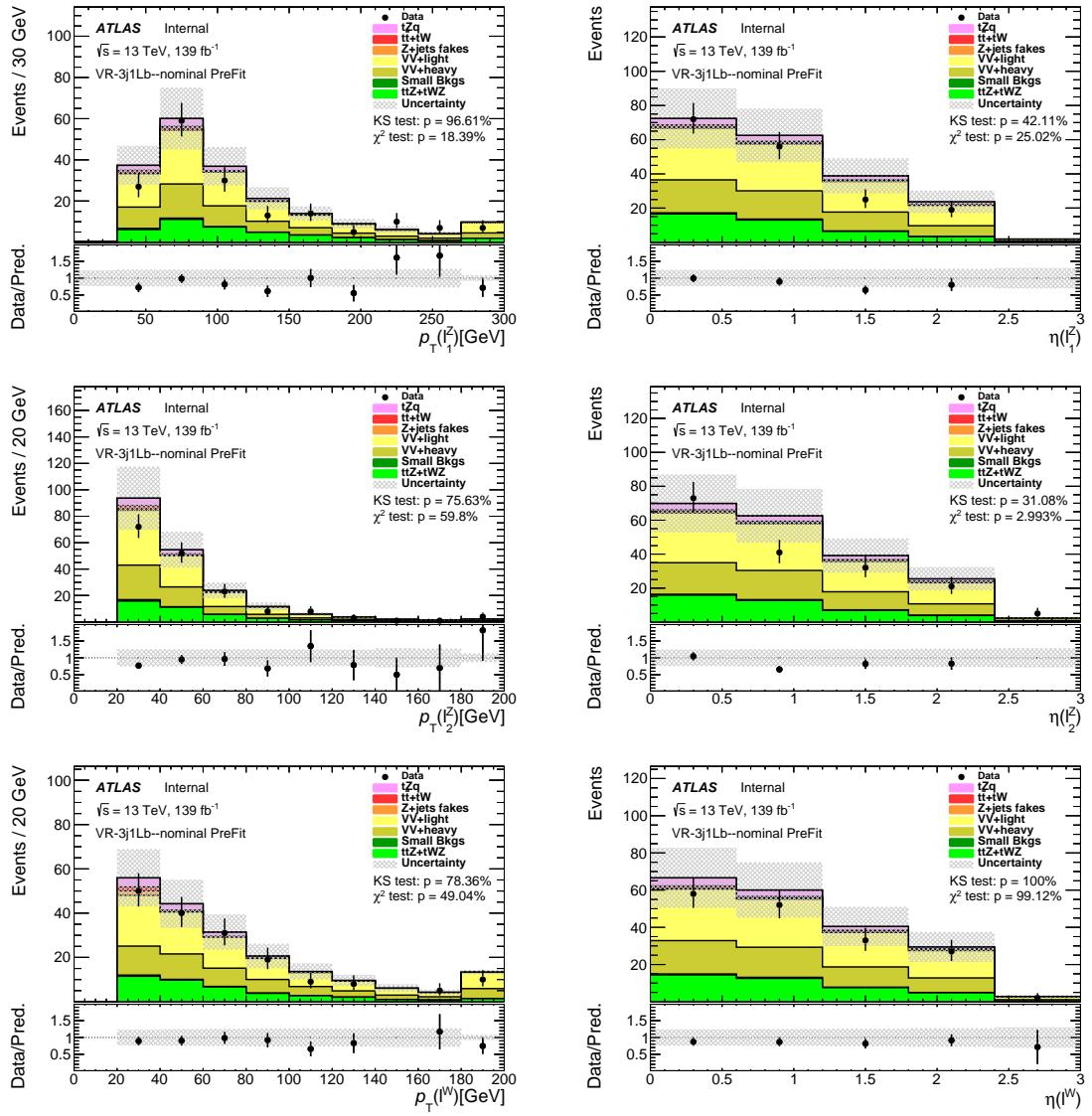


Figure 22: Comparison of data and MC predictions for reconstructed lepton-related quantities for events in the diboson 3j1Lb VR. Both signal and backgrounds are normalised to the expected number of events before the fit. The uncertainty band includes statistical uncertainties for signal and backgrounds and background normalization uncertainties due to the prior assumptions and the modeling systematics, with the exception of  $t\bar{t}$  and  $Z + \text{jets}$ , where only the statistical uncertainties are shown.

Not reviewed, for internal circulation only

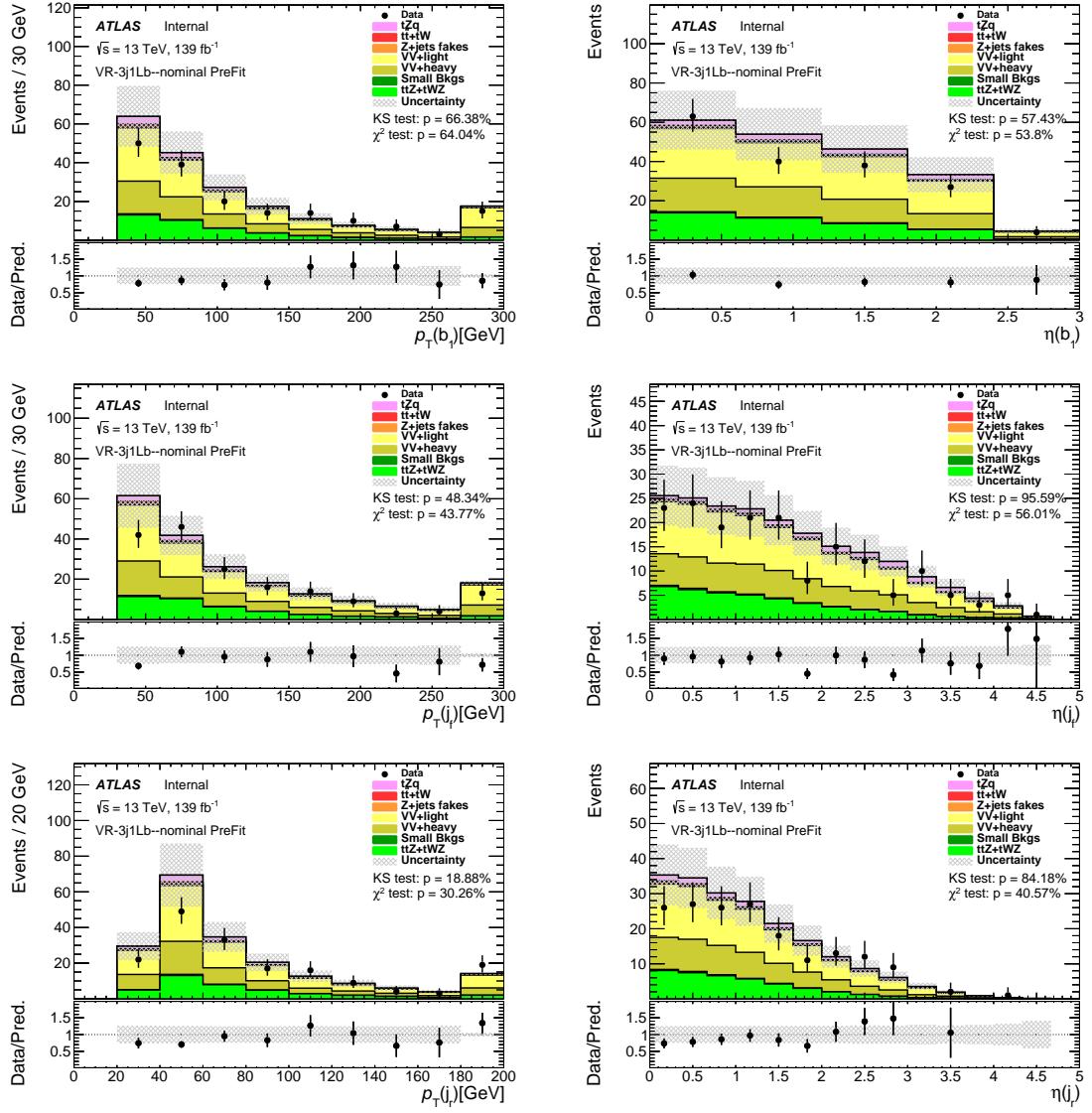


Figure 23: Comparison of data and MC predictions for reconstructed jet-related quantities for events in the diboson 3j1Lb VR. Both signal and backgrounds are normalised to the expected number of events before the fit. The uncertainty band includes statistical uncertainties for signal and backgrounds and background normalization uncertainties due to the prior assumptions and the modeling systematics, with the exception of  $t\bar{t}$  and  $Z + \text{jets}$ , where only the statistical uncertainties are shown.

Not reviewed, for internal circulation only

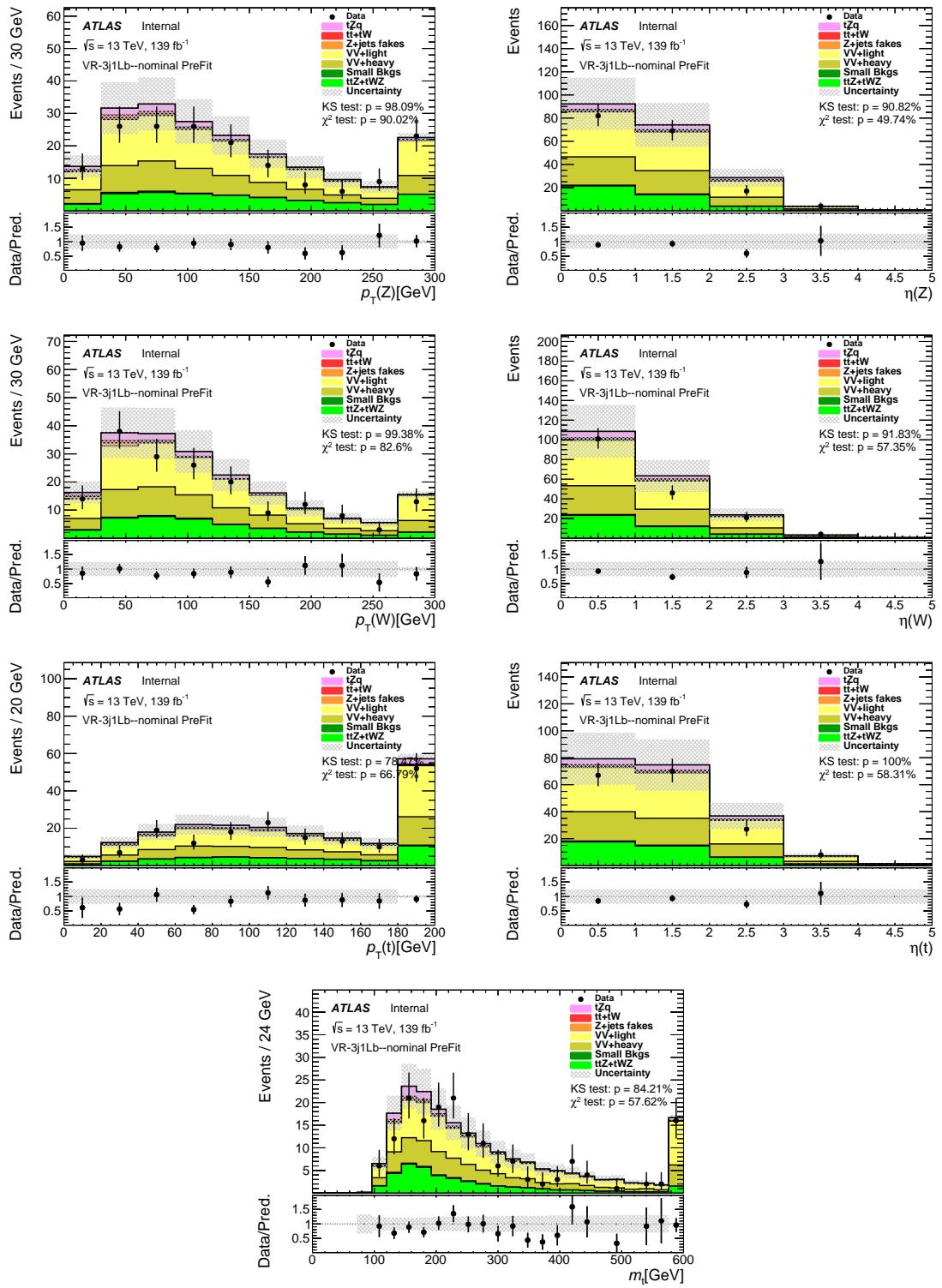


Figure 24: Comparison of data and MC predictions for reconstructed event-related quantities for events in the diboson 3j1Lb VR. Both signal and backgrounds are normalised to the expected number of events before the fit. The uncertainty band includes statistical uncertainties for signal and backgrounds and background normalization uncertainties due to the prior assumptions and the modeling systematics, with the exception of  $t\bar{t}$  and  $Z + \text{jets}$ , where only the statistical uncertainties are shown.

796 **7.3.4 Control-region yields**

797 The number of observed data events in the diboson control regions and expected numbers of signal and  
 798 background events for the luminosity of  $139 \text{ fb}^{-1}$  are listed in Tables 14 and 15 for the diboson Xj0b CRs.

Table 14: Number of observed and expected events in the diboson 2j0b CR. The left table shows the number of events after luminosity weighting, while the right table shows the raw number of events available. The uncertainties include only statistical uncertainties.

Process	Number of events		Process	Number of raw events	
$t\bar{t}Z$	42.2	$\pm 1.2$	$t\bar{t}Z$	31 829	
$t\bar{t}W$	1.8	$\pm 0.2$	$t\bar{t}W$	604	
$t\bar{t}H$	1.1	$\pm 0.1$	$t\bar{t}H$	2086	
$tWZ$	16.7	$\pm 1.0$	$tWZ$	2672	
$VV + \text{HF}$	382.1	$\pm 1.8$	$VV + \text{HF}$	146 671	
$VV + \text{LF}$	2039.7	$\pm 4.8$	$VV + \text{LF}$	792 748	
$Z + \text{jets}$	63.5	$\pm 0.2$	$Z + \text{jets}$	1 065 907	
$t\bar{t}$	13.8	$\pm 0.0$	$t\bar{t}$	234 791	
$tW$	0.5	$\pm 0.0$	$tW$	4561	
$tZq$	55.4	$\pm 0.6$	$tZq$	226 420	
Total expected	2616.8	$\pm 5.4$	Total expected	2 508 289	
Data	2703				

Table 15: Number of observed and expected events in the diboson 3j0b CR. The left table shows the number of events after luminosity weighting, while the right table shows the raw number of events available. The uncertainties include only statistical uncertainties.

Process	Number of events		Process	Number of raw events	
$t\bar{t}Z$	46.1	$\pm 1.3$	$t\bar{t}Z$	38 722	
$t\bar{t}W$	0.7	$\pm 0.1$	$t\bar{t}W$	287	
$t\bar{t}H$	1.0	$\pm 0.1$	$t\bar{t}H$	1766	
$tWZ$	12.5	$\pm 0.9$	$tWZ$	2277	
$VV + HF$	190.0	$\pm 1.1$	$VV + HF$	80 609	
$VV + LF$	708.0	$\pm 2.2$	$VV + LF$	310 959	
$Z + \text{jets}$	20.2	$\pm 0.1$	$Z + \text{jets}$	388 570	
$t\bar{t}$	6.8	$\pm 0.0$	$t\bar{t}$	91 122	
$tW$	0.3	$\pm 0.0$	$tW$	1345	
$tZq$	22.3	$\pm 0.4$	$tZq$	120 942	
Total expected	1008.0	$\pm 2.9$	Total expected	1 036 599	
Data	949				

Not reviewed, for internal circulation only

### 7.3.5 Control-region yields with pure Monte Carlo samples

As done in Section 5.4, event yields tables not using the BJR method are shown in the following. Event yields are shown in Tables 16 and 17 for the diboson Xj0b CRs.

Table 16: Number of observed and expected events in the diboson 2j0b CR. The left table shows the number of events after luminosity weighting, while the right table shows the raw number of events available. **For the  $Z + \text{jets}$  and  $t\bar{t}$  samples, the BJR method is not applied, in order to show the available statistics in the MC samples.** The uncertainties include only statistical uncertainties.

Process	Number of events		Process	Number of raw events	
$t\bar{t}Z$	$42.2 \pm$	1.2	$t\bar{t}Z$	31 829	
$t\bar{t}W$	$1.8 \pm$	0.2	$t\bar{t}W$	604	
$t\bar{t}H$	$1.1 \pm$	0.1	$t\bar{t}H$	2086	
$tWZ$	$16.7 \pm$	1.0	$tWZ$	2672	
$VV + \text{HF}$	$382.1 \pm$	1.8	$VV + \text{HF}$	146 671	
$VV + \text{LF}$	$2039.7 \pm$	4.8	$VV + \text{LF}$	792 748	
$Z + \text{jets}$	$63.5 \pm$	4.1	$Z + \text{jets}$	1673	
$t\bar{t}$	$13.8 \pm$	1.0	$t\bar{t}$	265	
$tW$	$0.5 \pm$	0.3	$tW$	3	
$tZq$	$0.0 \pm$	0.0	$tZq$	0	
Total expected	$2561.4 \pm$	6.9	Total expected	978 551	
Data	2703				

Table 17: Number of observed and expected events in the diboson 3j0b CR. The left table shows the number of events after luminosity weighting, while the right table shows the raw number of events available. **For the  $Z + \text{jets}$  and  $t\bar{t}$  samples, the BJR method is not applied, in order to show the available statistics in the MC samples.** The uncertainties include only statistical uncertainties.

Process	Number of events		Process	Number of raw events	
$t\bar{t}Z$	$46.1 \pm$	1.3	$t\bar{t}Z$	38 722	
$t\bar{t}W$	$0.7 \pm$	0.1	$t\bar{t}W$	287	
$t\bar{t}H$	$1.0 \pm$	0.1	$t\bar{t}H$	1766	
$tWZ$	$12.5 \pm$	0.9	$tWZ$	2277	
$VV + \text{HF}$	$190.0 \pm$	1.1	$VV + \text{HF}$	80 609	
$VV + \text{LF}$	$708.0 \pm$	2.2	$VV + \text{LF}$	310 959	
$Z + \text{jets}$	$20.2 \pm$	2.4	$Z + \text{jets}$	742	
$t\bar{t}$	$6.8 \pm$	0.8	$t\bar{t}$	130	
$tW$	$0.3 \pm$	0.2	$tW$	2	
$tZq$	$0.0 \pm$	0.0	$tZq$	0	
Total expected	$985.7 \pm$	3.9	Total expected	435 494	
Data	949				

802 **7.4 Modeling of  $t\bar{t}$  and  $t\bar{t}Z$** 803 **7.4.1 Validation-region yields**

804 The number of observed data events in the  $t\bar{t}V + t\bar{t}$  validation regions and expected numbers of signal and  
 805 background events for the luminosity of  $139 \text{ fb}^{-1}$  are listed in Tables 18 and 19 for the  $t\bar{t}V + t\bar{t}$  Xj1b VRs.

Table 18: Number of observed and expected events in the  $t\bar{t}V + t\bar{t}$  2j1b VR. The left table shows the number of events after luminosity weighting, while the right table shows the raw number of events available. The uncertainties include only statistical uncertainties.

Process	Number of events		Process	Number of raw events	
$t\bar{t}Z$	$19.3 \pm$	1.0	$t\bar{t}Z$	14 226	
$t\bar{t}W$	$22.6 \pm$	0.8	$t\bar{t}W$	7509	
$t\bar{t}H$	$7.6 \pm$	0.2	$t\bar{t}H$	17 754	
$tWZ$	$3.5 \pm$	0.4	$tWZ$	537	
$VV + HF$	$18.8 \pm$	0.4	$VV + HF$	9034	
$VV + LF$	$4.2 \pm$	0.2	$VV + LF$	1089	
$Z + \text{jets}$	$4.9 \pm$	0.1	$Z + \text{jets}$	20 883	
$t\bar{t}$	$81.0 \pm$	0.1	$t\bar{t}$	808 306	
$tW$	$3.4 \pm$	0.0	$tW$	9864	
$tZq$	$10.4 \pm$	0.2	$tZq$	40 982	
Total expected	$175.6 \pm$	1.4	Total expected	930 184	
Data	196				

Table 19: Number of observed and expected events in the  $t\bar{t}V + t\bar{t}$  3j1b VR. The left table shows the number of events after luminosity weighting, while the right table shows the raw number of events available. The uncertainties include only statistical uncertainties.

Process	Number of events		Process	Number of raw events	
$t\bar{t}Z$	$25.7 \pm$	1.2	$t\bar{t}Z$	20 433	
$t\bar{t}W$	$11.4 \pm$	0.6	$t\bar{t}W$	4240	
$t\bar{t}H$	$9.0 \pm$	0.2	$t\bar{t}H$	18 094	
$tWZ$	$3.0 \pm$	0.4	$tWZ$	534	
$VV + HF$	$10.8 \pm$	0.3	$VV + HF$	5244	
$VV + LF$	$2.2 \pm$	0.1	$VV + LF$	594	
$Z + \text{jets}$	$1.8 \pm$	0.0	$Z + \text{jets}$	9749	
$t\bar{t}$	$36.0 \pm$	0.1	$t\bar{t}$	363 899	
$tW$	$1.6 \pm$	0.0	$tW$	4239	
$tZq$	$6.2 \pm$	0.2	$tZq$	27 957	
Total expected	$107.7 \pm$	1.4	Total expected	454 983	
Data	126				

Not reviewed, for internal circulation only

806 **7.4.2 Validation-region yields with pure Monte Carlo samples**

807 As done in Section 5.4, event yields tables not using the BJR method are shown in the following. Event  
808 yields are shown in Tables 20 and 21 for the  $t\bar{t}V + t\bar{t}$  Xj1b VRs.

Table 20: Number of observed and expected events in the  $t\bar{t}V + t\bar{t}$  2j1b VR. The left table shows the number of events after luminosity weighting, while the right table shows the raw number of events available. **For the Z + jets and  $t\bar{t}$  samples, the BJR method is not applied, in order to show the available statistics in the MC samples.** The uncertainties include only statistical uncertainties.

Process	Number of events		Process	Number of raw events	
$t\bar{t}Z$	$19.3 \pm$	1.0	$t\bar{t}Z$	14 226	
$t\bar{t}W$	$22.6 \pm$	0.8	$t\bar{t}W$	7509	
$t\bar{t}H$	$7.6 \pm$	0.2	$t\bar{t}H$	17 754	
$tWZ$	$3.5 \pm$	0.4	$tWZ$	537	
$VV + HF$	$18.8 \pm$	0.4	$VV + HF$	9034	
$VV + LF$	$4.2 \pm$	0.2	$VV + LF$	1089	
$Z + jets$	$4.9 \pm$	1.2	$Z + jets$	170	
$t\bar{t}$	$81.0 \pm$	2.4	$t\bar{t}$	1597	
$tW$	$3.4 \pm$	0.7	$tW$	28	
$tZq$	$0.0 \pm$	0.0	$tZq$	0	
Total expected	$165.2 \pm$	3.1	Total expected	51 944	
Data	196				

Table 21: Number of observed and expected events in the  $t\bar{t}V + t\bar{t}$  3j1b VR. The left table shows the number of events after luminosity weighting, while the right table shows the raw number of events available. **For the Z + jets and  $t\bar{t}$  samples, the BJR method is not applied, in order to show the available statistics in the MC samples.** The uncertainties include only statistical uncertainties.

Process	Number of events		Process	Number of raw events	
$t\bar{t}Z$	$25.7 \pm$	1.2	$t\bar{t}Z$	20 433	
$t\bar{t}W$	$11.4 \pm$	0.6	$t\bar{t}W$	4240	
$t\bar{t}H$	$9.0 \pm$	0.2	$t\bar{t}H$	18 094	
$tWZ$	$3.0 \pm$	0.4	$tWZ$	534	
$VV + HF$	$10.8 \pm$	0.3	$VV + HF$	5244	
$VV + LF$	$2.2 \pm$	0.1	$VV + LF$	594	
$Z + jets$	$1.8 \pm$	0.5	$Z + jets$	75	
$t\bar{t}$	$36.0 \pm$	1.5	$t\bar{t}$	735	
$tW$	$1.6 \pm$	0.5	$tW$	12	
$tZq$	$0.0 \pm$	0.0	$tZq$	0	
Total expected	$101.5 \pm$	2.2	Total expected	49 961	
Data	126				

809 **7.4.3 Validation-region plots**

810 Distributions of lepton, jet and event variables in the  $t\bar{t}V + t\bar{t}$  validation regions are shown in Figs. 25 to 27  
 811 for the 2j1b VR and in Figs. 28 to 30 for the 3j1b VR.

Not reviewed, for internal circulation only

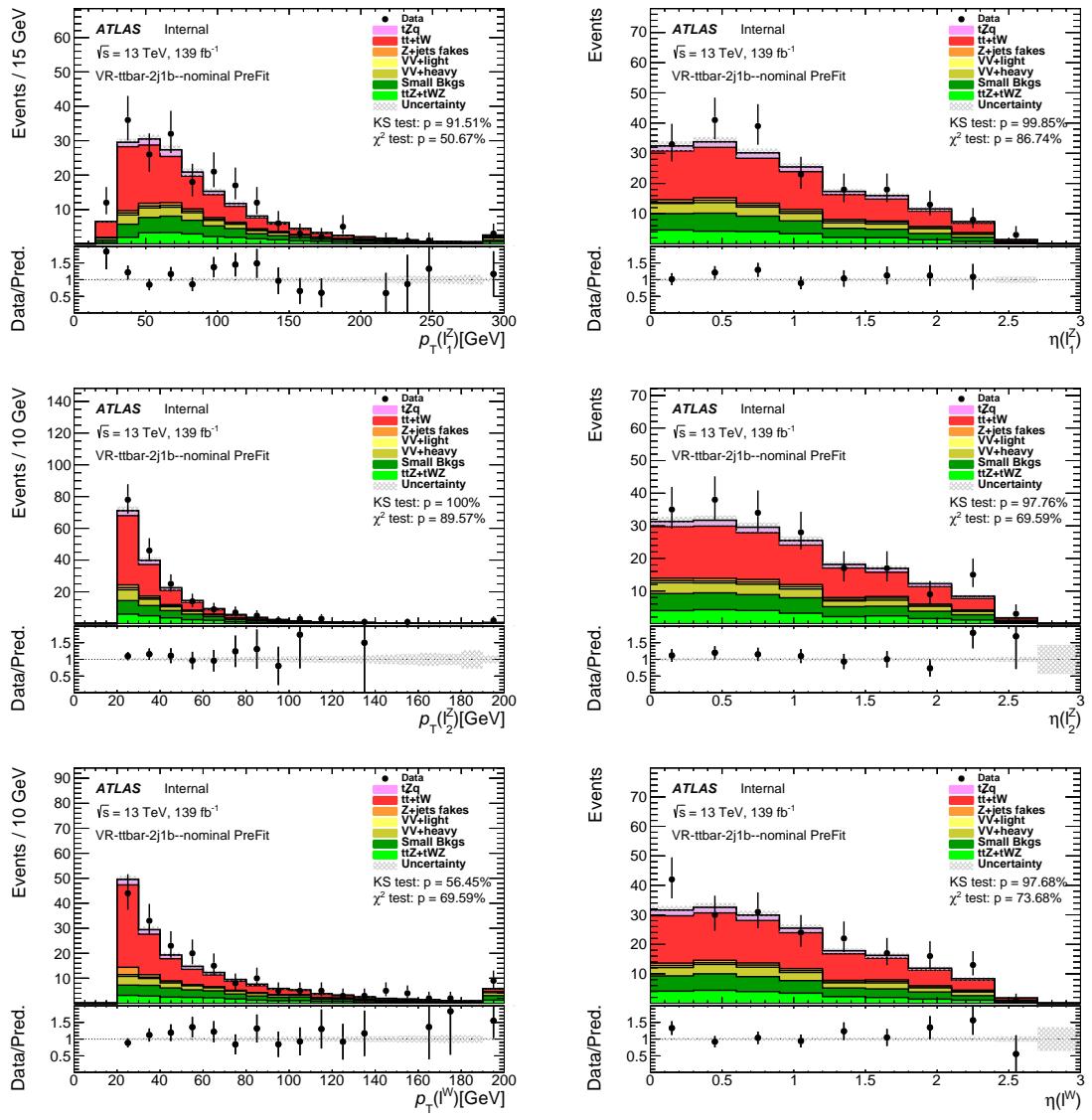


Figure 25: Comparison of data and MC predictions for reconstructed lepton-related quantities for events in the  $t\bar{t}V + t\bar{t}$  2j1b VR. Both signal and backgrounds are normalised to the expected number of events before the fit. The uncertainty band includes statistical uncertainties for signal and backgrounds and background normalization uncertainties due to the prior assumptions and the modeling systematics, with the exception of  $t\bar{t}$  and  $Z + \text{jets}$ , where only the statistical uncertainties are shown.

Not reviewed, for internal circulation only

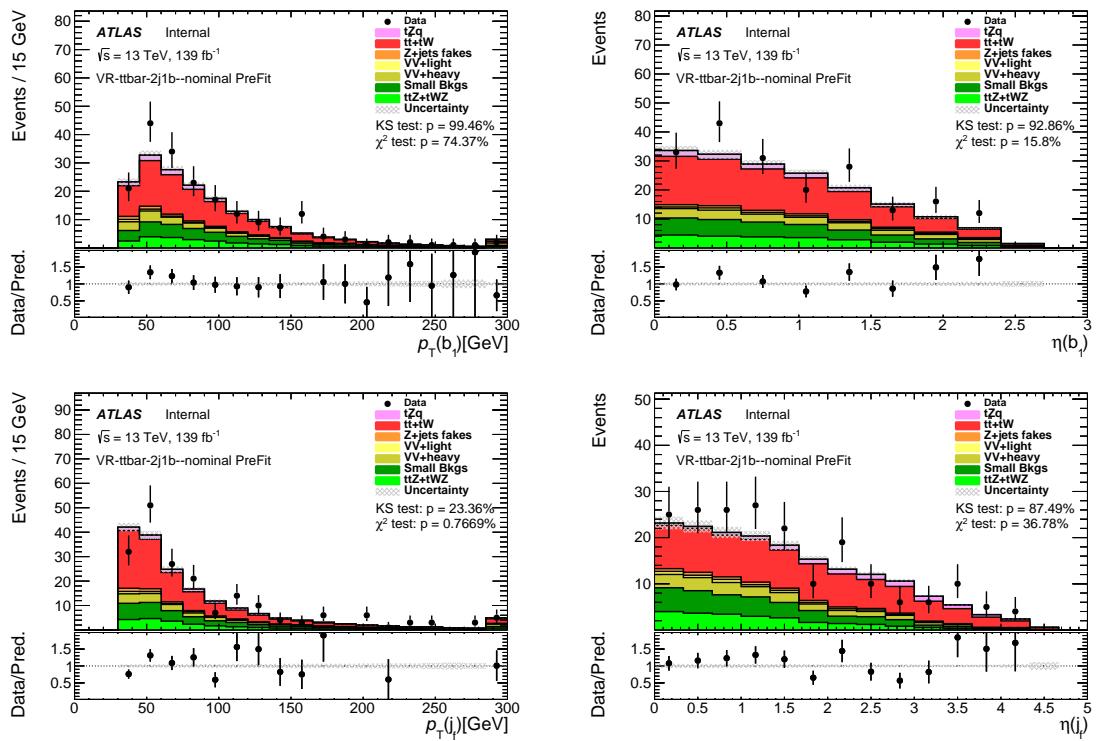


Figure 26: Comparison of data and MC predictions for reconstructed jet-related quantities for events in the  $t\bar{t}V + t\bar{t}$  2j1b VR. Both signal and backgrounds are normalised to the expected number of events before the fit. The uncertainty band includes statistical uncertainties for signal and backgrounds and background normalization uncertainties due to the prior assumptions and the modeling systematics, with the exception of  $t\bar{t}$  and  $Z + \text{jets}$ , where only the statistical uncertainties are shown.

Not reviewed, for internal circulation only

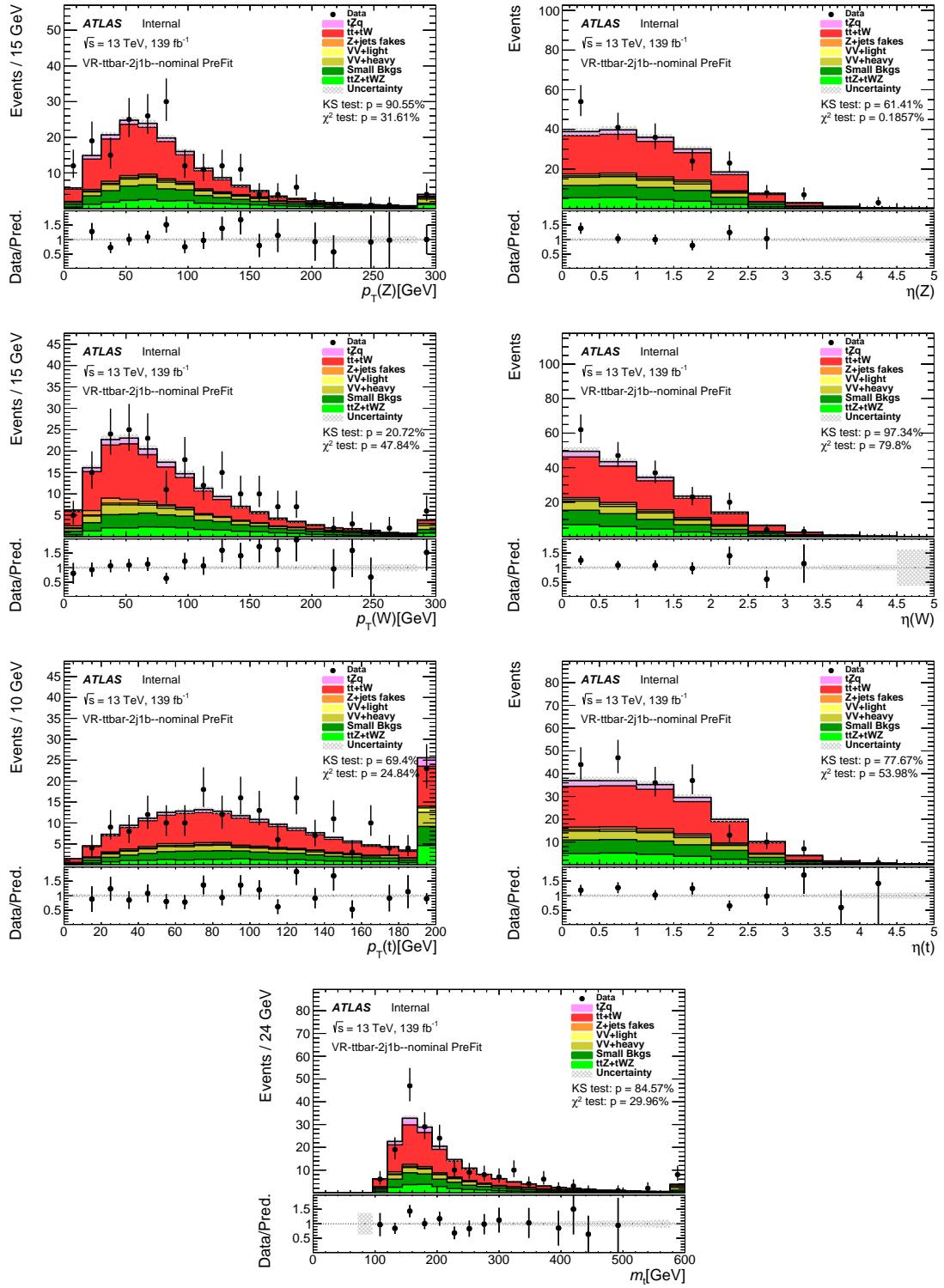


Figure 27: Comparison of data and MC predictions for reconstructed event-related quantities for events in the  $t\bar{t}V + t\bar{t}$  2j1b VR. Both signal and backgrounds are normalised to the expected number of events before the fit. The uncertainty band includes statistical uncertainties for signal and backgrounds and background normalization uncertainties due to the prior assumptions and the modeling systematics, with the exception of  $t\bar{t}$  and  $Z + \text{jets}$ , where only the statistical uncertainties are shown.

Not reviewed, for internal circulation only

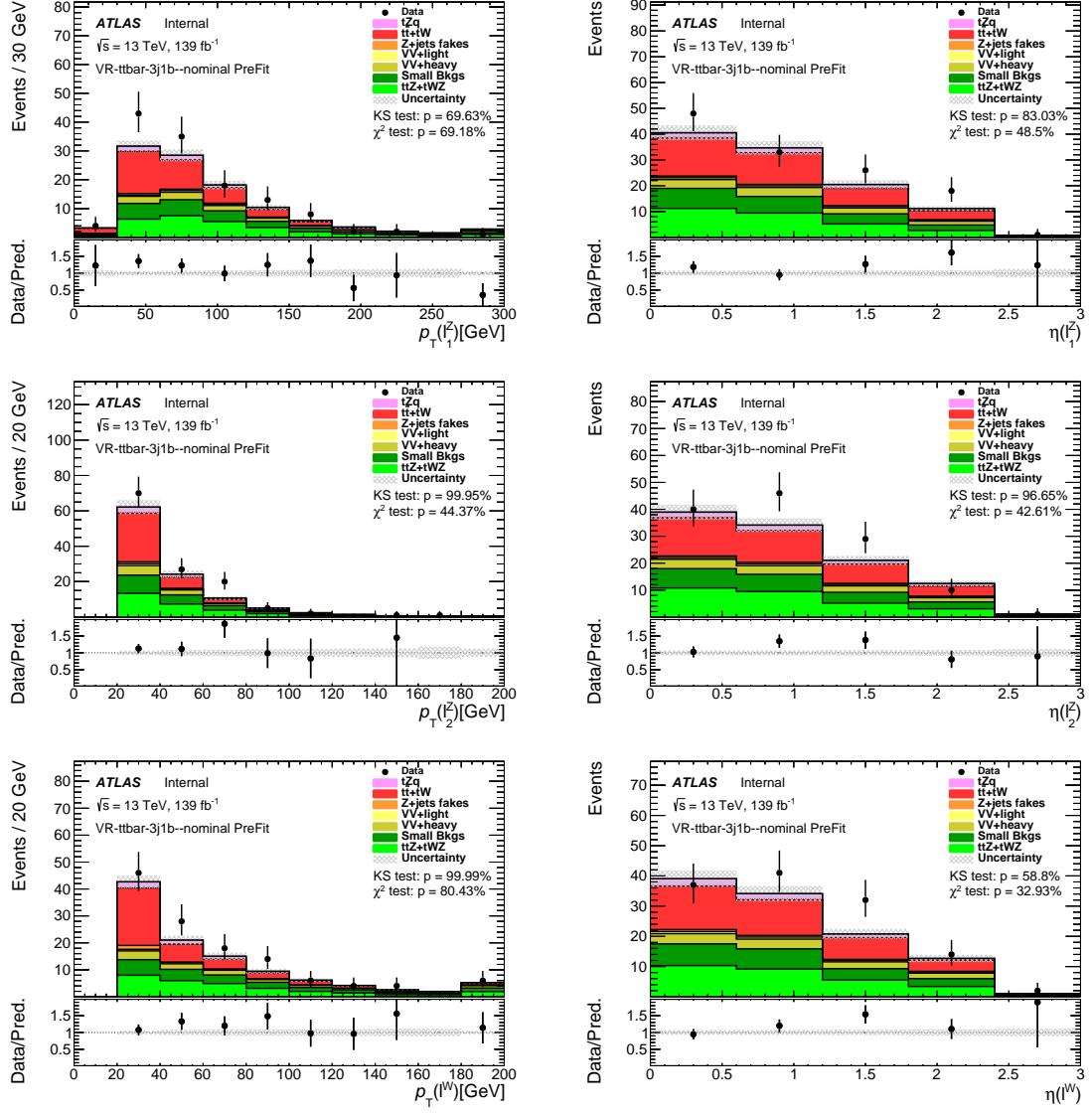


Figure 28: Comparison of data and MC predictions for reconstructed lepton-related quantities for events in the  $t\bar{t}V + t\bar{t}$  3j1b VR. Both signal and backgrounds are normalised to the expected number of events before the fit. The uncertainty band includes statistical uncertainties for signal and backgrounds and background normalization uncertainties due to the prior assumptions and the modeling systematics, with the exception of  $t\bar{t}$  and  $Z + \text{jets}$ , where only the statistical uncertainties are shown.

Not reviewed, for internal circulation only

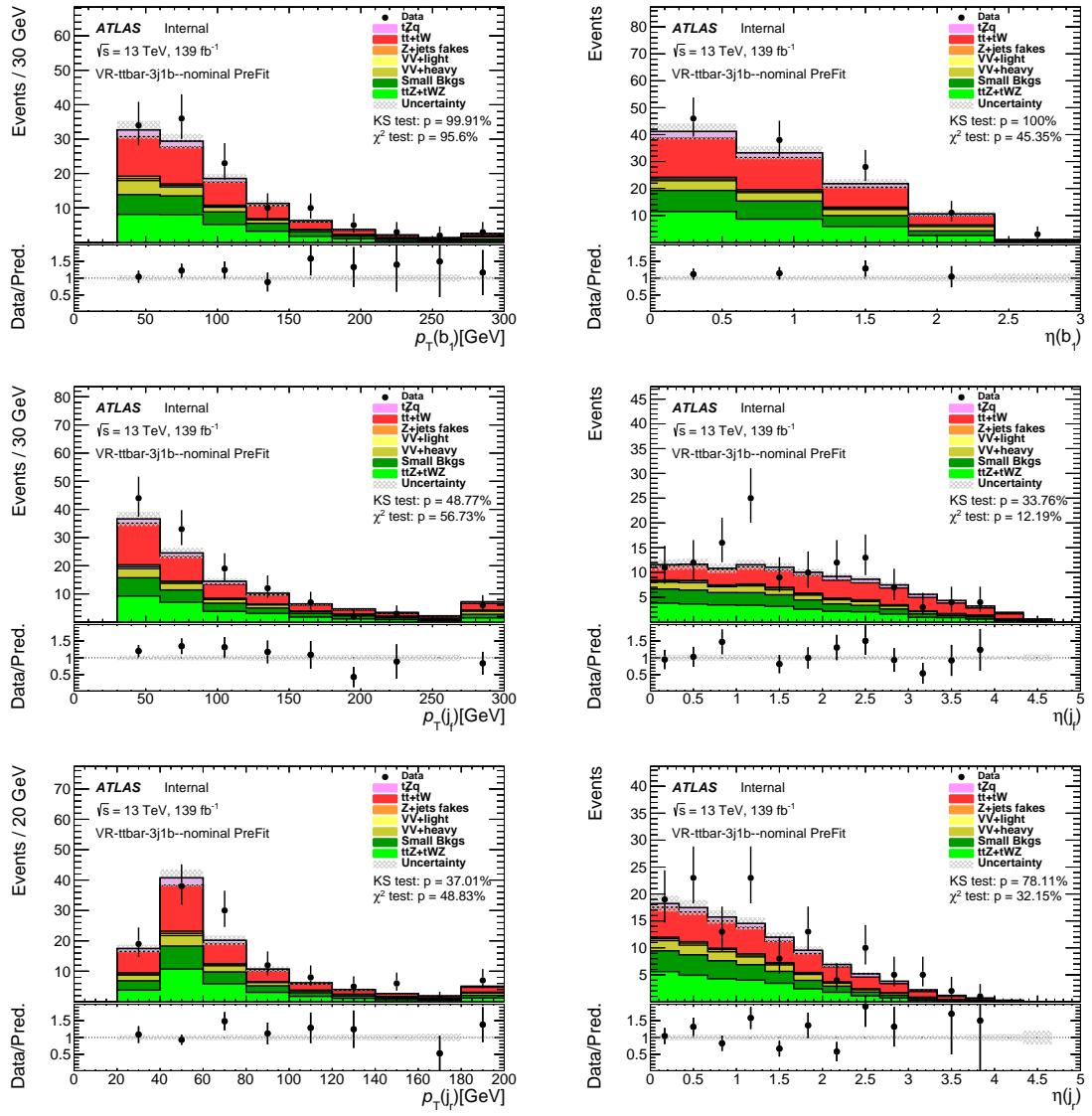


Figure 29: Comparison of data and MC predictions for reconstructed jet-related quantities for events in the  $t\bar{t}V + t\bar{t}$  3j1b VR. Both signal and backgrounds are normalised to the expected number of events before the fit. The uncertainty band includes statistical uncertainties for signal and backgrounds and background normalization uncertainties due to the prior assumptions and the modeling systematics, with the exception of  $t\bar{t}$  and  $Z + \text{jets}$ , where only the statistical uncertainties are shown.

Not reviewed, for internal circulation only

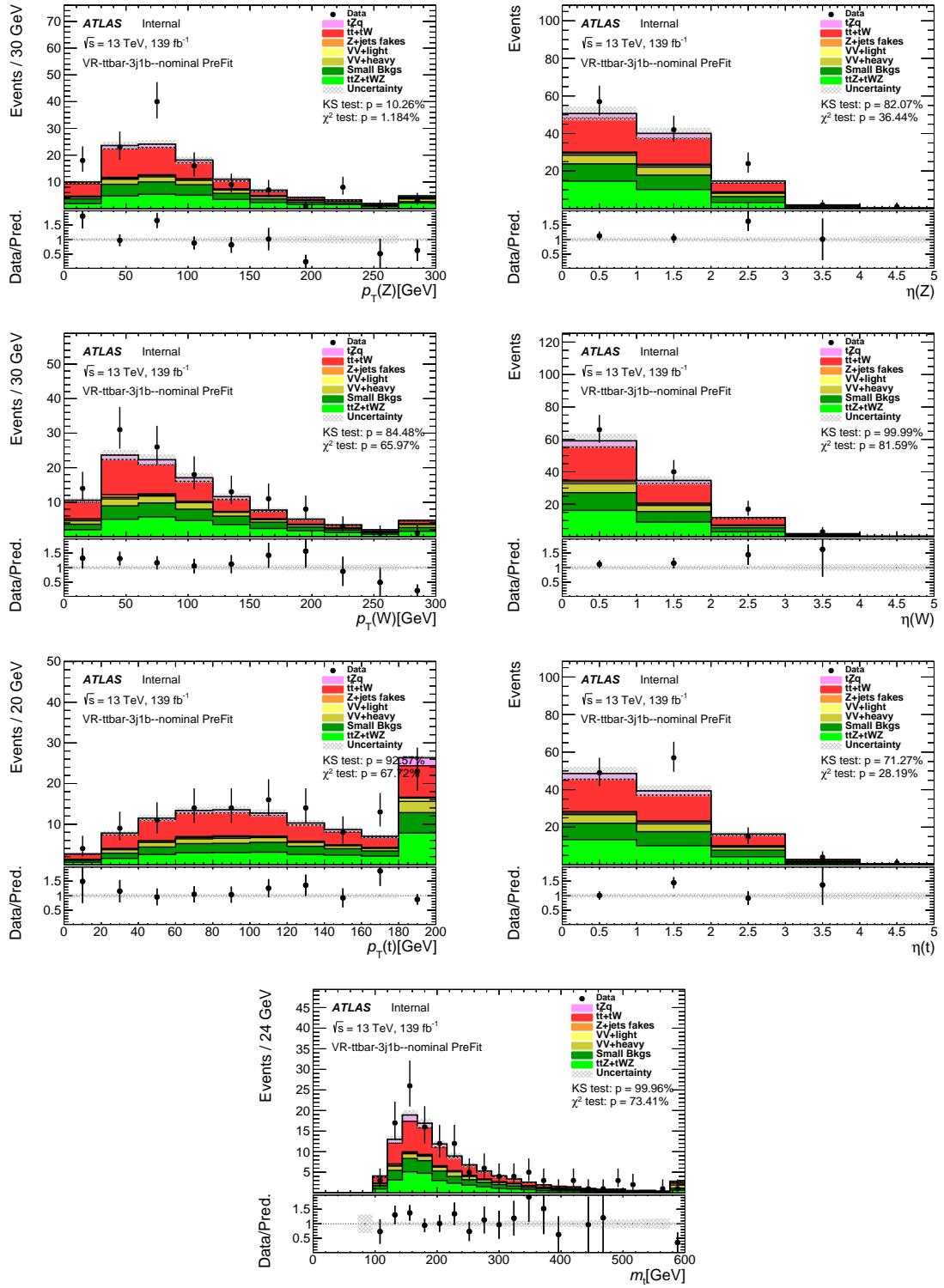


Figure 30: Comparison of data and MC predictions for reconstructed event-related quantities for events in the  $t\bar{t}V + t\bar{t}$  3j1b VR. Both signal and backgrounds are normalised to the expected number of events before the fit. The uncertainty band includes statistical uncertainties for signal and backgrounds and background normalization uncertainties due to the prior assumptions and the modeling systematics, with the exception of  $t\bar{t}$  and  $Z +$  jets, where only the statistical uncertainties are shown.

812 **7.4.4 Control-region yields**

813 The number of observed data events in the  $t\bar{t}$  and  $t\bar{t}Z$  control regions and expected numbers of signal and  
 814 background events for the luminosity of  $139\text{ fb}^{-1}$  are listed in Tables 22 and 23 for the  $t\bar{t}$  Xj1b CRs, and in  
 815 Tables 24 and 25 for the  $t\bar{t}Z$  Xj2b CRs.

Table 22: Number of observed and expected events in the  $t\bar{t}$  2j1b CR. The left table shows the number of events after luminosity weighting, while the right table shows the raw number of events available. The uncertainties include only statistical uncertainties.

Process	Number of events	Process	Number of raw events
$t\bar{t}Z$	$3.5 \pm 0.5$	$t\bar{t}Z$	2533
$t\bar{t}W$	$9.3 \pm 0.5$	$t\bar{t}W$	2914
$t\bar{t}H$	$2.8 \pm 0.1$	$t\bar{t}H$	6782
$tWZ$	$0.9 \pm 0.2$	$tWZ$	143
$VV + HF$	$0.4 \pm 0.1$	$VV + HF$	166
$VV + LF$	$0.1 \pm 0.0$	$VV + LF$	19
$Z + \text{jets}$	$0.0 \pm 0.0$	$Z + \text{jets}$	330
$t\bar{t}$	$34.0 \pm 0.1$	$t\bar{t}$	327 074
$tW$	$0.8 \pm 0.0$	$tW$	3935
$tZq$	$0.2 \pm 0.0$	$tZq$	1101
Total expected	$52.0 \pm 0.7$	Total expected	344 997
Data	49		

Table 23: Number of observed and expected events in the  $t\bar{t}$  3j1b CR. The left table shows the number of events after luminosity weighting, while the right table shows the raw number of events available. The uncertainties include only statistical uncertainties.

Process	Number of events		Process	Number of raw events	
$t\bar{t}Z$	$3.6 \pm$	0.5	$t\bar{t}Z$	2827	
$t\bar{t}W$	$4.7 \pm$	0.4	$t\bar{t}W$	1756	
$t\bar{t}H$	$3.3 \pm$	0.1	$t\bar{t}H$	6881	
$tWZ$	$0.2 \pm$	0.2	$tWZ$	80	
$VV + HF$	$0.3 \pm$	0.0	$VV + HF$	101	
$VV + LF$	$0.0 \pm$	0.0	$VV + LF$	8	
$Z + jets$	$0.0 \pm$	0.0	$Z + jets$	194	
$t\bar{t}$	$15.3 \pm$	0.0	$t\bar{t}$	146 886	
$tW$	$0.5 \pm$	0.0	$tW$	1677	
$tZq$	$0.2 \pm$	0.0	$tZq$	794	
Total expected	$28.1 \pm$	0.6	Total expected	161 204	
Data	31				

Table 24: Number of observed and expected events in the  $t\bar{t}Z$  3j2b CR. The left table shows the number of events after luminosity weighting, while the right table shows the raw number of events available. The uncertainties include only statistical uncertainties.

Process	Number of events		Process	Number of raw events	
$t\bar{t}Z$	$45.1 \pm$	1.2	$t\bar{t}Z$	35 187	
$t\bar{t}W$	$1.3 \pm$	0.2	$t\bar{t}W$	552	
$t\bar{t}H$	$1.4 \pm$	0.1	$t\bar{t}H$	2858	
$tWZ$	$4.4 \pm$	0.5	$tWZ$	663	
$VV + HF$	$5.3 \pm$	0.2	$VV + HF$	2682	
$VV + LF$	$0.1 \pm$	0.0	$VV + LF$	9	
$Z + jets$	$0.5 \pm$	0.0	$Z + jets$	2972	
$t\bar{t}$	$1.6 \pm$	0.0	$t\bar{t}$	2944	
$tW$	$0.1 \pm$	0.0	$tW$	28	
$tZq$	$13.2 \pm$	0.2	$tZq$	36 019	
Total expected	$73.1 \pm$	1.4	Total expected	83 914	
Data	92				

Table 25: Number of observed and expected events in the  $t\bar{t}Z$  4j2b CR. The left table shows the number of events after luminosity weighting, while the right table shows the raw number of events available. The uncertainties include only statistical uncertainties.

Process	Number of events		Process	Number of raw events	
$t\bar{t}Z$	$47.5 \pm$	1.3	$t\bar{t}Z$	42 202	
$t\bar{t}W$	$0.6 \pm$	0.1	$t\bar{t}W$	228	
$t\bar{t}H$	$1.3 \pm$	0.1	$t\bar{t}H$	2099	
$tWZ$	$4.0 \pm$	0.5	$tWZ$	762	
$VV + HF$	$3.3 \pm$	0.1	$VV + HF$	1630	
$VV + LF$	$0.1 \pm$	0.0	$VV + LF$	7	
$Z + \text{jets}$	$0.1 \pm$	0.0	$Z + \text{jets}$	2021	
$t\bar{t}$	$1.0 \pm$	0.0	$t\bar{t}$	1644	
$tW$	$0.0 \pm$	0.0	$tW$	15	
$tZq$	$8.6 \pm$	0.2	$tZq$	27 582	
Total expected	$66.6 \pm$	1.4	Total expected	78 190	
Data	75				

Not reviewed, for internal circulation only

#### 816 7.4.5 Control-region yields with pure Monte Carlo samples

817 As done in Section 5.4, event yields tables not using the BJR method are shown in the following. Event  
 818 yields are shown in Tables 26 and 27 for the  $t\bar{t}$  Xj1b CRs, and in Tables 28 and 29 for the  $t\bar{t}Z$  Xj2b CRs.

Table 26: Number of observed and expected events in the  $t\bar{t}$  2j1b CR. The left table shows the number of events after luminosity weighting, while the right table shows the raw number of events available. **For the  $Z + \text{jets}$  and  $t\bar{t}$  samples, the BJR method is not applied, in order to show the available statistics in the MC samples.** The uncertainties include only statistical uncertainties.

Process	Number of events		Process	Number of raw events	
$t\bar{t}Z$	$3.5 \pm$	0.5	$t\bar{t}Z$	2533	
$t\bar{t}W$	$9.3 \pm$	0.5	$t\bar{t}W$	2914	
$t\bar{t}H$	$2.8 \pm$	0.1	$t\bar{t}H$	6782	
$tWZ$	$0.9 \pm$	0.2	$tWZ$	143	
$VV + \text{HF}$	$0.4 \pm$	0.1	$VV + \text{HF}$	166	
$VV + \text{LF}$	$0.1 \pm$	0.0	$VV + \text{LF}$	19	
$Z + \text{jets}$	$0.0 \pm$	0.0	$Z + \text{jets}$	1	
$t\bar{t}$	$34.0 \pm$	1.5	$t\bar{t}$	682	
$tW$	$0.8 \pm$	0.3	$tW$	7	
$tZq$	$0.0 \pm$	0.0	$tZq$	0	
Total expected	$51.8 \pm$	1.7	Total expected	13 247	
Data	49				

Table 27: Number of observed and expected events in the  $t\bar{t}$  3j1b CR. The left table shows the number of events after luminosity weighting, while the right table shows the raw number of events available. **For the  $Z + \text{jets}$  and  $t\bar{t}$  samples, the BJR method is not applied, in order to show the available statistics in the MC samples.** The uncertainties include only statistical uncertainties.

Process	Number of events		Process	Number of raw events	
$t\bar{t}Z$	$3.6 \pm$	0.5	$t\bar{t}Z$	2827	
$t\bar{t}W$	$4.7 \pm$	0.4	$t\bar{t}W$	1756	
$t\bar{t}H$	$3.3 \pm$	0.1	$t\bar{t}H$	6881	
$tWZ$	$0.2 \pm$	0.2	$tWZ$	80	
$VV + \text{HF}$	$0.3 \pm$	0.0	$VV + \text{HF}$	101	
$VV + \text{LF}$	$0.0 \pm$	0.0	$VV + \text{LF}$	8	
$Z + \text{jets}$	$0.0 \pm$	0.0	$Z + \text{jets}$	0	
$t\bar{t}$	$15.3 \pm$	1.0	$t\bar{t}$	308	
$tW$	$0.5 \pm$	0.3	$tW$	4	
$tZq$	$0.0 \pm$	0.0	$tZq$	0	
Total expected	$27.9 \pm$	1.2	Total expected	11 965	
Data	31				

Table 28: Number of observed and expected events in the  $t\bar{t}Z$  3j2b CR. The left table shows the number of events after luminosity weighting, while the right table shows the raw number of events available. **For the  $Z + \text{jets}$  and  $t\bar{t}$  samples, the BJR method is not applied, in order to show the available statistics in the MC samples.** The uncertainties include only statistical uncertainties.

Process	Number of events		Process	Number of raw events	
$t\bar{t}Z$	$45.1 \pm$	1.2	$t\bar{t}Z$	35 187	
$t\bar{t}W$	$1.3 \pm$	0.2	$t\bar{t}W$	552	
$t\bar{t}H$	$1.4 \pm$	0.1	$t\bar{t}H$	2858	
$tWZ$	$4.4 \pm$	0.5	$tWZ$	663	
$VV + \text{HF}$	$5.3 \pm$	0.2	$VV + \text{HF}$	2682	
$VV + \text{LF}$	$0.1 \pm$	0.0	$VV + \text{LF}$	9	
$Z + \text{jets}$	$0.5 \pm$	0.1	$Z + \text{jets}$	21	
$t\bar{t}$	$1.6 \pm$	0.4	$t\bar{t}$	23	
$tW$	$0.1 \pm$	0.1	$tW$	1	
$tZq$	$13.2 \pm$	0.2	$tZq$	36 019	
Total expected	$73.1 \pm$	1.4	Total expected	78 015	
Data	92				

Table 29: Number of observed and expected events in the  $t\bar{t}Z$  4j2b CR. The left table shows the number of events after luminosity weighting, while the right table shows the raw number of events available. **For the  $Z + \text{jets}$  and  $t\bar{t}$  samples, the BJR method is not applied, in order to show the available statistics in the MC samples.** The uncertainties include only statistical uncertainties.

Process	Number of events		Process	Number of raw events	
$t\bar{t}Z$	$47.5 \pm$	1.3	$t\bar{t}Z$	42 202	
$t\bar{t}W$	$0.6 \pm$	0.1	$t\bar{t}W$	228	
$t\bar{t}H$	$1.3 \pm$	0.1	$t\bar{t}H$	2099	
$tWZ$	$4.0 \pm$	0.5	$tWZ$	762	
$VV + \text{HF}$	$3.3 \pm$	0.1	$VV + \text{HF}$	1630	
$VV + \text{LF}$	$0.1 \pm$	0.0	$VV + \text{LF}$	7	
$Z + \text{jets}$	$0.1 \pm$	0.1	$Z + \text{jets}$	6	
$t\bar{t}$	$1.0 \pm$	0.3	$t\bar{t}$	21	
$tW$	$0.0 \pm$	0.0	$tW$	0	
$tZq$	$8.6 \pm$	0.2	$tZq$	27 582	
Total expected	$66.6 \pm$	1.5	Total expected	74 537	
Data	75				

## 8 Multivariate analysis

In order to better separate signal and background, a multivariate analysis is used. To extract the  $tZq$  signal events from the background events, several kinematic variables are combined into one discriminant using a neural-network algorithm. This section contains a brief discussion of the neural-network technique used in this analysis and also contains a comparison between the observed and simulated distributions used to feed the neural network.

### 8.1 Implementation and input variables

The neural-network package NeuroBayes [58, 59] is used, which combines a three-layer feed-forward neural network with a complex robust preprocessing. The neural network uses Bayesian regularisation techniques for the training process to improve the performance and to avoid overtraining. The network consists of one input node for each input variable used plus one bias node, and can have an arbitrary, user-defined number of hidden nodes. There is one output node which gives a continuous output in the interval  $[-1, 1]$ . The ratio of signal to background events in the training is set to be 50:50, where the different background processes are weighted according to their number of expected events. All background processes are considered in the training.

To achieve the optimal network training, Neurobayes preprocesses the input variables. In the first step, variables are transformed to be distributed between 0 and 1, in order to reduce the influence of extreme values and to damp statistical fluctuations. In the next step, variables are converted to have a Gaussian distribution, in order to be able to place the bulk of the events in the linear part of the activation functions for the hidden nodes. In a last step, the importance of each variable is determined. The correlation matrix of the transformed input variables is calculated, including the correlation of all variables to the target. One variable after the other is omitted to determine the loss in the total correlation to the target caused by its removal. The variable with the smallest loss of correlation is discarded leading to an  $(n - 1)$ -dimensional correlation matrix. The same procedure is repeated with the reduced correlation matrix to find the least important of the  $(n - 1)$  remaining variables. At the end, a list of variables ordered according to their importance is obtained and the most contributing variables are selected. Only significant variables that are well modelled are taken into account in the final neural network. The modelling of the input variables is checked in the data set as described in the previous sections.

In this analysis, two NNs are trained, one for each signal region using the same setup and with the same list of the input variables. In the 2j1b SR, 15 variables are retained for the neural-network training and are listed and explained in Table 30; the number of nodes in the hidden layer is set to 25. Similarly, in the 3j1b SR, 15 variables are retained in the training and are listed and explained in Table 31; the number of nodes in the hidden layer is set to 25.

Using neural-network algorithms implies that the kinematic configuration of the events has to be learnt. This can lead to a bias if the statistics of the training sample are too small and the network training makes use of statistical fluctuations. To avoid overtraining bias, five-fold template assembly is used in this analysis and five NN are trained for each signal region. For each NN, 80 % of the available events are used for the training and 20 % of the available events are used to build statistically independent templates (test templates). Finally, the five statistically independent templates are added to make the final template which is then used in this analysis. The comparison between the five training templates built from the events used

Table 30: Variables used as input to the neural network of the 2j1b SR ordered by their importance. The 2nd column gives the correlation loss.

Variable	Corr. loss [%]	Definition
$m_{bj_f}$	43.3	Invariant mass of the $b$ -jet and the forward jet
$m_t$	34.7	Reconstructed top-quark mass
$ \eta(j_f) $	18.6	Absolute value of the forward jet $\eta$
$m_T(\ell, E_T^{\text{miss}})$	12.7	Transverse mass of the $W$ boson
$b$ -tagging score	9.5	$b$ -tagging score of the $b$ -jet
$H_T$	6.0	Scalar sum of the $p_T$ of the selected particles in the event
$q(\ell^W)$	6.0	Electric charge of the lepton from the $W$ -boson decay
$ \eta(\ell^W) $	4.9	Absolute value of the $\eta$ of the lepton from the $W$ -boson decay
$p_T(W)$	3.5	$p_T$ of the reconstructed $W$ boson
$p_T(\ell^W)$	4.5	$p_T$ of the lepton coming from the $W$ -boson decay
$m(\ell\ell)$	4.5	Mass of the reconstructed $Z$ boson
$ \eta(Z) $	4.4	Absolute value of the $\eta$ of the reconstructed $Z$ boson
$\Delta R(j_f, Z)$	4.1	$\Delta R$ between the forward jet and the reconstructed $Z$ boson
$E_T^{\text{miss}}$	3.8	Missing transverse momentum
$p_T(j_f)$	3.3	Forward jet $p_T$

Table 31: Variables used as input to the neural network of the 3j1b SR ordered by their importance. The 2nd column gives the correlation loss.

Variable	Corr. loss [%]	Definition
$m_{bj_f}$	43.0	Invariant mass of the $b$ -jet and the forward jet
$m_t$	31.8	Reconstructed top-quark mass
$ \eta(j_f) $	17.4	Absolute value of the forward jet $\eta$
$m_T(\ell, E_T^{\text{miss}})$	12.3	Transverse mass of $W$ -boson
$ \eta(j_r) $	12.0	Absolute value of the radiation jet $\eta$
$p_T(Z)$	10.2	$p_T$ of the reconstructed $Z$ boson
$\Delta R(j_f, Z)$	8.1	$\Delta R$ between the forward jet and the reconstructed $Z$ boson
$q(\ell^W)$	7.8	Electric charge of the lepton from the $W$ boson decay
$p_T(j_r)$	6.7	$p_T$ of the radiation jet
$p_T(j_f)$	5.6	$p_T$ of the forward jet
$b$ -tagging score	5.2	$b$ -tagging score of the $b$ -jet
$ \eta(\ell^W) $	4.2	Absolute value of the $\eta$ of the lepton coming from the $W$ -boson decay
$ \eta(Z) $	3.9	Absolute value of the $\eta$ of the reconstructed $Z$ boson
$p_T(\ell^W)$	2.5	$p_T$ of the lepton coming from the $W$ boson decay
$p_T(W)$	3.5	$p_T$ of the reconstructed $W$ boson

859 in the training and the test templates for the signal and background processes are shown in Figs. 49 and 50  
 860 for 2j1b SR and 3j1b SR, receptively.

861 In addition, the ROC curves for both signal regions are created and compared for both training and test  
 862 samples and again a good agreement is observed. This can be seen in Fig. 31.

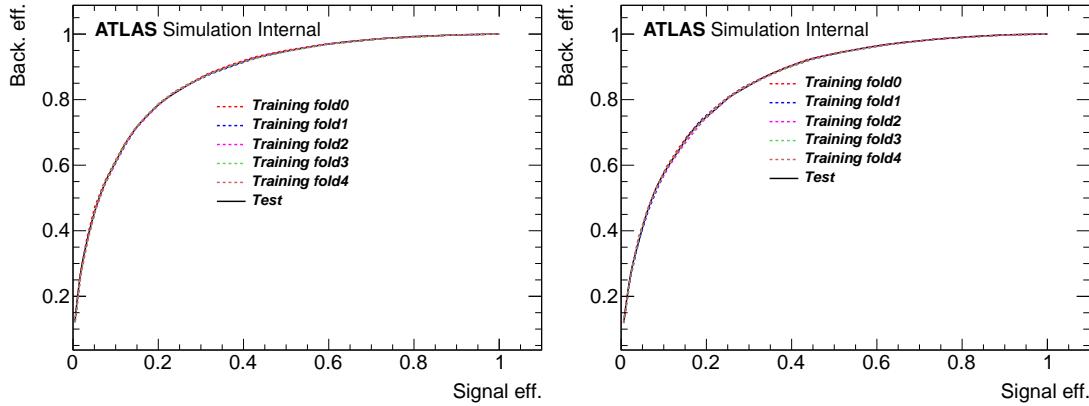


Figure 31: Neural-network ROC curve of the training and test samples of the 2 jet SR (left) and of the 3 jet SR (right). The hashed curves are created from the training samples of each fold and the solid curves are created from the test samples.

863 **8.1.1 Signal purity as a function of the NN output**

The quality of the training is checked by plotting the signal purity as a function of the neural network output as can be seen in Fig. 32. The signal purity is defined as the ratio between the number of signal events and the signal plus background events in a bin. If the NN is well trained, then the error function  $E(w)$  is minimal, i.e.  $\frac{dE}{dO_{\text{NN}}} = 0$ . It is shown in Ref. [58] that the purity for a well trained network at the minimum is a linear function of the network output,  $O_{\text{NN}}$ :

$$P = \frac{O_{\text{NN}} + 1}{2},$$

864 which can be interpreted as a probability to observe signal events as a function of the NN output. Thus, for  
865 a well trained network, all the points should lie on the diagonal, as can be seen in the figure.

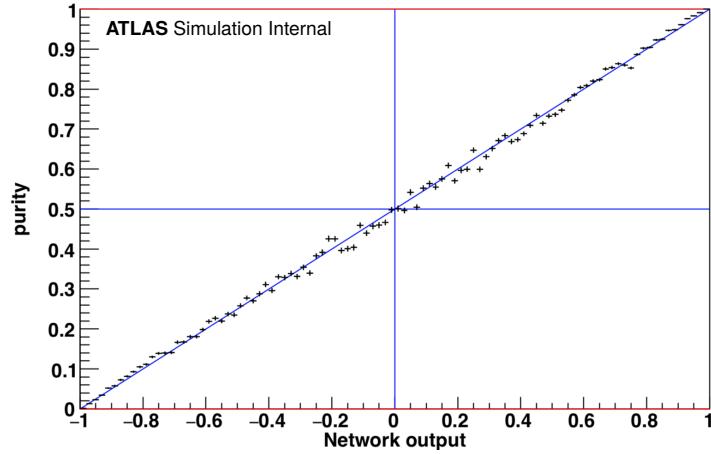
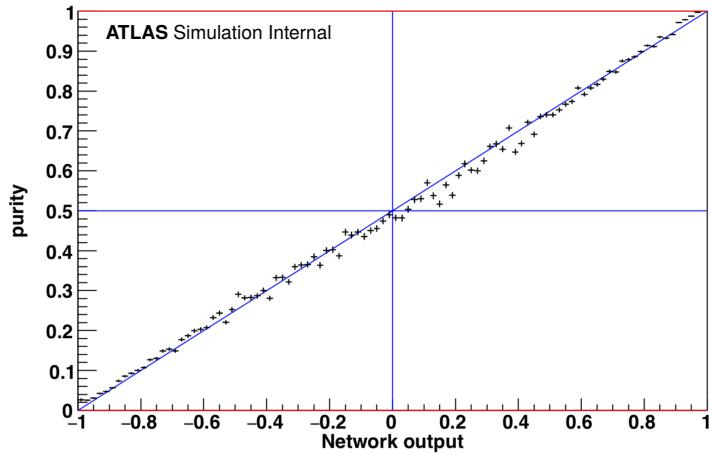


Figure 32: The signal purity as a function of the NN output (top) for the 2 jet SR and (bottom) for 3 jet SR. The expected linear behaviour is observed demonstrating that the network is well trained.

866 **8.2 Input variable distributions**

867 **8.2.1 Input variable normalised distributions in the SRs**

868 Figures 33 and 34 and Figs. 35 and 36 show the distributions of the input variables, normalised to unity, for  
869 the 2j1b SR and 3j1b SR, respectively. The shapes for the backgrounds with fake lepton contributions are  
870 taken from the  $b$ -jet replacement method (see Section 6).

Not reviewed, for internal circulation only

Not reviewed, for internal circulation only

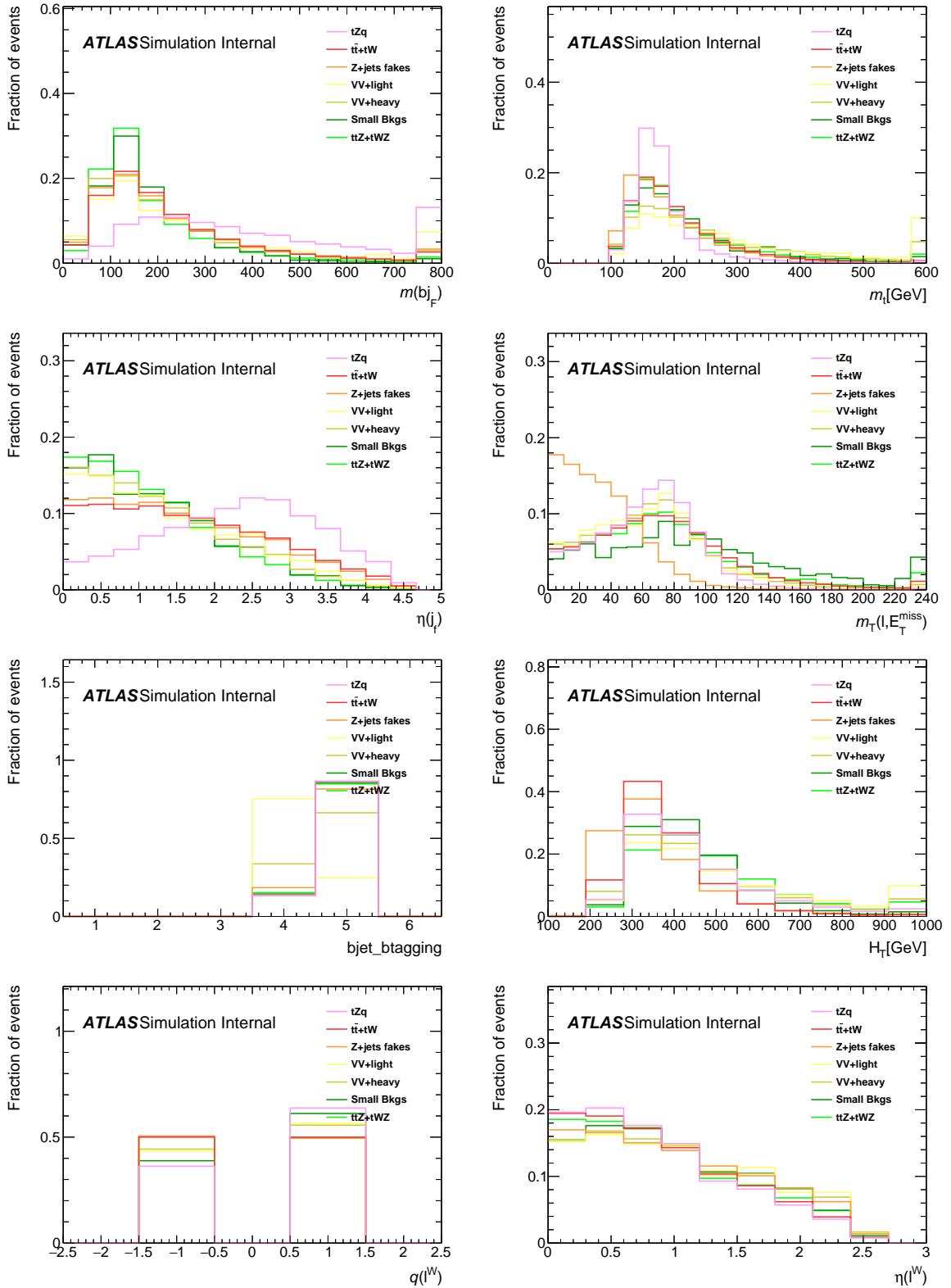


Figure 33: Normalised kinematic plots of neural-network training variables of the 2j1b SR, in order of significance. ‘bjet\_btagging’ refers to the pseudo-continuous b-tagging score.

Not reviewed, for internal circulation only

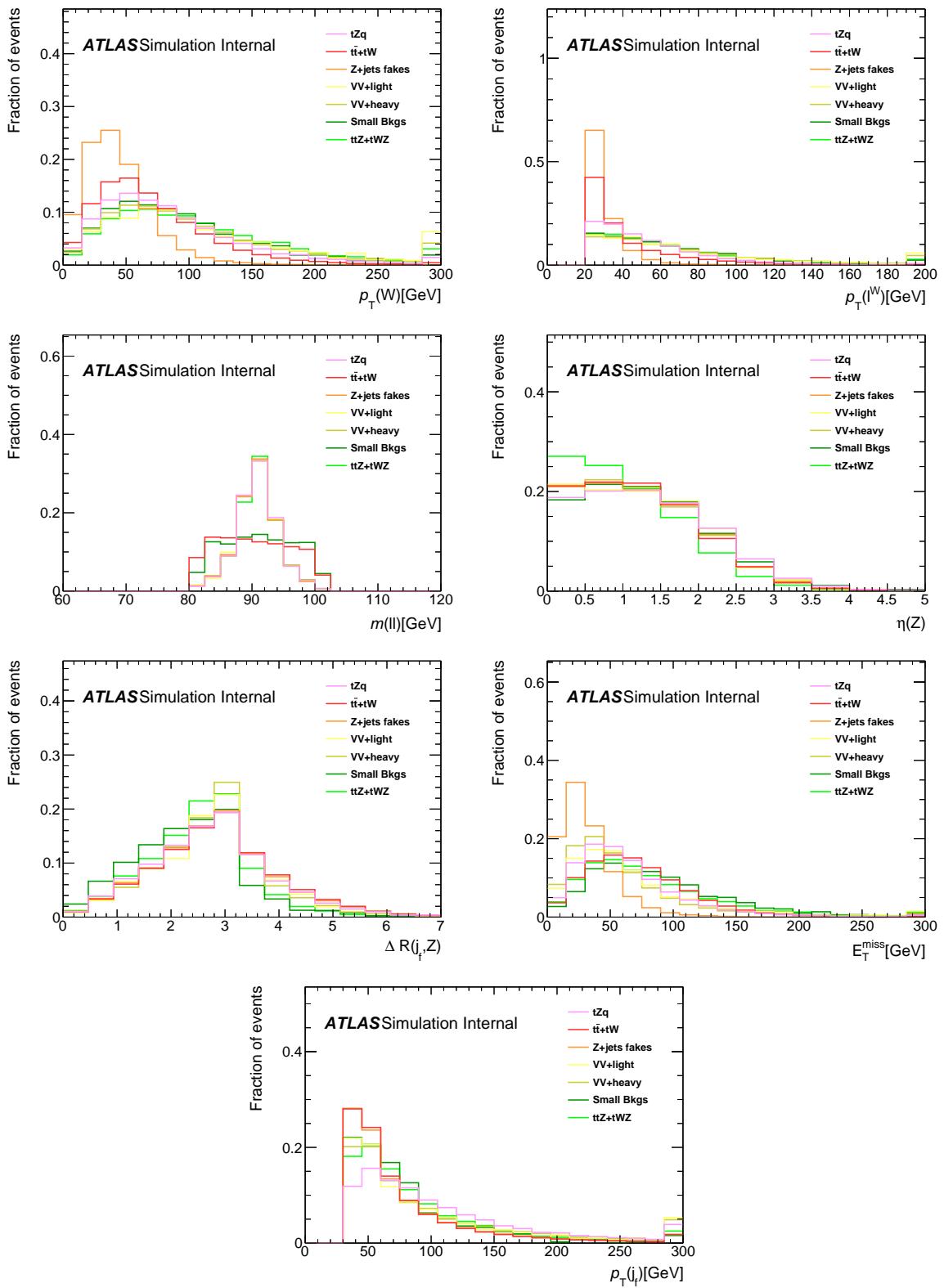


Figure 34: Normalised kinematic plots of neural-network training variables of the 2j1b SR, in order of significance.

Not reviewed, for internal circulation only

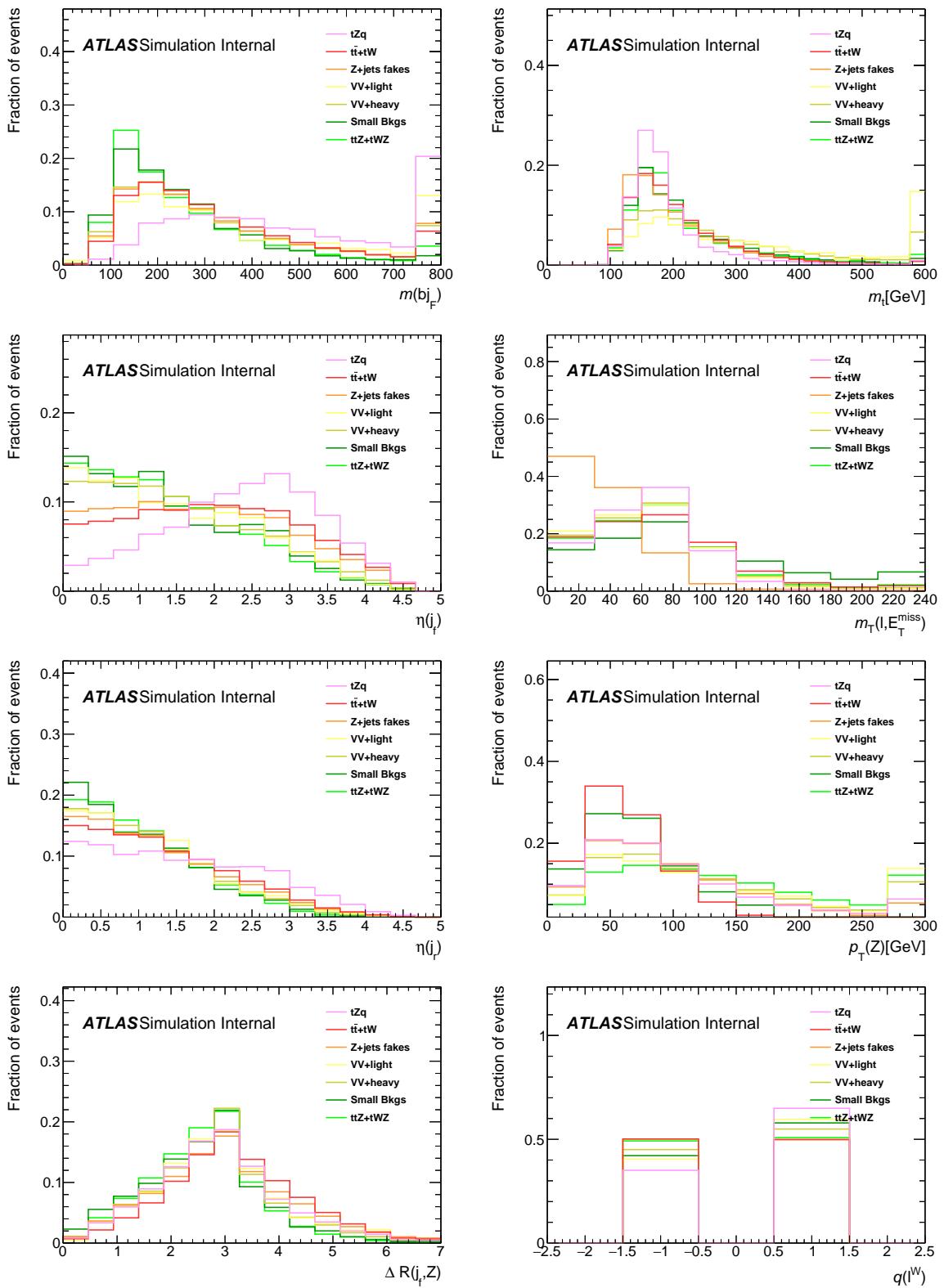


Figure 35: Normalised kinematic plots of neural-network training variables of the 3j1b SR, in order of significance.

Not reviewed, for internal circulation only

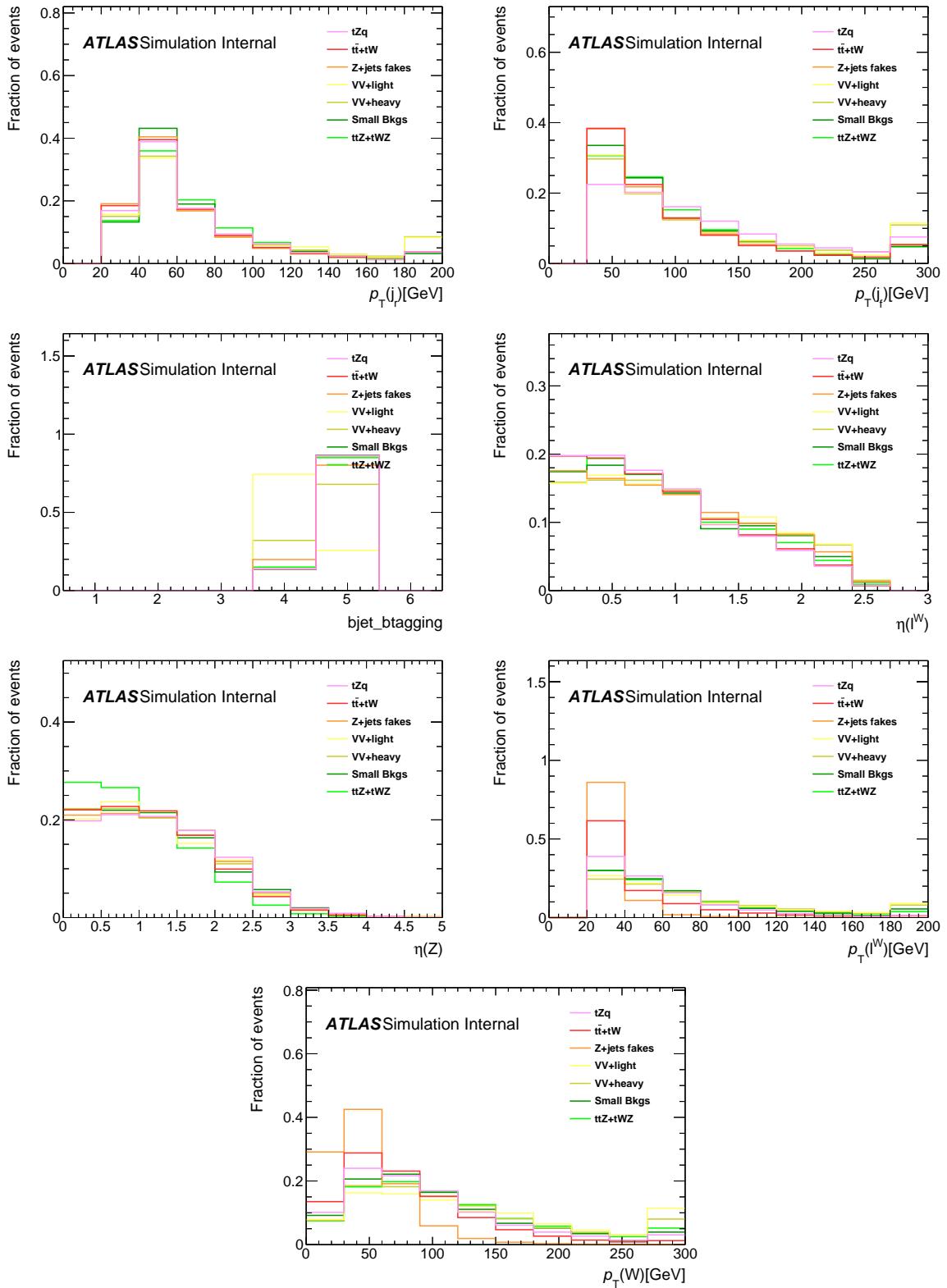


Figure 36: Normalised kinematic plots of neural-network training variables of the 3j1b SR, in order of significance. ‘bjet\_btagging’ refers to the pseudo-continuous b-tagging score.

871 **8.2.2 Input variable distributions in the SRs**

872 Figures 37 and 38 and Figs. 39 and 40 show the distributions of the input variables, scaled to the expected  
873 number of events for the 2j1b SR and 3j1b SR, respectively.

[Not reviewed, for internal circulation only]

Not reviewed, for internal circulation only

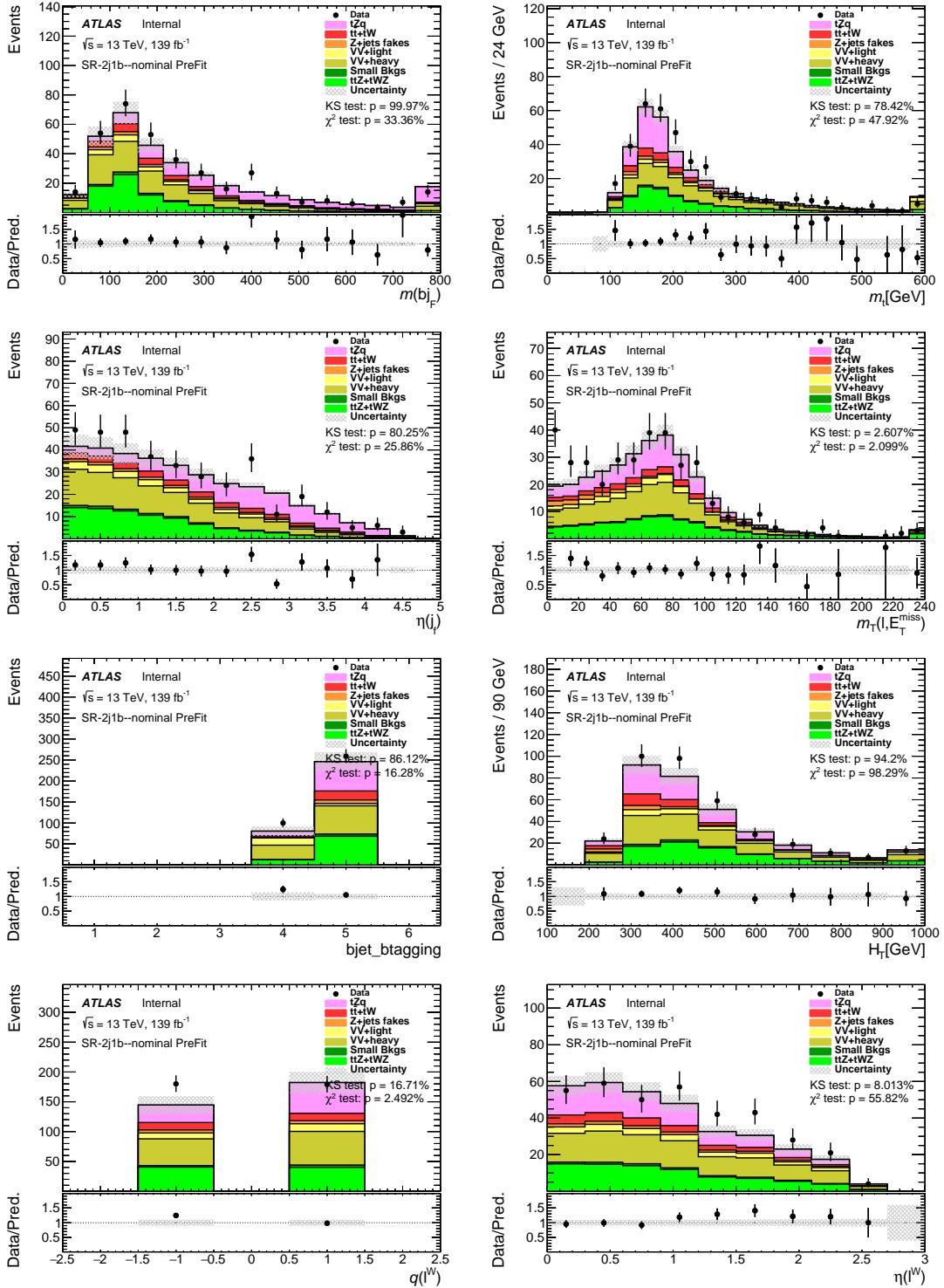


Figure 37: Stacked kinematic plots of neural-network training variables of the 2j1b SR, in order of significance. ‘bjet\_bttagging’ refers to the pseudo-continuous b-tagging score. Both signal and backgrounds are normalised to the expected number of events before the fit. The uncertainty band includes statistical uncertainties for signal and backgrounds and background normalization uncertainties due to the prior assumptions and the modeling systematics, with the exception of  $t\bar{t}$  and  $Z + \text{jets}$ , where only the statistical uncertainties are shown.

Not reviewed, for internal circulation only

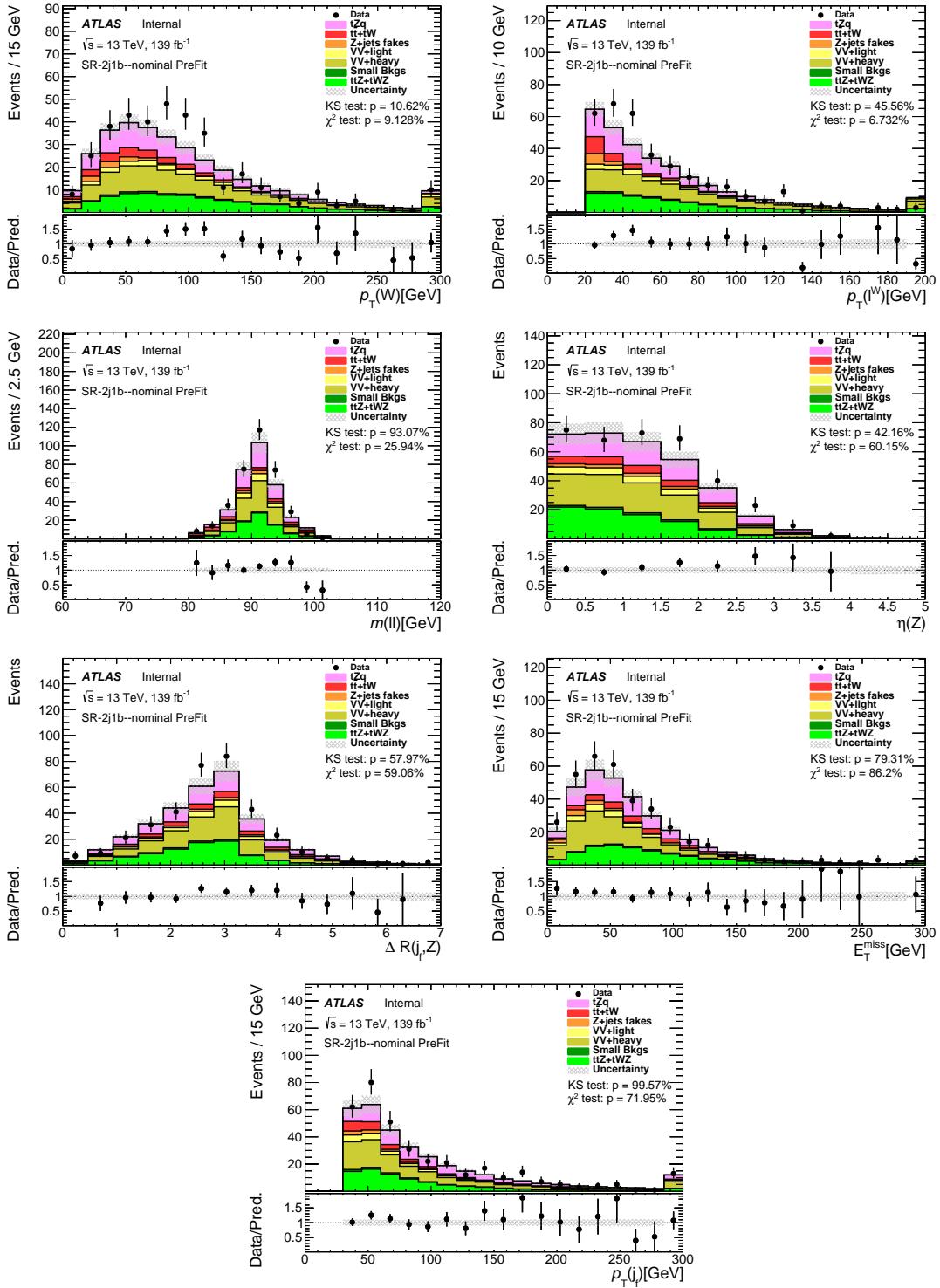


Figure 38: Stacked kinematic plots of neural-network training variables of the 2j1b SR, in order of significance. Both signal and backgrounds are normalised to the expected number of events before the fit. The uncertainty band includes statistical uncertainties for signal and backgrounds and background normalization uncertainties due to the prior assumptions and the modeling systematics, with the exception of  $t\bar{t}$  and  $Z + \text{jets}$ , where only the statistical uncertainties are shown.

Not reviewed, for internal circulation only

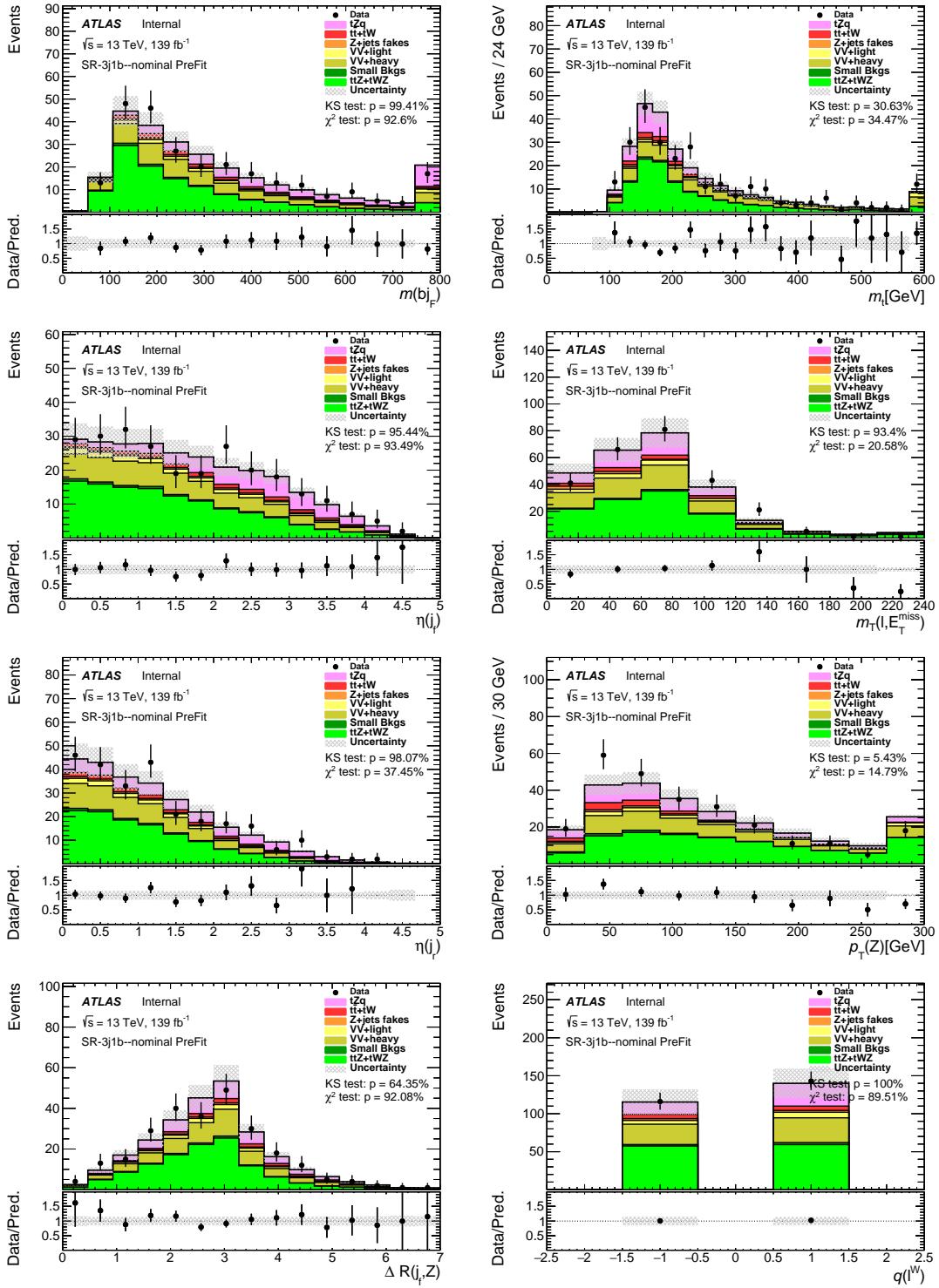


Figure 39: Stacked kinematic plots of neural-network training variables of the 3j1b SR, in order of significance. Both signal and backgrounds are normalised to the expected number of events before the fit. The uncertainty band includes statistical uncertainties for signal and backgrounds and background normalization uncertainties due to the prior assumptions and the modeling systematics, with the exception of  $t\bar{t}$  and  $Z + \text{jets}$ , where only the statistical uncertainties are shown.

Not reviewed, for internal circulation only

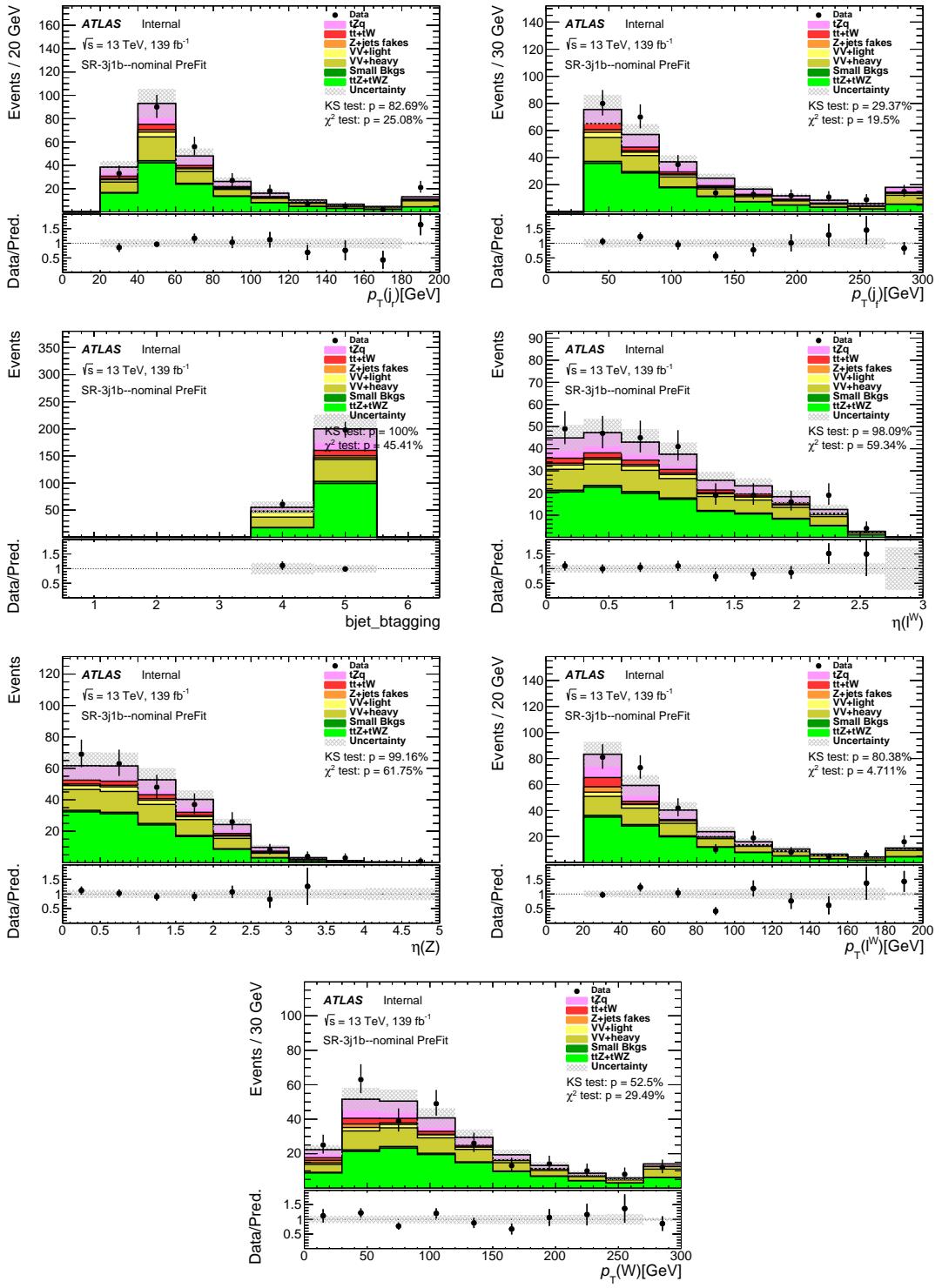


Figure 40: Stacked kinematic plots of neural-network training variables of the 3j1b SR, in order of significance. ‘bjet\_btagging’ refers to the pseudo-continuous b-tagging score. Both signal and backgrounds are normalised to the expected number of events before the fit. The uncertainty band includes statistical uncertainties for signal and backgrounds and background normalization uncertainties due to the prior assumptions and the modeling systematics, with the exception of  $t\bar{t}$  and  $Z + \text{jets}$ , where only the statistical uncertainties are shown.

<sup>874</sup> **8.2.3 Input variable distributions for the diboson VRs**

[Not reviewed, for internal circulation only]

Not reviewed, for internal circulation only

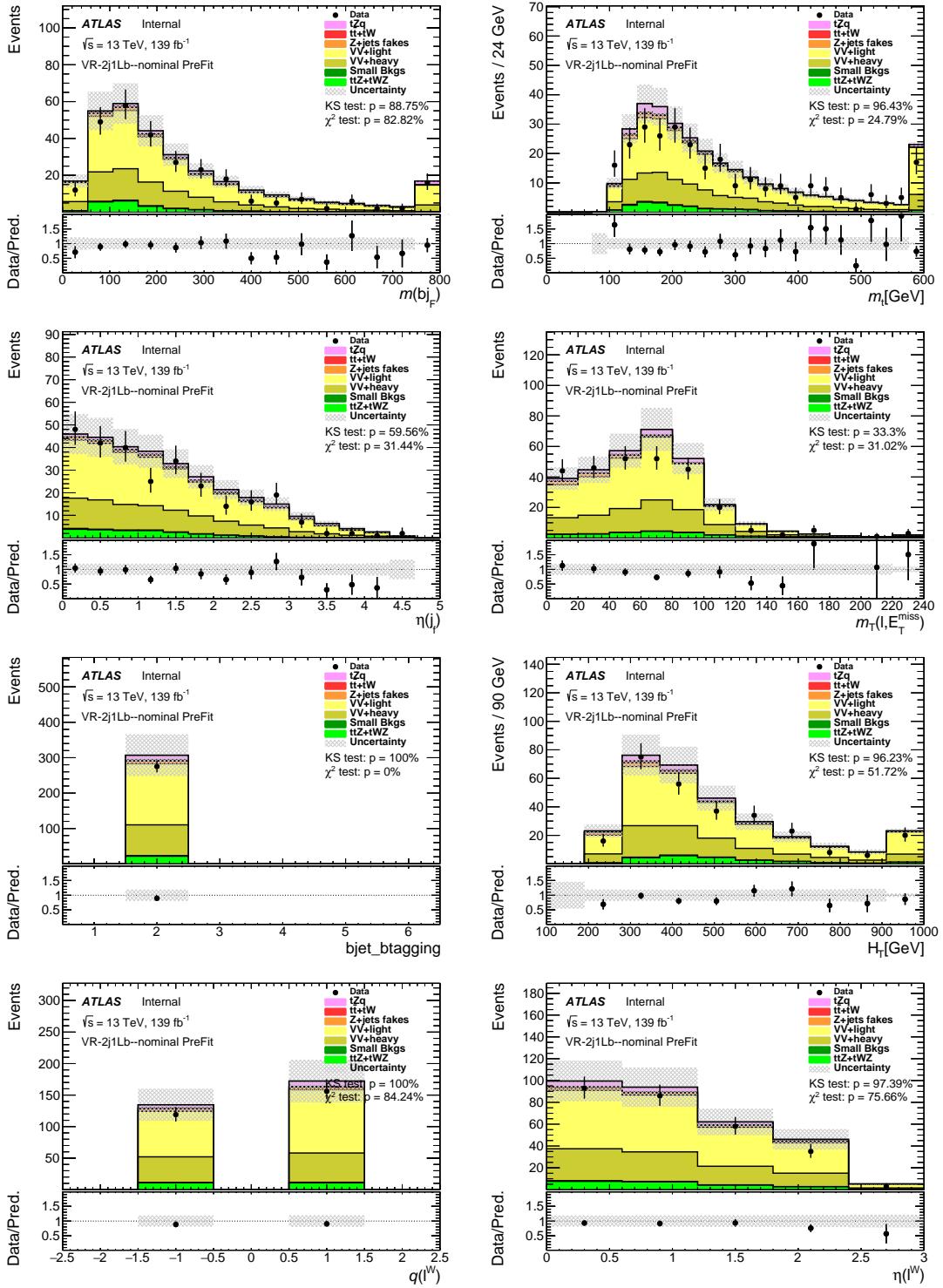


Figure 41: Stacked kinematic plots of neural-network training variables of the diboson 2j1Lb VR, in order of significance. ‘bjet\_bttagging’ refers to the pseudo-continuous b-tagging score. Both signal and backgrounds are normalised to the expected number of events before the fit. The uncertainty band includes statistical uncertainties for signal and backgrounds and background normalization uncertainties due to the prior assumptions and the modeling systematics, with the exception of  $t\bar{t}$  and  $Z + \text{jets}$ , where only the statistical uncertainties are shown.

Not reviewed, for internal circulation only

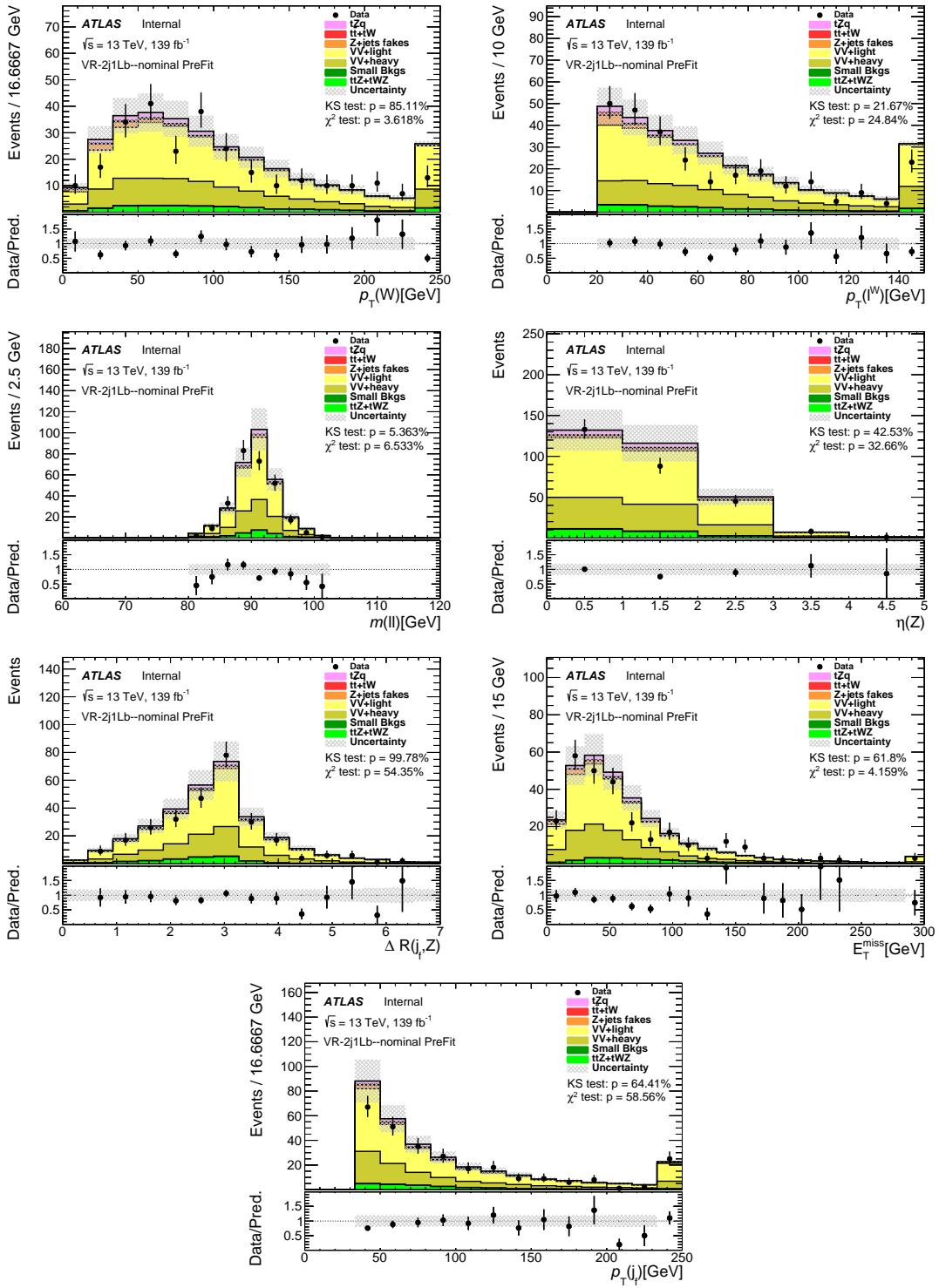


Figure 42: Stacked kinematic plots of neural-network training variables of the diboson 2j1Lb VR, in order of significance. Both signal and backgrounds are normalised to the expected number of events before the fit. The uncertainty band includes statistical uncertainties for signal and backgrounds and background normalization uncertainties due to the prior assumptions and the modeling systematics, with the exception of  $t\bar{t}$  and  $Z + \text{jets}$ , where only the statistical uncertainties are shown.

Not reviewed, for internal circulation only

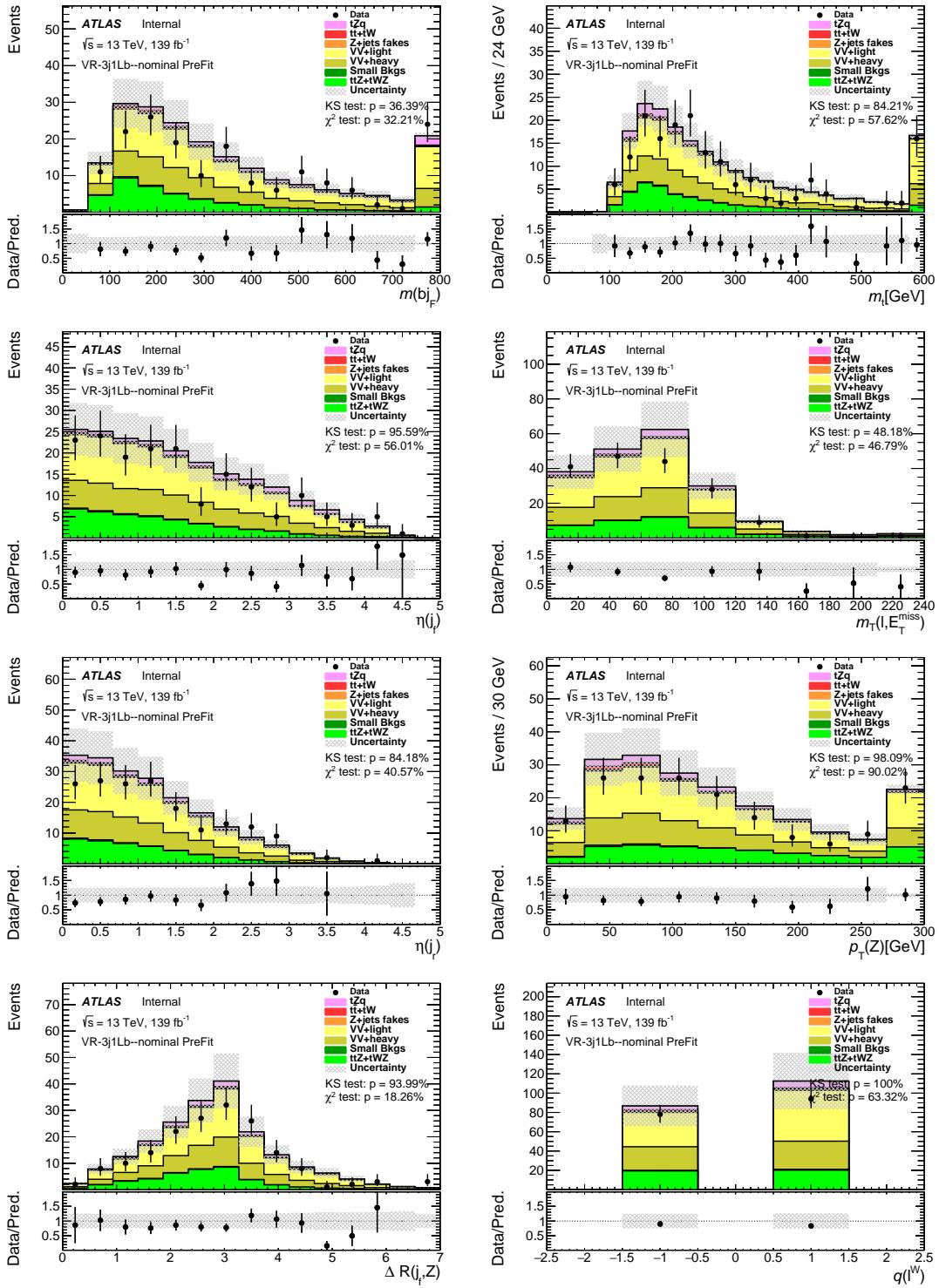


Figure 43: Stacked kinematic plots of neural-network training variables of the diboson 3j1Lb VR, in order of significance. Both signal and backgrounds are normalised to the expected number of events before the fit. The uncertainty band includes statistical uncertainties for signal and backgrounds and background normalization uncertainties due to the prior assumptions and the modeling systematics, with the exception of  $t\bar{t}$  and  $Z + \text{jets}$ , where only the statistical uncertainties are shown.

Not reviewed, for internal circulation only

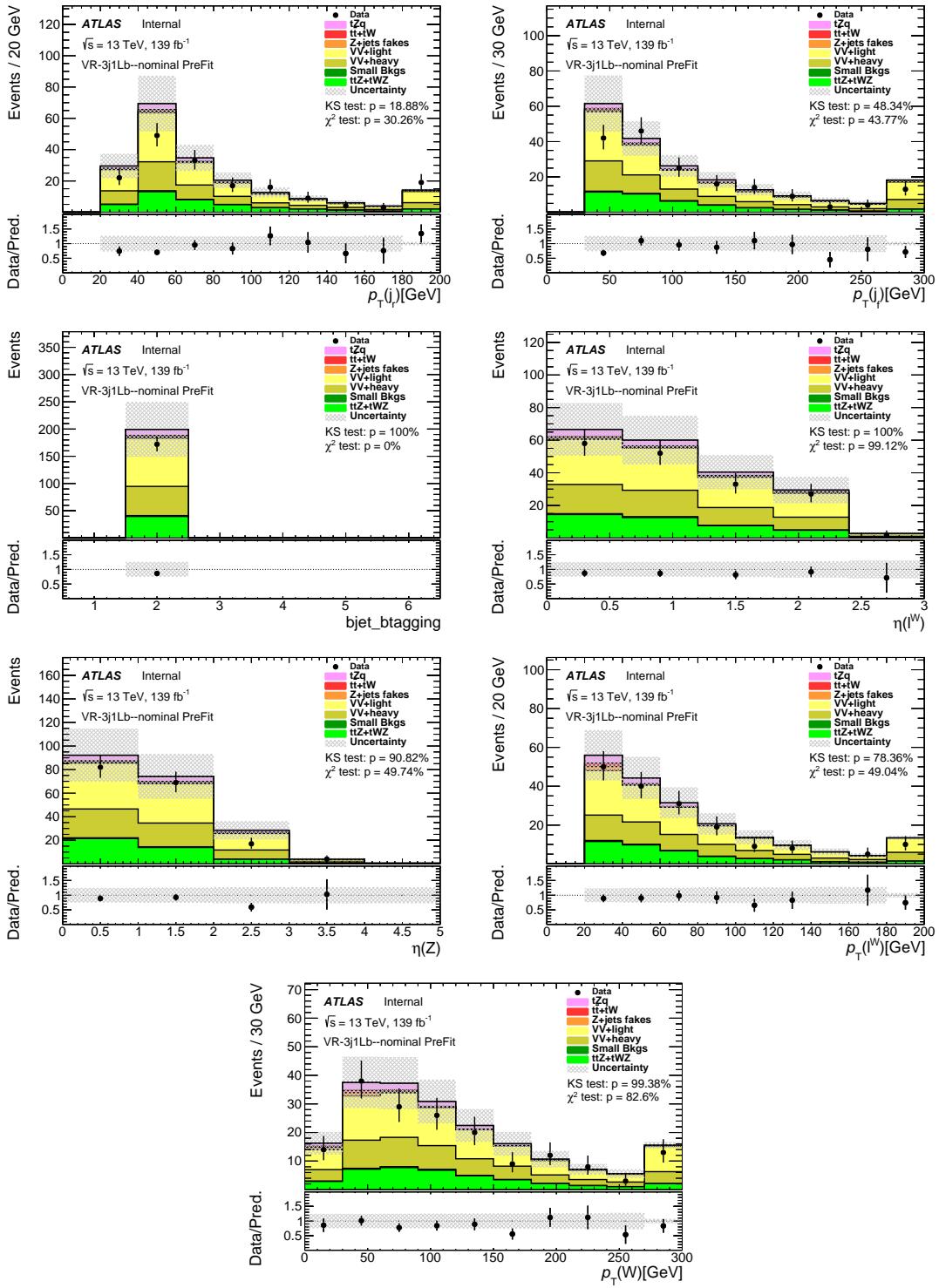


Figure 44: Stacked kinematic plots of neural-network training variables of the diboson 3j1Lb VR, in order of significance. ‘bjet\_bttagging’ refers to the pseudo-continuous b-tagging score. Both signal and backgrounds are normalised to the expected number of events before the fit. The uncertainty band includes statistical uncertainties for signal and backgrounds and background normalization uncertainties due to the prior assumptions and the modeling systematics, with the exception of  $t\bar{t}$  and  $Z + \text{jets}$ , where only the statistical uncertainties are shown.

875 **8.2.4 Input variable distributions for the  $t\bar{t}V + t\bar{t}$  VRs**

[Not reviewed, for internal circulation only]

Not reviewed, for internal circulation only

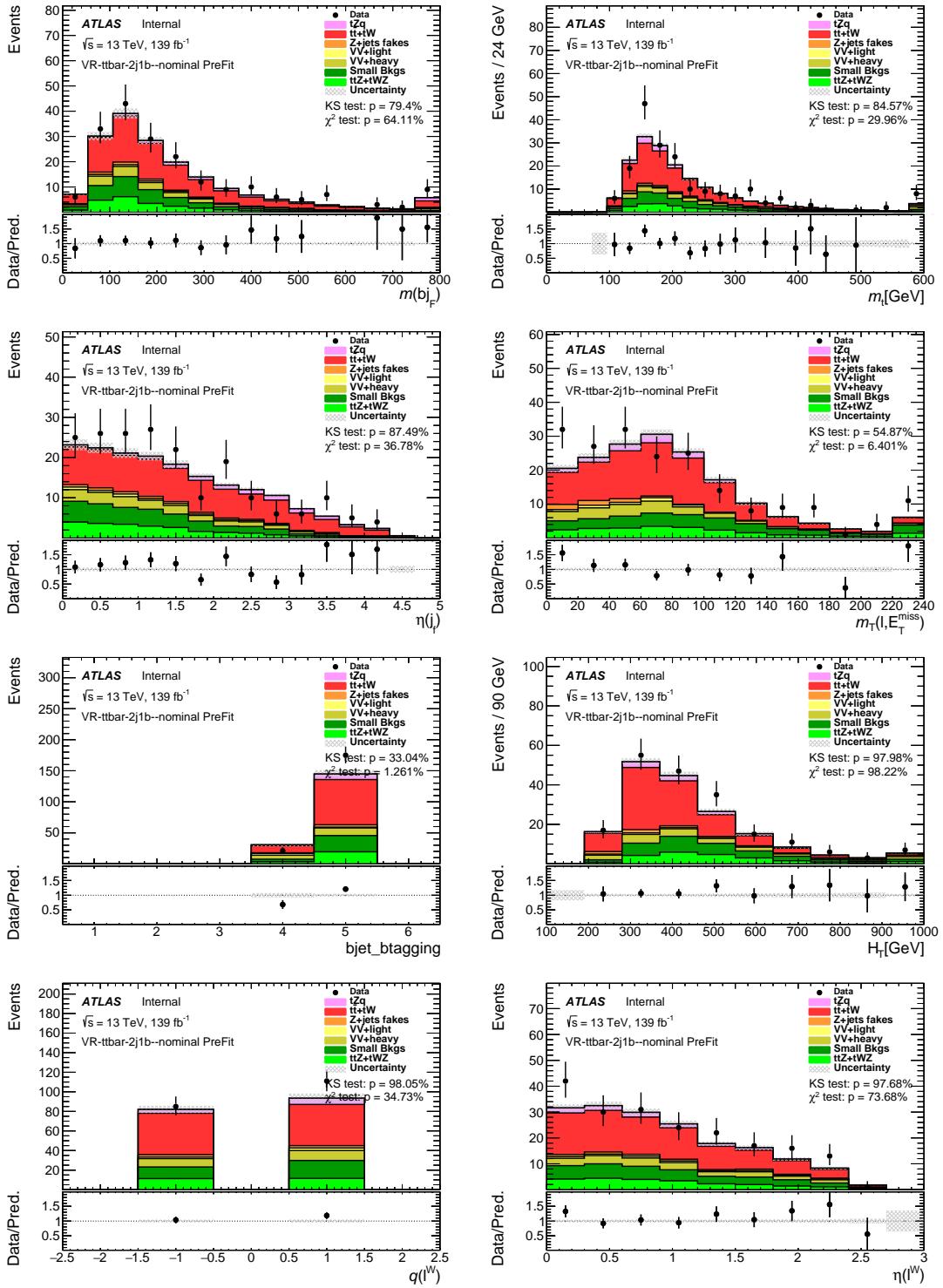


Figure 45: Stacked kinematic plots of neural-network training variables of the  $t\bar{t}V + t\bar{t}2j1b$  VR, in order of significance. ‘bjet\_btagging’ refers to the pseudo-continuous b-tagging score. Both signal and backgrounds are normalised to the expected number of events before the fit. The uncertainty band includes statistical uncertainties for signal and backgrounds and background normalization uncertainties due to the prior assumptions and the modeling systematics, with the exception of  $t\bar{t}$  and  $Z + \text{jets}$ , where only the statistical uncertainties are shown.

Not reviewed, for internal circulation only

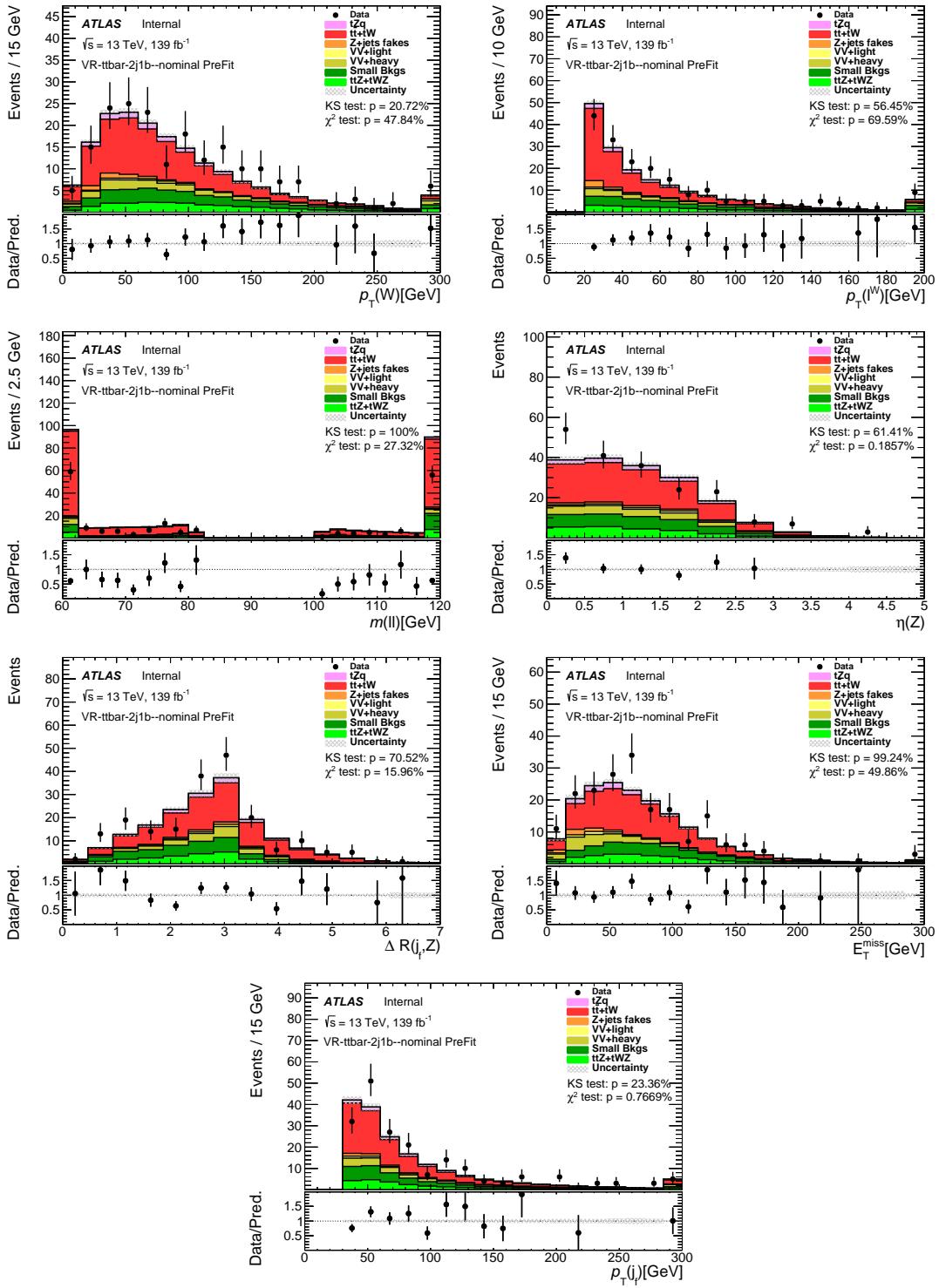


Figure 46: Stacked kinematic plots of neural-network training variables of the  $t\bar{t}V + t\bar{t}2j1b$  VR, in order of significance. Both signal and backgrounds are normalised to the expected number of events before the fit. The uncertainty band includes statistical uncertainties for signal and backgrounds and background normalization uncertainties due to the prior assumptions and the modeling systematics, with the exception of  $t\bar{t}$  and  $Z + \text{jets}$ , where only the statistical uncertainties are shown.

Not reviewed, for internal circulation only

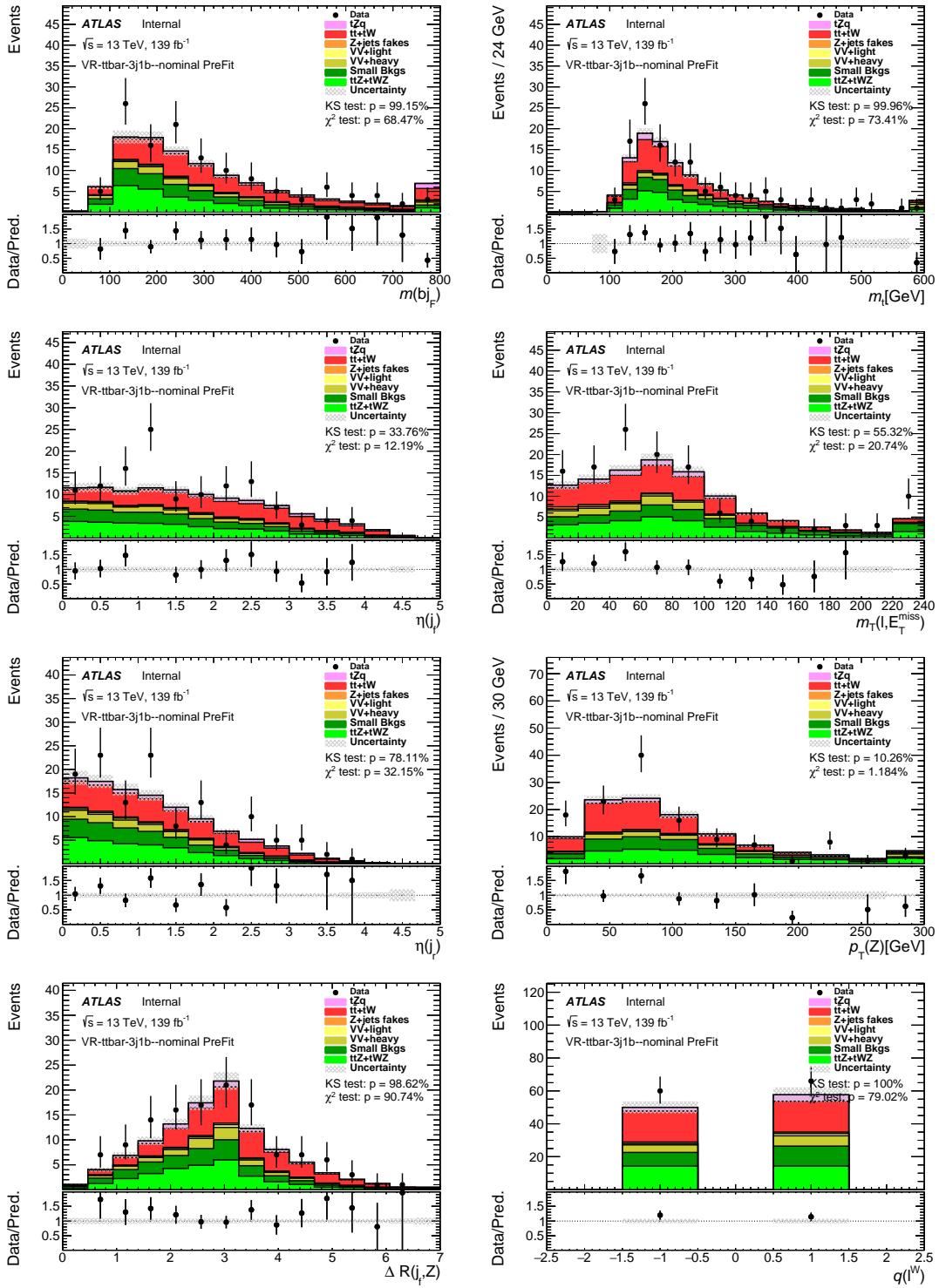


Figure 47: Stacked kinematic plots of neural-network training variables of the  $t\bar{t}V + t\bar{t}3j1b$  VR, in order of significance. Both signal and backgrounds are normalised to the expected number of events before the fit. The uncertainty band includes statistical uncertainties for signal and backgrounds and background normalization uncertainties due to the prior assumptions and the modeling systematics, with the exception of  $t\bar{t}$  and  $Z + \text{jets}$ , where only the statistical uncertainties are shown.

Not reviewed, for internal circulation only

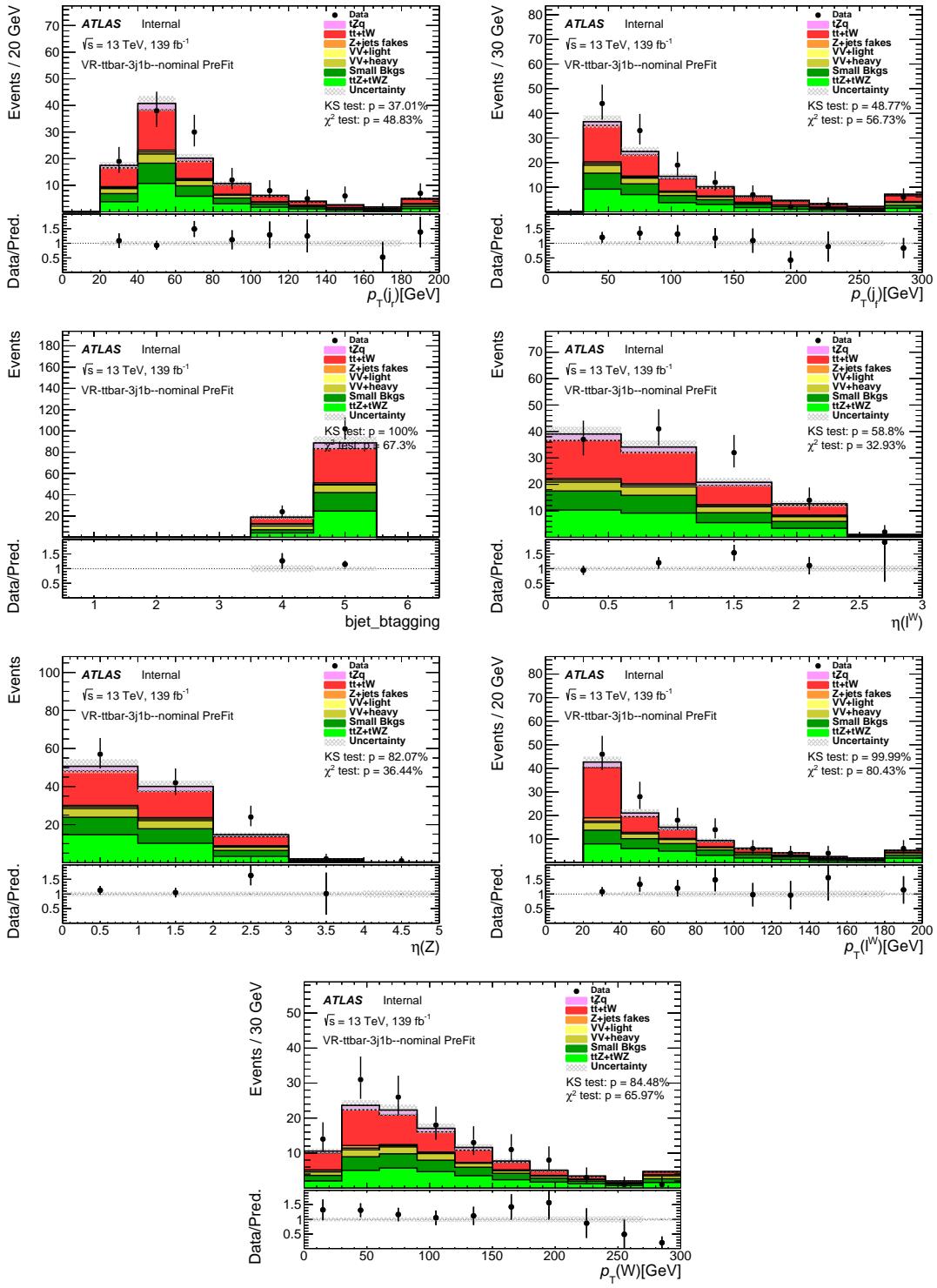


Figure 48: Stacked kinematic plots of neural-network training variables of the  $t\bar{t}V + t\bar{t}3j1b$  VR, in order of significance. ‘bjet\_btagging’ refers to the pseudo-continuous b-tagging score. Both signal and backgrounds are normalised to the expected number of events before the fit. The uncertainty band includes statistical uncertainties for signal and backgrounds and background normalization uncertainties due to the prior assumptions and the modeling systematics, with the exception of  $t\bar{t}$  and  $Z + \text{jets}$ , where only the statistical uncertainties are shown.

876 **8.3 Neural-network output distributions**877 **8.3.1 Neural-network output distributions in the SRs**

878 The distributions of the neural-network output of the 2j1b and 3j1b SRs for signal and backgrounds  
879 separately are shown in Fig. 49 and Fig. 50, respectively. A good separation between the signal and  
880 backgrounds is seen, demonstrating that using the neural network should lead to an improved cross-section  
881 measurement. In addition, the plot shows no significant difference between the training and test distributions  
882 which means that the NN did not suffer from overtraining. The separation power of the neural-network can  
883 be quantified in Gini index, which is approximately one half of the area under the receiver operating curve.  
884 The Gini index for the 2j1b region is 37.6% and for the 3j1b region is 37.5%.

885 Figure 52 shows the output of the NN, both the 2j1b and 3j1b SRs.

Not reviewed, for internal circulation only

Not reviewed, for internal circulation only

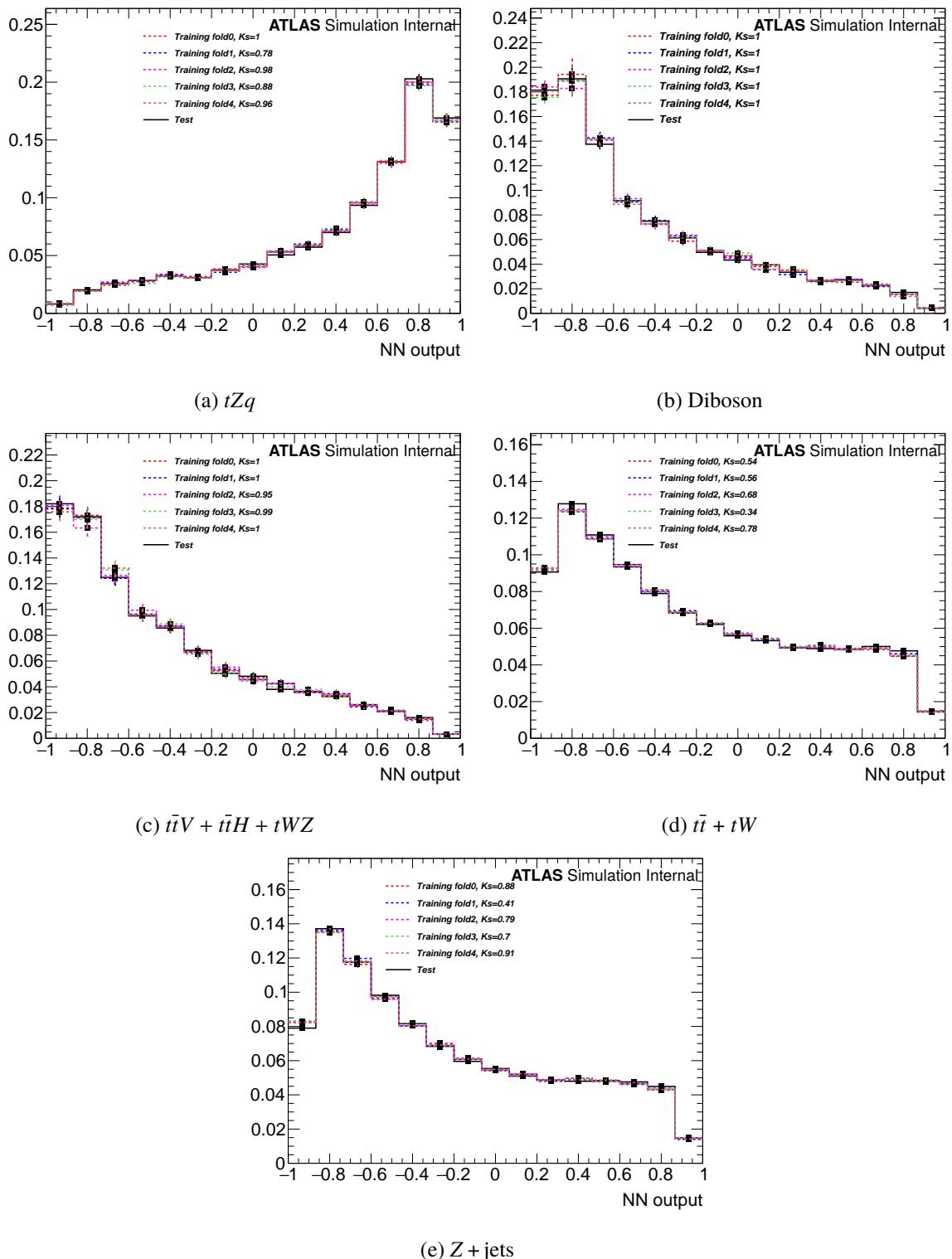


Figure 49: Neural-network training and test output distributions of the 2j1b SR normalised to unity. The black solid line is created from the test sample and the hashed lines created from the training samples.

Not reviewed, for internal circulation only

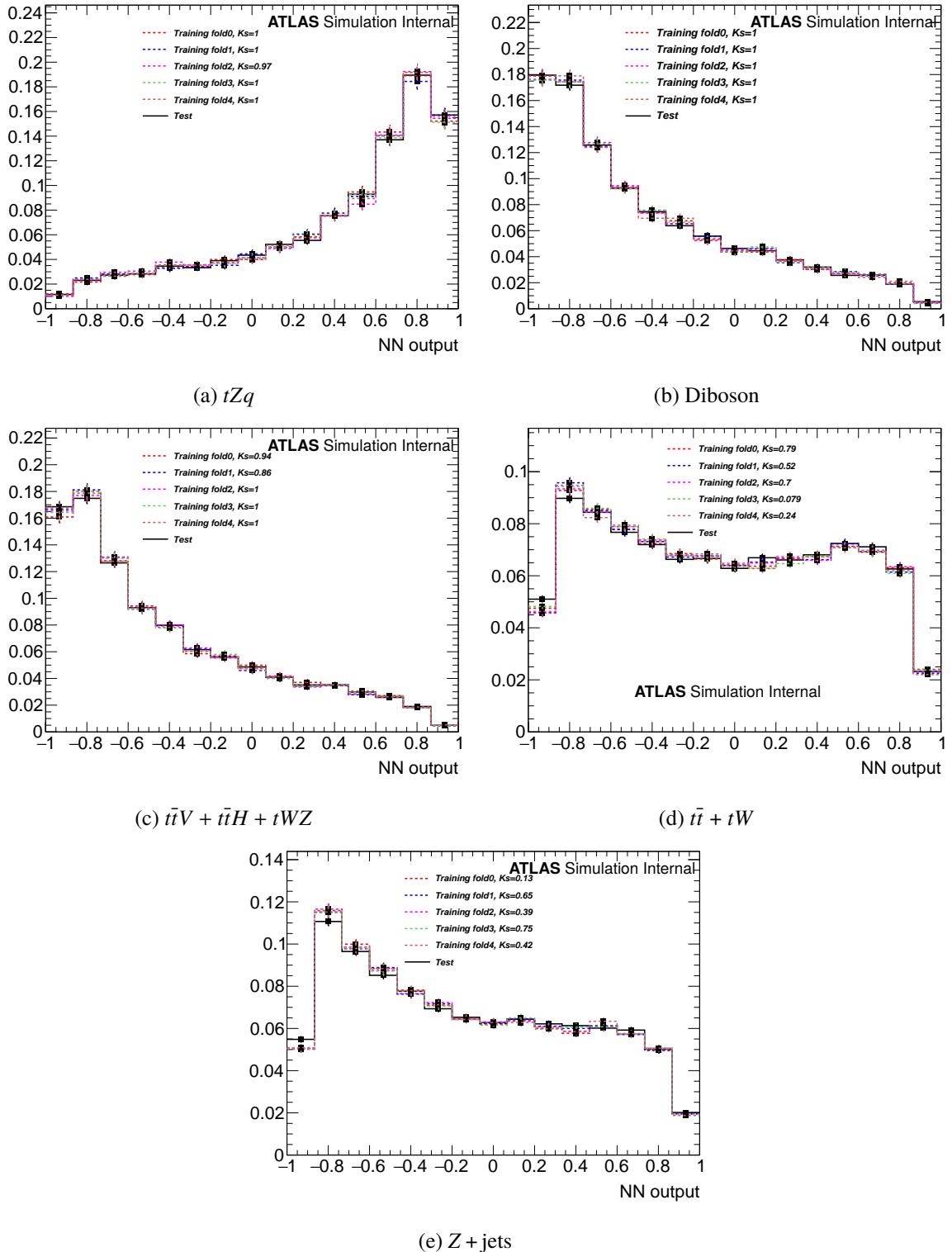


Figure 50: Neural-network training and test output distributions of the 3j1b SR normalised to unity. The black solid line is created from the test sample and the hashed lines created from the training samples.

Not reviewed, for internal circulation only

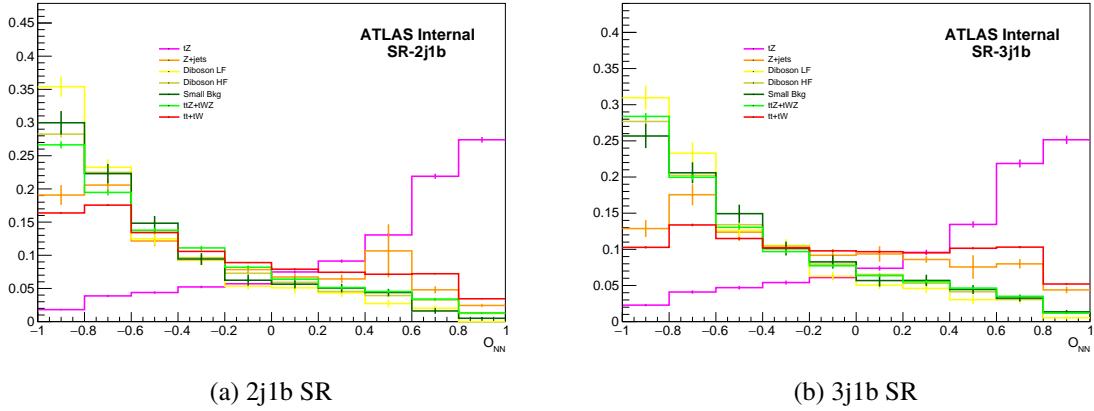


Figure 51: Shapes of the NN output in the SRs, in the 2j1b SR (left) and in the 3j1b SR (right).

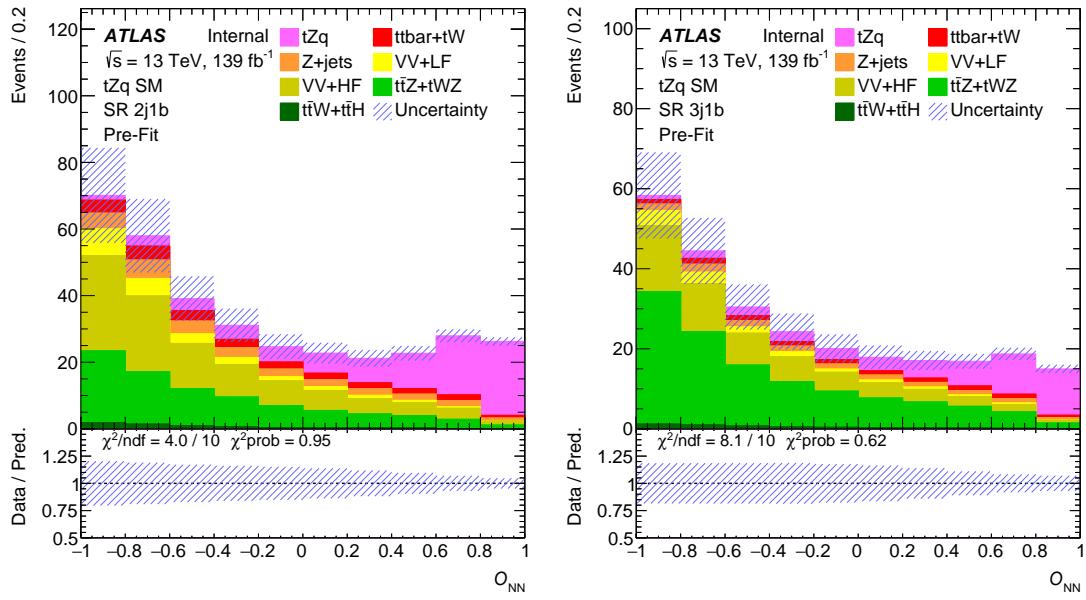


Figure 52: Output of the NN in the SRs, in the 2j1b SR (left) and in the 3j1b SR (right). The uncertainty band includes both statistical and systematic uncertainties.

### 886 8.3.2 Neural-network output distributions in the VRs

887 The NN trained in the SRs are applied on the events selected in both the the diboson and  $t\bar{t}V + t\bar{t}$  validation  
 888 regions using the same variables. The undefined variables due to the missing jets, etc. are replaced by  
 889 -999 value, and since this value has never seen during the NN trainings then that variable is not used by  
 890 NeuroBayes during the evaluation, the same argument is valid for the variables that have different range  
 891 such as  $b$ -tagging score. This test is meant to compare the observed distributions of the kinematic variables  
 892 and their correlations to the model of simulated events by using a none linear transformation applied  
 893 equally on data and MC, signal and background.

894 The output distributions of the data and all background and signal processes scaled to their predicted  
 895 numbers of events can be seen in Fig. 53 for the diboson VRs and in Fig. 54 for the  $t\bar{t}$  VRs.

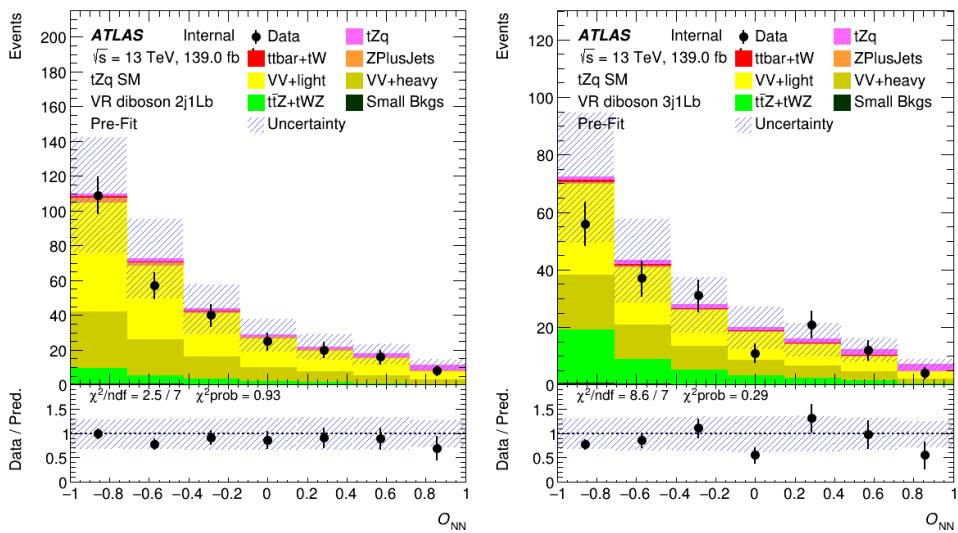


Figure 53: Neural-network output distribution of the events in the diboson VRs. Both signal and backgrounds are normalised to the expected number of events before the fit. The uncertainty band includes both statistical and systematic uncertainties.

Not reviewed, for internal circulation only

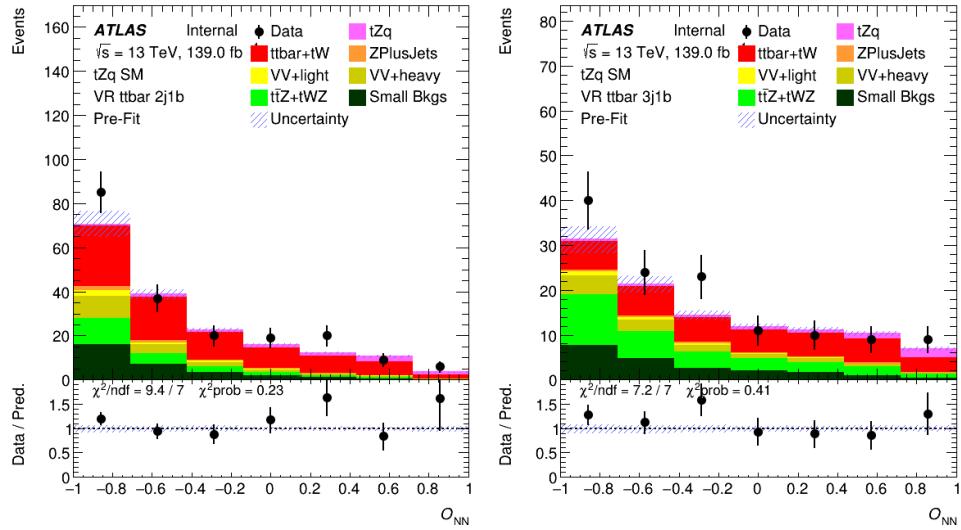


Figure 54: Neural-network output distribution of the events in the  $t\bar{t}V + t\bar{t}$  VRs. Both signal and backgrounds are normalised to the expected number of events before the fit. The uncertainty band includes both statistical and systematic uncertainties. Since the  $t\bar{t}$  background is free floating in the fit, there are no uncertainties on this background pre-fit.

## 896 9 Systematic uncertainties

### 897 9.1 Sources of systematic uncertainties

898 Many sources of systematic uncertainties are considered in the extraction of the  $tZq$  cross section. The  
 899 systematic uncertainties are evaluated using the common top group prescription and standard ATLAS  
 900 procedures. Systematic uncertainties are considered for the normalisation of the individual backgrounds  
 901 and the signal acceptance from various sources and standard ATLAS procedures as implemented in  
 902 `AnalysisTop-21.2.58`.

903 **Object energy scale/resolution and efficiencies:** Systematic uncertainties due to residual differences  
 904 between data and Monte Carlo simulations, for jets, electron and muon reconstruction after calibration, as  
 905 well as uncertainties on the calibration scale factors are propagated to the event yields and observables.

- 906 • **Lepton reconstruction:**

907 The mis-modelling of muon (electron) trigger, reconstruction and selection efficiencies in simulation  
 908 is corrected by introducing scale factors derived from measured efficiencies in data.  $Z \rightarrow \mu^+ \mu^-$   
 909 ( $Z \rightarrow e^+ e^-$ ) decays are used to obtain scale factors as functions of the lepton kinematics. The  
 910 uncertainties are evaluated by varying the lepton and signal selections and from the uncertainties in  
 911 the backgrounds evaluations.

- 912 • **Lepton momentum scale and resolution:**

913 The  $Z \rightarrow \ell\ell$  processes are used to measure the lepton momentum scale and resolution. Calibration  
 914 factors and associated uncertainties are derived to match the simulation to observed distributions  
 915 in collision data. The effect of momentum scale uncertainties is evaluated by repeating the event  
 916 selection after varying the lepton momentum up by  $1\sigma$  and down by  $1\sigma$ . For the momentum  
 917 resolution uncertainties the event selection is repeated by smearing the lepton momentum [60].

- 918 • **Jet energy scale (JES):**

919 The JES was derived using information from test-beam data, LHC collision data and simulation.  
 920 The JES calibration consists of several steps that account for detector problems, jet reconstruction  
 921 algorithms, jet fragmentation models, dense data-taking environment from high pile-up conditions  
 922 and response difference between data and MC simulation. The fractional uncertainty decreases  
 923 with the  $p_T$  of the reconstructed jet and is rather stable in  $\eta$  [61]. The JES uncertainty has various  
 924 components according to the factors it accounts for and the different steps used to compute it. The  
 925 jet calibration procedure is described in Ref. [62]. The sources of the JES uncertainties and the  
 926 effective number of parameters are summarised in Table 32. To take into account the fact that the  
 927 major backgrounds have different q/g fraction compositions, the JES flavour composition uncertainty  
 928 is decorrelated in the following way:  $VV + LF$ ,  $VV + HF$ ,  $t\bar{t}Z$  and a fourth NP which is correlated  
 929 among all other samples.

- 930 • **Jet energy resolution:**

931 The impact of the uncertainty on the jet energy resolution is evaluated by smearing the jet energy in  
 932 the MC samples. The number of the effective JER NP considered is 8.

- 933 • **Jet vertex tagger:**

934 The uncertainty for the JVT requirement is also applied. This uncertainty is eventually pruned for  
 935 each sample and in each region.

Table 32: Sources of JES uncertainties and the number of NP.

Source	Number of NP
BJES response	1
Detector	2
Mixed	3
Modelling	4
Statistical	6
Eta Intercalibration	5
Flavour composition	5
Pile-up	4
Punchthrough	1
Relative non-closure	1
Single particle high $p_T$	1

936 • **Missing transverse momentum:**

937 Uncertainties of the soft-track component are derived from the level of agreement between data  
 938 and MC simulation of the  $p_T$  balance between the hard and soft  $E_T^{\text{miss}}$  components. Three different  
 939 uncertainties are considered: an offset along the  $p_T$  (hard) axis, as well as the smearing resolution  
 940 along and perpendicular to the  $p_T$  (hard) axis.

941 •  **$b$ -tagging efficiency:**

942 The  $b$ -tagging efficiencies and mis-tag rate for the taggers have been measured in data using the same  
 943 methods as described in [63, 64]. The number of NP used for the  $b$ -tagging efficiencies is 45 while  
 944 the NP used for  $c$  and light quark jets mis-tag rates are 20 and 20, respectively. The impact on the  
 945  $tZq$  cross-section measurement due to the uncertainties of the  $b$ -tagging data/MC scale factors is  
 946 evaluated separately for  $b$ ,  $c$  and light-flavour quark jets in the MC samples.

947 **Monte Carlo modelling and parton densities:** Systematic effects from MC modelling are estimated by  
 948 comparing different generators and varying parameters for the event generation.

949 • **MC modelling uncertainties:**

950 For the signal sample the scale and showering are varied. Generator-level studies showed that the  
 951 settings:  $\mu = 0.5$  and ‘Var3cUp’;  $\mu = 2.0$  and ‘Var3cDown’ provide a reasonable estimate of the  
 952 systematic uncertainty [65]. The size of the effects was determined using AFII MC samples.

953 The effect of changing the MC generator for  $t\bar{t}$  events was investigated, and the difference between  
 954 PowHEG-Box and MADGRAPH5\_aMC@NLO prediction is included as  $t\bar{t}$  NLO matching systematic  
 955 uncertainty. The impact of the parton shower and hadronisation model is evaluated by comparing  
 956 samples generated with PowHEG-Box generator interfaced either with PYTHIA8 or HERWIG7. Scale  
 957 and showering systematics, obtained as for the signal, are also included. All the details about the  
 958 samples used for  $t\bar{t}$  modeling uncertainties are reported in Section 3.2.2.

959 The effect of changing the MC generator for  $t\bar{t}Z$  events was investigated, and the difference between  
 960 MADGRAPH5\_aMC@NLO and SHERPA prediction is included as  $t\bar{t}Z$  generator systematic  
 961 uncertainty. Scale and showering systematics, are also included. To obtain an uncertainties of the  
 962 renormalization and factorization scale, the renormalization and factorization scales values  $\mu_F$  and

963  $\mu_R$  are simultaneously varied by factors of 2.0 and 0.5. The uncertainty associated with the tuning  
 964 of the MC samples is derived by comparing the nominal signal sample to equivalent samples with an  
 965 up/down variation of the Var3c parameter in the A14 tune [17]. All the details about the samples  
 966 used for  $t\bar{t}Z$  modeling uncertainties are reported in Section 3.2.2.

967 The effect of changing the MC generator for diboson events was investigated, and the difference  
 968 between SHERPA and PowHEG-Box prediction is included as diboson generator systematic uncertainty.  
 969 All the details about the samples used for diboson modeling uncertainties are reported in Section 3.2.2.

970 • **PDF uncertainty:**

971 The systematic uncertainties related to the parton distribution functions are taking into account for  
 972 the signal. The events are reweighted according to each of the PDF uncertainty eigenvectors. The  
 973 uncertainties are calculated using the formula given in Equation 43 of Ref. [66]. The uncertainty is  
 974 calculated, following the new PDF4LHC recommendation [67], of the estimated uncertainties for  
 975 the PDF4LHC15 PDF set.

976 • **Monte Carlo statistics:**

977 The uncertainty due to the limited size of the Monte Carlo samples is included.

978 **Background rate uncertainty:** For the backgrounds that are floated in the fit ( $Z + \text{jets}$  and  $t\bar{t}$ ), normalization  
 979 uncertainty of 15 % for  $Z + \text{jets}$  and 7 % for  $t\bar{t}$ . These values correspond to the highest Monte Carlo  
 980 statistical uncertainty of the  $Z + \text{jets}$  and  $t\bar{t}$  samples in SRs and the relevant CRs. Four NPs are added  
 981 for  $Z + \text{jets}$  (one for each SR and one for each diboson CR) and four NPs are added for  $t\bar{t}$  (one for each  
 982 SR and one for each  $t\bar{t}$  CR). The four NPs are de-correlated for each region. The overall  $Z + \text{jets}$  and  $t\bar{t}$   
 983 normalization is one single parameter, but the normalizations in each region has the freedom to move w.r.t.  
 984 the other regions within the MC statistical uncertainty.

985 For the other backgrounds (diboson and  $t\bar{t}Z$ ), the uncertainty on the normalization is kept correlated among  
 986 regions.

987 For  $t\bar{t}Z$ , the normalization uncertainty is taken from [68], where a 12 % theory uncertainty is quoted.

988 For diboson, the normalization uncertainty is taken from ATLAS results [69]. From Figure 6, showing  
 989 the differential cross-section as a function of the number of jets, the uncertainties applied are 20 % for  
 990 the light diboson component and 30 % for the heavy diboson component. The latter is justified by the  
 991 observation that a 30 % normalization scale is obtained for  $V+HF$ , as discussed in [70]. On top of that,  
 992 modeling uncertainties are also used in the fit, as mentioned above.

993 For  $t\bar{t}W$  and  $t\bar{t}H$  a 15 % systematic uncertainty on the normalization is used.

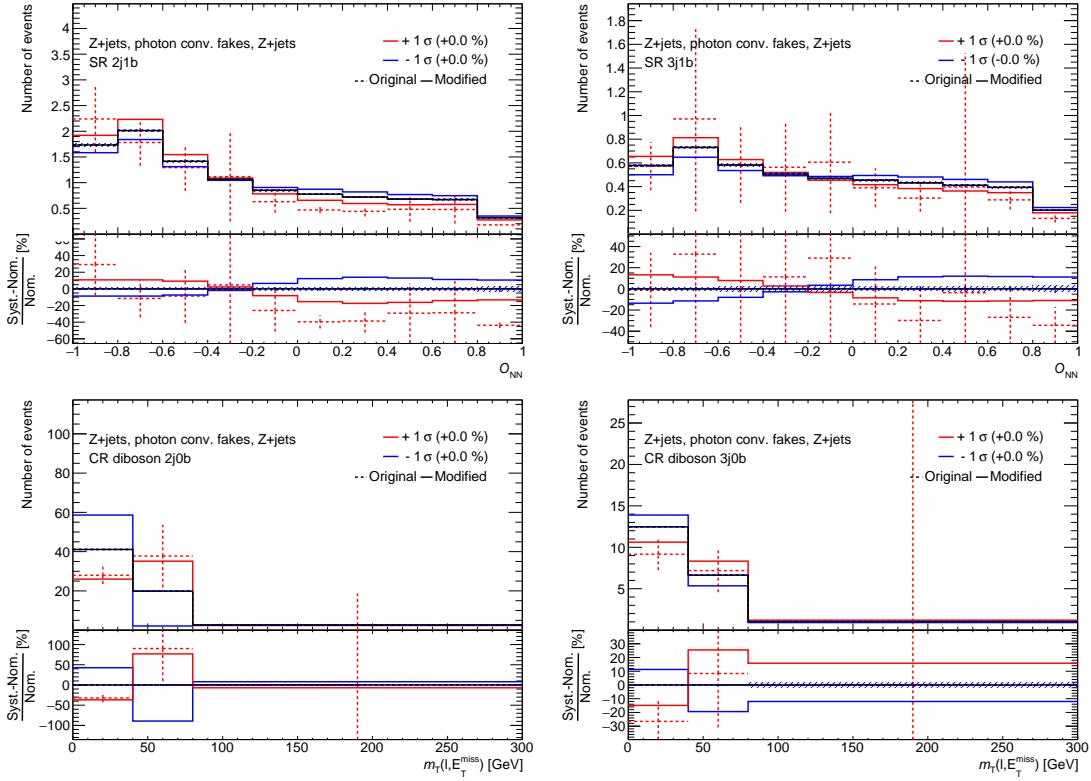
994 The uncertainties used are summarised in Table 33.

995 **BJR shape uncertainty:** To account for the possible slight differences in shape of  $Z + \text{jets}$  events  
 996 originating from sources other than semi-leptonic  $B$  decays, a systematic uncertainty on the shape of the  
 997  $Z + \text{jets}$  distribution is applied. The systematic uncertainty is constructed by comparing the shapes of  
 998 Monte Carlo events from different sources separated by their origin of the fake lepton in the event (e.g.:  
 999 heavy flavor decay, photon conversion, etc.). The magnitude of the difference in the shape, (i.e. bin-by-bin  
 1000 scale factors), is scaled by the relative contribution of non-semi-leptonic  $b$  decays' relative contribution of  
 1001 total  $Z + \text{jets}$  events, which is taken to be approximately 25 % for SR-Xj1b and 50 % for CR-Xj0b. These

Table 33: Uncertainties on the normalisation of all background processes.

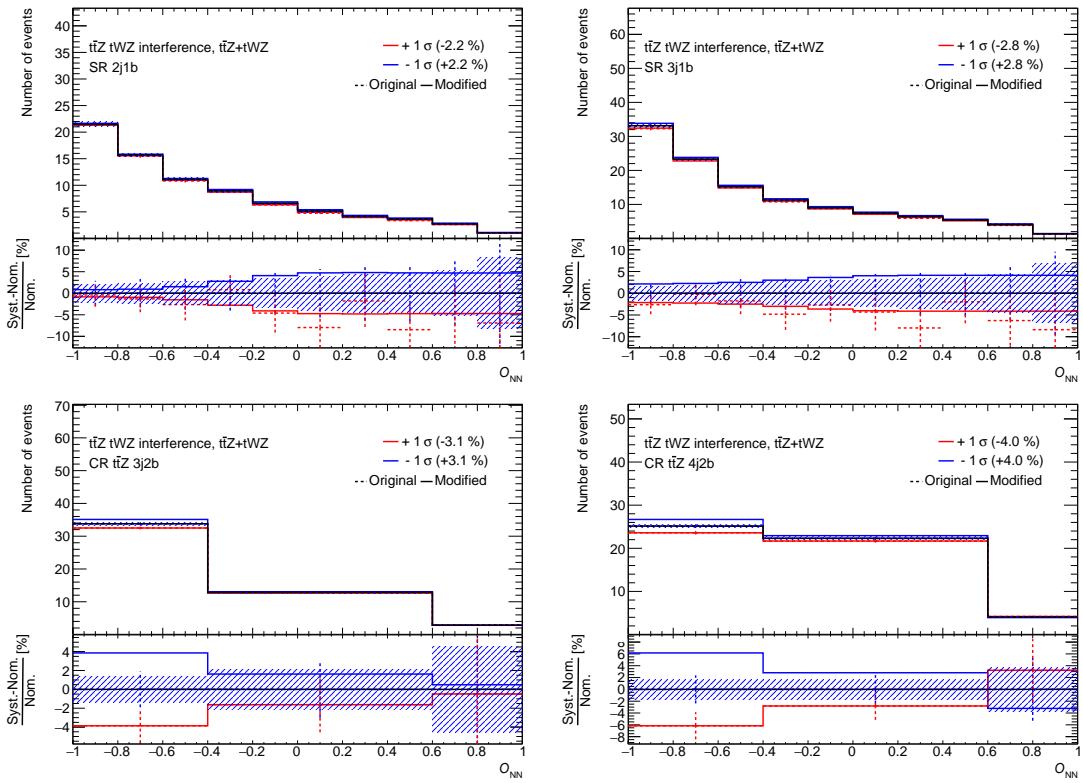
Process	Uncertainty
$t\bar{t}Z$	12 %
Small backgrounds	15 %
$VV + LF$	20 %
$VV + HF$	30 %
$Z + \text{jets}$	15 % (uncorrelated between regions)
$t\bar{t}/ tW\text{-channel}$	7 % (uncorrelated between regions)

1002 weighted scale factors are then applied to the nominal BJR  $Z + \text{jets}$  templates to create a 2 point systematic  
 1003 in the control and signal regions. Theese uncertainties are shown in Fig. 55.

Figure 55:  $Z + \text{jets}$  BJR shape uncertainty.

1004  **$tWZ$  and  $t\bar{t}Z$  interference:** To take into account the interference of the  $tWZ$  and  $t\bar{t}Z$  processes,  $tWZ$   
 1005 samples with DR1 and DR2 interference treatment schemes are compared and the difference used as a  
 1006 systematic uncertainty. The shapes of this uncertainty are shown in Fig. 56.

1007 **Luminosity:** The uncertainty in the combined 2015–2018 integrated luminosity is 1.7 %. It is derived,  
 1008 following a methodology similar to that detailed in Ref. [71], from the calibration of the luminosity scale  
 1009 using  $x$ – $y$  beam-separation scans.

Figure 56:  $tWZ$  DR1/DR2 shape uncertainty.

1010 **Uncertainty on pile-up reweighting:** The uncertainty of the pile-up reweighting in simulated samples  
 1011 is included.

## 1012 9.2 Acceptance and shape uncertainties

1013 The systematic uncertainties discussed above cause variations on the signal acceptance, the background  
 1014 rates, and the shape of the distributions that are fed to the fit. We denote the relative variation of the  
 1015 acceptance of process  $j$  due to a systematic source  $i$   $\alpha_{ij+}$  and  $\alpha_{ij-}$  for a positive or negative variation of the  
 1016 systematic uncertainty.

1017 The only systematic uncertainty that has acceptance uncertainty without a shape is luminosity.

1018 The MC statistics is related to the statistical uncertainty in each bin of the distributions that are used  
 1019 in the fit, so it can change the shape of the distributions. For all other systematics listed, rate and shape  
 1020 differences are taken into account.

1021 The values of the uncertainties in terms of the fraction of the nominal value that are input to the fit are  
 1022 given in ????.

1023 **Smoothing and symmetrisation of shape uncertainties:** Due to low statistics shape systematic uncer-  
 1024 tainties can suffer from fluctuations in individual bins. A smoothing of systematic shape uncertainties is

1025 performed using the default smoothing algorithm present in the `TRExFitter` package to average adjacent  
1026 bins to remove statistical fluctuations.

1027 When including the acceptance and shape uncertainties in the fit, the templates are symmetrised by taking  
1028 half the difference between the up and down variation around the nominal template. For bins where both the  
1029 initial up and down variation are on the same side from the nominal, the largest variation is symmetrically  
1030 assigned for the final templates.

1031 All systematic uncertainties containing up and down systematic variations are symmetrised by via  
1032  $(\alpha_{ij-} + \alpha_{ij+})/2 = \alpha_{ij-} = \alpha_{ij+}$ . One sided systematics are symmetrised by defining  $\alpha_{ij-} = \alpha_{ij+}$ .

1033 **Pruning:** A 0.5 % level pruning is applied.

Not reviewed, for internal circulation only

## 1034 10 Profiled likelihood fit

### 1035 10.1 Introduction

1036 In order to extract the  $tZq$  cross-section, a binned maximum likelihood fit is performed using the MC  
 1037 templates for both signal and background predictions. The software framework used for performing the fit  
 1038 is **TRExFitter** [72]. This combines the functionalities of **RooFit** [73] and **RooStats** [74] and is designed  
 1039 to build probability density functions that are automatically fit to data and interpreted with statistical tests.  
 1040 The likelihood function comprises histogram bins from both SRs and CRs. Binning optimization studies  
 1041 were performed using the ‘Transform D’ algorithm [72] using anywhere from 7-12 bins. No significant  
 1042 changes in the uncertainty on the  $tZq$  cross section measurement are obtained. The final choice for binning  
 1043 will be 10 equally spaced bins.

1044 **Regions** The regions included in the fit, as well as the distributions that are fit, are summarised in  
 1045 Table 34. The definitions of the various regions are shown in Table 4. Some regions are used to control the  
 1046 overall normalisation of various backgrounds. In the diboson CRs,  $m_T(\ell, E_T^{\text{miss}})$  is used instead of  $O_{\text{NN}}$  to  
 1047 better separate the diboson contribution from  $Z + \text{jets}$ .

Table 34: Overview of the regions included in the fit.

Region	Distribution	Additional info
2j1b SR	$O_{\text{NN}}$	–
3j1b SR	$O_{\text{NN}}$	–
2j0b diboson CR	$m_T(\ell, E_T^{\text{miss}})$	–
3j0b diboson CR	$m_T(\ell, E_T^{\text{miss}})$	–
2j1b $t\bar{t}$ CR	–	single bin
3j1b $t\bar{t}$ CR	–	single bin
3j2b $t\bar{t}Z$ CR	$O_{\text{NN}}$	–
4j2b $t\bar{t}Z$ CR	$O_{\text{NN}}$	–

1048 **Inputs** The inputs to the fit consist of binned distributions, including the signal and all background  
 1049 channels. Additionally, for each MC sample, separate templates that take into account the systematic  
 1050 variations discussed in Section 9 are created and included in the fit.

1051 **POI** The global likelihood function describing the agreement between data and prediction as a function of  
 1052 the parameter of interest,  $\mu_{\text{SIG}}$ , and the set of nuisance parameters describing the effect of the corresponding  
 1053 systematic uncertainty sources is constructed and fitted. The signal strength parameter,  $\mu_{\text{SIG}}$ , is defined as  
 1054 the ratio between the measured cross-section and the theoretical prediction,  $\mu_{\text{SIG}} = \sigma_{tZq}/\sigma_{tZq}^{\text{pred}}$ .

1055 **Systematic uncertainty NPs** The impact of the systematic uncertainties on the extracted  $\mu_{\text{SIG}}$  is estimated  
 1056 in the following way.

1057 A nuisance parameter (NP) is associated to each systematic uncertainty. These NPs have a central value and  
 1058 an associated uncertainty pre-fit. The fit is able to change the central value of the NPs (this is called *pull*)  
 1059 and the uncertainty on the NP can change (this is called *constraint* if the uncertainty becomes smaller), to  
 1060 better describe the data. The change in each NP central value and its uncertainty are shown in figures such  
 1061 as Fig. 353 as a dot (central value) and a black line (uncertainty). If no pull and no constraint are present,  
 1062 the black dot is at 0 and the black line at  $\pm 1$ . This part of the figure helps in understanding what the fit  
 1063 learns about the systematic uncertainties from data.

1064 To understand the impact of the NPs on the extracted  $\mu_{\text{SIG}}$  the following procedure is used: the fit is re-run  
 1065 several times, separately for each NP, changing the central value of each NP up and down by the pre-fit  
 1066 (post-fit)  $\pm 1\sigma$  uncertainties, fixing it to that value and re-running the fit to  $\mu_{\text{SIG}}$ . The difference between  
 1067 this  $\mu_{\text{SIG}}$  and the one extracted from the standard fit is the pre-fit (post-fit) impact on  $\mu_{\text{SIG}}$ . The reference  
 1068 scale for this information in the figure is the bottom  $x$ -axis, labelled  $\Delta\mu_{\text{SIG}}$ . This part of the plot helps to  
 1069 understand the size of the effect that the uncertainty has on the signal strength.

1070 To prevent statistical fluctuations increasing the systematic uncertainties and wasted computation on fitting  
 1071 insignificant NPs, systematic uncertainties are pruned from the fit if they have an impact of less than 2 %  
 1072 on the result of  $\mu_{\text{SIG}}$ .

1073 **Statistical uncertainty NPs** The same procedure is applied to the *gamma* parameters, which represent  
 1074 the background statistical uncertainty in each bin of the NN output distribution. There is therefore one  
 1075 gamma parameter per bin of each input distribution.

1076 **Background treatment in the fit** The  $t\bar{t}Z + tWZ$  and diboson (still split into two components, heavy  
 1077 and light) backgrounds have pre-fit normalizations with uncertainties, while  $t\bar{t}$  and  $Z + \text{jets}$  are free floating  
 1078 in the fit. A single NP is associated to each one of these backgrounds, namely  $\mu_{t\bar{t}}$  and  $\mu_{Z+\text{jets}}$ . For the  
 1079 values of the pre-fit normalization uncertainties, please see Section 9 and Table 33.

1080 In the past, another approach was used, where all backgrounds were floating. A background normalization  
 1081 parameter is associated to each background, namely  $\mu_{t\bar{t}}$ ,  $\mu_{t\bar{t}V}$ ,  $\mu_{Z+\text{jets}}$ ,  $\mu_{VV+\text{HF}}$  and  $\mu_{VV+\text{LF}}$ . The results  
 1082 for this approach are reported in Appendix G. Please note that in this fit,  $t\bar{t}V$  includes  $t\bar{t}Z$ ,  $t\bar{t}W$ ,  $tWZ$  and  
 1083  $t\bar{t}H$ .

## 1084 10.2 Asimov fit

1085 In order to compute the expected significance, an Asimov dataset is used. The Asimov dataset is constructed  
 1086 by scaling each background to the value obtained in the signal-depleted fit described in Appendix G.4,  
 1087 with  $\mu_{\text{SIG}}$  set to 1.

1088 The MINOS function is used to calculate the uncertainties on both the parameters of interest and on all the  
 1089 nuisance parameters.

1090 The values of the post-fit normalization parameters for the free floating backgrounds are shown in Fig. 57.  
 1091 The correlation matrix of the parameters included in the fit is shown in Fig. 58.

1092 The pull distributions for the all nuisance parameters can be seen in Figs. 59 to 66 and Fig. 67.

1093 The list of the systematic shapes that are dropped from the fit for each sample and for each region is shown  
 1094 in Fig. 68.

1095 Event yields pre- and post-fit are shown in Tables 35 and 38. Pre-fit and post-fit distributions of the fitted  
 1096 distributions in the various regions are shown in Appendix G.2.1

1097 A fit including both statistical and systematical uncertainties leads to an uncertainty on  $\mu_{\text{SIG}}$  of  $^{+14}_{-13}$  %. A  
 1098 fit to determine the expected significance yields a value of 9.2.

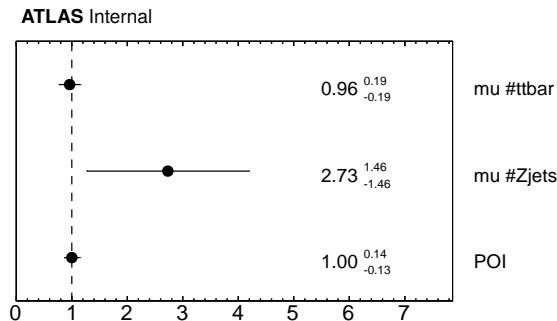


Figure 57: Normalisation factors of the Asimov fit.

Not reviewed, for internal circulation only

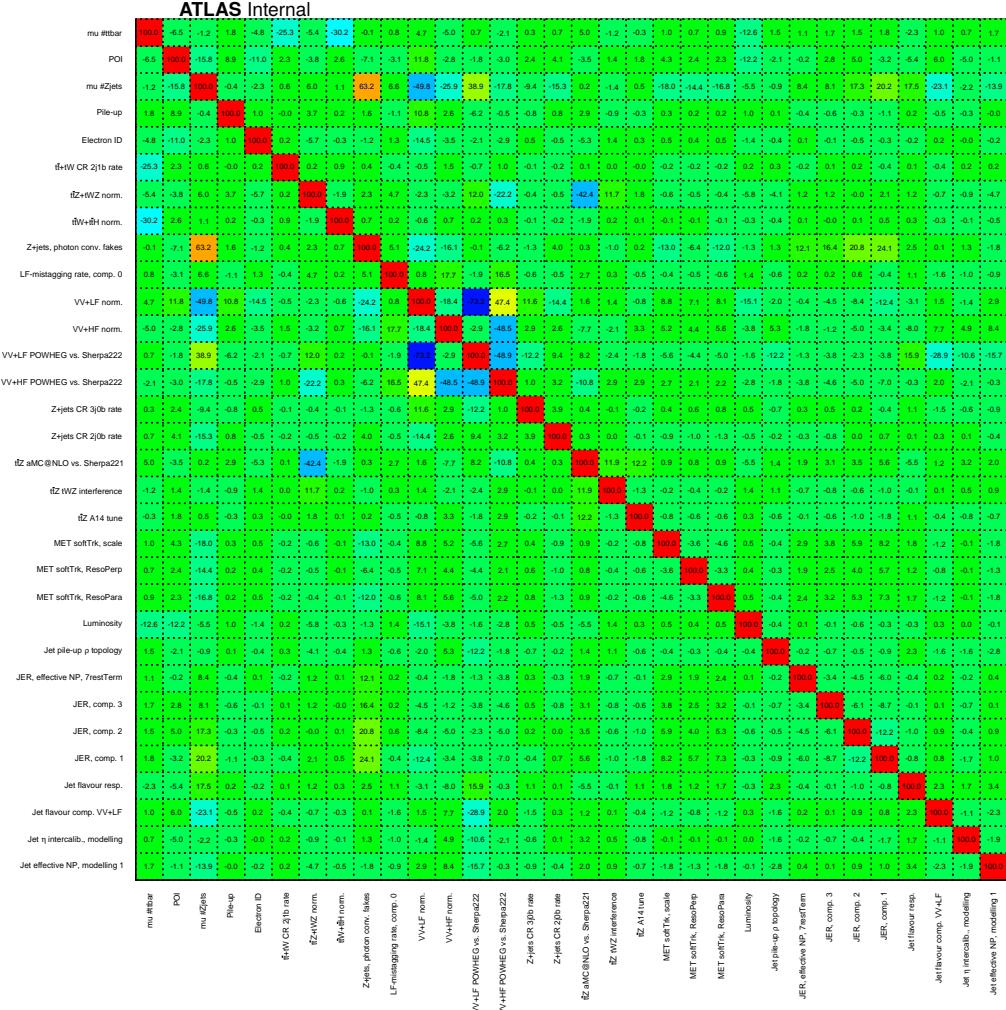


Figure 58: Correlation matrix of the Asimov fit. Only NPs with a correlation coefficient larger than 10 % with some other NP are shown.

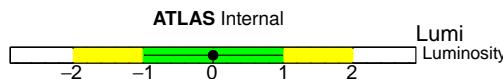


Figure 59: Pulls and constraints of the nuisance parameters of the Asimov fit: luminosity.

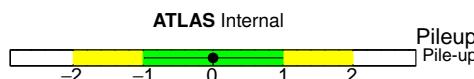


Figure 60: Pulls and constraints of the nuisance parameters of the Asimov fit: pile-up.

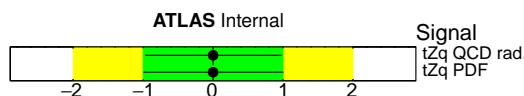


Figure 61: Pulls and constraints of the nuisance parameters of the Asimov fit: signal systematics.

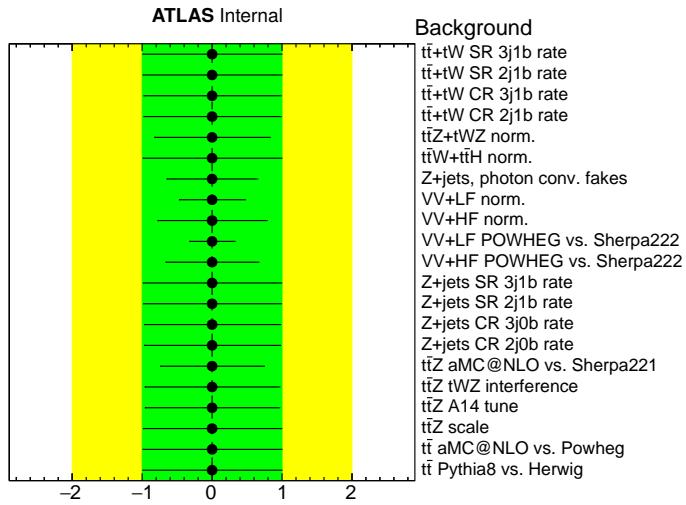
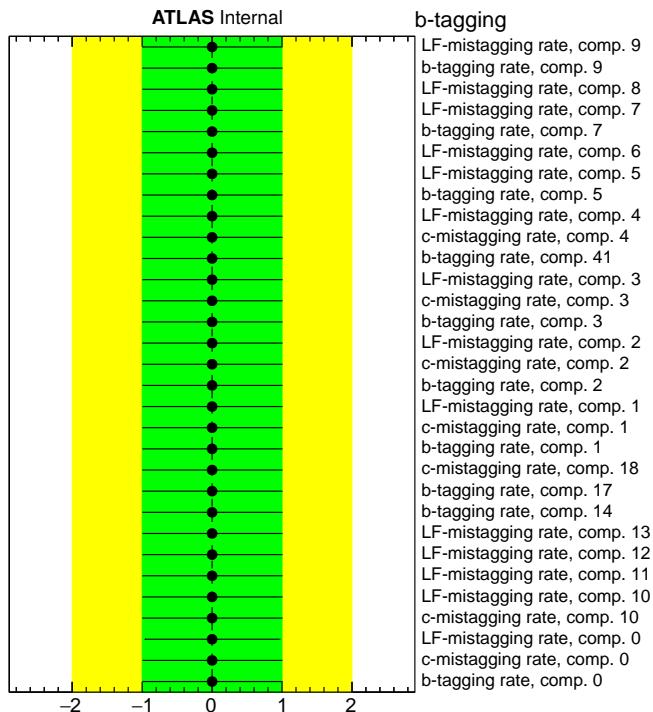


Figure 62: Pulls and constraints of the nuisance parameters of the Asimov fit: background modeling systematics.

Figure 63: Pulls and constraints of the nuisance parameters of the Asimov fit:  $b$ -tagging systematics.

Not reviewed, for internal circulation only

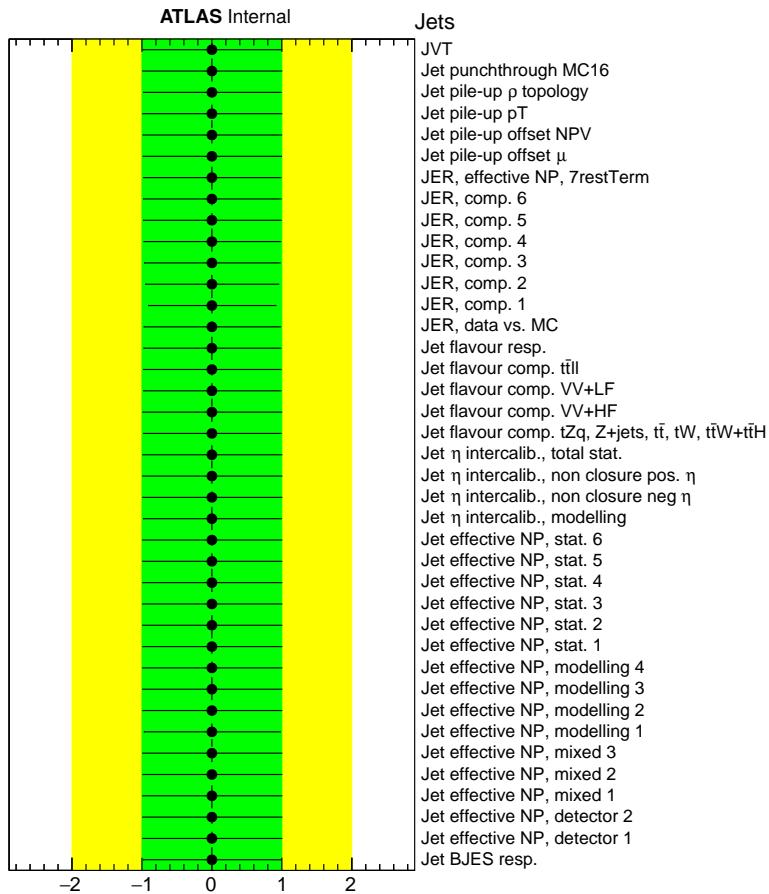


Figure 64: Pulls and constraints of the nuisance parameters of the Asimov fit: jet systematics.

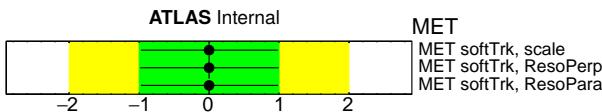
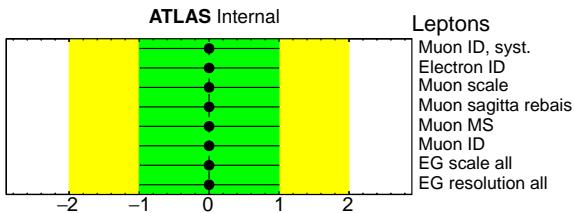
Figure 65: Pulls and constraints of the nuisance parameters of the Asimov fit:  $E_T^{\text{miss}}$  systematics.

Figure 66: Pulls and constraints of the nuisance parameters of the Asimov fit: lepton systematics.

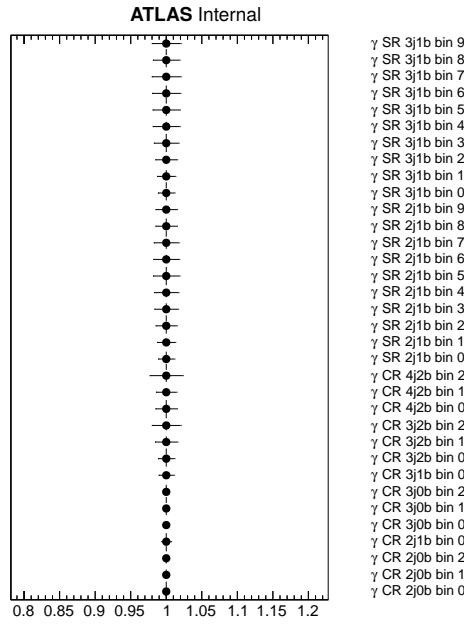
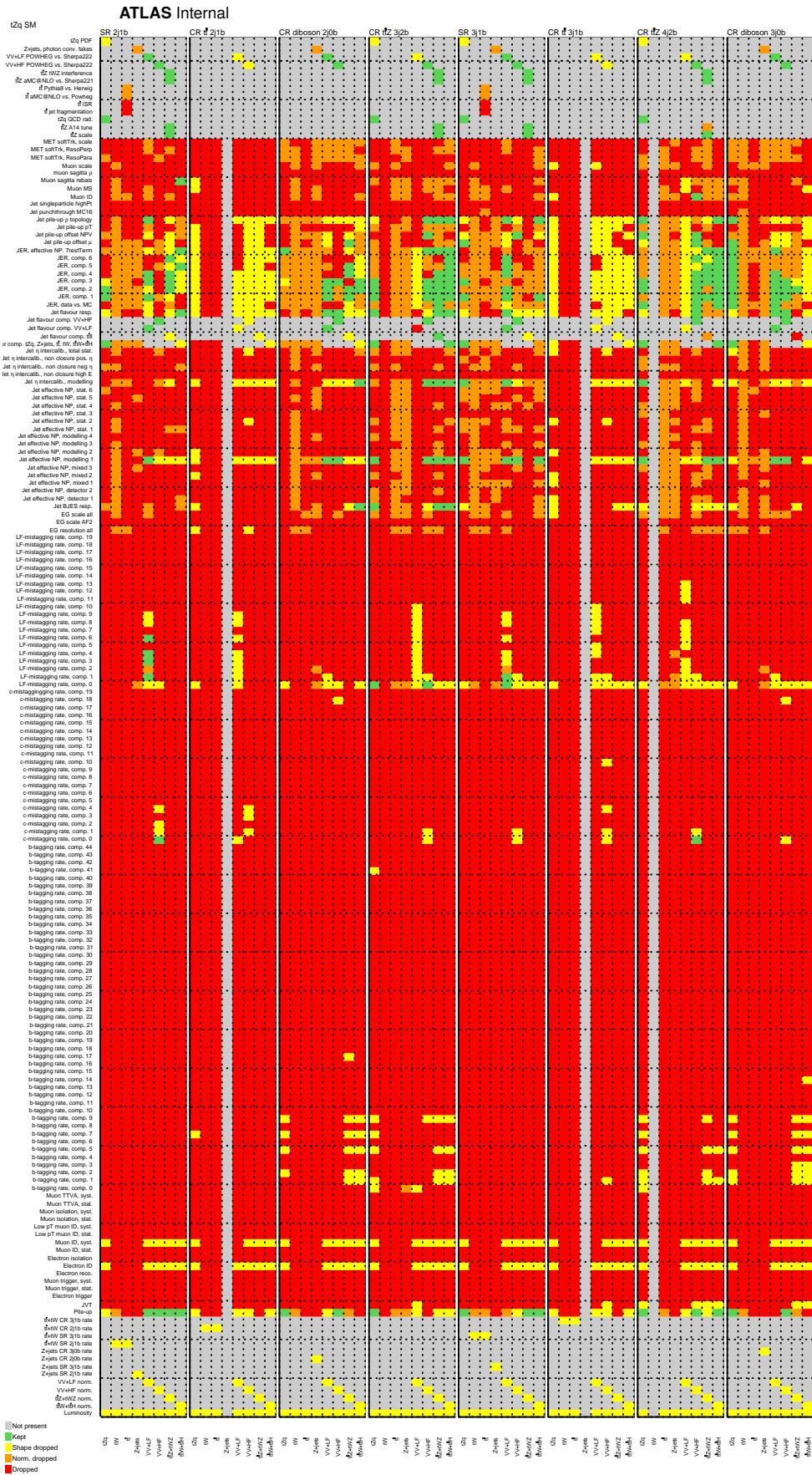


Figure 67: Gamma parameters of the Asimov fit.

Table 35: Pre-fit (left) and post-fit (right) event yields in the SRs for the Asimov fit. The uncertainties include both statistical and systematic uncertainties.

	SR 2j1b	SR 2j1b
$tZq$	$81.1 \pm 3.3$	$81.1 \pm 11.3$
$tW$	$1.0 \pm 0.1$	$1.0 \pm 0.2$
$t\bar{t}$	$22.7 \pm 1.6$	$22.7 \pm 4.8$
$Z + \text{jets}$	$28.0 \pm 4.2$	$28.0 \pm 15.4$
$VV + \text{LF}$	$22.7 \pm 15.7$	$22.7 \pm 9.0$
$VV + \text{HF}$	$101.3 \pm 43.1$	$101.3 \pm 22.1$
$t\bar{t}Z + tWZ$	$80.6 \pm 18.0$	$80.6 \pm 10.1$
$t\bar{t} H + t\bar{t} W$	$6.3 \pm 1.0$	$6.3 \pm 1.0$
Total	$343.7 \pm 50.5$	$343.7 \pm 15.3$
	SR 3j1b	SR 3j1b
$tZq$	$46.1 \pm 2.6$	$46.1 \pm 6.5$
$tW$	$0.4 \pm 0.0$	$0.4 \pm 0.1$
$t\bar{t}$	$10.6 \pm 0.8$	$10.6 \pm 2.2$
$Z + \text{jets}$	$13.0 \pm 2.0$	$13.0 \pm 7.2$
$VV + \text{LF}$	$12.3 \pm 9.3$	$12.3 \pm 5.1$
$VV + \text{HF}$	$59.4 \pm 34.6$	$59.4 \pm 17.6$
$t\bar{t}Z + tWZ$	$116.7 \pm 18.6$	$116.7 \pm 10.7$
$t\bar{t} H + t\bar{t} W$	$4.6 \pm 0.7$	$4.6 \pm 0.7$
Total	$263.1 \pm 41.2$	$263.1 \pm 11.5$

Not reviewed, for internal circulation only



31st October 2019 – 16:44 Figure 68: Pruning of the nuisance parameters of the Asimov fit.

Table 36: Pre-fit (left) and post-fit (right) event yields in the diboson CRs for the Asimov fit. The uncertainties include both statistical and systematic uncertainties.

CR diboson 2j0b			CR diboson 2j0b		
$tZq$	$55.4 \pm 1.9$		$tZq$	$55.4 \pm 7.6$	
$tW$	$0.5 \pm 0.0$		$tW$	$0.5 \pm 0.1$	
$t\bar{t}$	$13.2 \pm 0.2$		$t\bar{t}$	$13.2 \pm 2.6$	
$Z + \text{jets}$	$173.4 \pm 26.2$		$Z + \text{jets}$	$173.4 \pm 92.4$	
$VV + \text{LF}$	$2039.7 \pm 628.5$		$VV + \text{LF}$	$2039.7 \pm 104.9$	
$VV + \text{HF}$	$382.1 \pm 139.6$		$VV + \text{HF}$	$382.1 \pm 79.8$	
$t\bar{t}Z + tWZ$	$58.9 \pm 7.9$		$t\bar{t}Z + tWZ$	$58.9 \pm 6.7$	
$t\bar{t} H + t\bar{t} W$	$2.9 \pm 0.5$		$t\bar{t} H + t\bar{t} W$	$2.9 \pm 0.5$	
Total	$2726.2 \pm 646.6$		Total	$2726.2 \pm 53.4$	
CR diboson 3j0b			CR diboson 3j0b		
$tZq$	$22.3 \pm 1.9$		$tZq$	$22.3 \pm 3.4$	
$tW$	$0.3 \pm 0.0$		$tW$	$0.3 \pm 0.1$	
$t\bar{t}$	$6.6 \pm 0.1$		$t\bar{t}$	$6.6 \pm 1.3$	
$Z + \text{jets}$	$55.0 \pm 8.3$		$Z + \text{jets}$	$55.0 \pm 29.8$	
$VV + \text{LF}$	$708.0 \pm 351.8$		$VV + \text{LF}$	$708.0 \pm 54.6$	
$VV + \text{HF}$	$190.0 \pm 101.2$		$VV + \text{HF}$	$190.0 \pm 51.9$	
$t\bar{t}Z + tWZ$	$58.7 \pm 7.4$		$t\bar{t}Z + tWZ$	$58.7 \pm 6.1$	
$t\bar{t} H + t\bar{t} W$	$1.7 \pm 0.3$		$t\bar{t} H + t\bar{t} W$	$1.7 \pm 0.3$	
Total	$1042.6 \pm 367.7$		Total	$1042.6 \pm 31.9$	

Table 37: Pre-fit (left) and post-fit (right) event yields in the  $t\bar{t}$  CRs for the Asimov fit. The uncertainties include both statistical and systematic uncertainties.

CR $t\bar{t}$ 2j1b			CR $t\bar{t}$ 2j1b		
$tZq$	$0.2 \pm 0.1$		$tZq$	$0.2 \pm 0.1$	
$tW$	$0.7 \pm 0.1$		$tW$	$0.7 \pm 0.1$	
$t\bar{t}$	$32.7 \pm 2.4$		$t\bar{t}$	$32.7 \pm 6.3$	
$Z + \text{jets}$	$0 \pm 0$		$Z + \text{jets}$	$0 \pm 0$	
$VV + \text{LF}$	$0.1 \pm 0.0$		$VV + \text{LF}$	$0.1 \pm 0.0$	
$VV + \text{HF}$	$0.4 \pm 0.2$		$VV + \text{HF}$	$0.4 \pm 0.1$	
$t\bar{t}Z + tWZ$	$4.4 \pm 0.6$		$t\bar{t}Z + tWZ$	$4.4 \pm 0.5$	
$t\bar{t} H + t\bar{t} W$	$12.1 \pm 1.9$		$t\bar{t} H + t\bar{t} W$	$12.1 \pm 1.9$	
Total	$50.6 \pm 3.2$		Total	$50.6 \pm 6.1$	
CR $t\bar{t}$ 3j1b			CR $t\bar{t}$ 3j1b		
$tZq$	$0.2 \pm 0.1$		$tZq$	$0.2 \pm 0.1$	
$tW$	$0.5 \pm 0.0$		$tW$	$0.5 \pm 0.1$	
$t\bar{t}$	$14.7 \pm 1.1$		$t\bar{t}$	$14.7 \pm 3.0$	
$Z + \text{jets}$	$0 \pm 0$		$Z + \text{jets}$	$0 \pm 0$	
$VV + \text{LF}$	$0.0 \pm 0.0$		$VV + \text{LF}$	$0.0 \pm 0.0$	
$VV + \text{HF}$	$0.3 \pm 0.2$		$VV + \text{HF}$	$0.3 \pm 0.1$	
$t\bar{t}Z + tWZ$	$3.7 \pm 0.6$		$t\bar{t}Z + tWZ$	$3.7 \pm 0.5$	
$t\bar{t} H + t\bar{t} W$	$8.0 \pm 1.3$		$t\bar{t} H + t\bar{t} W$	$8.0 \pm 1.3$	
Total	$27.5 \pm 1.8$		Total	$27.5 \pm 3.0$	

Table 38: Pre-fit (left) and post-fit (right) event yields in the  $t\bar{t}Z$  CRs for the Asimov fit. The uncertainties include both statistical and systematic uncertainties.

CR $t\bar{t}Z$ 3j2b			CR $t\bar{t}Z$ 3j2b		
$tZq$	$13.2 \pm 0.9$		$tZq$	$13.2 \pm 2.0$	
$tW$	$0.1 \pm 0.0$		$tW$	$0.1 \pm 0.0$	
$t\bar{t}$	$1.6 \pm 0.0$		$t\bar{t}$	$1.6 \pm 0.3$	
$Z + \text{jets}$	$1.4 \pm 0.0$		$Z + \text{jets}$	$1.4 \pm 0.8$	
$VV + \text{LF}$	$0.1 \pm 0.1$		$VV + \text{LF}$	$0.1 \pm 0.1$	
$VV + \text{HF}$	$5.3 \pm 3.4$		$VV + \text{HF}$	$5.3 \pm 1.7$	
$t\bar{t}Z + tWZ$	$49.5 \pm 11.8$		$t\bar{t}Z + tWZ$	$49.5 \pm 6.3$	
$t\bar{t} H + t\bar{t} W$	$2.8 \pm 0.5$		$t\bar{t} H + t\bar{t} W$	$2.8 \pm 0.5$	
Total	$73.9 \pm 12.5$		Total	$73.9 \pm 5.7$	
CR $t\bar{t}Z$ 4j2b			CR $t\bar{t}Z$ 4j2b		
$tZq$	$8.6 \pm 0.8$		$tZq$	$8.6 \pm 1.4$	
$tW$	$0 \pm 0$		$tW$	$0 \pm 0$	
$t\bar{t}$	$1.0 \pm 0.0$		$t\bar{t}$	$1.0 \pm 0.2$	
$Z + \text{jets}$	$0.4 \pm 0.0$		$Z + \text{jets}$	$0.4 \pm 0.2$	
$VV + \text{LF}$	$0.1 \pm 0.1$		$VV + \text{LF}$	$0.1 \pm 0.1$	
$VV + \text{HF}$	$3.3 \pm 2.0$		$VV + \text{HF}$	$3.3 \pm 1.0$	
$t\bar{t}Z + tWZ$	$51.5 \pm 8.5$		$t\bar{t}Z + tWZ$	$51.5 \pm 4.9$	
$t\bar{t} H + t\bar{t} W$	$1.9 \pm 0.3$		$t\bar{t} H + t\bar{t} W$	$1.9 \pm 0.3$	
Total	$66.8 \pm 8.9$		Total	$66.8 \pm 4.6$	

### 1099 10.3 Unblinded fit

1100 This section contains the results of the unblinded fit.

1101 The MINOS function is used to calculate the uncertainties on both the parameters of interest and on all the  
1102 nuisance parameters.

1103  $tZq$  production has been observed with a significance of 9.1.

1104 The measured  $\mu_{\text{SIG}}$  is  $0.96^{+0.144}_{-0.13}$ , from which the measured cross section is extracted to be  $97^{+13}_{-12}$  (stat.)  $\pm 7$  (syst.) fb,  
1105 which has a relative uncertainty of 14 %.

1106 The values of the post-fit normalization parameters for the free floating backgrounds are shown in Fig. 69.

1107 The  $t\bar{t}$  background is scaled down by 4 %, still compatible is 1 within uncertainty. The  $Z + \text{jets}$  background  
1108 instead is scaled up by 270 %.

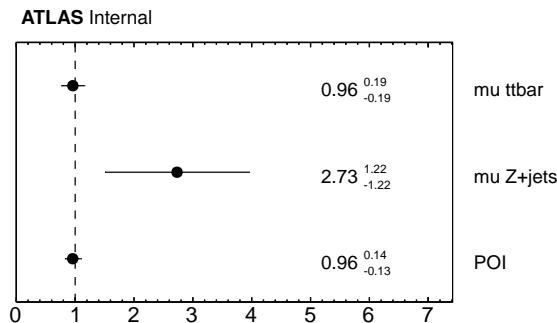


Figure 69: Normalisation factors of the unblinded fit.

<sup>4</sup> The value of  $\mu_{\text{SIG}}$  is not considered an observable that will be published, but only an intermediate result.

1109 **10.3.1 Correlation matrix**

1110 The correlation matrix of the parameters included in the fit is shown in Fig. 70.

1111 The highest correlations happen between the diboson HF and LF component uncertainties, namely the  
 1112 normalization (called VV+LF/HF norm.) and the modeling (called diboson LF/HF powhegVSsherpa222)  
 1113 NPs. Diboson LF NPs are also correlated to  $Z + \text{jets}$  background NPs, namely the normalization (called  
 1114 SR/CR  $Z + \text{jets}$  norm) and the photon conversion NPs. This is expected as the diboson LF and the  $Z + \text{jets}$   
 1115 background are constrained in the same CRs (the 2/3j0b CRs). The NP for the jet flavour composition for  
 1116 the diboson + LF component is also correlated with the other diboson LF NPs, as expected.

1117  $E_T^{\text{miss}}$  NPs are correlated with the  $Z + \text{jets}$  background.

ATLAS Internal

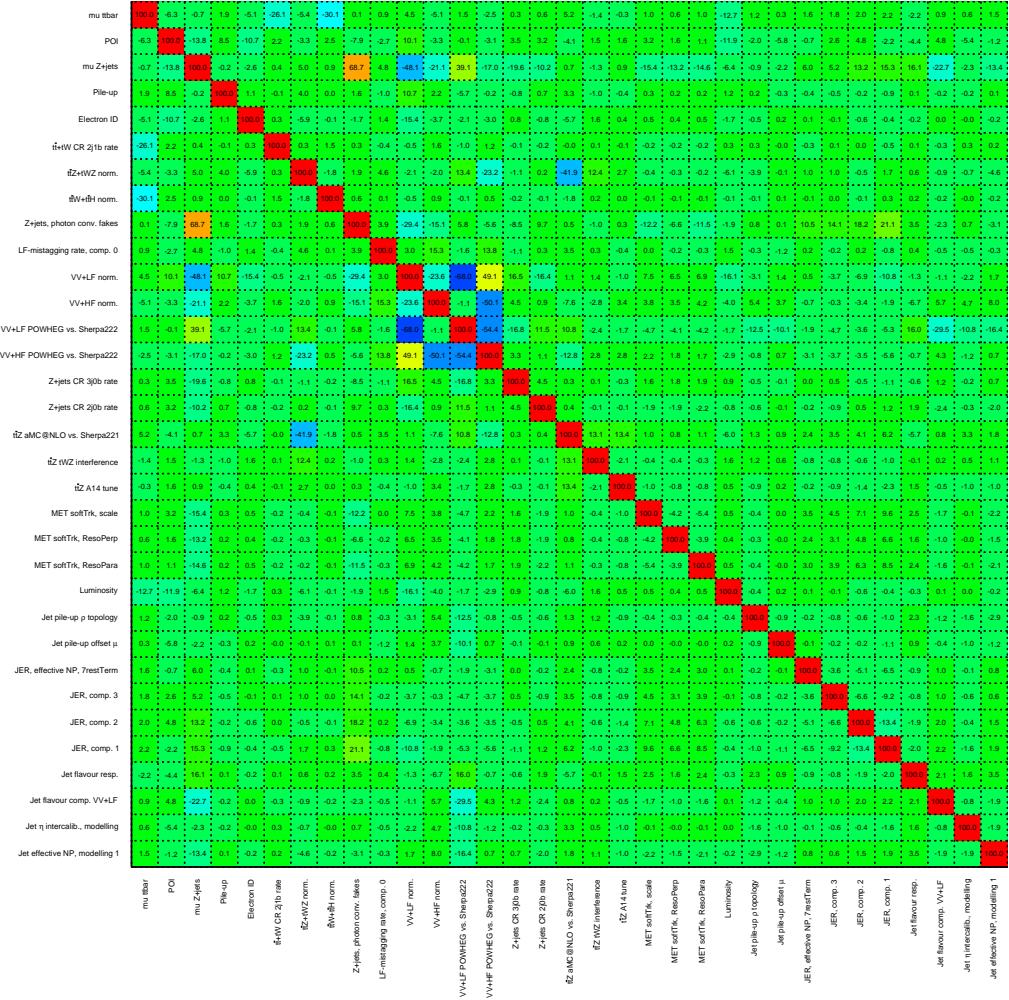


Figure 70: Correlation matrix of the unblinded fit. Only NPs with a correlation coefficient larger than 10 % with some other NP are shown.

### 1118 10.3.2 Nuisance parameters pulls and constraints

1119 The pull distributions for the all nuisance parameters can be seen in Figs. 71 to 78 and Fig. 79.

1120 The luminosity NP, shown in Fig. 71 is slightly pulled, by 12 % and constrained by 2 %. It was studied that,  
1121 when including more free floating backgrounds in the fit, the luminosity pull was reduced.

1122 For the signal NPs, shown in Fig. 73 the only NP that is pulled by 40 % is the NP for the scale and shower  
1123 uncertainties. Because of the way the systematic signal sample was generated, it is not possible to split this  
1124 uncertainty into two separate NPs.

1125 Figure 74 shows the NPs related to the background modeling. The main pulls are for the  $t\bar{t}Z$  normalization  
1126 (40 %) and generator uncertainty (60 %), which are related to the pre-fit disagreement shown in the  $t\bar{t}Z$   
1127 CRs (Fig. 89). Also the NP for the  $Z + \text{jets}$  photon conversions is pulled (50 %) and constrained (40 %), as  
1128 already mentioned before. Also some diboson related NPs are pulled and constrained.

1129 The jet NPs are all well behaved, especially after having split the flavour composition NP in four separate  
1130 components, as described in Section 9.

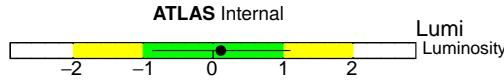


Figure 71: Pulls and constraints of the nuisance parameters of the unblinded fit: luminosity.

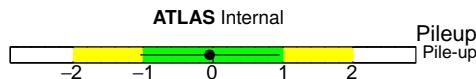


Figure 72: Pulls and constraints of the nuisance parameters of the unblinded fit: pile-up.

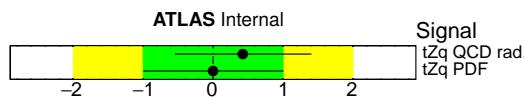


Figure 73: Pulls and constraints of the nuisance parameters of the unblinded fit: signal systematics.

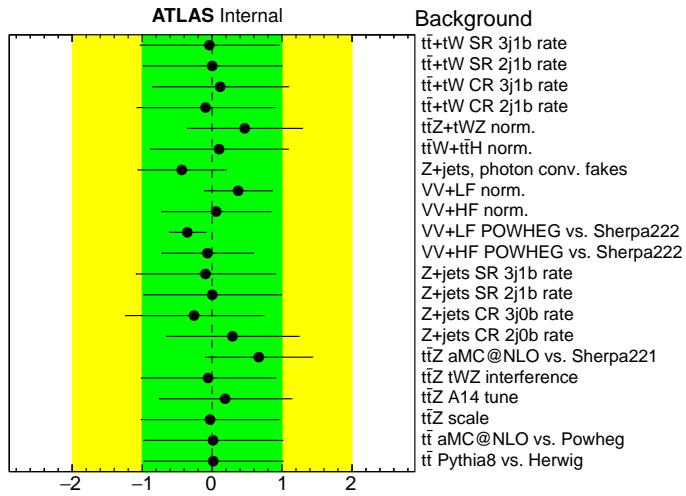


Figure 74: Pulls and constraints of the nuisance parameters of the unblinded fit: background modeling systematics.

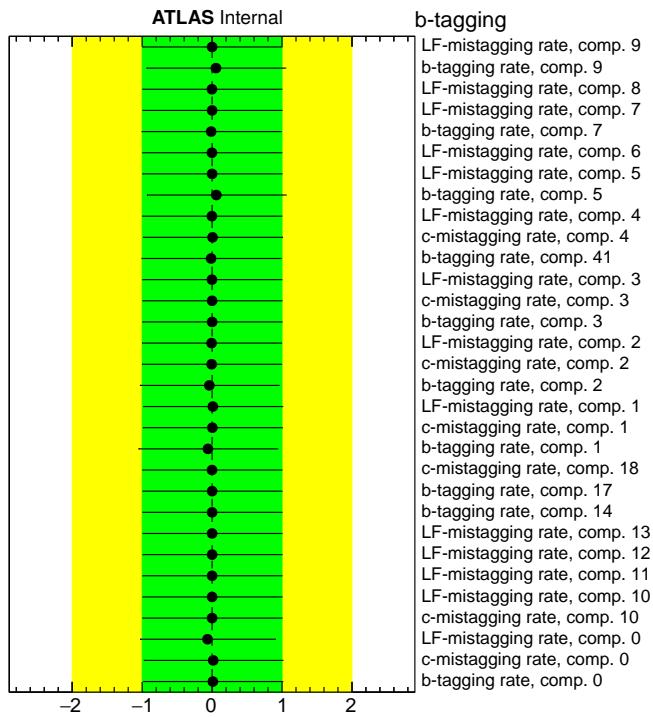


Figure 75: Pulls and constraints of the nuisance parameters of the unblinded fit:  $b$ -tagging systematics.

Not reviewed, for internal circulation only

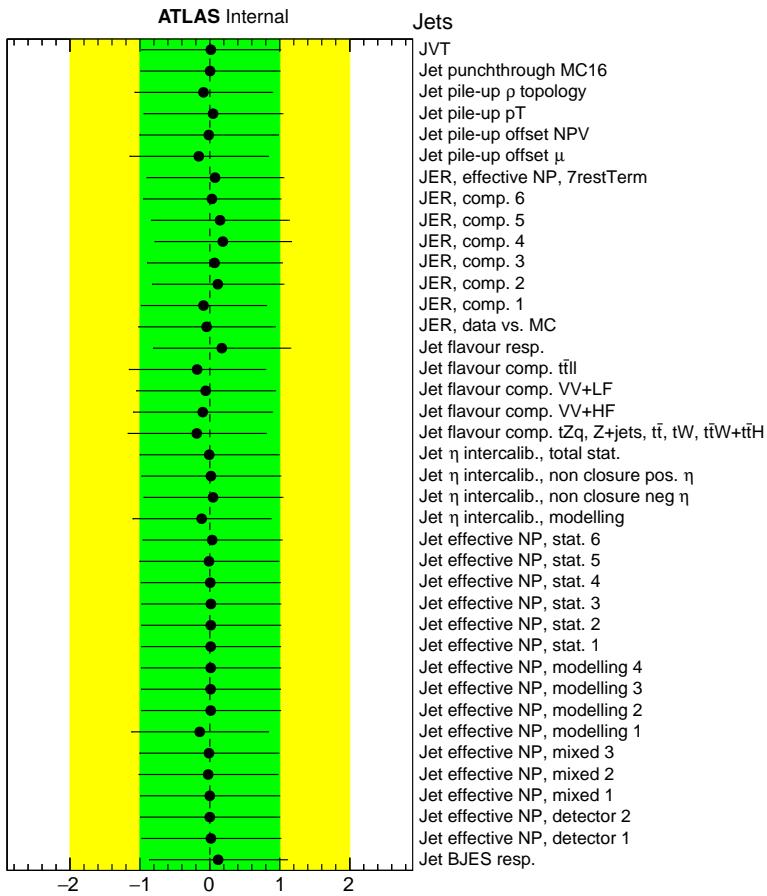


Figure 76: Pulls and constraints of the nuisance parameters of the unblinded fit: jet systematics.

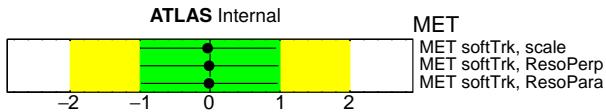


Figure 77: Pulls and constraints of the nuisance parameters of the unblinded fit:  $E_T^{\text{miss}}$  systematics.

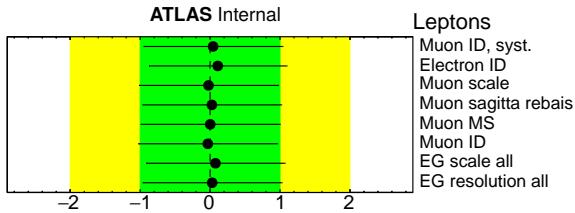


Figure 78: Pulls and constraints of the nuisance parameters of the unblinded fit: lepton systematics.

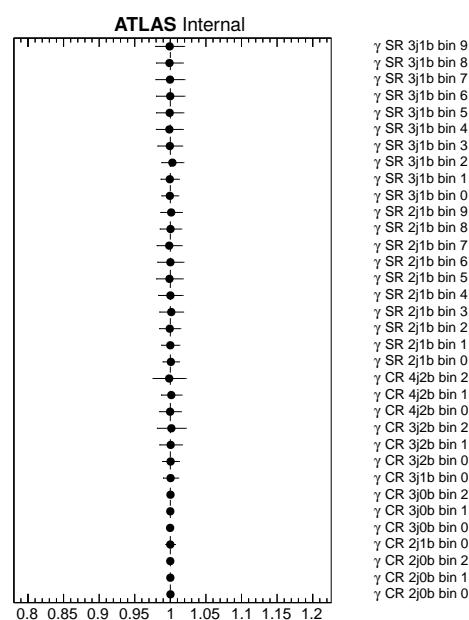


Figure 79: Gamma parameters of the unblinded fit.

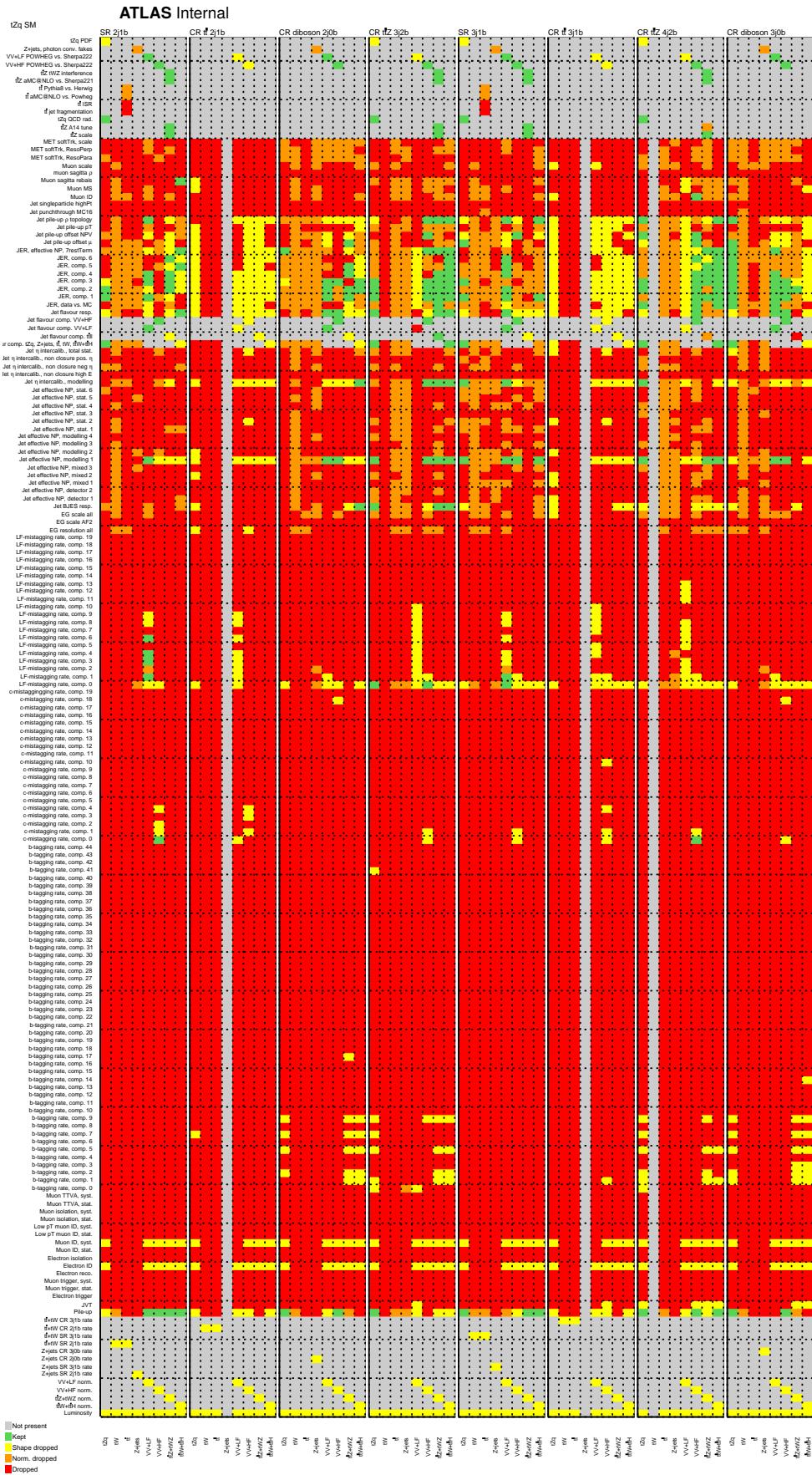
---

**1131 10.3.3 Nuisance parameters pruning**

1132 The list of the systematic shapes that are dropped from the fit for each sample and for each region is shown  
1133 in Fig. 80. A 0.5 % level pruning is applied. For more studies about the pruning, see Section 10.3.12.

1134 As it can be noticed, the  $tW$  sample is dropped from the 4j2b CR and  $Z + \text{jets}$  samples is dropped from the  
1135 2j1b and 3j1b CRs. This is due to the lack of simulated events surviving the selection cuts.

Not reviewed, for internal circulation only



31st October 2019 – 16:44 Figure 80: Pruning of the nuisance parameters of the unblinded fit.

1136 **10.3.4 Nuisance parameters ranking**

1137 The ranking of the impact of the systematic uncertainties is shown in Fig. 81.

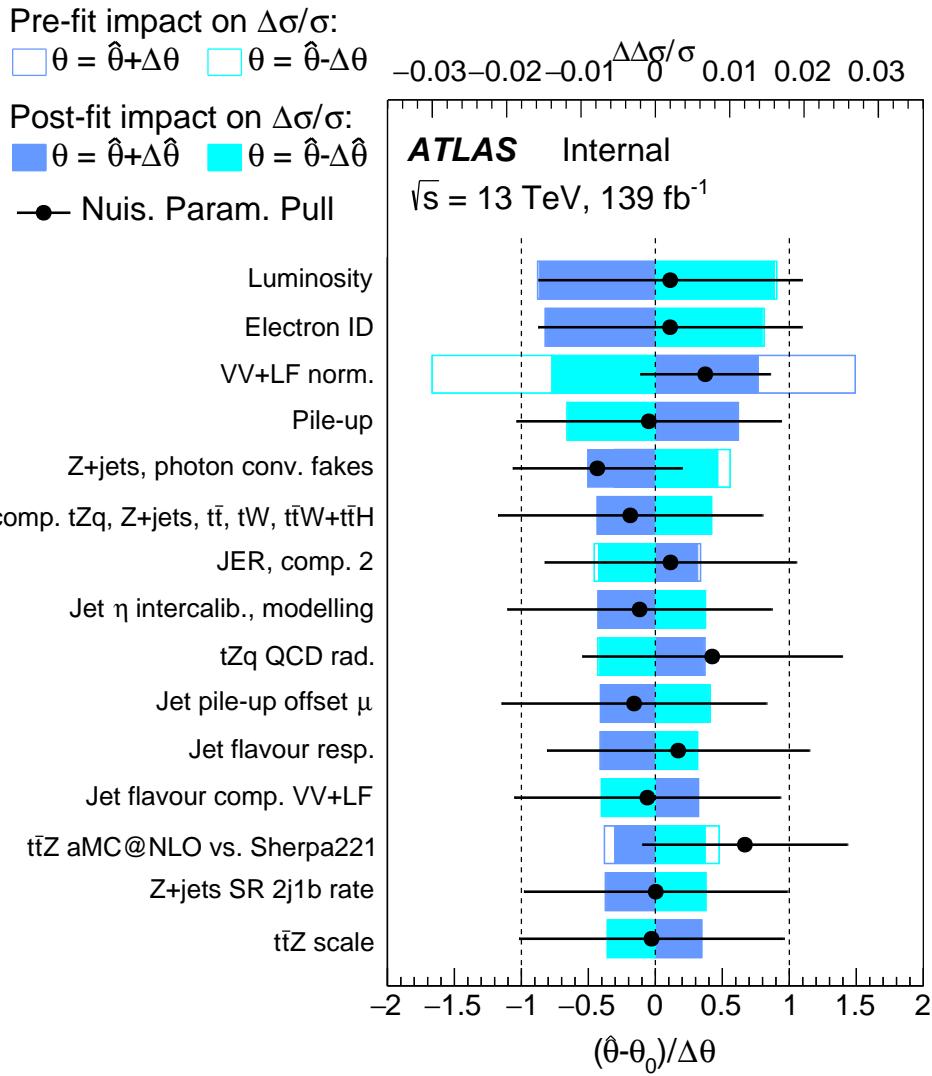
1138 The highest ranked uncertainty is the  $Z + \text{jets}$  normalization parameter. It should be noted though that the  
1139 impact on  $\mu_{\text{SIG}}$  is lower than 2 %. The uncertainty is actually dominated by the statistical uncertainty, as  
1140 shown in Section 10.3.6.

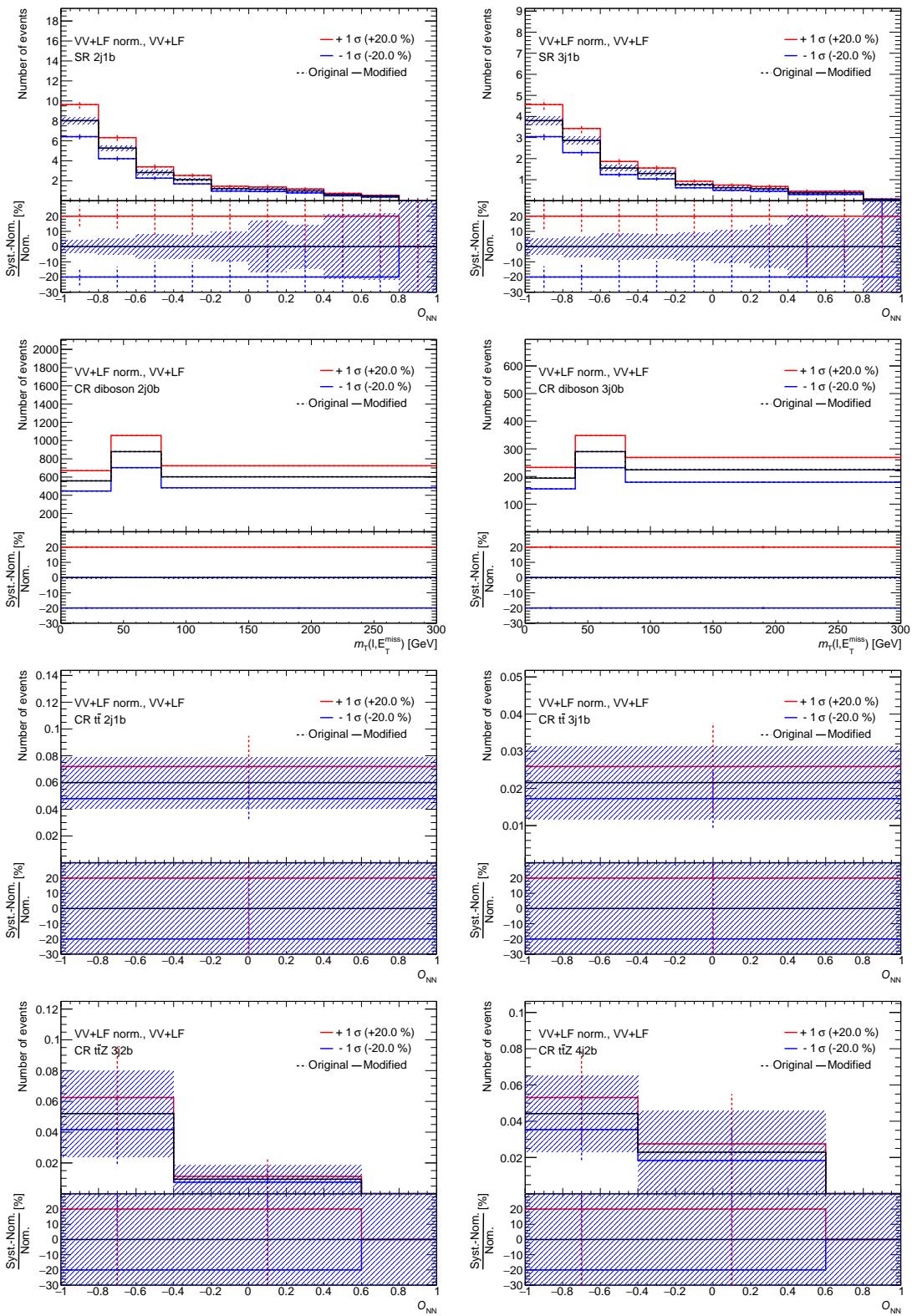
Figure 81: Ranking of the nuisance parameters of the unblinded fit.

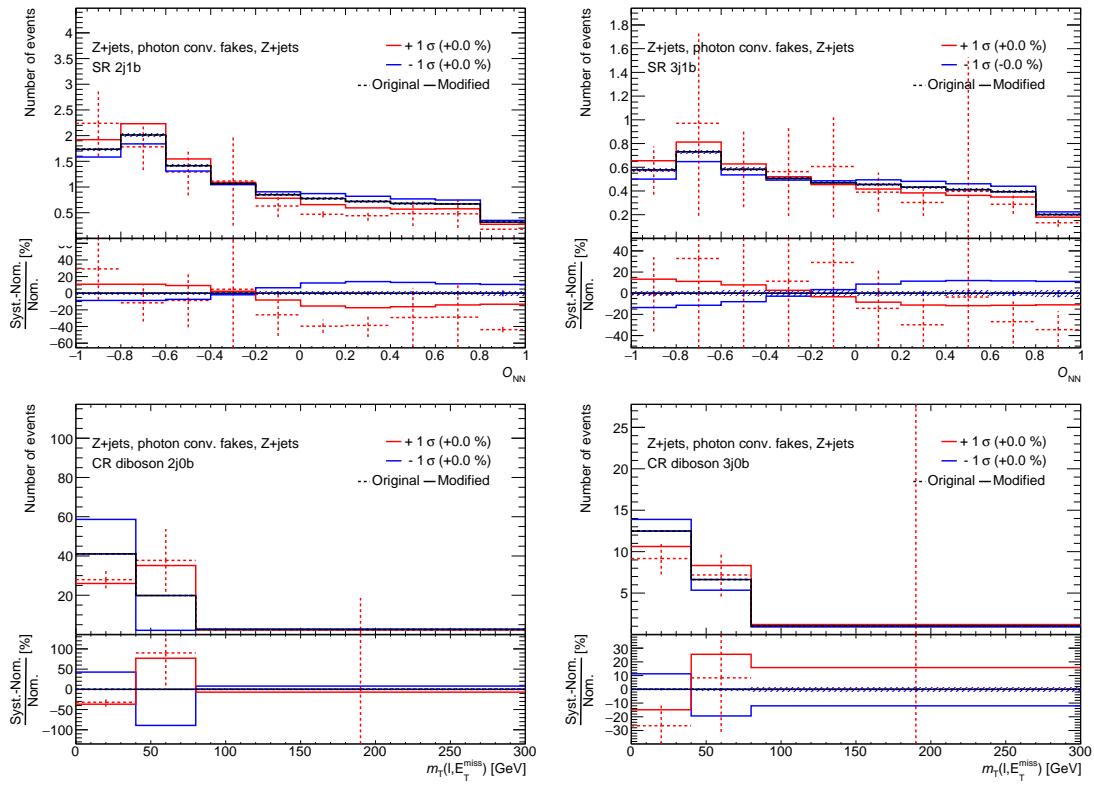
---

**1141 10.3.5 Red and blue plots**

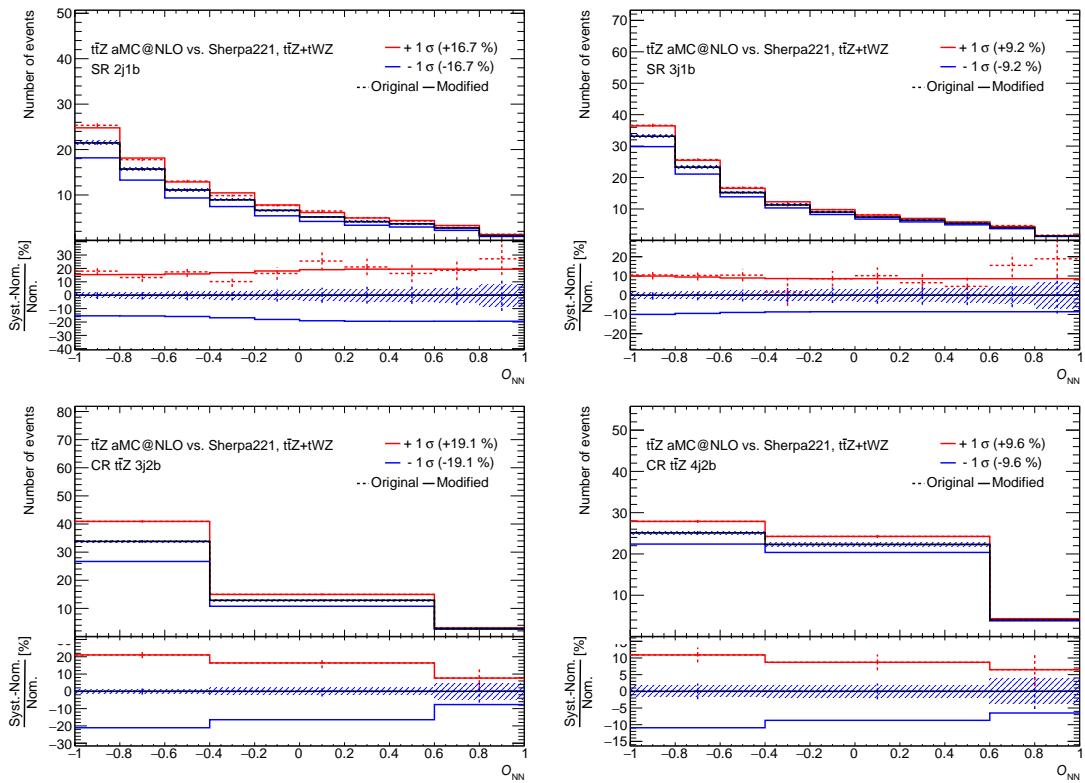
1142 The red and blue plots for those NPs that are either constrained or pulled are reported in Appendix G.3,  
1143 while those for the highly ranked uncertainties are shown in Figs. 82 to 84. It should be noted that,  
1144 even though highly ranked, these uncertainties have a very small impact on the final uncertainty, as the  
1145 uncertainty is dominated by the statistical uncertainty. The  $VV + LF$  normalization uncertainty (shown in  
1146 Fig. 82) is constrained mainly in the diboson CRs and it is pulled by 40 % and constrained by 50 %. The  
1147  $Z + \text{jets}$  photon conversion uncertainty (shown in Fig. 83) is constrained mainly in the diboson CRs. It is  
1148 pulled by 50 % and constrained by 40 %.

Not reviewed, for internal circulation only

Figure 82:  $VV + LF$  normalization uncertainty.

Figure 83:  $Z + \text{jets}$  BJR shape uncertainty.

Not reviewed, for internal circulation only

Figure 84:  $t\bar{t}Z$  McAtNLO vs Sherpa uncertainty.

### 1149 10.3.6 Fractional uncertainties

1150 Figures 85 and 86 show the uncertainty breakdown in the SRs and in the CRs too.

1151 As it can be noticed, the uncertainty is dominated by the statistical uncertainty in the SRs and in the  $t\bar{t}$   
 1152 and  $t\bar{t}V$  CRs. In the high statistics diboson CRs instead, as expected the diboson modeling uncertainties  
 1153 dominate the uncertainty.

1154 A table with the breakdown of uncertainties is available in Table 43.

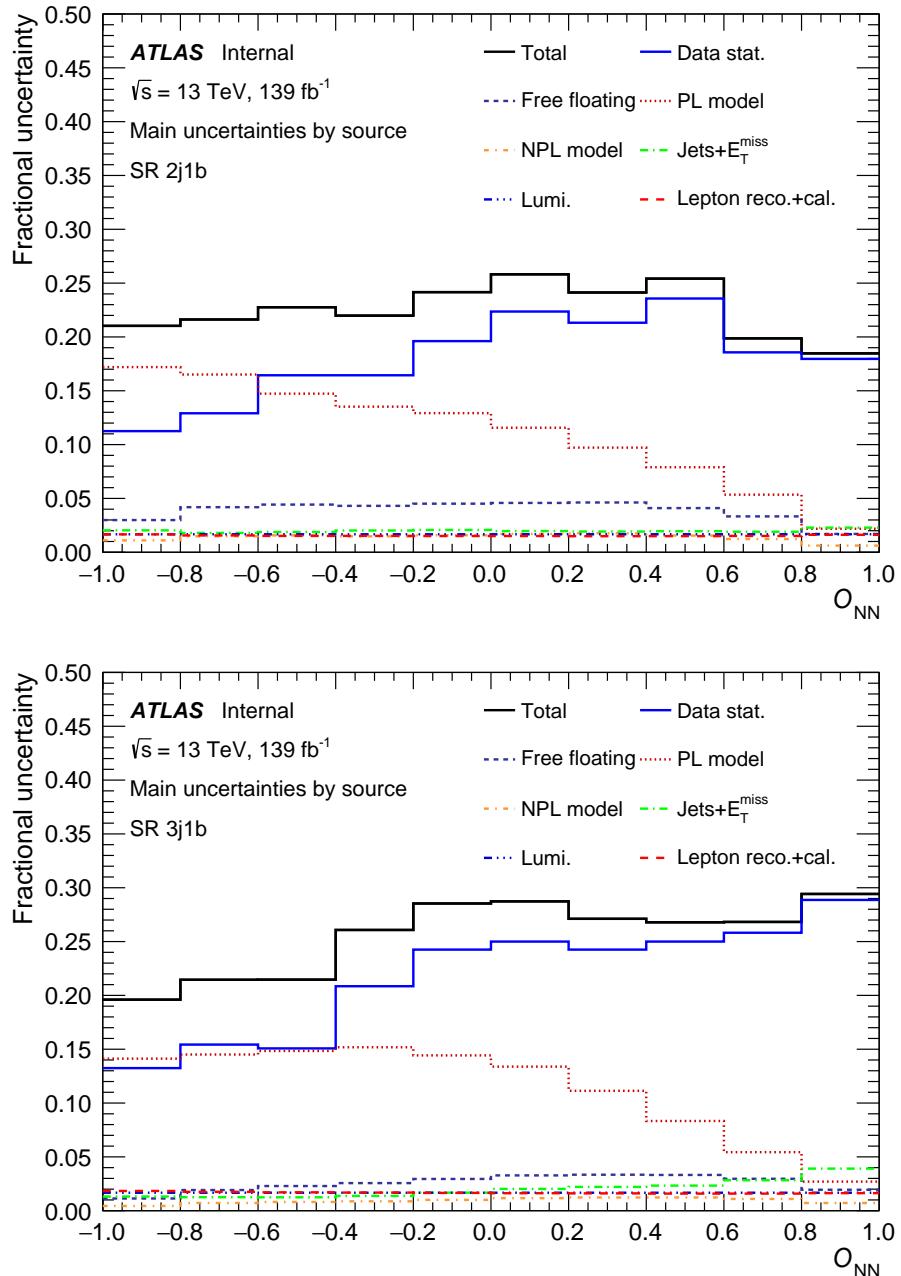


Figure 85: Breakdown of uncertainties in the signal regions.

Not reviewed, for internal circulation only

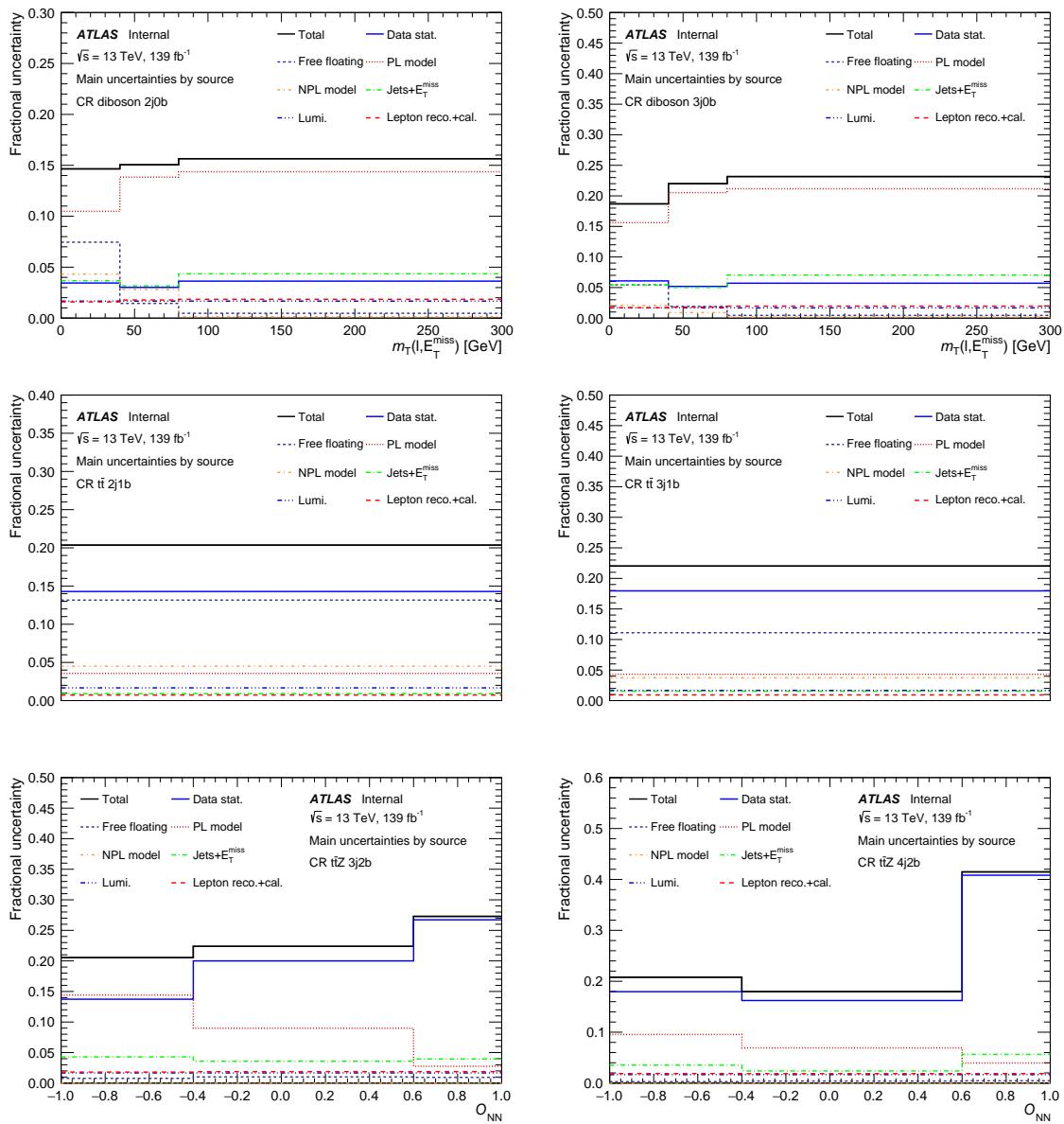


Figure 86: Breakdown of uncertainties in the control regions.

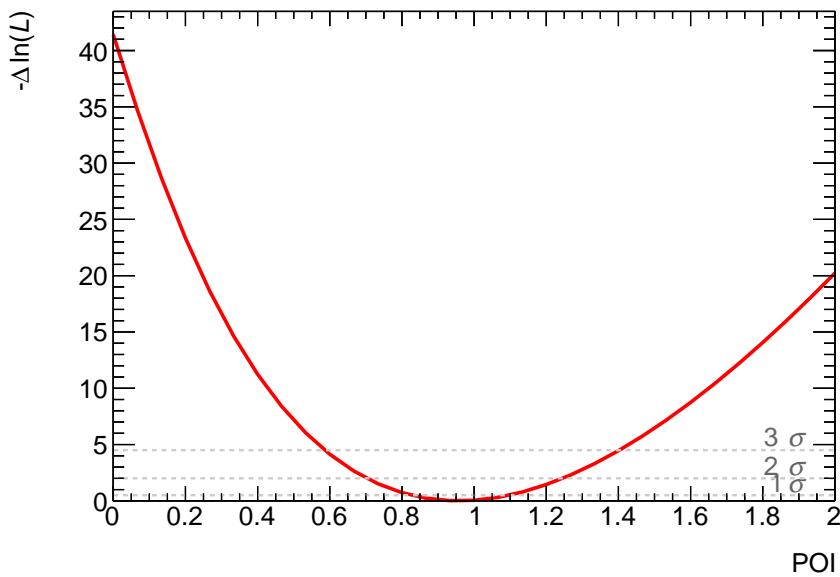


Figure 87: Likelihood scan curve.

1155 **10.3.7 Pre- and post-fit plots of fitted variables in fit regions**

1156 Event yields pre- and post-fit are shown in Tables 39 and 42. Pre-fit and post-fit distributions of the fitted  
 1157 distributions in the various regions are shown in Figs. 88 to 91.

Table 39: Pre-fit (left) and post-fit (right) event yields in the SRs for the unblinded fit. The uncertainties include both statistical and systematic uncertainties.

	SR 2j1b	SR 2j1b
$tZq$	$81.1 \pm 3.3$	$78.9 \pm 11.3$
$tW$	$1.1 \pm 0.1$	$1.0 \pm 0.2$
$t\bar{t}$	$23.7 \pm 1.7$	$22.8 \pm 4.8$
$Z + \text{jets}$	$10.2 \pm 1.5$	$28.0 \pm 13.1$
$VV + \text{LF}$	$22.7 \pm 15.7$	$19.7 \pm 7.9$
$VV + \text{HF}$	$101.3 \pm 43.1$	$101.3 \pm 21.6$
$t\bar{t}Z + tWZ$	$80.6 \pm 18.0$	$95.5 \pm 11.4$
$t\bar{t} H + t\bar{t} W$	$6.3 \pm 1.0$	$6.5 \pm 1.0$
Total	$327.0 \pm 50.3$	$353.8 \pm 15.6$
Data	359	359
	SR 3j1b	SR 3j1b
$tZq$	$46.1 \pm 2.6$	$43.4 \pm 6.2$
$tW$	$0.4 \pm 0.0$	$0.4 \pm 0.1$
$t\bar{t}$	$11.1 \pm 0.8$	$10.6 \pm 2.2$
$Z + \text{jets}$	$4.8 \pm 0.7$	$12.8 \pm 6.0$
$VV + \text{LF}$	$12.3 \pm 9.3$	$10.1 \pm 4.2$
$VV + \text{HF}$	$59.4 \pm 34.6$	$58.3 \pm 17.3$
$t\bar{t}Z + tWZ$	$116.7 \pm 18.6$	$131.7 \pm 11.5$
$t\bar{t} H + t\bar{t} W$	$4.6 \pm 0.7$	$4.7 \pm 0.7$
Total	$255.3 \pm 41.2$	$272.1 \pm 11.6$
Data	259	259

Table 40: Pre-fit (left) and post-fit (right) event yields in the diboson CRs for the unblinded fit. The uncertainties include both statistical and systematic uncertainties.

CR diboson 2j0b			CR diboson 2j0b		
$tZq$	$55.4 \pm 1.9$		$tZq$	$53.1 \pm 7.5$	
$tW$	$0.5 \pm 0.0$		$tW$	$0.5 \pm 0.1$	
$t\bar{t}$	$13.8 \pm 0.2$		$t\bar{t}$	$13.3 \pm 2.7$	
$Z + \text{jets}$	$63.5 \pm 9.6$		$Z + \text{jets}$	$181.3 \pm 82.4$	
$VV + \text{LF}$	$2039.7 \pm 628.5$		$VV + \text{LF}$	$1999.9 \pm 104.6$	
$VV + \text{HF}$	$382.1 \pm 139.6$		$VV + \text{HF}$	$383.0 \pm 78.3$	
$t\bar{t}Z + tWZ$	$58.9 \pm 7.9$		$t\bar{t}Z + tWZ$	$63.2 \pm 7.0$	
$t\bar{t} H + t\bar{t} W$	$2.9 \pm 0.5$		$t\bar{t} H + t\bar{t} W$	$3.0 \pm 0.5$	
Total	$2616.8 \pm 646.0$		Total	$2697.2 \pm 56.2$	
Data	2703		Data	2703	
CR diboson 3j0b			CR diboson 3j0b		
$tZq$	$22.3 \pm 1.9$		$tZq$	$21.2 \pm 3.3$	
$tW$	$0.3 \pm 0.0$		$tW$	$0.3 \pm 0.1$	
$t\bar{t}$	$6.8 \pm 0.1$		$t\bar{t}$	$6.6 \pm 1.3$	
$Z + \text{jets}$	$20.2 \pm 3.0$		$Z + \text{jets}$	$53.0 \pm 23.5$	
$VV + \text{LF}$	$708.0 \pm 351.8$		$VV + \text{LF}$	$624.1 \pm 53.3$	
$VV + \text{HF}$	$190.0 \pm 101.2$		$VV + \text{HF}$	$186.2 \pm 50.5$	
$t\bar{t}Z + tWZ$	$58.7 \pm 7.4$		$t\bar{t}Z + tWZ$	$61.9 \pm 6.2$	
$t\bar{t} H + t\bar{t} W$	$1.7 \pm 0.3$		$t\bar{t} H + t\bar{t} W$	$1.7 \pm 0.3$	
Total	$1008.0 \pm 367.6$		Total	$955.0 \pm 29.2$	
Data	949		Data	949	

Table 41: Pre-fit (left) and post-fit (right) event yields in the  $t\bar{t}$  CRs for the unblinded fit. The uncertainties include both statistical and systematic uncertainties.

	CR $t\bar{t}$ 2j1b	CR $t\bar{t}$ 2j1b	
$tZq$	$0.2 \pm 0.1$	$tZq$	$0.2 \pm 0.1$
$tW$	$0.8 \pm 0.1$	$tW$	$0.7 \pm 0.1$
$t\bar{t}$	$34.0 \pm 2.5$	$t\bar{t}$	$32.5 \pm 6.3$
$Z + \text{jets}$	$0 \pm 0$	$Z + \text{jets}$	$0 \pm 0$
$VV + \text{LF}$	$0.1 \pm 0.0$	$VV + \text{LF}$	$0.1 \pm 0.0$
$VV + \text{HF}$	$0.4 \pm 0.2$	$VV + \text{HF}$	$0.4 \pm 0.1$
$t\bar{t}Z + tWZ$	$4.4 \pm 0.6$	$t\bar{t}Z + tWZ$	$4.8 \pm 0.5$
$t\bar{t} H + t\bar{t} W$	$12.1 \pm 1.9$	$t\bar{t} H + t\bar{t} W$	$12.4 \pm 1.9$
Total	$52.0 \pm 3.3$	Total	$51.1 \pm 6.1$
Data	49	Data	49
	CR $t\bar{t}$ 3j1b	CR $t\bar{t}$ 3j1b	
$tZq$	$0.2 \pm 0.1$	$tZq$	$0.2 \pm 0.1$
$tW$	$0.5 \pm 0.0$	$tW$	$0.5 \pm 0.1$
$t\bar{t}$	$15.3 \pm 1.1$	$t\bar{t}$	$14.9 \pm 3.1$
$Z + \text{jets}$	$0 \pm 0$	$Z + \text{jets}$	$0 \pm 0$
$VV + \text{LF}$	$0.0 \pm 0.0$	$VV + \text{LF}$	$0.0 \pm 0.0$
$VV + \text{HF}$	$0.3 \pm 0.2$	$VV + \text{HF}$	$0.3 \pm 0.1$
$t\bar{t}Z + tWZ$	$3.7 \pm 0.6$	$t\bar{t}Z + tWZ$	$3.9 \pm 0.5$
$t\bar{t} H + t\bar{t} W$	$8.0 \pm 1.3$	$t\bar{t} H + t\bar{t} W$	$8.2 \pm 1.3$
Total	$28.1 \pm 1.9$	Total	$28.0 \pm 3.0$
Data	31	Data	31

Table 42: Pre-fit (left) and post-fit (right) event yields in the  $t\bar{t}Z$  CRs for the unblinded fit. The uncertainties include both statistical and systematic uncertainties.

	CR $t\bar{t}Z$ 3j2b	CR $t\bar{t}Z$ 3j2b
$tZq$	$13.2 \pm 0.9$	$12.9 \pm 2.0$
$tW$	$0.1 \pm 0.0$	$0.1 \pm 0.0$
$t\bar{t}$	$1.6 \pm 0.0$	$1.6 \pm 0.3$
$Z + \text{jets}$	$0.5 \pm 0.0$	$1.4 \pm 0.6$
$VV + \text{LF}$	$0.1 \pm 0.1$	$0.1 \pm 0.1$
$VV + \text{HF}$	$5.3 \pm 3.4$	$5.2 \pm 1.7$
$t\bar{t}Z + tWZ$	$49.5 \pm 11.8$	$59.3 \pm 7.1$
$t\bar{t} H + t\bar{t} W$	$2.8 \pm 0.5$	$2.8 \pm 0.5$
Total	$73.1 \pm 12.5$	$83.5 \pm 6.4$
Data	92	92
	CR $t\bar{t}Z$ 4j2b	CR $t\bar{t}Z$ 4j2b
$tZq$	$8.6 \pm 0.8$	$8.0 \pm 1.3$
$tW$	$0 \pm 0$	$0 \pm 0$
$t\bar{t}$	$1.0 \pm 0.0$	$1.0 \pm 0.2$
$Z + \text{jets}$	$0.1 \pm 0.0$	$0.4 \pm 0.2$
$VV + \text{LF}$	$0.1 \pm 0.1$	$0.1 \pm 0.1$
$VV + \text{HF}$	$3.3 \pm 2.0$	$3.4 \pm 1.0$
$t\bar{t}Z + tWZ$	$51.5 \pm 8.5$	$58.1 \pm 5.3$
$t\bar{t} H + t\bar{t} W$	$1.9 \pm 0.3$	$2.0 \pm 0.3$
Total	$66.6 \pm 8.9$	$72.8 \pm 5.0$
Data	75	75

Not reviewed, for internal circulation only

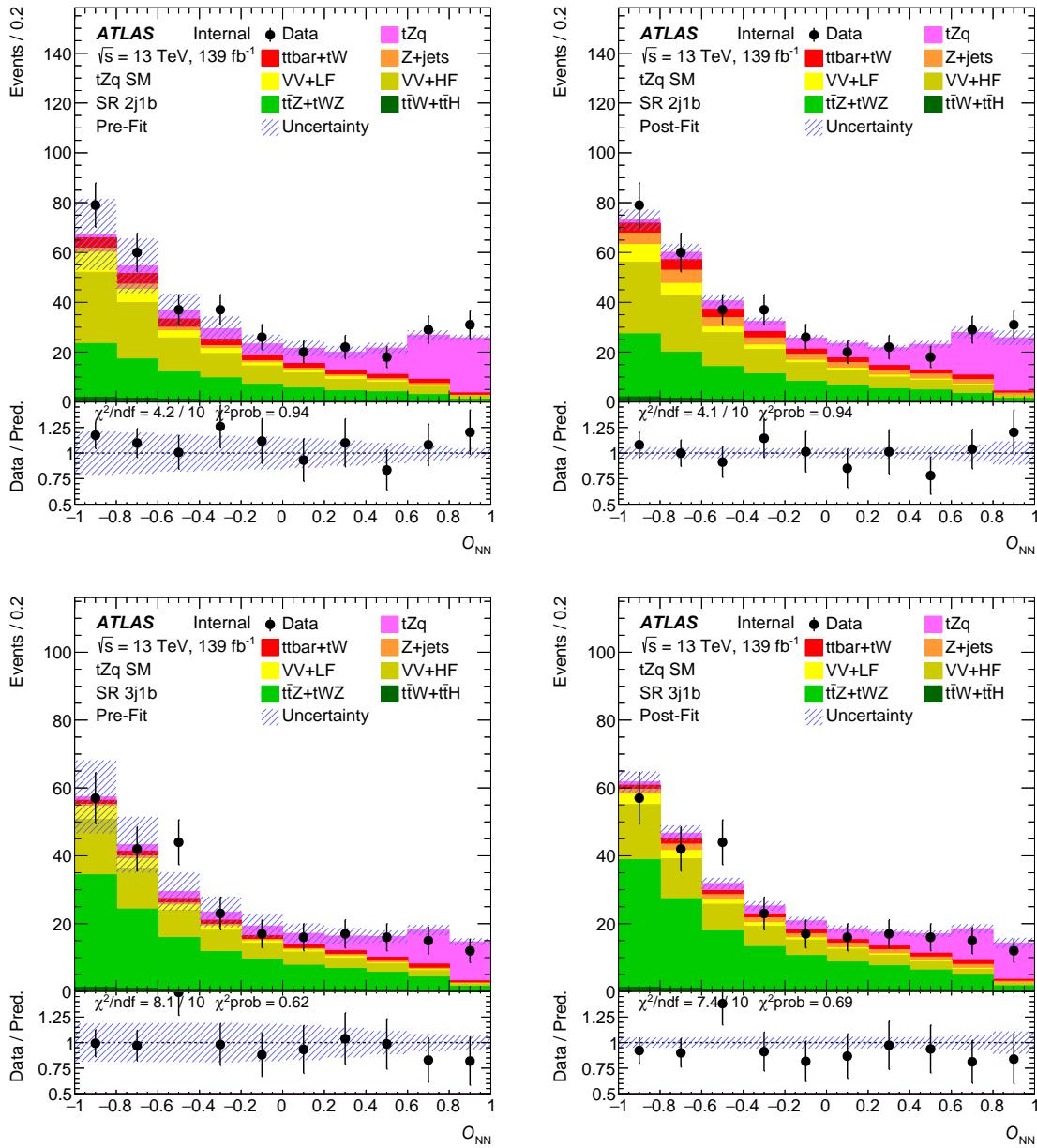


Figure 88: Pre-fit (left) and post-fit (right) NN output distributions in the signal regions. The uncertainty band includes both statistical and systematic uncertainties.

Not reviewed, for internal circulation only

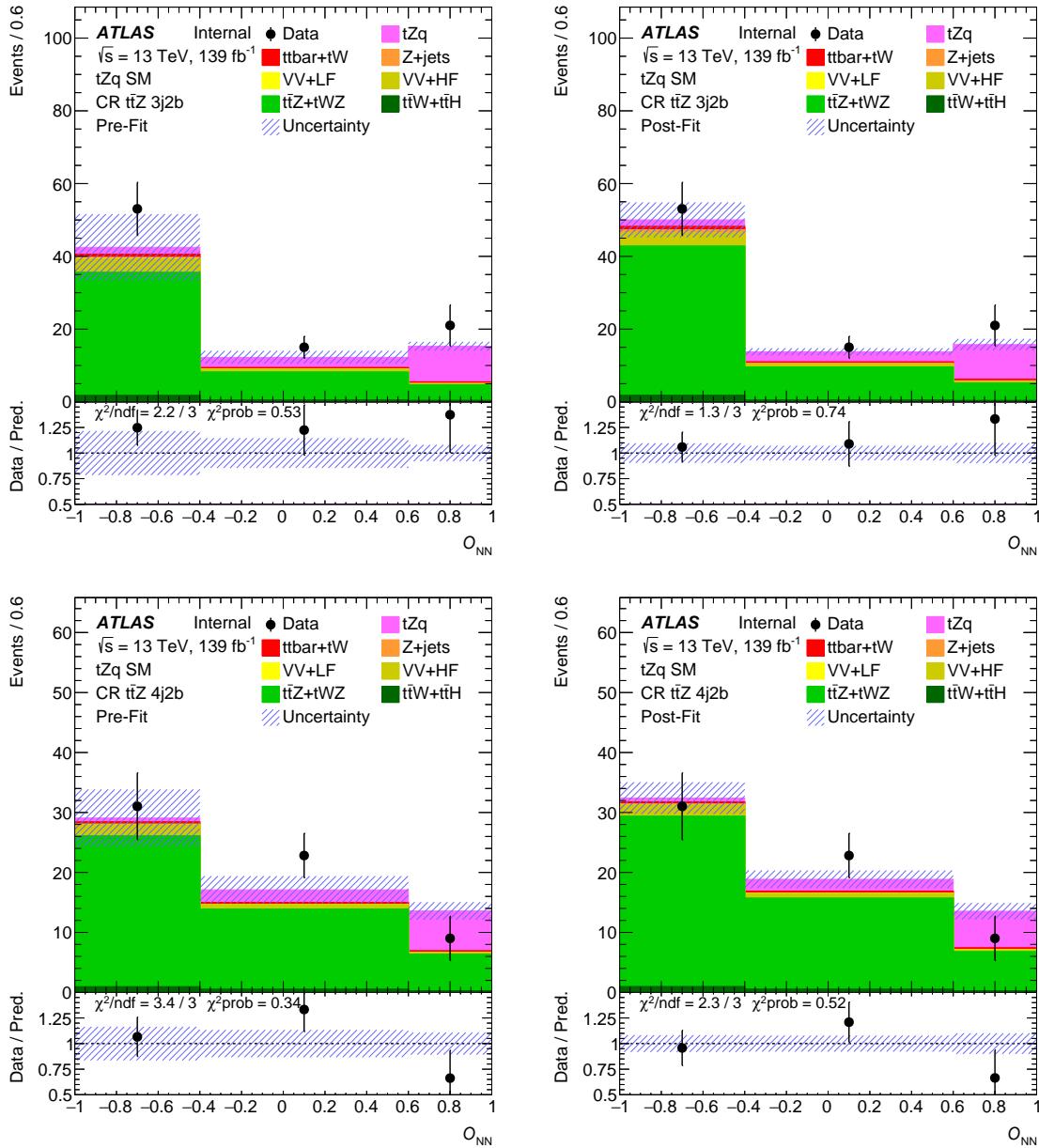


Figure 89: Pre-fit (left) and post-fit (right) NN output distributions in the  $t\bar{t}Z$  control regions. The uncertainty band includes both statistical and systematic uncertainties.

Not reviewed, for internal circulation only

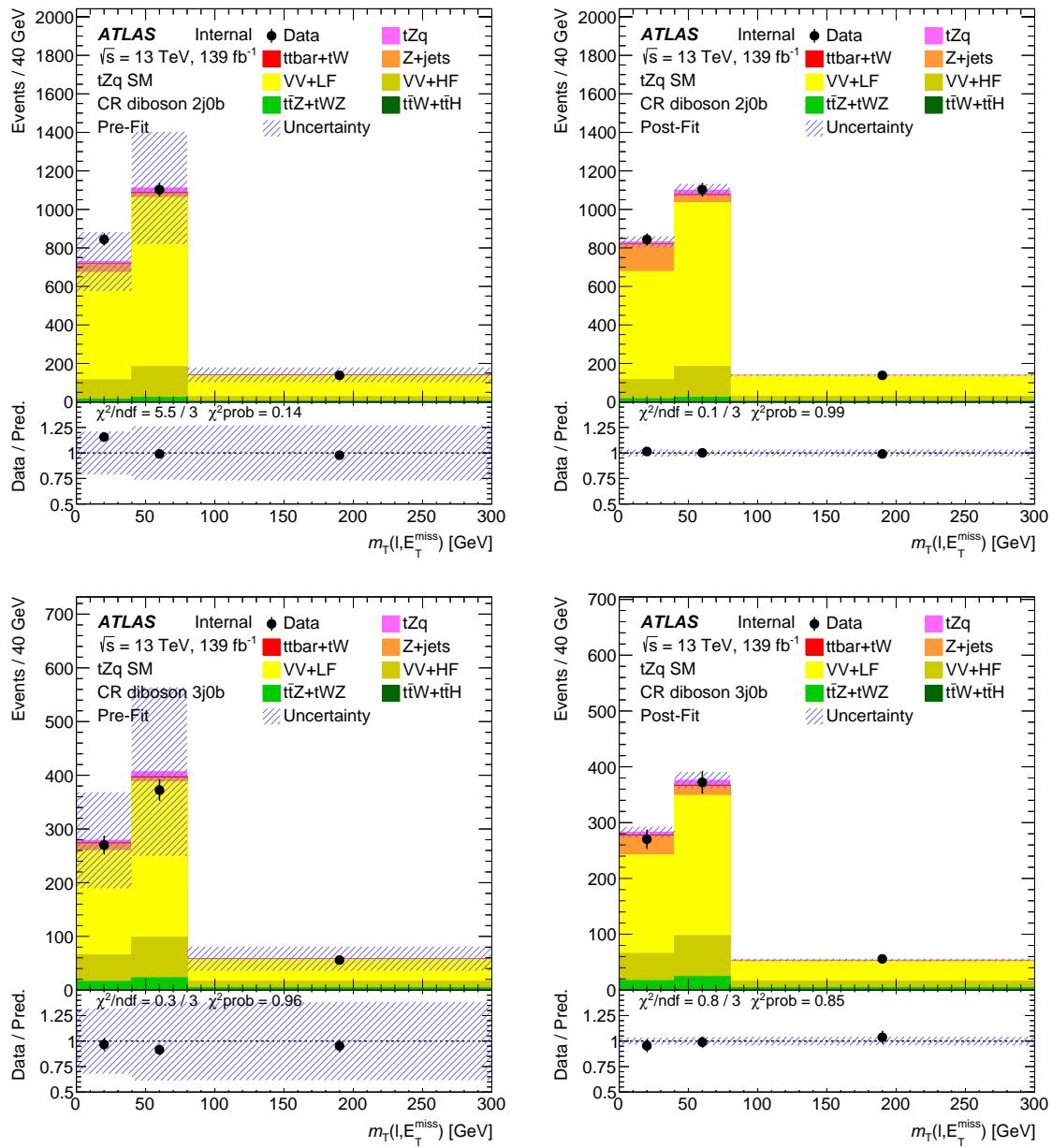


Figure 90: Pre-fit (left) and post-fit (right)  $E_T^{\text{miss}}$  distributions in the diboson control regions. The uncertainty band includes both statistical and systematic uncertainties.

Not reviewed, for internal circulation only

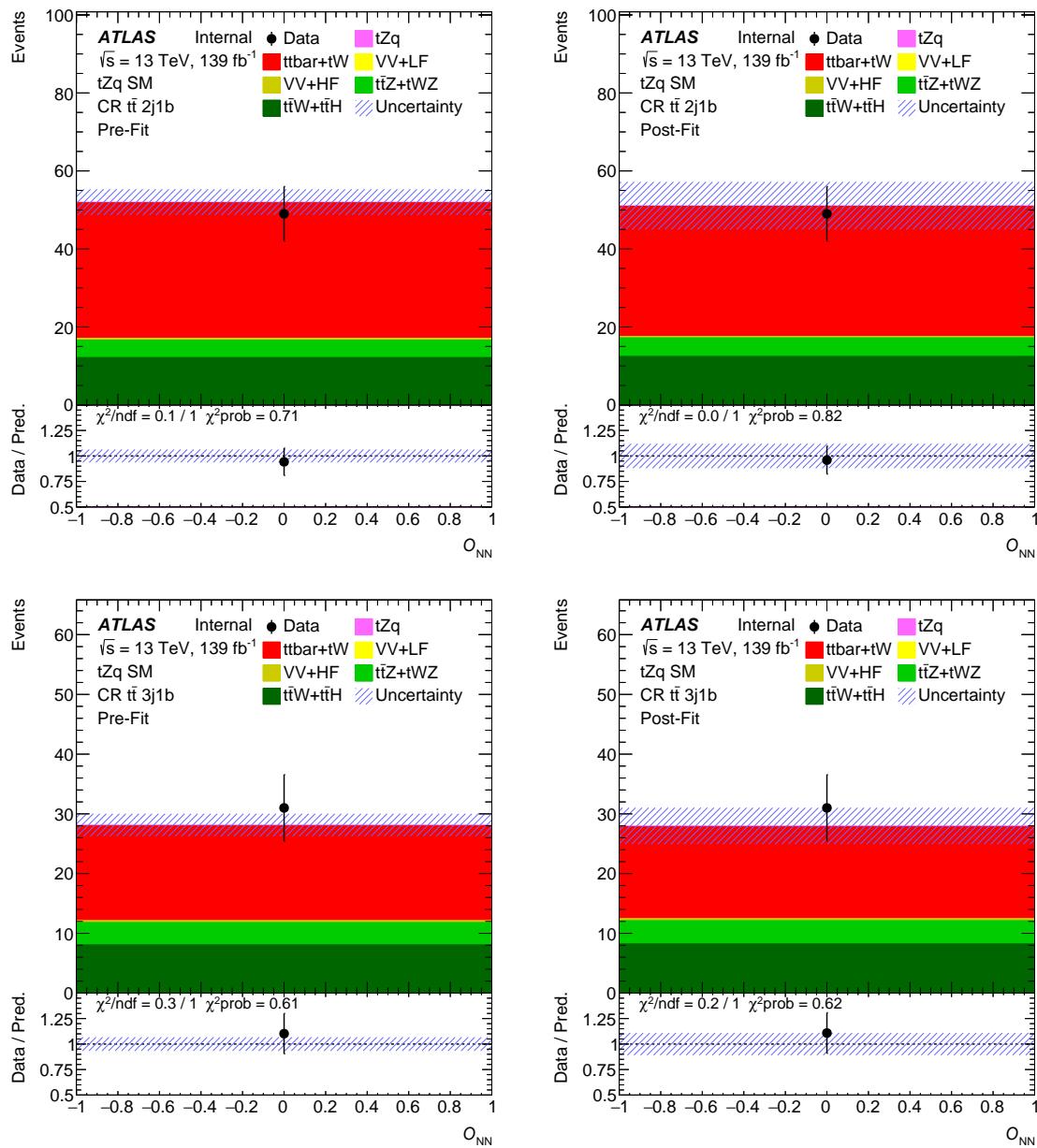


Figure 91: Pre-fit (left) and post-fit (right) NN output distributions in the  $t\bar{t}$  control regions. The uncertainty band includes both statistical and systematic uncertainties. Since the  $t\bar{t}$  background is free floating in the fit, there are no uncertainties on this background pre-fit.

1158 **10.3.8 Pre- and post-fit distributions of the 4 highest ranked NN input variables in the SRs**

1159 Figures 92 to 95 show the distributions of the four highest ranked NN input variables in the SRs.

Not reviewed, for internal circulation only

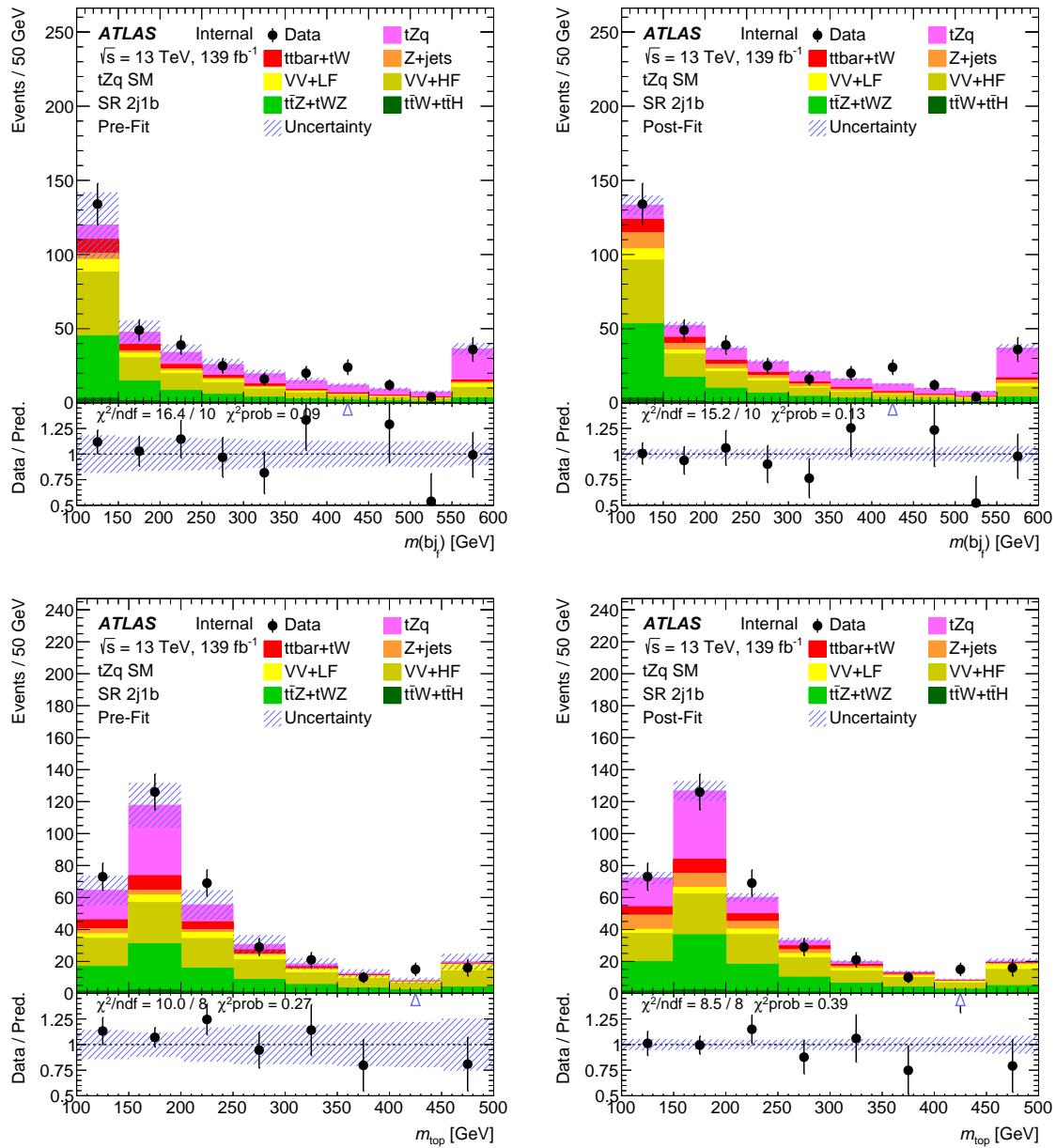


Figure 92: Pre-fit (left) and post-fit (right) NN input variable distributions in the 2j1b signal region. The uncertainty band includes both statistical and systematic uncertainties.

Not reviewed, for internal circulation only

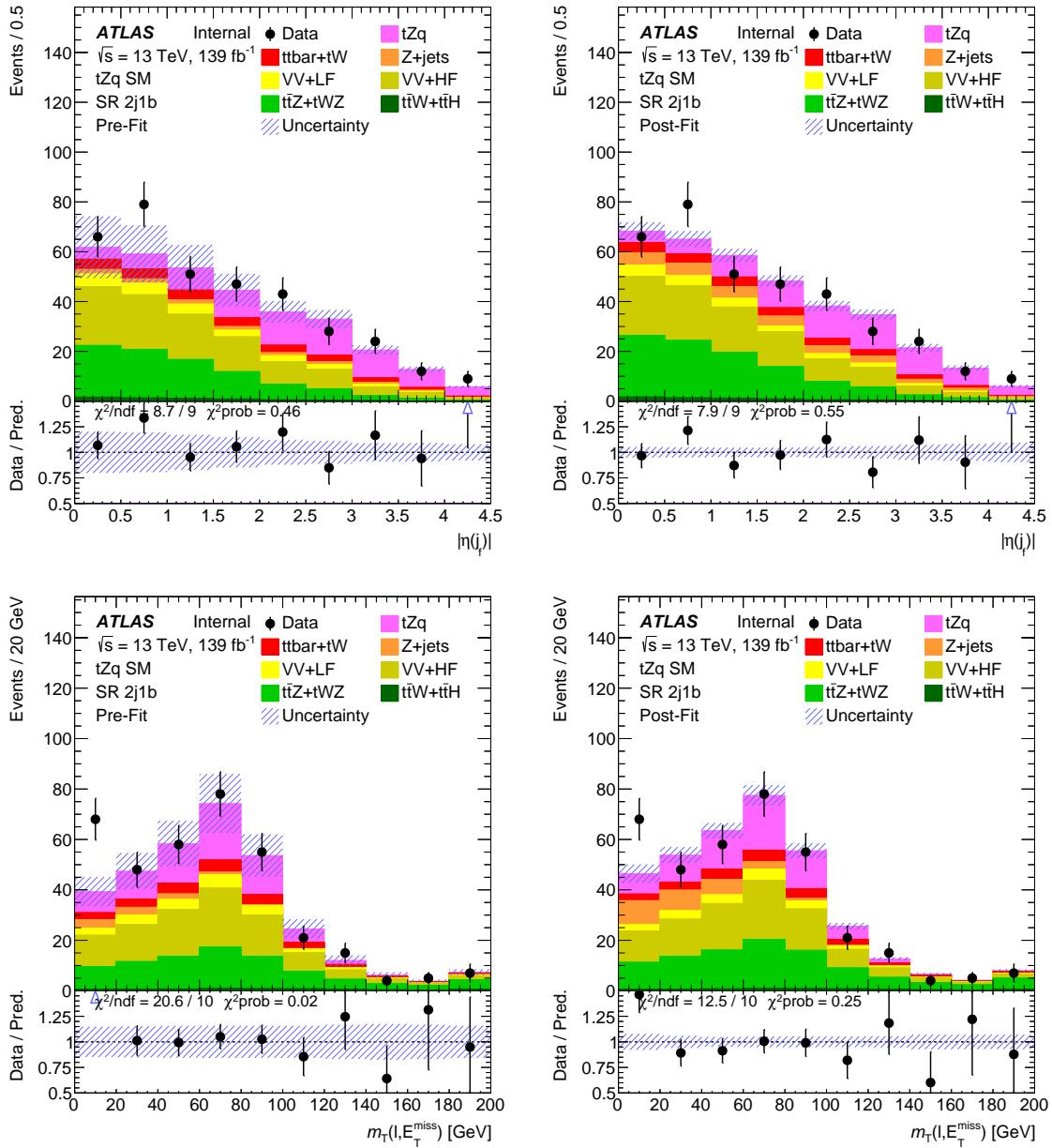


Figure 93: Pre-fit (left) and post-fit (right) NN input variable distributions in the 2j1b signal region. The uncertainty band includes both statistical and systematic uncertainties.

Not reviewed, for internal circulation only

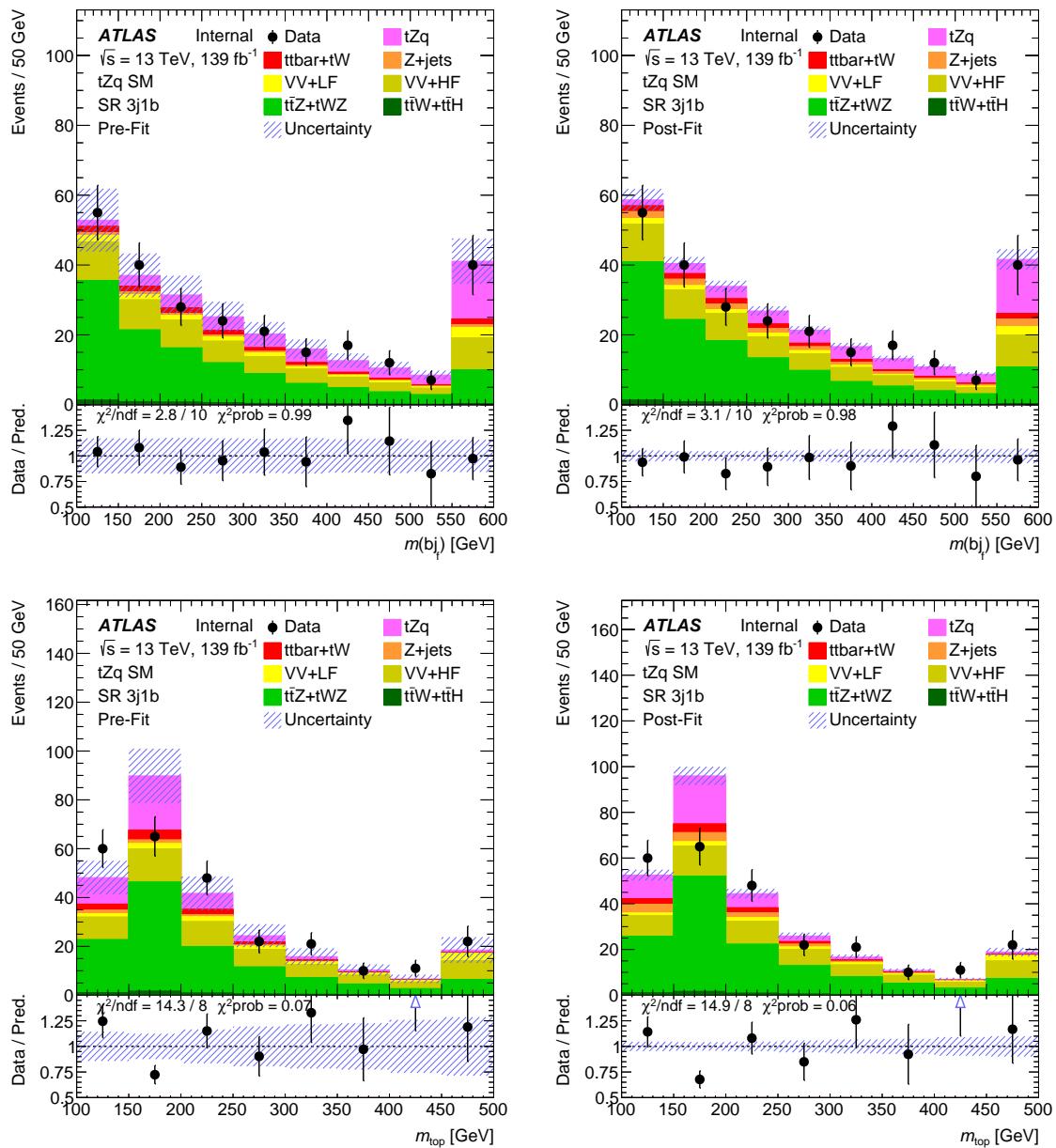


Figure 94: Pre-fit (left) and post-fit (right) NN input variable distributions in the 3j1b signal region. The uncertainty band includes both statistical and systematic uncertainties.

Not reviewed, for internal circulation only

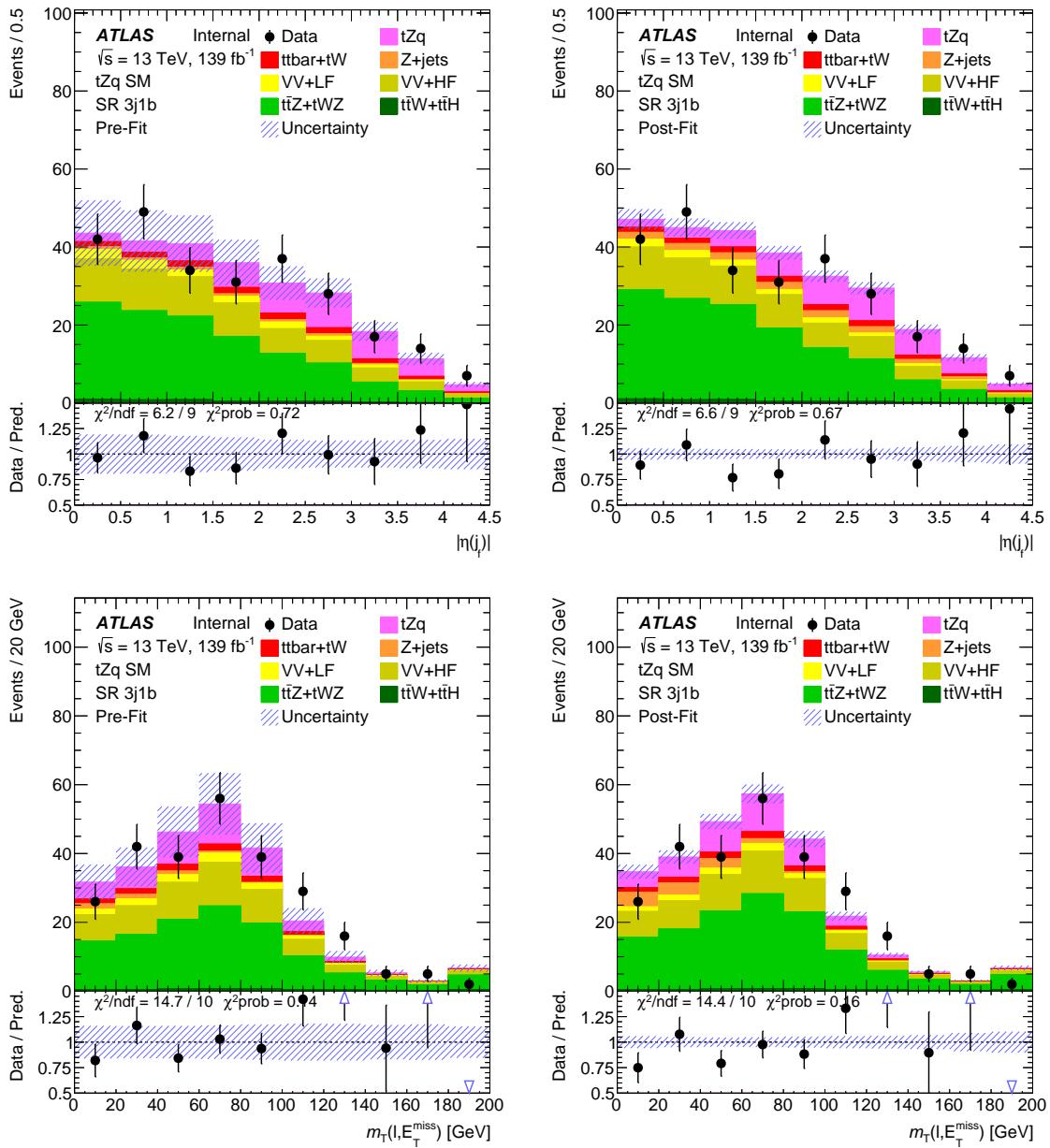


Figure 95: Pre-fit (left) and post-fit (right) NN input variable distributions in the 3j1b signal region. The uncertainty band includes both statistical and systematic uncertainties.

1160 **10.3.9 Pre- and post-fit distributions of the 4 highest ranked NN input variables in the VRs**

1161 Figures 96 to 99 show the distributions of the four highest ranked NN input variables in the diboson VRs.  
 1162 Figures 100 to 103 show the distributions of the four highest ranked NN input variables in the diboson  
 1163 VRs.

Not reviewed, for internal circulation only

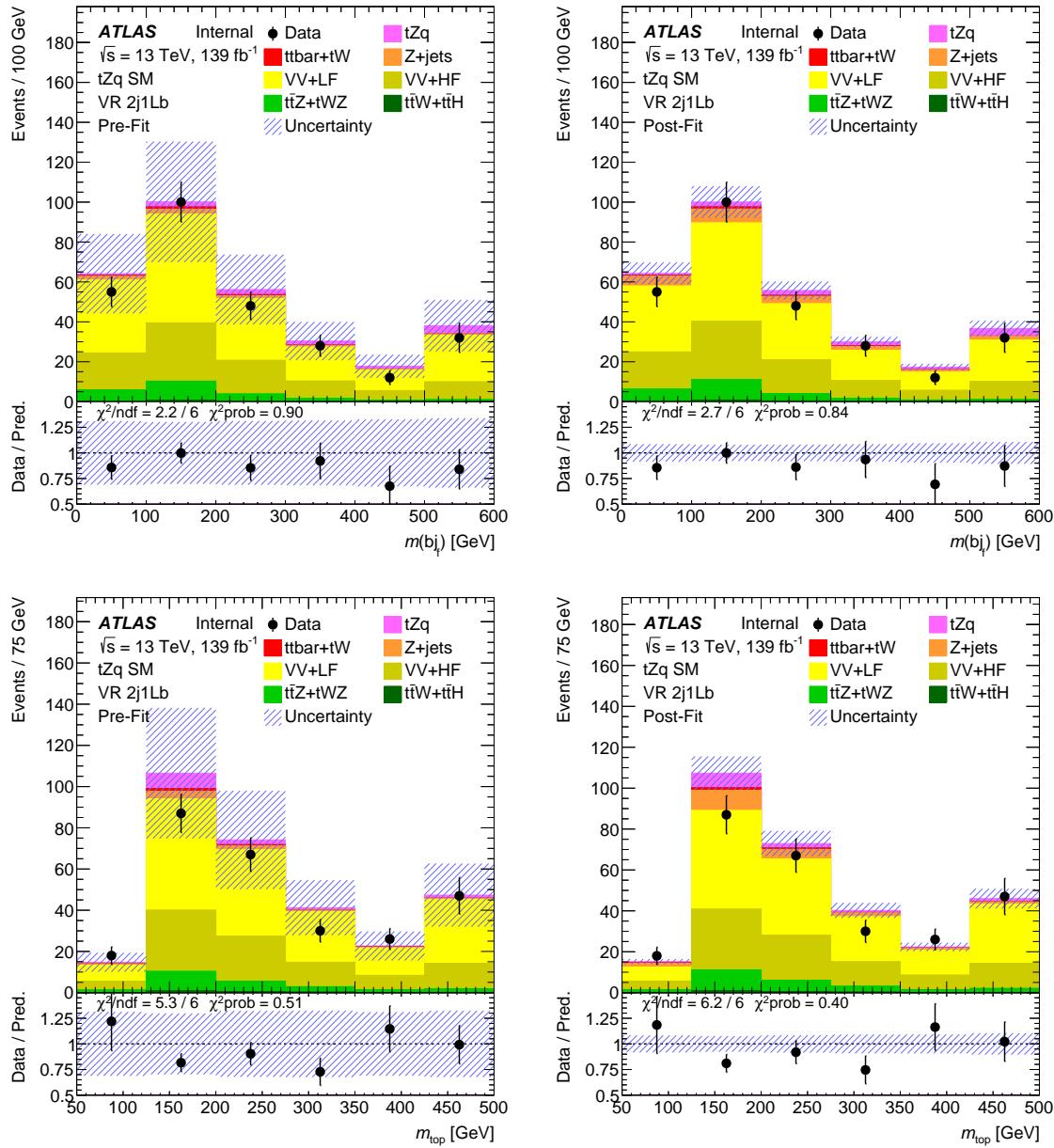


Figure 96: Pre-fit (left) and post-fit (right) NN input variable distributions in the diboson 2j1Lb validation region. The uncertainty band includes both statistical and systematic uncertainties.

Not reviewed, for internal circulation only

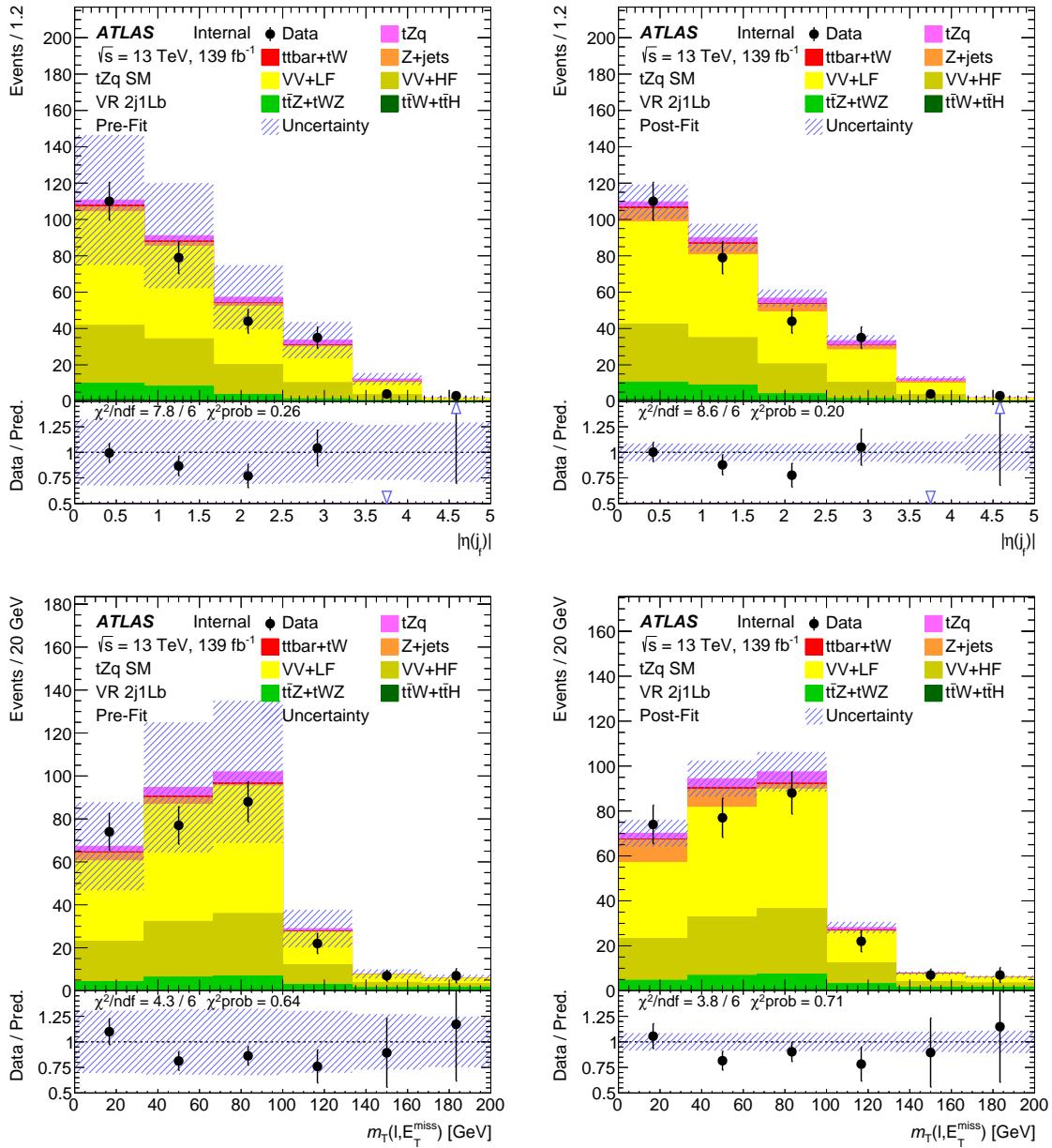


Figure 97: Pre-fit (left) and post-fit (right) NN input variable distributions in the diboson 2j1Lb validation region. The uncertainty band includes both statistical and systematic uncertainties.

Not reviewed, for internal circulation only

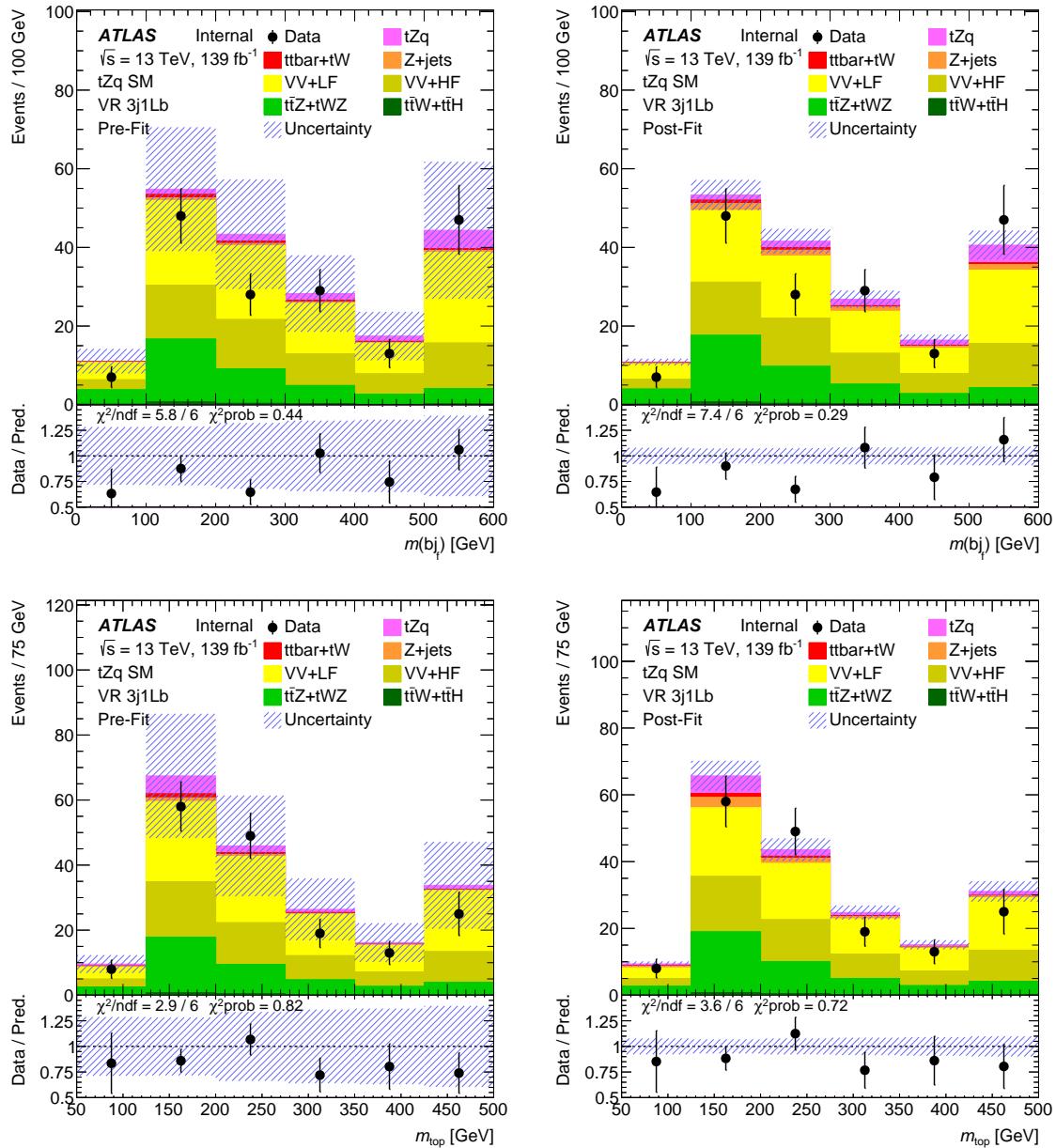


Figure 98: Pre-fit (left) and post-fit (right) NN input variable distributions in the diboson 3j1Lb validation region. The uncertainty band includes both statistical and systematic uncertainties.

Not reviewed, for internal circulation only

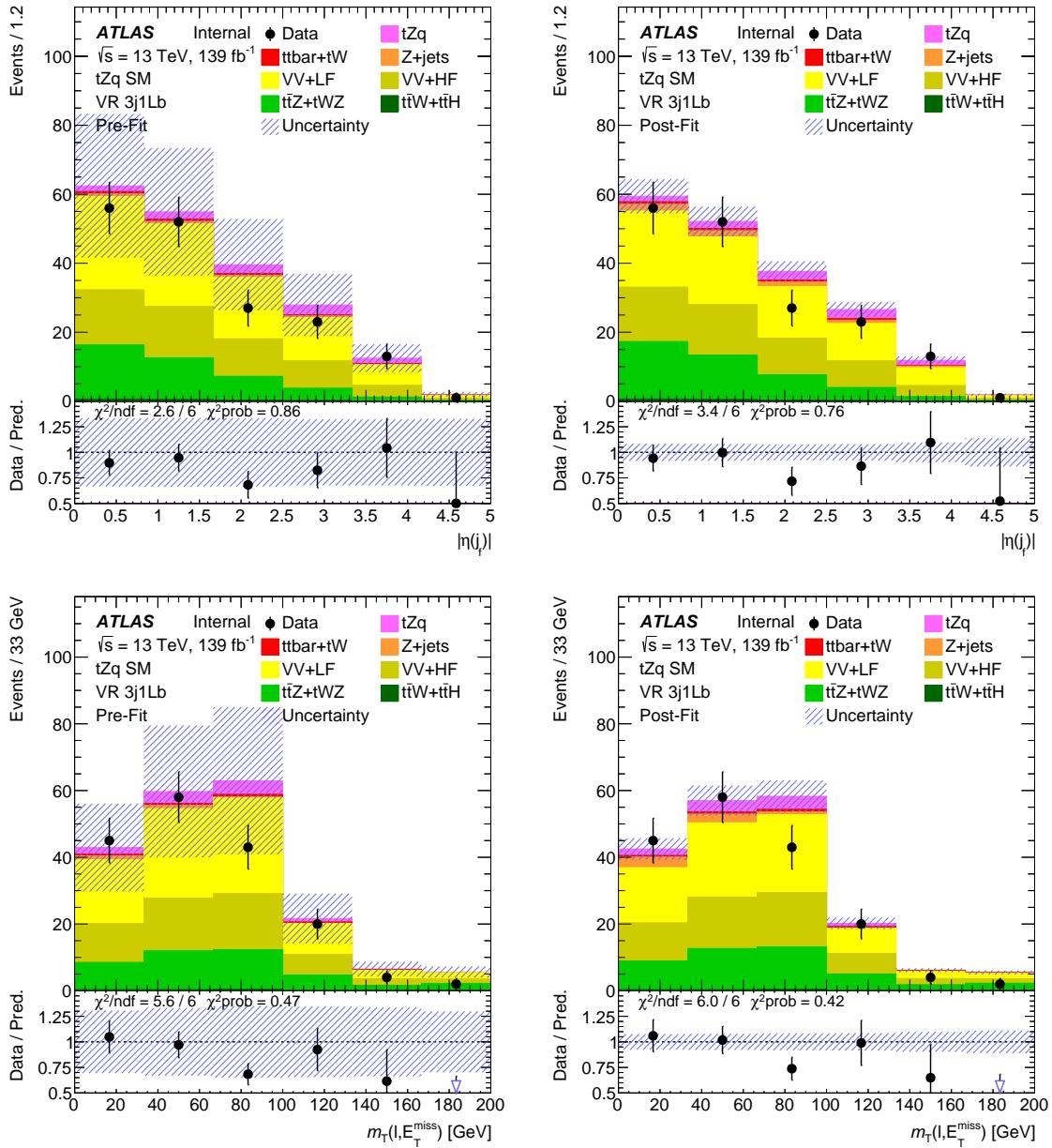


Figure 99: Pre-fit (left) and post-fit (right) NN input variable distributions in the diboson 3j1Lb validation region. The uncertainty band includes both statistical and systematic uncertainties.

Not reviewed, for internal circulation only

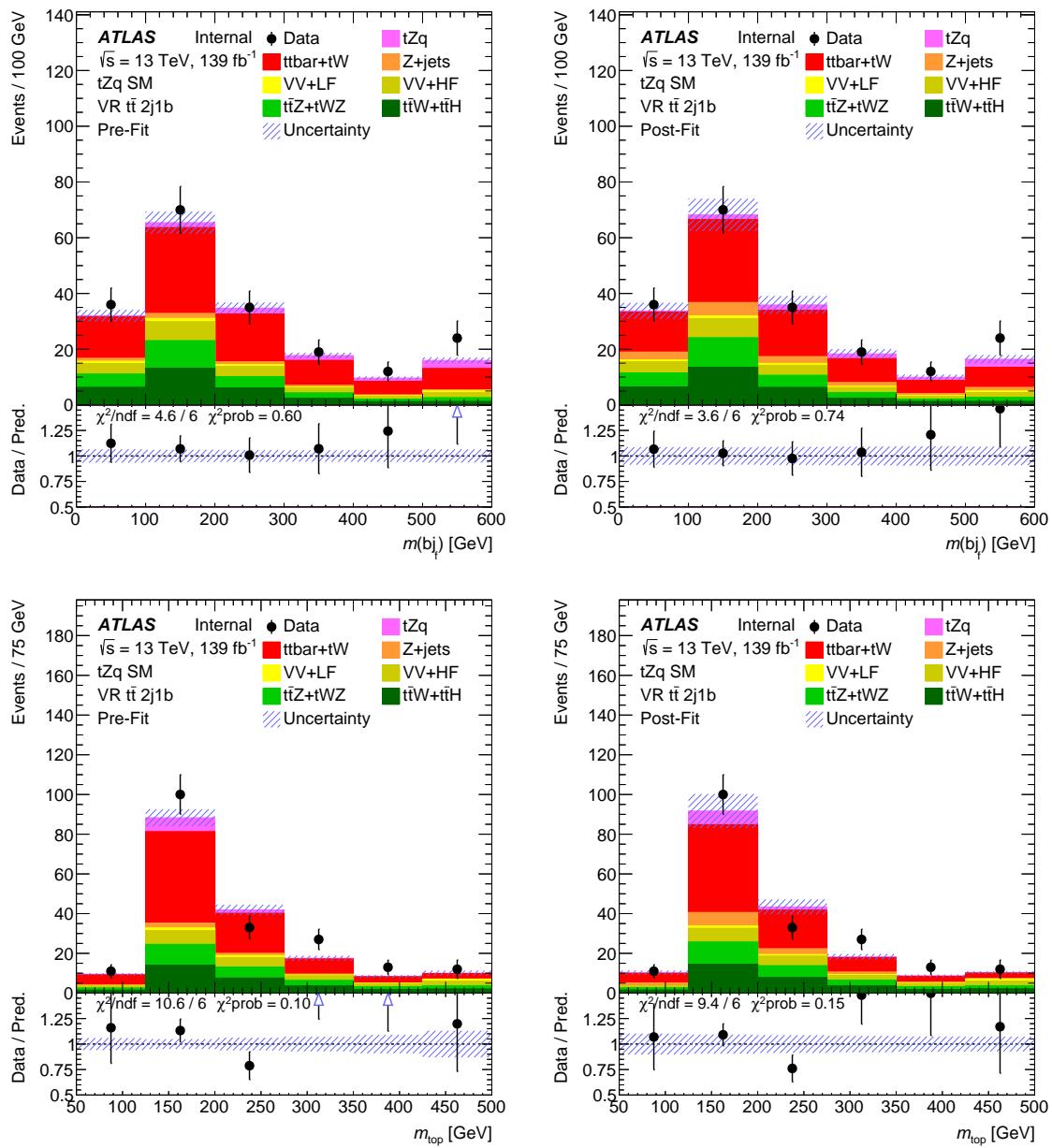


Figure 100: Pre-fit (left) and post-fit (right) NN input variable distributions in the  $t\bar{t}V + t\bar{t}$  2j1b validation region. The uncertainty band includes both statistical and systematic uncertainties. Since the  $t\bar{t}$  background is free floating in the fit, there are no uncertainties on this background pre-fit.

Not reviewed, for internal circulation only

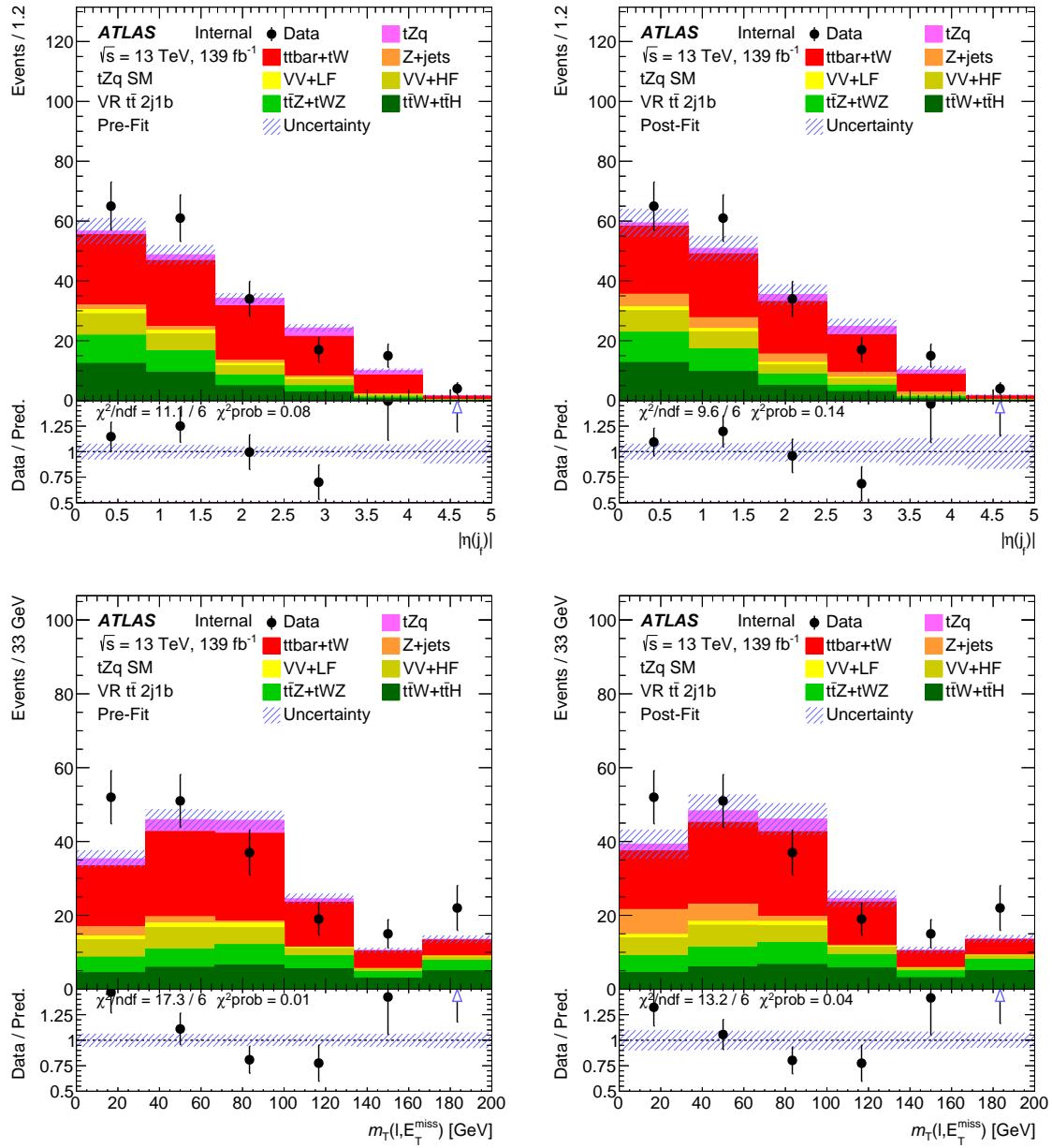


Figure 101: Pre-fit (left) and post-fit (right) NN input variable distributions in the  $t\bar{t}V + t\bar{t}$  2j1b validation region. The uncertainty band includes both statistical and systematic uncertainties. Since the  $t\bar{t}$  background is free floating in the fit, there are no uncertainties on this background pre-fit.

Not reviewed, for internal circulation only

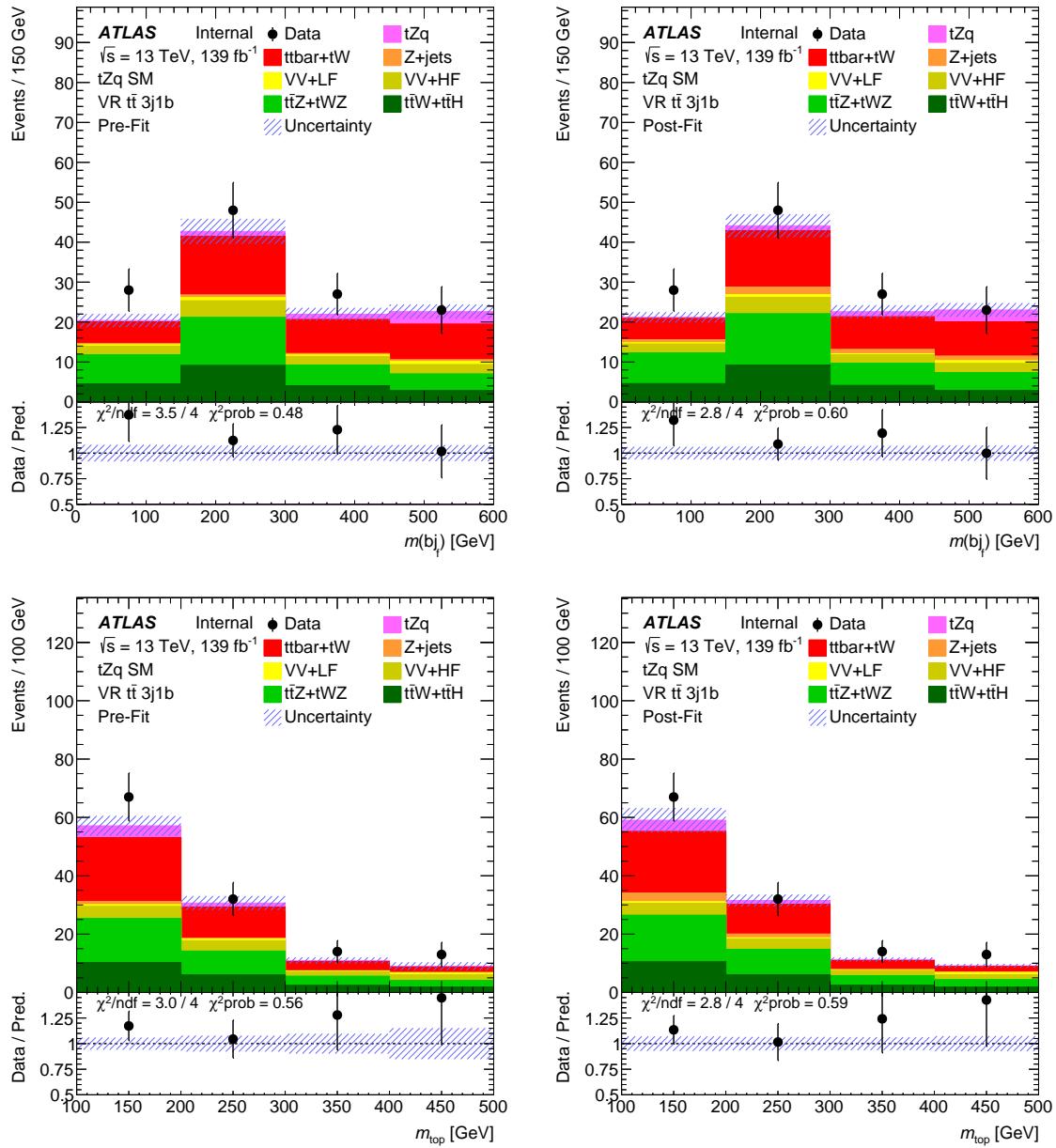


Figure 102: Pre-fit (left) and post-fit (right) NN input variable distributions in the  $t\bar{t}V + t\bar{t} 3j1b$  validation regions. The uncertainty band includes both statistical and systematic uncertainties. Since the  $t\bar{t}$  background is free floating in the fit, there are no uncertainties on this background pre-fit.

Not reviewed, for internal circulation only

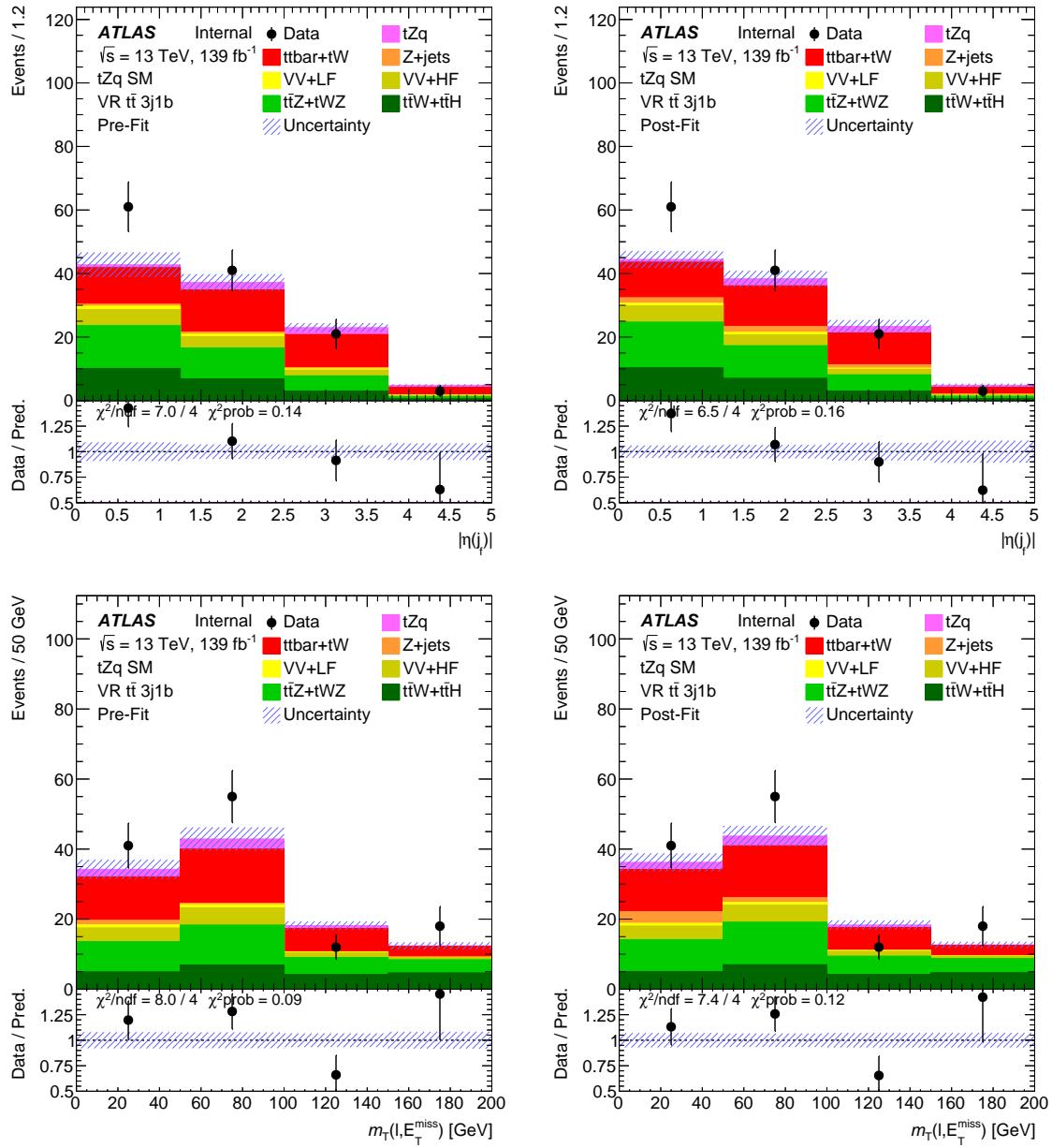


Figure 103: Pre-fit (left) and post-fit (right) NN input variable distributions in the  $t\bar{t}V + t\bar{t}$  3j1b validation regions. The uncertainty band includes both statistical and systematic uncertainties. Since the  $t\bar{t}$  background is free floating in the fit, there are no uncertainties on this background pre-fit.

## 1164 10.3.10 NN output variable distributions in VRs pre- and post-fit

Not reviewed, for internal circulation only

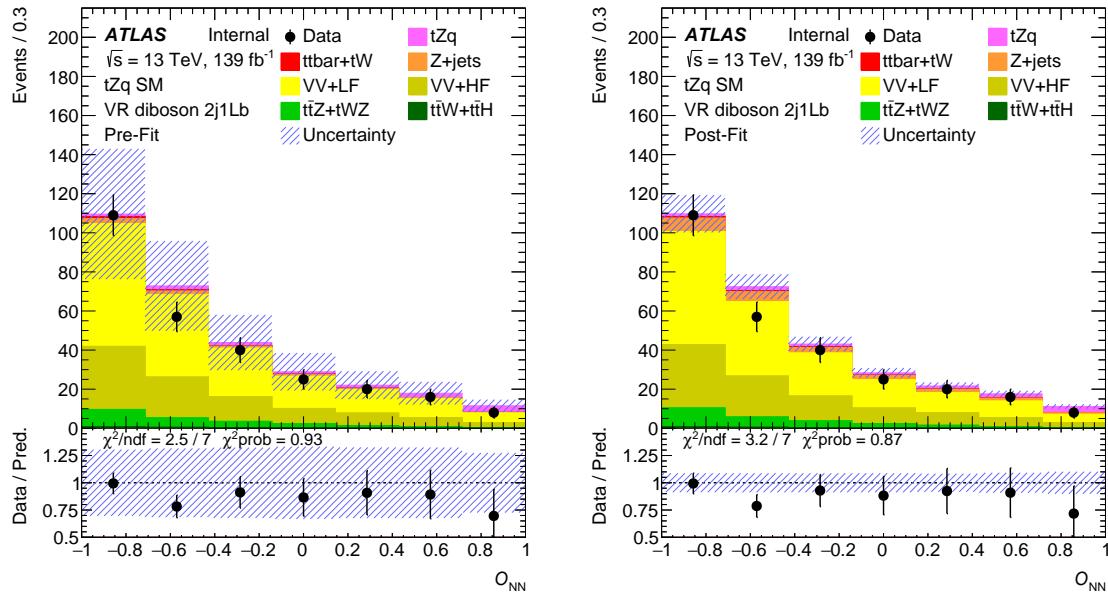


Figure 104: Pre-fit (left) and post-fit (right) NN output variable distributions in the diboson 2j1Lb validation region. The uncertainty band includes both statistical and systematic uncertainties.

Not reviewed, for internal circulation only

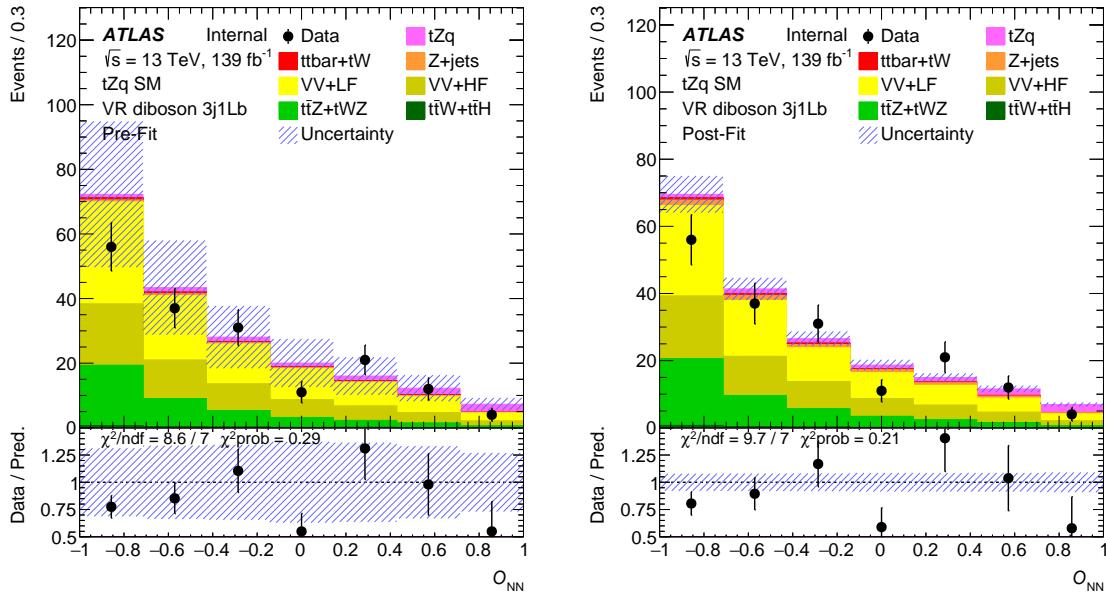


Figure 105: Pre-fit (left) and post-fit (right) NN output variable distributions in the diboson 3j1Lb validation region. The uncertainty band includes both statistical and systematic uncertainties.

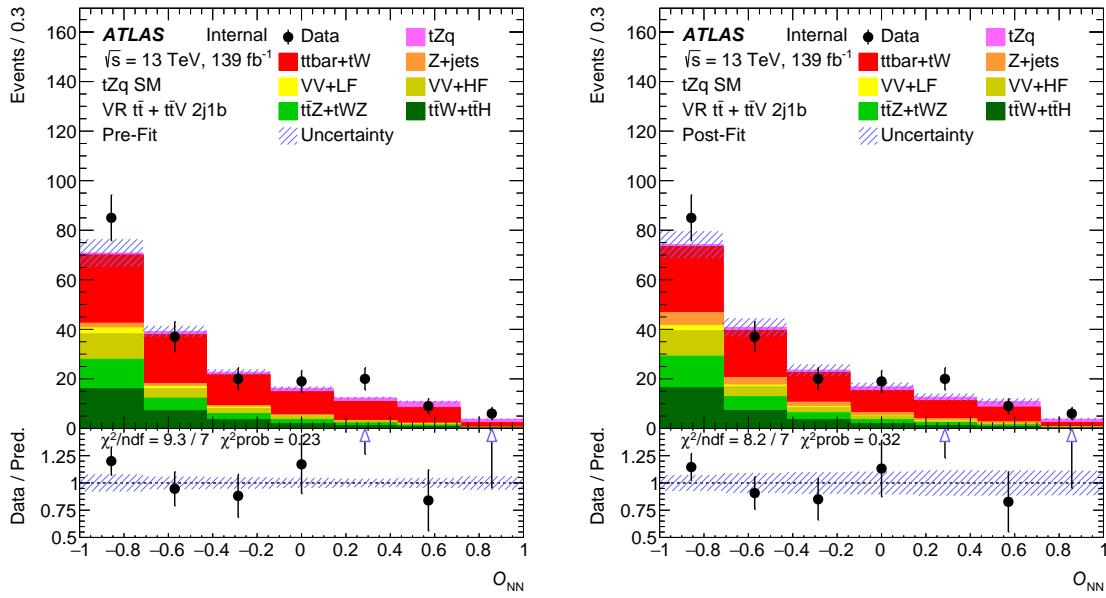


Figure 106: Pre-fit (left) and post-fit (right) NN output variable distributions in the  $t\bar{t}V + t\bar{t}$  2j1b validation region. The uncertainty band includes both statistical and systematic uncertainties. Since the  $t\bar{t}$  background is free floating in the fit, there are no uncertainties on this background pre-fit.

Not reviewed, for internal circulation only

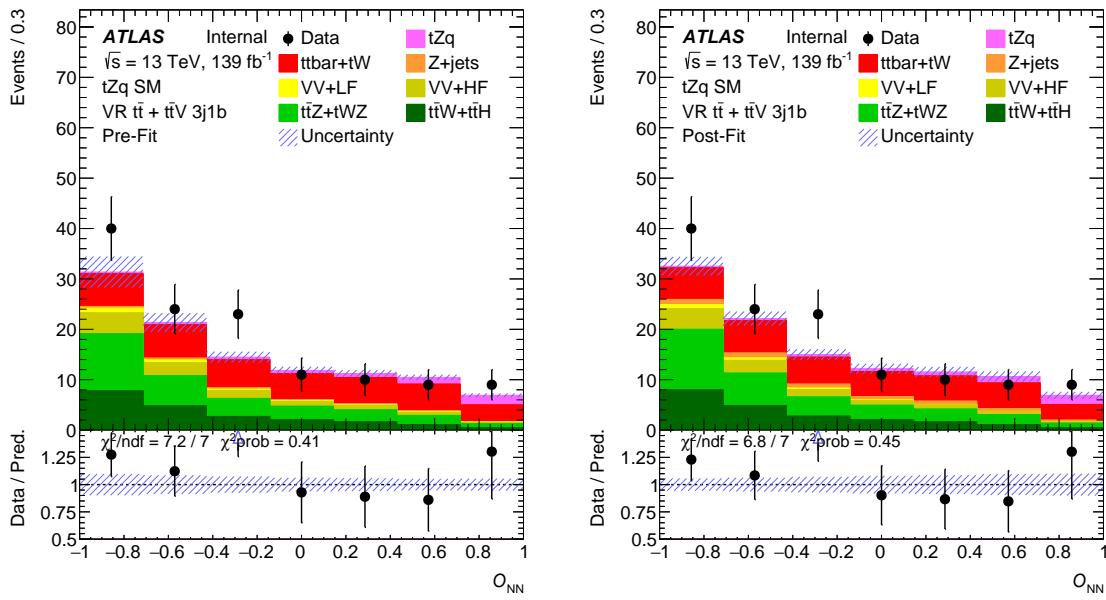


Figure 107: Pre-fit (left) and post-fit (right) NN output variable distributions in the  $t\bar{t}V + t\bar{t}$  3j1b validation regions. The uncertainty band includes both statistical and systematic uncertainties. Since the  $t\bar{t}$  background is free floating in the fit, there are no uncertainties on this background pre-fit.

1165 **10.3.11 Checks - Diboson HF rescaling**

1166 Given that typically a 10 % correction is required for the diboson HF contribution, a test was done scaling  
 1167 the  $VV + HF$  contribution by 10 % before the fit and checking the effect on  $\mu_{SIG}$  and on the pulls.

1168 In the fit setup of INT note v0.8,  $\mu$  went from 0.9663 to 0.9649, giving a relative change of 0.15 %. The  
 1169 changes in the pulls are as expected.

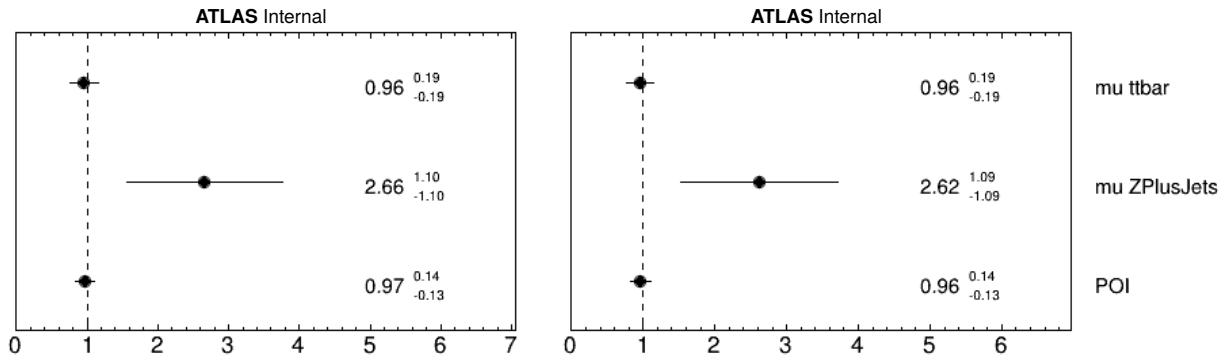


Figure 108: Normalisation factors of the unblinded fit, on the left for the default fit, on the right for the fit with diboson HF scaled down by 10 %.

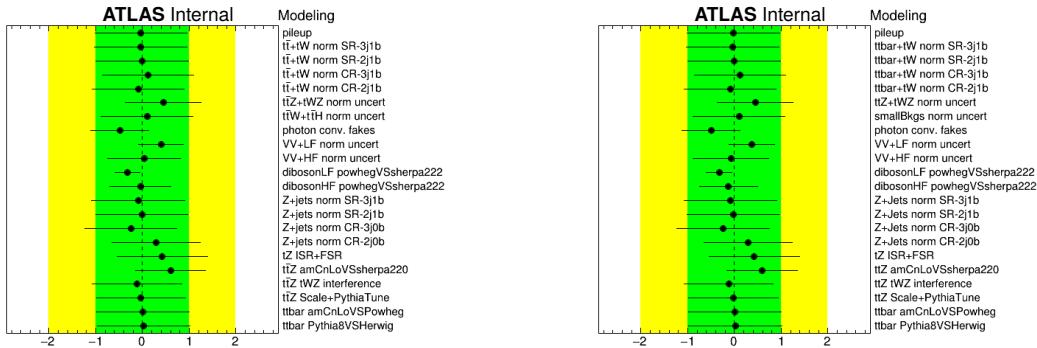


Figure 109: Pulls and constraints of the nuisance parameters of the unblinded fit: background modeling systematics, on the left for the default fit, on the right for the fit with diboson HF scaled down by 10 %.

1170 **10.3.12 Checks - Pruning**1171 The following check was not repeated after fixing the signal PDF uncertainty after the CONF note was  
1172 released.

1173 The pruning level used in the analysis is 0.5 %. A test was performed applying a pruning level of 1.0 %.

1174 The POI changes of 0.3 % while the uncertainty on the POI decreases by 4 %.

1175 The increase in the uncertainty mainly comes from jet and signal PDF uncertainties, as shown in Table 43.

Table 43: Overview of the impact of each systematic uncertainty category on the POI. Pruning levels of 1 % and 0.5 % are compared.

Uncertainty	Pruning 1 %		Pruning 0.5 %	
	Absolute impact	Relative impact	Absolute impact	Relative impact
Fakes	0.01969	2.0 %	0.02242	2.3 %
Jets+MET	0.01115	1.2 %	0.02038	2.1 %
Leptons	0.01496	1.5 %	0.01600	1.7 %
Lumi	0.01646	1.7 %	0.01626	1.7 %
Prompt	0.03187	3.3 %	0.03243	3.4 %
PileUp	0.01212	1.3 %	0.01139	1.2 %
b-tagging	0.00528	0.5 %	0.00422	0.4 %
tZ PDF	0.02110	2.2 %	0.04006	4.1 %
tZ Radiation	0.00650	0.7 %	0.00753	0.8 %
Gammas	0.00999	1.0 %	0.00996	1.0 %
FullSyst	0.06762	7.0 %	0.07743	8.0 %

1176 **10.3.13 Checks - Split into years**

1177 Given the fact that the reconstructed  $t$ -quark mass in the 3j1b SR shows some mismodeling, this distribution  
 1178 is shown separately for the three years of data taking. As it can be seen, the mismodeling is just present in  
 1179 part of the dataset, giving the confidence that it's a statistical fluctuation.

Not reviewed, for internal circulation only

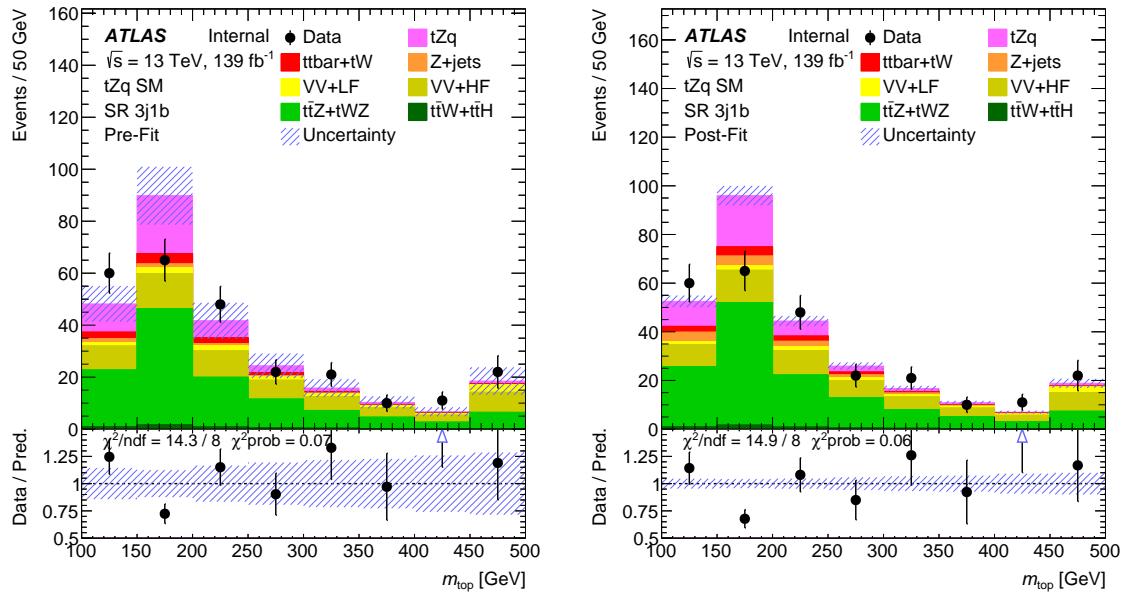


Figure 110: Pre-fit (left) and post-fit (right) NN input variable distributions in the 3j1b signal region. The full Run2 dataset is shown. The uncertainty band includes both statistical and systematic uncertainties.

Not reviewed, for internal circulation only

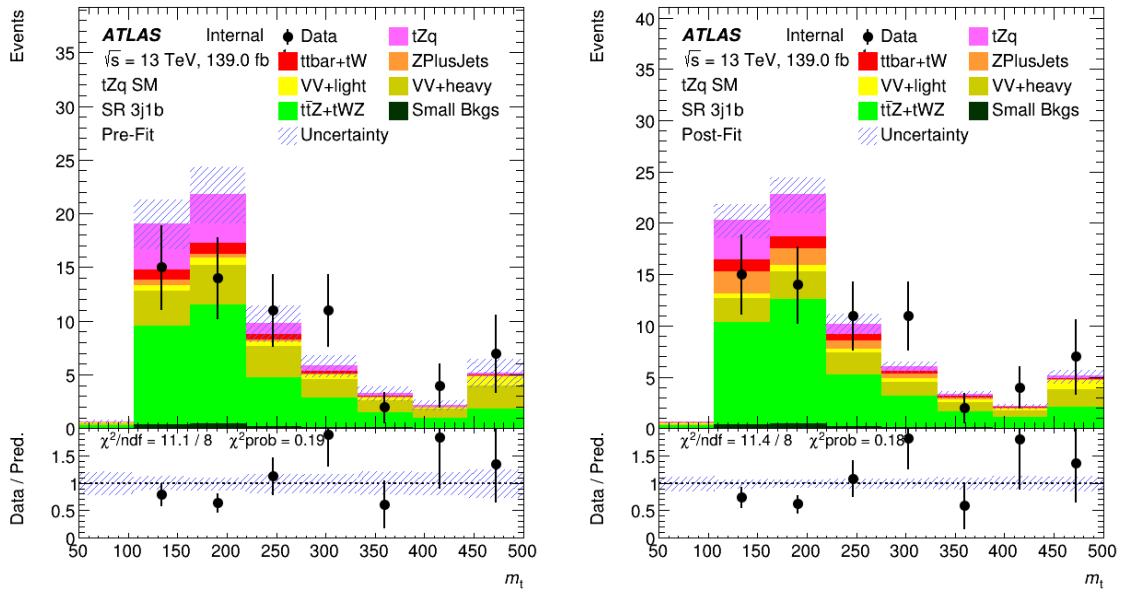


Figure 111: Pre-fit (left) and post-fit (right) NN input variable distributions in the 3j1b signal region. Only the 2015+2016 data is shown. The uncertainty band includes both statistical and systematic uncertainties.

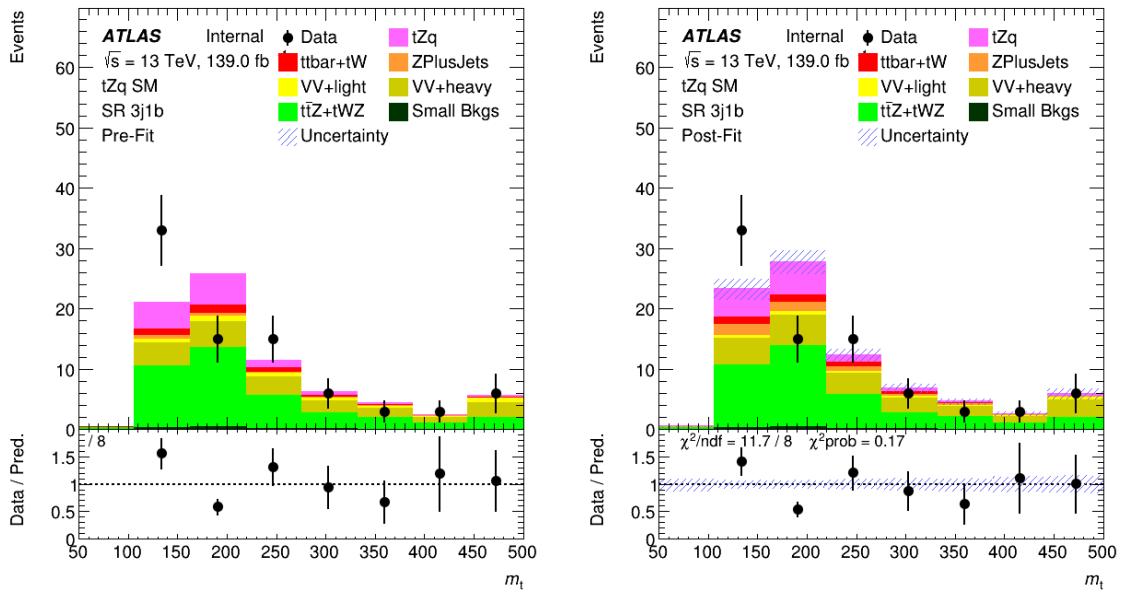


Figure 112: Pre-fit (left) and post-fit (right) NN input variable distributions in the 3j1b signal region. Only the 2017 data is shown. The uncertainty band includes both statistical and systematic uncertainties.

Not reviewed, for internal circulation only

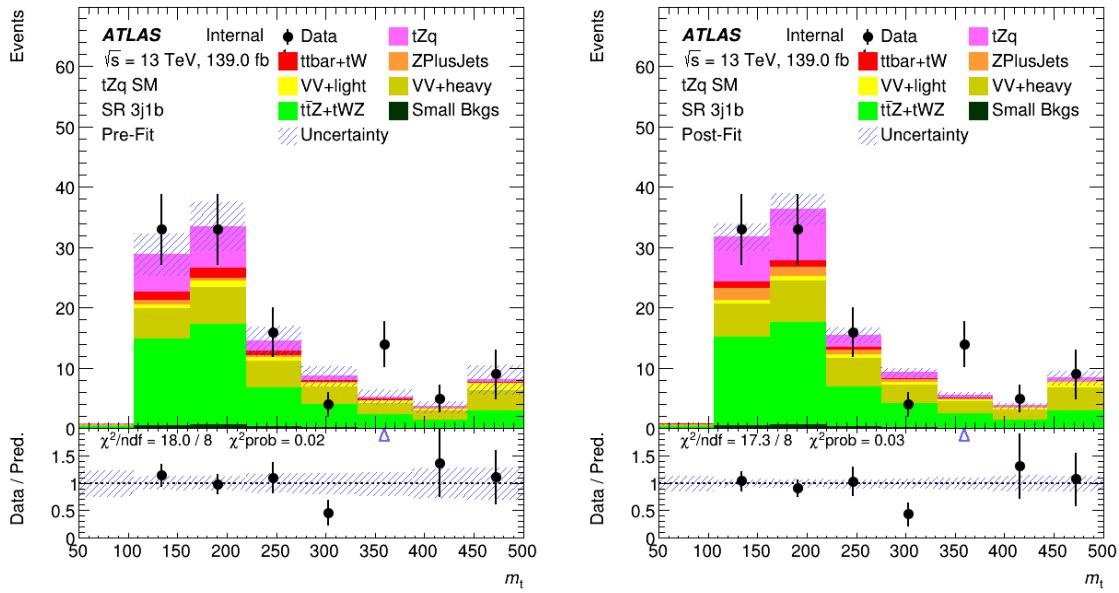


Figure 113: Pre-fit (left) and post-fit (right) NN input variable distributions in the 3j1b signal region. Only the 2018 data is shown. The uncertainty band includes both statistical and systematic uncertainties.

---

**1180 11 Conclusion**

1181  $tZq$  production has been observed with a significance of 9.1, while the expected significance is 9.2. The  
1182 latter is computed scaling all backgrounds to their post-fit value from the fully unblinded fit.

1183 The measured cross section is  $97^{+13}_{-12}$  (stat.)  $\pm 7$  (syst.)  $\text{fb} = 97^{+14}_{-13} \text{ fb}$ , which has a relative uncertainty of  
1184 14 %, to be compared with the Standard Model expectation of  $101.7 \text{ fb}^{+5.2\%}_{-1.3\%}$  (scale)  $\pm 1.0\%$  (PDF).

1185 **References**

- [1] ATLAS Collaboration, *Measurement of the production cross-section of a single top quark in association with a Z boson in proton–proton collisions at 13 TeV with the ATLAS detector*, *Phys. Lett. B* **780** (2018) 557, arXiv: [1710.03659 \[hep-ex\]](https://arxiv.org/abs/1710.03659) (cit. on pp. 9, 11).
- [2] CMS Collaboration, *Measurement of the associated production of a single top quark and a Z boson in pp collisions at  $\sqrt{s} = 13$  TeV*, *Phys. Lett. B* **779** (2018) 358, arXiv: [1712.02825 \[hep-ex\]](https://arxiv.org/abs/1712.02825) (cit. on p. 9).
- [3] CMS Collaboration, *Observation of single top quark production in association with a Z boson in proton–proton collisions at  $\sqrt{s} = 13$  TeV*, *Phys. Rev. Lett.* (2018), arXiv: [1812.05900 \[hep-ex\]](https://arxiv.org/abs/1812.05900) (cit. on pp. 9, 426).
- [4] URL: [https://indico.cern.ch/event/672140/contributions/2755063/attachments/1552019/2438680/Lidia\\_LHCTopWG\\_20171003.pdf](https://indico.cern.ch/event/672140/contributions/2755063/attachments/1552019/2438680/Lidia_LHCTopWG_20171003.pdf) (cit. on p. 9).
- [5] J. Campbell, R. K. Ellis and R. Röntsch, *Single top production in association with a Z boson at the LHC*, *Phys. Rev. D* **87** (2013) 114006, arXiv: [1302.3856 \[hep-ph\]](https://arxiv.org/abs/1302.3856) (cit. on p. 9).
- [6] C. Degrande, F. Maltoni, K. Mimasu, E. Vryonidou and C. Zhang, *Single-top associated production with a Z or H boson at the LHC: the SMEFT interpretation*, *Journal of High Energy Physics* **2018** (2018) 5, ISSN: 1029-8479, URL: [https://doi.org/10.1007/JHEP10\(2018\)005](https://doi.org/10.1007/JHEP10(2018)005) (cit. on p. 9).
- [7] *TopWGBindingGuidelines*, URL: <https://twiki.cern.ch/twiki/bin/viewauth/AtlasProtected/TopWGBindingGuidelines> (cit. on p. 12).
- [8] *SgTopRun2NtupleContents*, URL: <https://twiki.cern.ch/twiki/bin/view/AtlasProtected/SgTopRun2NtupleContents> (cit. on p. 13).
- [9] *SgTopRun2NtupleSamples*, URL: <https://twiki.cern.ch/twiki/bin/view/AtlasProtected/SgTopRun2NtupleSamples> (cit. on p. 13).
- [10] *TOPQ derivations*, URL: [https://twiki.cern.ch/twiki/bin/view/AtlasProtected/TopDerivations#4\\_TOPQ\\_derivations\\_overview](https://twiki.cern.ch/twiki/bin/view/AtlasProtected/TopDerivations#4_TOPQ_derivations_overview) (cit. on p. 13).
- [11] ATLAS Collaboration, *Performance of the ATLAS trigger system in 2015*, *Eur. Phys. J. C* **77** (2017) 317, arXiv: [1611.09661 \[hep-ex\]](https://arxiv.org/abs/1611.09661) (cit. on p. 13).
- [12] ATLAS Collaboration, *2015 start-up trigger menu and initial performance assessment of the ATLAS trigger using Run-2 data*, ATL-DAQ-PUB-2016-001, 2016, URL: <https://cds.cern.ch/record/2136007> (cit. on p. 13).
- [13] ATLAS Collaboration, *Trigger Menu in 2016*, ATL-DAQ-PUB-2017-001, 2017, URL: <https://cds.cern.ch/record/2242069> (cit. on p. 13).
- [14] J. Alwall et al., *The automated computation of tree-level and next-to-leading order differential cross sections, and their matching to parton shower simulations*, *JHEP* **1407** (2014) 079, arXiv: [1405.0301 \[hep-ph\]](https://arxiv.org/abs/1405.0301) (cit. on pp. 14, 16).
- [15] NNPDF Collaboration, R.D. Ball et al., *Parton distributions for the LHC Run II*, *JHEP* **04** (2015) 040, arXiv: [1410.8849 \[hep-ph\]](https://arxiv.org/abs/1410.8849) (cit. on pp. 14–17).
- [16] T. Sjöstrand et al., *An Introduction to PYTHIA 8.2*, *Comput. Phys. Commun.* **191** (2015) 159, arXiv: [1410.3012 \[hep-ph\]](https://arxiv.org/abs/1410.3012) (cit. on pp. 14–16).
- [17] ATLAS Collaboration, *ATLAS Pythia 8 tunes to 7 TeV data*, ATL-PHYS-PUB-2014-021, 2014, URL: <https://cds.cern.ch/record/1966419> (cit. on pp. 14–16, 104).

- 1226 [18] S. Frixione, E. Laenen, P. Motylinski and B. R. Webber, *Angular correlations of lepton pairs from*  
 1227 *vector boson and top quark decays in Monte Carlo simulations*, **JHEP 0704** (2007) 081, arXiv:  
 1228 [hep-ph/0702198](https://arxiv.org/abs/hep-ph/0702198) (cit. on p. 14).
- 1229 [19] P. Artoisenet, R. Frederix, O. Mattelaer and R. Rietkerk, *Automatic spin-entangled decays of heavy*  
 1230 *resonances in Monte Carlo simulations*, **JHEP 1303** (2013) 015, arXiv: [1212.3460](https://arxiv.org/abs/1212.3460) [hep-ph]  
 1231 (cit. on p. 14).
- 1232 [20] R. Frederix, E. Re and P. Torrielli, *Single-top t-channel hadroproduction in the four-flavour scheme*  
 1233 *with POWHEG and aMC@NLO*, **JHEP 09** (2012) 130, arXiv: [1207.5391](https://arxiv.org/abs/1207.5391) [hep-ph] (cit. on p. 14).
- 1234 [21] D. J. Lange, *The EvtGen particle decay simulation package*, **Nucl. Instrum. Meth. A 462** (2001) 152  
 1235 (cit. on p. 14).
- 1236 [22] URL: <https://indico.cern.ch/event/708573/contributions/2995420/attachments/1649998/2638496/VryonidoutZjsm.pdf> (cit. on p. 14).
- 1238 [23] S. Frixione et al., *A positive-weight next-to-leading-order Monte Carlo for heavy flavour hadroproduc-*  
 1239 *tion*, **JHEP 09** (2007) 126, arXiv: [0707.3088](https://arxiv.org/abs/0707.3088) [hep-ph] (cit. on pp. 15, 16).
- 1240 [24] P. Nason, *A New method for combining NLO QCD with shower Monte Carlo algorithms*, **JHEP 0411**  
 1241 (2004) 040, arXiv: [hep-ph/0409146](https://arxiv.org/abs/hep-ph/0409146) (cit. on pp. 15, 16).
- 1242 [25] S. Frixione, P. Nason and C. Oleari, *Matching NLO QCD computations with Parton Shower*  
 1243 *simulations: the POWHEG method*, **JHEP 11** (2007) 070, arXiv: [0709.2092](https://arxiv.org/abs/0709.2092) [hep-ph] (cit. on  
 1244 pp. 15, 16).
- 1245 [26] S. Alioli, P. Nason, C. Oleari and E. Re, *A general framework for implementing NLO calculations in*  
 1246 *shower Monte Carlo programs: the POWHEG BOX*, **JHEP 1006** (2010) 043, arXiv: [1002.2581](https://arxiv.org/abs/1002.2581)  
 1247 [hep-ph] (cit. on pp. 15, 16).
- 1248 [27] ATLAS Collaboration, *Studies on top-quark Monte Carlo modelling for Top2016*, ATL-PHYS-PUB-  
 1249 2016-020, 2016, URL: <https://cds.cern.ch/record/2216168> (cit. on pp. 15, 16).
- 1250 [28] ATLAS Collaboration, *Studies on top-quark Monte Carlo modelling with Sherpa and MG5\_aMC@NLO*,  
 1251 ATL-PHYS-PUB-2017-007, 2017, URL: <https://cds.cern.ch/record/2261938> (cit. on p. 15).
- 1252 [29] M. Bahr et al., *Herwig++ Physics and Manual*, **Eur. Phys. J. C 58** (2008) 639, arXiv: [0803.0883](https://arxiv.org/abs/0803.0883)  
 1253 [hep-ph] (cit. on p. 15).
- 1254 [30] J. Bellm et al., *Herwig 7.0/Herwig++ 3.0 release note*, **Eur. Phys. J. C 76** (2016) 196, arXiv:  
 1255 [1512.01178](https://arxiv.org/abs/1512.01178) [hep-ph] (cit. on p. 15).
- 1256 [31] L. Harland-Lang, A. Martin, P. Motylinski and R. Thorne, *Parton distributions in the LHC era: MMHT 2014 PDFs*, **Eur. Phys. J. C 75** (2015) 204, arXiv: [1412.3989](https://arxiv.org/abs/1412.3989) [hep-ph] (cit. on p. 15).
- 1258 [32] E. Re, *Single-top Wt-channel production matched with parton showers using the POWHEG method*,  
 1259 **Eur. Phys. J. C 71** (2011) 1547, arXiv: [1009.2450](https://arxiv.org/abs/1009.2450) [hep-ph] (cit. on p. 16).
- 1260 [33] S. Frixione, E. Laenen, P. Motylinski, B. R. Webber and C. D. White, *Single-top hadroproduction in*  
 1261 *association with a W boson*, **JHEP 0807** (2008) 029, arXiv: [0805.3067](https://arxiv.org/abs/0805.3067) [hep-ph] (cit. on p. 16).
- 1262 [34] T. Gleisberg et al., *Event generation with SHERPA 1.1*, **JHEP 02** (2009) 007, arXiv: [0811.4622](https://arxiv.org/abs/0811.4622)  
 1263 [hep-ph] (cit. on pp. 16, 17).
- 1264 [35] T. Gleisberg and S. Höche, *Comix, a new matrix element generator*, **JHEP 12** (2008) 039, arXiv:  
 1265 [0808.3674](https://arxiv.org/abs/0808.3674) [hep-ph] (cit. on pp. 16, 17).

- 1266 [36] S. Schumann and F. Krauss, *A Parton shower algorithm based on Catani-Seymour dipole factorisation*,  
 1267 *JHEP* **03** (2008) 038, arXiv: [0709.1027 \[hep-ph\]](https://arxiv.org/abs/0709.1027) (cit. on pp. 16, 17).
- 1268 [37] S. Höche, F. Krauss, M. Schonherr and F. Siegert, *A critical appraisal of NLO+PS matching methods*,  
 1269 *JHEP* **09** (2012) 049, arXiv: [1111.1220 \[hep-ph\]](https://arxiv.org/abs/1111.1220) (cit. on pp. 16, 17).
- 1270 [38] S. Höche, F. Krauss, M. Schonherr and F. Siegert, *QCD matrix elements + parton showers: The*  
 1271 *NLO case*, *JHEP* **04** (2013) 027, arXiv: [1207.5030 \[hep-ph\]](https://arxiv.org/abs/1207.5030) (cit. on pp. 16, 17).
- 1272 [39] S. Catani, F. Krauss, R. Kuhn and B. R. Webber, *QCD matrix elements + parton showers*, *JHEP* **11**  
 1273 (2001) 063, arXiv: [hep-ph/0109231](https://arxiv.org/abs/hep-ph/0109231) (cit. on pp. 16, 17).
- 1274 [40] S. Höche, F. Krauss, S. Schumann and F. Siegert, *QCD matrix elements and truncated showers*,  
 1275 *JHEP* **05** (2009) 053, arXiv: [0903.1219 \[hep-ph\]](https://arxiv.org/abs/0903.1219) (cit. on pp. 16, 17).
- 1276 [41] F. Caccioli, P. Maierhofer and S. Pozzorini, *Scattering Amplitudes with Open Loops*, *Phys. Rev. Lett.*  
 1277 **108** (2012) 111601, arXiv: [1111.5206 \[hep-ph\]](https://arxiv.org/abs/1111.5206) (cit. on pp. 16, 17).
- 1278 [42] A. Denner, S. Dittmaier and L. Hofer, *Collier: a fortran-based Complex One-Loop Library in*  
 1279 *Extended Regularizations*, *Comput. Phys. Commun.* **212** (2017) 220, arXiv: [1604.06792 \[hep-ph\]](https://arxiv.org/abs/1604.06792)  
 1280 (cit. on pp. 16, 17).
- 1281 [43] *TopCommonObjects13TeV*, URL: <https://twiki.cern.ch/twiki/bin/view/AtlasProtected/TopCommonObjects13TeV> (cit. on p. 18).
- 1283 [44] ATLAS Collaboration, *Electron identification measurements in ATLAS using  $\sqrt{s} = 13$  TeV data with*  
 1284 *50 ns bunch spacing*, ATL-PHYS-PUB-2015-041, 2015, URL: <https://cds.cern.ch/record/2048202> (cit. on p. 18).
- 1286 [45] ATLAS Collaboration, *Electron and photon energy calibration with the ATLAS detector using data*  
 1287 *collected in 2015 at  $\sqrt{s} = 13$  TeV*, ATL-PHYS-PUB-2016-015, 2016, URL: <https://cds.cern.ch/record/2203514> (cit. on p. 18).
- 1289 [46] ATLAS Collaboration, *Electron efficiency measurements with the ATLAS detector using the 2015*  
 1290 *LHC proton–proton collision data*, ATLAS-CONF-2016-024, 2016, URL: <https://cds.cern.ch/record/2157687> (cit. on p. 18).
- 1292 [47] ATLAS Collaboration, *Muon reconstruction performance in early  $\sqrt{s} = 13$  TeV data*, ATL-PHYS-  
 1293 PUB-2015-037, 2015, URL: <https://cds.cern.ch/record/2047831> (cit. on p. 18).
- 1294 [48] W. Lampl et al., *Calorimeter Clustering Algorithms: Description and Performance*, ATL-LARG-  
 1295 PUB-2008-002, 2008, URL: <https://cds.cern.ch/record/1099735> (cit. on p. 19).
- 1296 [49] ATLAS Collaboration, *Identification and rejection of pile-up jets at high pseudorapidity with the*  
 1297 *ATLAS detector*, *Eur. Phys. J. C* **77** (2017) 580, arXiv: [1705.02211 \[hep-ex\]](https://arxiv.org/abs/1705.02211) (cit. on p. 19),  
 1298 Erratum: *Eur. Phys. J. C* **77** (2017) 712.
- 1299 [50] ATLAS Collaboration, *Optimisation of the ATLAS b-tagging performance for the 2016 LHC Run*,  
 1300 ATL-PHYS-PUB-2016-012, 2016, URL: <https://cds.cern.ch/record/2160731> (cit. on  
 1301 p. 19).
- 1302 [51] ATLAS Collaboration, *Commissioning of the ATLAS high performance b-tagging algorithms in*  
 1303 *the 7 TeV collision data*, ATLAS-CONF-2011-102, 2011, URL: <https://cds.cern.ch/record/1369219> (cit. on p. 19).

- 1305 [52] J. Ferrando, J. Geisen, C. S. Pollard, M. Saimpert and J. C. Schmoeckel, *Measurement of the*  
 1306 *b-jet identification efficiency with  $t\bar{t}$  events using an improved likelihood method: Calibration*  
 1307 *INT note of ANA-FTAG-2018-01*, tech. rep. ATL-COM-PHYS-2018-1072, CERN, 2018, URL:  
 1308 <https://cds.cern.ch/record/2631547> (cit. on p. 19).
- 1309 [53] ATLAS Collaboration, *Performance of missing transverse momentum reconstruction in proton–*  
 1310 *proton collisions at  $\sqrt{s} = 7$  TeV with ATLAS*, *Eur. Phys. J. C* **72** (2012) 1844, arXiv: [1108.5602](https://arxiv.org/abs/1108.5602) [hep-ex] (cit. on p. 19).
- 1312 [54] ATLAS Collaboration, *Performance of algorithms that reconstruct missing transverse momentum in*  
 1313  *$\sqrt{s} = 8$  TeV proton–proton collisions in the ATLAS detector*, *Eur. Phys. J. C* **77** (2017) 241, arXiv:  
 1314 [1609.09324](https://arxiv.org/abs/1609.09324) [hep-ex] (cit. on p. 19).
- 1315 [55] ATLAS Collaboration, *Performance of missing transverse momentum reconstruction with the ATLAS*  
 1316 *detector in the first proton–proton collisions at  $\sqrt{s} = 13$  TeV*, ATL-PHYS-PUB-2015-027, 2015,  
 1317 URL: <https://cds.cern.ch/record/2037904> (cit. on p. 19).
- 1318 [56] URL: <https://twiki.cern.ch/twiki/bin/viewauth/AtlasProtected/MCTruthClassifier>  
 1319 (cit. on p. 33).
- 1320 [57] N. F. Castro et al., *Search for flavour-changing  $tZ$  interactions in proton–proton collisions at*  
 1321  *$\sqrt{s} = 13$  TeV with the ATLAS detector*, URL: <https://cds.cern.ch/record/2222281> (cit. on  
 1322 p. 33).
- 1323 [58] M. Feindt, *A Neural Bayesian Estimator for Conditional Probability Densities*, 2004, arXiv:  
 1324 [0402093v1](https://arxiv.org/abs/0402093v1) (cit. on pp. 72, 75).
- 1325 [59] M. Feindt and U. Kerzel, *The NeuroBayes Neural Network Package*, *Nucl. Instrum. Meth.* **A559**  
 1326 (2006) 190 (cit. on p. 72).
- 1327 [60] ATLAS Collaboration, *Electron and photon energy calibration with the ATLAS detector using LHC*  
 1328 *Run 1 data*, *Eur. Phys. J. C* **74** (2014) 3071, arXiv: [1407.5063](https://arxiv.org/abs/1407.5063) [hep-ex] (cit. on p. 102).
- 1329 [61] *JetPubPlots*, URL: <https://atlas.web.cern.ch/Atlas/GROUPS/PHYSICS/PLOTS/JETM-2018-006> (cit. on p. 102).
- 1331 [62] ATLAS Collaboration, *Jet energy scale measurements and their systematic uncertainties in proton–*  
 1332 *proton collisions at  $\sqrt{s} = 13$  TeV with the ATLAS detector*, *Phys. Rev. D* **96** (2017) 072002, arXiv:  
 1333 [1703.09665](https://arxiv.org/abs/1703.09665) [hep-ex] (cit. on p. 102).
- 1334 [63] ATLAS Collaboration, *Calibration of the performance of b-tagging for c and light-flavour jets in*  
 1335 *the 2012 ATLAS data*, ATLAS-CONF-2014-046, 2014, URL: <https://cds.cern.ch/record/1741020> (cit. on p. 103).
- 1337 [64] ATLAS Collaboration, *Calibration of b-tagging using dileptonic top pair events in a combinatorial*  
 1338 *likelihood approach with the ATLAS experiment*, ATLAS-CONF-2014-004, 2014, URL: <https://cds.cern.ch/record/1664335> (cit. on p. 103).
- 1340 [65] ATLAS Collaboration, *Simulation of top-quark production for the ATLAS experiment at  $\sqrt{s} = 13$  TeV*,  
 1341 ATL-PHYS-PUB-2016-004, 2016, URL: <https://cds.cern.ch/record/2120417> (cit. on  
 1342 p. 103).
- 1343 [66] J. M. Campbell, J. Huston and W. Stirling, *Hard Interactions of Quarks and Gluons: A Primer for*  
 1344 *LHC Physics*, *Rept. Prog. Phys.* **70** (2007) 89, arXiv: [hep-ph/0611148](https://arxiv.org/abs/hep-ph/0611148) (cit. on p. 104).
- 1345 [67] J. Butterworth et al., *PDF4LHC recommendations for LHC Run II*, *J. Phys. G* **43** (2016) 023001,  
 1346 arXiv: [1510.03865](https://arxiv.org/abs/1510.03865) [hep-ph] (cit. on p. 104).

- 1347 [68] D. de Florian et al., *Handbook of LHC Higgs cross sections: 4. Deciphering the nature of the Higgs*  
1348 *sector*, (2016), arXiv: [1610.07922 \[hep-ph\]](https://arxiv.org/abs/1610.07922) (cit. on p. 104).
- 1349 [69] ATLAS Collaboration, *Measurement of  $W^\pm Z$  production cross sections and gauge boson polarisation*  
1350 *in  $pp$  collisions at  $\sqrt{s} = 13$  TeV with the ATLAS detector*, (2019), arXiv: [1902.05759 \[hep-ex\]](https://arxiv.org/abs/1902.05759)  
1351 (cit. on p. 104).
- 1352 [70] ATLAS Collaboration, *Evidence for the  $H \rightarrow b\bar{b}$  decay with the ATLAS detector*, *JHEP* **12**  
1353 (2017) 024, arXiv: [1708.03299 \[hep-ex\]](https://arxiv.org/abs/1708.03299) (cit. on p. 104).
- 1354 [71] ATLAS Collaboration, *Luminosity determination in  $pp$  collisions at  $\sqrt{s} = 8$  TeV using the ATLAS*  
1355 *detector at the LHC*, *Eur. Phys. J. C* **76** (2016) 653, arXiv: [1608.03953 \[hep-ex\]](https://arxiv.org/abs/1608.03953) (cit. on p. 105).
- 1356 [72] *TRExFitter*, URL: <https://twiki.cern.ch/twiki/bin/viewauth/AtlasProtected/TtHFitter> (cit. on p. 108).
- 1358 [73] W. Verkerke and D. P. Kirkby, *The RooFit toolkit for data modeling*, eConf **C0303241** (2003)  
1359 MOLT007, [,186(2003)], arXiv: [physics/0306116 \[physics\]](https://arxiv.org/abs/physics/0306116) (cit. on p. 108).
- 1360 [74] L. Moneta et al., *The RooStats Project*, PoS **ACAT2010** (2010) 057, arXiv: [1009.1003 \[physics.data-an\]](https://arxiv.org/abs/1009.1003)  
1361 (cit. on p. 108).

<sup>1362</sup> **Appendices**

[Not reviewed, for internal circulation only]

## 1363 A List of Monte Carlo datasets

1364 This appendix summarises the MC datasets for signal and background. Table 44 shows the nominal  
 1365 samples produced in full simulation, for mc16a, mc16d and mc16e.

1366 Table 44: Overview of the signal and background simulated samples (full simulation).

Process	Sample ID	Generator	$\sigma$ [pb]	$k$ -factor	$N$ -generated
$tZq$	412063	MadGraphPy8Ev–A14–tllq–NLO	0.0300	1.00	mc16a: 4.99 M mc16d: 6.23 M mc16e: 8.26 M
$t\bar{t}$	410472	PowPy8Ev–A14–ttbar–hdamp258p75–dil	77.0	1.14	mc16a: 79.83 M mc16d: 44.88 M * mc16e: 99.25 M
$tW$	410648	PowPy8Ev–A14–Wt–t–dil	4.00	0.94	mc16a: 1.00 M mc16d: 1.25 M mc16e: 1.66 M
	410649	PowPy8Ev–A14–Wt–tbar–dil	3.99	0.94	mc16a: 1.00 M mc16d: 1.25 M mc16e: 1.65 M
$ttH$	346343	PowPy8Ev–A14–ttH125–allhad	0.0534	1.00	mc16a: 4.98 M mc16d: 6.49 M mc16e: 8.25 M
	346344	PowPy8Ev–A14–ttH125–sl	0.223	1.00	mc16a: 4.99 M mc16d: 6.50 M mc16e: 8.26 M
1367	346345	PowPy8Ev–A14–ttH125–dilep	0.231	1.00	mc16a: 4.99 M mc16d: 6.49 M mc16e: 8.28 M
$ttV$	410155	aMcAtNloPy8Ev–A14–ttW	0.548	1.10	mc16a: 7.50 M mc16d: 7.50 M mc16e: 12.04 M
	410156	aMcAtNloPy8Ev–A14–ttZnunu	0.155	1.11	mc16a: 1.50 M mc16d: 1.50 M mc16e: 2.00 M
	410157	aMcAtNloPy8Ev–A14–ttZqq	0.528	1.11	mc16a: 3.00 M mc16d: 3.00 M mc16e: 3.59 M
	410218	aMcAtNloPy8Ev–A14–ttee	0.0369	1.12	mc16a: 1.41 M mc16d: 1.34 M mc16e: 2.17 M
	410219	aMcAtNloPy8Ev–A14–ttmumu	0.0369	1.12	mc16a: 1.41 M mc16d: 1.34 M mc16e: 2.17 M
	410220	aMcAtNloPy8Ev–A14–tttautau	0.0365	1.12	mc16a: 0.94 M mc16d: 0.90 M mc16e: 0.96 M

Not reviewed, for internal circulation only

Process	Sample ID	Generator	$\sigma$ [pb]	k-factor	$N$ -generated
$tWZ$	410408	aMcAtNloPy8Ev–A14–tWZ–Ztoll–DR1	0.0200	1.00	mc16a: 0.10 M mc16d: 0.12 M mc16e: 0.16 M
Diboson	363356	Sherpa221–ZqqZll	15.6	0.14	mc16a: 5.40 M mc16d: 5.40 M mc16e: 8.95 M
	363358	Sherpa221–WqqZll	3.44	1.00	mc16a: 5.40 M mc16d: 26.91 M mc16e: 8.96 M
	364250	Sherpa222–llll	1.25	1.00	mc16a: 17.84 M mc16d: 36.00 M mc16e: 25.68 M
	364253	Sherpa222–lllv	4.58	1.00	mc16a: 15.54 M mc16d: 32.11 M mc16e: 26.79 M
	364254	Sherpa222–llvv	12.5	1.00	mc16a: 15.00 M mc16d: 29.98 M mc16e: 24.89 M
Z + jets	364114	Sherpa221–Zee–maxHtPtV0_70–L	1630	0.98	mc16a: 8.00 M mc16d: 10.00 M mc16e: 13.27 M
1368	364115	Sherpa221–Zee–maxHtPtV0_70–C	224	0.98	mc16a: 5.00 M mc16d: 6.24 M mc16e: 8.31 M
	364116	Sherpa221–Zee–maxHtPtV0_70–B	126	0.98	mc16a: 8.00 M mc16d: 9.99 M mc16e: 13.28 M
	364117	Sherpa221–Zee–maxHtPtV70_140–L	76.3	0.98	mc16a: 5.96 M mc16d: 7.38 M mc16e: 9.95 M
	364118	Sherpa221–Zee–maxHtPtV70_140–C	20.3	0.98	mc16a: 2.00 M mc16d: 2.50 M mc16e: 3.33 M
	364119	Sherpa221–Zee–maxHtPtV70_140–B	12.6	0.98	mc16a: 5.97 M mc16d: 7.49 M mc16e: 9.91 M
	364120	Sherpa221–Zee–maxHtPtV140_280–L	25.0	0.98	mc16a: 5.00 M mc16d: 6.25 M mc16e: 8.36 M
	364121	Sherpa221–Zee–maxHtPtV140_280–C	9.37	0.98	mc16a: 3.00 M mc16d: 3.75 M mc16e: 4.99 M
	364122	Sherpa221–Zee–maxHtPtV140_280–B	6.08	0.98	mc16a: 12.44 M mc16d: 15.66 M mc16e: 20.74 M
	364123	Sherpa221–Zee–maxHtPtV280_500–L	4.87	0.98	mc16a: 2.00 M mc16d: 2.50 M mc16e: 2.78 M

Process	Sample ID	Generator	$\sigma$ [pb]	$k$ -factor	$N$ -generated
1369	364124	Sherpa221–Zee–maxHtPtV280_500–C	2.28	0.98	mc16a: 1.00 M mc16d: 1.25 M mc16e: 1.74 M
	364125	Sherpa221–Zee–maxHtPtV280_500–B	1.49	0.98	mc16a: 2.00 M mc16d: 2.50 M mc16e: 3.33 M
	364126	Sherpa221–Zee–maxHtPtV500_1000	1.81	0.98	mc16a: 3.00 M mc16d: 3.71 M mc16e: 4.98 M
	364127	Sherpa221–Zee–maxHtPtV1000_Ecms	0.150	0.98	mc16a: 1.00 M mc16d: 1.25 M mc16e: 1.67 M
	364100	Sherpa221–Zmumu–maxHtPtV0_70–L	1630	0.98	mc16a: 7.97 M mc16d: 9.91 M mc16e: 13.26 M
	364101	Sherpa221–Zmumu–maxHtPtV0_70–C	224	0.98	mc16a: 4.98 M mc16d: 6.20 M mc16e: 8.28 M
	364102	Sherpa221–Zmumu–maxHtPtV0_70–B	127	0.98	mc16a: 7.98 M mc16d: 9.26 M mc16e: 13.24 M
	364103	Sherpa221–Zmumu–maxHtPtV70_140–L	75.0	0.98	mc16a: 5.98 M mc16d: 7.48 M mc16e: 9.94 M
	364104	Sherpa221–Zmumu–maxHtPtV70_140–C	20.4	0.98	mc16a: 2.00 M mc16d: 2.49 M mc16e: 3.31 M
	364105	Sherpa221–Zmumu–maxHtPtV70_140–B	12.4	0.98	mc16a: 5.98 M mc16d: 7.47 M mc16e: 9.94 M
	364106	Sherpa221–Zmumu–maxHtPtV140_280–L	24.3	0.98	mc16a: 5.00 M mc16d: 6.24 M mc16e: 8.29 M
	364107	Sherpa221–Zmumu–maxHtPtV140_280–C	9.28	0.98	mc16a: 3.00 M mc16d: 3.75 M mc16e: 4.99 M
	364108	Sherpa221–Zmumu–maxHtPtV140_280–B	6.01	0.98	mc16a: 12.46 M mc16d: 15.63 M mc16e: 20.74 M
	364109	Sherpa221–Zmumu–maxHtPtV280_500–L	4.77	0.98	mc16a: 2.00 M mc16d: 2.46 M mc16e: 3.32 M
	364110	Sherpa221–Zmumu–maxHtPtV280_500–C	2.27	0.98	mc16a: 1.00 M mc16d: 1.25 M mc16e: 1.67 M
	364111	Sherpa221–Zmumu–maxHtPtV280_500–B	1.49	0.98	mc16a: 2.00 M mc16d: 2.50 M mc16e: 3.33 M

Not reviewed, for internal circulation only

Not reviewed, for internal circulation only

Process	Sample ID	Generator	$\sigma$ [pb]	k-factor	$N$ -generated
	364112	Sherpa221–Zmumu–maxHtPtV500_1000	1.79	0.98	mc16a: 3.00 M mc16d: 3.75 M mc16e: 5.09 M
	364113	Sherpa221–Zmumu–maxHtPtV1000_Ecms	0.150	0.98	mc16a: 1.00 M mc16d: 1.25 M mc16e: 1.67 M
	364128	Sherpa221–Ztautau–maxHtPtV0_70–L	1630	0.98	mc16a: 7.99 M mc16d: 10.00 M mc16e: 13.27 M
	364129	Sherpa221–Ztautau–maxHtPtV0_70–C	224	0.98	mc16a: 4.98 M mc16d: 6.14 M mc16e: 8.27 M
	364130	Sherpa221–Ztautau–maxHtPtV0_70–B	128	0.98	mc16a: 8.00 M mc16d: 9.99 M mc16e: 13.28 M
	364131	Sherpa221–Ztautau–maxHtPtV70_140–L	76.0	0.98	mc16a: 6.00 M mc16d: 7.50 M mc16e: 9.97 M
	364132	Sherpa221–Ztautau–maxHtPtV70_140–C	20.2	0.98	mc16a: 2.00 M mc16d: 2.50 M mc16e: 3.33 M
	364133	Sherpa221–Ztautau–maxHtPtV70_140–B	12.3	0.98	mc16a: 5.97 M mc16d: 7.50 M mc16e: 9.96 M
1370	364134	Sherpa221–Ztautau–maxHtPtV140_280–L	24.8	0.98	mc16a: 4.94 M mc16d: 6.23 M mc16e: 8.30 M
	364135	Sherpa221–Ztautau–maxHtPtV140_280–C	9.33	0.98	mc16a: 3.00 M mc16d: 3.75 M mc16e: 4.99 M
	364136	Sherpa221–Ztautau–maxHtPtV140_280–B	5.48	0.98	mc16a: 4.99 M mc16d: 6.21 M mc16e: 8.29 M
	364137	Sherpa221–Ztautau–maxHtPtV280_500–L	4.79	0.98	mc16a: 2.00 M mc16d: 2.50 M mc16e: 3.32 M
	364138	Sherpa221–Ztautau–maxHtPtV280_500–C	2.28	0.98	mc16a: 1.00 M mc16d: 1.23 M mc16e: 1.67 M
	364139	Sherpa221–Ztautau–maxHtPtV280_500–B	1.50	0.98	mc16a: 1.98 M mc16d: 2.50 M mc16e: 3.32 M
	364140	Sherpa221–Ztautau–maxHtPtV500_1000	1.81	0.98	mc16a: 3.00 M mc16d: 3.75 M mc16e: 4.96 M
	364141	Sherpa221–Ztautau–maxHtPtV1000_Ecms	0.150	0.98	mc16a: 1.00 M mc16d: 1.25 M mc16e: 1.67 M

1371 Table 45 shows the samples used for systematic uncertainty evaluation, which are produced in fast  
 1372 simulation, for mc16a, mc16d and mc16e.

1373 Table 45: Overview of the signal and background simulated samples used for systematic uncertainty evaluation (fast  
 simulation).

Process	Sample ID	Generator	$\sigma$ [pb]	k-factor	$N$ -generated
$tZq$	412064	MadGraphPy8Ev–A14–tllq–NLO–Var3cDown	0.0300	1.00	mc16a: 5.00 M mc16d: 6.24 M mc16e: 8.13 M
	412065	MadGraphPy8Ev–A14–tllq–NLO–Var3cUp	0.0300	1.00	mc16a: 5.00 M mc16d: 6.25 M mc16e: 8.29 M
$t\bar{t}$	410482	PowPy8Ev–A14–ttbar–hdamp517p5–dil	76.9	1.14	mc16a: 20.00 M mc16d: 24.70 M mc16e: 33.20 M
	410558	PowH7Ev–H7UE–ttbar–hdamp258p75–dil	77.0	1.14	mc16a: 19.95 M mc16d: 24.97 M mc16e: 33.14 M
	410465	aMcPy8Ev–A14–ttbar–dil	76.3	1.17	mc16a: 20.00 M mc16d: 25.00 M mc16e: 24.88 M
$t\bar{t}Z$	410142	Sherpa221–tll–LO	0.110	1.09	mc16a: 1.80 M mc16d: 1.80 M mc16e: 3.00 M
	410370	aMcAtNloPy8Ev–A14–ttee–Var3cUp			mc16a: XX M mc16d: XX M mc16e: XX M
	410371	aMcAtNloPy8Ev–A14–ttee–Var3cDown			mc16a: XX M mc16d: XX M mc16e: XX M
	410372	aMcAtNloPy8Ev–A14–ttmumu–Var3cUp			mc16a: XX M mc16d: XX M mc16e: XX M
	410373	aMcAtNloPy8Ev–A14–ttmumu–Var3cDown			mc16a: XX M mc16d: XX M mc16e: XX M
	410374	aMcAtNloPy8Ev–A14–tttautau–Var3cUp			mc16a: XX M mc16d: XX M mc16e: XX M
	410375	aMcAtNloPy8Ev–A14–tttautau–Var3cDown			mc16a: XX M mc16d: XX M mc16e: XX M
	410408	aMcAtNloPy8Ev–A14–tWZ–Ztoll–DR1	0.0200	1.00	mc16a: 0.10 M mc16d: 0.12 M mc16e: 0.16 M
	412119	aMcAtNloPy8Ev–A14–tWZ–Ztoll–DR2	0.0200	1.00	mc16a: XX M mc16d: XX M

1375

Process	Sample ID	Generator	$\sigma$ [pb]	<i>k</i> -factor	<i>N</i> -generated
mc16e: XX M					
Diboson	361601	PowPy8Ev-CT10-WlvZll	4.46	1.00	mc16a: 10.01 M mc16d: 10.00 M mc16e: 10.03 M

[Not reviewed, for internal circulation only]

1376 Table 46 shows the samples used for additional studies, like closure tests, for mc16a, mc16d and mc16e. If  
 1377 the samples are produced in fast simulation, this is indicated in the table.

1378 Table 46: Overview of the alternative signal and background simulated samples.

Process	Sample ID	Generator	$\sigma$ [pb]	$k$ -factor	$N$ -generated
$tZq$	410049	MadGraphPy6Ev–P2012– $tZq$ –trilepton–LO	0.0200	1.00	mc15 FullSim: 1 M
$tZq$	410050	MadGraphPy6Ev–P2012– $tZq$ –noAllHad–LO	0.240	1.00	mc15 FullSim: 1 M
$tZq$	410550	MadGraphPy8Ev–A14– $tZq$ –trilepton–LO	0.0200	1.00	mc16a FullSim: 1 M mc16d FullSim: 1 M
$tZq$	410263	MadGraphPy8Ev–A14– $tllq$ –NLO	0.0300	1.00	mc16a AF2: 5.00 M mc16d AF2: 6.52 M mc16d AF2: 8.29 M

Not reviewed, for internal circulation only

## 1381 B Grouping of background sources

1382 To decide how to group background sources in plots and, more importantly, in the fit, comparisons of  
 1383 shapes of kinematic variables are done, in both SRs.

1384 **B.1  $tWZ, t\bar{t}Z, t\bar{t}W$  and  $t\bar{t}H$**

1385 Studies presented in the following were done on events with  $m_T(W) > 20$  GeV.

1386 As can be seen from the breakdown of the contribution of each background in the two SRs shown in  
 1387 Tables 47 and 48, the contribution of  $t\bar{t}Z$  is the dominant contribution both in the 2j1b and in the 3j1b SRs.  
 1388 The  $tWZ$  contribution is also important, while  $t\bar{t}W$  and  $t\bar{t}H$  just contribute with few events.

Table 47: Numbers of expected events in the 2j1b SR broken down by process. The uncertainties include only statistical uncertainties.

Process	Number of events		Process	Number of raw events	
$t\bar{t}Z$	55.5	± 1.4	$t\bar{t}Z$	40 535	
$t\bar{t}W$	3.9	± 0.3	$t\bar{t}W$	1378	
$t\bar{t}H$	1.8	± 0.1	$t\bar{t}H$	4019	
$tWZ$	16.2	± 1.0	$tWZ$	2661	
$VV + HF$	88.9	± 0.9	$VV + HF$	33 090	
$VV + LF$	19.9	± 0.6	$VV + LF$	4249	
$Z + jets$	7.1	± 0.1	$Z + jets$	114 379	
$t\bar{t}$	21.8	± 0.1	$t\bar{t}$	153 210	
$tW$	1.0	± 0.0	$tW$	1744	
$tZq$	63.3	± 0.5	$tZq$	275 446	
Total expected	279.3	± 2.1	Total expected	630 711	

Table 48: Numbers of expected events in the 3j1b SR broken down by process. The uncertainties include only statistical uncertainties.

Process	Number of events		Process	Number of raw events	
$t\bar{t}Z$	85.0	± 1.7	$t\bar{t}Z$	68 557	
$t\bar{t}W$	2.0	± 0.2	$t\bar{t}W$	696	
$t\bar{t}H$	2.2	± 0.1	$t\bar{t}H$	4018	
$tWZ$	17.6	± 1.1	$tWZ$	3168	
$VV + HF$	51.7	± 0.6	$VV + HF$	21 070	
$VV + LF$	10.7	± 0.3	$VV + LF$	2592	
$Z + jets$	3.1	± 0.1	$Z + jets$	51 841	
$t\bar{t}$	10.4	± 0.0	$t\bar{t}$	64 770	
$tW$	0.4	± 0.0	$tW$	662	
$tZq$	35.8	± 0.4	$tZq$	185 167	
Total expected	218.9	± 2.2	Total expected	402 541	

1389 The question is therefore how to treat  $t\bar{t}Z$  and  $tWZ$ , if separately or together, as done for  $t\bar{t}$  and  $tW$ .  
 1390 Figure 114 show various kinematical distributions in the 2j1b SR, while Fig. 116 shows the four highest  
 1391 ranked variables in the 2j1b SR. Figure 117 show various kinematical distributions in the 3j1b SR, while  
 1392 Fig. 119 shows the four highest ranked variables in the 3j1b SR. Figure 120 shows the  $O_{NN}$  distributions in  
 1393 the two SRs.

1394 As can be seen, the shapes are similar for  $t\bar{t}Z$  and  $tWZ$ , while they are different for the *small backgrounds*,  
 1395 which include  $t\bar{t}W$  and  $t\bar{t}H$ . Therefore it is decided to keep  $t\bar{t}Z$  and  $tWZ$  contributions together and separate  
 1396 them from  $t\bar{t}W$  and  $t\bar{t}H$ . The  $t\bar{t}Z$  modeling uncertainties applied in the fit only effect the  $t\bar{t}Z$  component of  
 1397 the  $t\bar{t}Z + tWZ$  grouping.

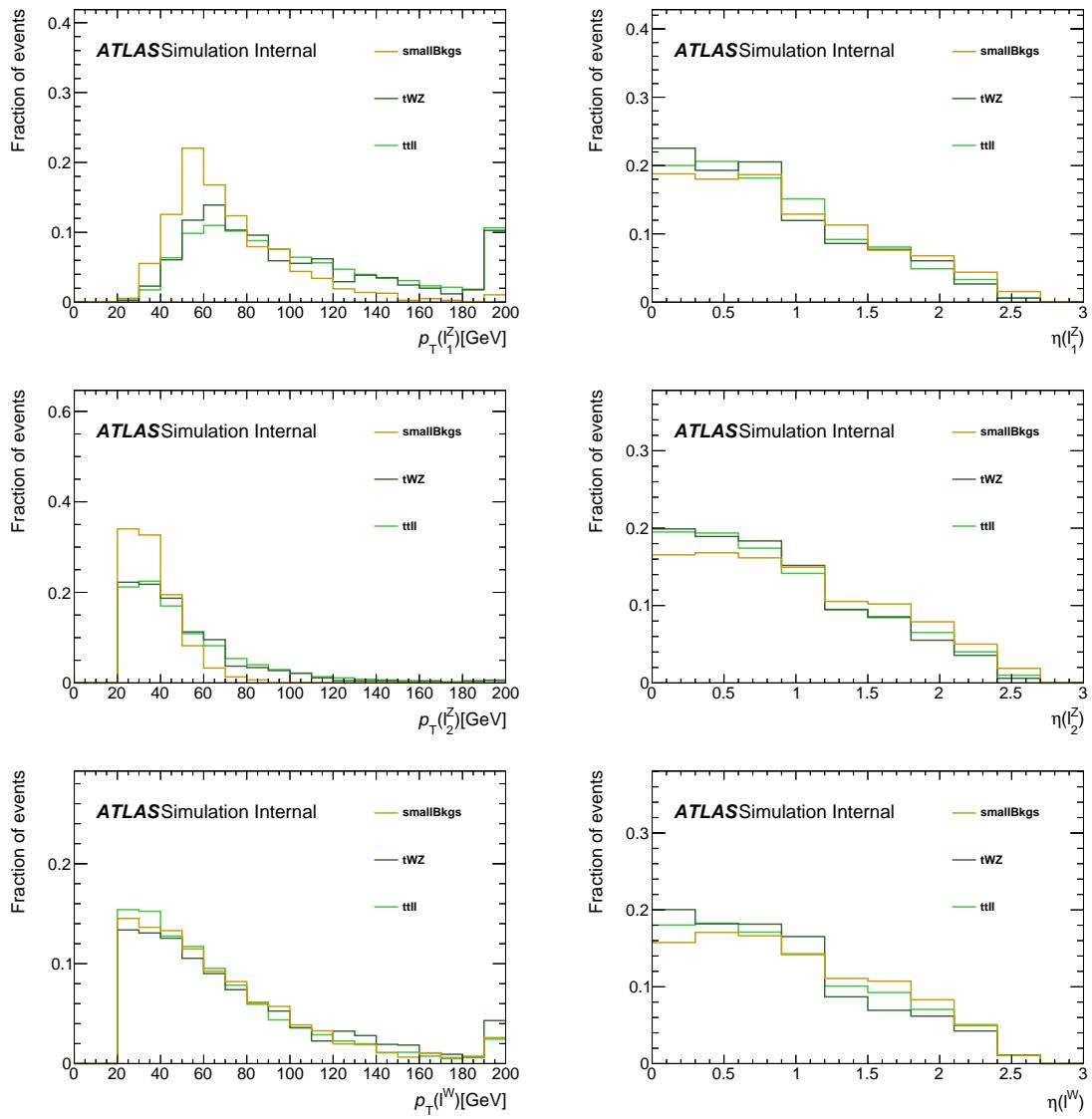


Figure 114: Normalised kinematic plots of reconstructed lepton-related quantities for events in the 2j1b SR.

Not reviewed, for internal circulation only

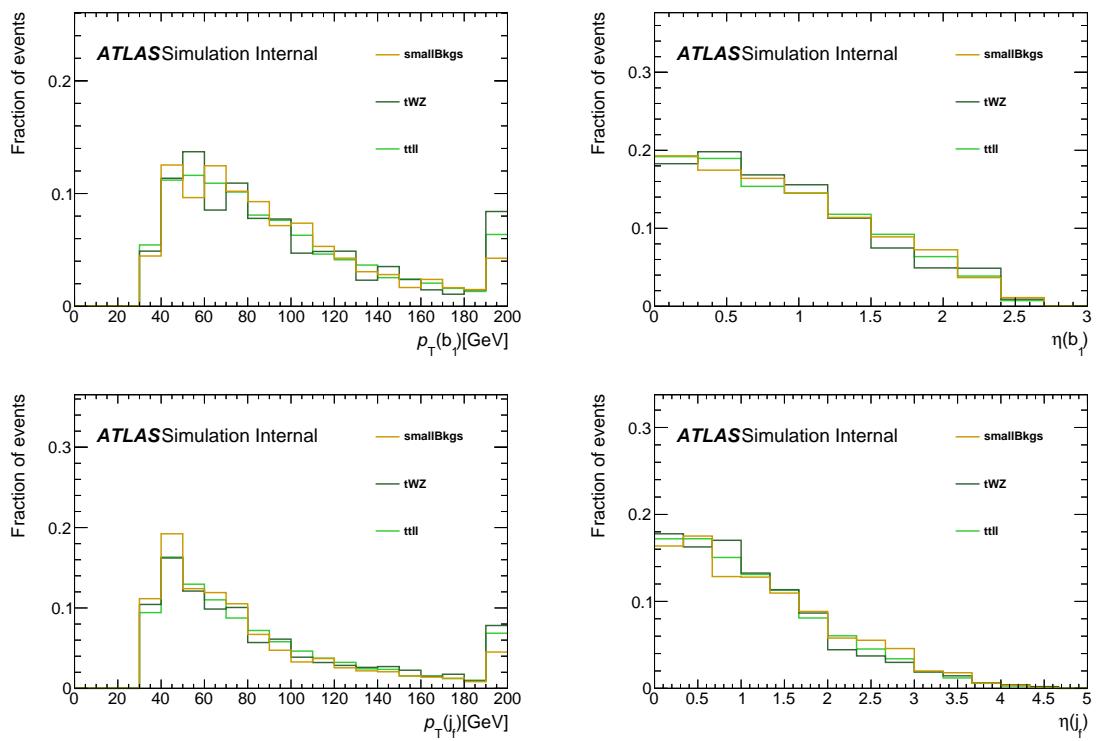


Figure 115: Normalised kinematic plots of reconstructed jet-related quantities for events in the 2j1b SR.

Not reviewed, for internal circulation only

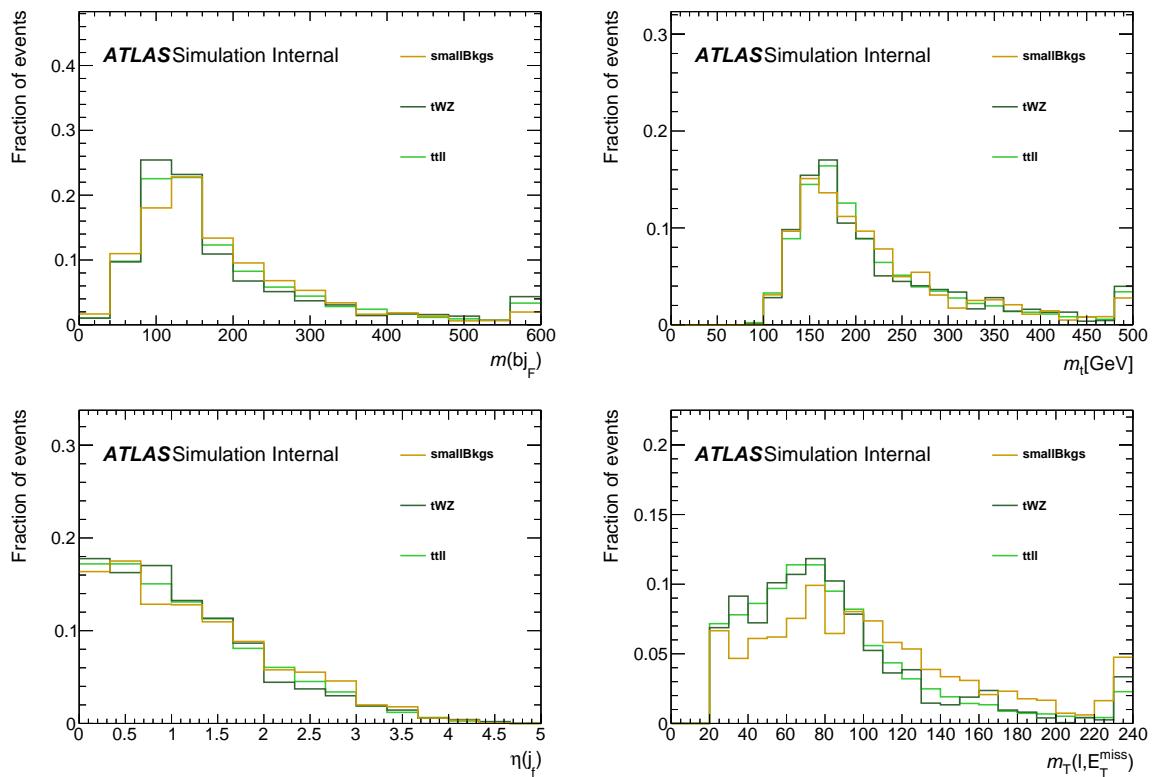


Figure 116: Normalised kinematic plots of neural-network training variables of the 2j1b SR, in order of significance.

Not reviewed, for internal circulation only

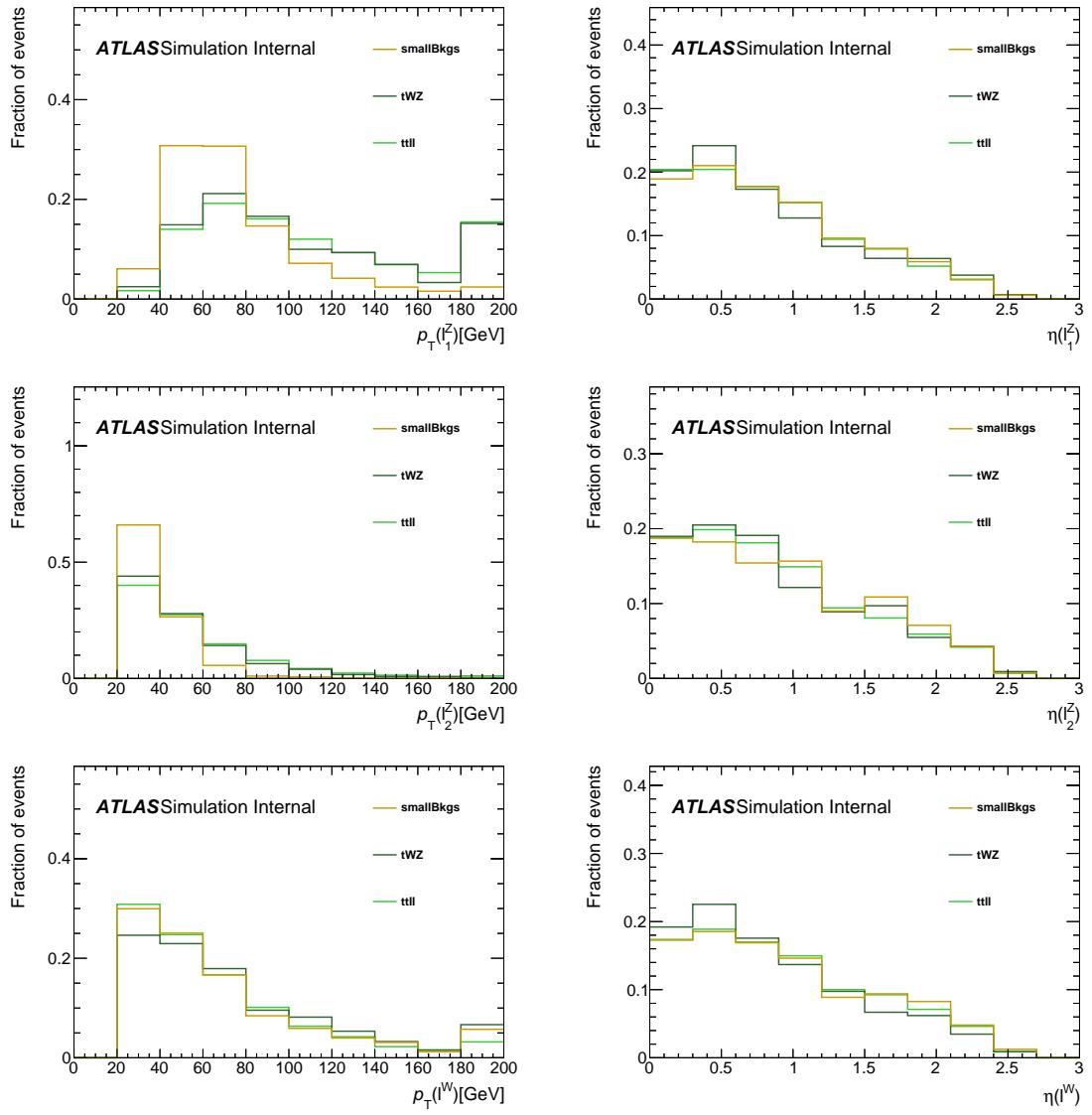


Figure 117: Normalised kinematic plots of reconstructed lepton-related quantities for events in the 3j1b SR.

Not reviewed, for internal circulation only

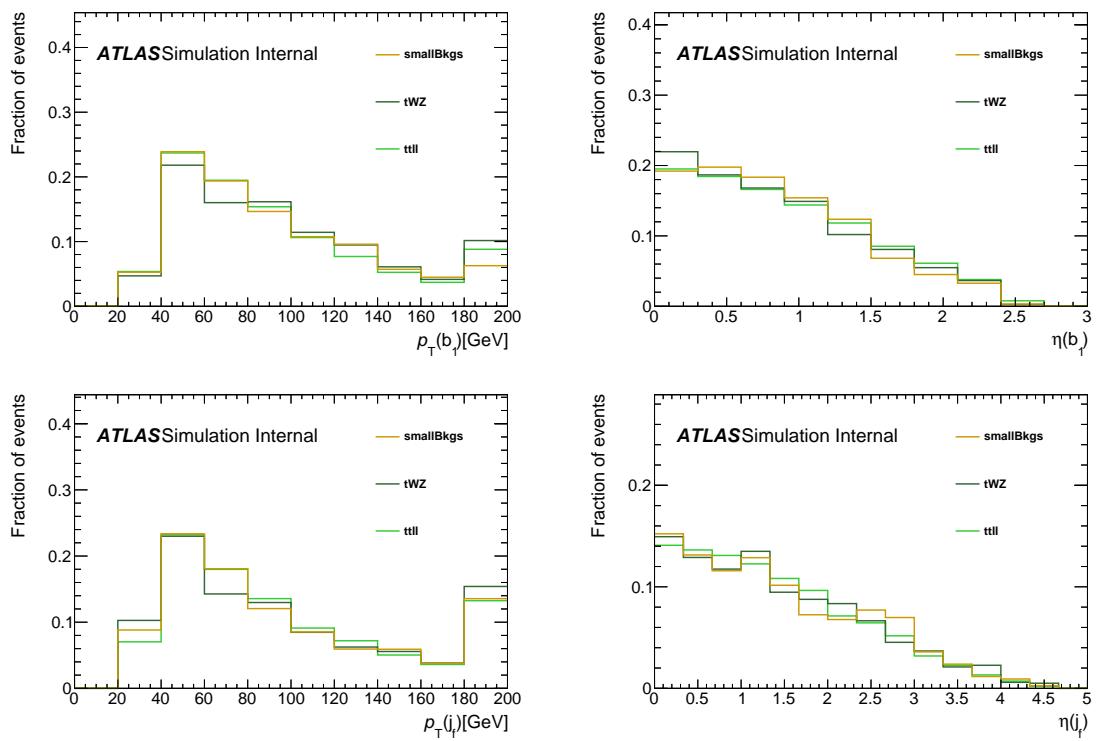


Figure 118: Normalised kinematic plots of reconstructed jet-related quantities for events in the 3j1b SR.

Not reviewed, for internal circulation only

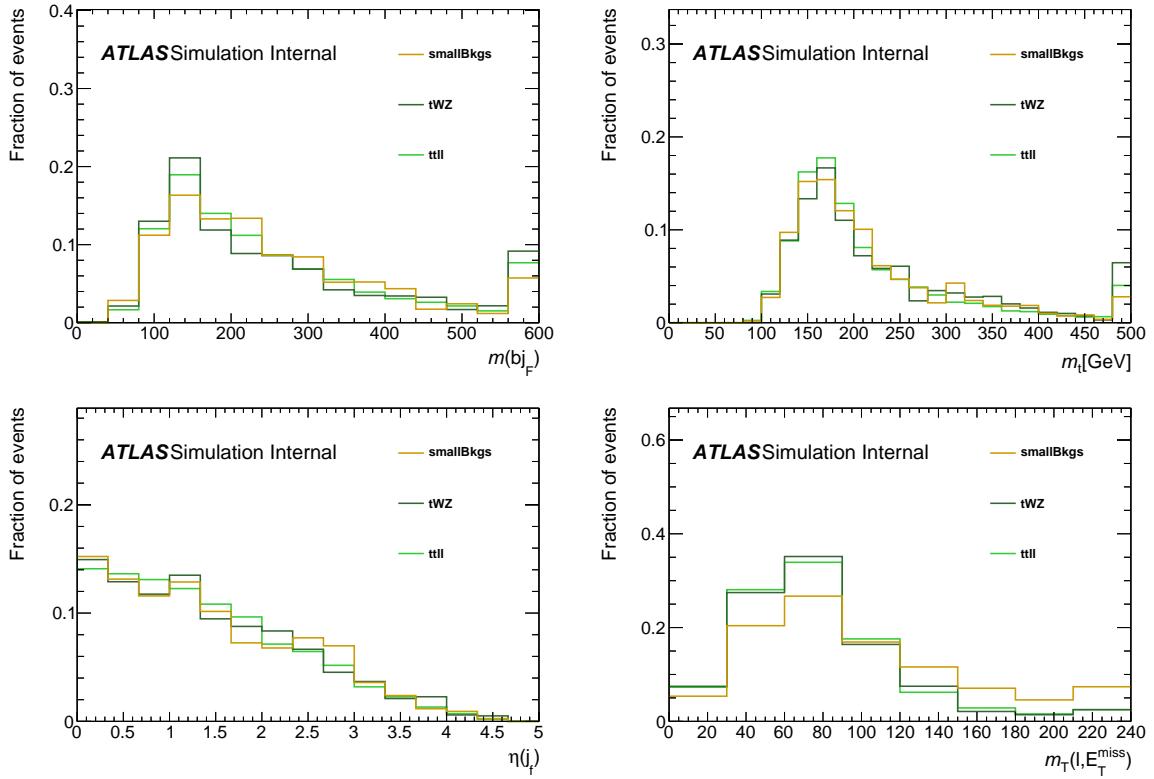


Figure 119: Normalised kinematic plots of neural-network training variables of the 3j1b SR, in order of significance.

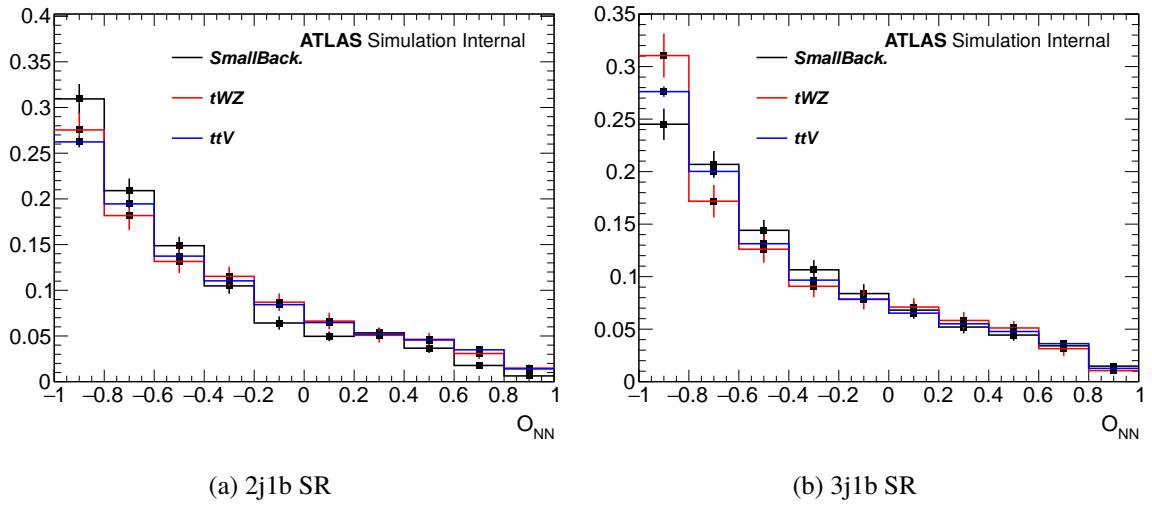


Figure 120: Neural-network output distributions in the 2j1b and 3j1b SRs normalised to unity.

1398 **B.2  $t\bar{t}$  and  $tW$** 1399 Studies presented in the following were done on events with  $m_T(W) > 20$  GeV.1400 Due to the almost insignificant contribution of  $tW$  and its lack of distinction from  $t\bar{t}$  at NLO,  $t\bar{t}$  and  
1401  $tW$  are grouped and treated as a single background source. The  $t\bar{t}$  modeling systematics effect only the  
1402 overwhelming dominate  $t\bar{t}$  component of this grouping.

Not reviewed, for internal circulation only

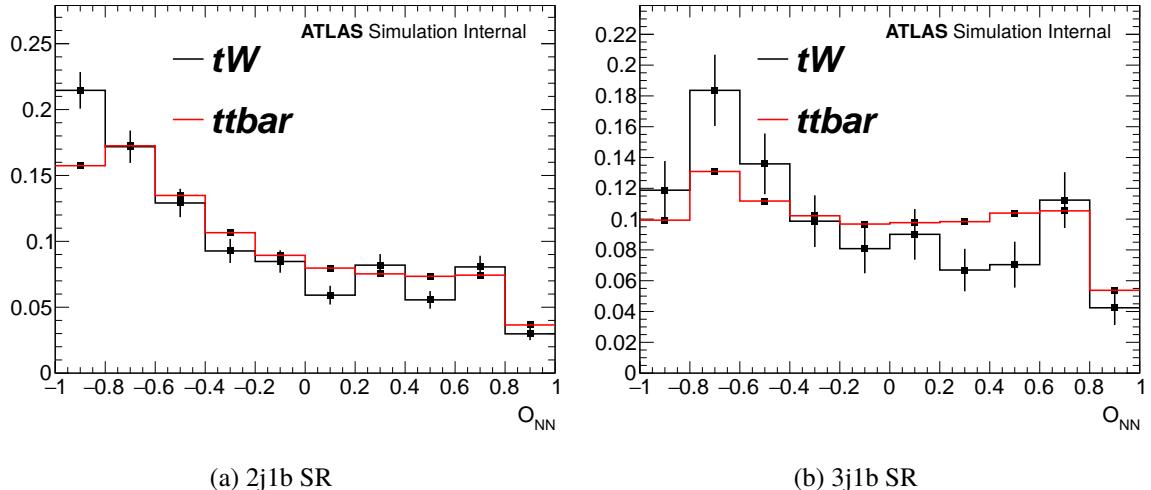


Figure 121: Neural-network output distributions in the 2j1b and 3j1b SRs normalised to unity.

### 1403 B.3 Diboson flavours

1404 As mentioned in Section 3.2, the diboson +  $b$ ,  $c$  and light components are grouped into  $VV + HF$  (heavy  
 1405 flavour) and  $VV + LF$  (light flavour) based on the types of jets associated: if one of the associated  
 1406 jets originated from  $b$ -quark or  $c$ -quark then it is considered as  $VV + HF$ , otherwise it is considered as  
 1407  $VV + LF$ .

1408 Figures 122 to 124 show the  $O_{NN}$  distributions in the SRs and diboson CRs and VRs. Three three diboson  
 1409 +  $b$ ,  $c$  and light components are shown separately. The SRs are dominated by diboson +  $b$  and diboson  
 1410 +  $c$  in similar fractions, while the diboson + light component is smaller. In the CRs instead, given that  
 1411 a 0b requirement is applied, the diboson + light component is the dominant one, with a smaller fraction  
 1412 of diboson +  $c$ . In the VRs, given the 1Lb requirement, the composition is similar to the CRs, with an  
 1413 increased diboson +  $c$  contribution.

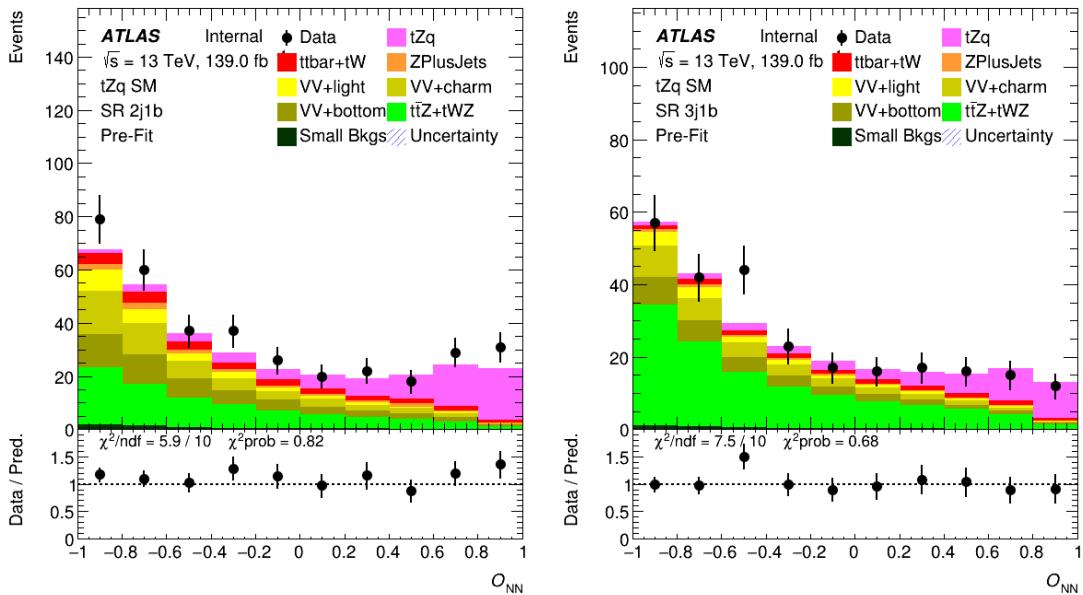


Figure 122:  $O_{NN}$  distributions with diboson +  $b$ ,  $c$  and light components split in the 2j1b SR (left) and 3j1b SR (right). The plots do not show the uncertainty because of a temporary glitch when creating the plots.

1414 In Figs. 125 to 127 the shapes of either  $O_{NN}$  or  $m_T(W)$  in the SRs and diboson CRs and VRs are shown,  
 1415 split into the three components. The similar shapes of diboson +  $b$  and diboson +  $c$  justify the grouping.  
 1416 Having two diboson components in the fit gives enough freedom to adjust for the relative fractions. Detailed  
 1417 studies about the splitting were done and it was seen that additional splitting (i.e. three components treated  
 1418 separately) brings no improvement to the analysis.

Not reviewed, for internal circulation only

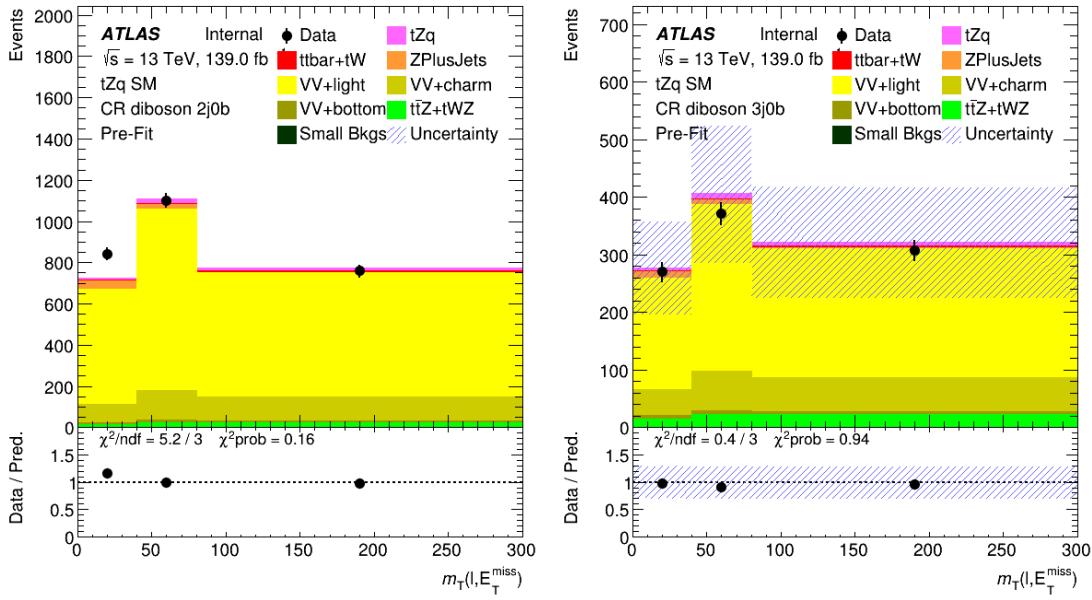


Figure 123:  $O_{\text{NN}}$  distributions with diboson +  $b, c$  and light components split in the 2j0b CR (left) and 3j0b CR (right). [The plot in the 2j0b CR does not show the uncertainty because of a temporary glitch when creating the plots.](#)

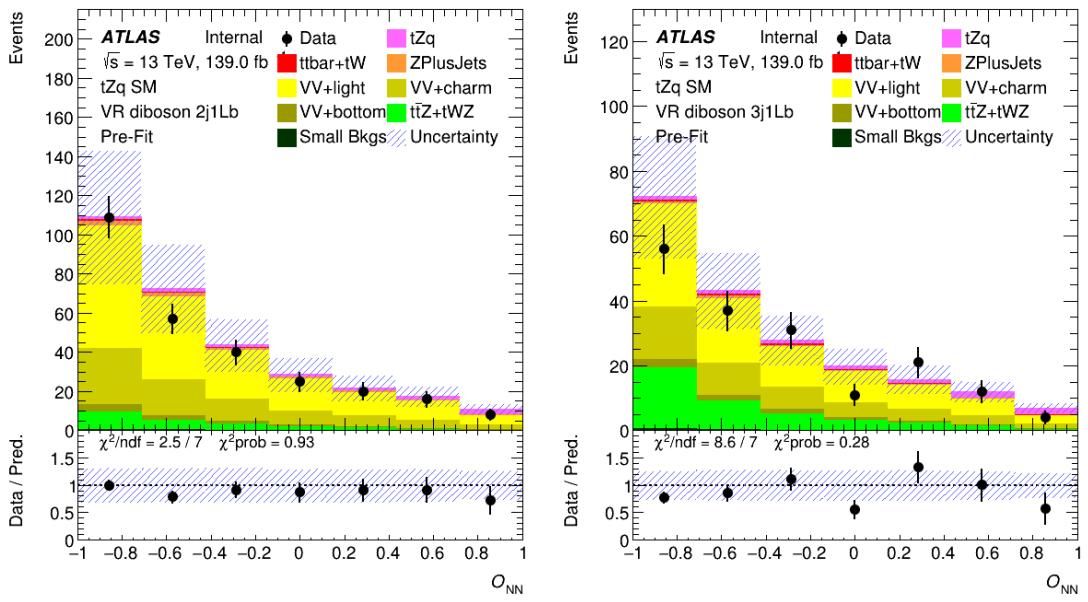


Figure 124:  $O_{\text{NN}}$  distributions with diboson +  $b, c$  and light components split in the 2j1Lb VR (left) and 3j1Lb VR (right).

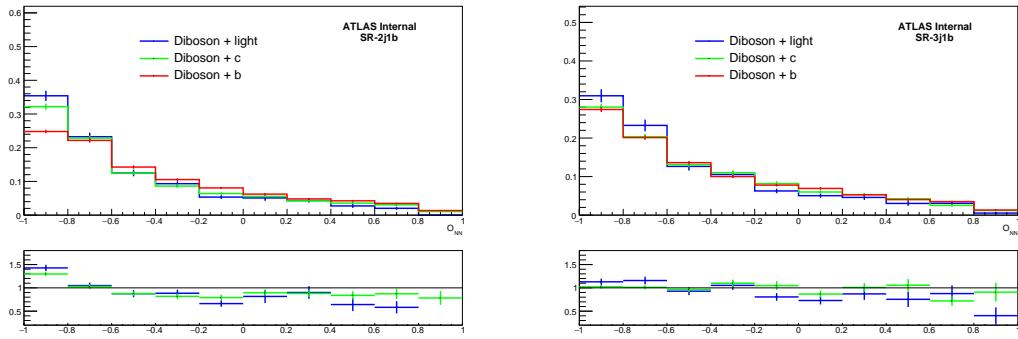


Figure 125: Comparison of  $O_{NN}$  shape for the diboson +  $b$ ,  $c$  and light components in the 2j1b SR (left) and 3j1b SR (right).

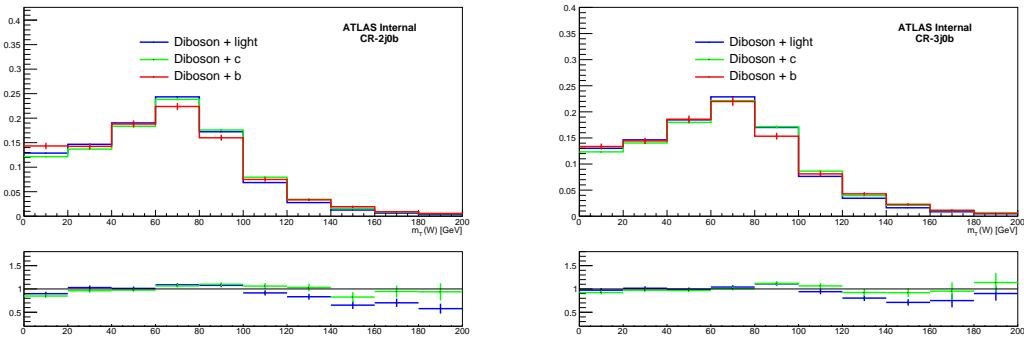


Figure 126: Comparison of  $m_T(W)$  shape for the diboson +  $b$ ,  $c$  and light components in the 2j0b CR (left) and 3j0b CR (right).

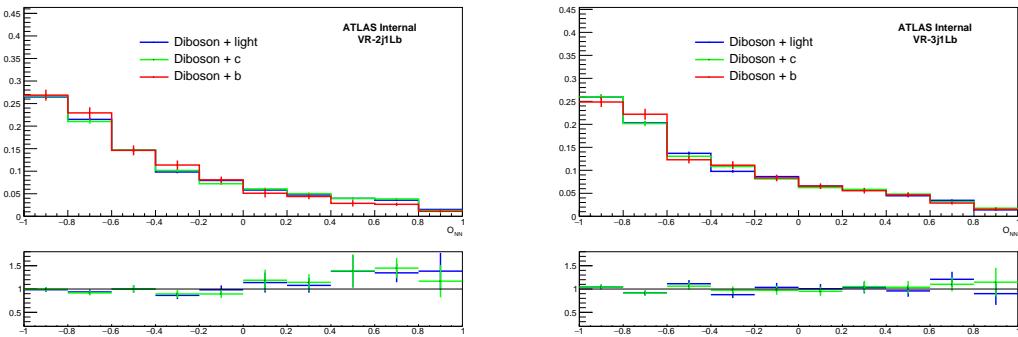


Figure 127: Comparison of  $O_{NN}$  shape for the diboson +  $b$ ,  $c$  and light components in the 2j1Lb VR (left) and 3j1Lb VR (right).

1419 **C More plots in SRs and VRs**

1420 In this appendix, more control plots for the signal regions and validation regions are shown.

1421 **C.1 Signal regions**

Not reviewed, for internal circulation only

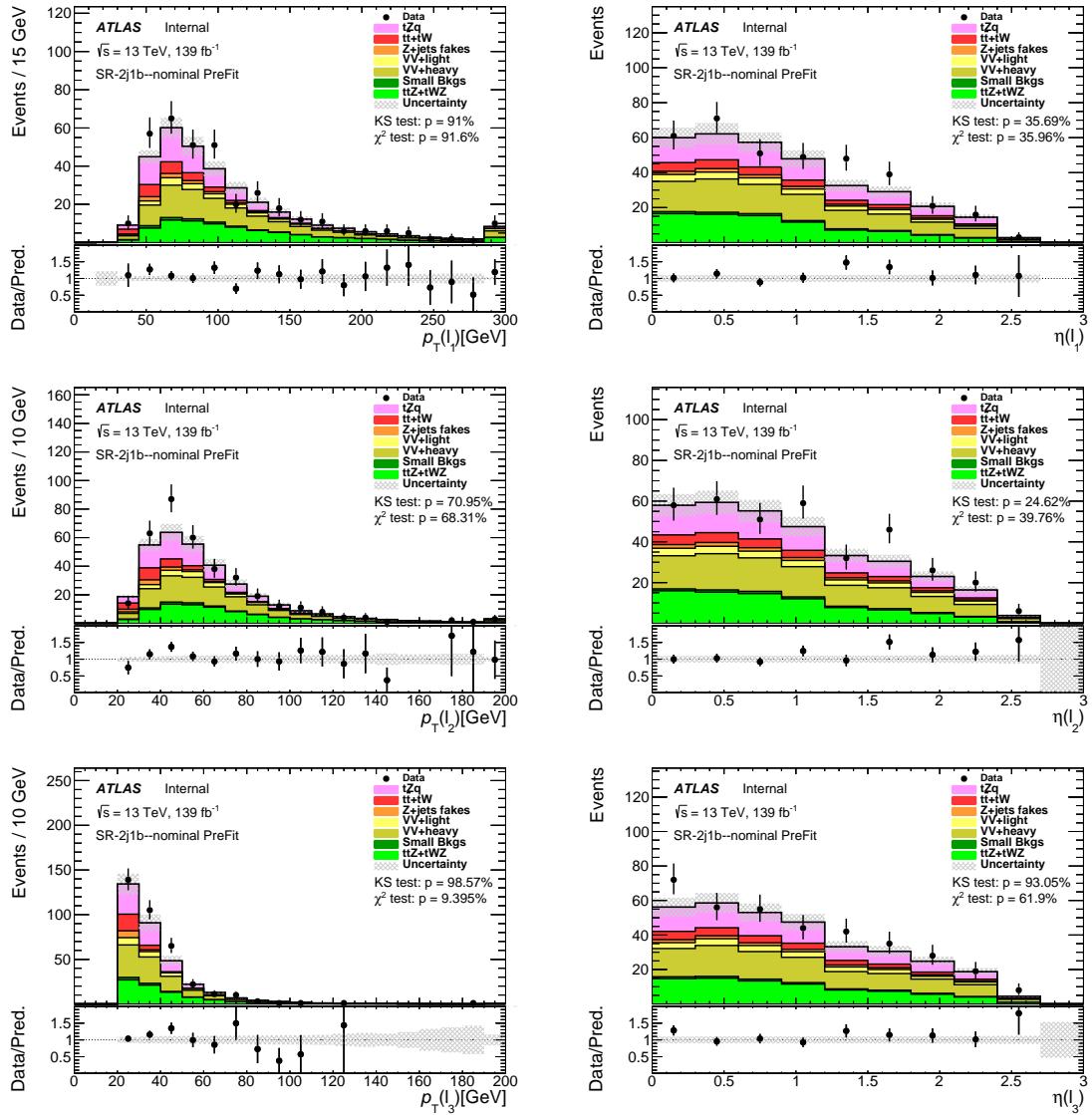


Figure 128: Comparison of data and MC predictions for reconstructed lepton-related quantities for events in the 2j1b SR. Both signal and backgrounds are normalised to the expected number of events before the fit. The uncertainty band includes statistical uncertainties for signal and backgrounds and background normalization uncertainties due to the prior assumptions and the modeling systematics, with the exception of  $t\bar{t}$  and  $Z + \text{jets}$ , where only the statistical uncertainties are shown.

Not reviewed, for internal circulation only

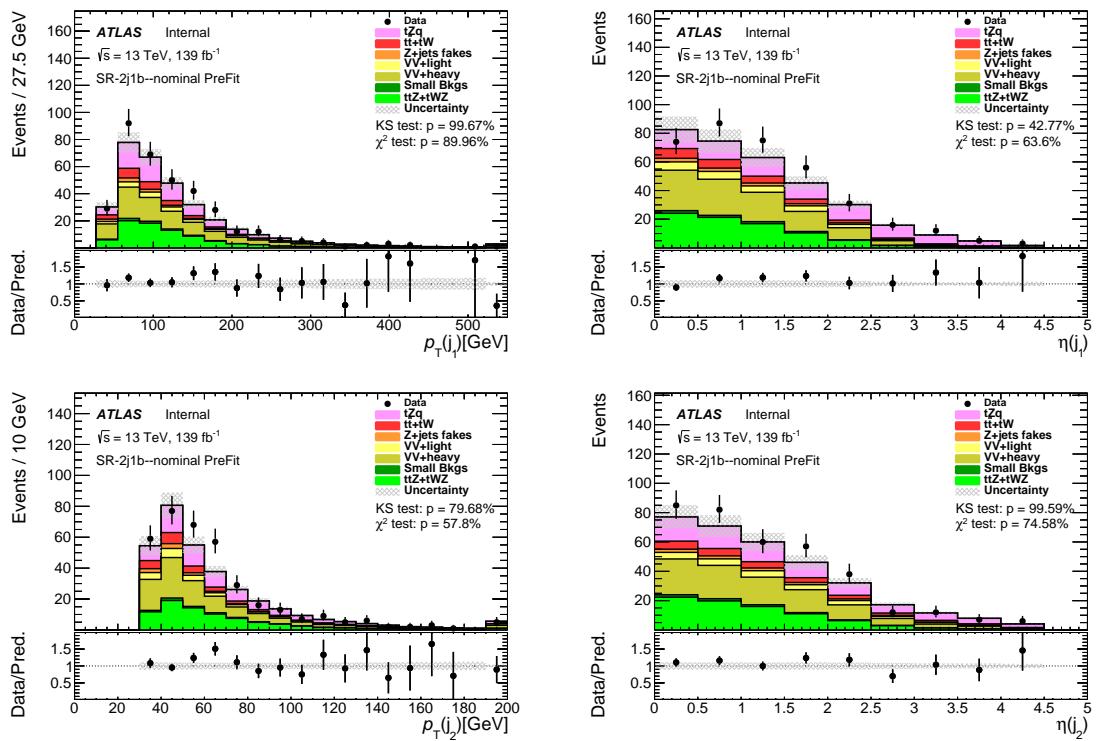


Figure 129: Comparison of data and MC predictions for reconstructed jet-related quantities for events in the 2j1b SR. Both signal and backgrounds are normalised to the expected number of events before the fit. The uncertainty band includes statistical uncertainties for signal and backgrounds and background normalization uncertainties due to the prior assumptions and the modeling systematics, with the exception of  $t\bar{t}$  and  $Z+jets$ , where only the statistical uncertainties are shown.

Not reviewed, for internal circulation only

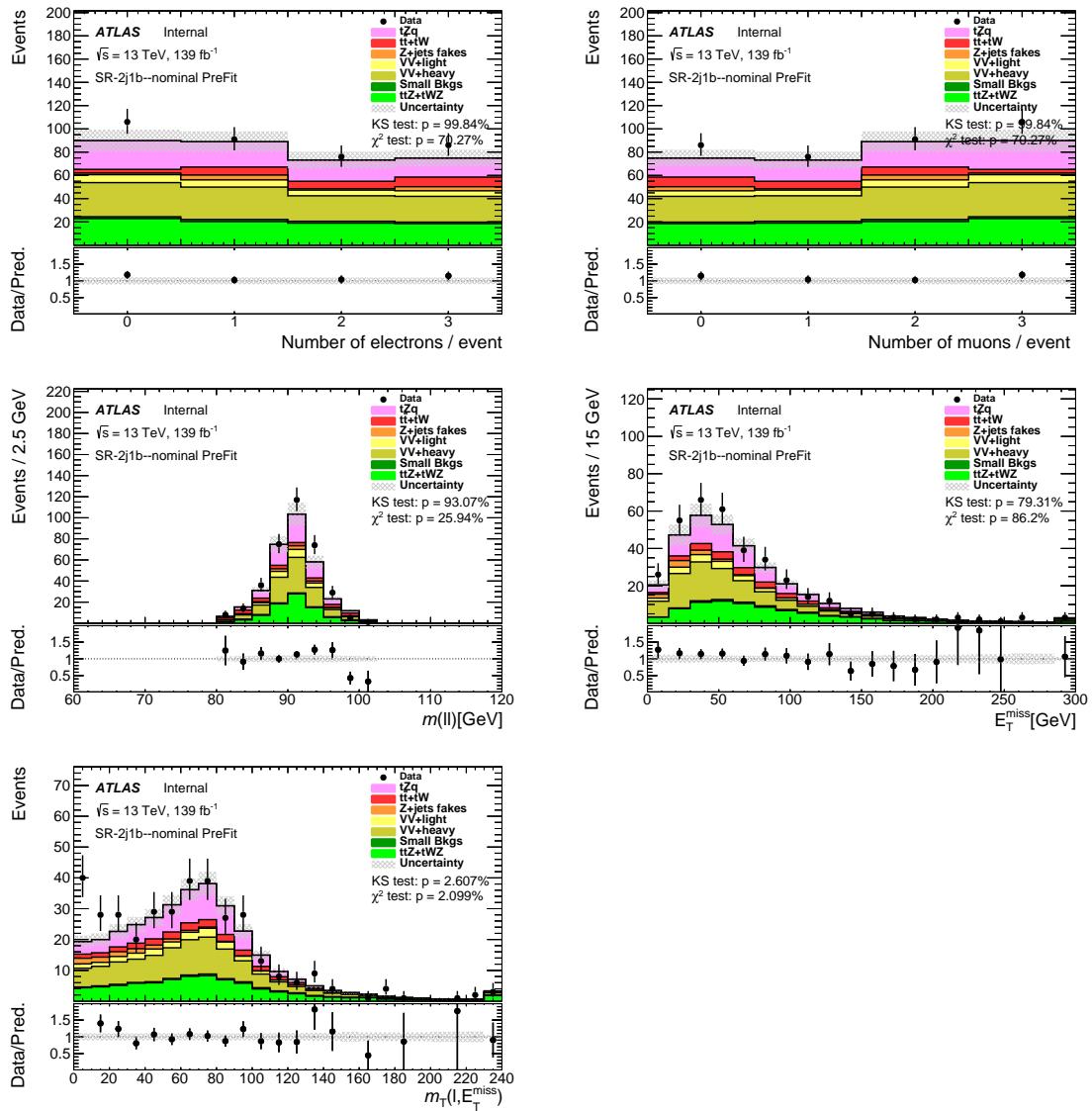


Figure 130: Comparison of data and MC predictions for reconstructed event-related quantities for events in the 2j1b SR. Both signal and backgrounds are normalised to the expected number of events before the fit. The uncertainty band includes statistical uncertainties for signal and backgrounds and background normalization uncertainties due to the prior assumptions and the modeling systematics, with the exception of  $t\bar{t}$  and  $Z + \text{jets}$ , where only the statistical uncertainties are shown.

Not reviewed, for internal circulation only

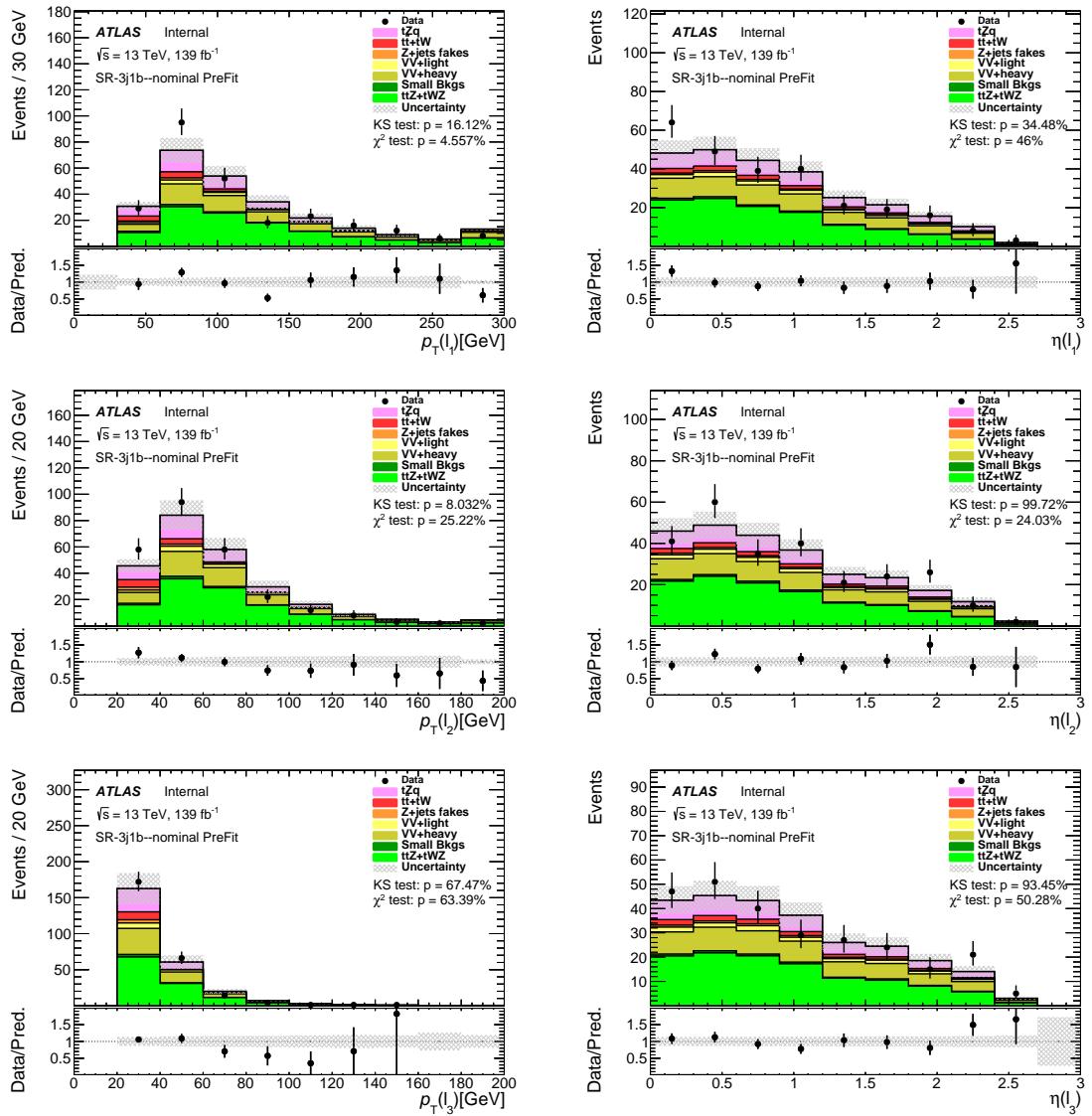


Figure 131: Comparison of data and MC predictions for reconstructed lepton-related quantities for events in the 3j1b SR. Both signal and backgrounds are normalised to the expected number of events before the fit. The uncertainty band includes statistical uncertainties for signal and backgrounds and background normalization uncertainties due to the prior assumptions and the modeling systematics, with the exception of  $t\bar{t}$  and  $Z + \text{jets}$ , where only the statistical uncertainties are shown.

Not reviewed, for internal circulation only

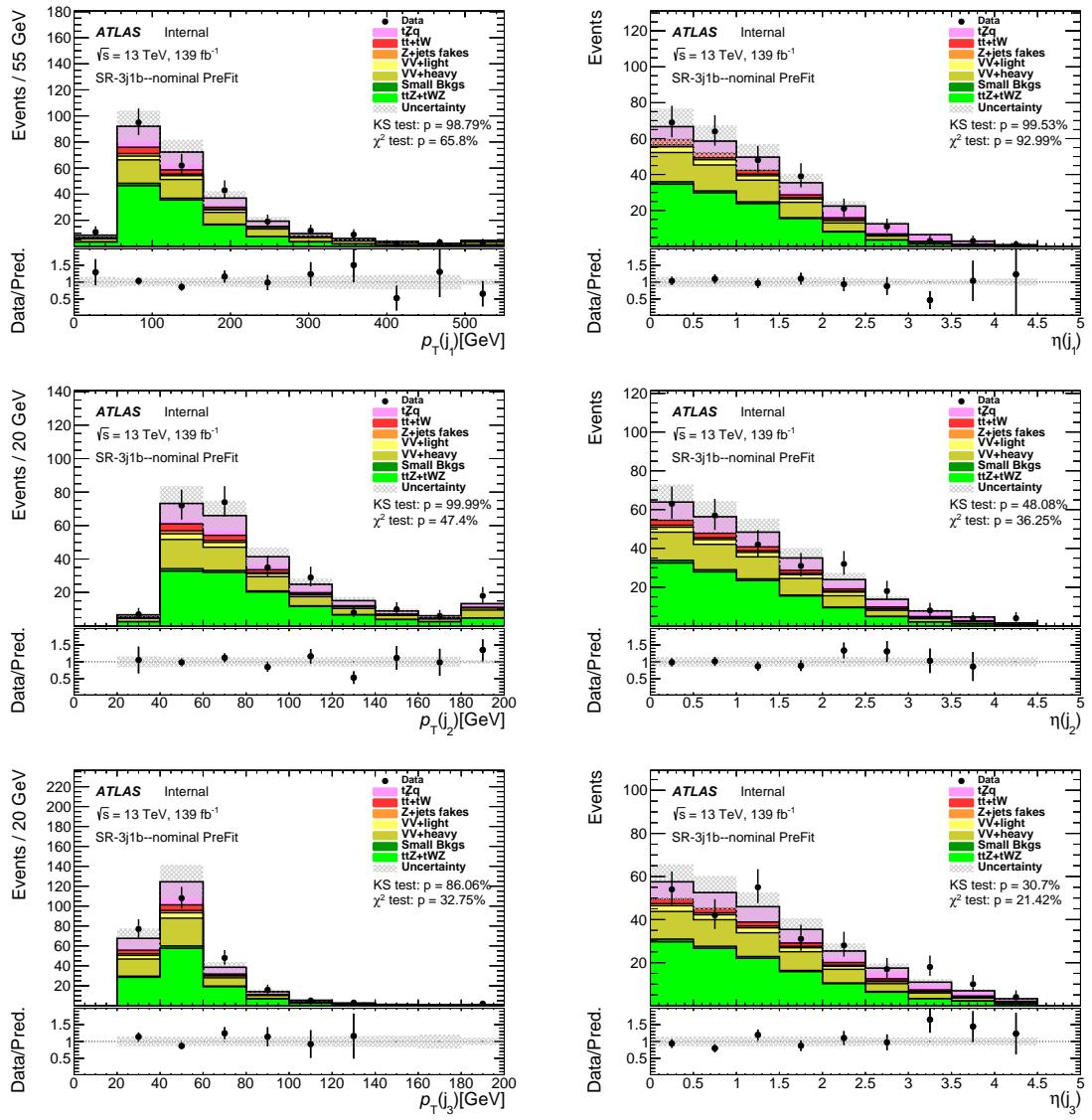


Figure 132: Comparison of data and MC predictions for reconstructed jet-related quantities for events in the 3j1b SR. Both signal and backgrounds are normalised to the expected number of events before the fit. The uncertainty band includes statistical uncertainties for signal and backgrounds and background normalization uncertainties due to the prior assumptions and the modeling systematics, with the exception of  $t\bar{t}$  and  $Z + \text{jets}$ , where only the statistical uncertainties are shown.

Not reviewed, for internal circulation only

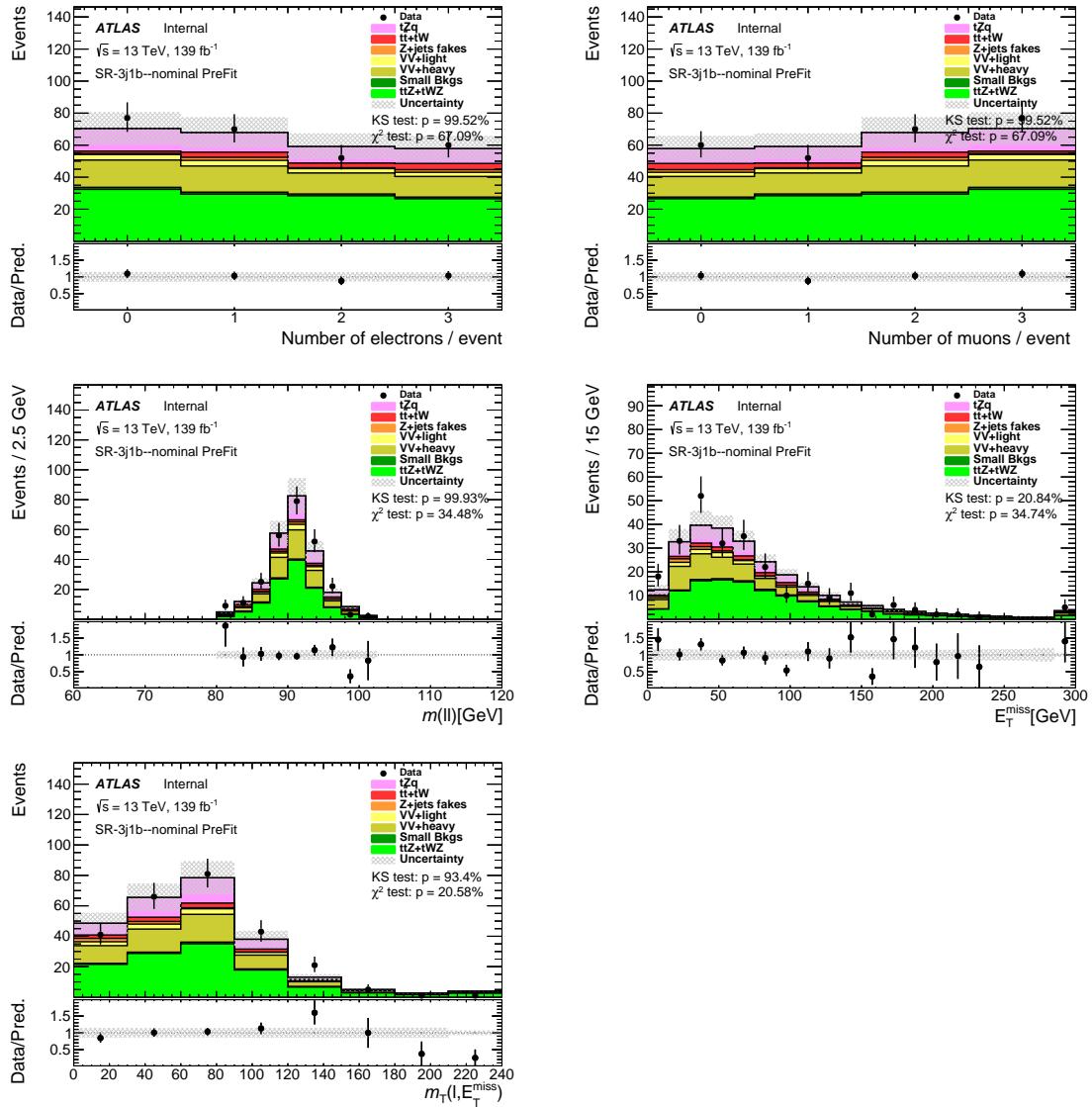


Figure 133: Comparison of data and MC predictions for reconstructed event-related quantities for events in the 3j1b SR. Both signal and backgrounds are normalised to the expected number of events before the fit. The uncertainty band includes statistical uncertainties for signal and backgrounds and background normalization uncertainties due to the prior assumptions and the modeling systematics, with the exception of  $t\bar{t}$  and  $Z + \text{jets}$ , where only the statistical uncertainties are shown.

1422 **C.2 Validation regions**1423 **C.2.1 Diboson VRs**

Not reviewed, for internal circulation only

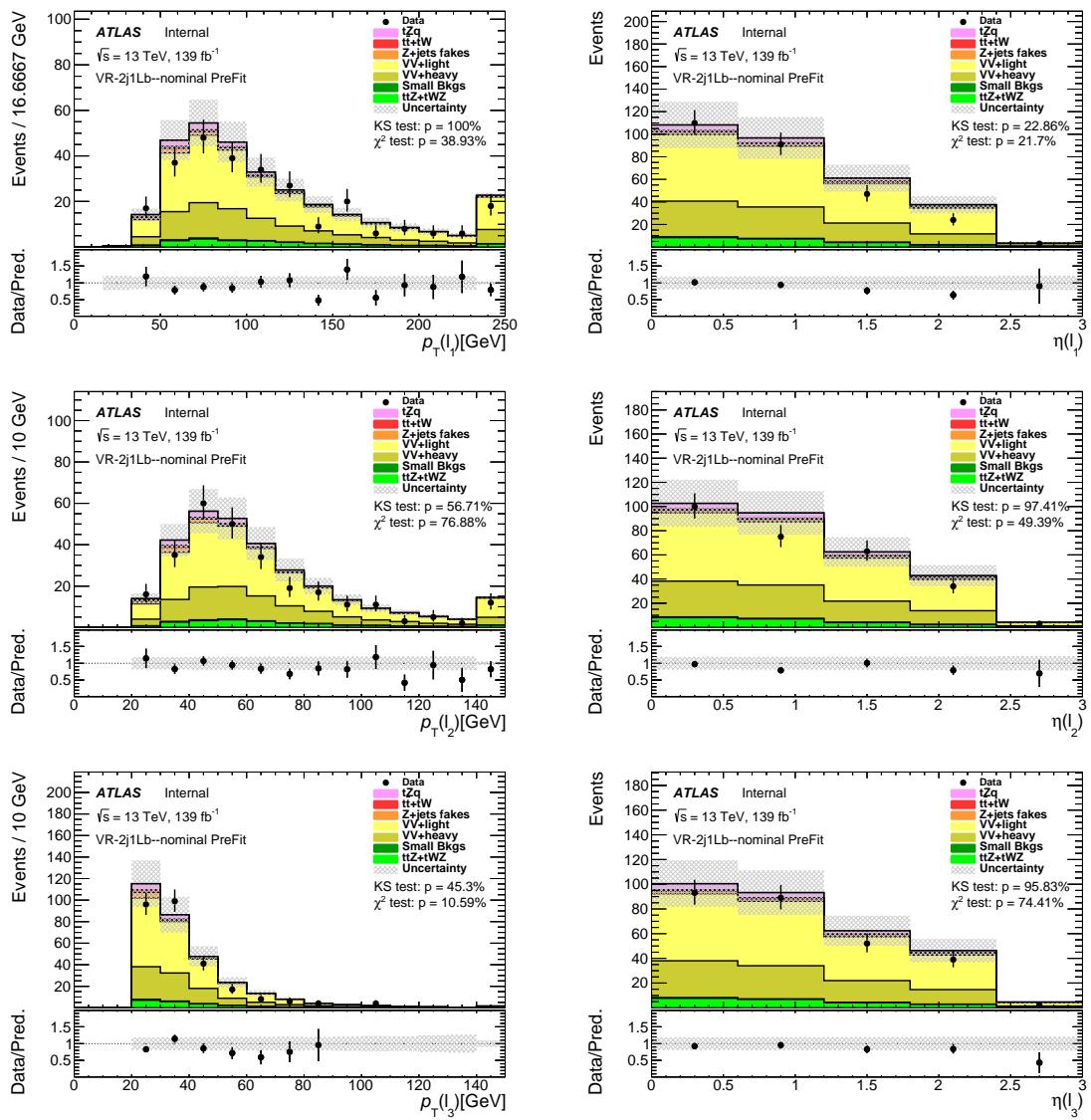


Figure 134: Comparison of data and MC predictions for reconstructed lepton-related quantities for events in the diboson 2j1Lb VR. Both signal and backgrounds are normalized to the expected number of events before the fit. The uncertainty band includes statistical uncertainties for signal and backgrounds and background normalization uncertainties due to the prior assumptions and the modeling systematics, with the exception of  $t\bar{t}$  and  $Z + \text{jets}$ , where only the statistical uncertainties are shown.

Not reviewed, for internal circulation only

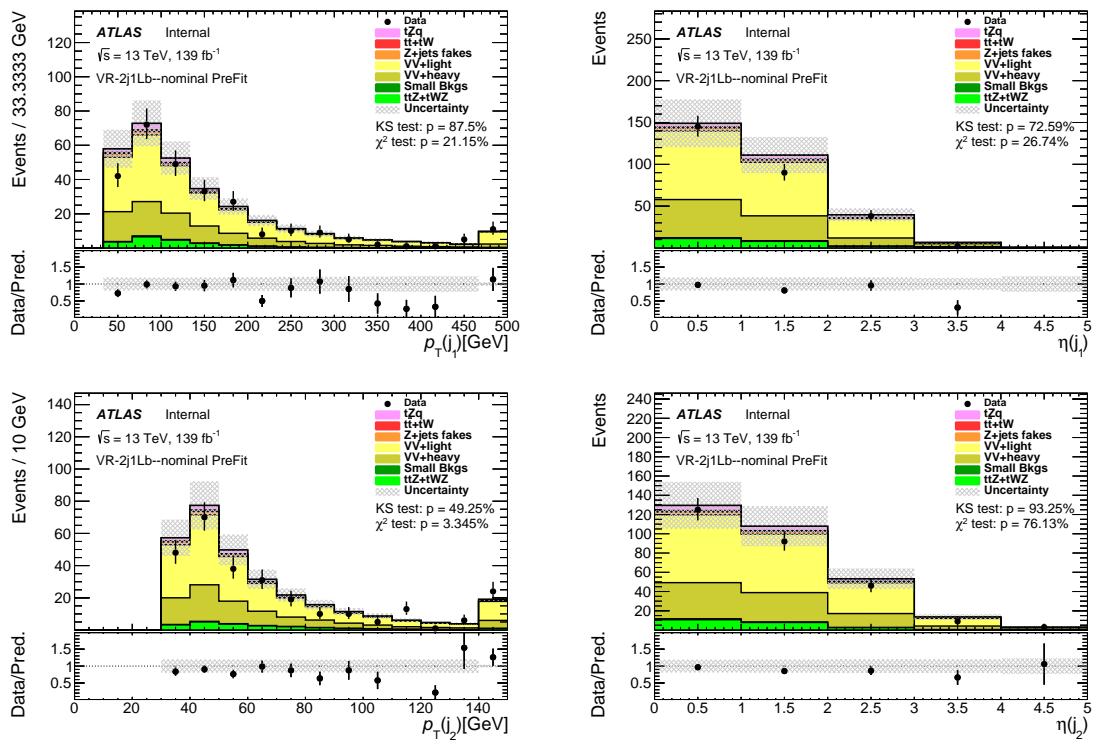


Figure 135: Comparison of data and MC predictions for reconstructed jet-related quantities for events in the diboson 2j1Lb VR. Both signal and backgrounds are normalised to the expected number of events before the fit. The uncertainty band includes statistical uncertainties for signal and backgrounds and background normalization uncertainties due to the prior assumptions and the modeling systematics, with the exception of  $t\bar{t}$  and  $Z + \text{jets}$ , where only the statistical uncertainties are shown.

1424 **C.2.2  $t\bar{t}V + t\bar{t}$  VRs**

Not reviewed, for internal circulation only

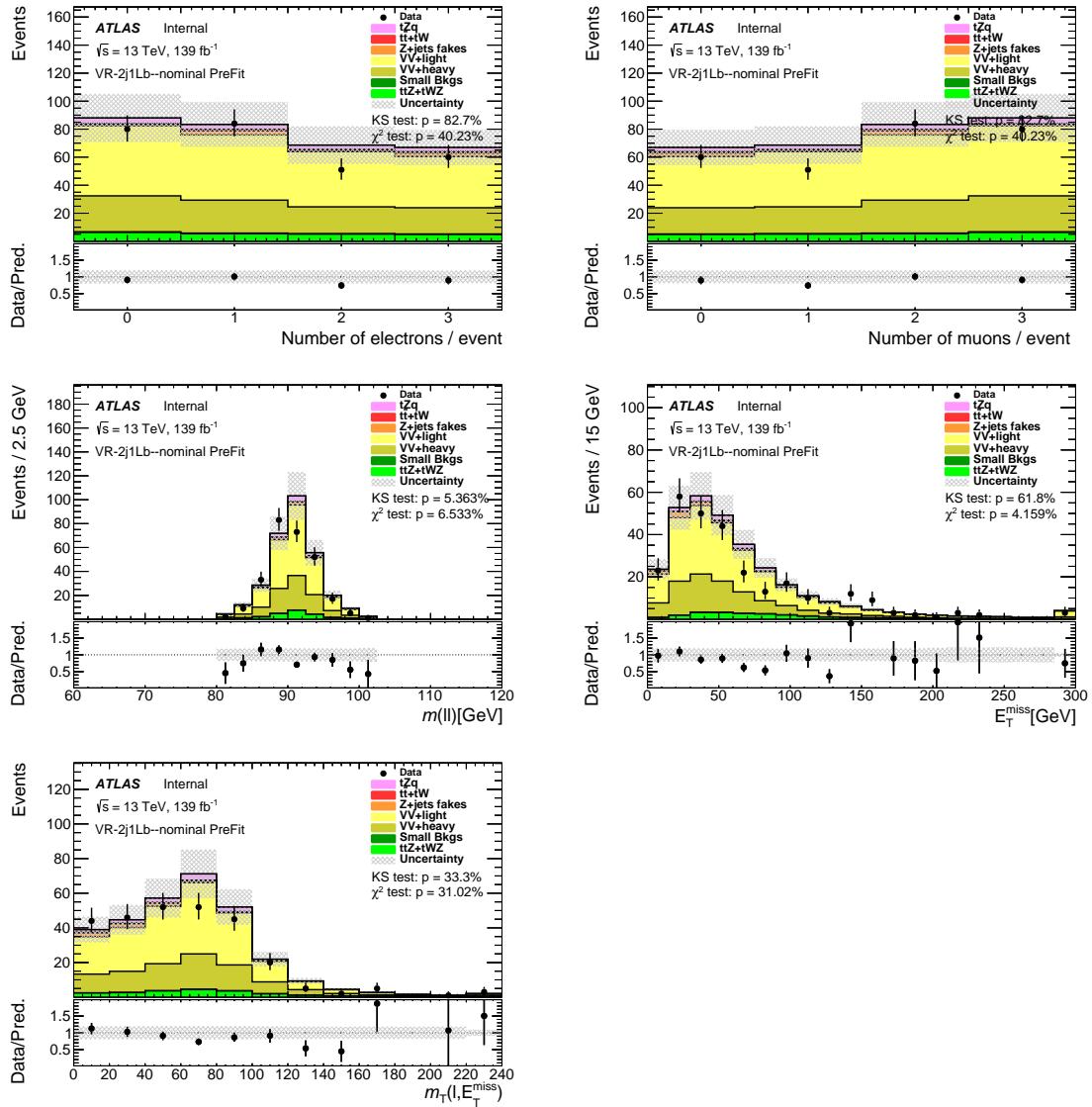


Figure 136: Comparison of data and MC predictions for reconstructed event-related quantities for events in the diboson 2j1Lb VR. Both signal and backgrounds are normalised to the expected number of events before the fit. The uncertainty band includes statistical uncertainties for signal and backgrounds and background normalization uncertainties due to the prior assumptions and the modeling systematics, with the exception of  $t\bar{t}$  and  $Z + \text{jets}$ , where only the statistical uncertainties are shown.

Not reviewed, for internal circulation only

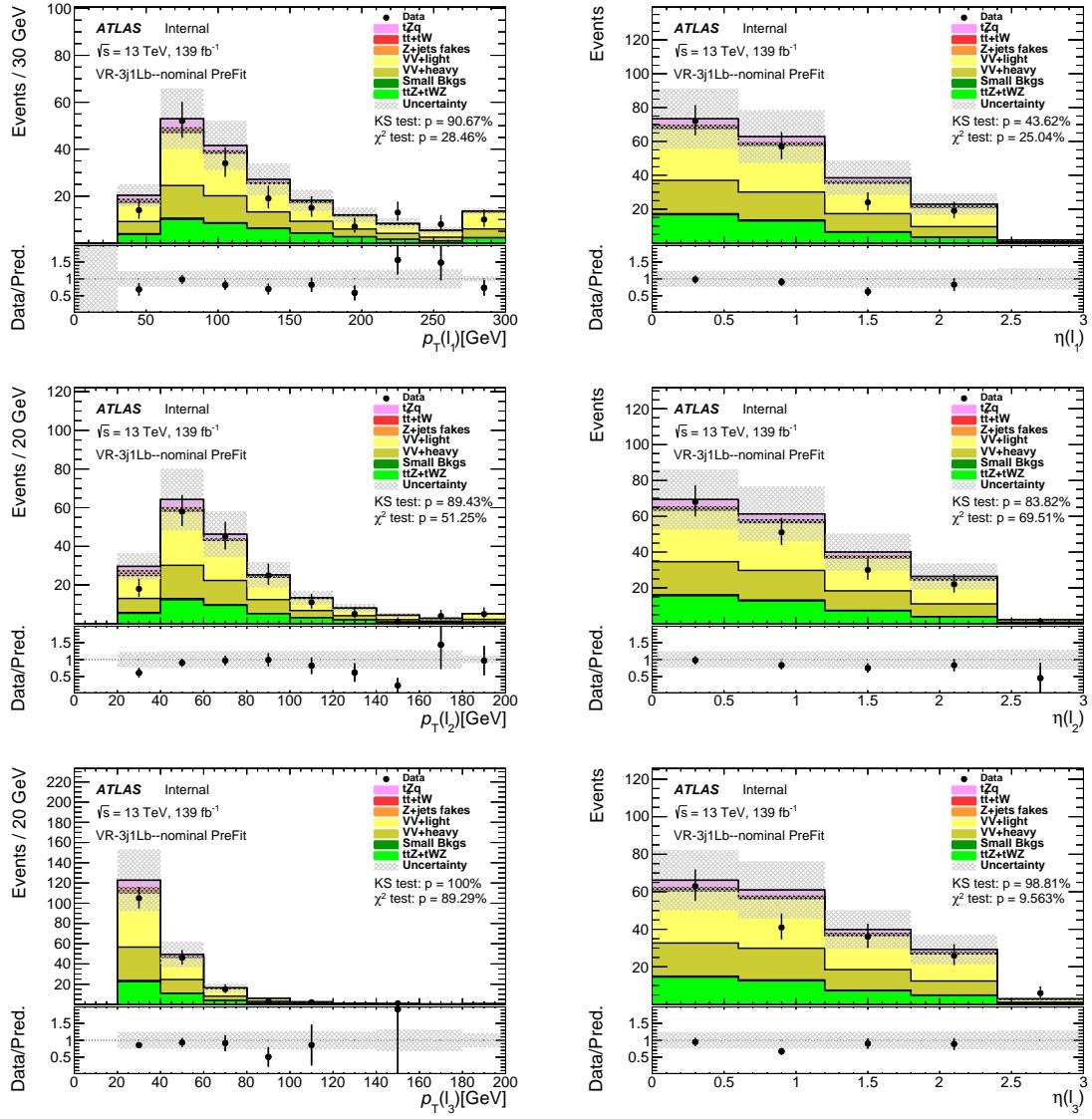


Figure 137: Comparison of data and MC predictions for reconstructed lepton-related quantities for events in the diboson 3j1Lb VR. Both signal and backgrounds are normalised to the expected number of events before the fit. The uncertainty band includes statistical uncertainties for signal and backgrounds and background normalization uncertainties due to the prior assumptions and the modeling systematics, with the exception of  $t\bar{t}$  and  $Z + \text{jets}$ , where only the statistical uncertainties are shown.

Not reviewed, for internal circulation only

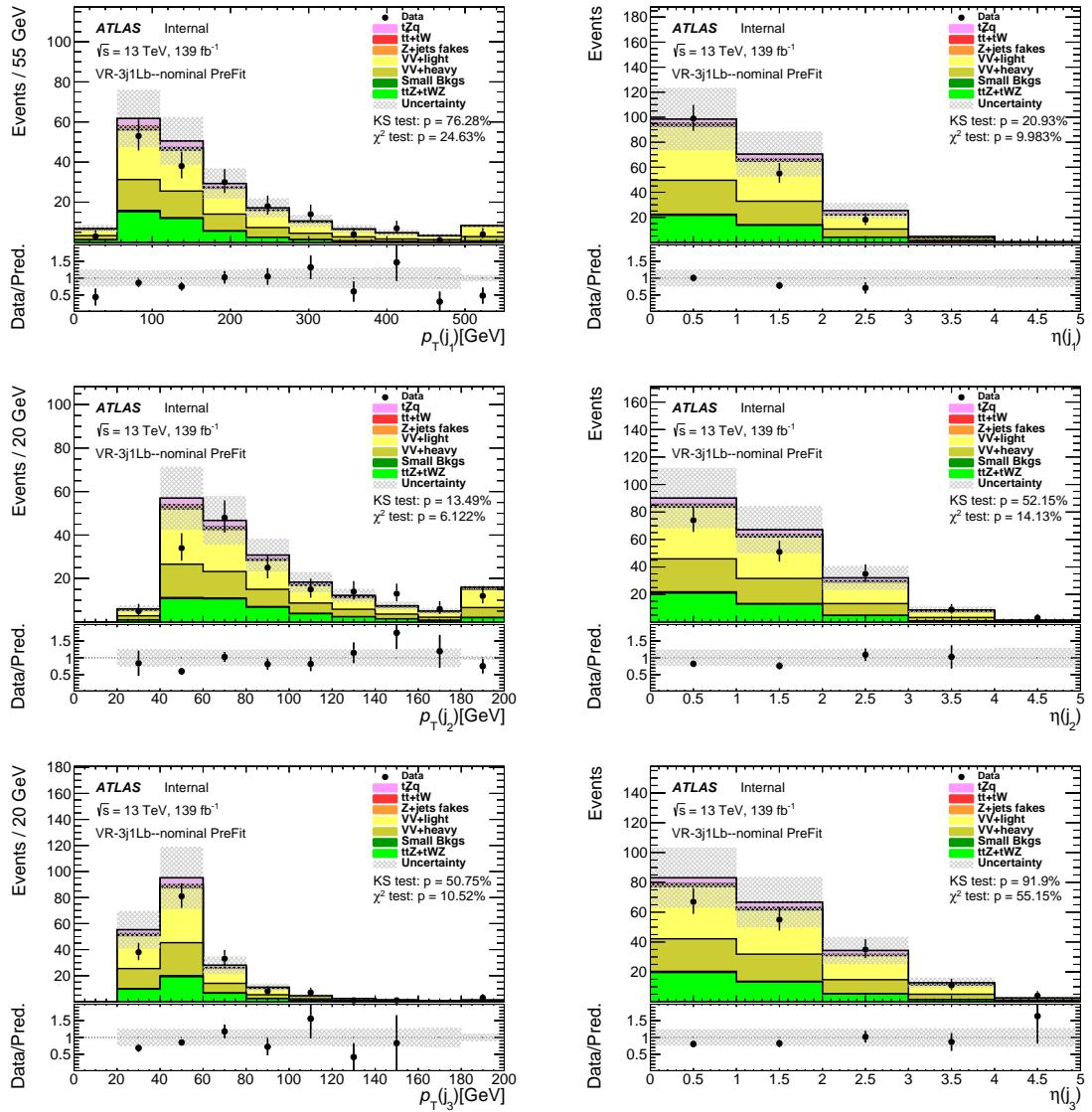


Figure 138: Comparison of data and MC predictions for reconstructed jet-related quantities for events in the diboson 3j1Lb VR. Both signal and backgrounds are normalised to the expected number of events before the fit. The uncertainty band includes statistical uncertainties for signal and backgrounds and background normalization uncertainties due to the prior assumptions and the modeling systematics, with the exception of  $t\bar{t}$  and  $Z + \text{jets}$ , where only the statistical uncertainties are shown.

Not reviewed, for internal circulation only

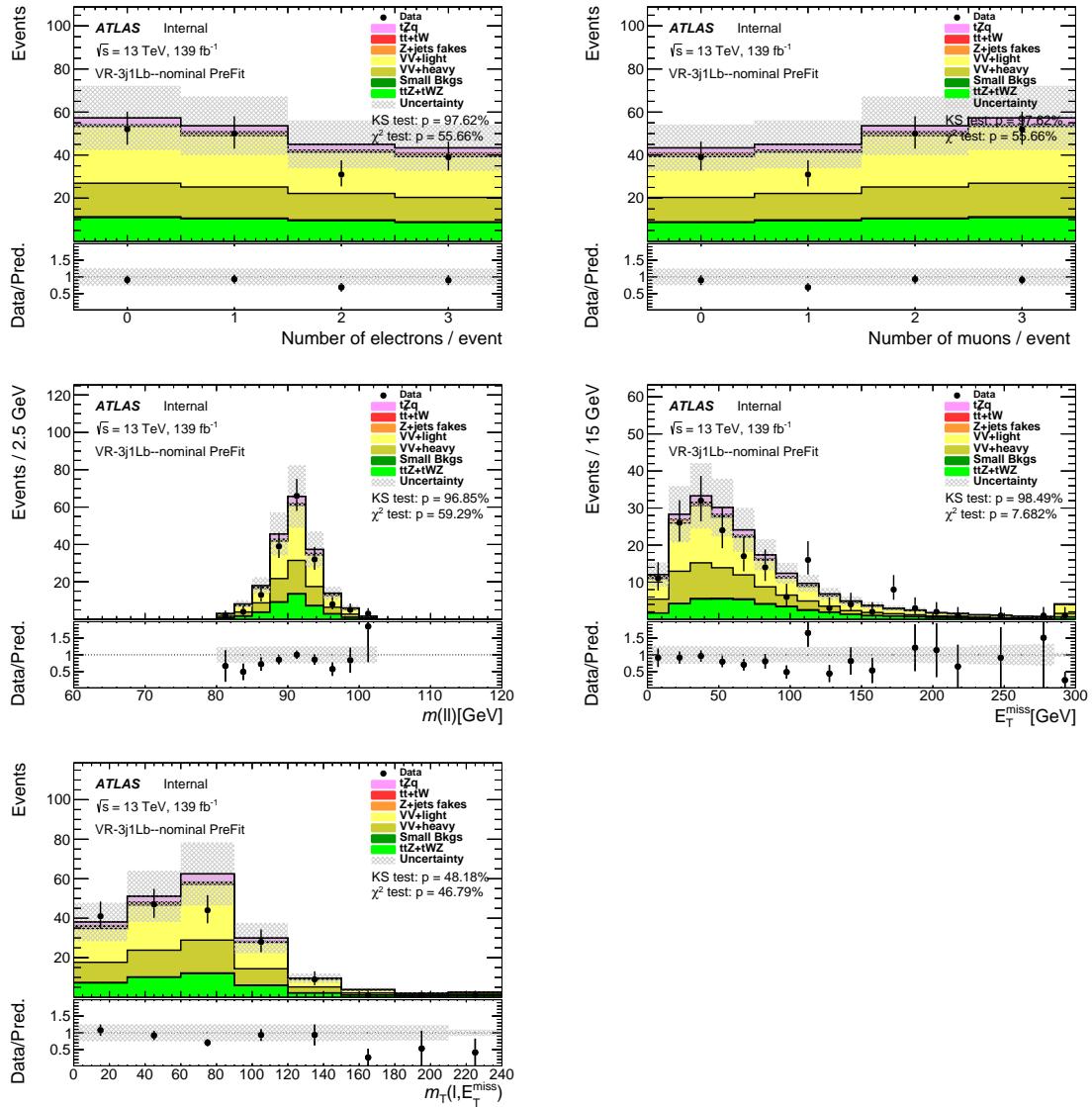


Figure 139: Comparison of data and MC predictions for reconstructed event-related quantities for events in the diboson 3j1Lb VR. Both signal and backgrounds are normalised to the expected number of events before the fit. The uncertainty band includes statistical uncertainties for signal and backgrounds and background normalization uncertainties due to the prior assumptions and the modeling systematics, with the exception of  $t\bar{t}$  and  $Z + \text{jets}$ , where only the statistical uncertainties are shown.

Not reviewed, for internal circulation only

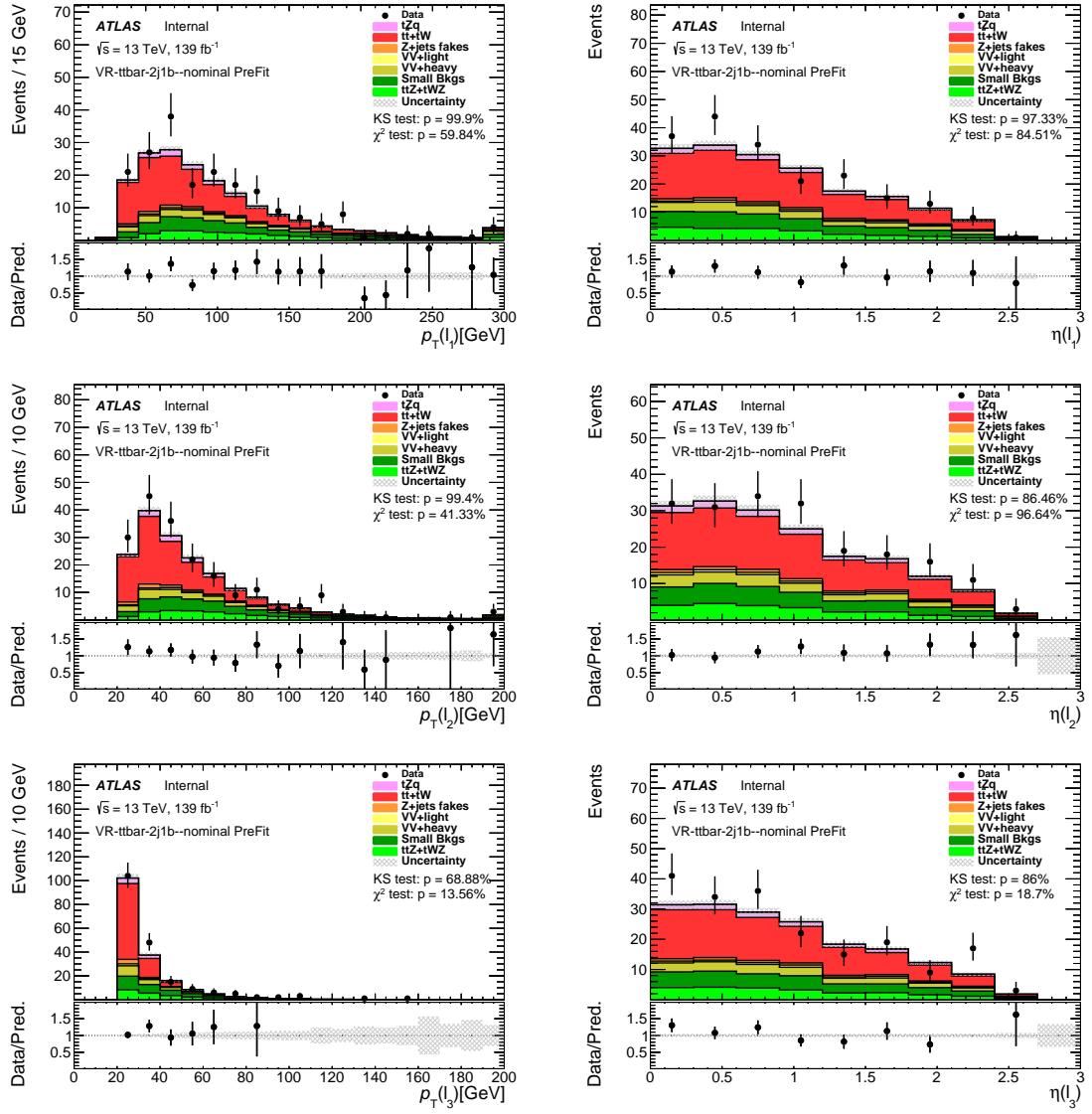


Figure 140: Comparison of data and MC predictions for reconstructed lepton-related quantities for events in the  $ttV + t\bar{t}$  2j1b VR. Both signal and backgrounds are normalised to the expected number of events before the fit. The uncertainty band includes statistical uncertainties for signal and backgrounds and background normalization uncertainties due to the prior assumptions and the modeling systematics, with the exception of  $t\bar{t}$  and  $Z + jets$ , where only the statistical uncertainties are shown.

Not reviewed, for internal circulation only

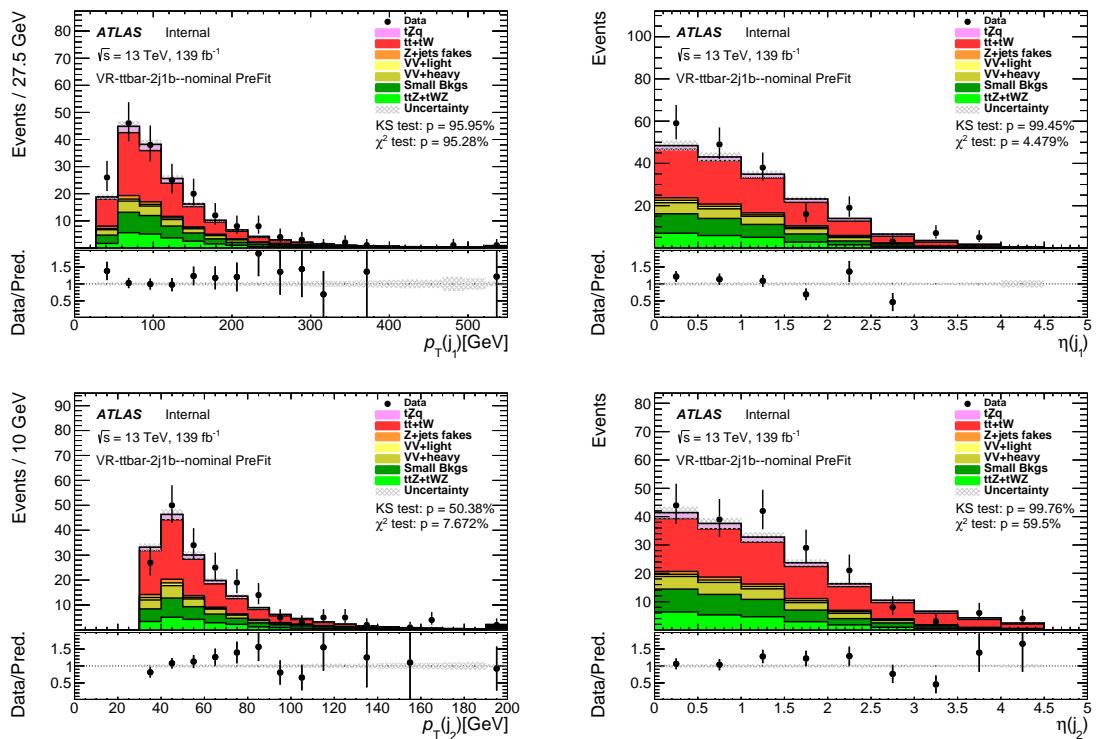


Figure 141: Comparison of data and MC predictions for reconstructed jet-related quantities for events in the  $t\bar{t}V + t\bar{t}$  2j1b VR. Both signal and backgrounds are normalised to the expected number of events before the fit. The uncertainty band includes statistical uncertainties for signal and backgrounds and background normalization uncertainties due to the prior assumptions and the modeling systematics, with the exception of  $t\bar{t}$  and  $Z + \text{jets}$ , where only the statistical uncertainties are shown.

Not reviewed, for internal circulation only

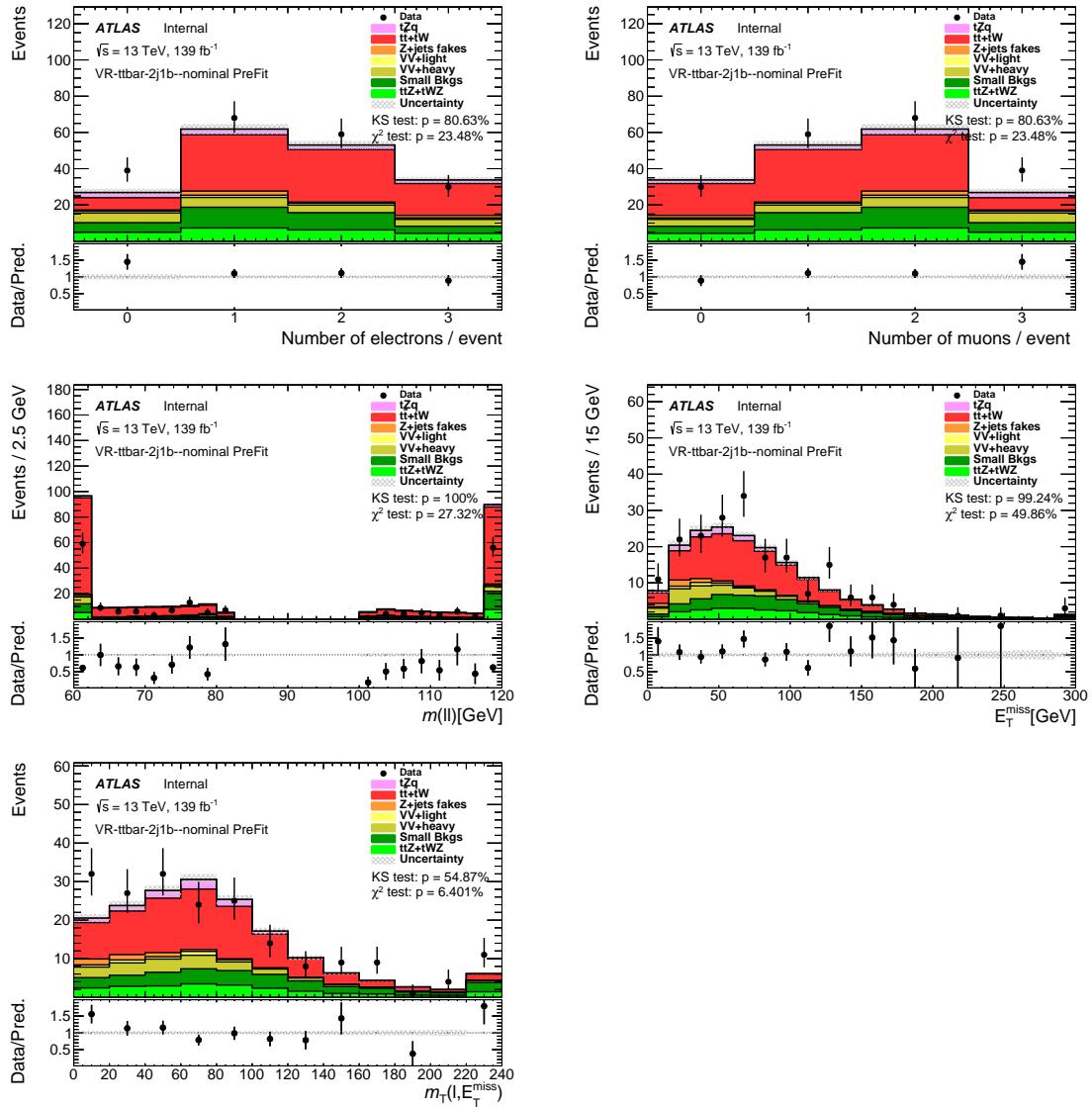


Figure 142: Comparison of data and MC predictions for reconstructed event-related quantities for events in the  $t\bar{t}V + t\bar{t}$  2j1b VR. Both signal and backgrounds are normalised to the expected number of events before the fit. The uncertainty band includes statistical uncertainties for signal and backgrounds and background normalization uncertainties due to the prior assumptions and the modeling systematics, with the exception of  $t\bar{t}$  and  $Z + \text{jets}$ , where only the statistical uncertainties are shown.

Not reviewed, for internal circulation only

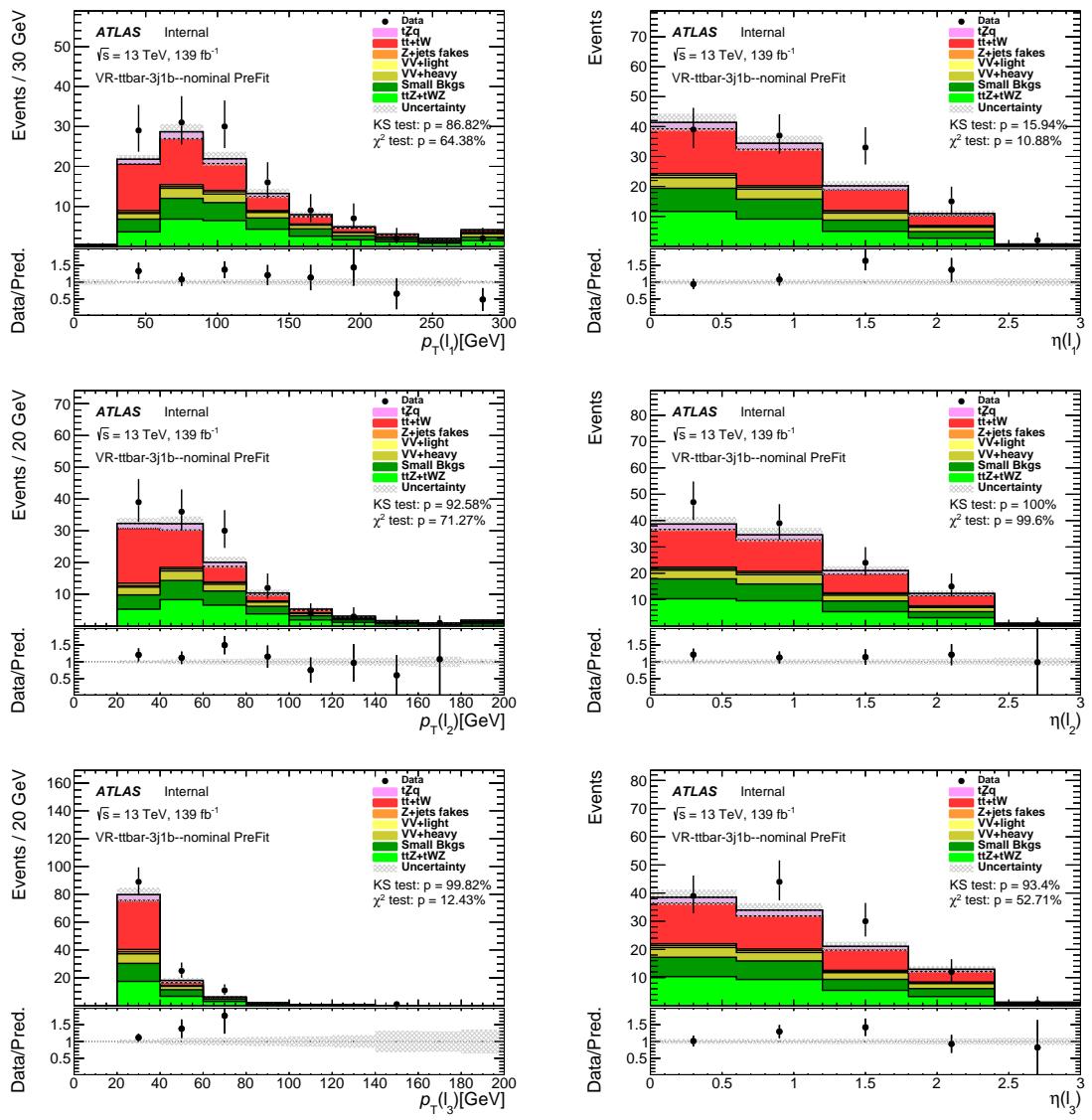


Figure 143: Comparison of data and MC predictions for reconstructed lepton-related quantities for events in the  $t\bar{t}V + t\bar{t}$  3j1b VR. Both signal and backgrounds are normalised to the expected number of events before the fit. The uncertainty band includes statistical uncertainties for signal and backgrounds and background normalization uncertainties due to the prior assumptions and the modeling systematics, with the exception of  $t\bar{t}$  and  $Z + \text{jets}$ , where only the statistical uncertainties are shown.

Not reviewed, for internal circulation only

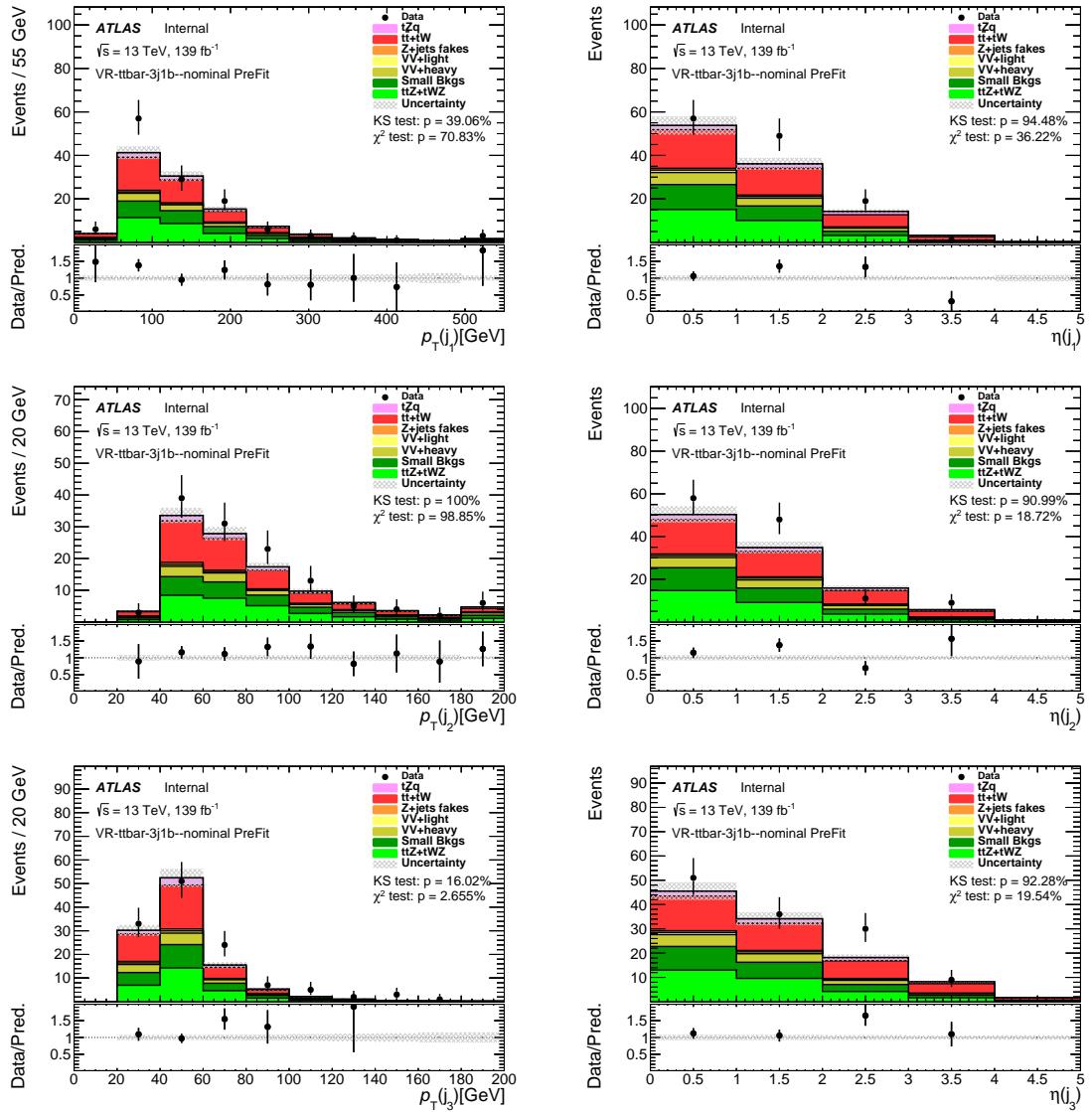


Figure 144: Comparison of data and MC predictions for reconstructed jet-related quantities for events in the  $t\bar{t}V + t\bar{t}$  3j1b VR. Both signal and backgrounds are normalised to the expected number of events before the fit. The uncertainty band includes statistical uncertainties for signal and backgrounds and background normalization uncertainties due to the prior assumptions and the modeling systematics, with the exception of  $t\bar{t}$  and  $Z + \text{jets}$ , where only the statistical uncertainties are shown.

Not reviewed, for internal circulation only

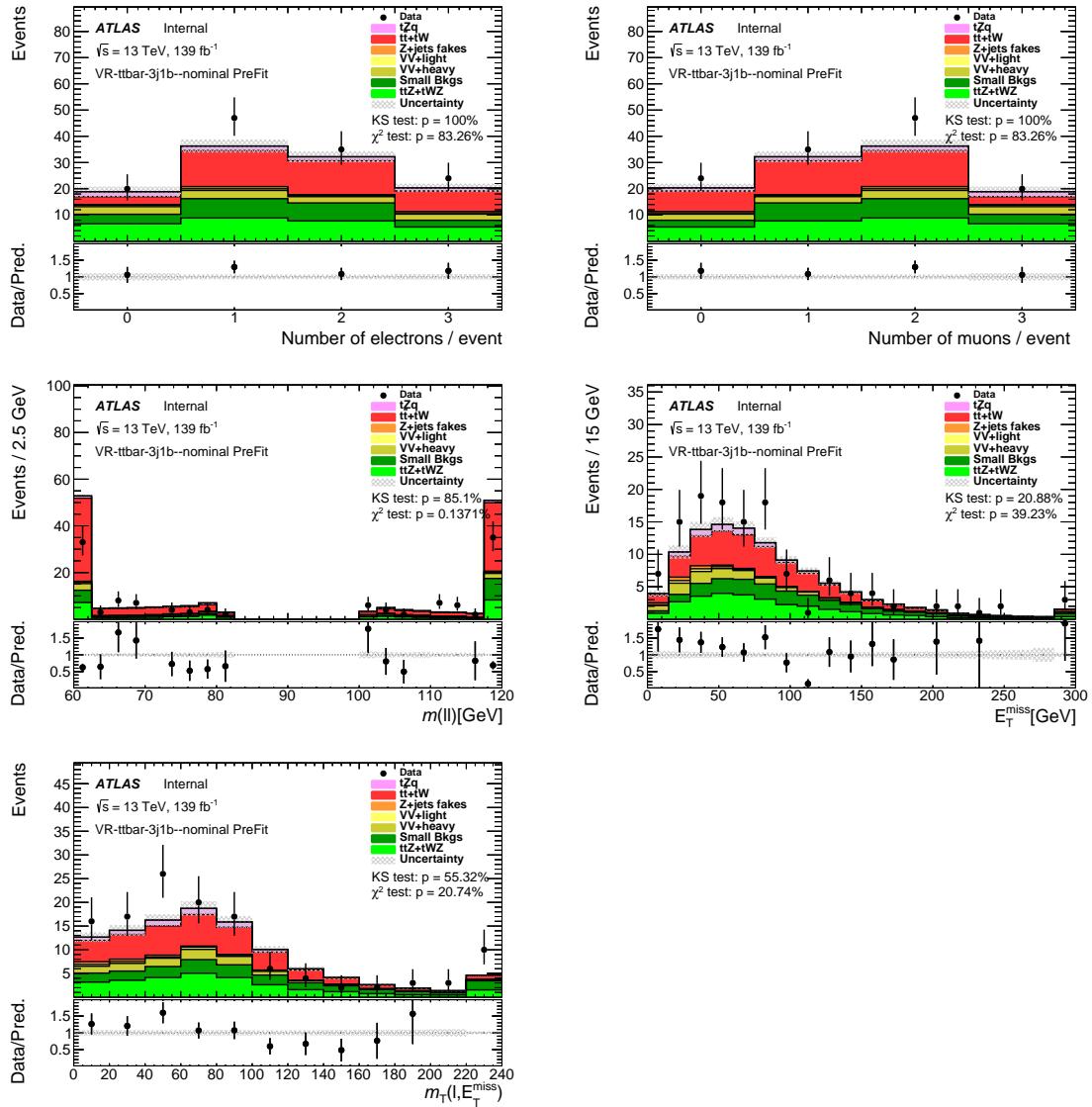


Figure 145: Comparison of data and MC predictions for reconstructed event-related quantities for events in the  $t\bar{t}V + t\bar{t}$  3j1b VR. Both signal and backgrounds are normalised to the expected number of events before the fit. The uncertainty band includes statistical uncertainties for signal and backgrounds and background normalization uncertainties due to the prior assumptions and the modeling systematics, with the exception of  $t\bar{t}$  and  $Z + \text{jets}$ , where only the statistical uncertainties are shown.

1425 **D Plots in CRs**

1426 In this appendix, plots in the control regions are shown.

Not reviewed, for internal circulation only

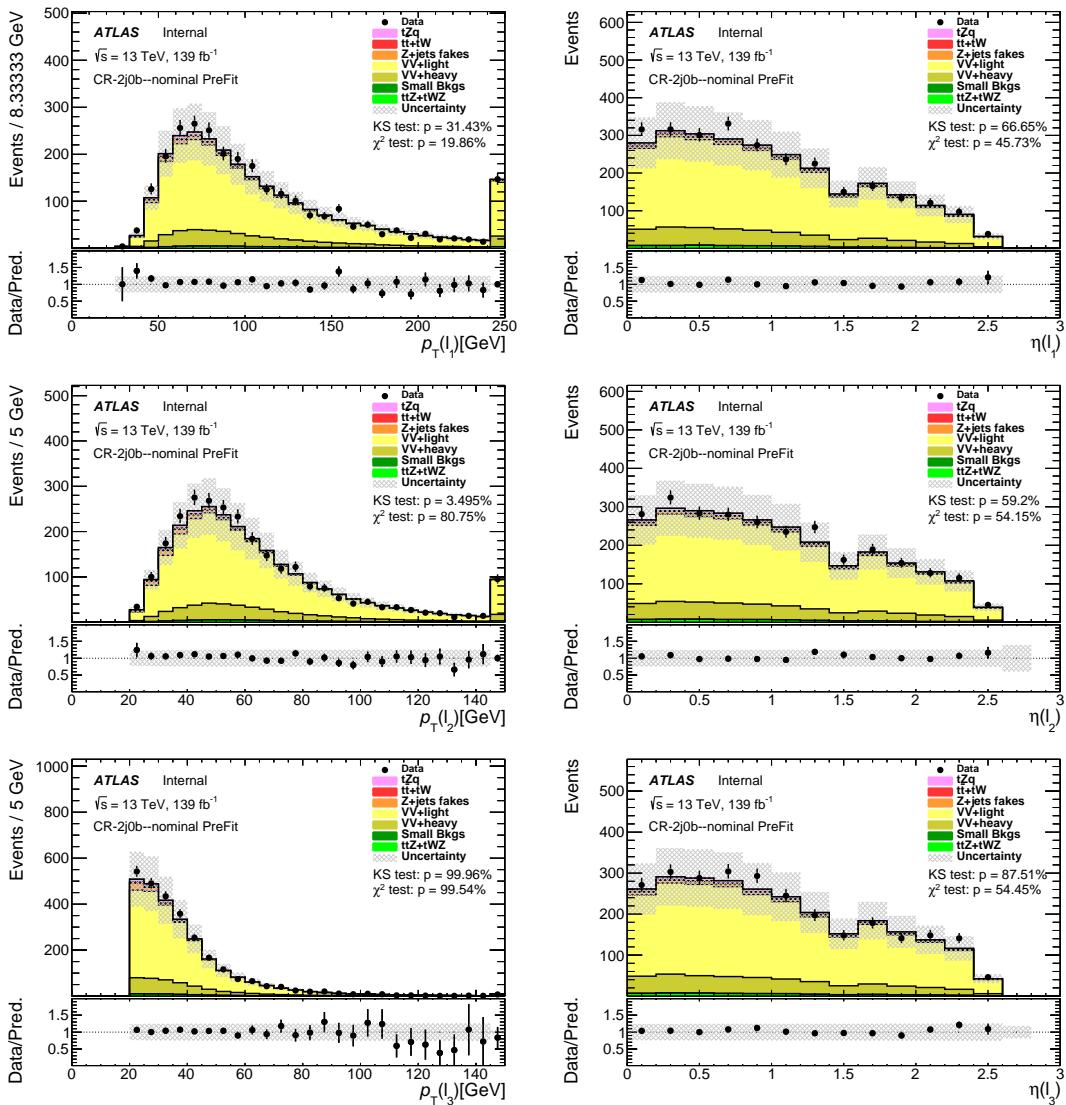
1427 **D.1 Basic kinematic plots**1428 **D.1.1 Diboson CRs**

Figure 146: Comparison of data and MC predictions for reconstructed lepton-related quantities for events in the diboson 2j0b CR. Both signal and backgrounds are normalised to the expected number of events before the fit. The uncertainty band includes statistical uncertainties for signal and backgrounds and background normalization uncertainties due to the prior assumptions and the modeling systematics, with the exception of  $t\bar{t}$  and  $Z + \text{jets}$ , where only the statistical uncertainties are shown.

Not reviewed, for internal circulation only

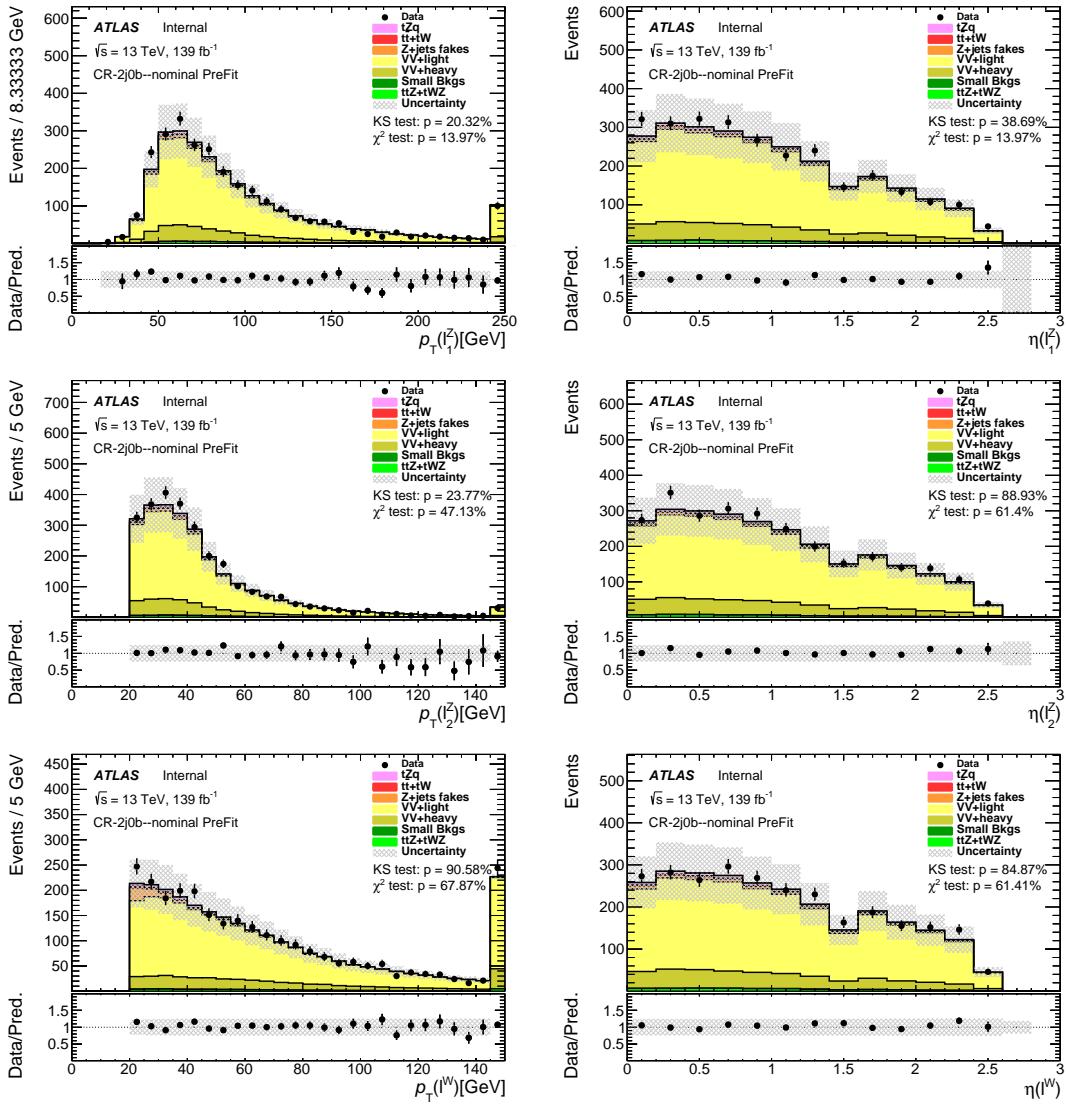


Figure 147: Comparison of data and MC predictions for reconstructed lepton-related quantities for events in the diboson 2j0b CR. Both signal and backgrounds are normalised to the expected number of events before the fit. The uncertainty band includes statistical uncertainties for signal and backgrounds and background normalization uncertainties due to the prior assumptions and the modeling systematics, with the exception of  $t\bar{t}$  and  $Z + \text{jets}$ , where only the statistical uncertainties are shown.

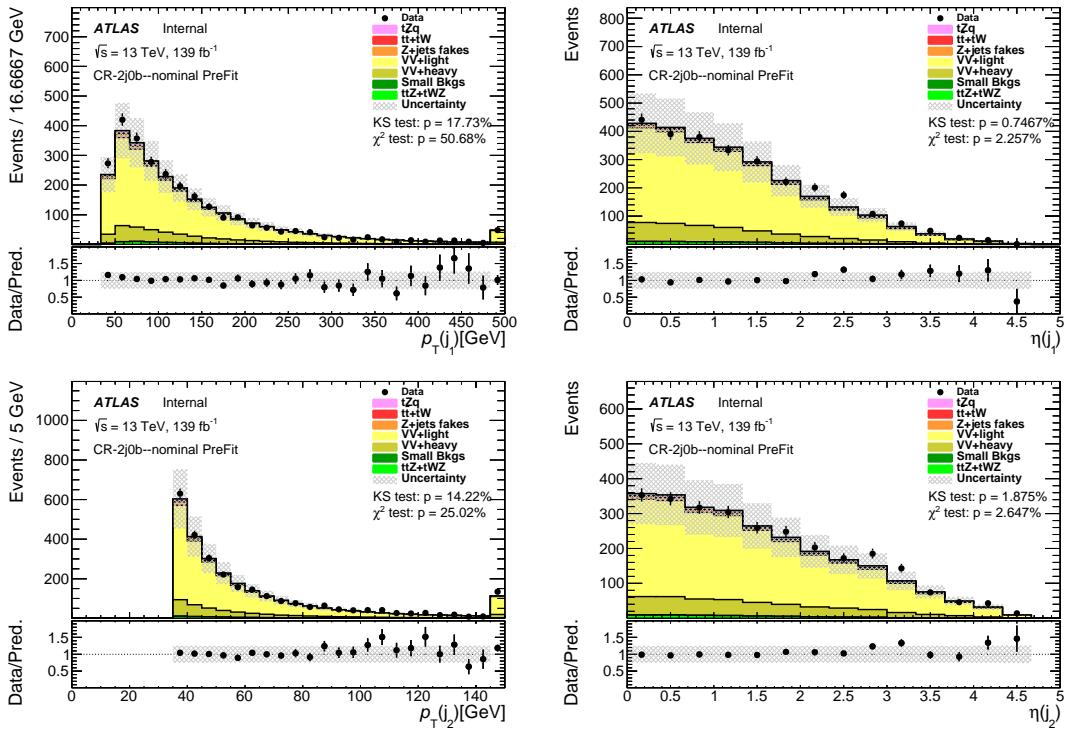


Figure 148: Comparison of data and MC predictions for reconstructed jet-related quantities for events in the diboson 2j0b CR. Both signal and backgrounds are normalised to the expected number of events before the fit. The uncertainty band includes statistical uncertainties for signal and backgrounds and background normalization uncertainties due to the prior assumptions and the modeling systematics, with the exception of  $t\bar{t}$  and  $Z + \text{jets}$ , where only the statistical uncertainties are shown.

Not reviewed, for internal circulation only

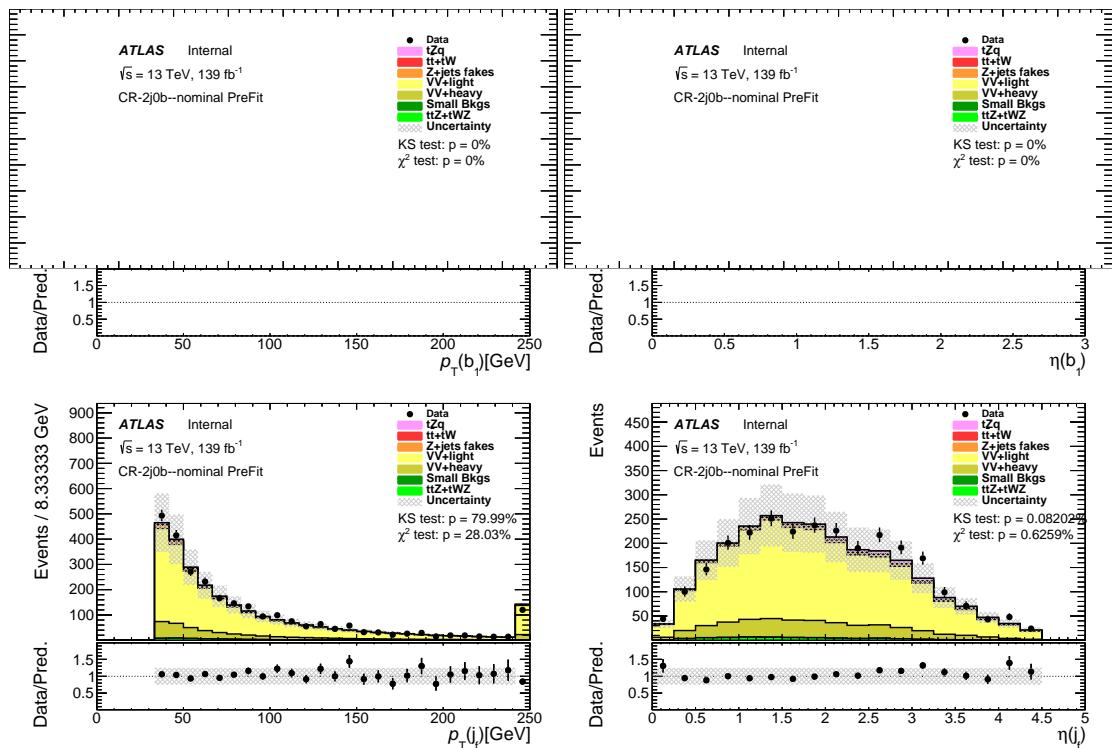


Figure 149: Comparison of data and MC predictions for reconstructed jet-related quantities for events in the diboson 2j0b CR. Both signal and backgrounds are normalised to the expected number of events before the fit. The uncertainty band includes statistical uncertainties for signal and backgrounds and background normalization uncertainties due to the prior assumptions and the modeling systematics, with the exception of  $t\bar{t}$  and  $Z + \text{jets}$ , where only the statistical uncertainties are shown. The distribution(s) with a  $b$ -jet are not filled, as there are no  $b$ -tagged jets in this region.

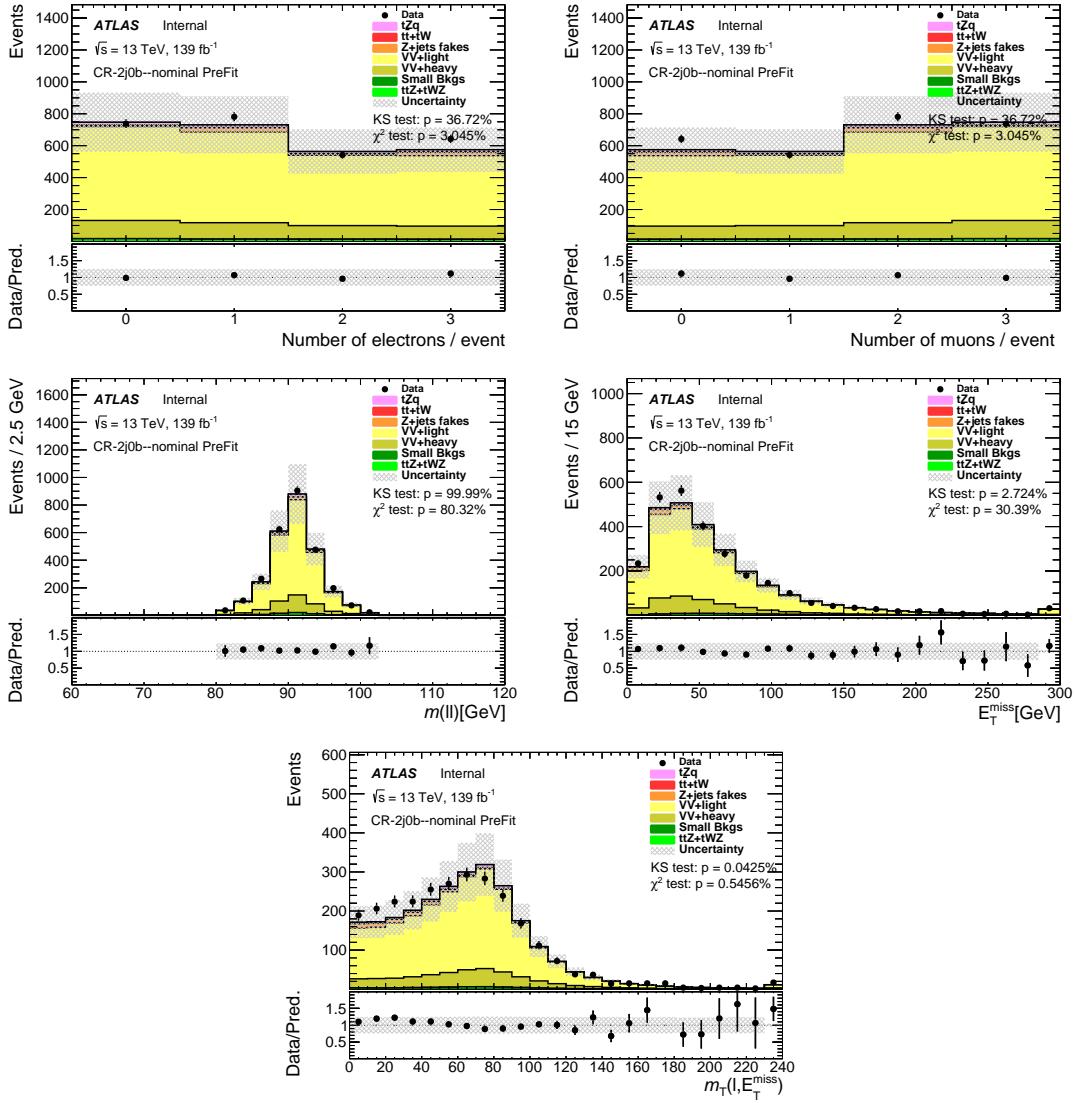


Figure 150: Comparison of data and MC predictions for reconstructed event-related quantities for events in the diboson 2j0b CR. Both signal and backgrounds are normalised to the expected number of events before the fit. The uncertainty band includes statistical uncertainties for signal and backgrounds and background normalization uncertainties due to the prior assumptions and the modeling systematics, with the exception of  $t\bar{t}$  and  $Z + \text{jets}$ , where only the statistical uncertainties are shown.

Not reviewed, for internal circulation only

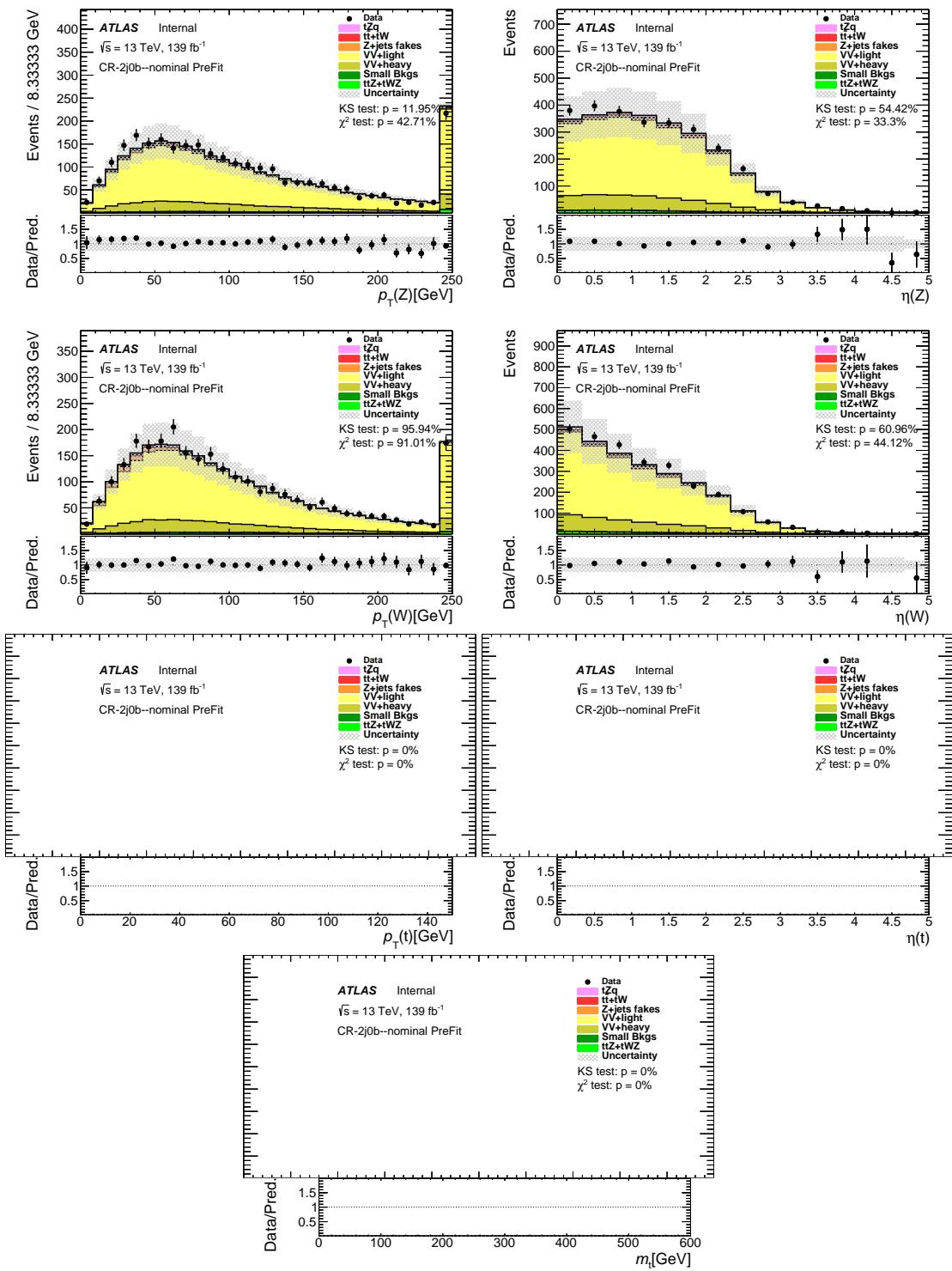


Figure 151: Comparison of data and MC predictions for reconstructed event-related quantities for events in the diboson 2j0b CR. Both signal and backgrounds are normalised to the expected number of events before the fit. The uncertainty band includes statistical uncertainties for signal and backgrounds and background normalization uncertainties due to the prior assumptions and the modeling systematics, with the exception of  $t\bar{t}$  and  $Z + \text{jets}$ , where only the statistical uncertainties are shown. The distribution(s) with a  $b$ -jet are not filled, as there are no  $b$ -tagged jets in this region.

Not reviewed, for internal circulation only

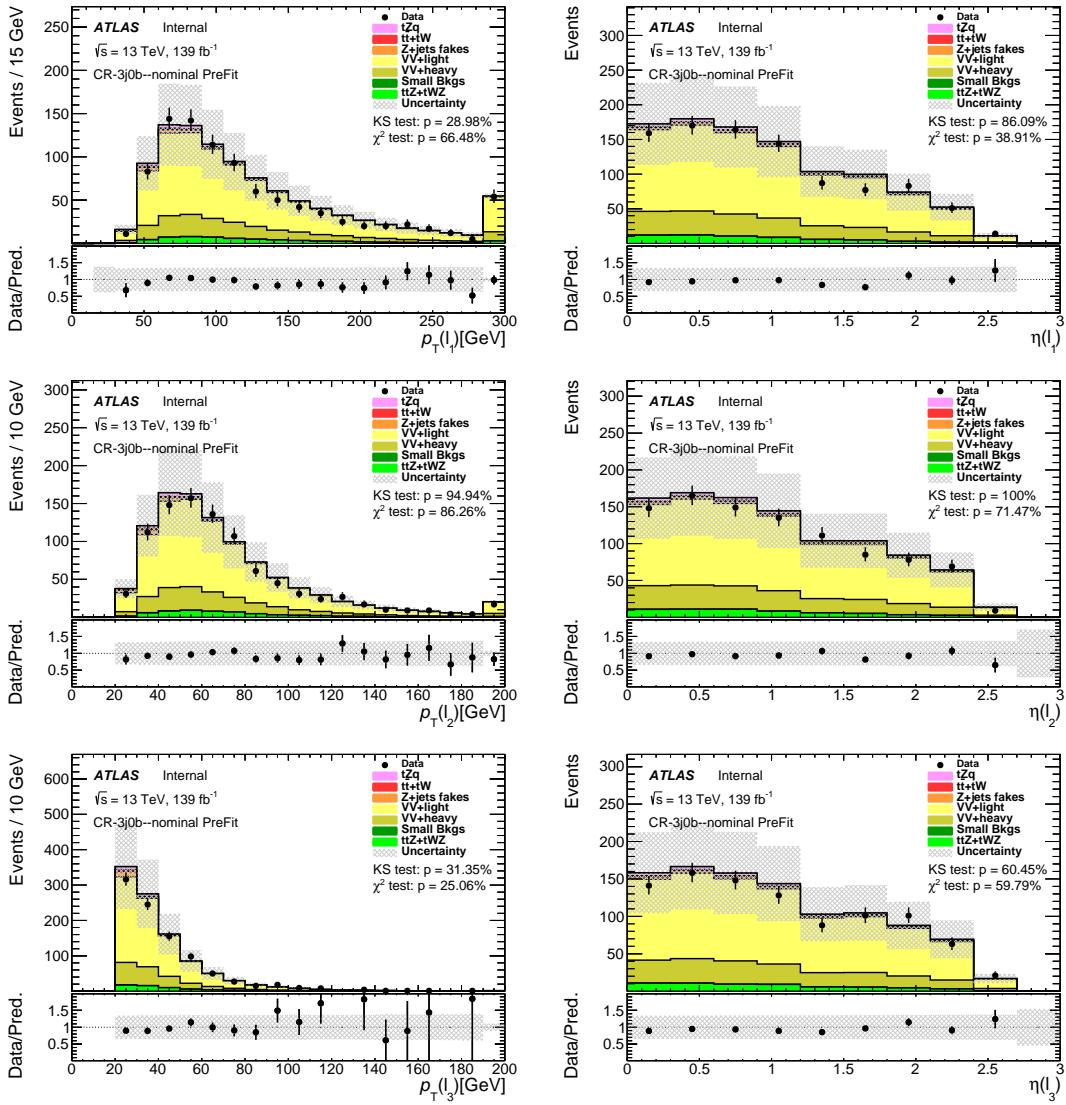


Figure 152: Comparison of data and MC predictions for reconstructed lepton-related quantities for events in the diboson 3j0b CR. Both signal and backgrounds are normalised to the expected number of events before the fit. The uncertainty band includes statistical uncertainties for signal and backgrounds and background normalization uncertainties due to the prior assumptions and the modeling systematics, with the exception of  $t\bar{t}$  and  $Z + \text{jets}$ , where only the statistical uncertainties are shown.

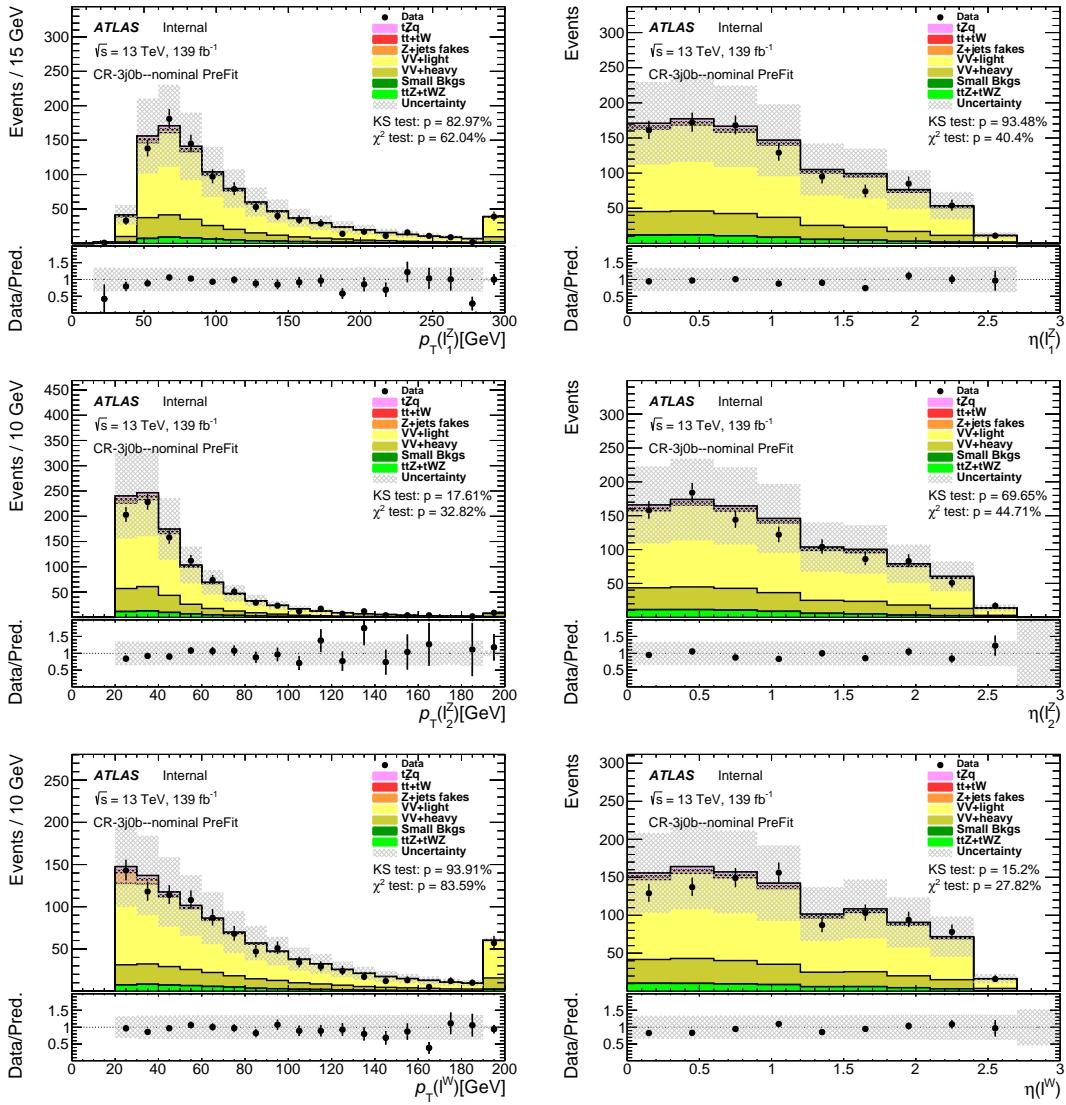


Figure 153: Comparison of data and MC predictions for reconstructed lepton-related quantities for events in the diboson 3j0b CR. Both signal and backgrounds are normalised to the expected number of events before the fit. The uncertainty band includes statistical uncertainties for signal and backgrounds and background normalization uncertainties due to the prior assumptions and the modeling systematics, with the exception of  $t\bar{t}$  and  $Z + \text{jets}$ , where only the statistical uncertainties are shown.

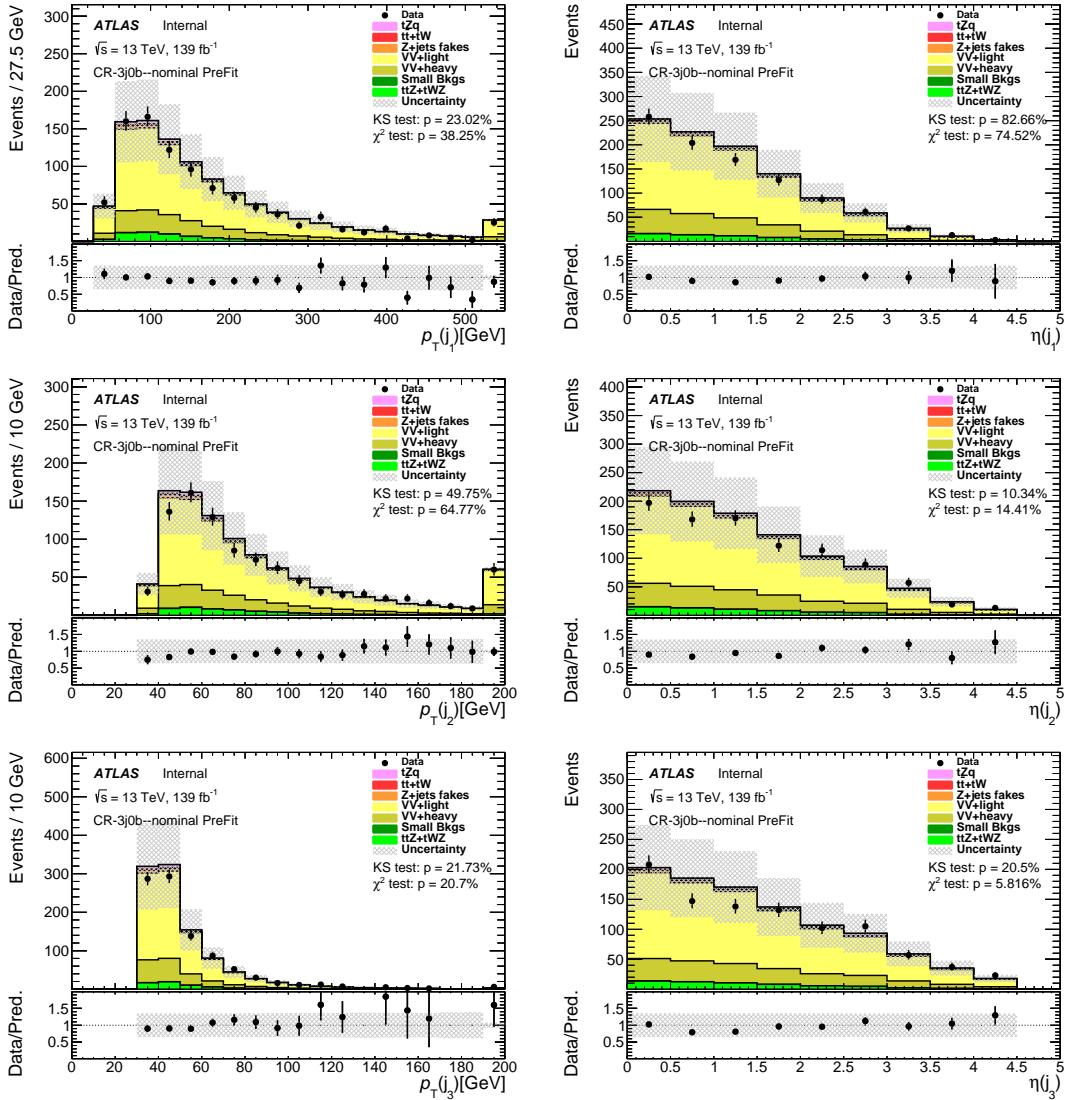


Figure 154: Comparison of data and MC predictions for reconstructed jet-related quantities for events in the diboson 3j0b CR. Both signal and backgrounds are normalised to the expected number of events before the fit. The uncertainty band includes statistical uncertainties for signal and backgrounds and background normalization uncertainties due to the prior assumptions and the modeling systematics, with the exception of  $t\bar{t}$  and  $Z + \text{jets}$ , where only the statistical uncertainties are shown.

Not reviewed, for internal circulation only

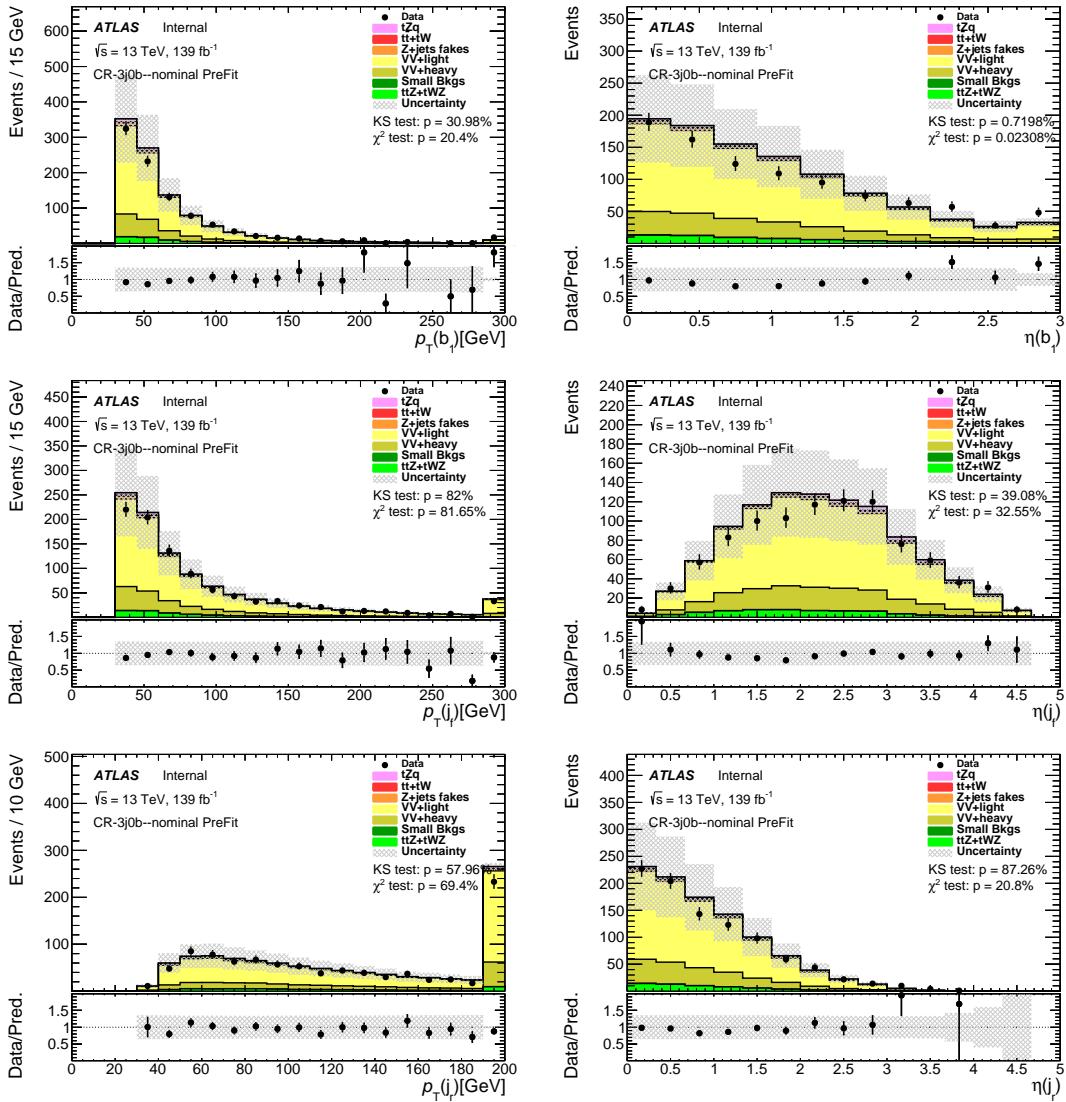


Figure 155: Comparison of data and MC predictions for reconstructed jet-related quantities for events in the diboson 3j0b CR. Both signal and backgrounds are normalised to the expected number of events before the fit. The uncertainty band includes statistical uncertainties for signal and backgrounds and background normalization uncertainties due to the prior assumptions and the modeling systematics, with the exception of  $t\bar{t}$  and  $Z + \text{jets}$ , where only the statistical uncertainties are shown.

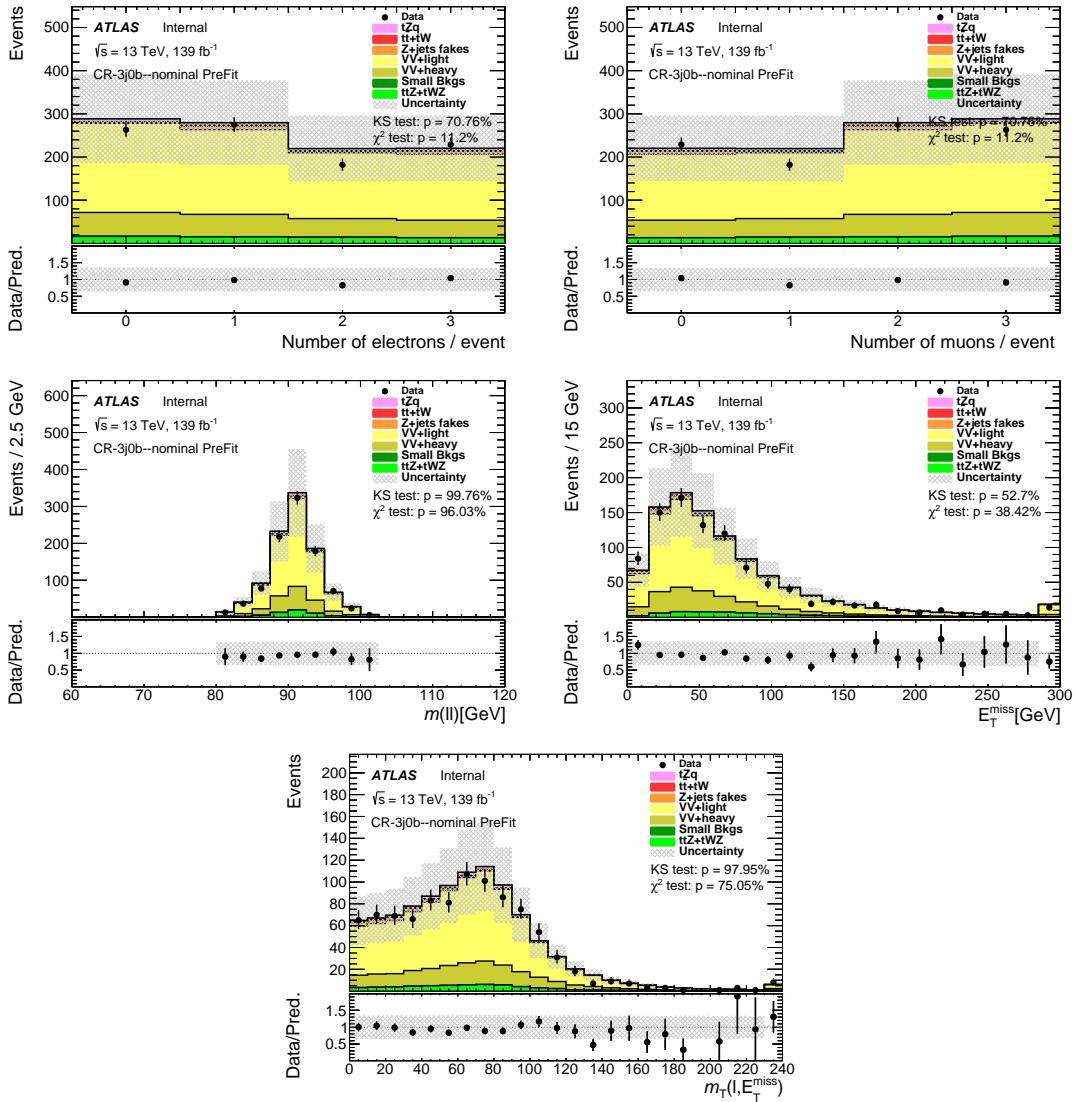


Figure 156: Comparison of data and MC predictions for reconstructed event-related quantities for events in the diboson 3j0b CR. Both signal and backgrounds are normalised to the expected number of events before the fit. The uncertainty band includes statistical uncertainties for signal and backgrounds and background normalization uncertainties due to the prior assumptions and the modeling systematics, with the exception of  $t\bar{t}$  and  $Z + \text{jets}$ , where only the statistical uncertainties are shown.

Not reviewed, for internal circulation only

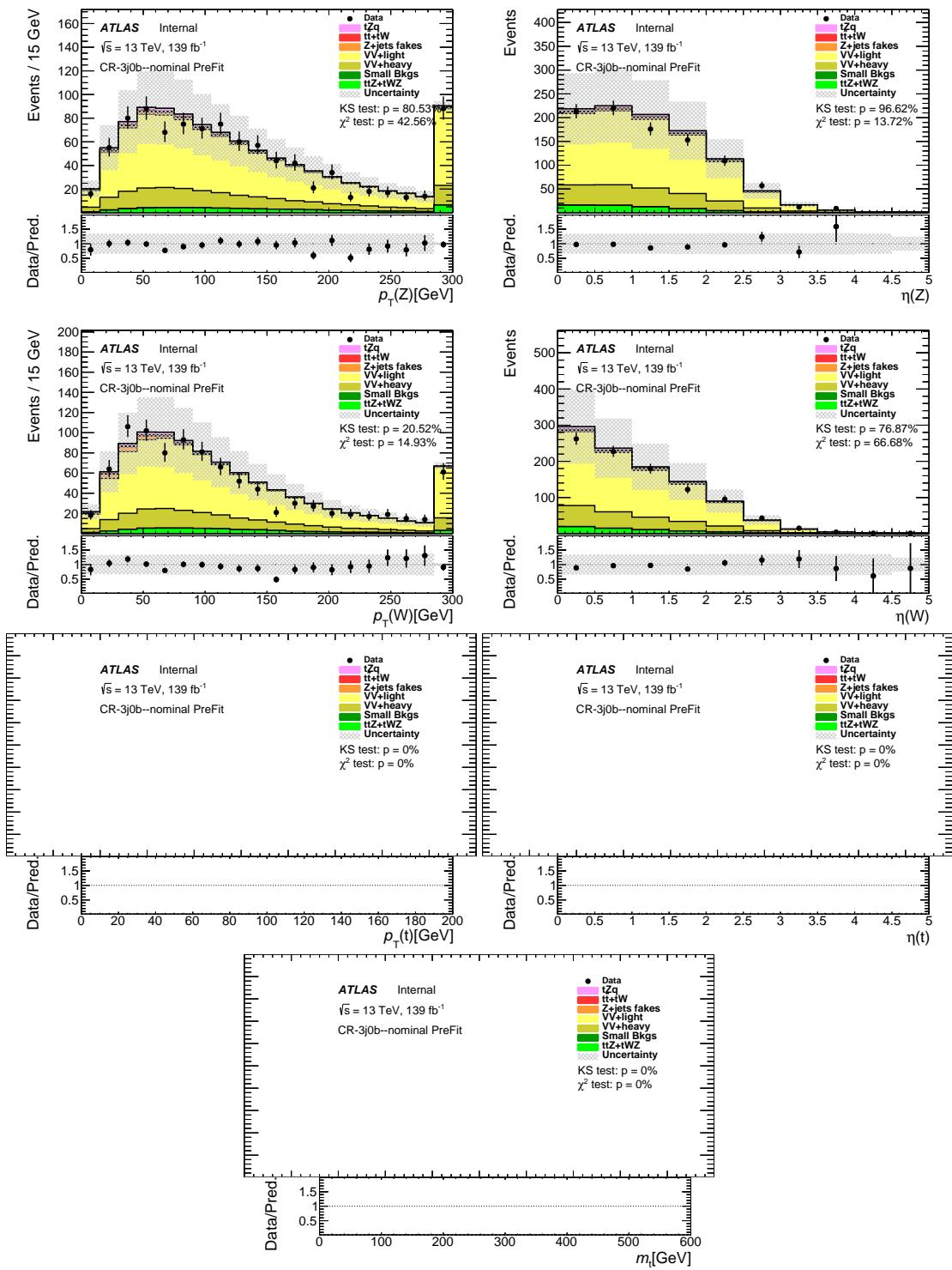


Figure 157: Comparison of data and MC predictions for reconstructed event-related quantities for events in the diboson 3j0b CR. Both signal and backgrounds are normalised to the expected number of events before the fit. The uncertainty band includes statistical uncertainties for signal and backgrounds and background normalization uncertainties due to the prior assumptions and the modeling systematics, with the exception of  $t\bar{t}$  and  $Z + jets$ , where only the statistical uncertainties are shown. The distribution(s) with a  $b$ -jet are not filled, as there are no  $b$ -tagged jets in this region.

1429 D.1.2  $t\bar{t}$  CRs

Not reviewed, for internal circulation only

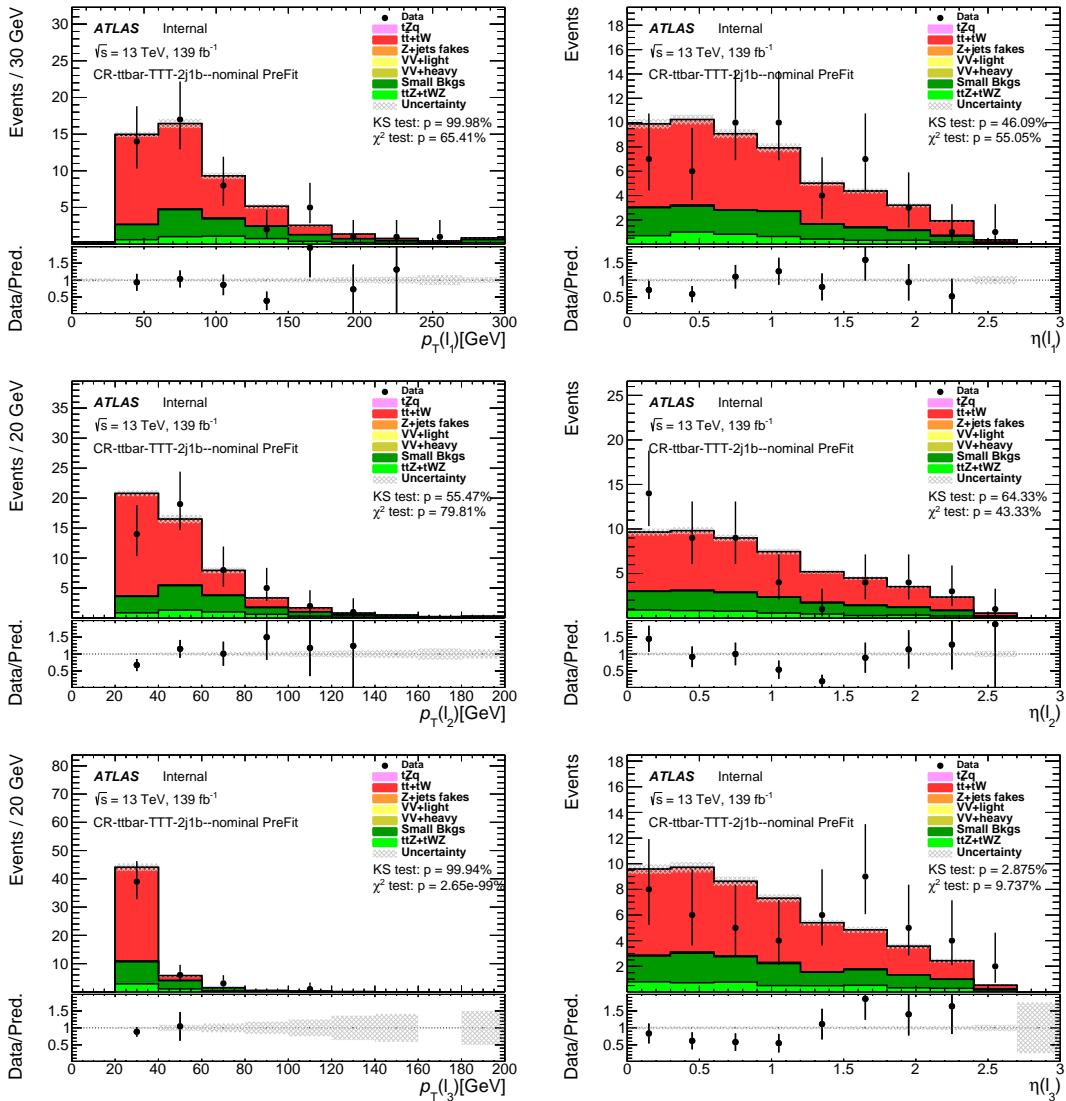


Figure 158: Comparison of data and MC predictions for reconstructed lepton-related quantities for events in the  $t\bar{t}$  2j1b CR. Both signal and backgrounds are normalised to the expected number of events before the fit. The uncertainty band includes statistical uncertainties for signal and backgrounds and background normalization uncertainties due to the prior assumptions and the modeling systematics, with the exception of  $t\bar{t}$  and  $Z + \text{jets}$ , where only the statistical uncertainties are shown.

Not reviewed, for internal circulation only

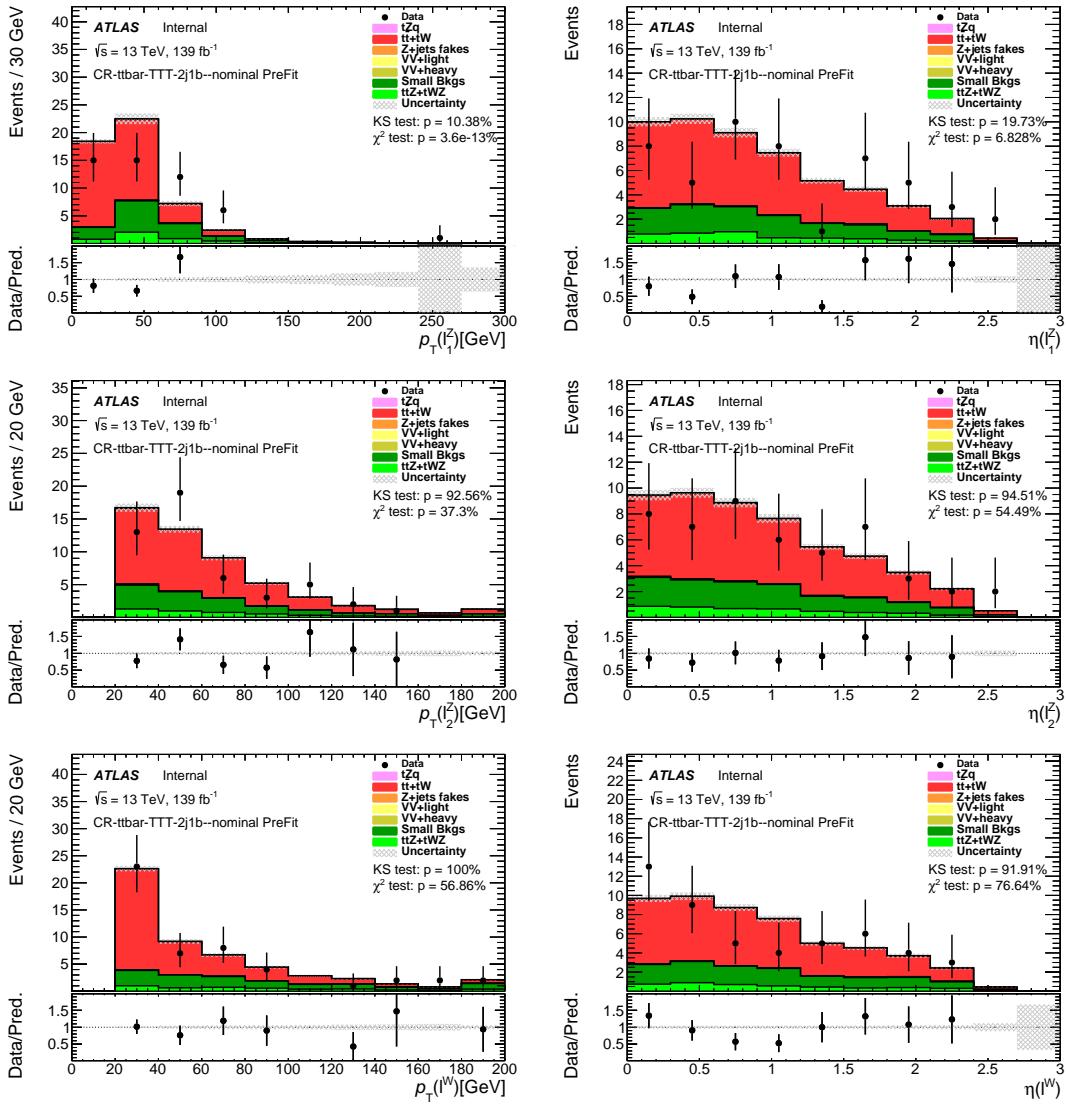


Figure 159: Comparison of data and MC predictions for reconstructed lepton-related quantities for events in the  $t\bar{t}$  2j1b CR. Both signal and backgrounds are normalised to the expected number of events before the fit. The uncertainty band includes statistical uncertainties for signal and backgrounds and background normalization uncertainties due to the prior assumptions and the modeling systematics, with the exception of  $t\bar{t}$  and  $Z + \text{jets}$ , where only the statistical uncertainties are shown.

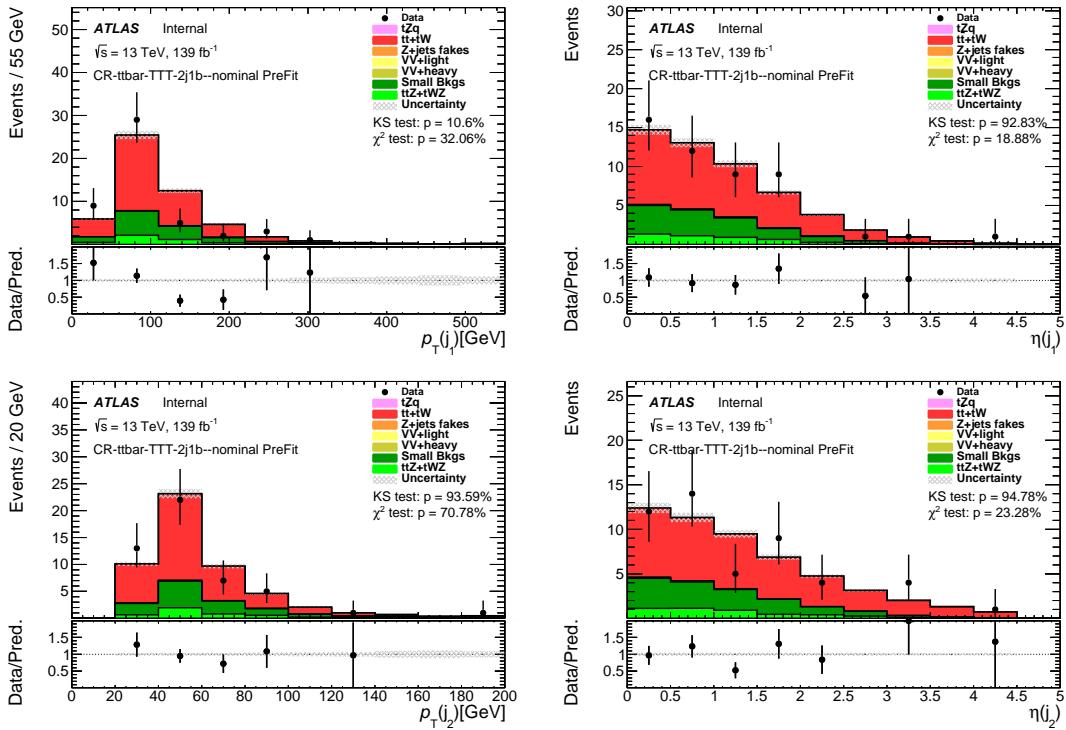


Figure 160: Comparison of data and MC predictions for reconstructed jet-related quantities for events in the  $t\bar{t}$  2j1b CR. Both signal and backgrounds are normalised to the expected number of events before the fit. The uncertainty band includes statistical uncertainties for signal and backgrounds and background normalization uncertainties due to the prior assumptions and the modeling systematics, with the exception of  $t\bar{t}$  and  $Z + \text{jets}$ , where only the statistical uncertainties are shown.

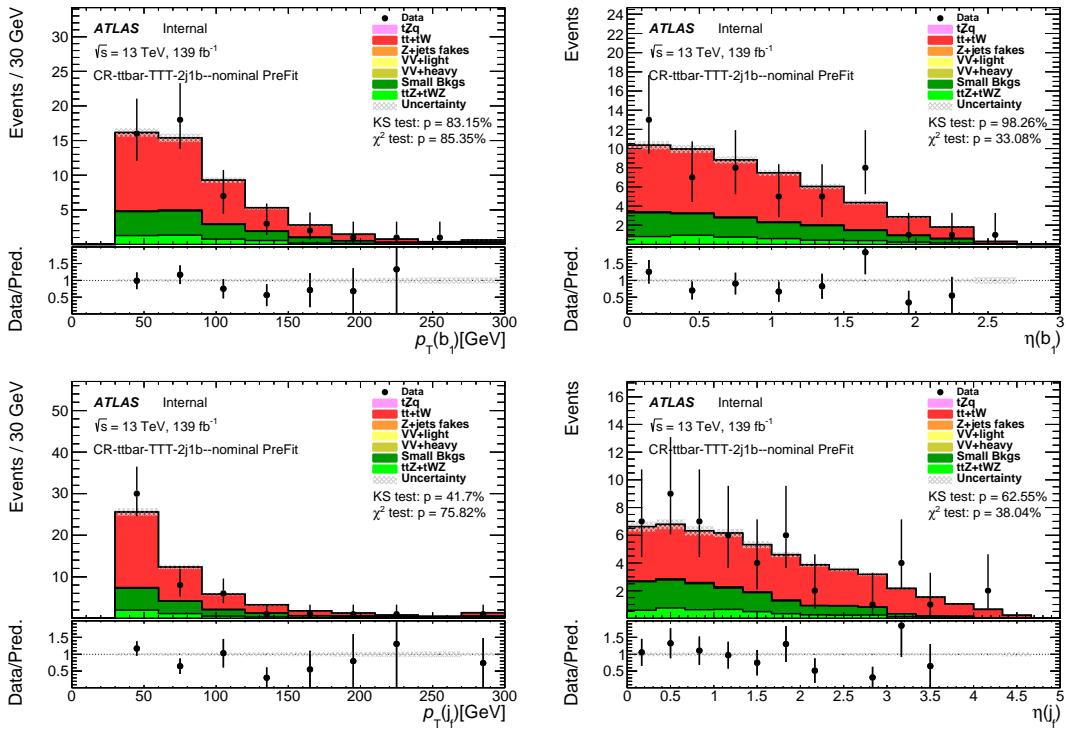


Figure 161: Comparison of data and MC predictions for reconstructed jet-related quantities for events in the  $t\bar{t}$  2j1b CR. Both signal and backgrounds are normalised to the expected number of events before the fit. The uncertainty band includes statistical uncertainties for signal and backgrounds and background normalization uncertainties due to the prior assumptions and the modeling systematics, with the exception of  $t\bar{t}$  and  $Z + \text{jets}$ , where only the statistical uncertainties are shown.

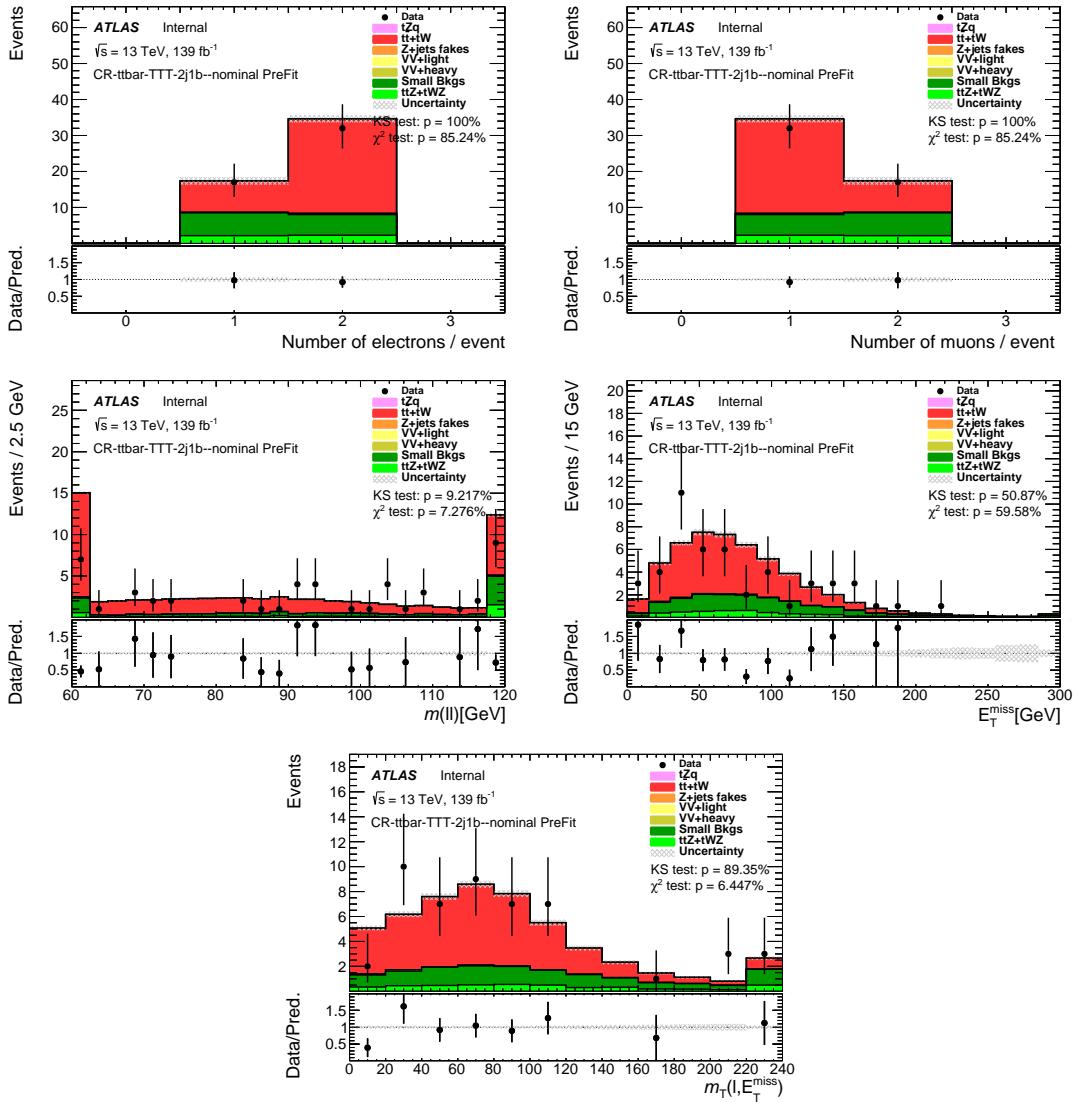


Figure 162: Comparison of data and MC predictions for reconstructed event-related quantities for events in the  $t\bar{t}$  2j1b CR. Both signal and backgrounds are normalised to the expected number of events before the fit. The uncertainty band includes statistical uncertainties for signal and backgrounds and background normalization uncertainties due to the prior assumptions and the modeling systematics, with the exception of  $t\bar{t}$  and  $Z + \text{jets}$ , where only the statistical uncertainties are shown.

Not reviewed, for internal circulation only

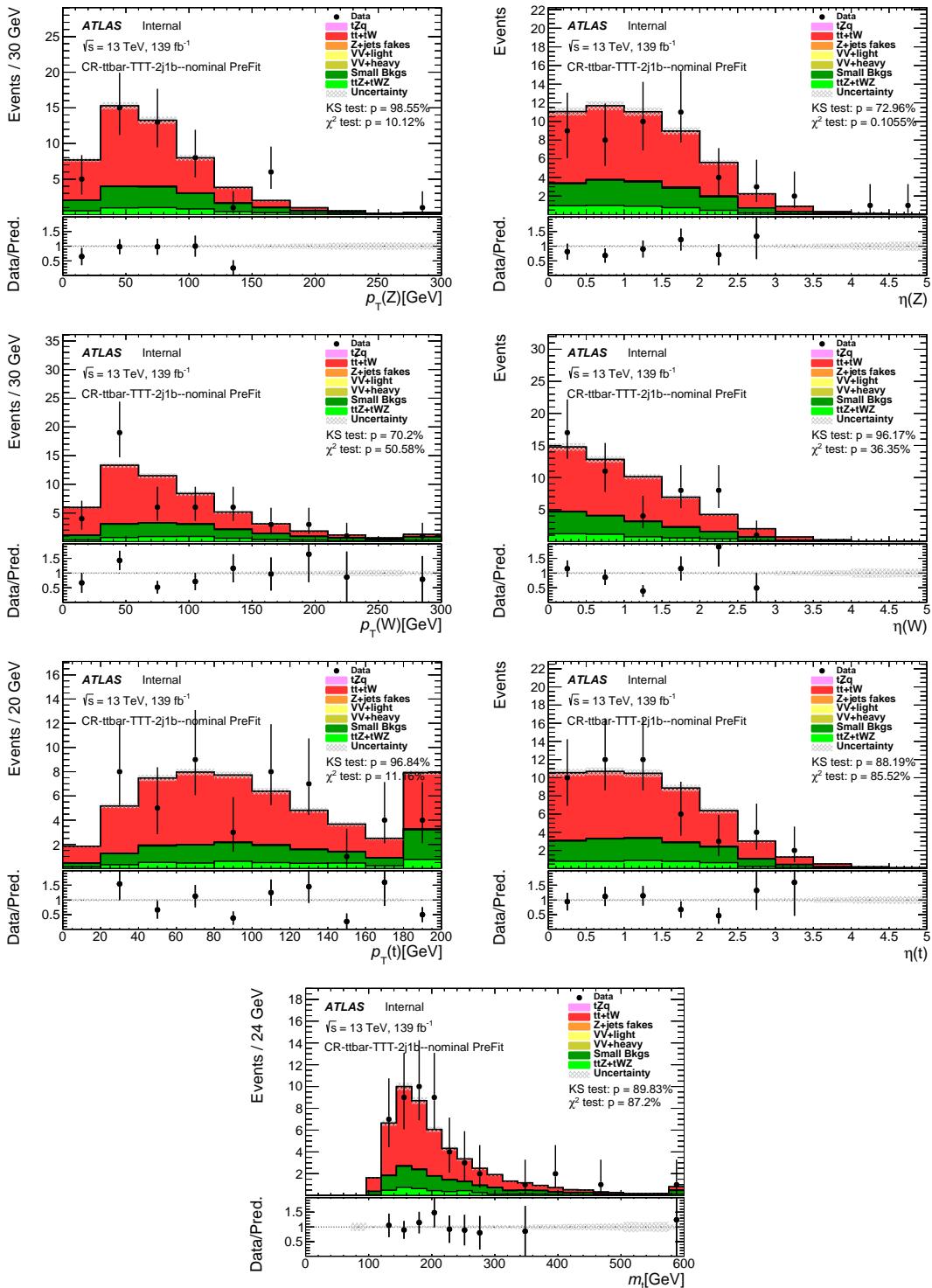


Figure 163: Comparison of data and MC predictions for reconstructed event-related quantities for events in the  $t\bar{t}$  2j1b CR. Both signal and backgrounds are normalised to the expected number of events before the fit. The uncertainty band includes statistical uncertainties for signal and backgrounds and background normalization uncertainties due to the prior assumptions and the modeling systematics, with the exception of  $t\bar{t}$  and  $Z + \text{jets}$ , where only the statistical uncertainties are shown.

Not reviewed, for internal circulation only

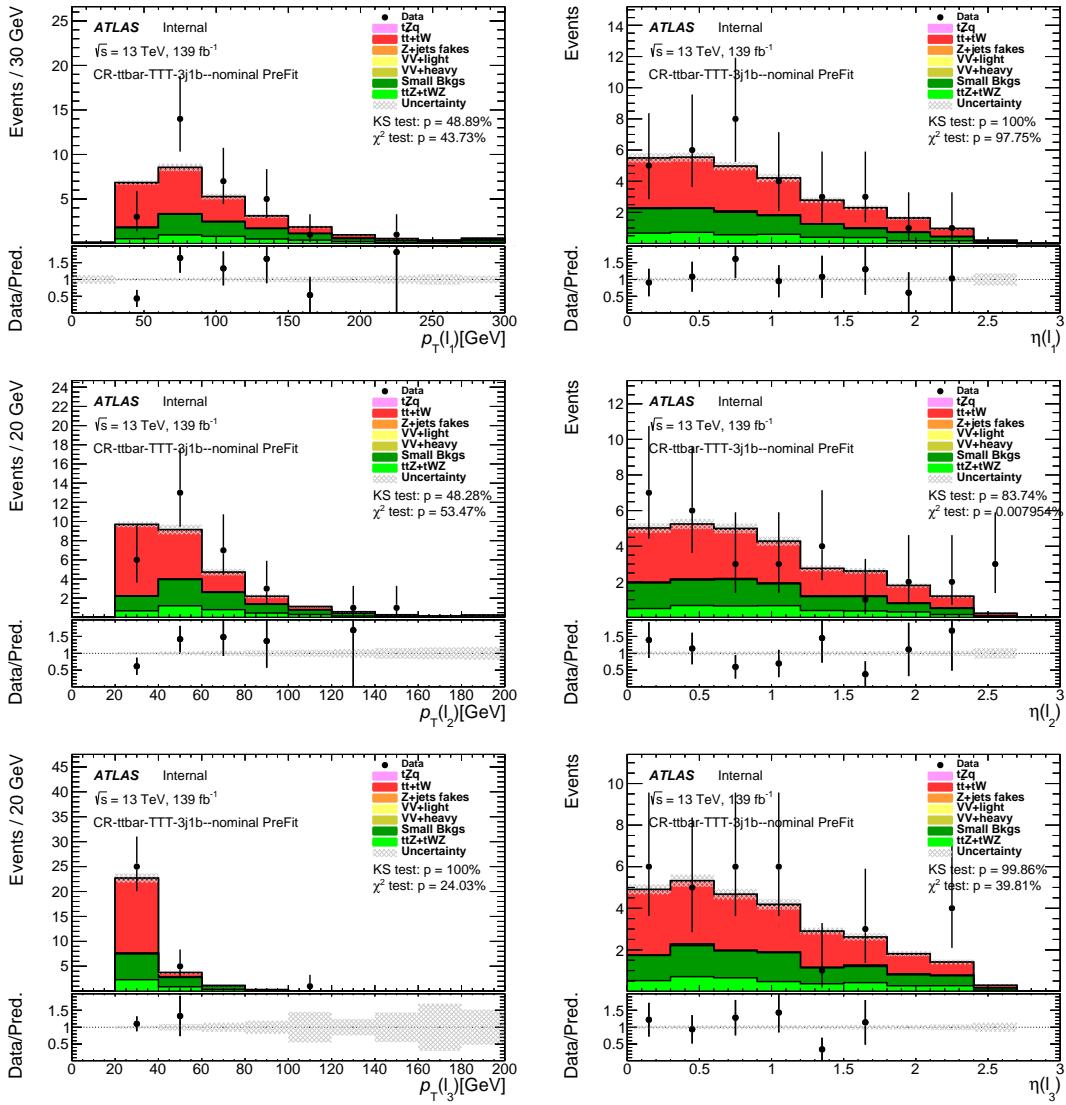


Figure 164: Comparison of data and MC predictions for reconstructed lepton-related quantities for events in the  $t\bar{t}$  3j1b CR. Both signal and backgrounds are normalised to the expected number of events before the fit. The uncertainty band includes statistical uncertainties for signal and backgrounds and background normalization uncertainties due to the prior assumptions and the modeling systematics, with the exception of  $t\bar{t}$  and  $Z + \text{jets}$ , where only the statistical uncertainties are shown.

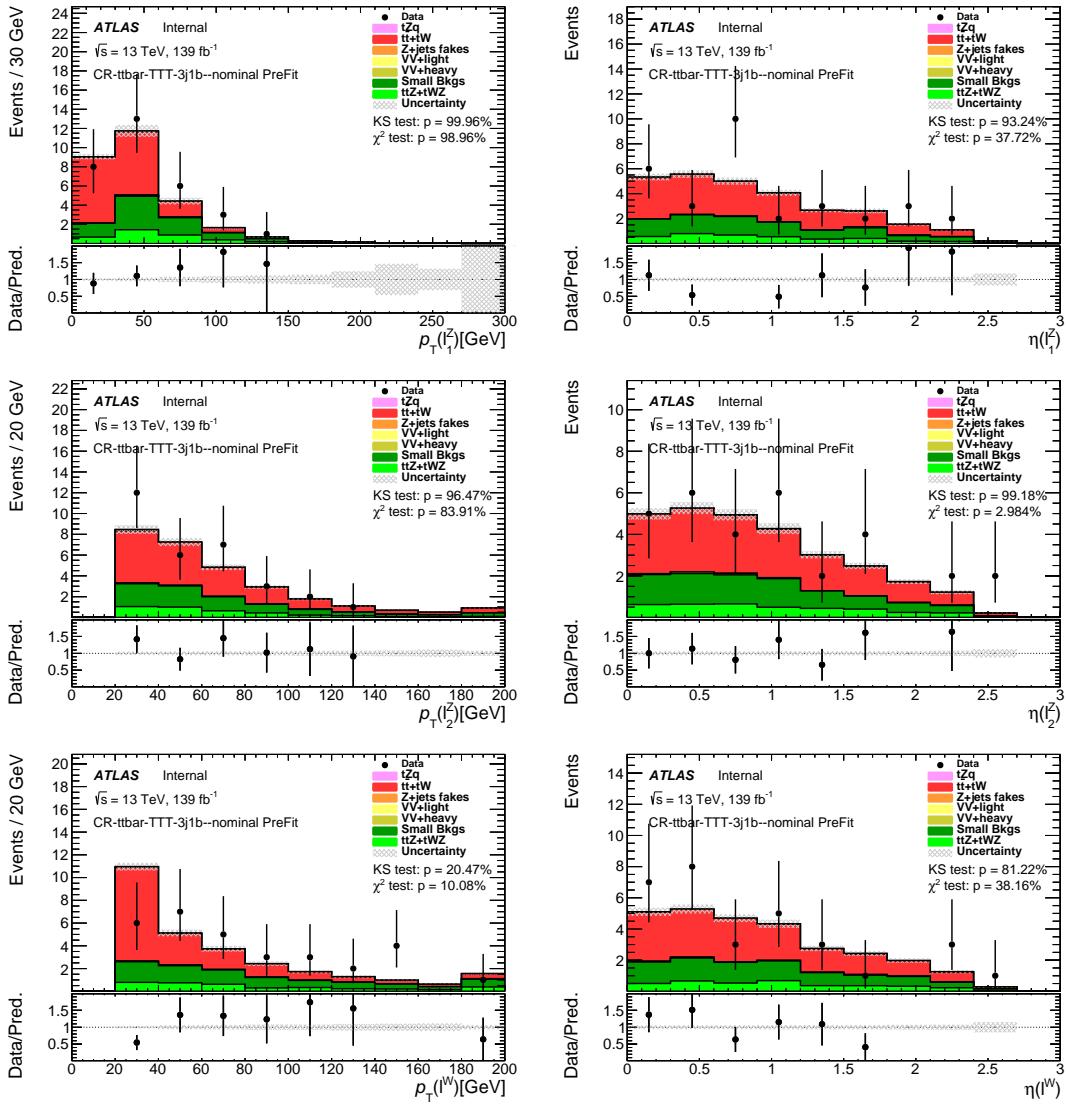


Figure 165: Comparison of data and MC predictions for reconstructed lepton-related quantities for events in the  $t\bar{t}$  3j1b CR. Both signal and backgrounds are normalised to the expected number of events before the fit. The uncertainty band includes statistical uncertainties for signal and backgrounds and background normalization uncertainties due to the prior assumptions and the modeling systematics, with the exception of  $t\bar{t}$  and  $Z + \text{jets}$ , where only the statistical uncertainties are shown.

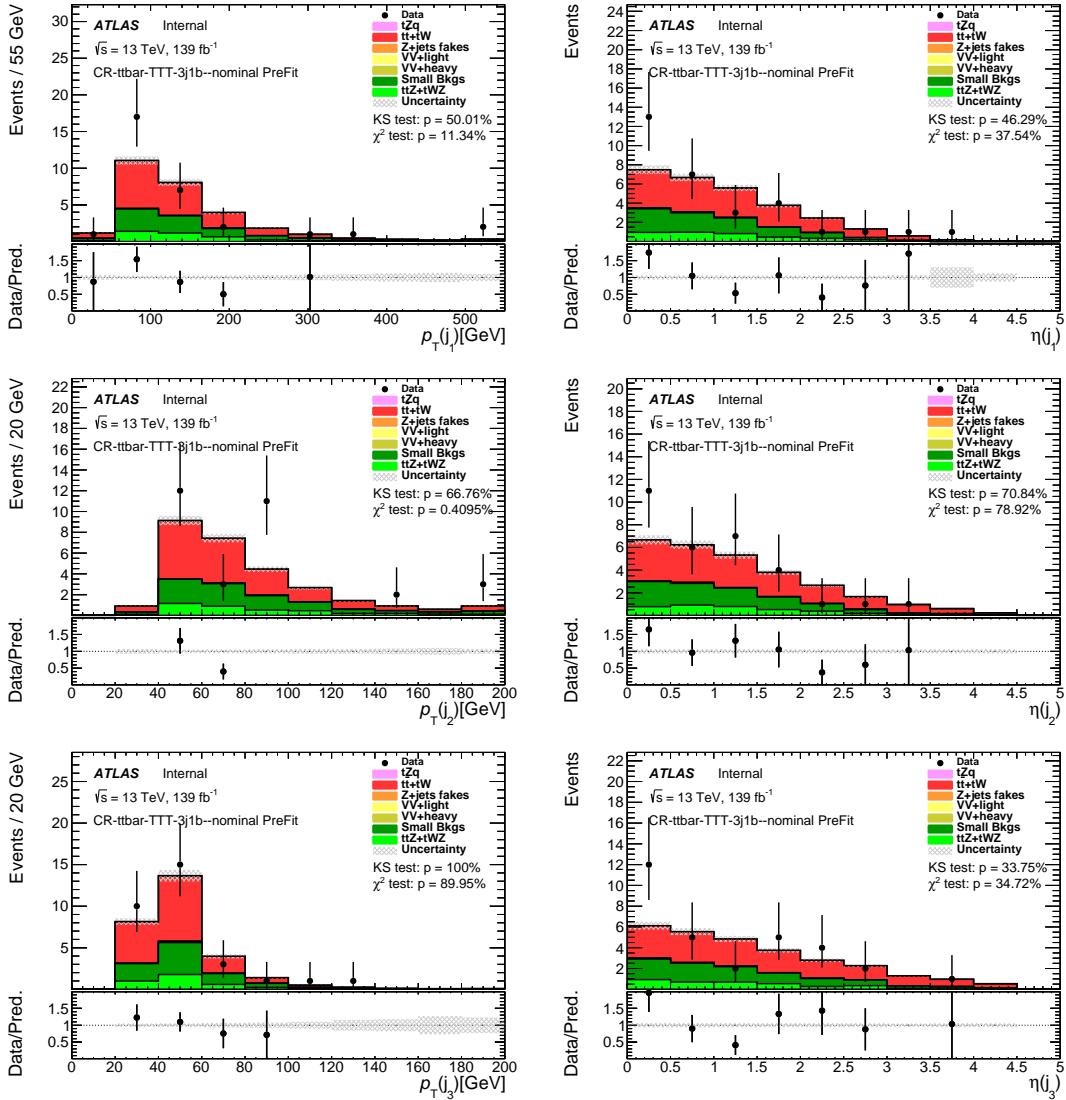


Figure 166: Comparison of data and MC predictions for reconstructed jet-related quantities for events in the  $t\bar{t}$  3j1b CR. Both signal and backgrounds are normalised to the expected number of events before the fit. The uncertainty band includes statistical uncertainties for signal and backgrounds and background normalization uncertainties due to the prior assumptions and the modeling systematics, with the exception of  $t\bar{t}$  and  $Z + \text{jets}$ , where only the statistical uncertainties are shown.

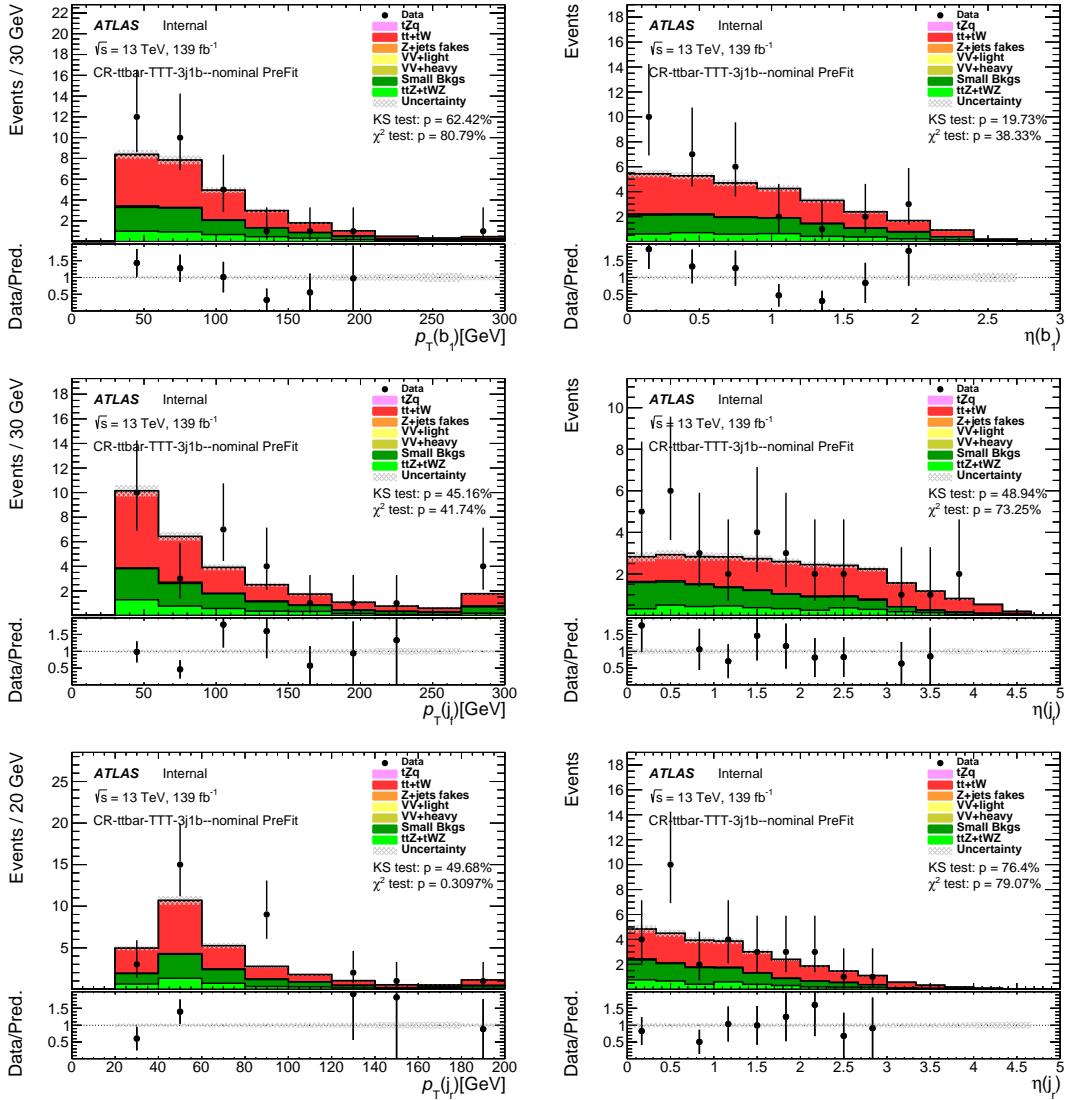


Figure 167: Comparison of data and MC predictions for reconstructed jet-related quantities for events in the  $t\bar{t}$  3j1b CR. Both signal and backgrounds are normalised to the expected number of events before the fit. The uncertainty band includes statistical uncertainties for signal and backgrounds and background normalization uncertainties due to the prior assumptions and the modeling systematics, with the exception of  $t\bar{t}$  and  $Z + \text{jets}$ , where only the statistical uncertainties are shown.

Not reviewed, for internal circulation only

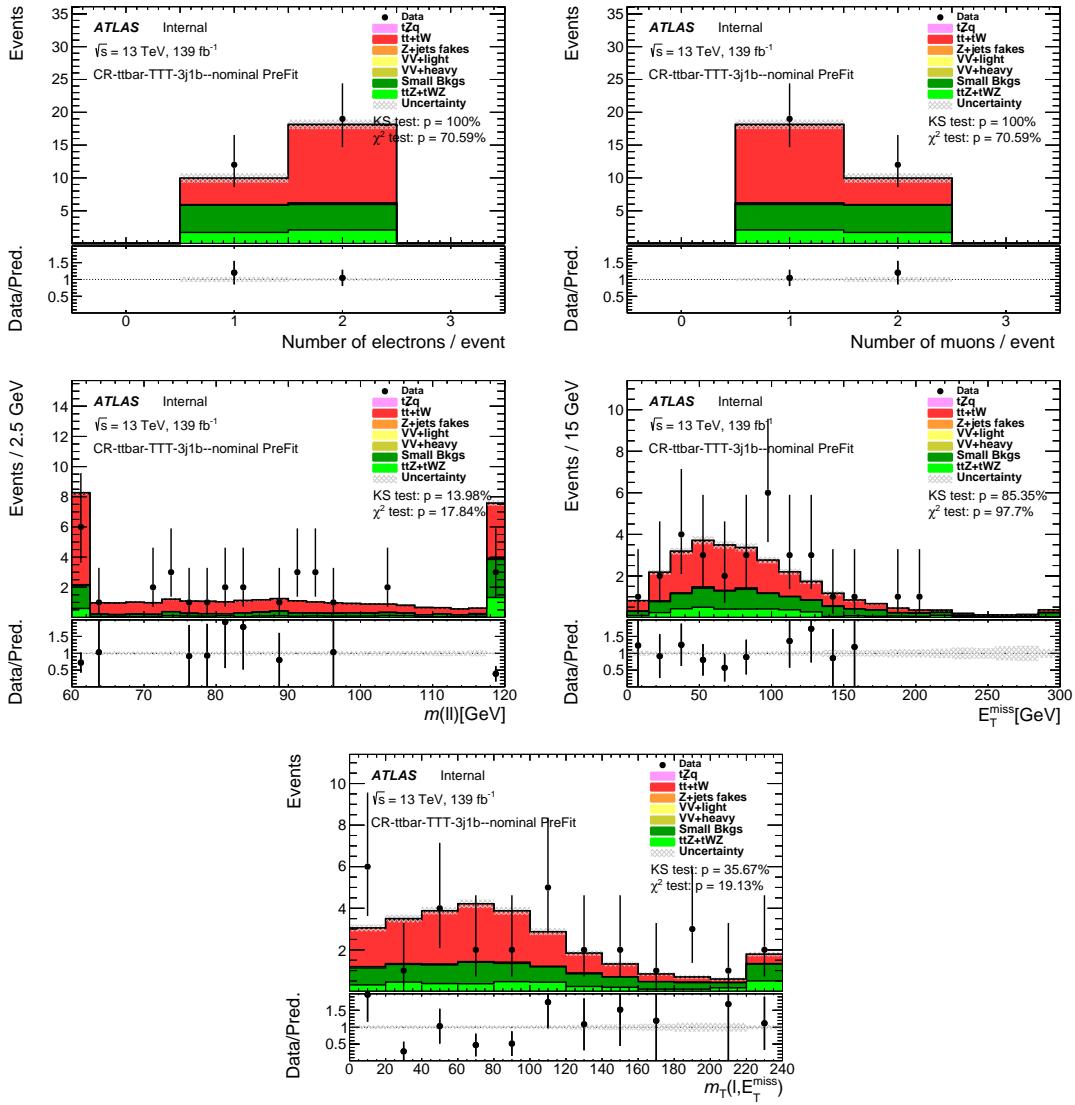


Figure 168: Comparison of data and MC predictions for reconstructed event-related quantities for events in the  $t\bar{t}$  3j1b CR. Both signal and backgrounds are normalised to the expected number of events before the fit. The uncertainty band includes statistical uncertainties for signal and backgrounds and background normalization uncertainties due to the prior assumptions and the modeling systematics, with the exception of  $t\bar{t}$  and  $Z + \text{jets}$ , where only the statistical uncertainties are shown.

Not reviewed, for internal circulation only

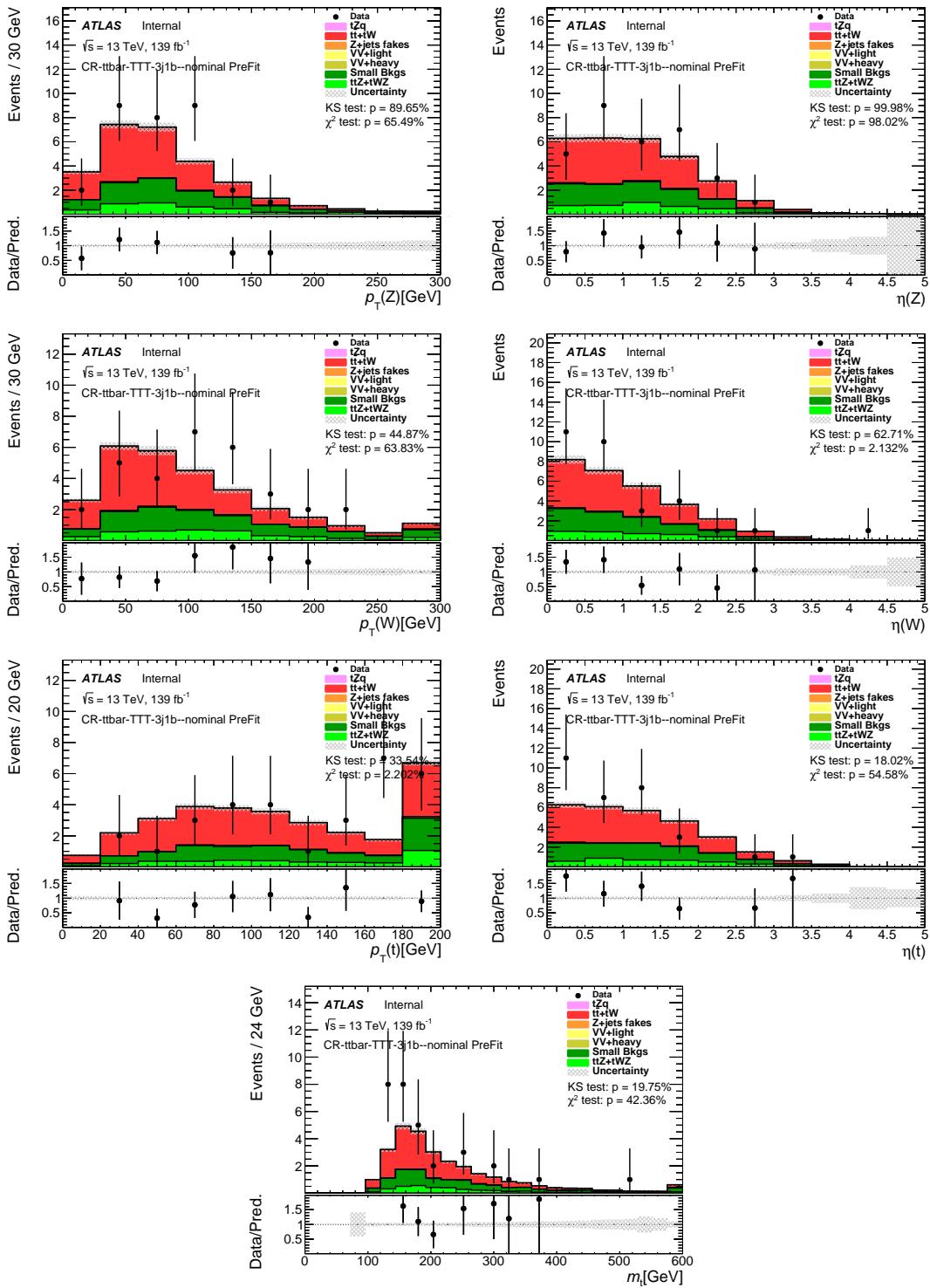


Figure 169: Comparison of data and MC predictions for reconstructed event-related quantities for events in the  $t\bar{t}$  3j1b CR. Both signal and backgrounds are normalised to the expected number of events before the fit. The uncertainty band includes statistical uncertainties for signal and backgrounds and background normalization uncertainties due to the prior assumptions and the modeling systematics, with the exception of  $t\bar{t}$  and  $Z + \text{jets}$ , where only the statistical uncertainties are shown.

1430 D.1.3  $t\bar{t}Z$  CRs

Not reviewed, for internal circulation only

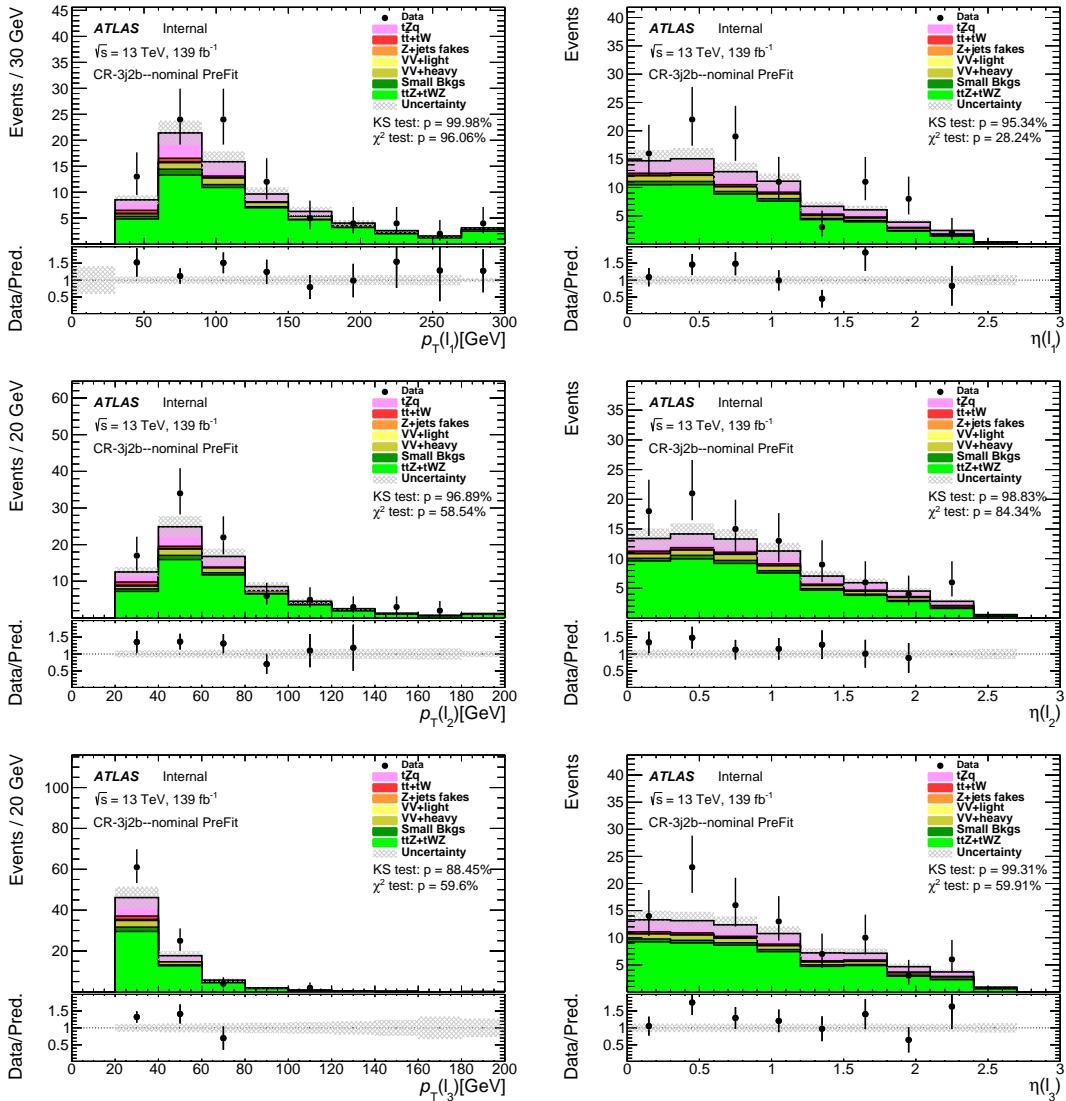


Figure 170: Comparison of data and MC predictions for reconstructed lepton-related quantities for events in the  $t\bar{t}Z$  3j2b CR. Both signal and backgrounds are normalised to the expected number of events before the fit. The uncertainty band includes statistical uncertainties for signal and backgrounds and background normalization uncertainties due to the prior assumptions and the modeling systematics, with the exception of  $t\bar{t}$  and  $Z + \text{jets}$ , where only the statistical uncertainties are shown.

Not reviewed, for internal circulation only

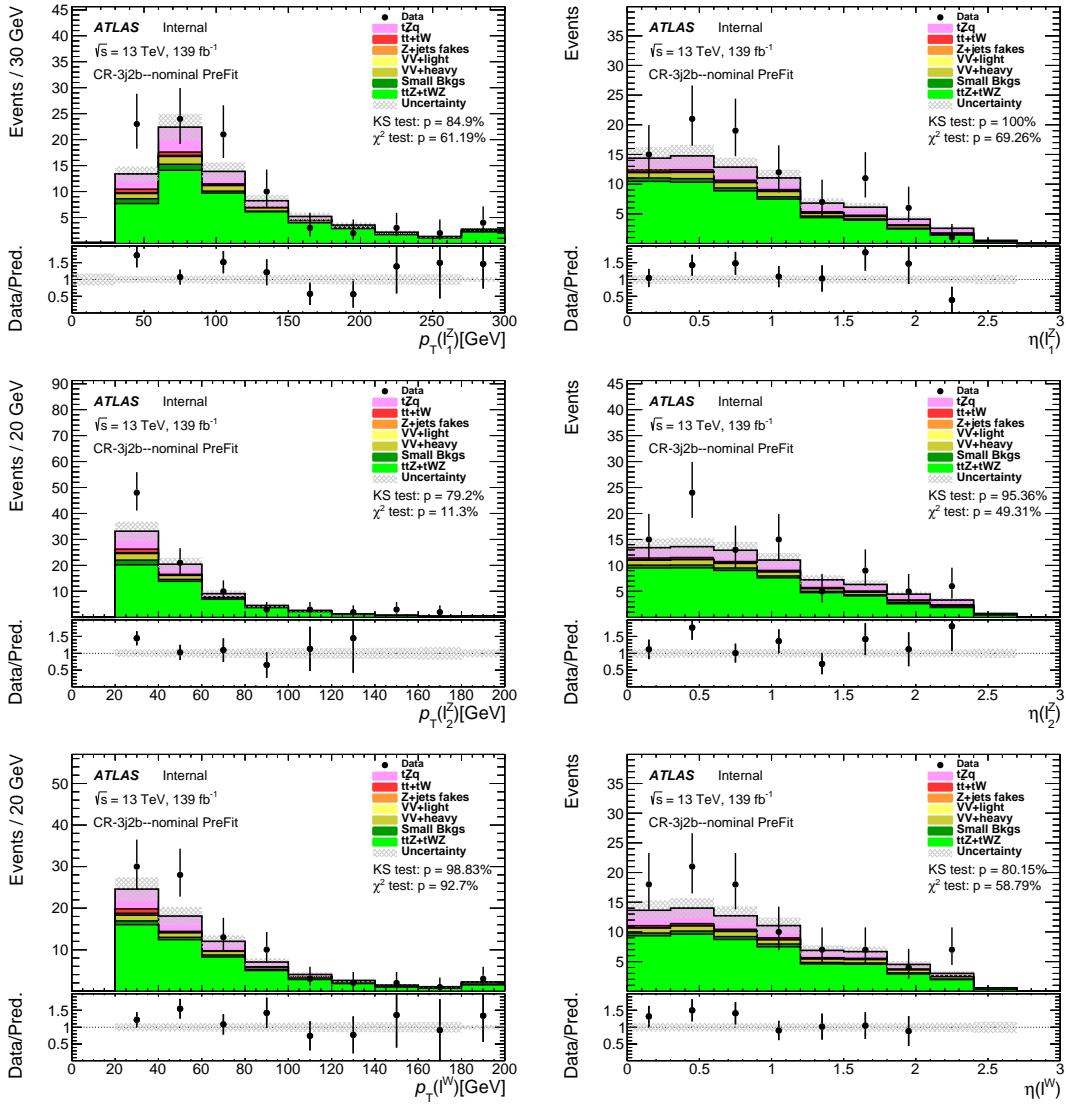


Figure 171: Comparison of data and MC predictions for reconstructed lepton-related quantities for events in the  $t\bar{t}Z$  3j2b CR. Both signal and backgrounds are normalised to the expected number of events before the fit. The uncertainty band includes statistical uncertainties for signal and backgrounds and background normalization uncertainties due to the prior assumptions and the modeling systematics, with the exception of  $t\bar{t}$  and  $Z + \text{jets}$ , where only the statistical uncertainties are shown.

Not reviewed, for internal circulation only

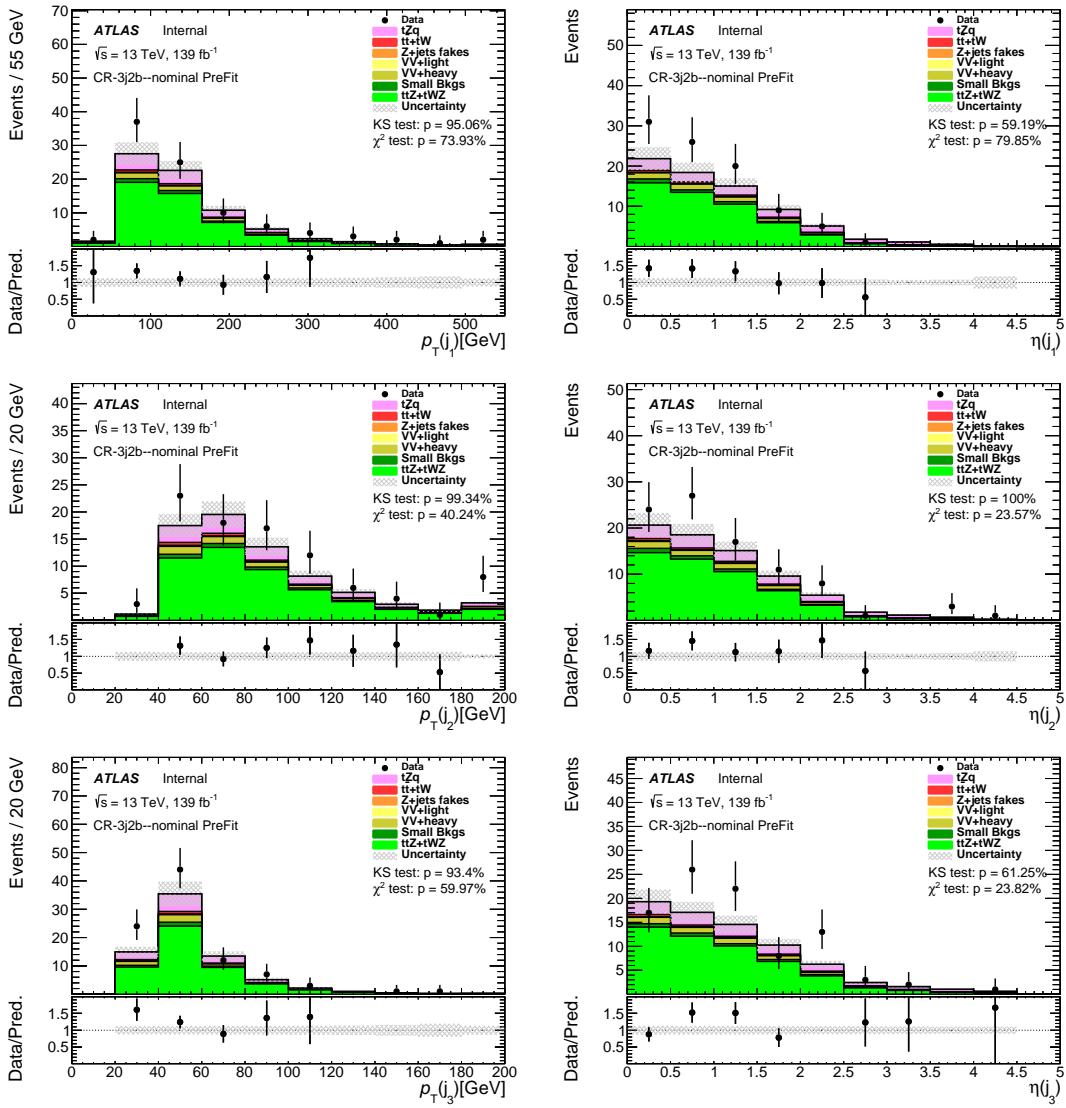


Figure 172: Comparison of data and MC predictions for reconstructed jet-related quantities for events in the  $t\bar{t}Z$  3j2b CR. Both signal and backgrounds are normalised to the expected number of events before the fit. The uncertainty band includes statistical uncertainties for signal and backgrounds and background normalization uncertainties due to the prior assumptions and the modeling systematics, with the exception of  $t\bar{t}$  and  $Z + \text{jets}$ , where only the statistical uncertainties are shown.

Not reviewed, for internal circulation only

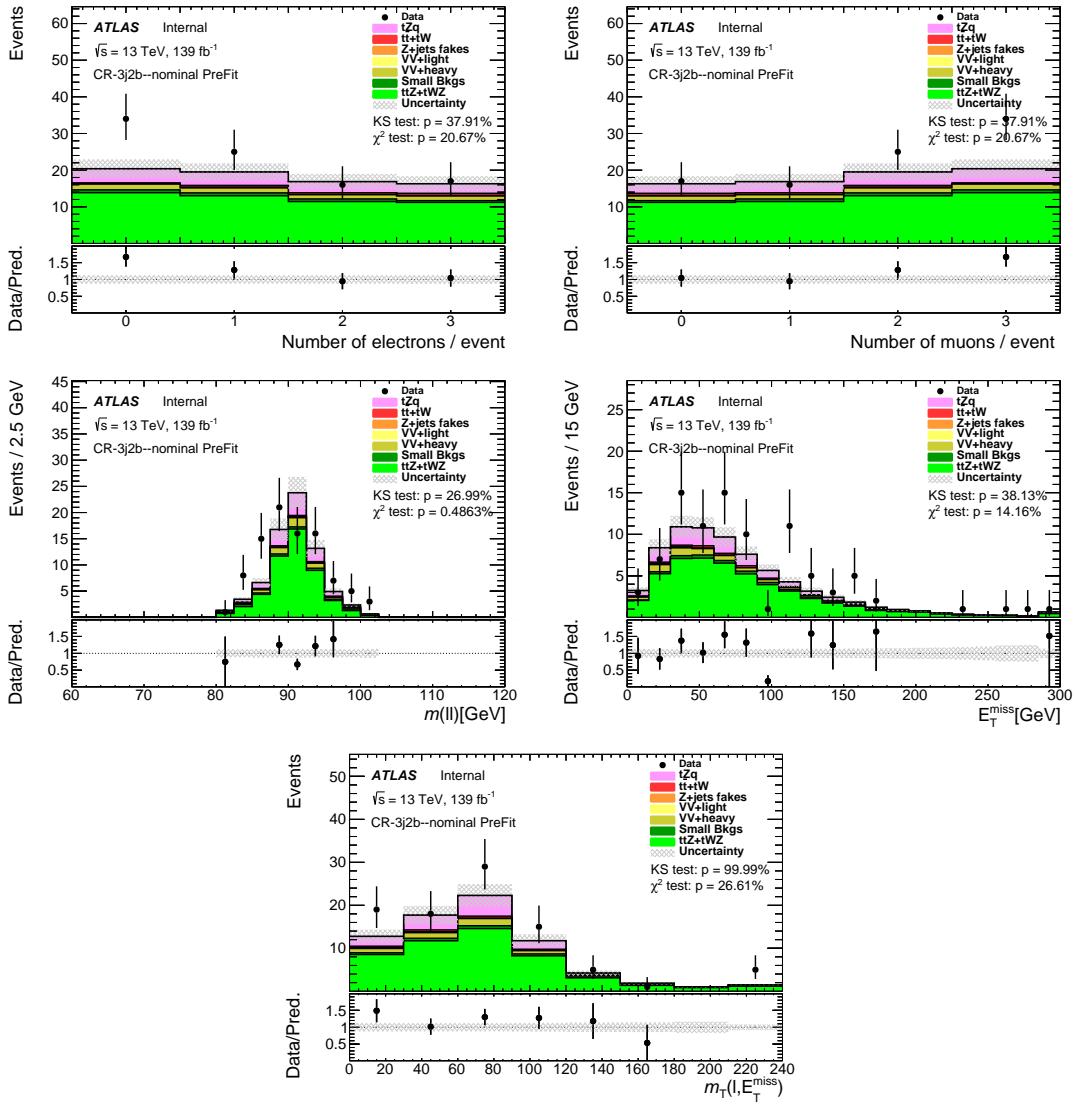


Figure 173: Comparison of data and MC predictions for reconstructed event-related quantities for events in the  $t\bar{t}Z$  3j2b CR. Both signal and backgrounds are normalised to the expected number of events before the fit. The uncertainty band includes statistical uncertainties for signal and backgrounds and background normalization uncertainties due to the prior assumptions and the modeling systematics, with the exception of  $t\bar{t}$  and  $Z + \text{jets}$ , where only the statistical uncertainties are shown.

Not reviewed, for internal circulation only

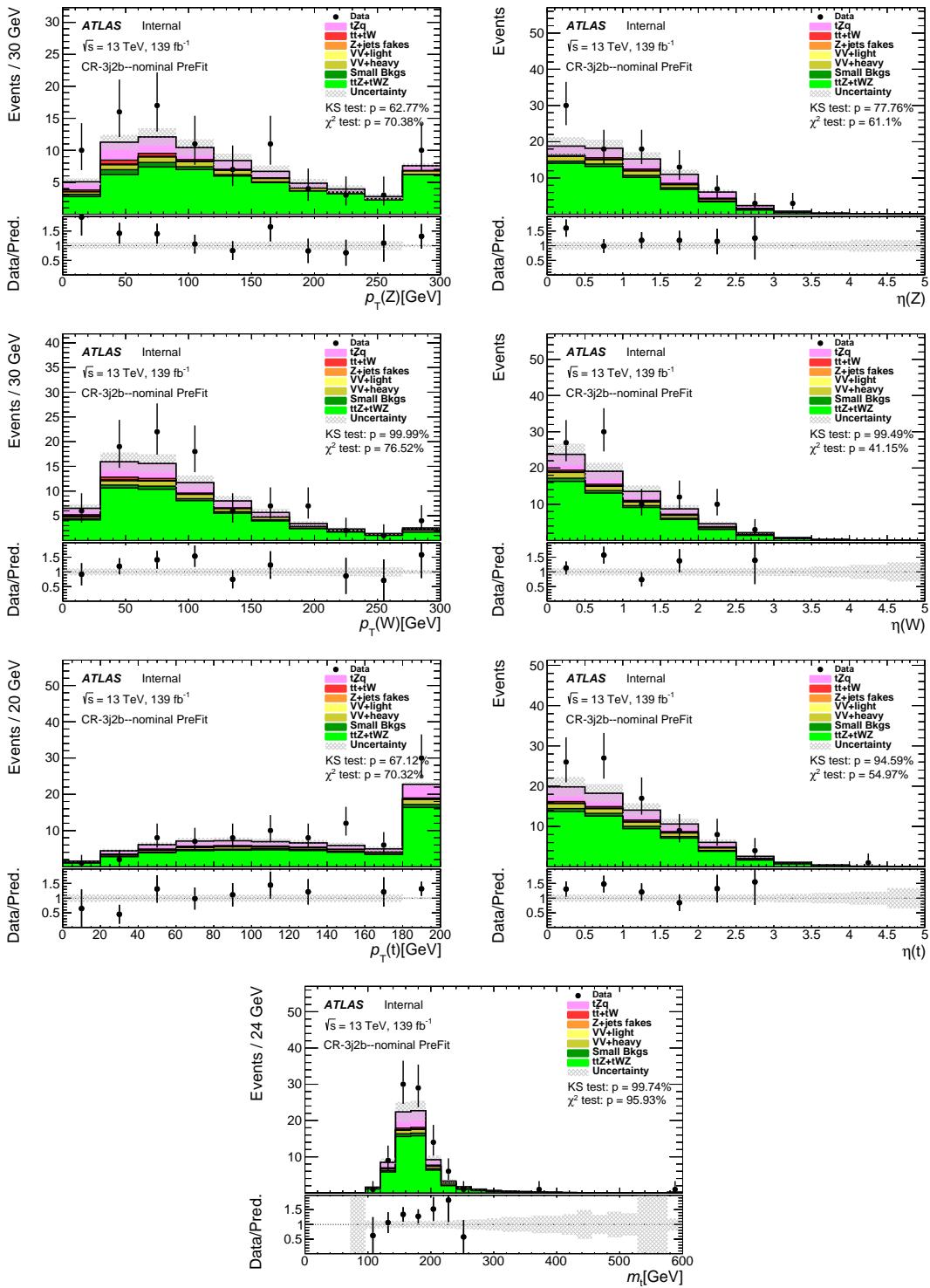


Figure 174: Comparison of data and MC predictions for reconstructed event-related quantities for events in the  $t\bar{t}Z$  3j2b CR. Both signal and backgrounds are normalised to the expected number of events before the fit. The uncertainty band includes statistical uncertainties for signal and backgrounds and background normalization uncertainties due to the prior assumptions and the modeling systematics, with the exception of  $t\bar{t}$  and  $Z + \text{jets}$ , where only the statistical uncertainties are shown.

Not reviewed, for internal circulation only

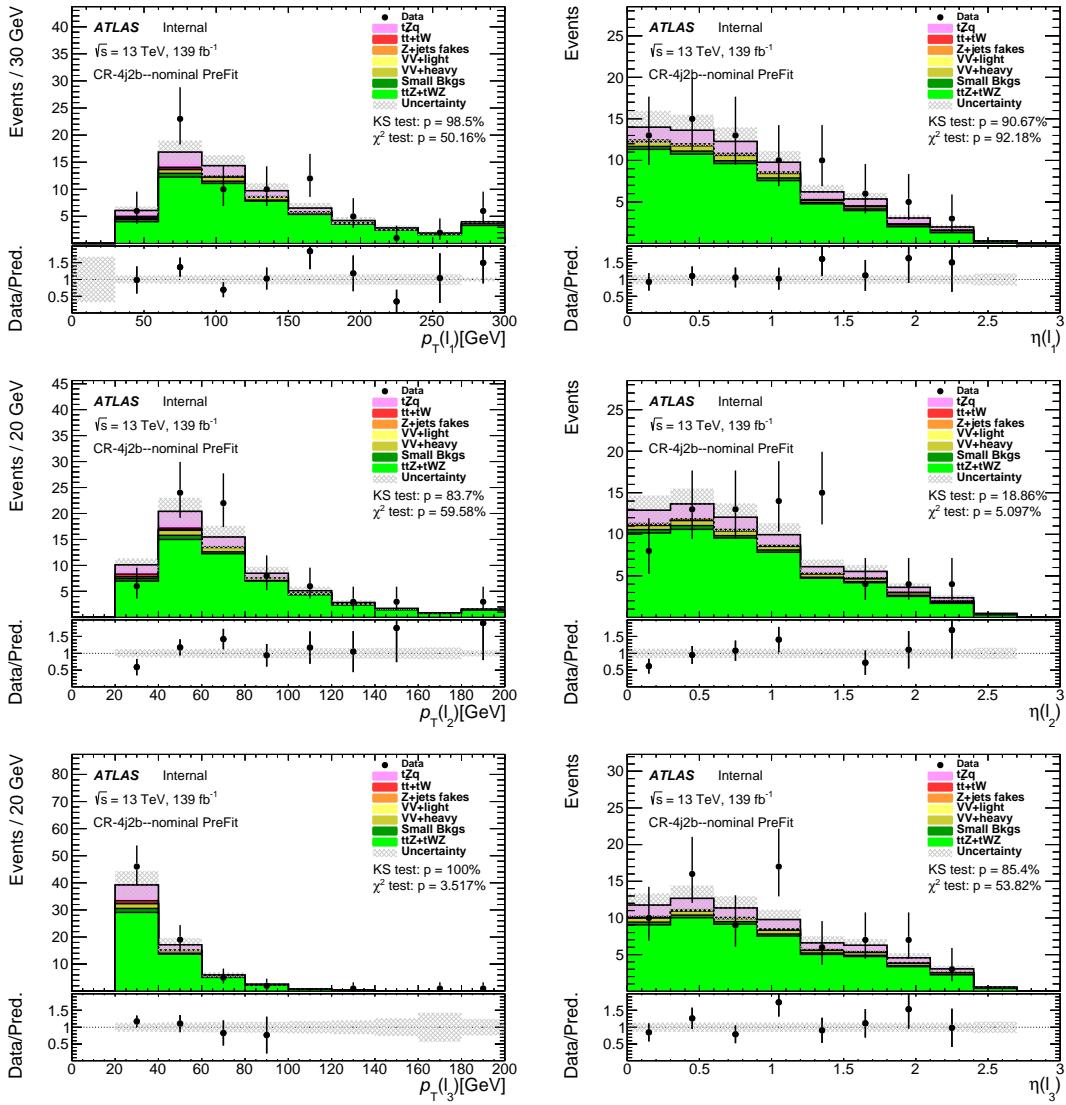


Figure 175: Comparison of data and MC predictions for reconstructed lepton-related quantities for events in the  $t\bar{t}Z$  4j2b CR. Both signal and backgrounds are normalised to the expected number of events before the fit. The uncertainty band includes statistical uncertainties for signal and backgrounds and background normalization uncertainties due to the prior assumptions and the modeling systematics, with the exception of  $t\bar{t}$  and  $Z + \text{jets}$ , where only the statistical uncertainties are shown.

Not reviewed, for internal circulation only

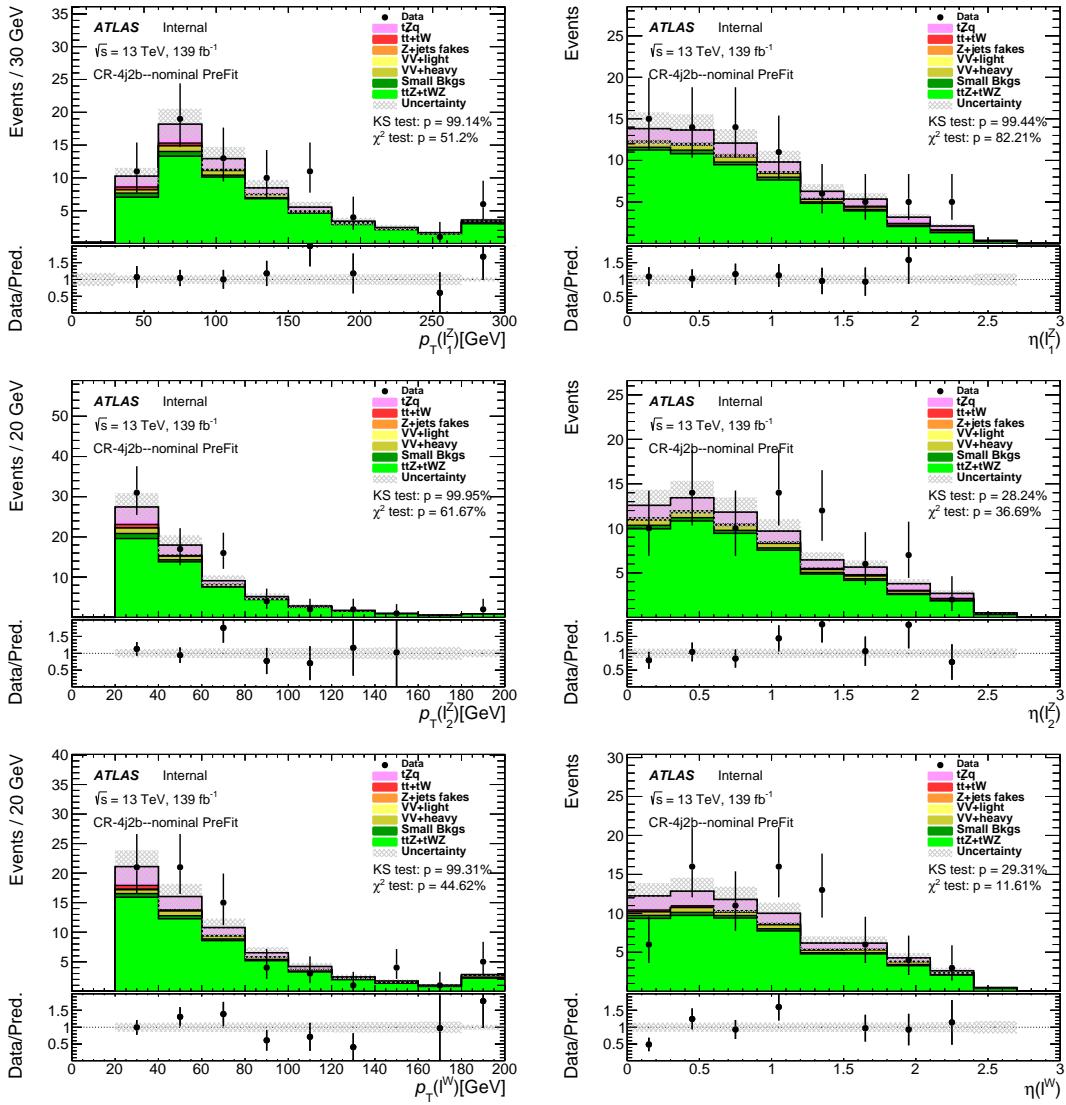


Figure 176: Comparison of data and MC predictions for reconstructed lepton-related quantities for events in the  $t\bar{t}Z$  4j2b CR. Both signal and backgrounds are normalised to the expected number of events before the fit. The uncertainty band includes statistical uncertainties for signal and backgrounds and background normalization uncertainties due to the prior assumptions and the modeling systematics, with the exception of  $t\bar{t}$  and  $Z + \text{jets}$ , where only the statistical uncertainties are shown.

Not reviewed, for internal circulation only

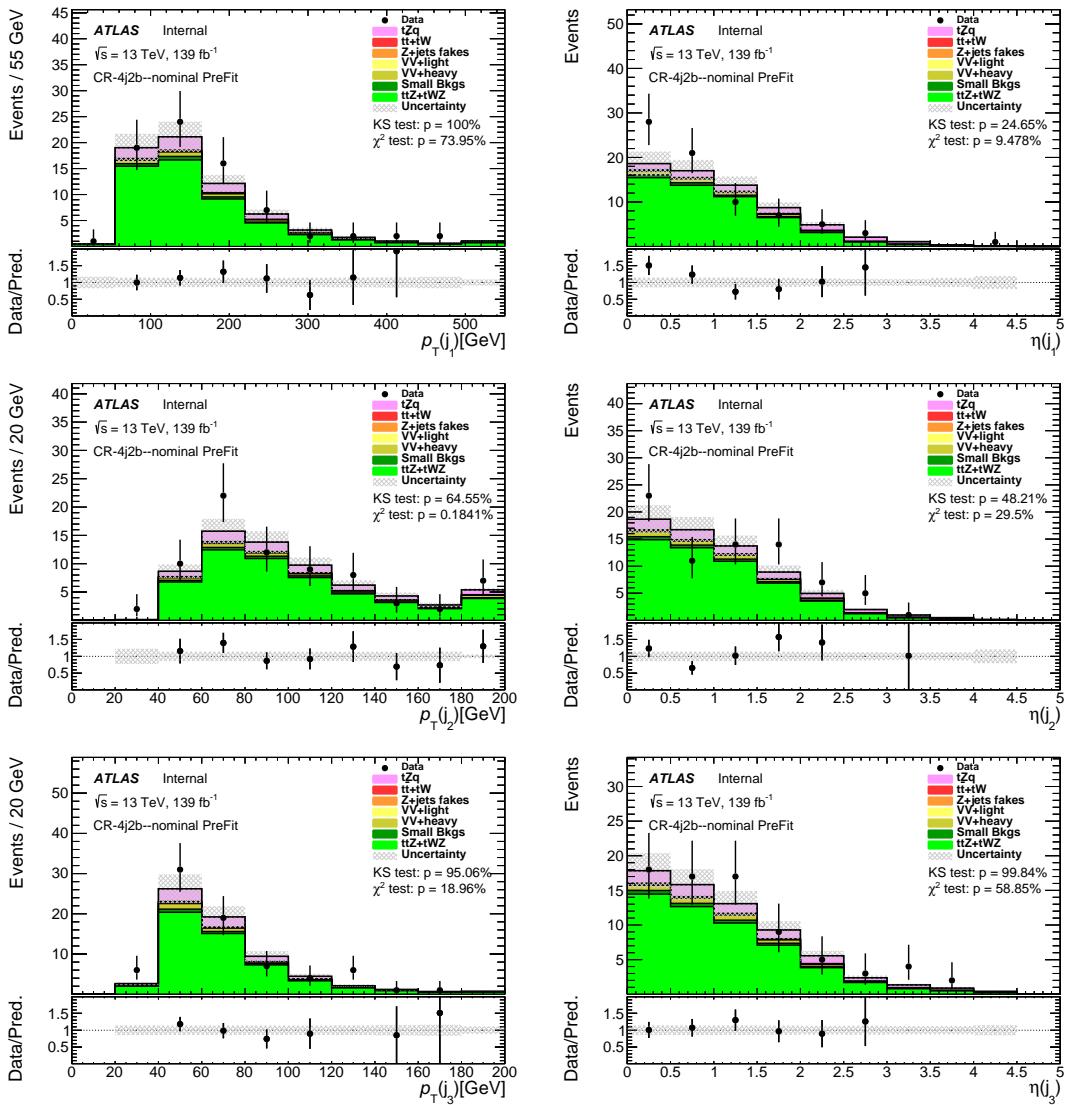


Figure 177: Comparison of data and MC predictions for reconstructed jet-related quantities for events in the  $t\bar{t}Z$  4j2b CR. Both signal and backgrounds are normalised to the expected number of events before the fit. The uncertainty band includes statistical uncertainties for signal and backgrounds and background normalization uncertainties due to the prior assumptions and the modeling systematics, with the exception of  $t\bar{t}$  and  $Z+jets$ , where only the statistical uncertainties are shown.

Not reviewed, for internal circulation only

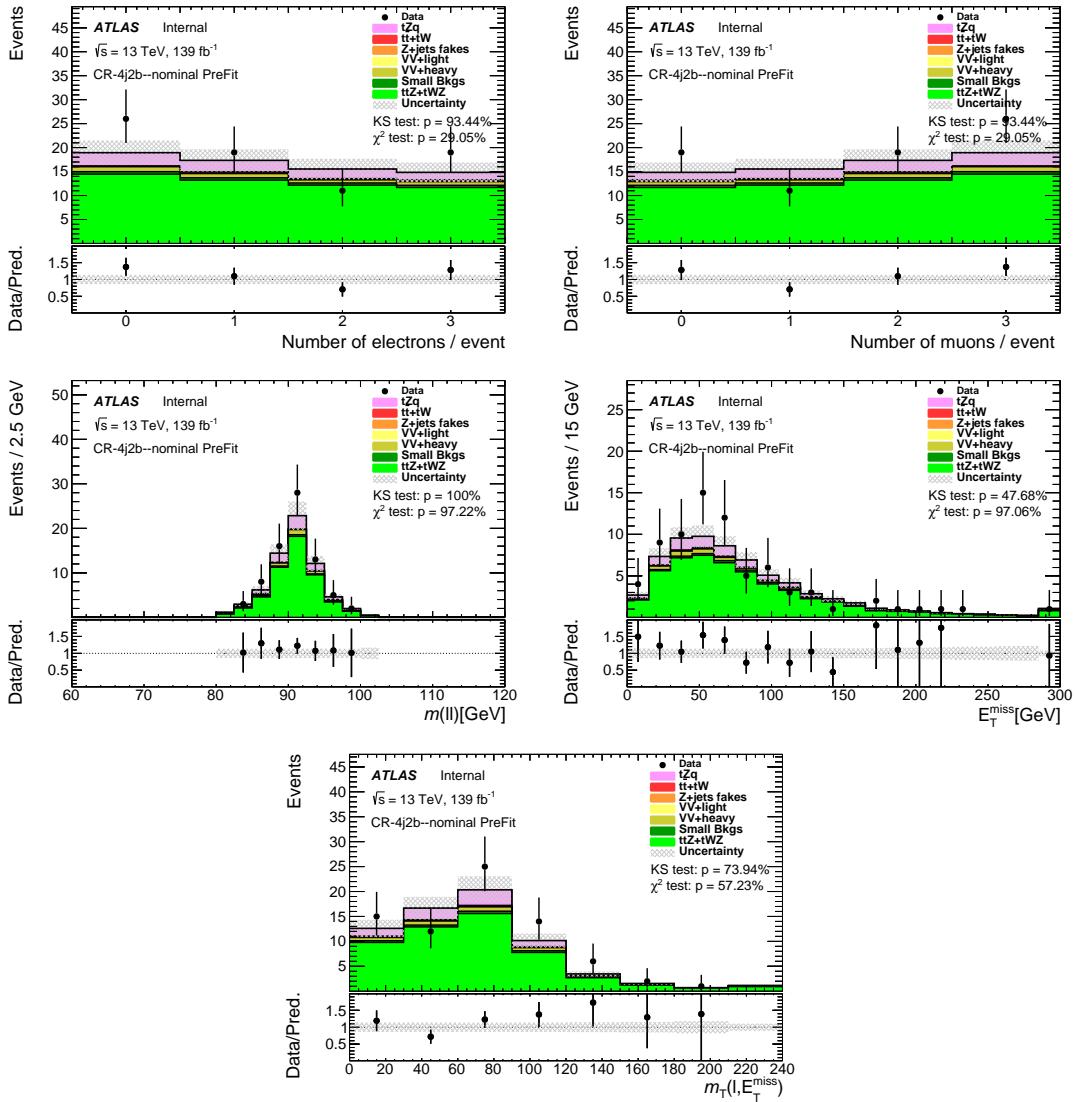


Figure 178: Comparison of data and MC predictions for reconstructed event-related quantities for events in the  $t\bar{t}Z$  4j2b CR. Both signal and backgrounds are normalised to the expected number of events before the fit. The uncertainty band includes statistical uncertainties for signal and backgrounds and background normalization uncertainties due to the prior assumptions and the modeling systematics, with the exception of  $t\bar{t}$  and  $Z + \text{jets}$ , where only the statistical uncertainties are shown.

Not reviewed, for internal circulation only

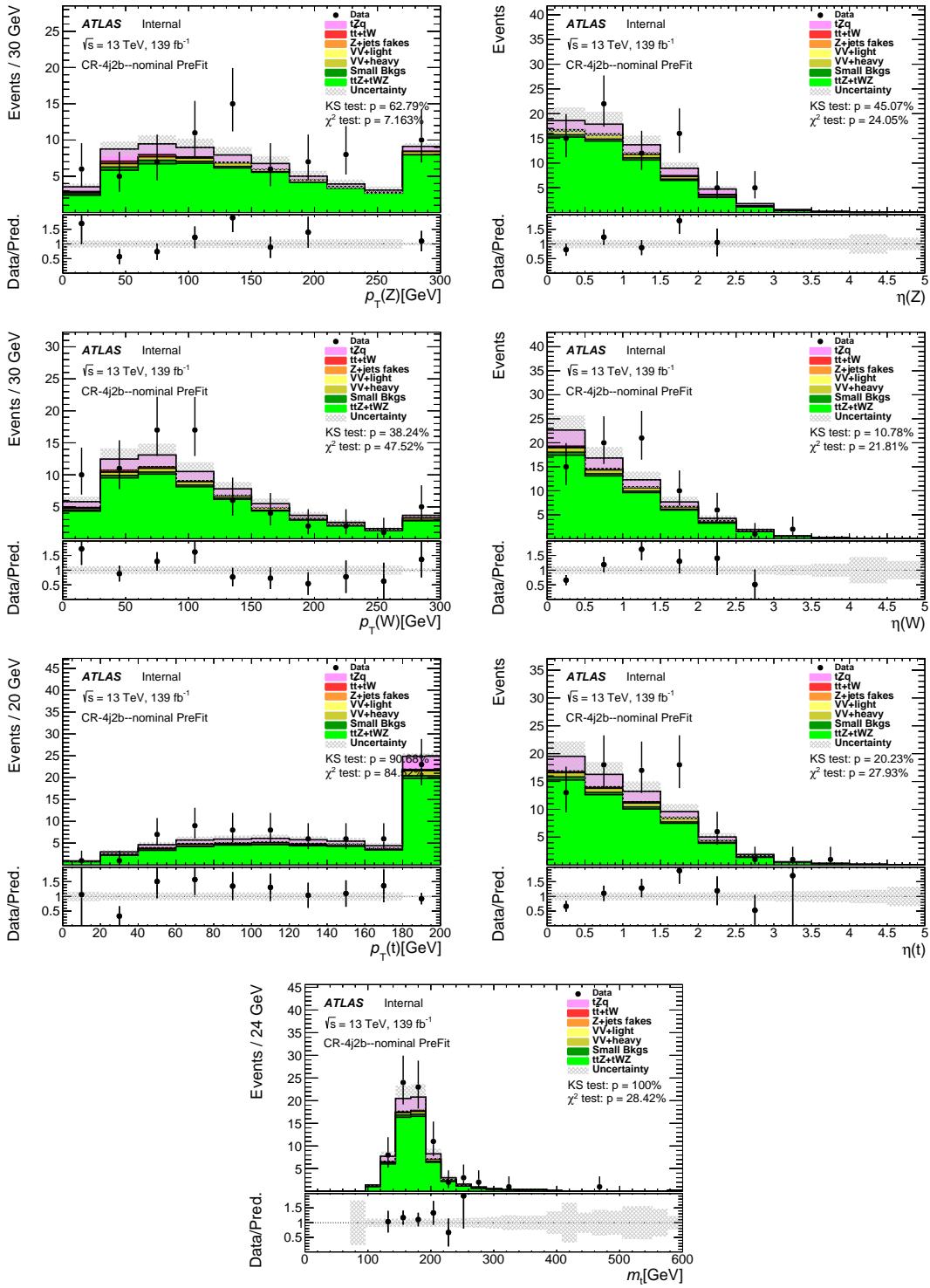


Figure 179: Comparison of data and MC predictions for reconstructed event-related quantities for events in the  $t\bar{t}Z$  4j2b CR. Both signal and backgrounds are normalised to the expected number of events before the fit. The uncertainty band includes statistical uncertainties for signal and backgrounds and background normalization uncertainties due to the prior assumptions and the modeling systematics, with the exception of  $t\bar{t}$  and  $Z + \text{jets}$ , where only the statistical uncertainties are shown.

1431 **D.2 NN input variable plots**

1432 **D.2.1 Diboson CRs**

[Not reviewed, for internal circulation only]

Not reviewed, for internal circulation only

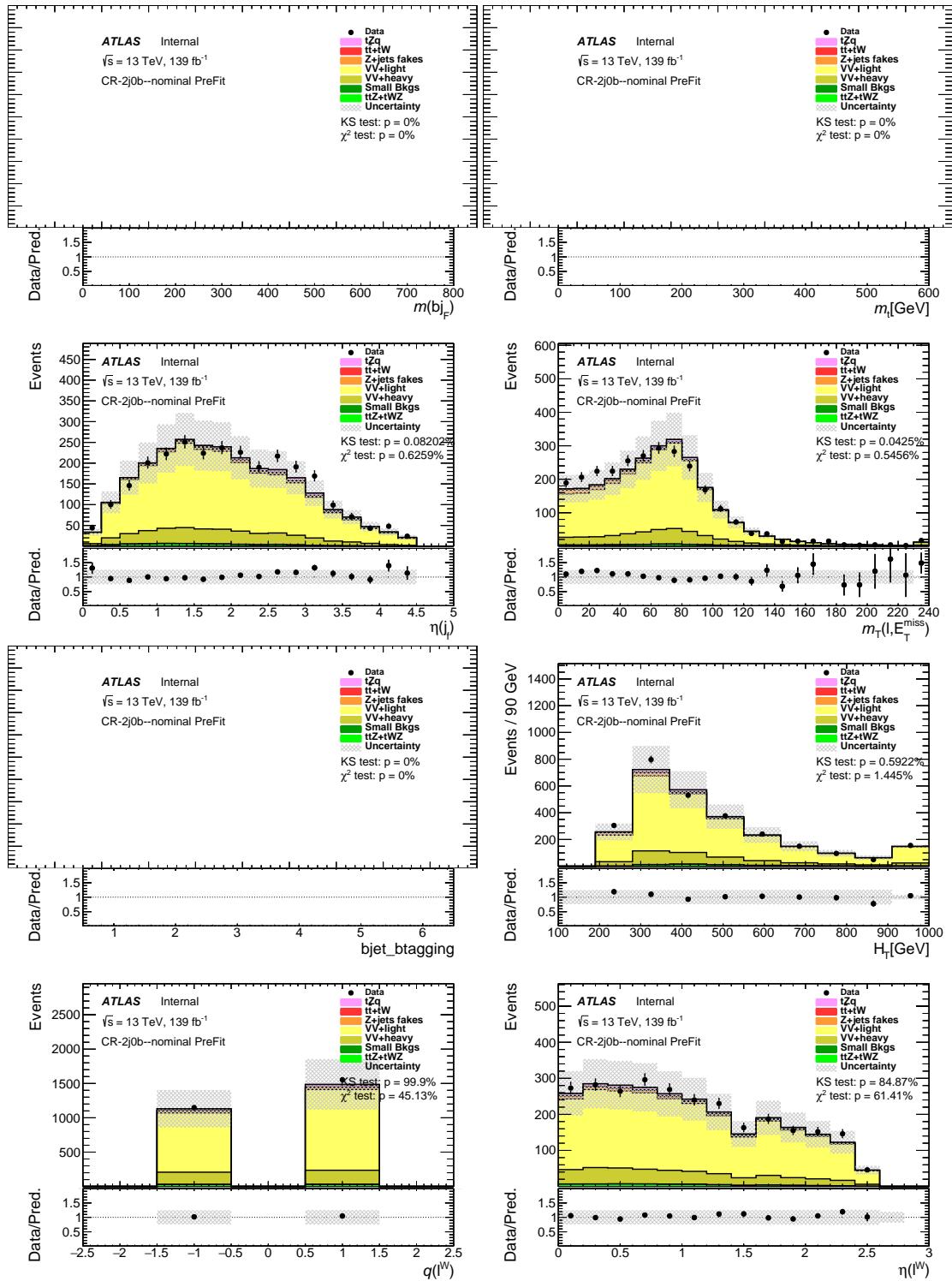


Figure 180: Stacked kinematic plots of neural-network training variables of the diboson 2j0b CR, in order of significance. Both signal and backgrounds are normalised to the expected number of events before the fit. The uncertainty band includes statistical uncertainties for signal and backgrounds and background normalization uncertainties due to the prior assumptions and the modeling systematics, with the exception of  $t\bar{t}$  and  $Z + \text{jets}$ , where only the statistical uncertainties are shown. The distribution(s) with a  $b$ -jet are not filled, as there are no  $b$ -tagged jets in this region.

Not reviewed, for internal circulation only

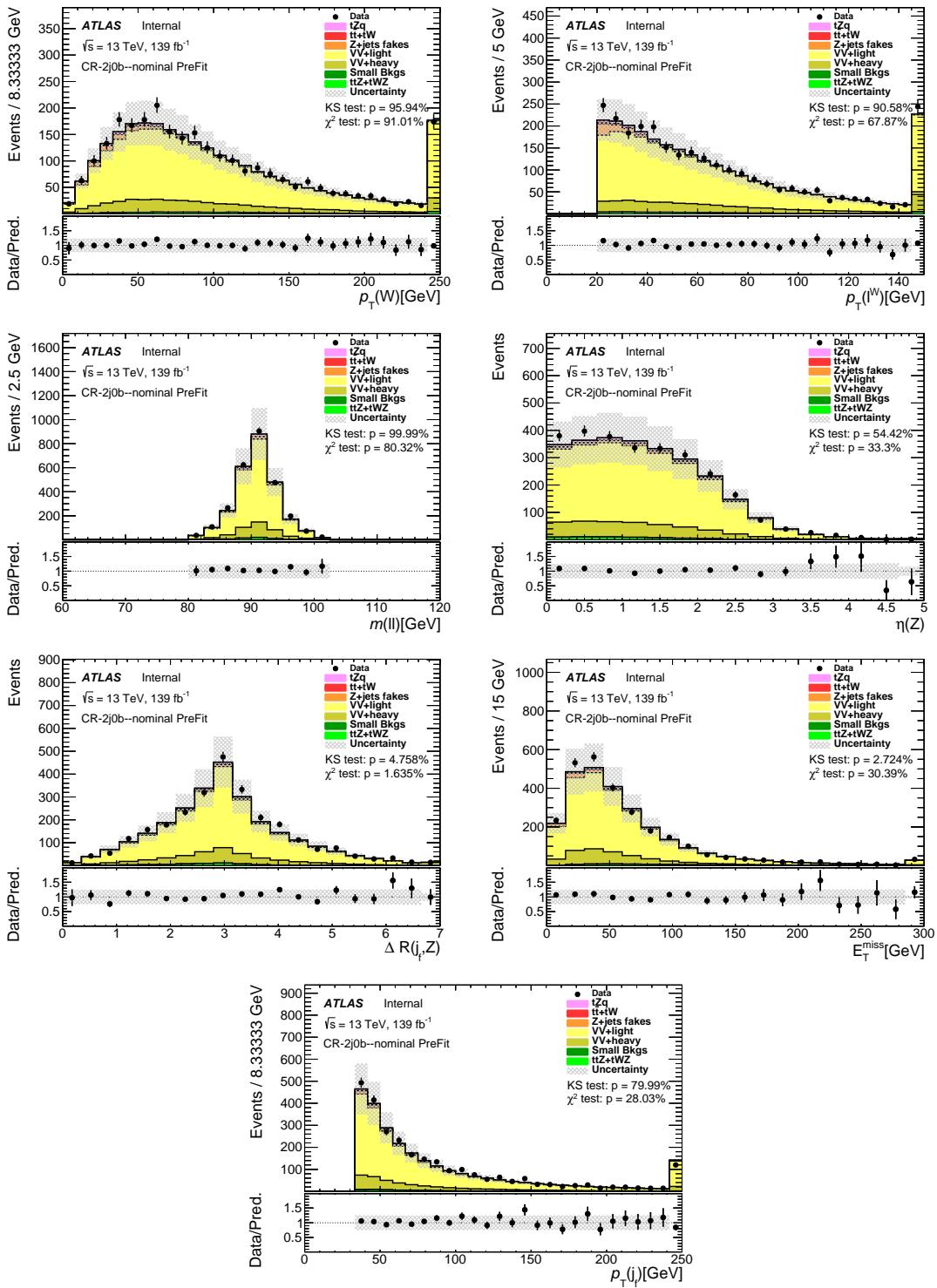


Figure 181: Stacked kinematic plots of neural-network training variables of the diboson 2j0b CR, in order of significance. Both signal and backgrounds are normalised to the expected number of events before the fit. The uncertainty band includes statistical uncertainties for signal and backgrounds and background normalization uncertainties due to the prior assumptions and the modeling systematics, with the exception of  $tt$  and  $Z + \text{jets}$ , where only the statistical uncertainties are shown.

Not reviewed, for internal circulation only

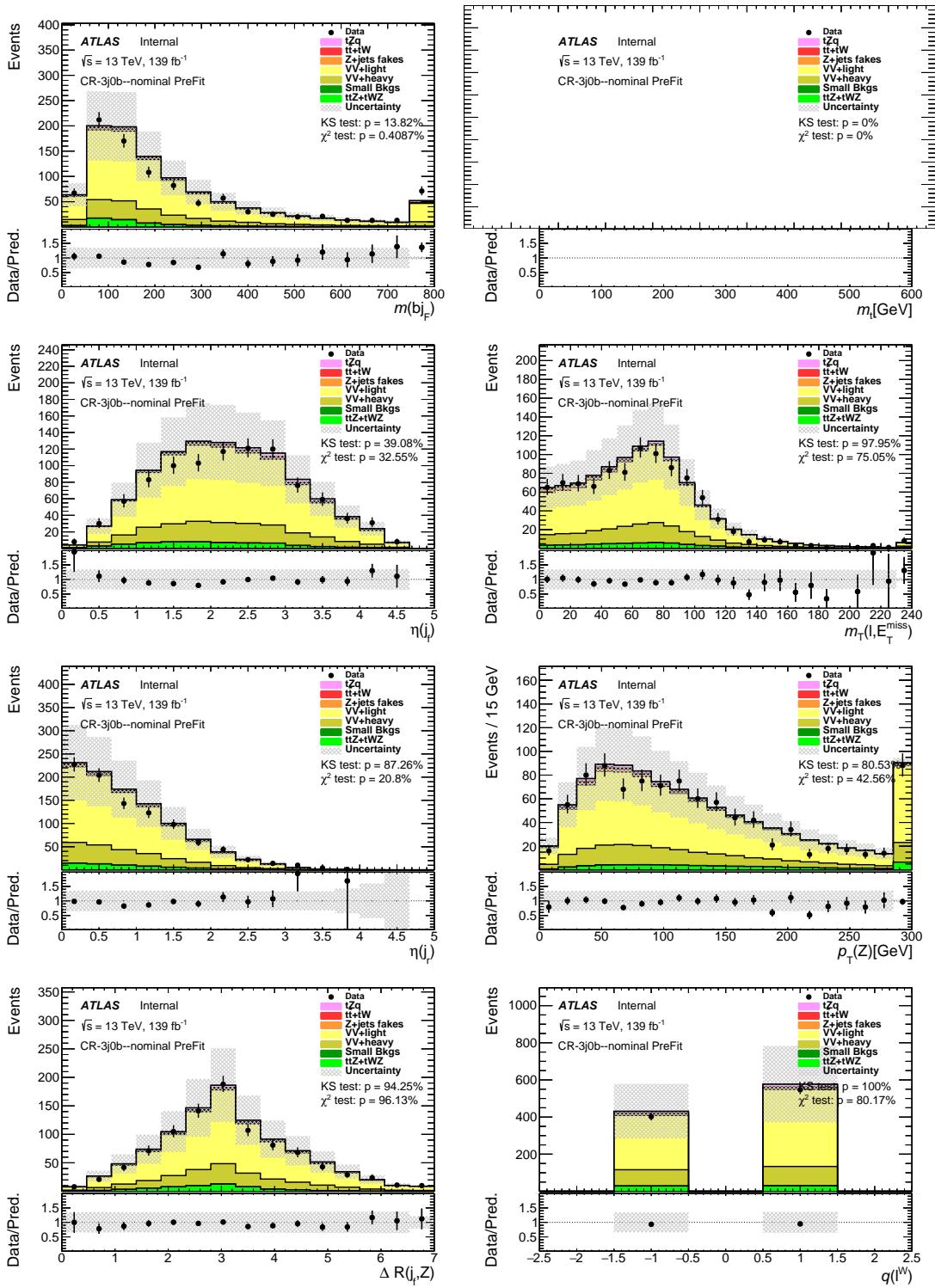


Figure 182: Stacked kinematic plots of neural-network training variables of the diboson 3j0b CR, in order of significance. Both signal and backgrounds are normalised to the expected number of events before the fit. The uncertainty band includes statistical uncertainties for signal and backgrounds and background normalization uncertainties due to the prior assumptions and the modeling systematics, with the exception of  $t\bar{t}$  and  $Z + \text{jets}$ , where only the statistical uncertainties are shown. The distribution(s) with a  $b$ -jet are not filled, as there are no  $b$ -tagged jets in this region.

Not reviewed, for internal circulation only

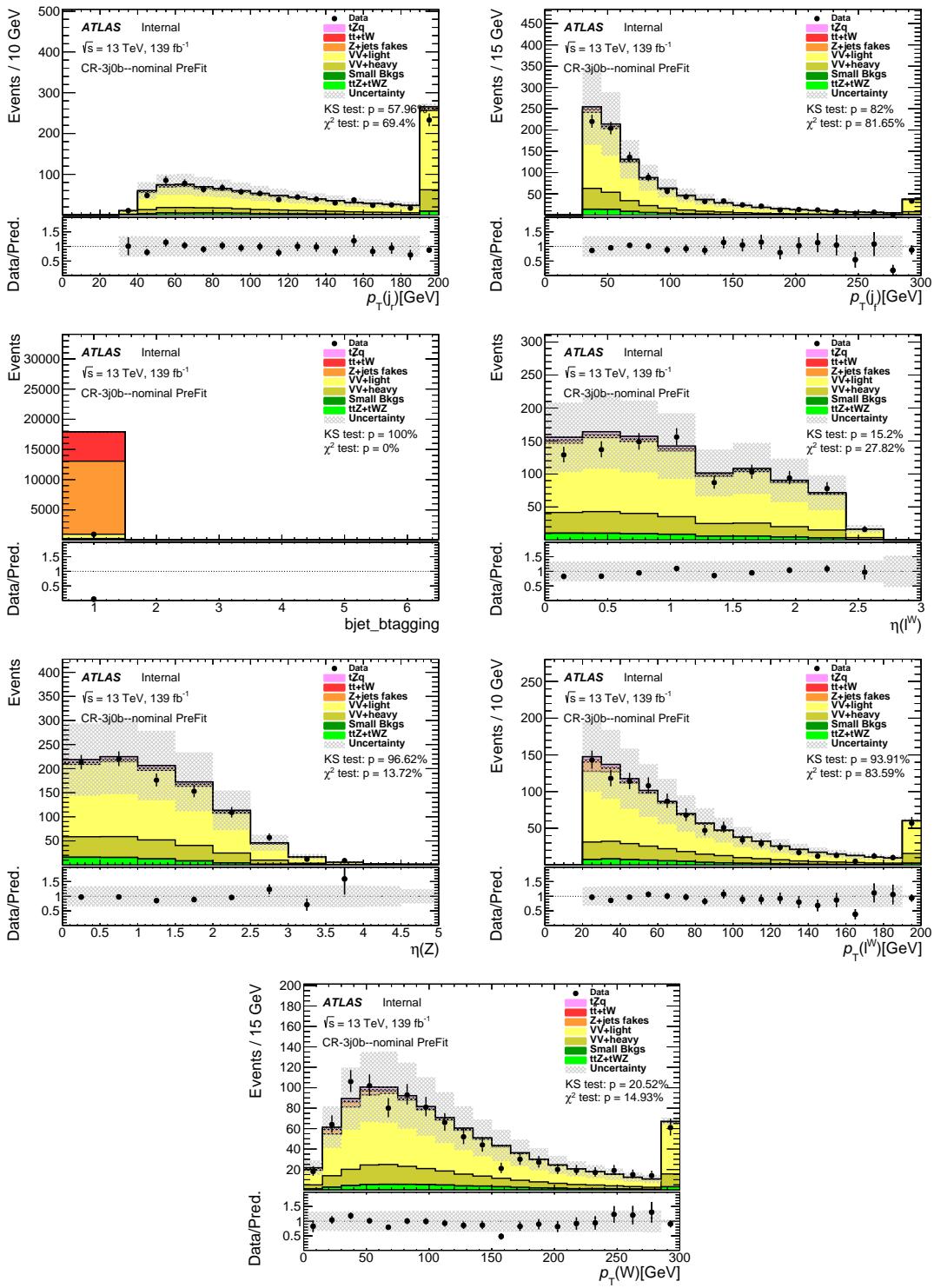


Figure 183: Stacked kinematic plots of neural-network training variables of the diboson 3j0b CR, in order of significance. Both signal and backgrounds are normalised to the expected number of events before the fit. The uncertainty band includes statistical uncertainties for signal and backgrounds and background normalization uncertainties due to the prior assumptions and the modeling systematics, with the exception of  $t\bar{t}$  and  $Z + \text{jets}$ , where only the statistical uncertainties are shown.

1433 **D.2.2  $t\bar{t}$  CRs**

[Not reviewed, for internal circulation only]

Not reviewed, for internal circulation only

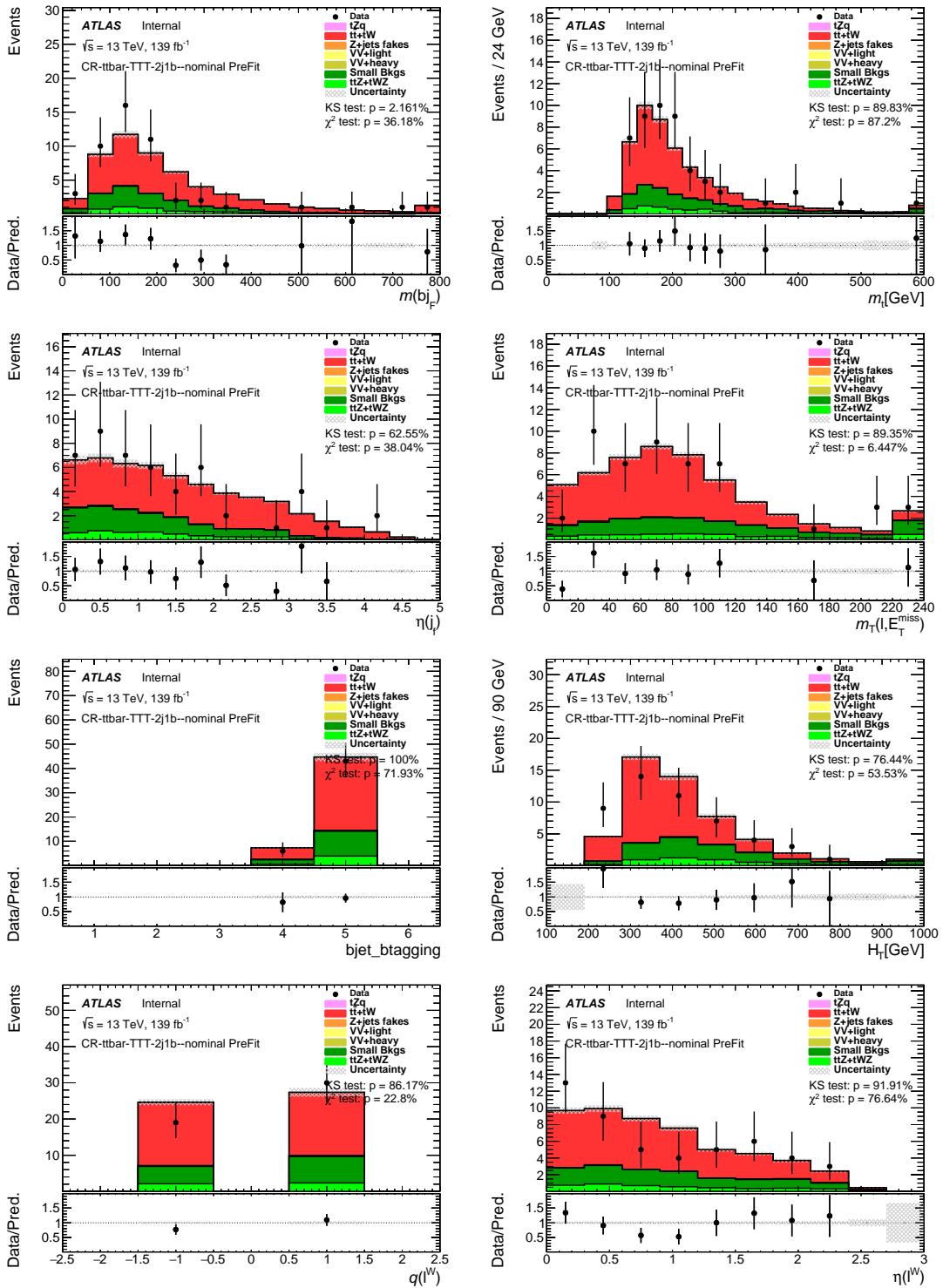


Figure 184: Stacked kinematic plots of neural-network training variables of the  $t\bar{t}$  2j1b CR, in order of significance. Both signal and backgrounds are normalised to the expected number of events before the fit. The uncertainty band includes statistical uncertainties for signal and backgrounds and background normalization uncertainties due to the prior assumptions and the modeling systematics, with the exception of  $t\bar{t}$  and  $Z + \text{jets}$ , where only the statistical uncertainties are shown.

Not reviewed, for internal circulation only

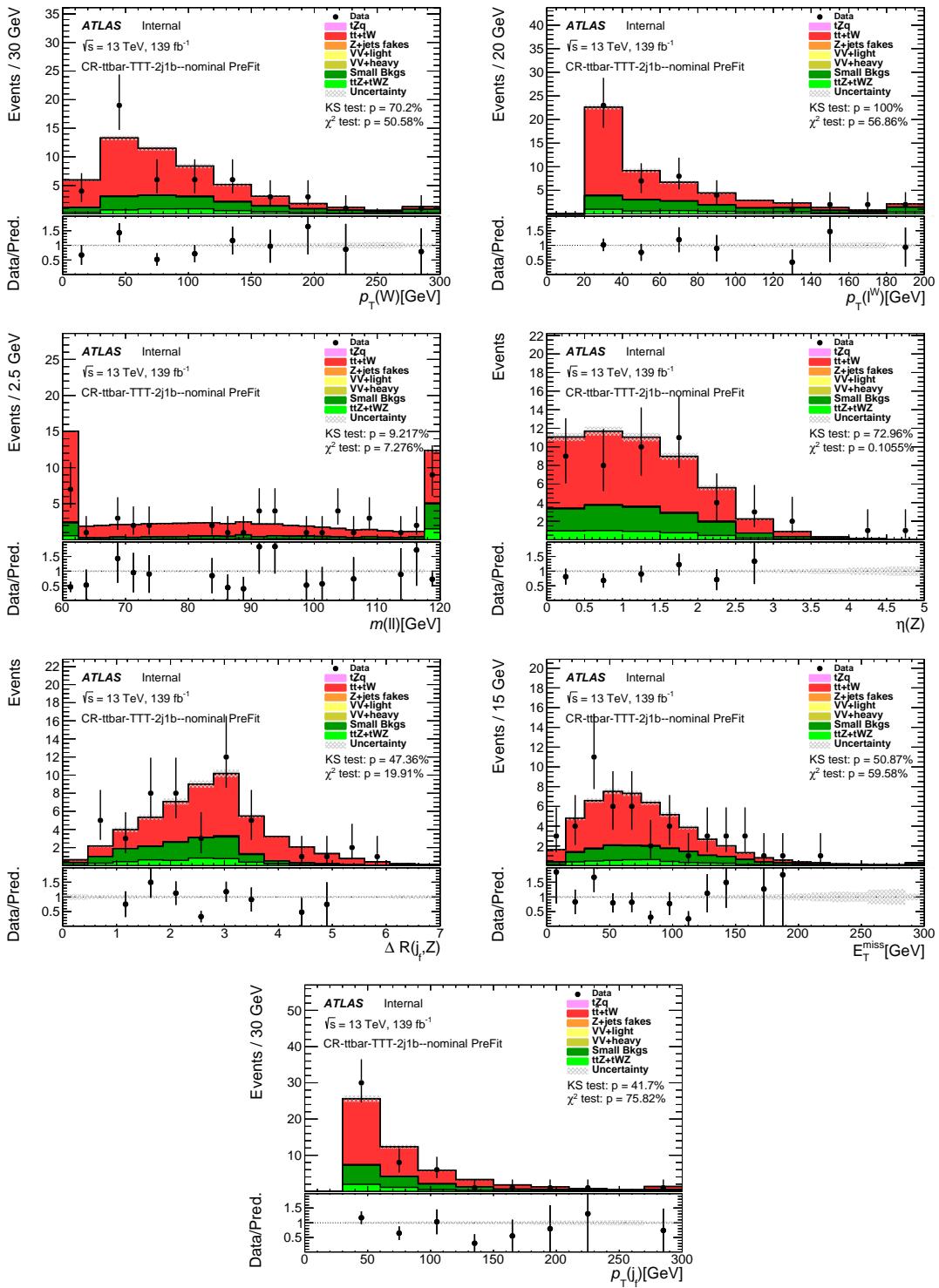


Figure 185: Stacked kinematic plots of neural-network training variables of the  $t\bar{t}$  2j1b CR, in order of significance. Both signal and backgrounds are normalised to the expected number of events before the fit. The uncertainty band includes statistical uncertainties for signal and backgrounds and background normalization uncertainties due to the prior assumptions and the modeling systematics, with the exception of  $t\bar{t}$  and  $Z + \text{jets}$ , where only the statistical uncertainties are shown.

Not reviewed, for internal circulation only

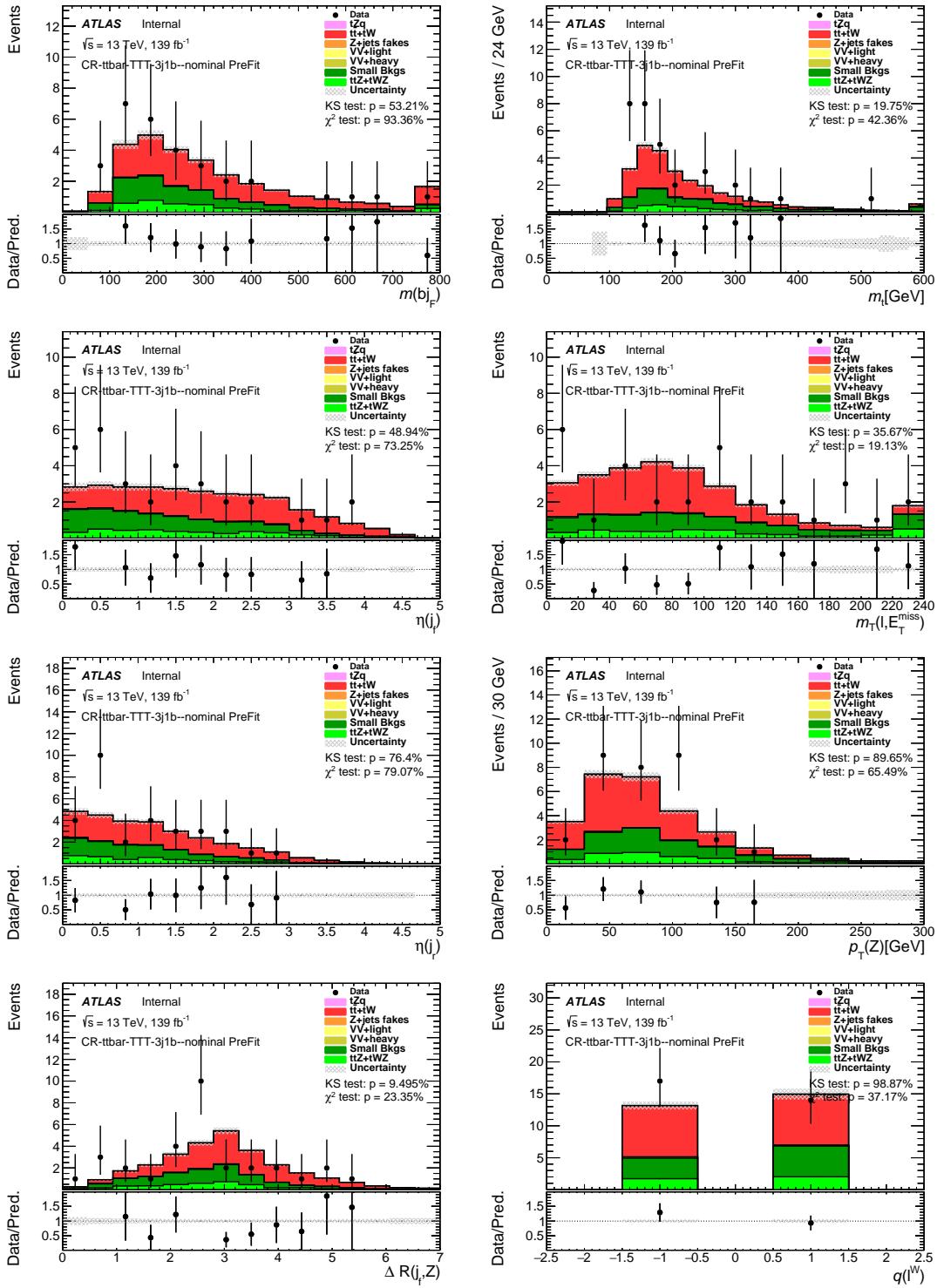


Figure 186: Stacked kinematic plots of neural-network training variables of the  $t\bar{t}$  3j1b CR, in order of significance. Both signal and backgrounds are normalised to the expected number of events before the fit. The uncertainty band includes statistical uncertainties for signal and backgrounds and background normalization uncertainties due to the prior assumptions and the modeling systematics, with the exception of  $t\bar{t}$  and  $Z + \text{jets}$ , where only the statistical uncertainties are shown.

Not reviewed, for internal circulation only

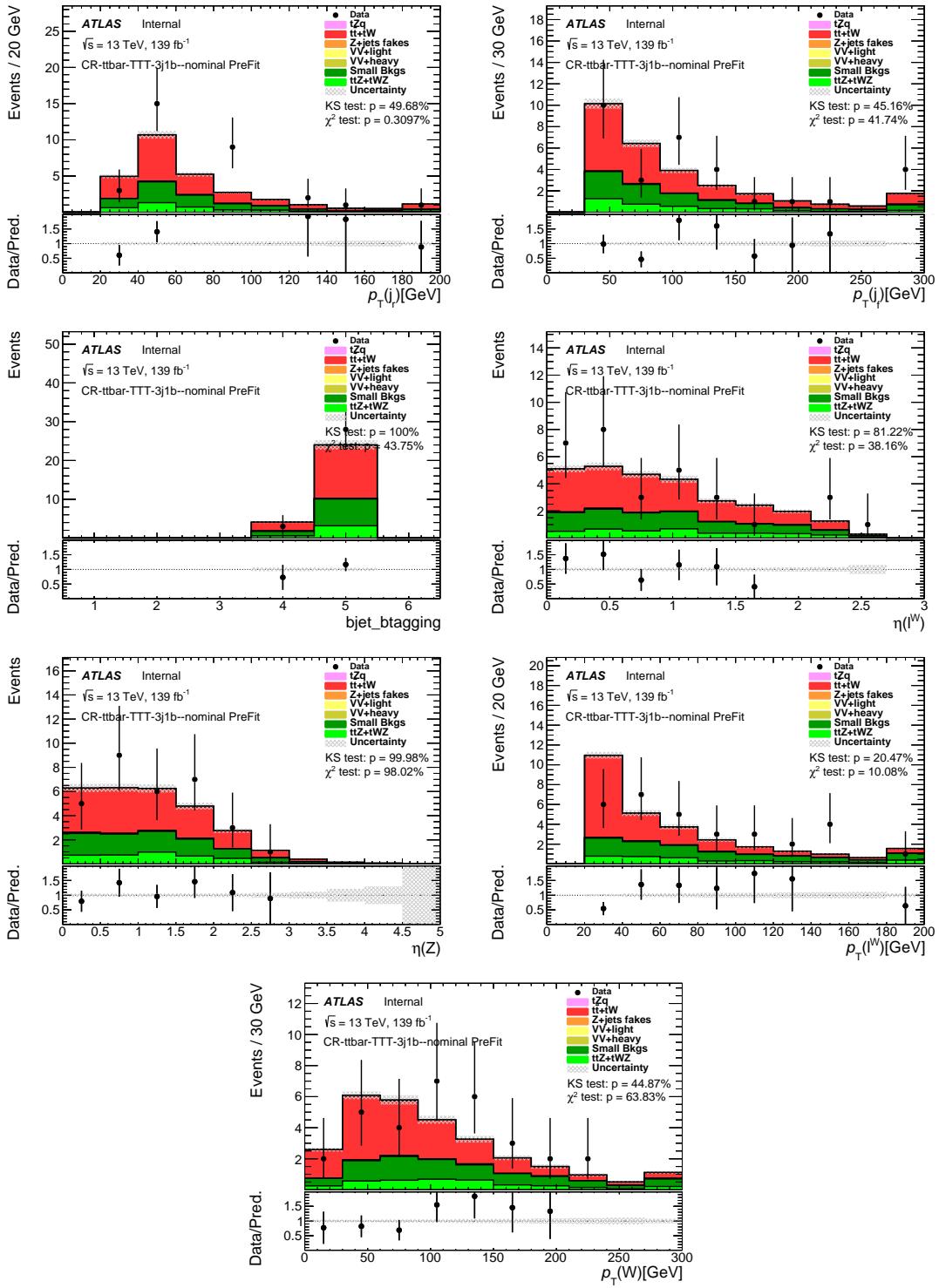


Figure 187: Stacked kinematic plots of neural-network training variables of the  $t\bar{t}$  3j1b CR, in order of significance. Both signal and backgrounds are normalised to the expected number of events before the fit. The uncertainty band includes statistical uncertainties for signal and backgrounds and background normalization uncertainties due to the prior assumptions and the modeling systematics, with the exception of  $t\bar{t}$  and  $Z + jets$ , where only the statistical uncertainties are shown.

1434 **D.2.3  $t\bar{t}Z$  CRs**

[Not reviewed, for internal circulation only]

Not reviewed, for internal circulation only

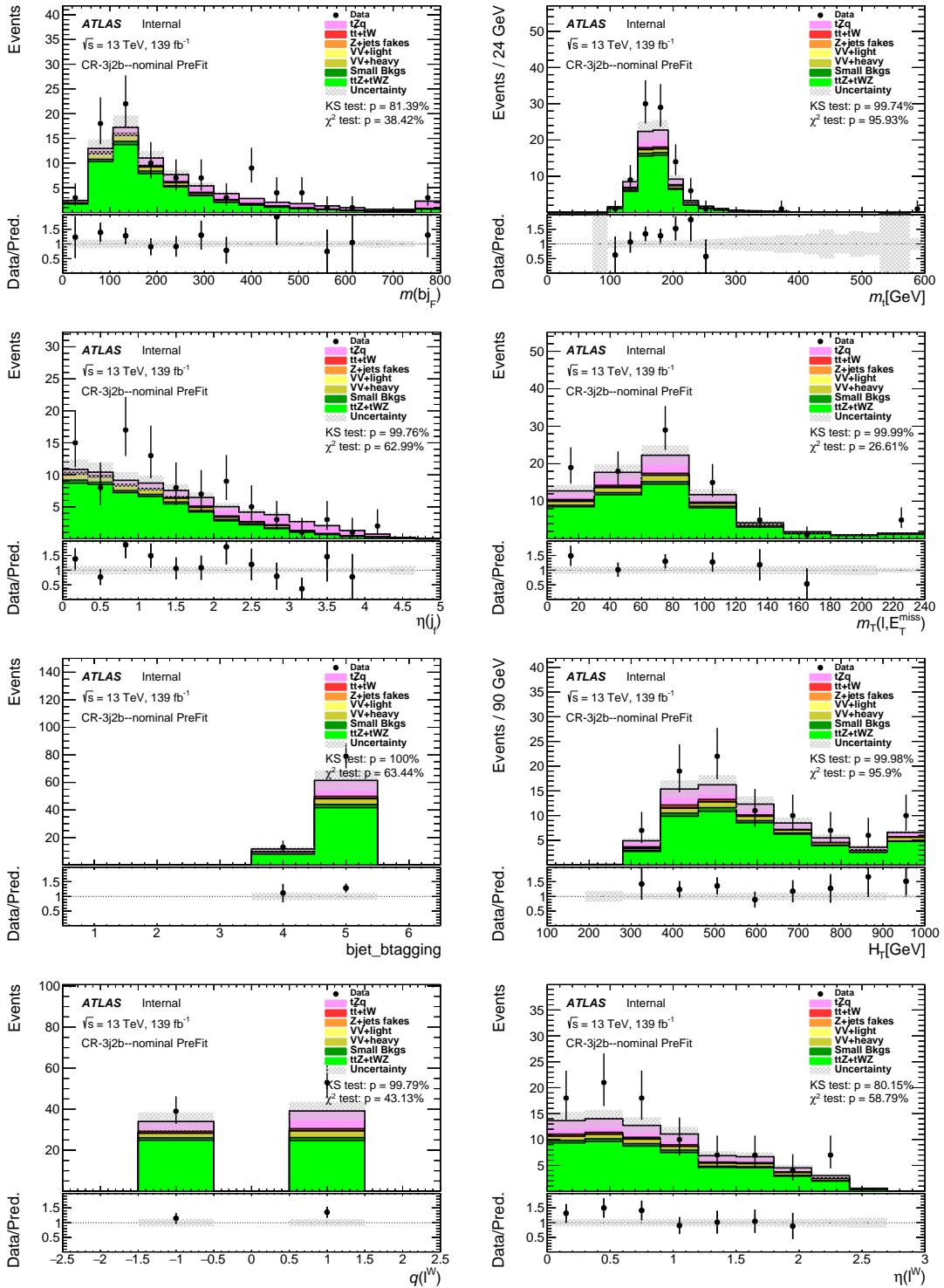


Figure 188: Stacked kinematic plots of neural-network training variables of the  $t\bar{t}Z$  3j2b CR, in order of significance. Both signal and backgrounds are normalised to the expected number of events before the fit. The uncertainty band includes statistical uncertainties for signal and backgrounds and background normalization uncertainties due to the prior assumptions and the modeling systematics, with the exception of  $t\bar{t}$  and  $Z + \text{jets}$ , where only the statistical uncertainties are shown.

Not reviewed, for internal circulation only

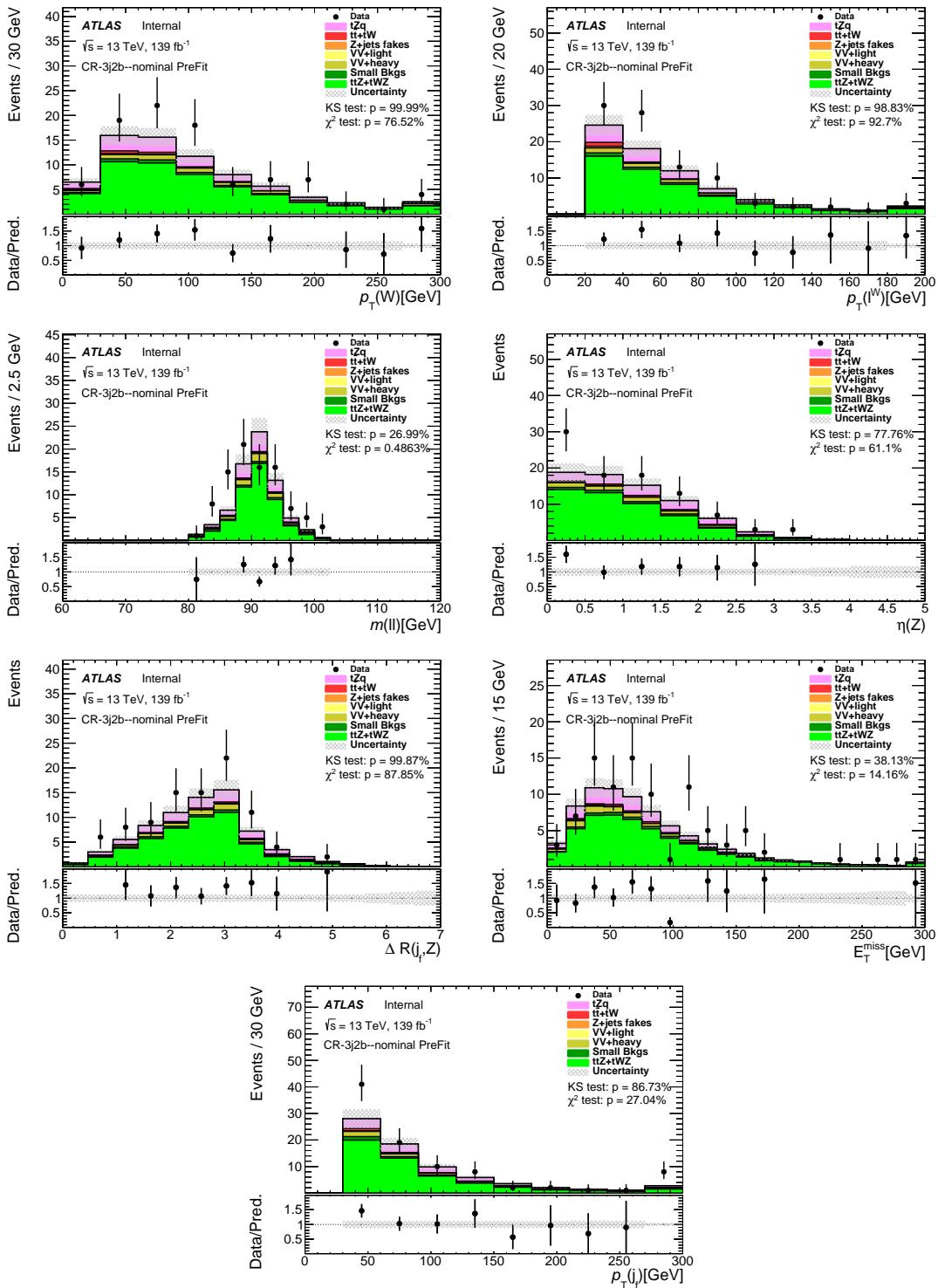


Figure 189: Stacked kinematic plots of neural-network training variables of the  $t\bar{t}Z$  3j2b CR, in order of significance. Both signal and backgrounds are normalised to the expected number of events before the fit. The uncertainty band includes statistical uncertainties for signal and backgrounds and background normalization uncertainties due to the prior assumptions and the modeling systematics, with the exception of  $t\bar{t}$  and  $Z + \text{jets}$ , where only the statistical uncertainties are shown.

Not reviewed, for internal circulation only

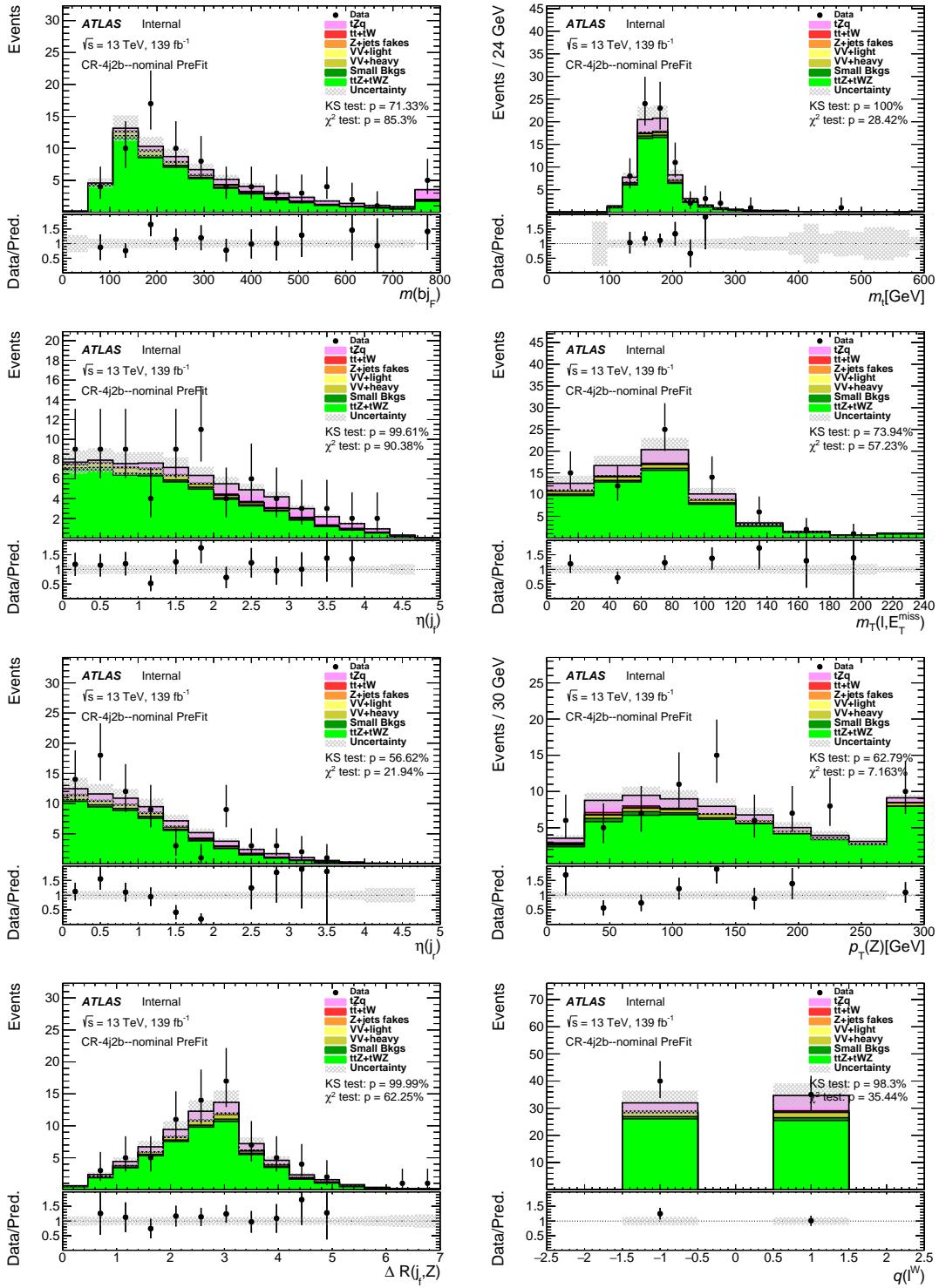


Figure 190: Stacked kinematic plots of neural-network training variables of the  $t\bar{t}Z$  4j2b CR, in order of significance. Both signal and backgrounds are normalised to the expected number of events before the fit. The uncertainty band includes statistical uncertainties for signal and backgrounds and background normalization uncertainties due to the prior assumptions and the modeling systematics, with the exception of  $t\bar{t}$  and  $Z + \text{jets}$ , where only the statistical uncertainties are shown.

Not reviewed, for internal circulation only

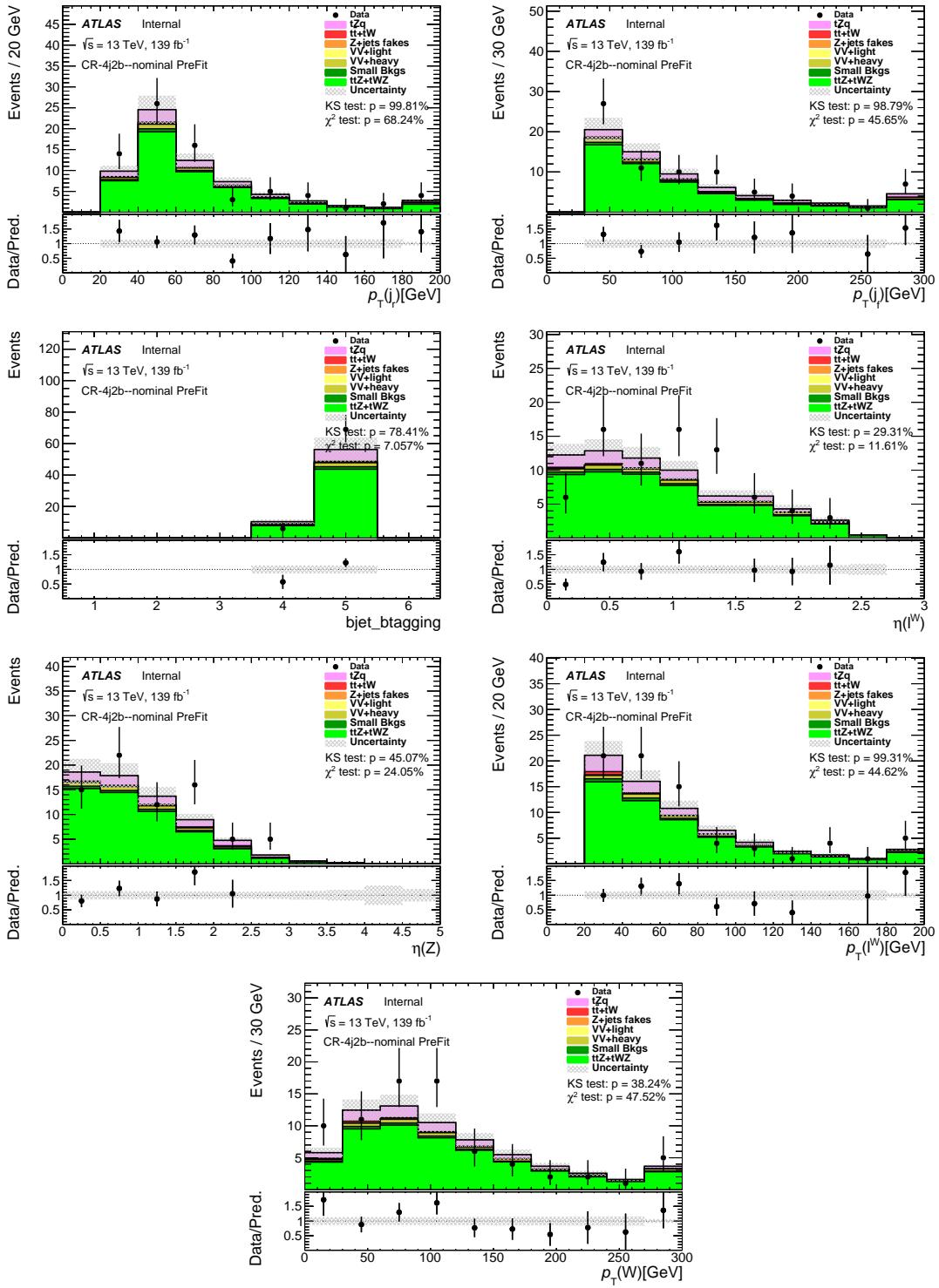


Figure 191: Stacked kinematic plots of neural-network training variables of the  $t\bar{t}Z$  4j2b CR, in order of significance. Both signal and backgrounds are normalised to the expected number of events before the fit. The uncertainty band includes statistical uncertainties for signal and backgrounds and background normalization uncertainties due to the prior assumptions and the modeling systematics, with the exception of  $t\bar{t}$  and  $Z + \text{jets}$ , where only the statistical uncertainties are shown.

1435 **E Additional BJR validation plots**1436 **E.1 Plots in SR-LTT regions**

1437 In this section, to show the validity of the  $b$ -jet replacement method, control regions are shown with the  
 1438 same cuts as the signal region but requiring '1' loose 2 'tight' leptons (LTT).

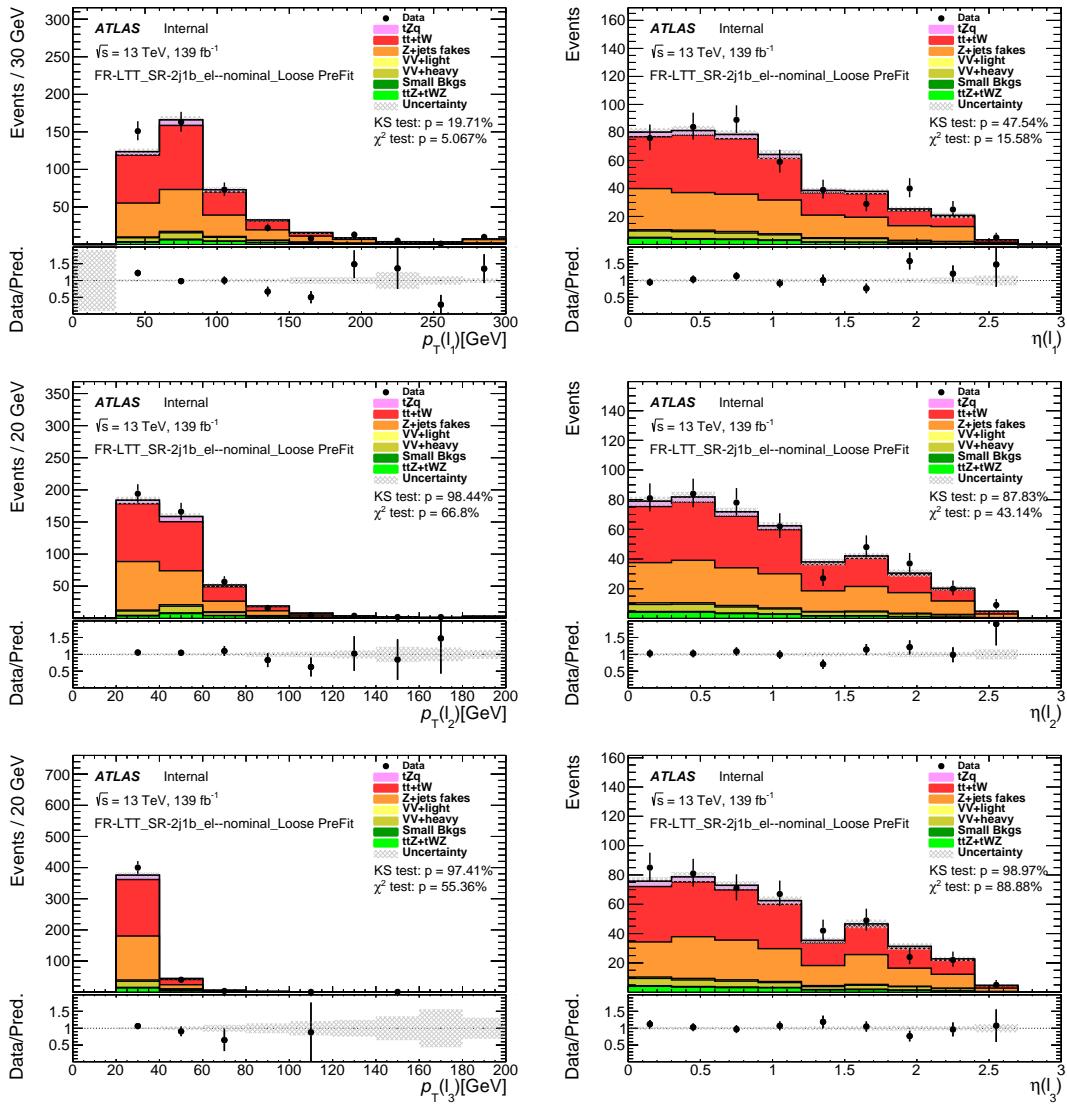
1439 **E.1.1 SR LTTs with electron fake**

Figure 192: Comparison of data and MC predictions for reconstructed lepton-related quantities for events in the SR-2j1b-LTT\_el.

Not reviewed, for internal circulation only

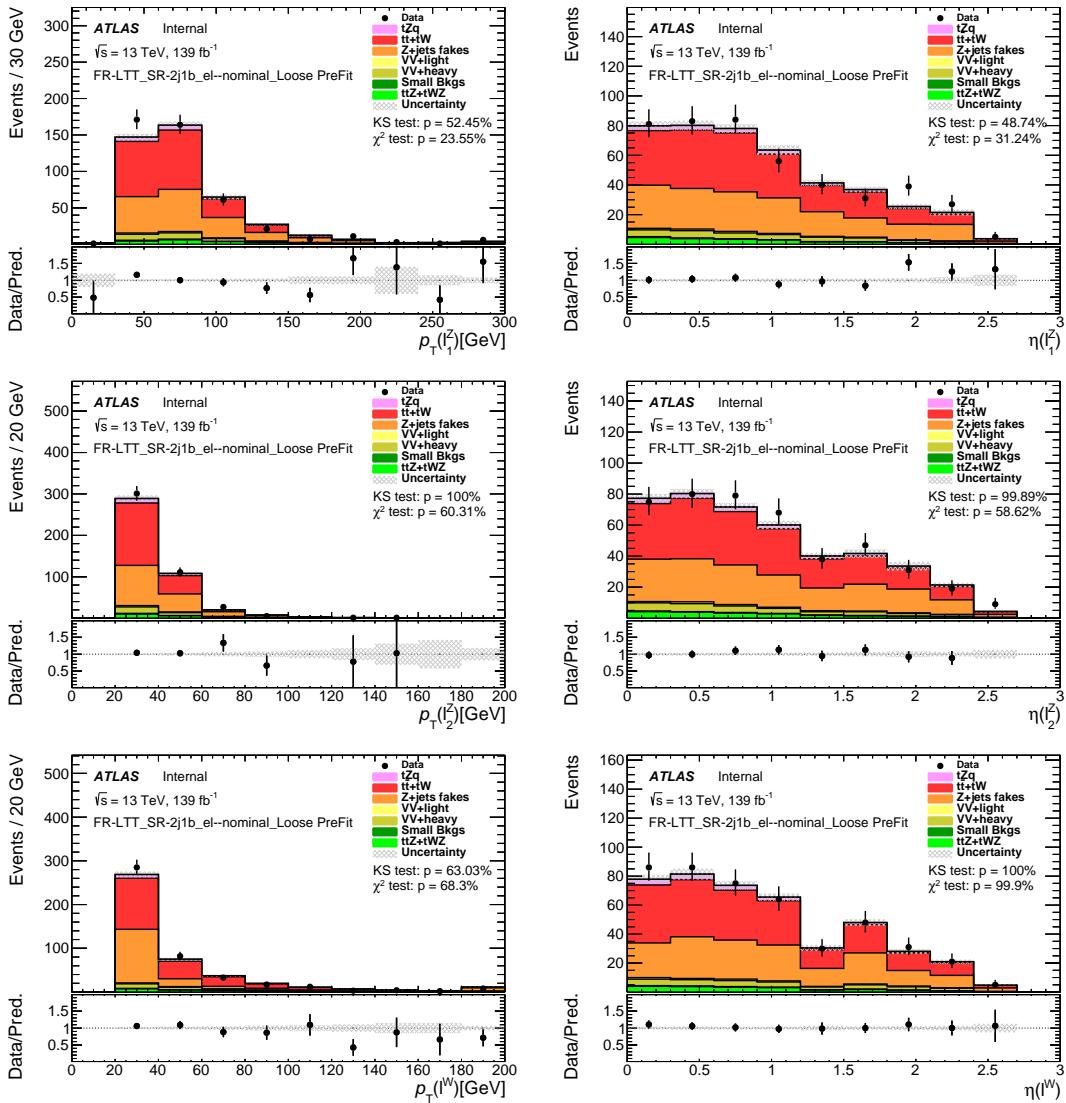


Figure 193: Comparison of data and MC predictions for reconstructed lepton-related quantities for events in the SR-2j1b-LTT\_el.

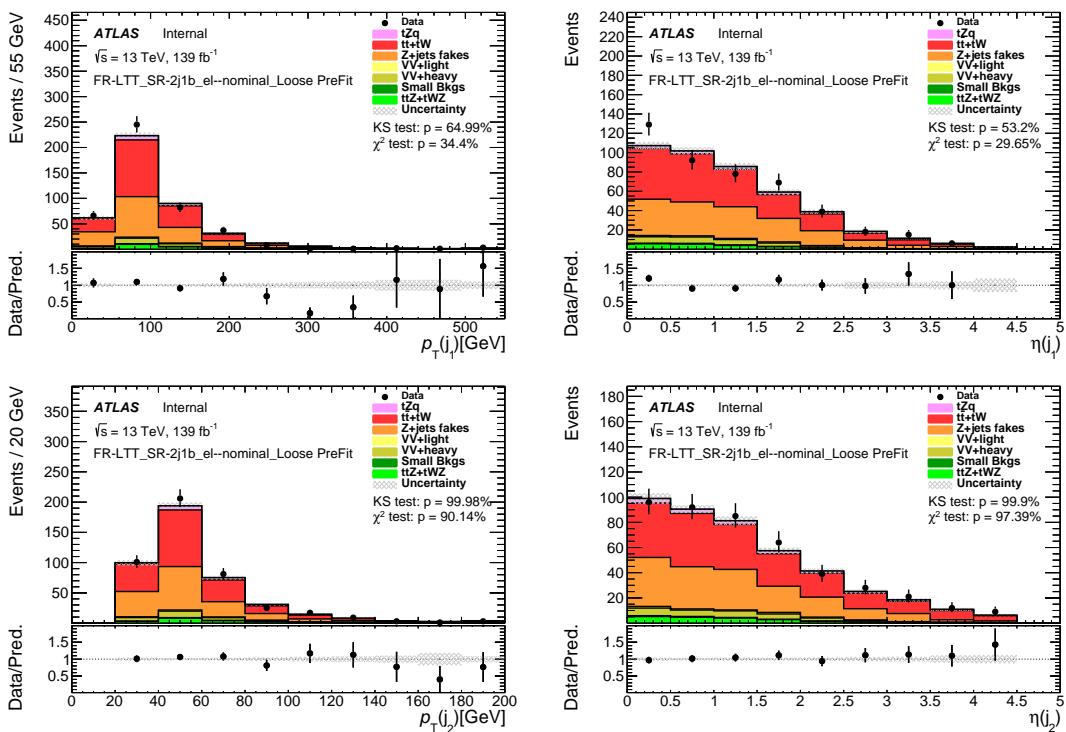


Figure 194: Comparison of data and MC predictions for reconstructed jet-related quantities for events in the SR-2j1b-LTT\_el.

Not reviewed, for internal circulation only

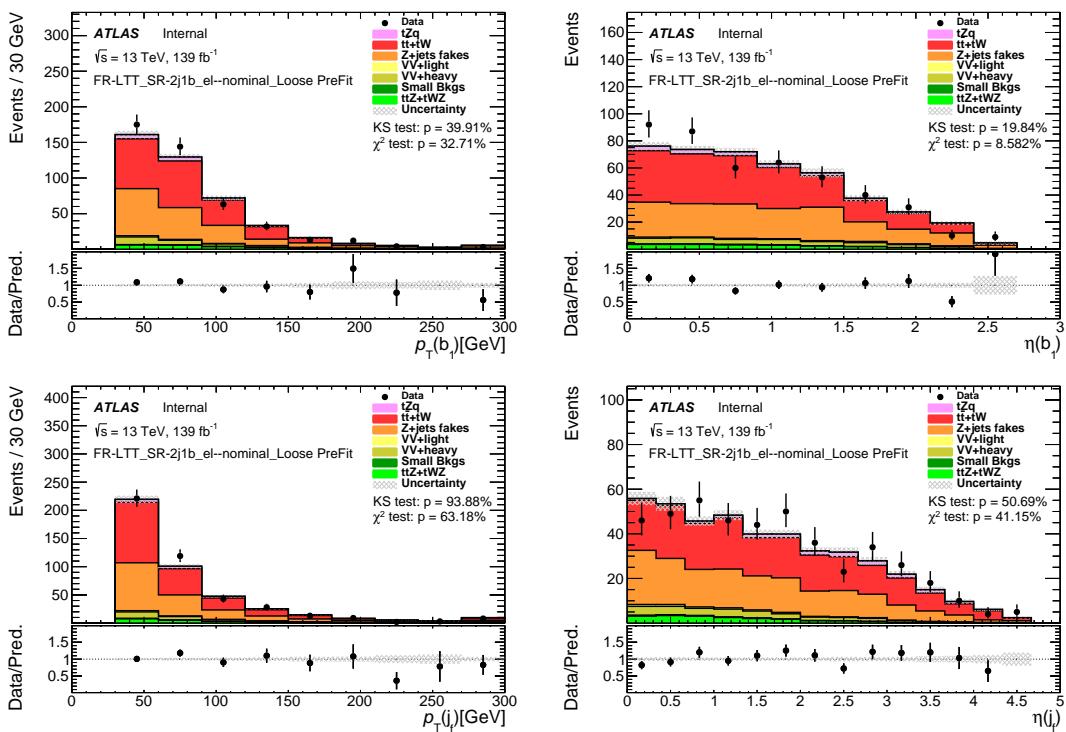


Figure 195: Comparison of data and MC predictions for reconstructed jet-related quantities for events in the SR-2j1b-LTT\_el.

Not reviewed, for internal circulation only

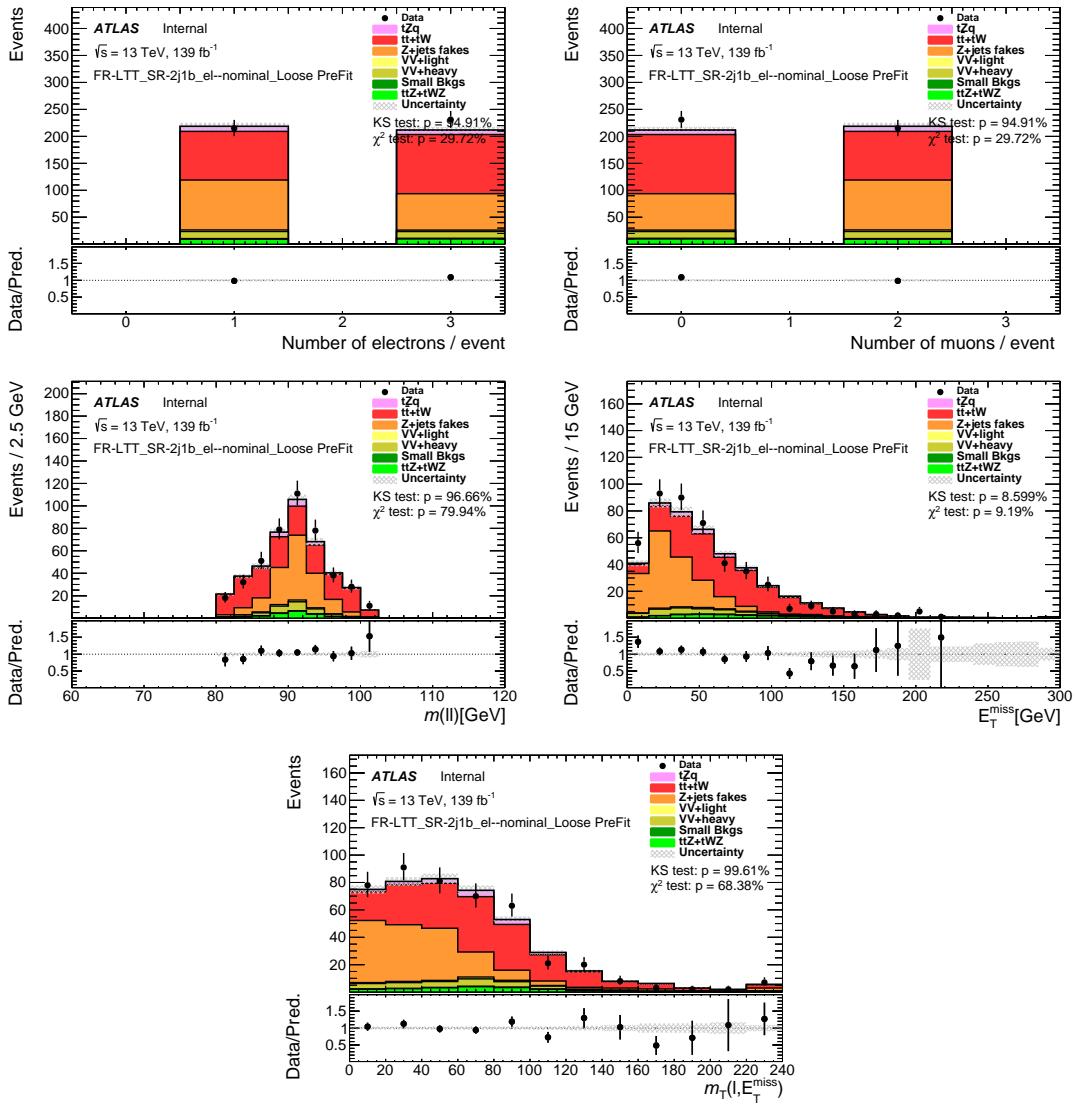


Figure 196: Comparison of data and MC predictions for reconstructed event-related quantities for events in the SR-2j1b-LTT\_el.

Not reviewed, for internal circulation only

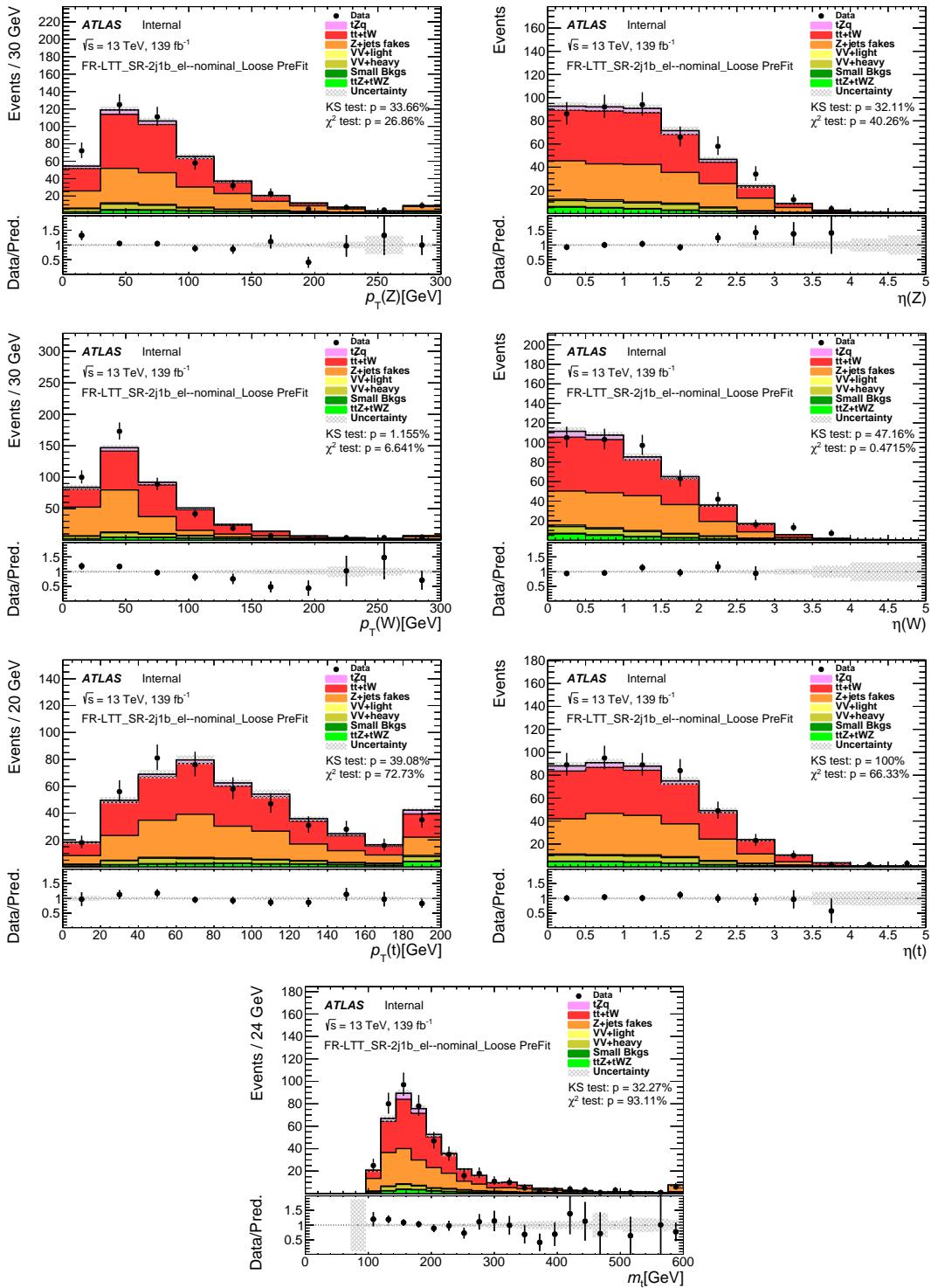


Figure 197: Comparison of data and MC predictions for reconstructed event-related quantities for events in the SR-2j1b-LTT\_el.

Not reviewed, for internal circulation only

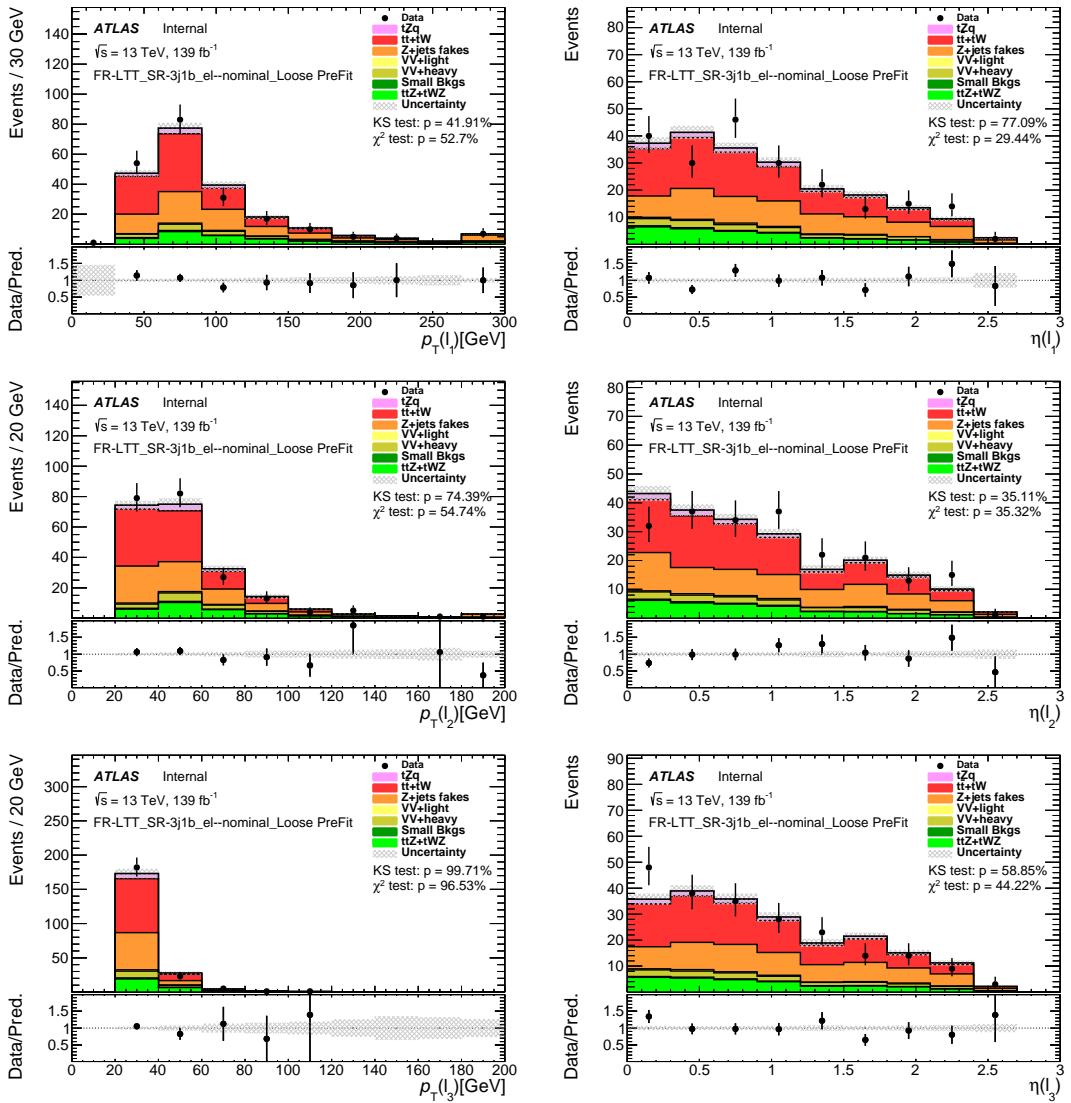


Figure 198: Comparison of data and MC predictions for reconstructed lepton-related quantities for events in the SR-3j1b-LTT\_el.

Not reviewed, for internal circulation only

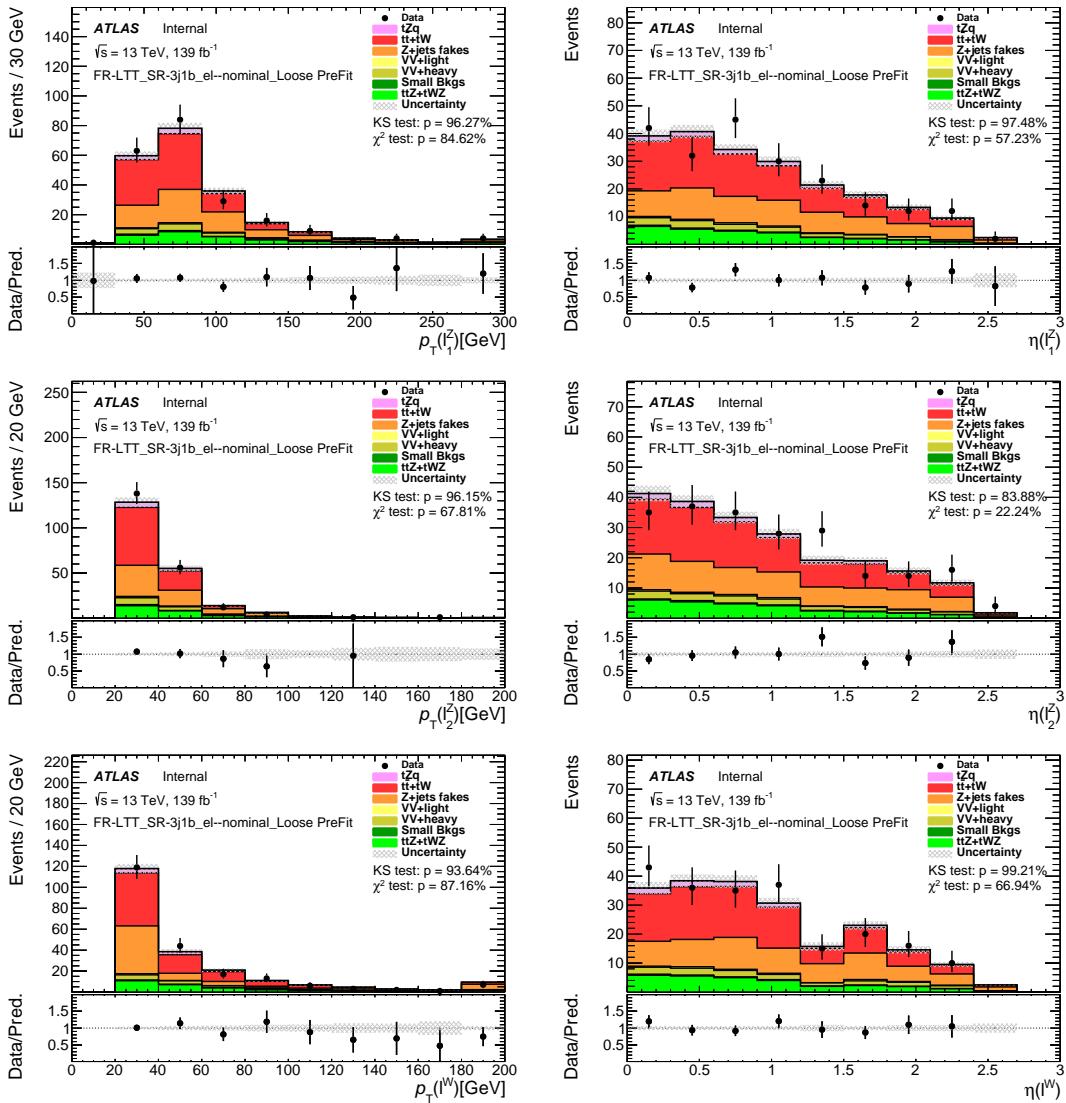


Figure 199: Comparison of data and MC predictions for reconstructed lepton-related quantities for events in the SR-3j1b-LTT\_el.

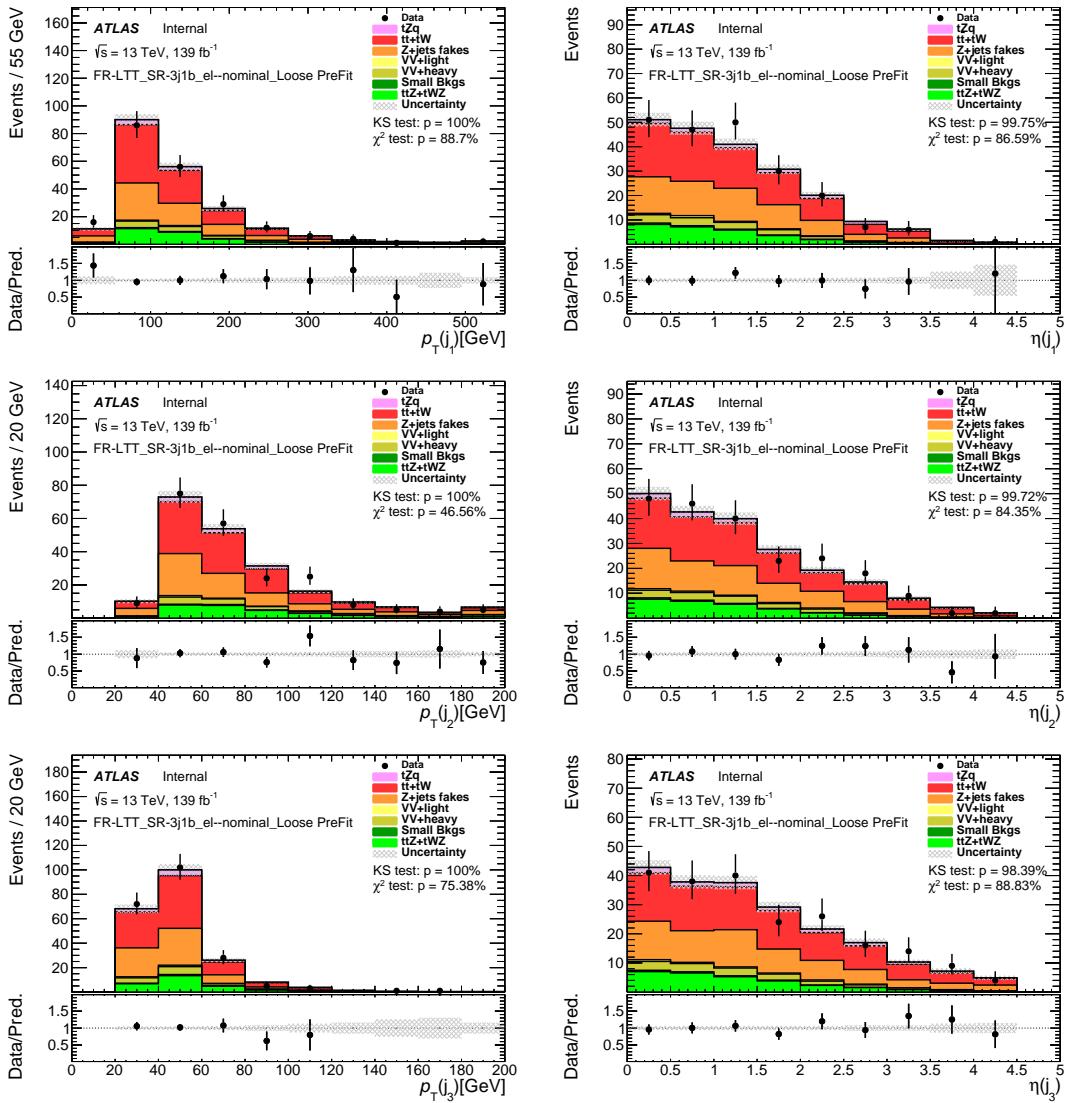


Figure 200: Comparison of data and MC predictions for reconstructed jet-related quantities for events in the SR-3j1b-LTT\_el.

Not reviewed, for internal circulation only

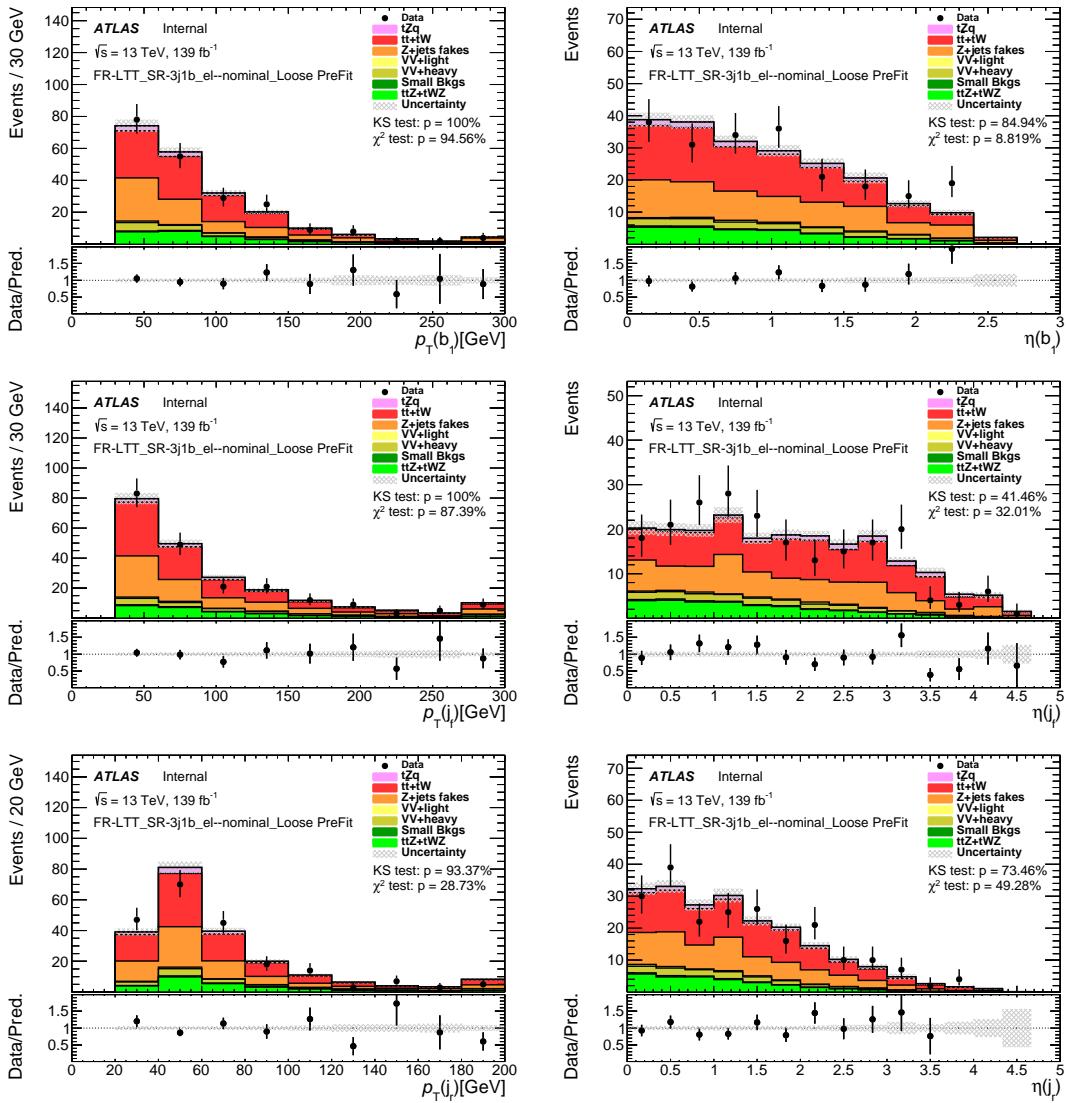


Figure 201: Comparison of data and MC predictions for reconstructed jet-related quantities for events in the SR-3j1b-LTT\_el.

Not reviewed, for internal circulation only

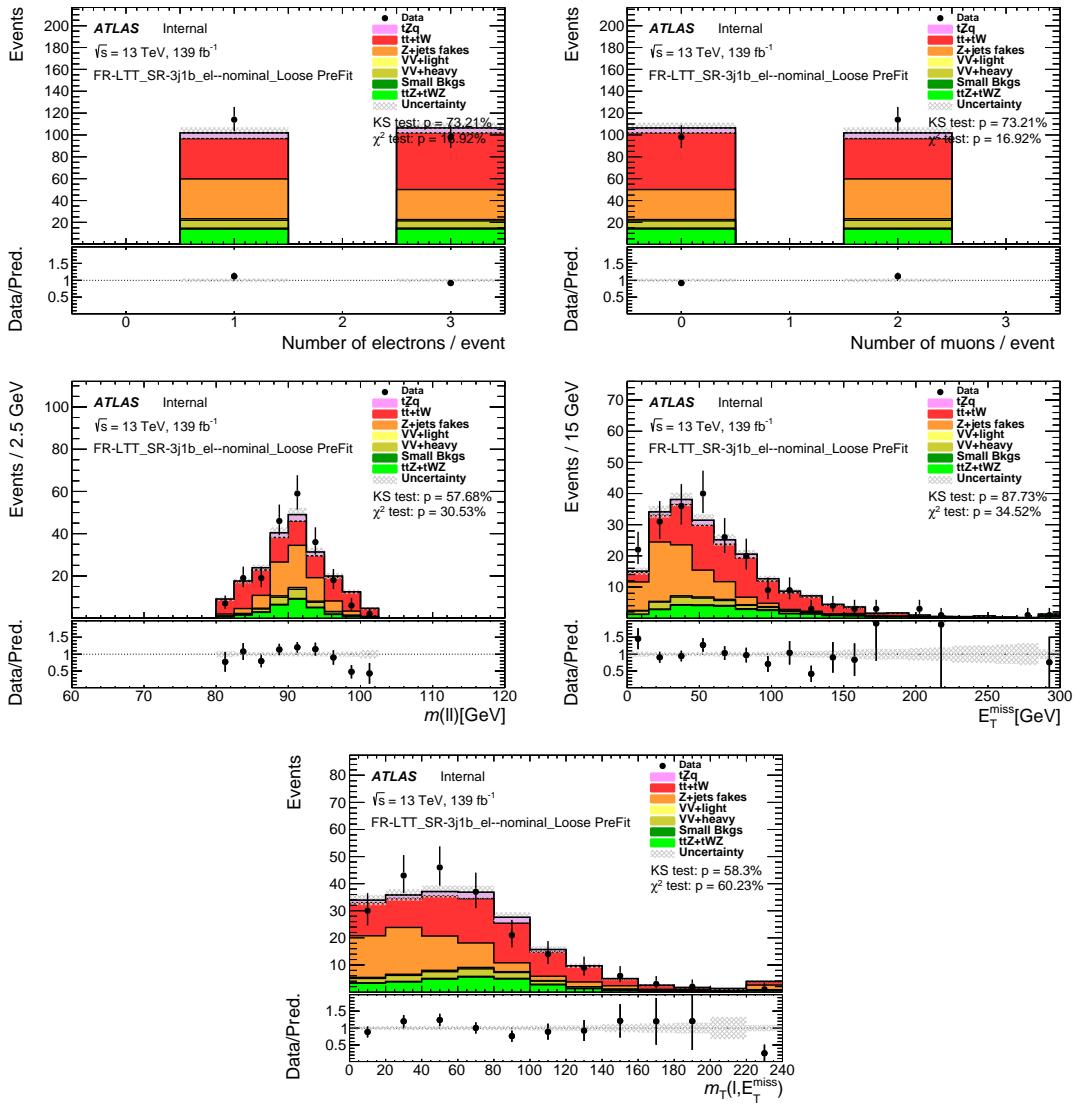


Figure 202: Comparison of data and MC predictions for reconstructed event-related quantities for events in the SR-3j1b-LTT\_el.

Not reviewed, for internal circulation only

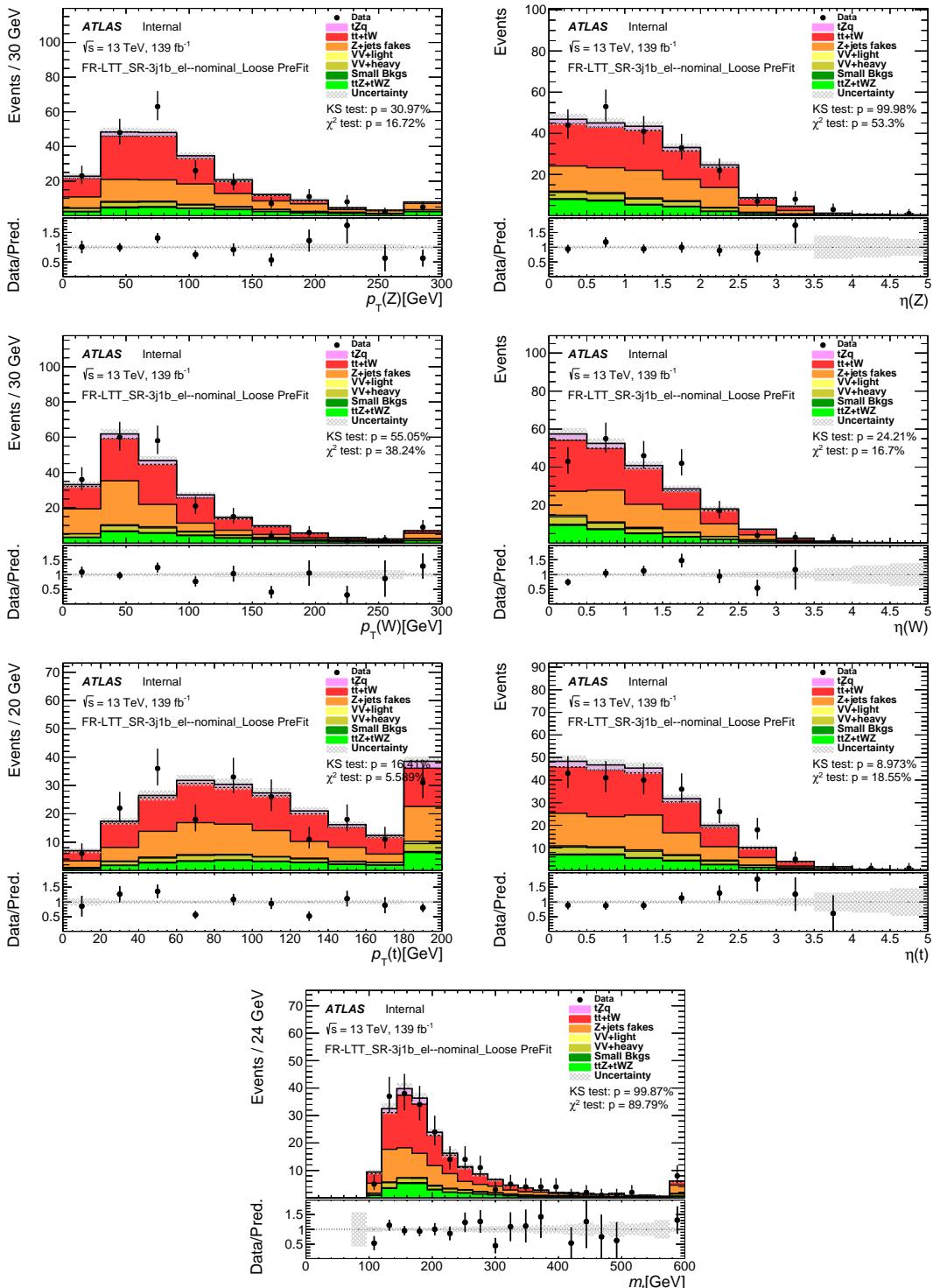


Figure 203: Comparison of data and MC predictions for reconstructed event-related quantities for events in the SR-3j1b-LTT\_el.

Not reviewed, for internal circulation only

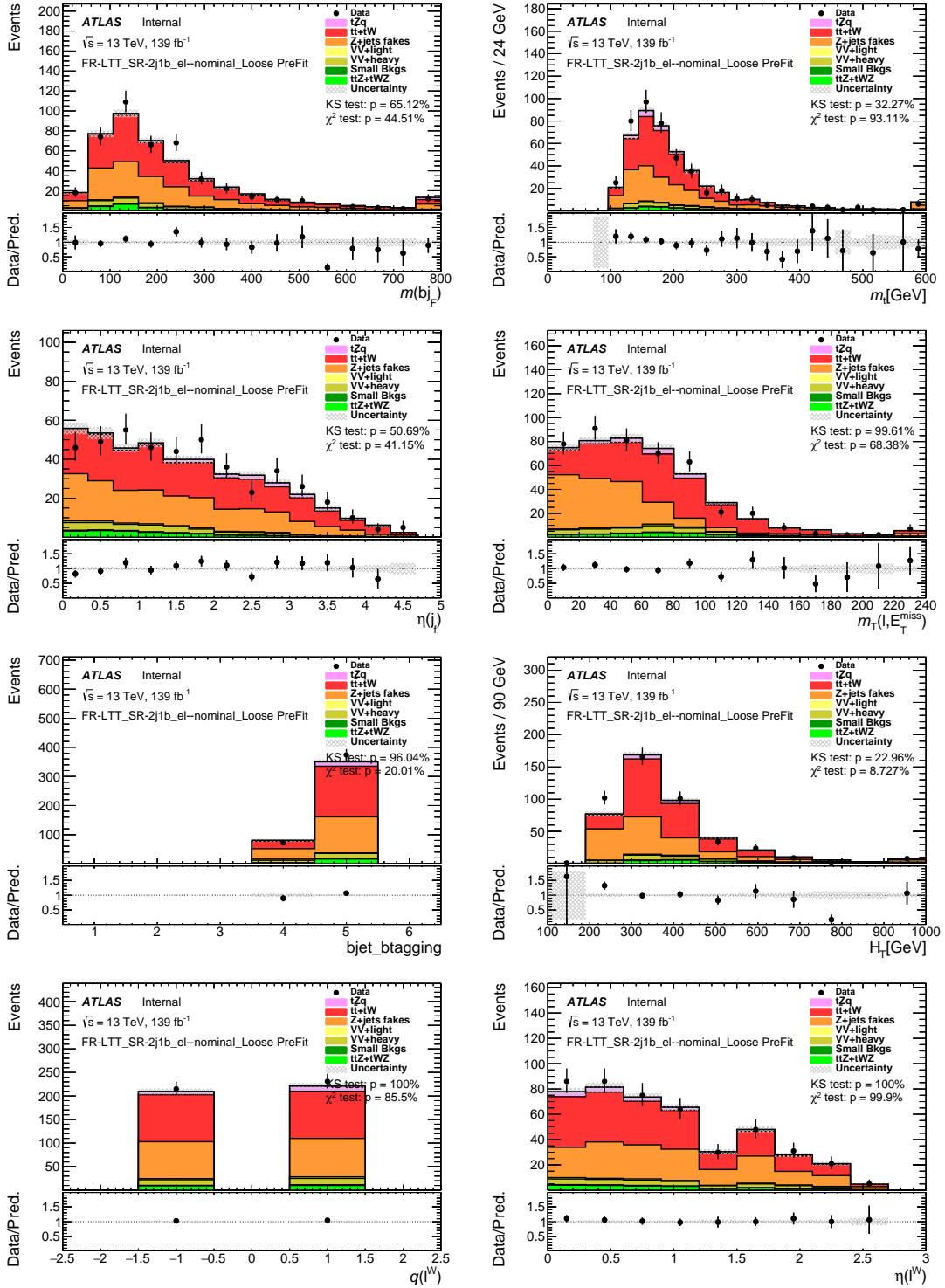


Figure 204: Stacked kinematic plots of neural-network training variables of the SR-2j1b-LTT\_el, in order of significance.

Not reviewed, for internal circulation only

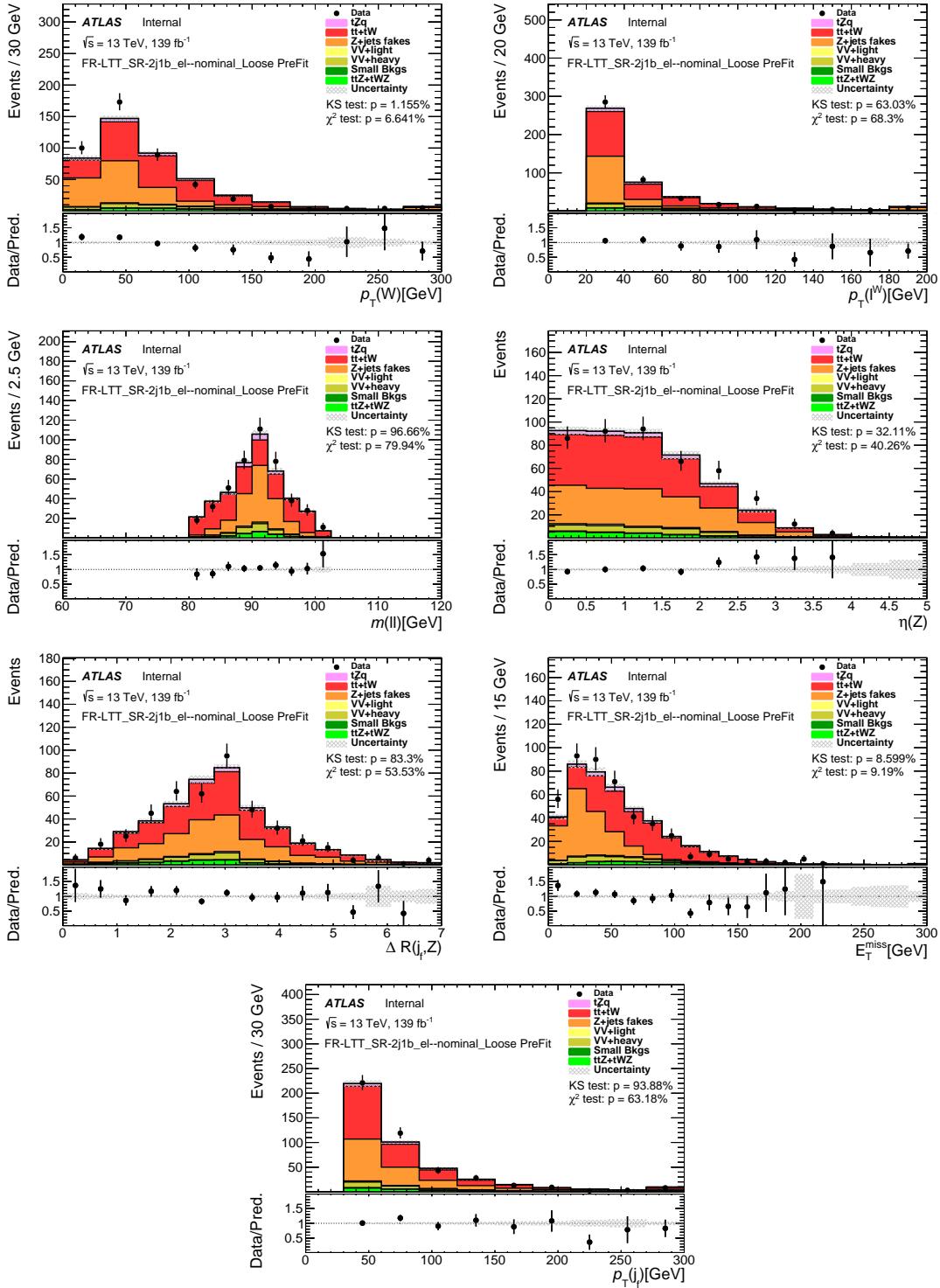


Figure 205: Stacked kinematic plots of neural-network training variables of the SR-2j1b-LTT\_el, in order of significance.

Not reviewed, for internal circulation only

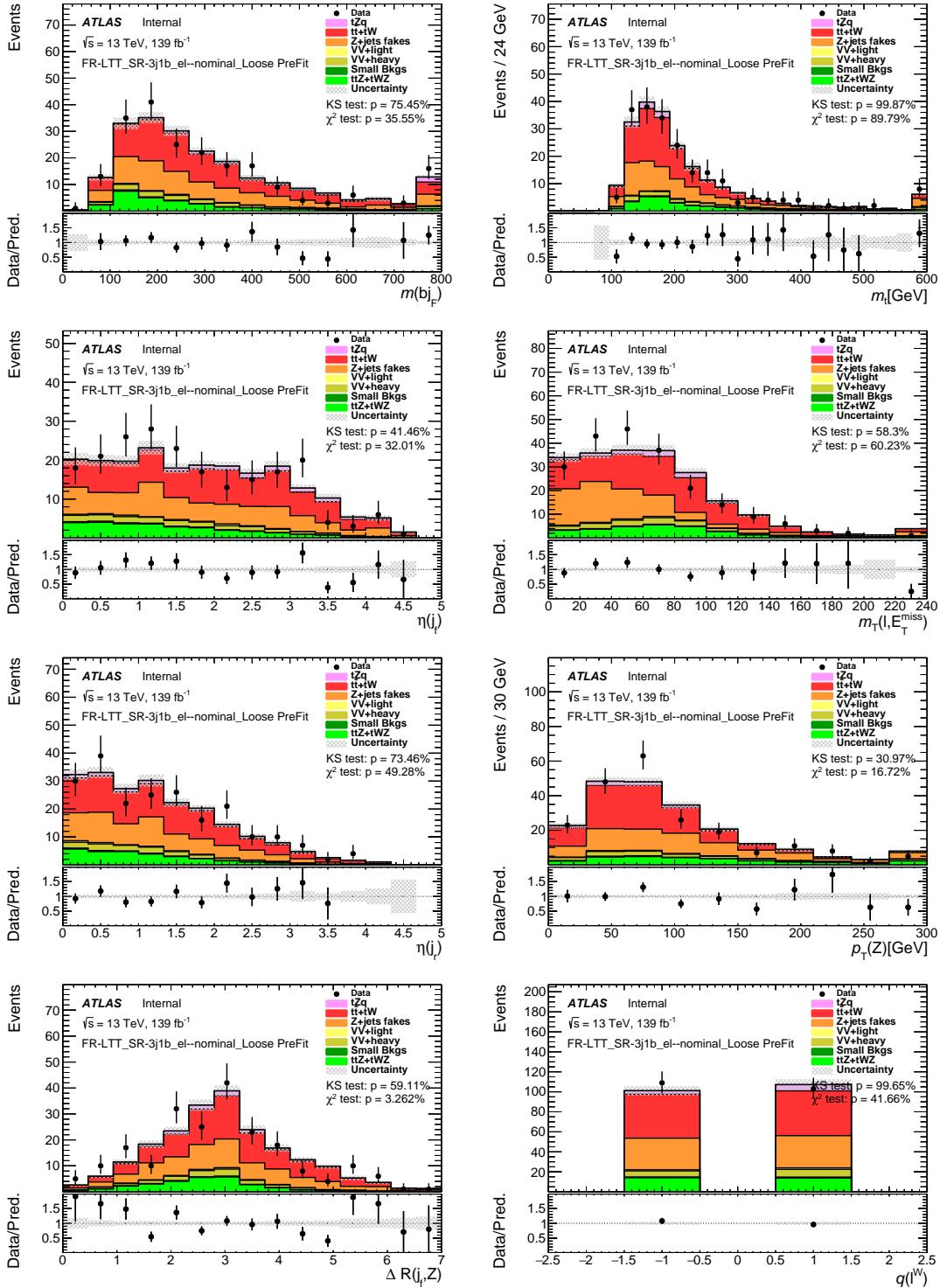


Figure 206: Stacked kinematic plots of neural-network training variables of the SR-3j1b-LTT\_el, in order of significance.

Not reviewed, for internal circulation only

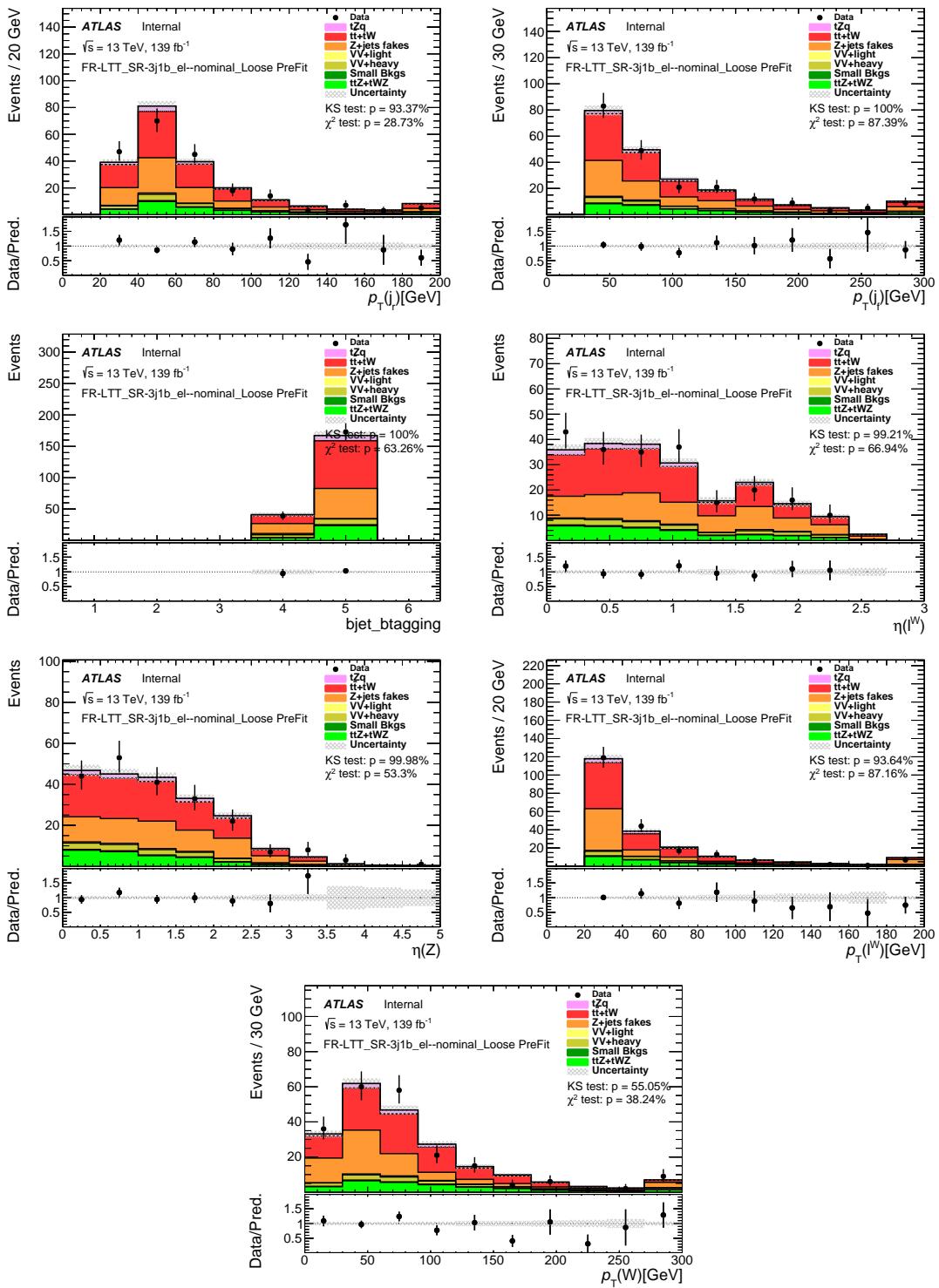


Figure 207: Stacked kinematic plots of neural-network training variables of the SR-3j1b-LTT\_el, in order of significance.

## 1440 E.1.2 SR LTTs with muon fake

Not reviewed, for internal circulation only

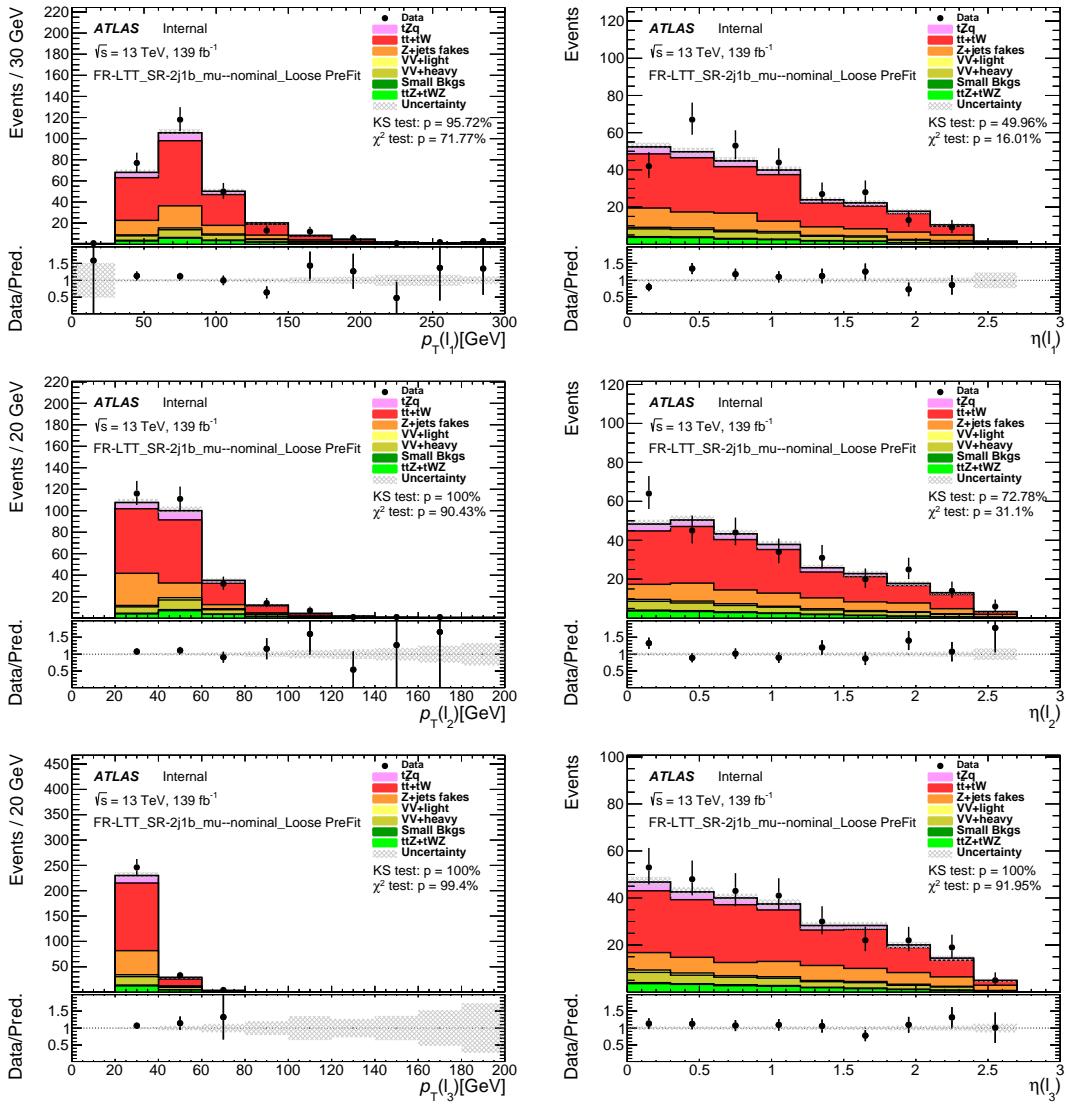


Figure 208: Comparison of data and MC predictions for reconstructed lepton-muon quantities for events in the SR-2j1b-LTT\_mu.

Not reviewed, for internal circulation only

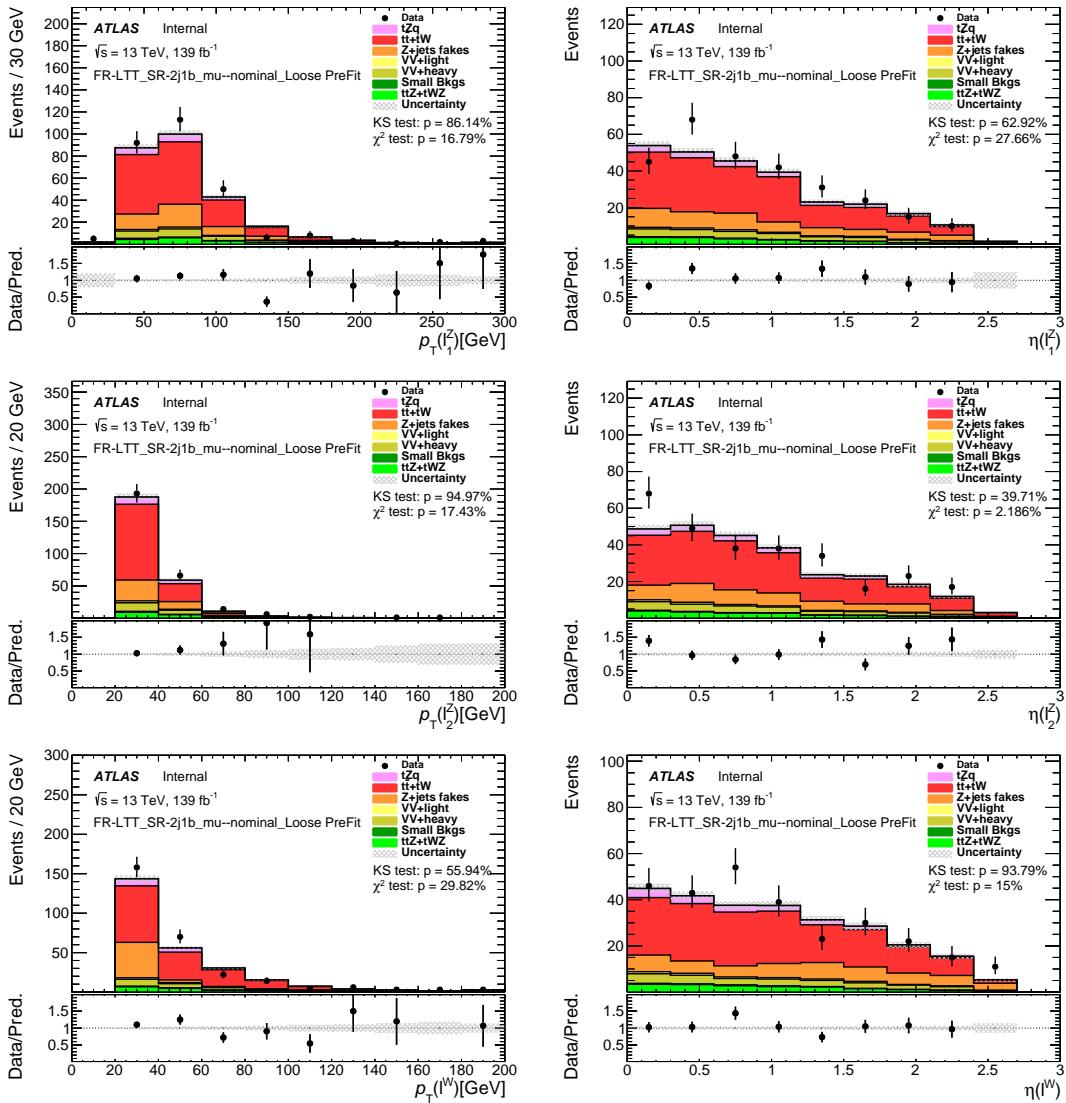


Figure 209: Comparison of data and MC predictions for reconstructed lepton-related quantities for events in the SR-2j1b-LTT\_mu.

Not reviewed, for internal circulation only

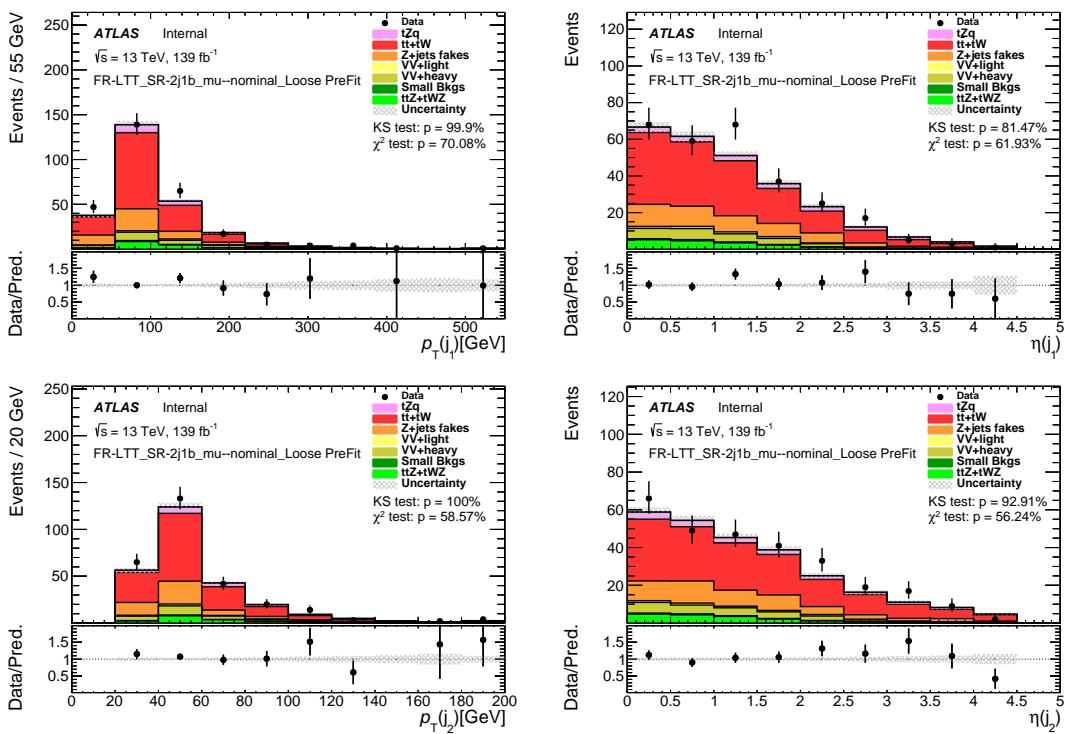


Figure 210: Comparison of data and MC predictions for reconstructed jet-related quantities for events in the SR-2j1b-LTT\_mu.

Not reviewed, for internal circulation only

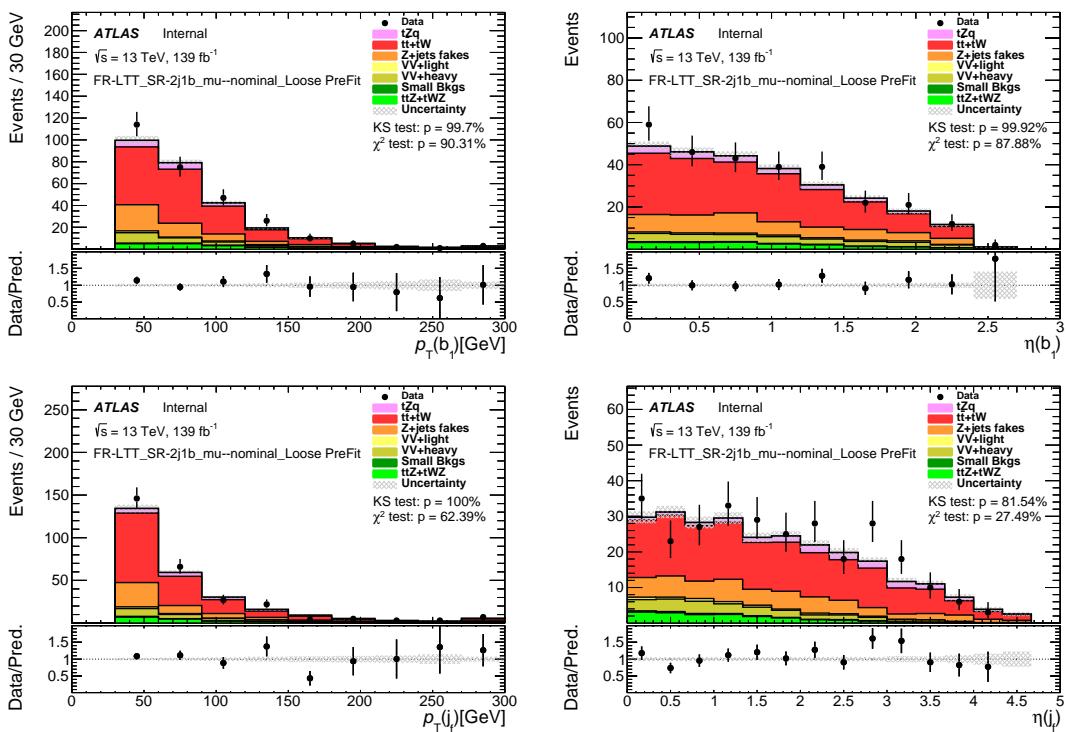


Figure 211: Comparison of data and MC predictions for reconstructed jet-related quantities for events in the SR-2j1b-LTT\_mu.

Not reviewed, for internal circulation only

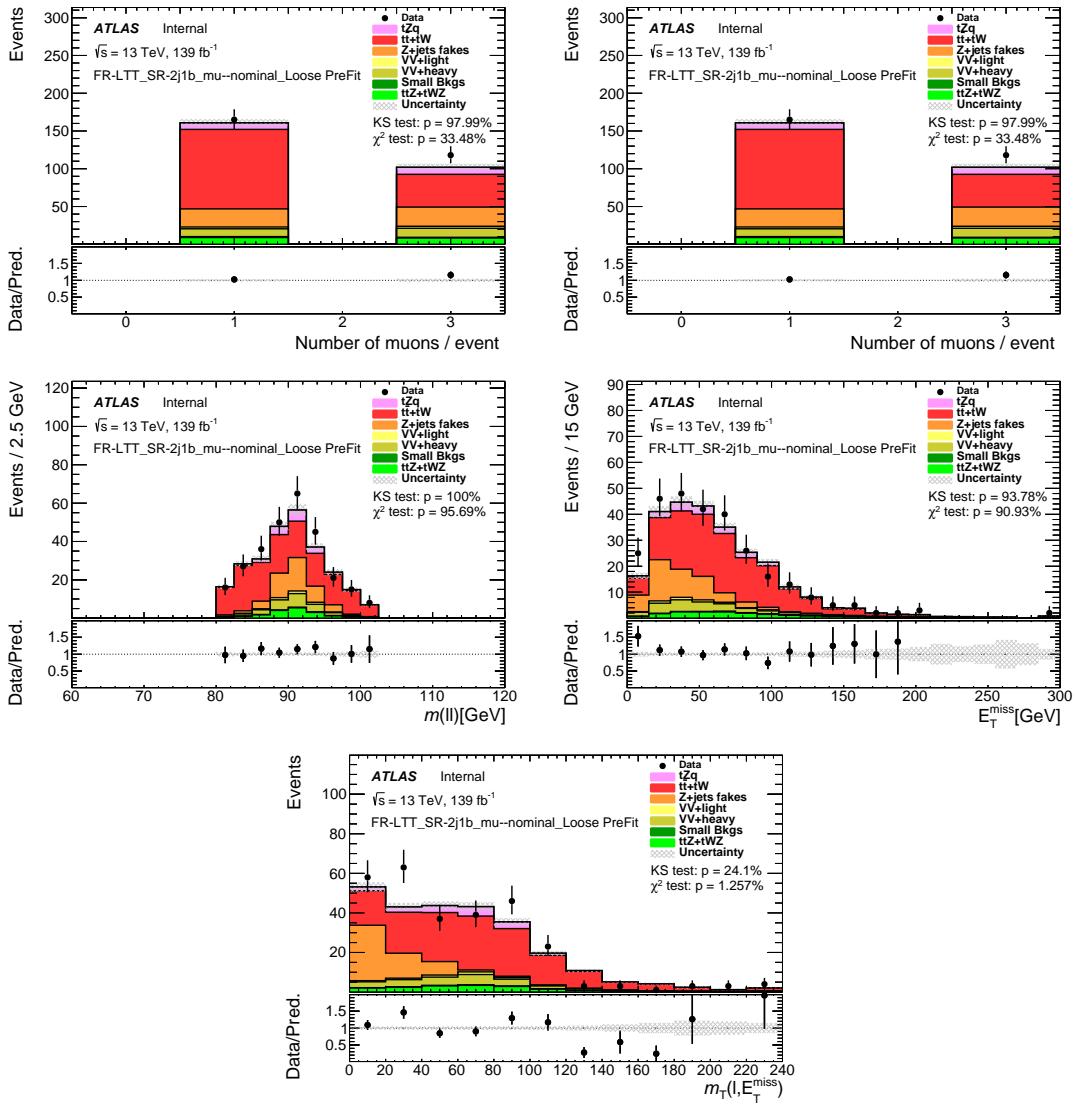


Figure 212: Comparison of data and MC predictions for reconstructed event-ruinated quantities for events in the SR-2j1b-LTT\_mu.

Not reviewed, for internal circulation only

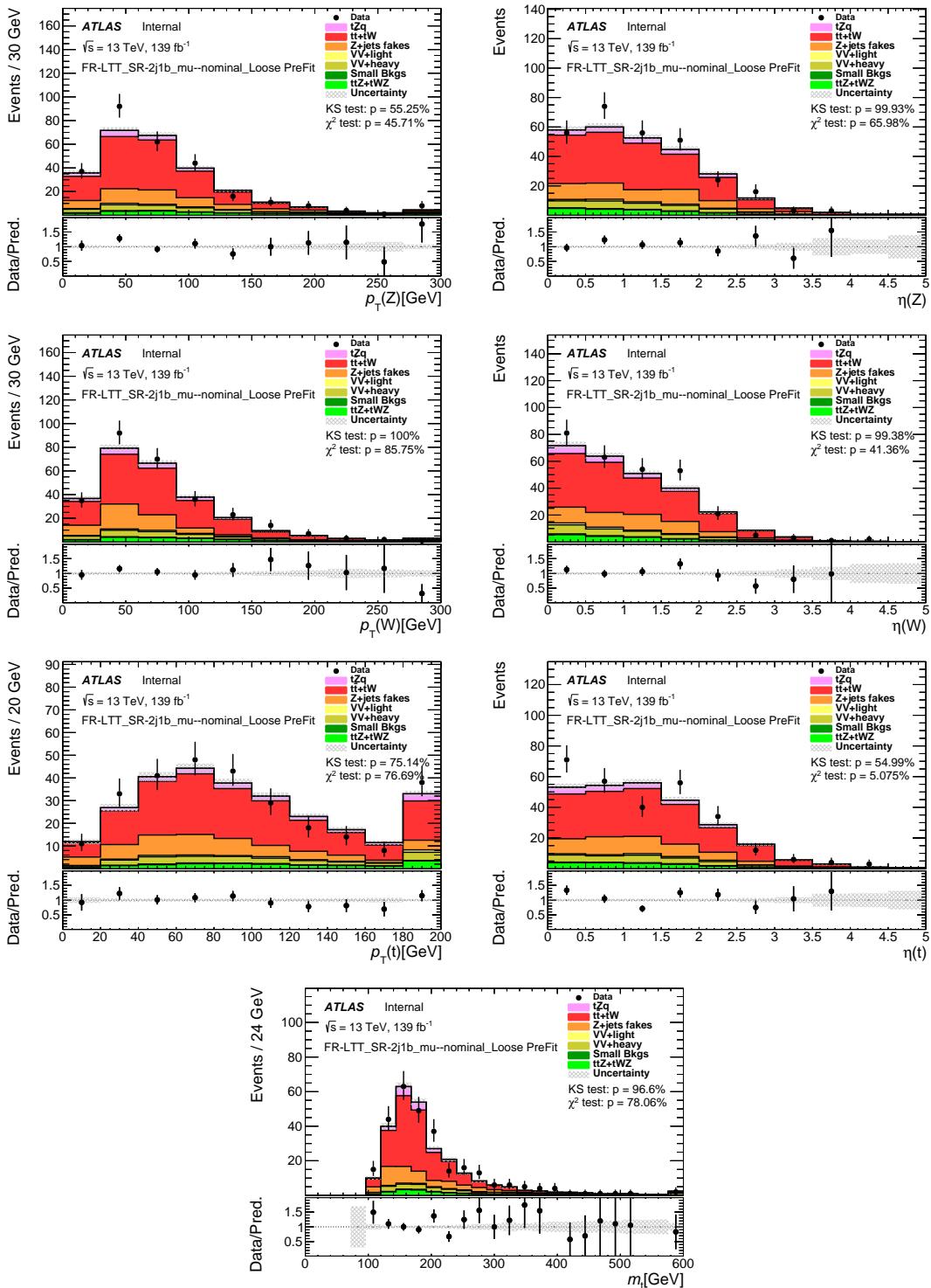


Figure 213: Comparison of data and MC predictions for reconstructed event-ruated quantities for events in the SR-2j1b-LTT\_mu.

Not reviewed, for internal circulation only

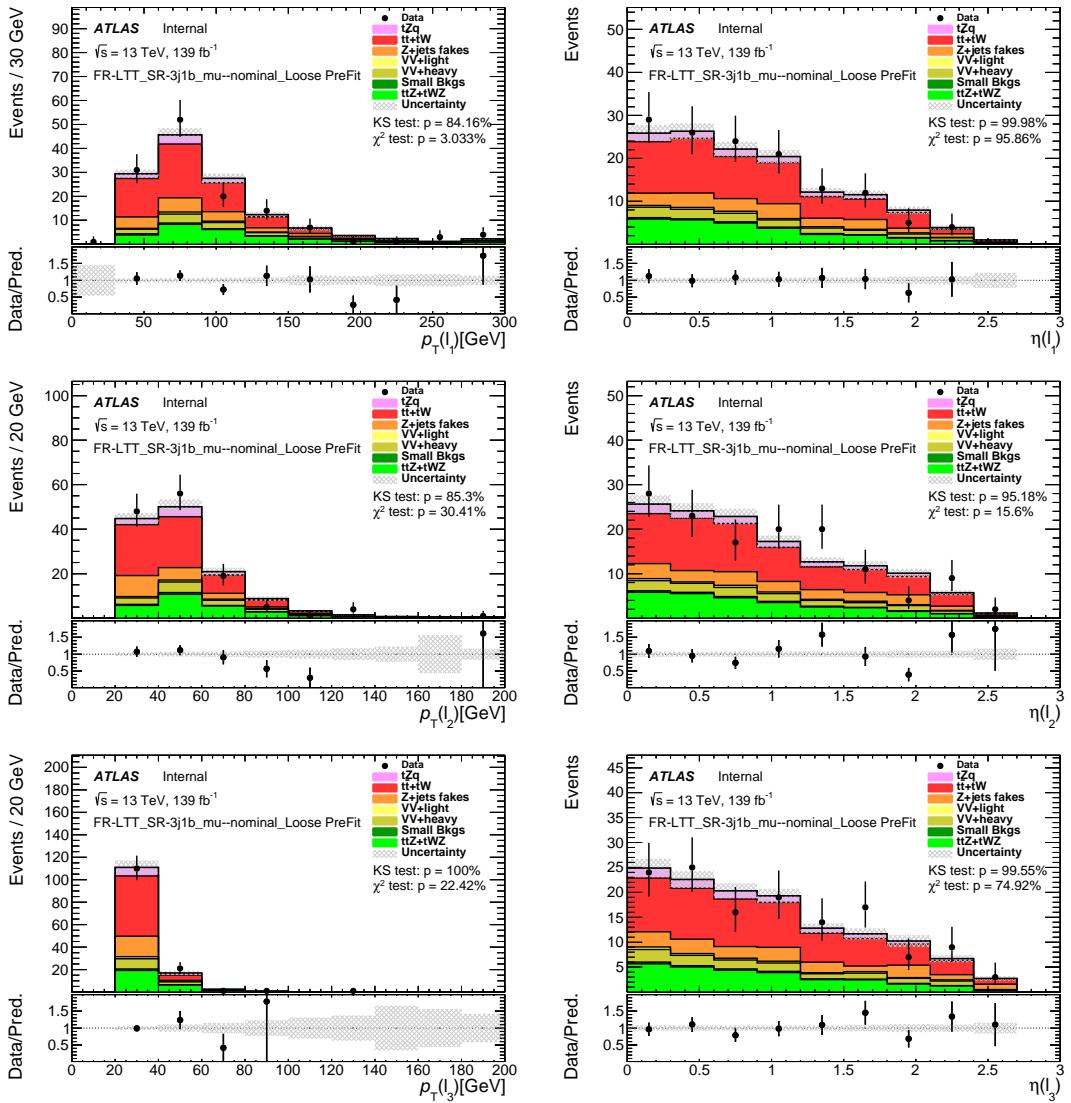


Figure 214: Comparison of data and MC predictions for reconstructed lepton-related quantities for events in the SR-3j1b-LTT\_mu.

Not reviewed, for internal circulation only

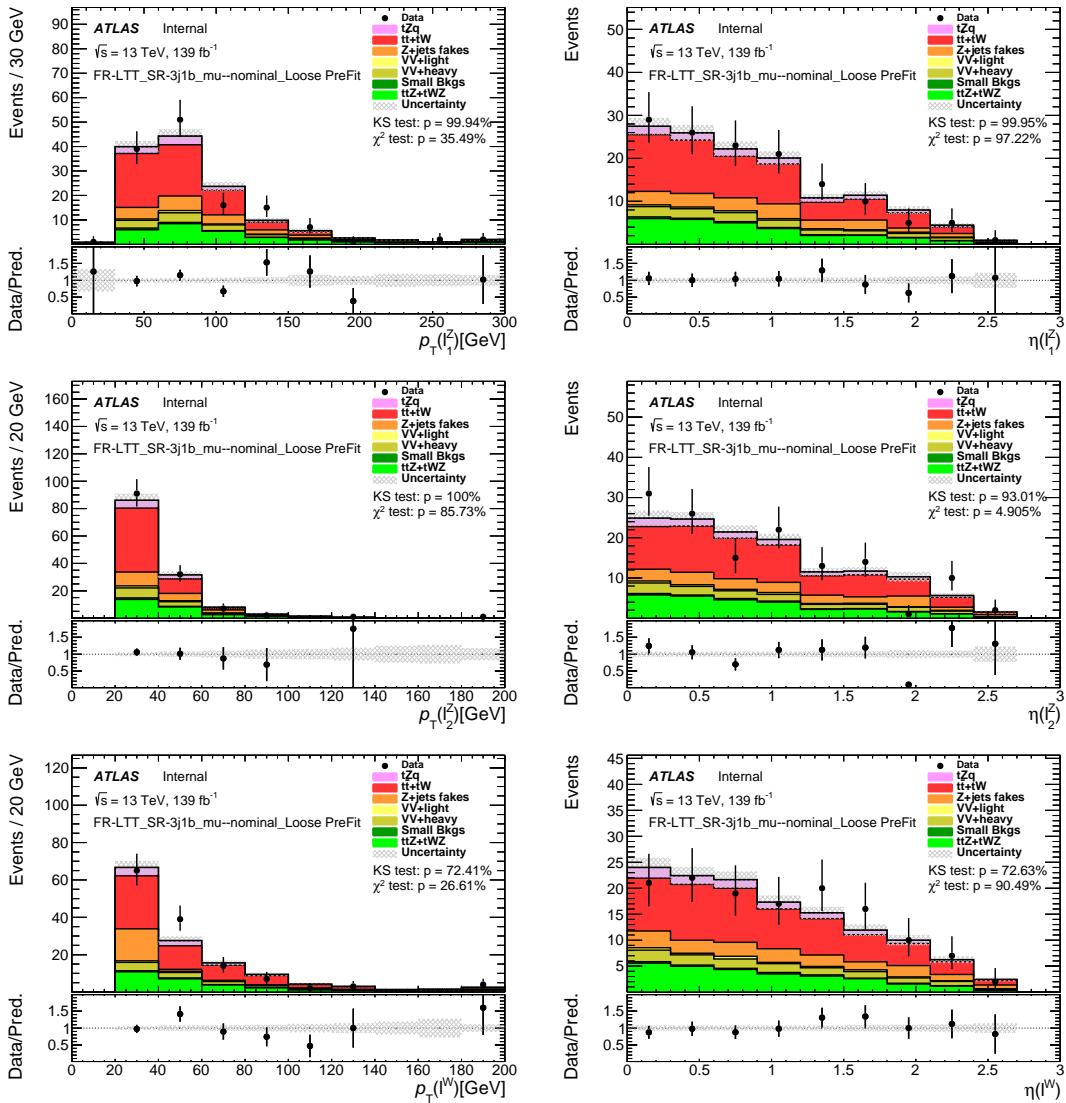


Figure 215: Comparison of data and MC predictions for reconstructed lepton-related quantities for events in the SR-3j1b-LTT\_mu.

Not reviewed, for internal circulation only

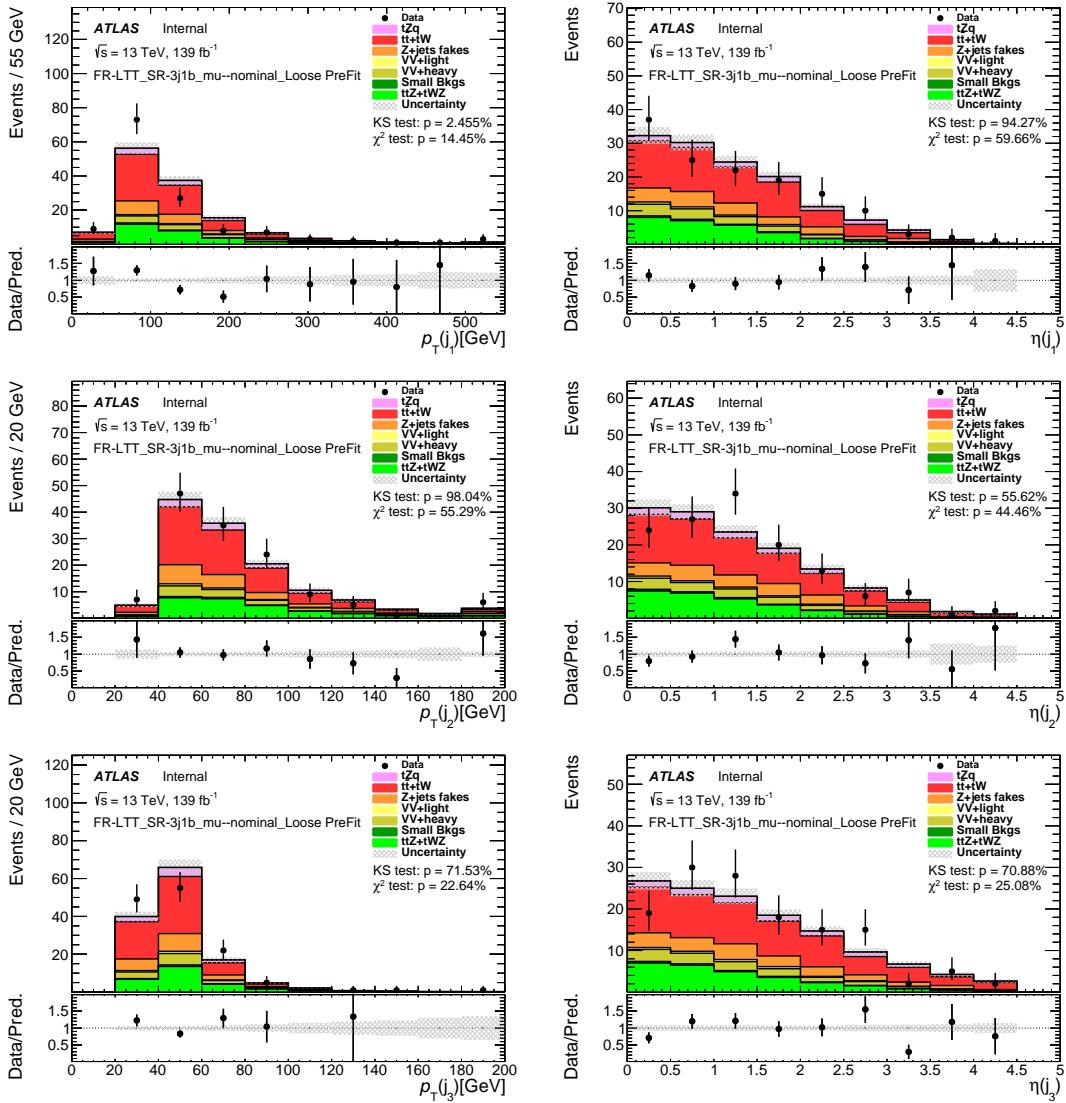


Figure 216: Comparison of data and MC predictions for reconstructed jet-related quantities for events in the SR-3j1b-LTT\_mu.

Not reviewed, for internal circulation only

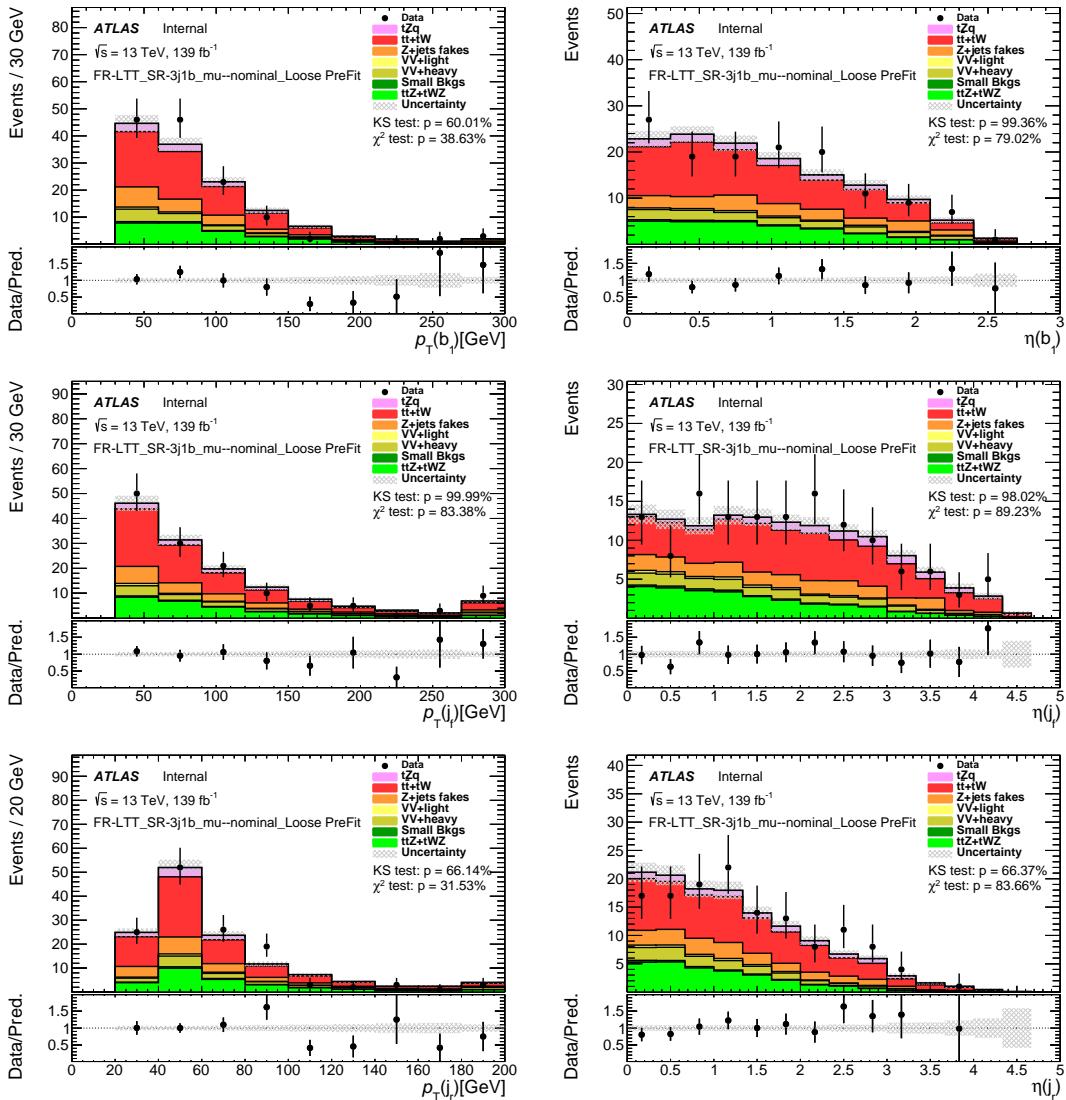


Figure 217: Comparison of data and MC predictions for reconstructed jet-related quantities for events in the SR-3j1b-LTT\_mu.

Not reviewed, for internal circulation only

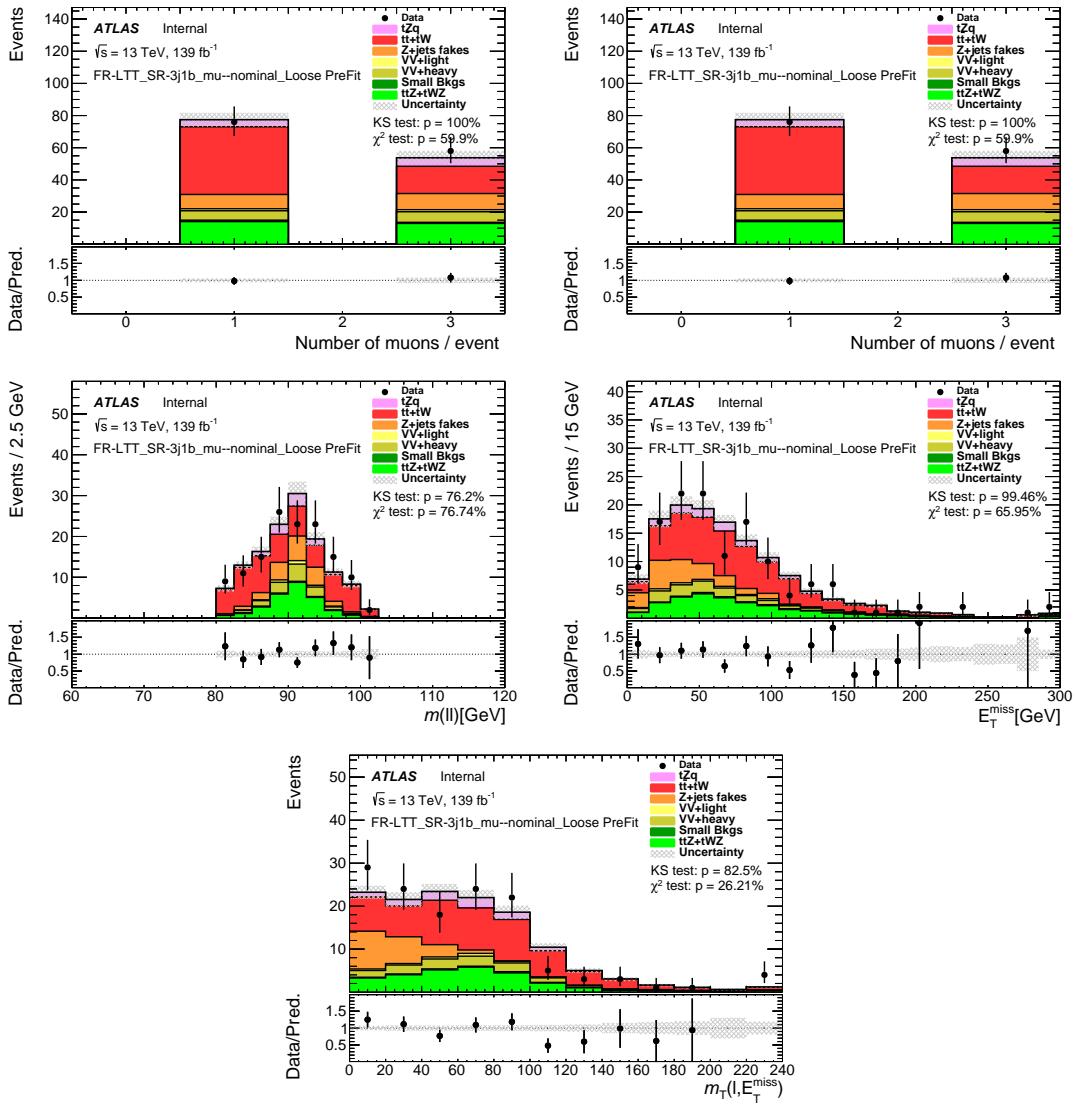


Figure 218: Comparison of data and MC predictions for reconstructed event-ruinated quantities for events in the SR-3j1b-LTT\_mu.

Not reviewed, for internal circulation only

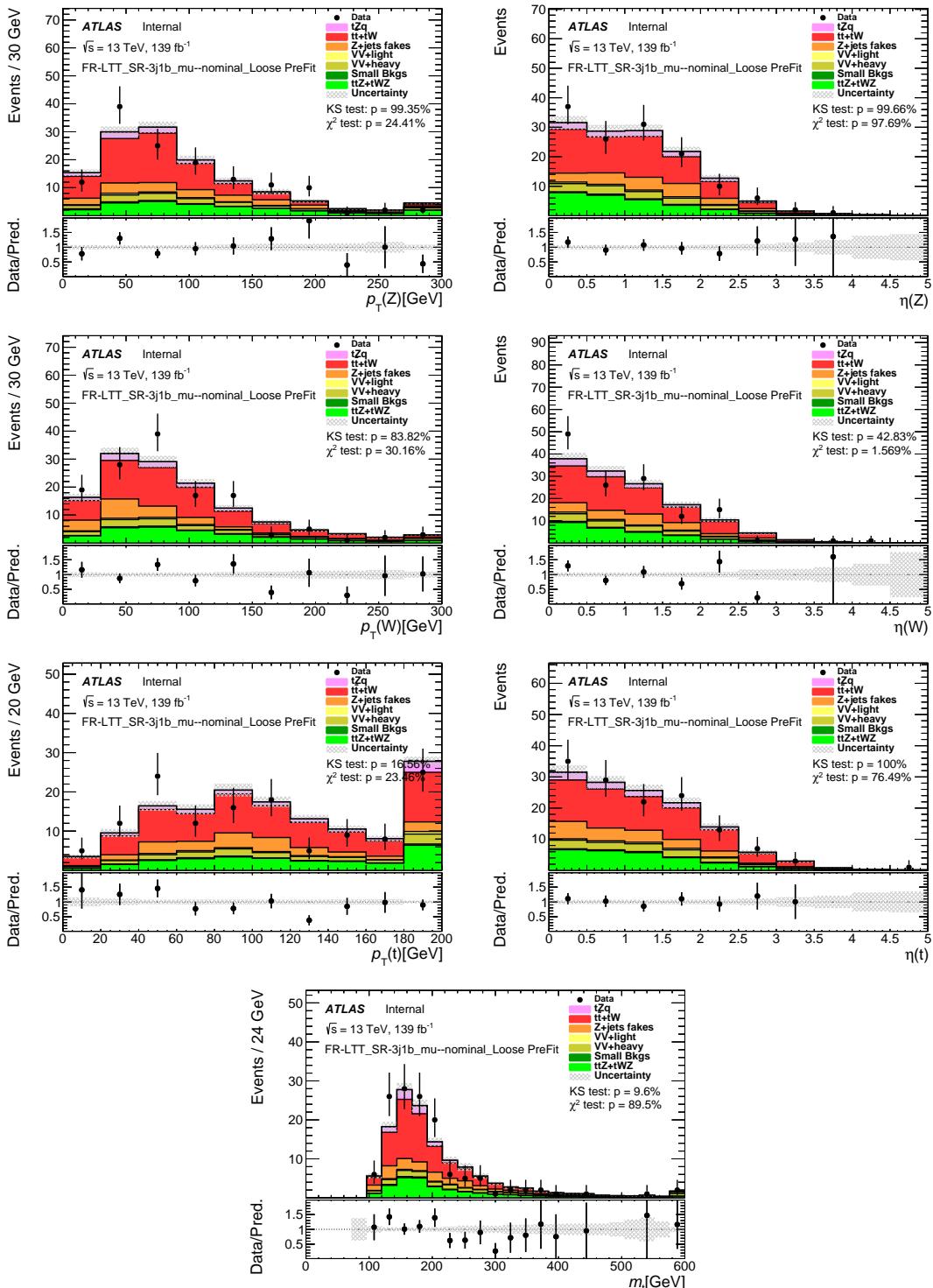


Figure 219: Comparison of data and MC predictions for reconstructed event-ruated quantities for events in the SR-3j1b-LTT\_mu.

Not reviewed, for internal circulation only

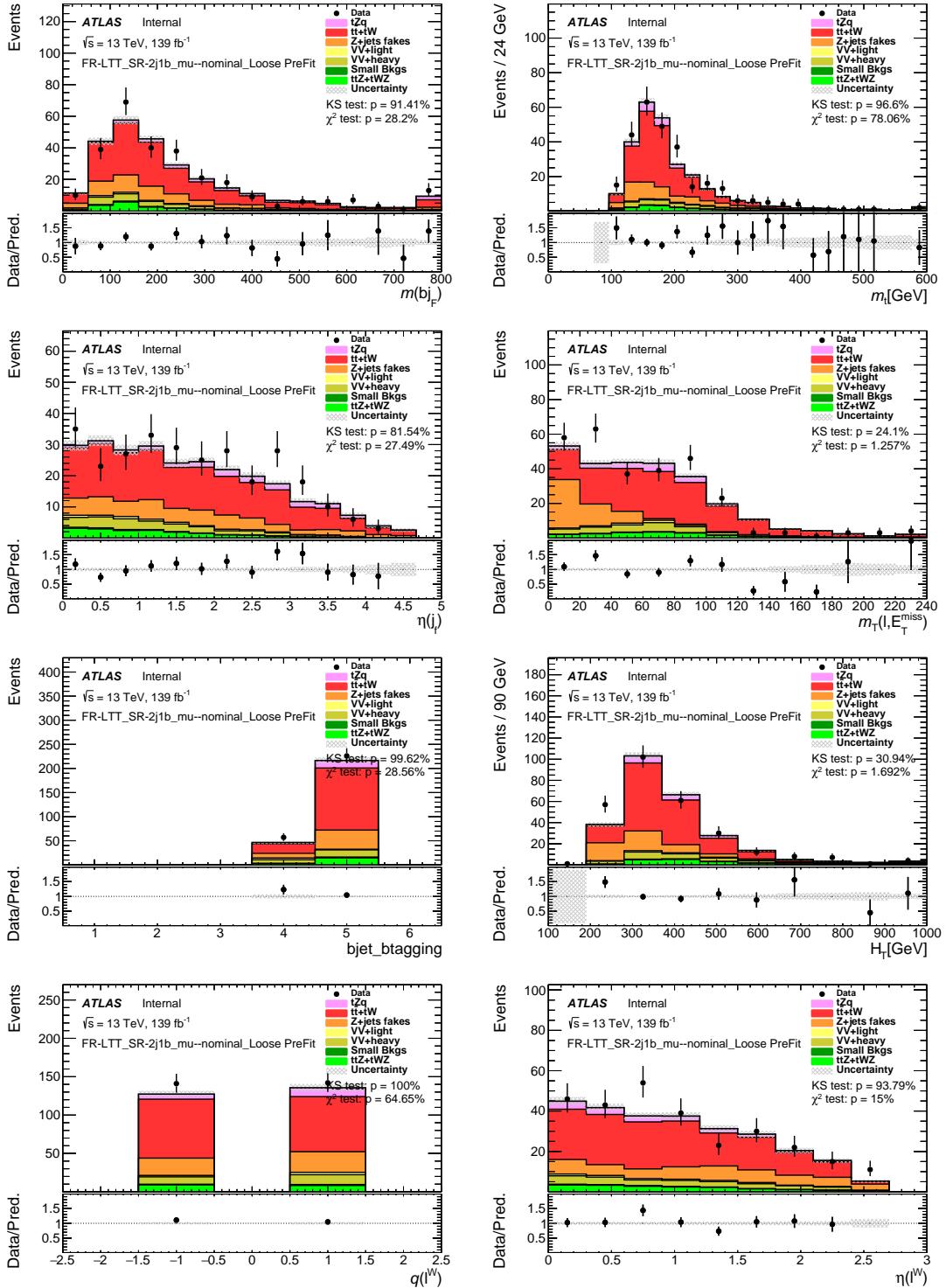


Figure 220: Stacked kinematic plots of neural-network training variables of the SR-2j1b-LTT\_mu, in order of significance.

Not reviewed, for internal circulation only

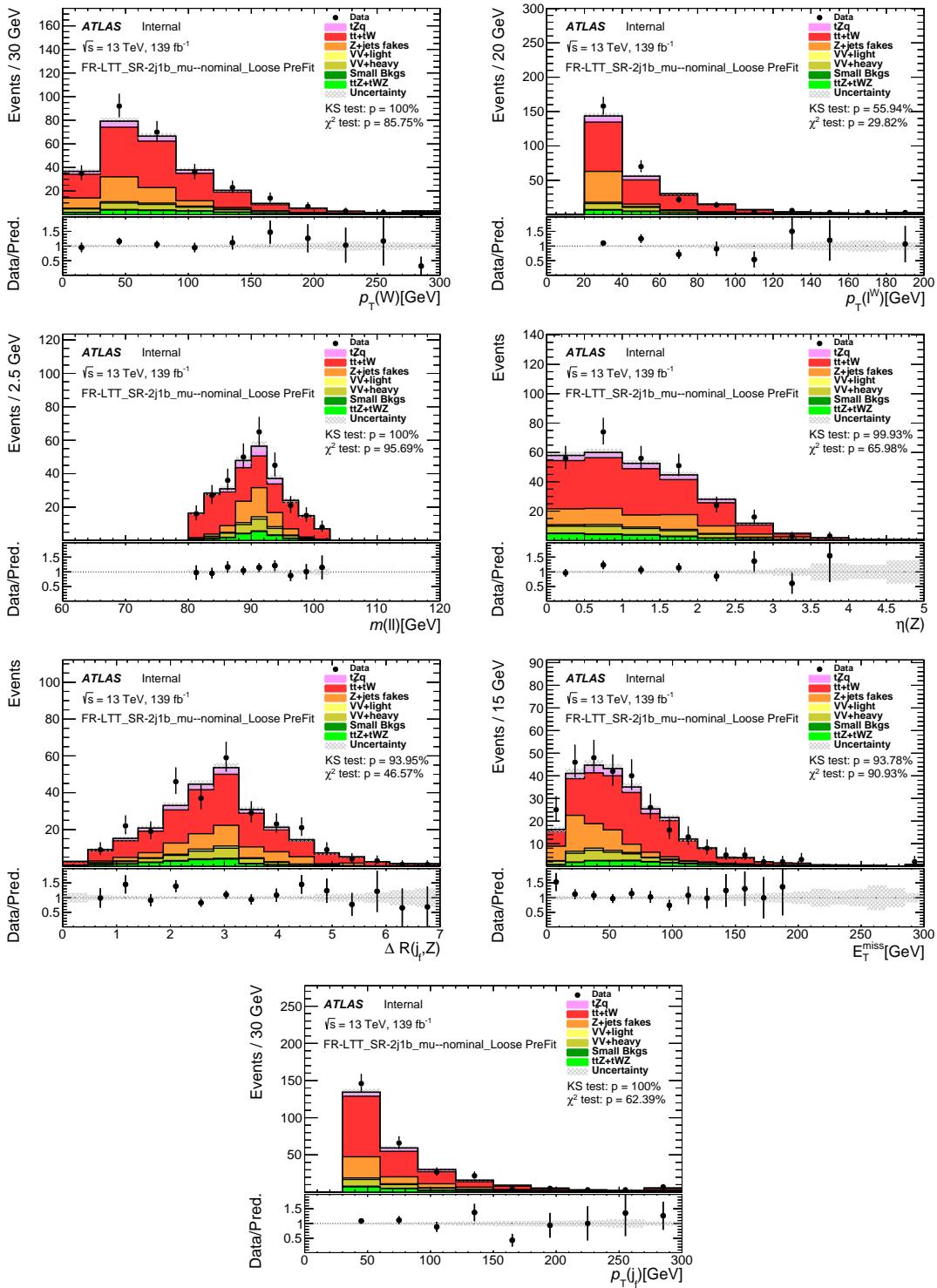


Figure 221: Stacked kinematic plots of neural-network training variables of the SR-2j1b-LTT\_mu, in order of significance.

Not reviewed, for internal circulation only

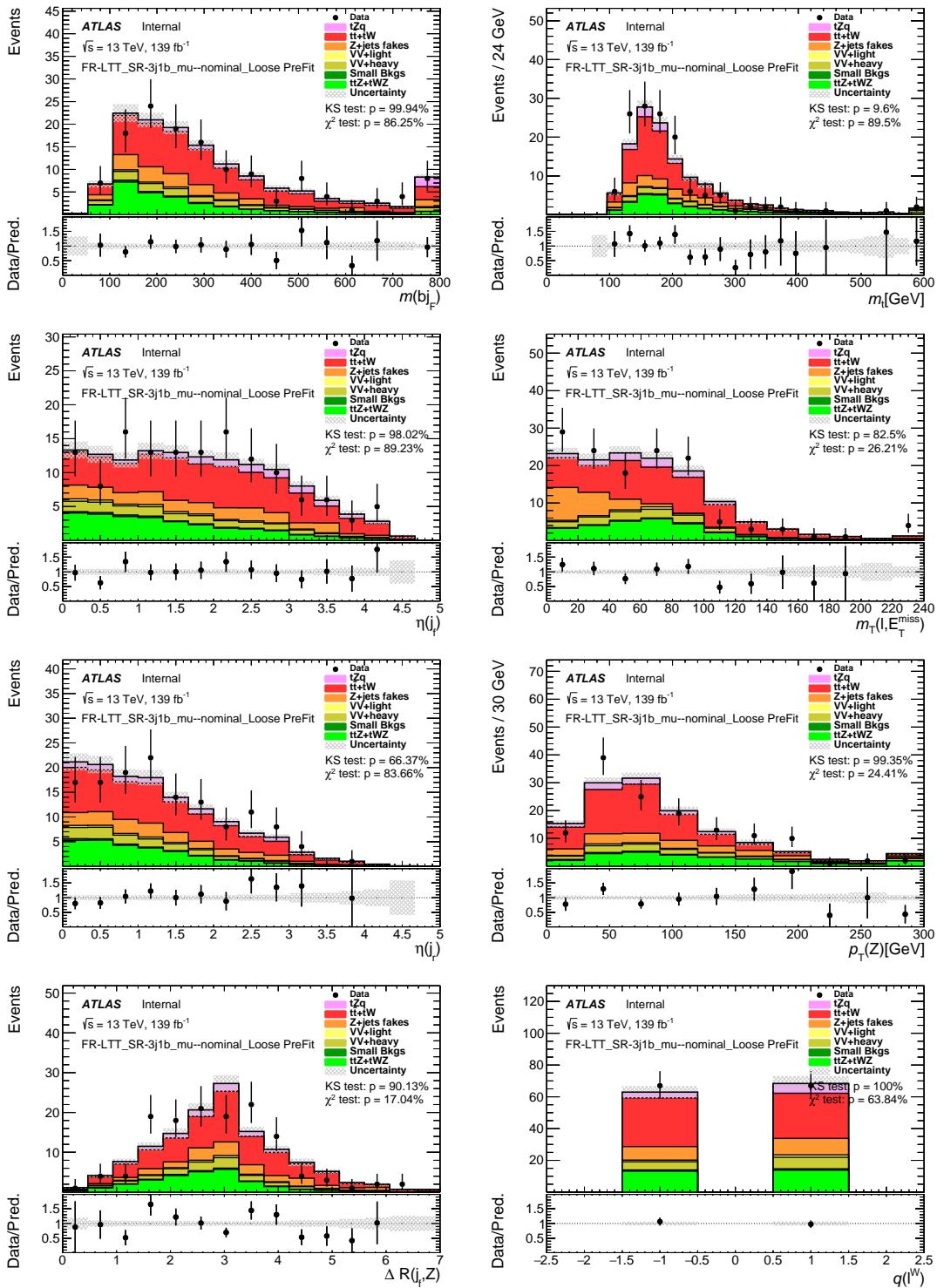


Figure 222: Stacked kinematic plots of neural-network training variables of the SR-2j1b-LTT\_mu, in order of significance.

Not reviewed, for internal circulation only

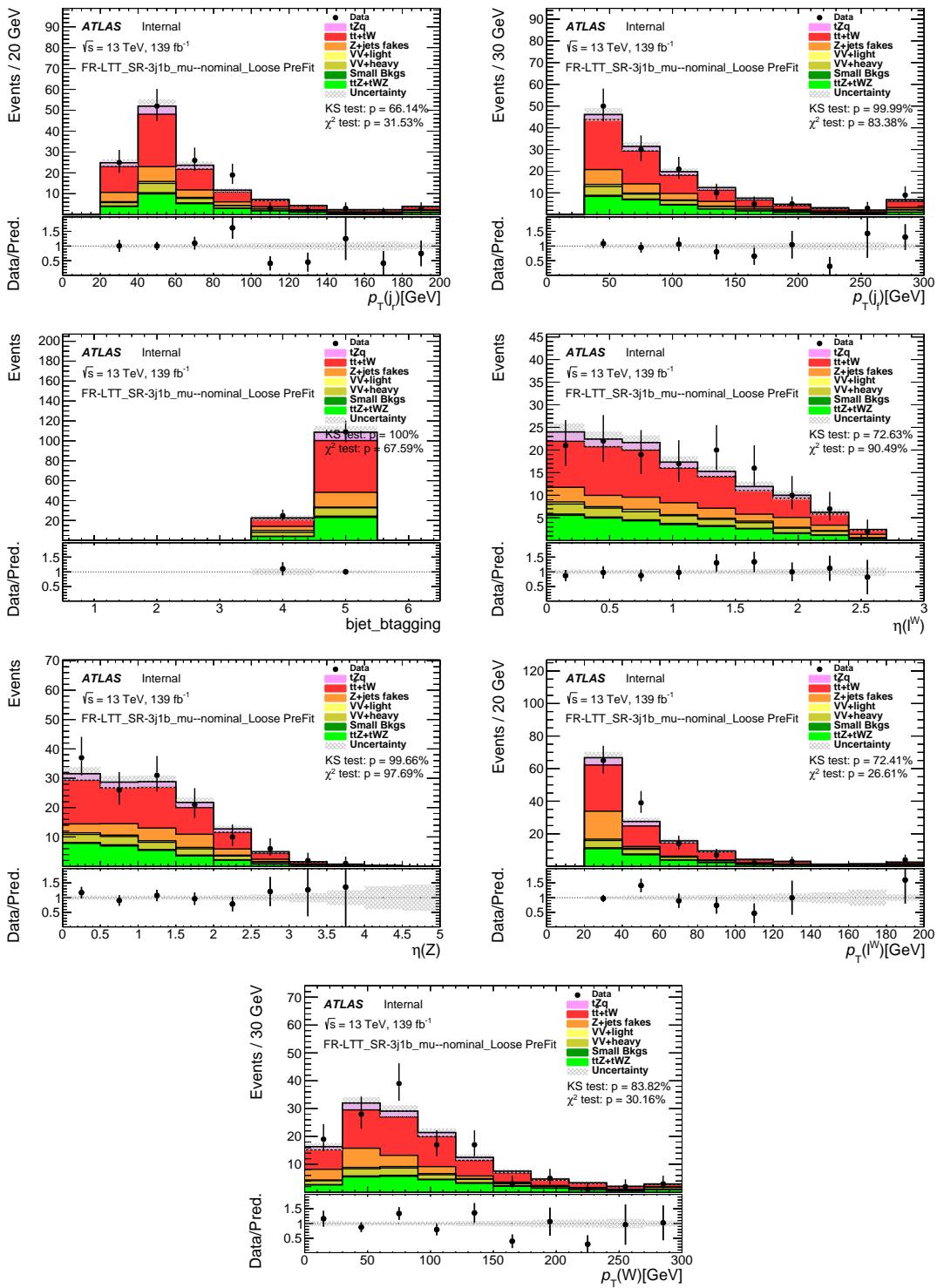


Figure 223: Stacked kinematic plots of neural-network training variables of the SR-2j1b-LTT\_mu, in order of significance.

## 1441 E.2 BJR vs MC shape comparisons

### 1442 E.2.1 Shape comparison between $b$ -jet replacement and MC for $t\bar{t}$

1443 Studies presented in the following were done on events with  $m_T(W) > 20$  GeV.

1444 In order to validate the method, the kinematic distributions for  $t\bar{t}$  events processed using the BJR method  
 1445 are compared with distribution obtained from the  $t\bar{t}$  MC sample, after applying the standard trilepton  
 1446 selection. The plots are shown in Figs. 224 to 226 for the 2j1b SR and Figs. 227 to 229 for the 3j1b SR.  
 1447 Reasonable agreement is observed between the BJR and MC  $t\bar{t}$  samples and the statistical fluctuations are  
 1448 considerably reduced when using BJR with respect to the pure MC estimate.

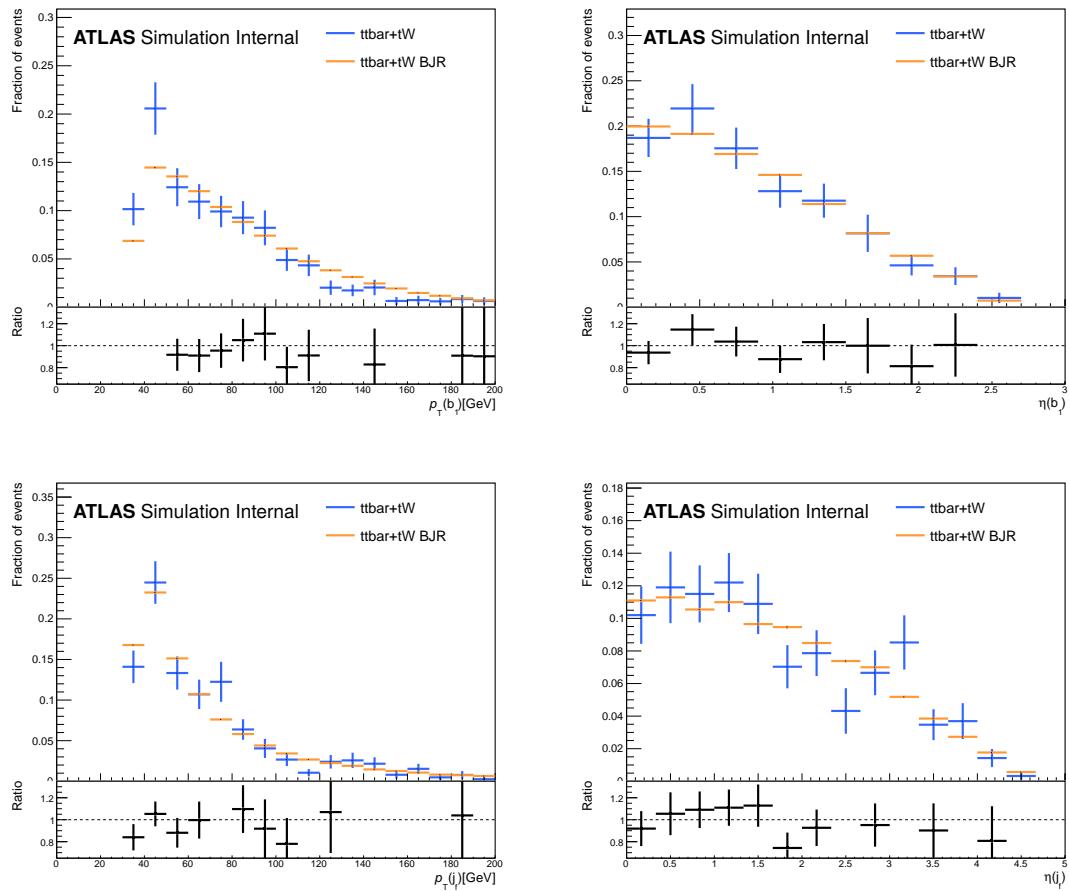
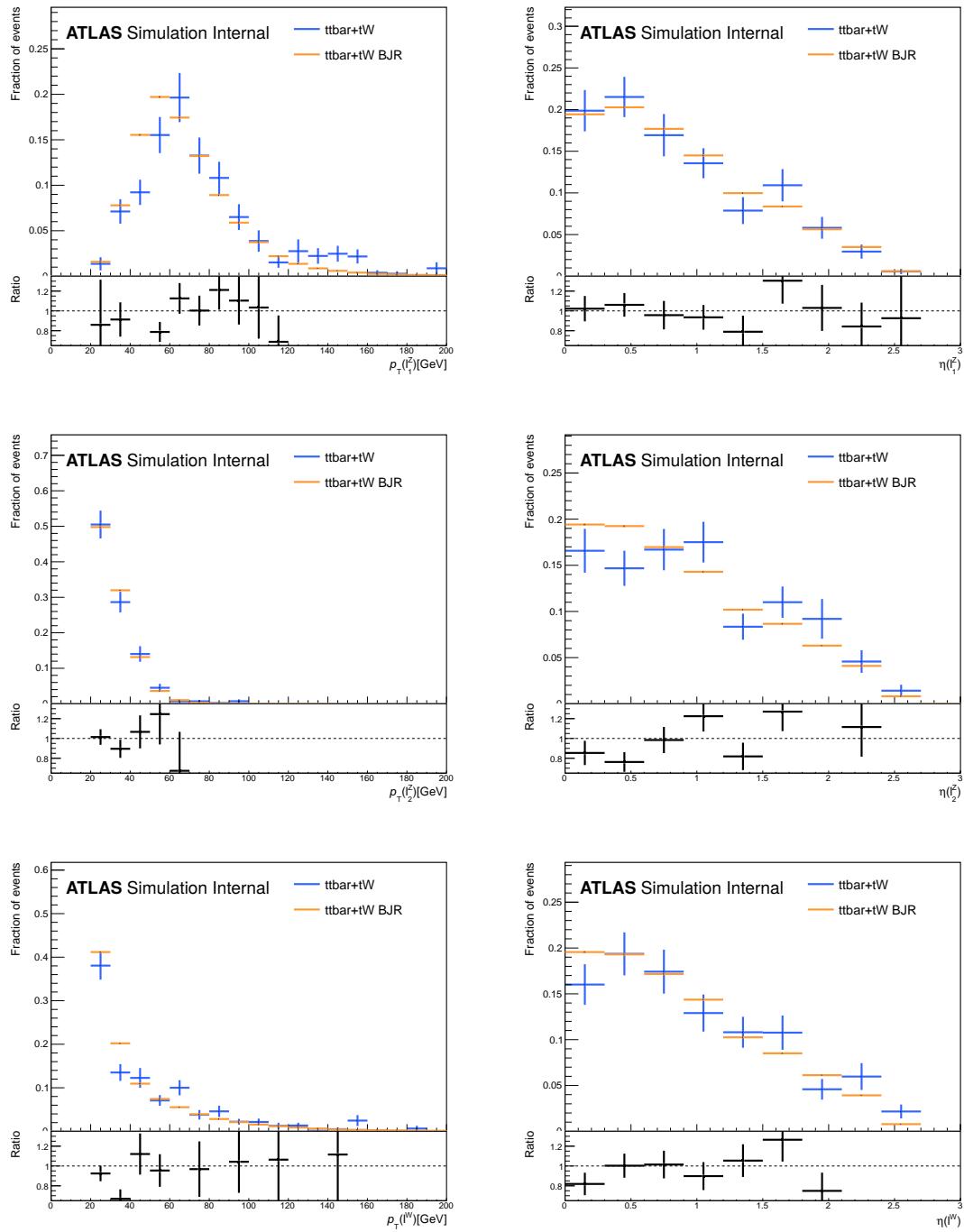
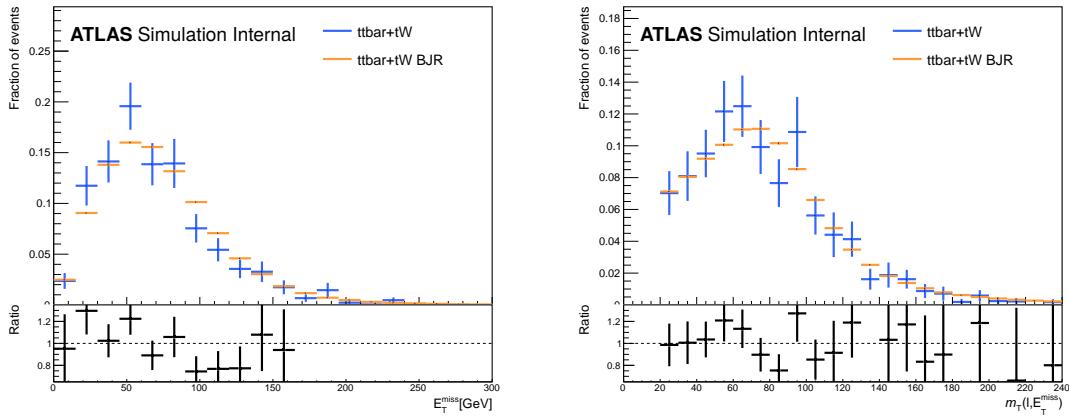
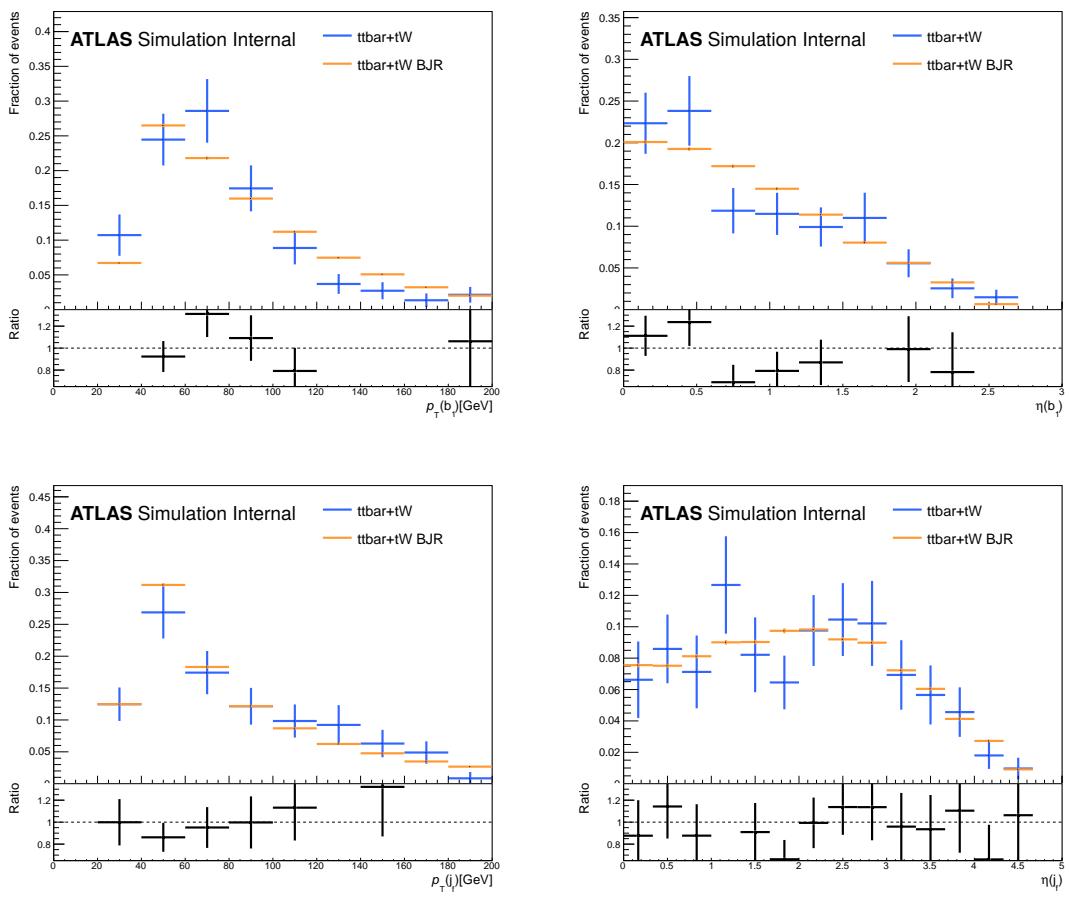


Figure 224: Kinematic distribution of jet related quantities in  $t\bar{t}$  events in the 2j1b SR.

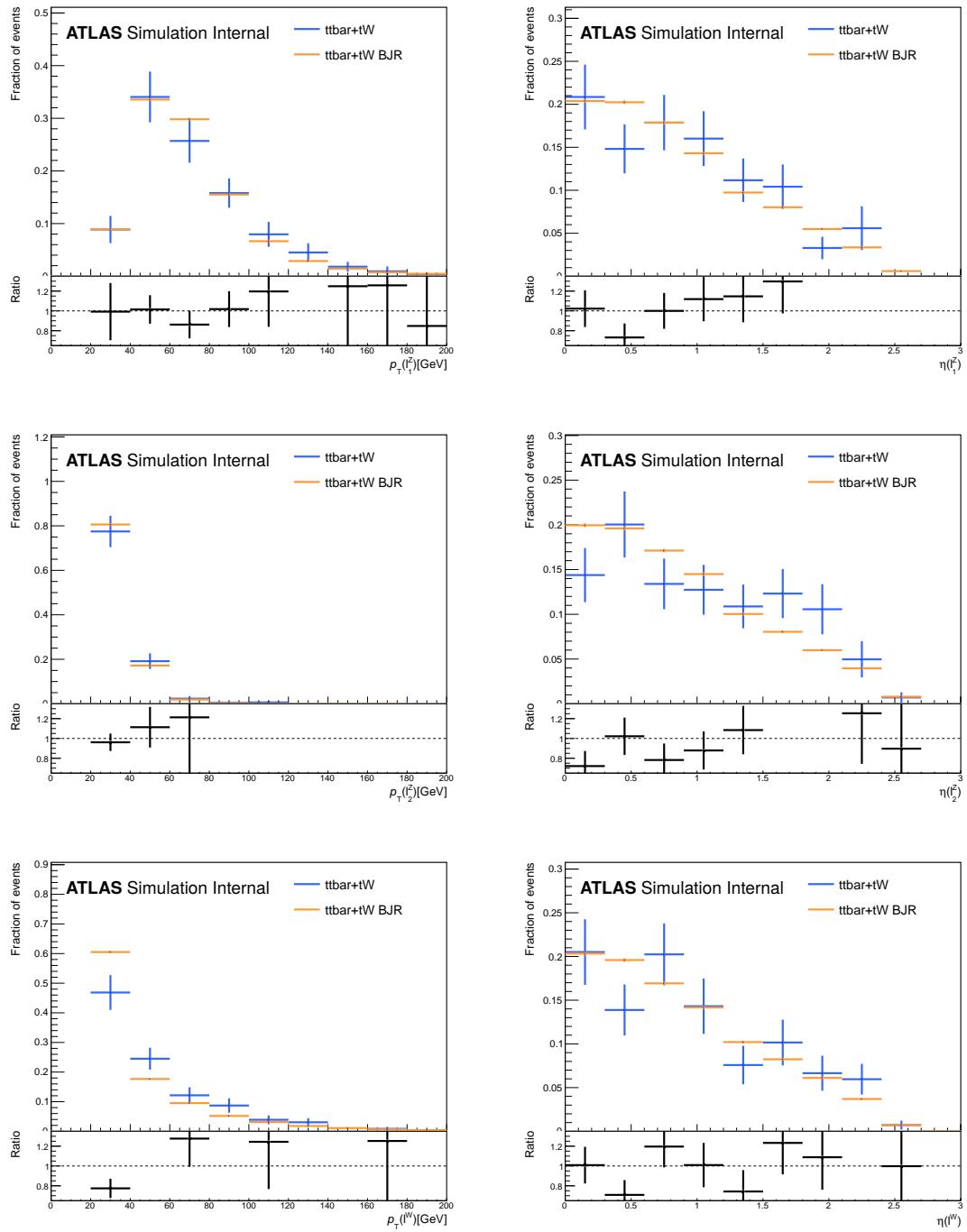
Not reviewed, for internal circulation only

Figure 225: Kinematic distribution of lepton related quantities in  $t\bar{t}$  events in the 2j1b SR.

Not reviewed, for internal circulation only

Figure 226:  $E_T^{\text{miss}}$  and  $m_T(W)$  distributions in  $t\bar{t}$  events in the 2j1b SR.Figure 227: Kinematic distribution of jet related quantities in  $t\bar{t}$  events in the 3j1b SR.

Not reviewed, for internal circulation only

Figure 228: Kinematic distribution of lepton related quantities in  $t\bar{t}$  events in the 3j1b SR.

Not reviewed, for internal circulation only

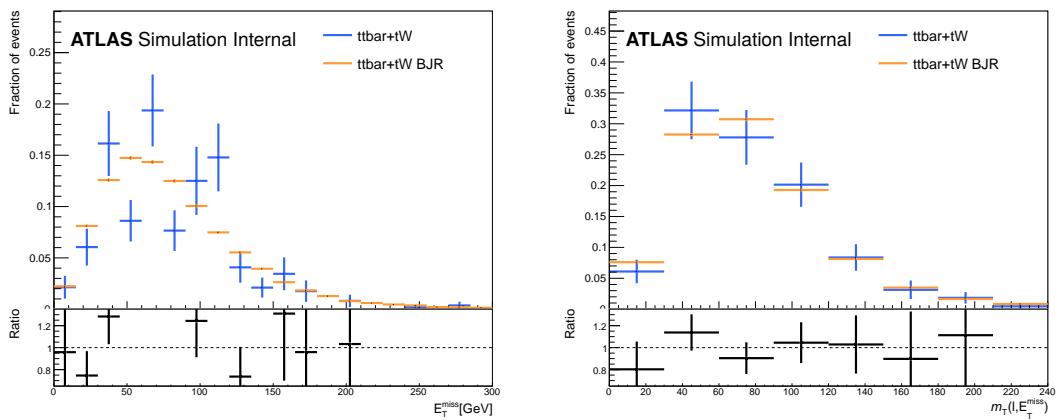
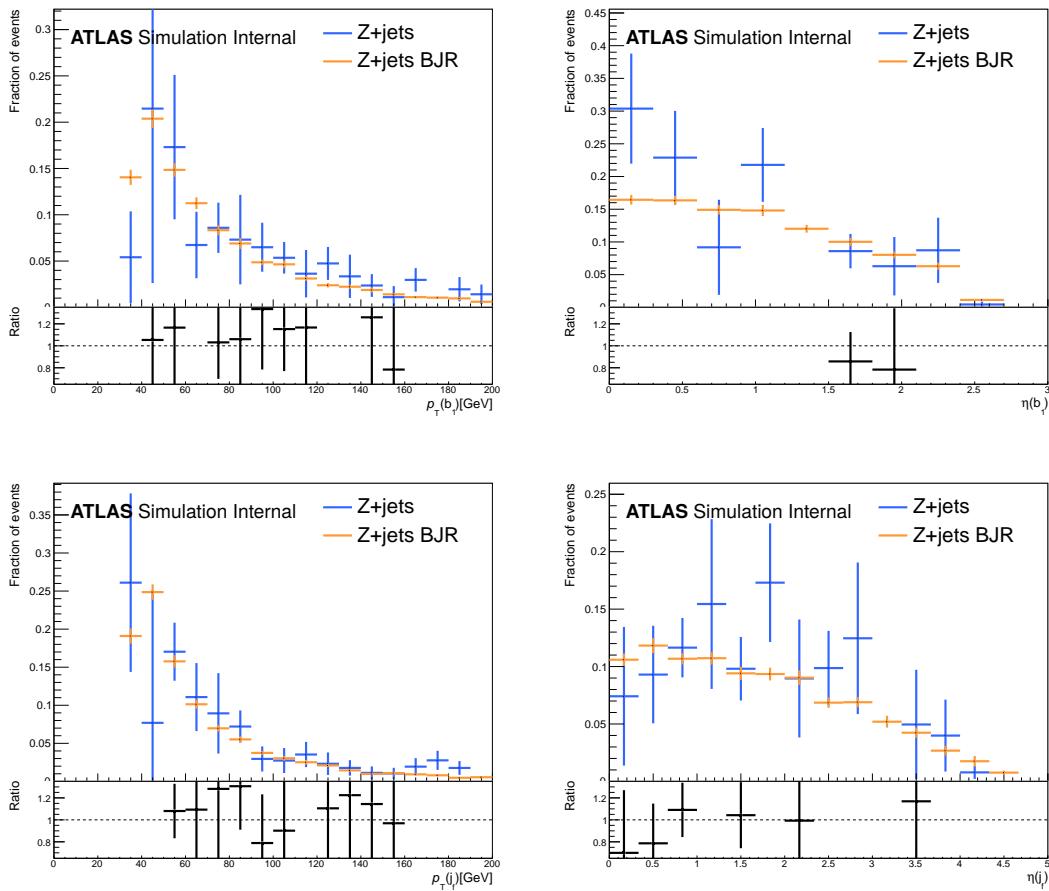


Figure 229:  $E_T^{\text{miss}}$  and  $m_T(W)$  distributions in  $t\bar{t}$  events in the 3j1b SR.

1449 **E.2.2 Shape comparison between  $b$ -jet replacement and MC for  $Z + \text{jets}$** 1450 Studies presented in the following were done on events with  $m_T(W) > 20 \text{ GeV}$ .

1451 Similar plots showing a comparison between the MC and the BJR sample for  $Z + \text{jets}$  events are shown in  
 1452 Figs. 230 to 232 for the 2j1b SR and Figs. 233 to 235 for the 3j1b SR. As it can be seen in these plots, a  
 1453 very low number of events pass the trilepton selection in the  $Z + \text{jets}$  MC. Further validation of this method  
 1454 is given by the very good agreement between data and MC observed in all the control and validation  
 1455 regions.

Not reviewed, for internal circulation only

Figure 230: Kinematic distribution of jet related quantities in  $Z + \text{jets}$  events in the 2j1b SR.

Not reviewed, for internal circulation only

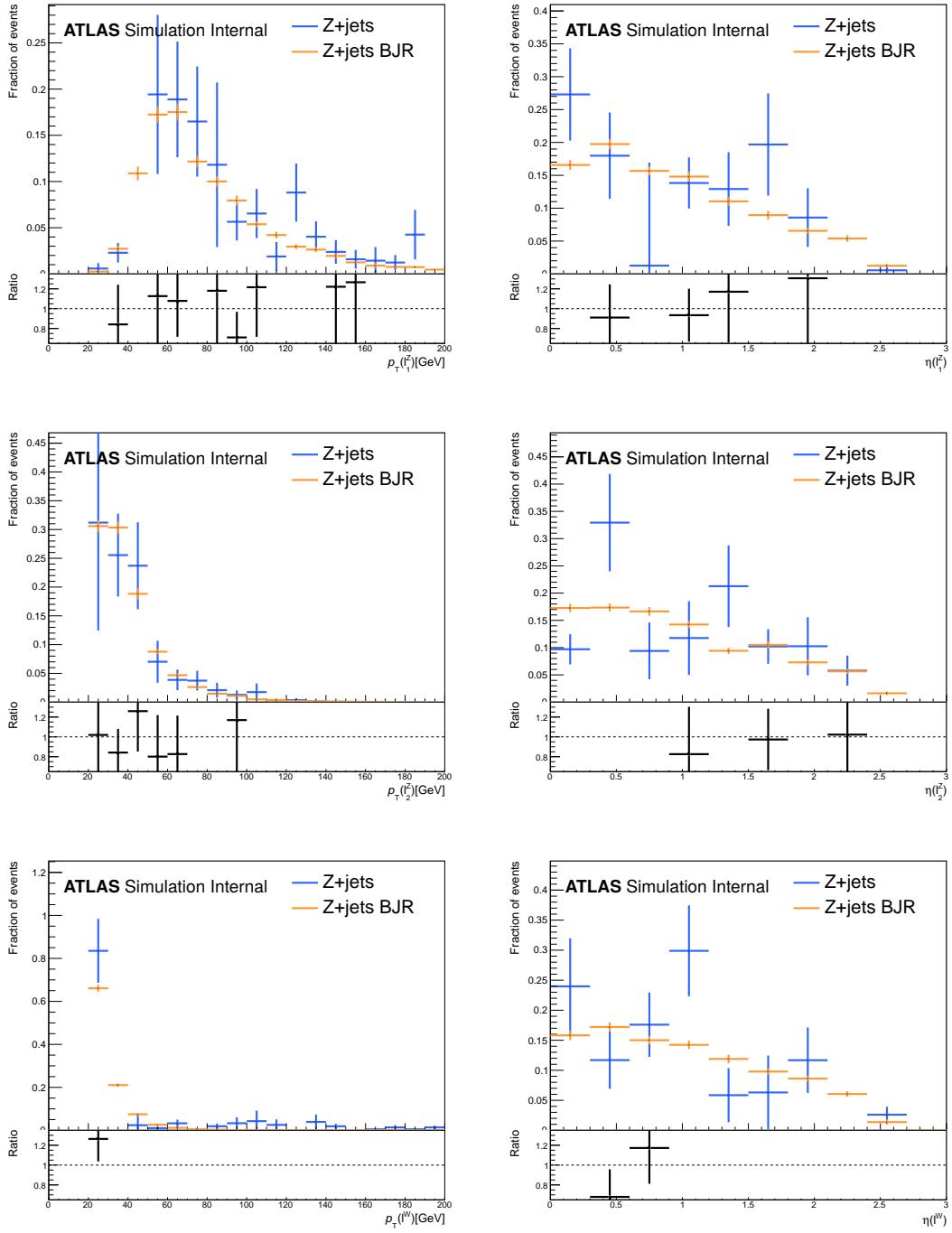
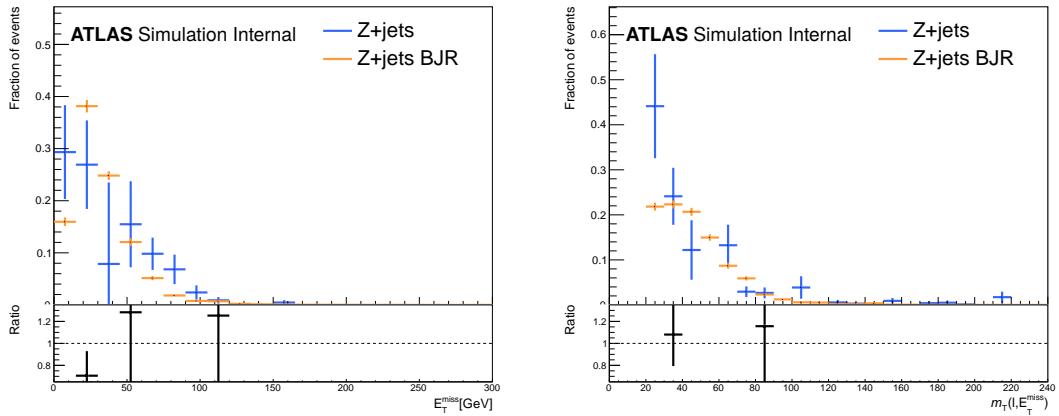
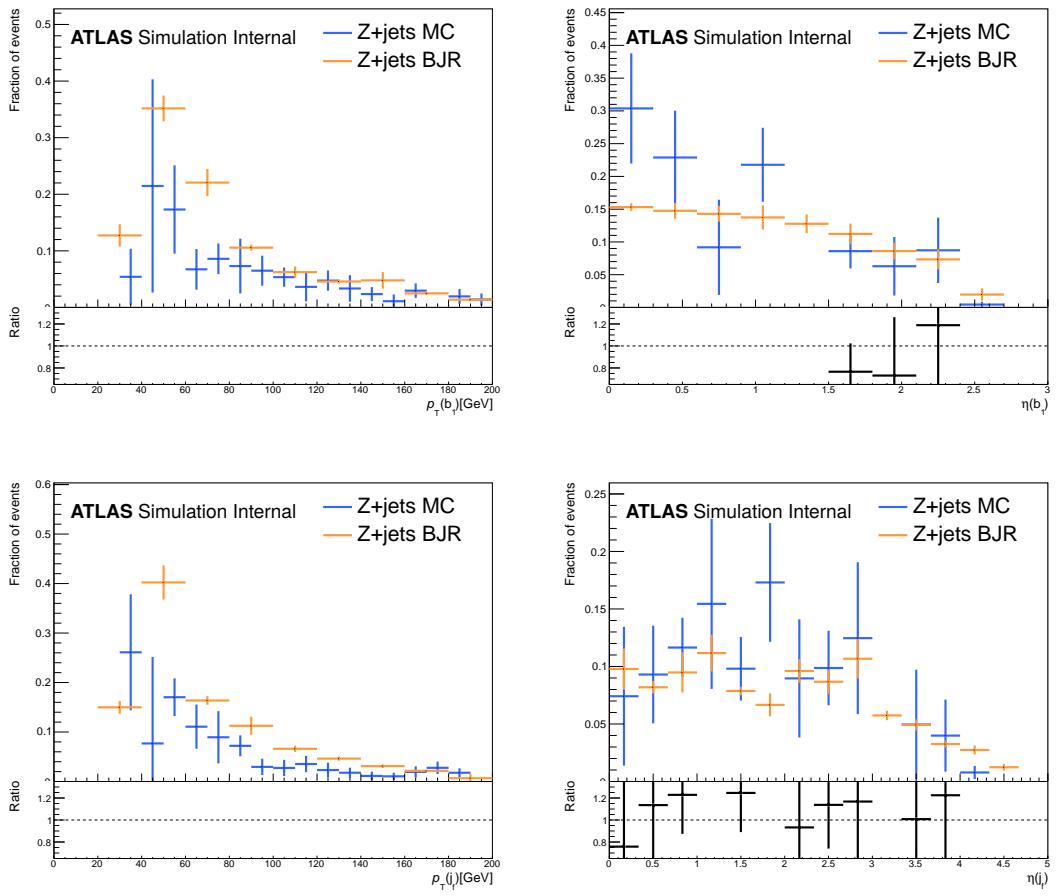


Figure 231: Kinematic distribution of lepton related quantities in  $Z + \text{jets}$  events in the 2j1b SR.

Not reviewed, for internal circulation only

Figure 232:  $E_T^{\text{miss}}$  and  $m_T(W)$  distributions in  $Z + \text{jets}$  events in the 2j1b SR.Figure 233: Kinematic distribution of jet related quantities in  $Z + \text{jets}$  events in the 3j1b SR.

Not reviewed, for internal circulation only

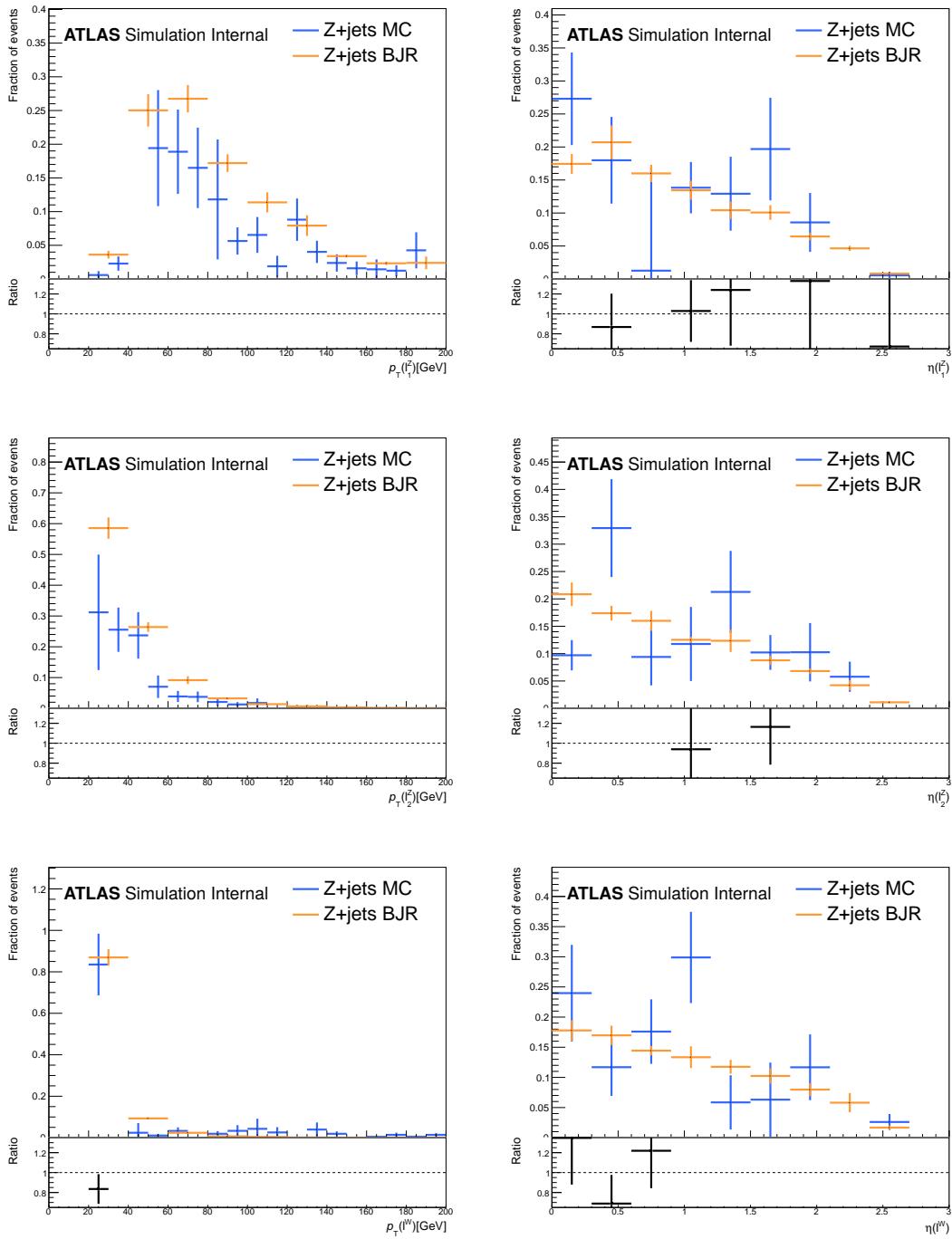


Figure 234: Kinematic distribution of lepton related quantities in Z + jets events in the 3j1b SR.

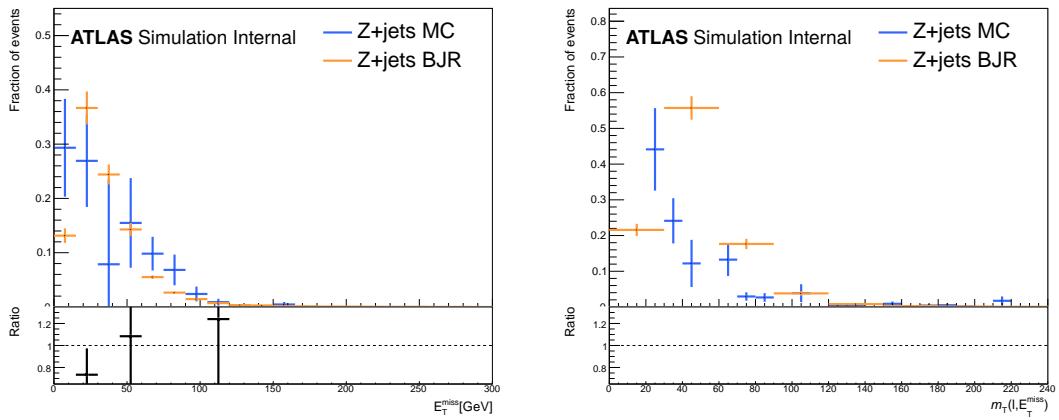


Figure 235:  $E_T^{\text{miss}}$  and  $m_T(W)$  distributions in  $Z + \text{jets}$  events in the 3j1b SR.

## 1456 F $Z + \text{jets}$ background estimation using the fake factor method

1457 In the previous analysis, the ‘fake-factor’ method was used to estimate the  $Z + \text{jets}$  background. In this  
 1458 section, the  $Z + \text{jets}$  background estimation using this method, instead of the  $b$ -jet replacement method, is  
 1459 shown.  
 1460 *2019-3-22: This Appendix still needs a bit of work. Some captions are missing and some plots still have to*  
 1461 *be added.*

### 1462 F.1 Introduction

1463 The fake-factor method tries to measure how often a fake lepton is misidentified as real, by deriving a fake  
 1464 factor from the data. This is derived in a region that is enriched in events that have at least one such fake  
 1465 lepton and is applied to a dedicated control region, resulting in a complete estimation of the fake-lepton  
 1466 contribution in the signal region. The fake-factor method provides an estimate of both the normalisation  
 1467 and the shape of the  $Z + \text{jets}$  fake-lepton background.

1468 In order to understand the procedure, it is important to differentiate between the ‘fake-factor region’ (FF)  
 1469 and the dedicated control region. A schematic representation is shown in Fig. 236. The fake-factor region  
 1470 for this analysis is obtained by inverting the cut on the transverse mass of the  $W$  boson that has been  
 1471 reconstructed from its associated lepton and  $E_T^{\text{miss}}$ . This is required to be greater than 20 GeV in the SR  
 1472 and  $< 20$  GeV for the FF selection.

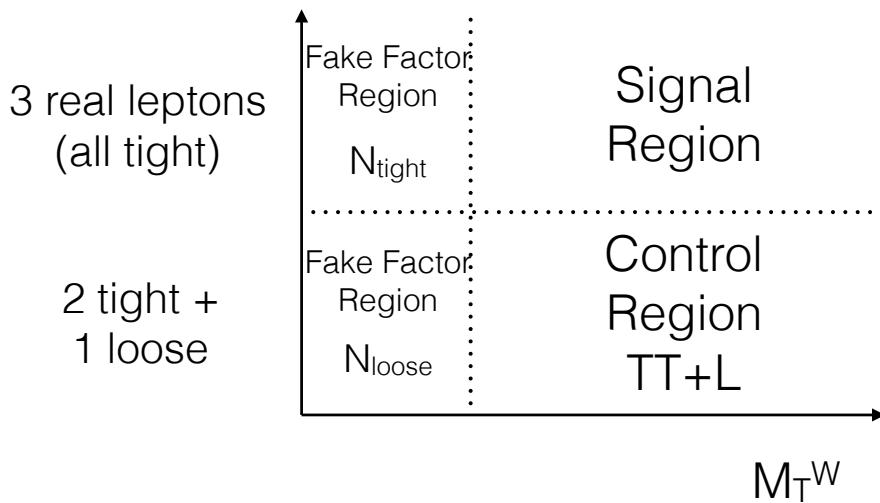


Figure 236: Schematic view of the definition of the control and fake factor regions.

1473 The factor is calculated using

$$F = \frac{N_{\text{tight}}^{\text{FF}}}{N_{\text{loose}}^{\text{FF}}}, \quad N^{\text{FF}} = N_{\text{data}} - N_{\text{MC}}^{\text{all}} \quad (5)$$

1474 where  $N_{\text{tight}}$  gives the number of events in which all leptons pass the ‘tight’ isolation and identification  
 1475 criteria and  $N_{\text{loose}}$  stands for the events in which one of the leptons only fulfils the ‘loose’ requirements.

1476 In order to obtain the total number of  $Z + \text{jets}$  events in the signal region, this factor will be applied to  
 1477 the  $Z + \text{jets}$  control region that has the same cuts as the signal region, except for the requirement of two  
 1478 tight and one loose-not-tight lepton. As shown in Table 49, the tight requirements consist of passing the  
 1479 ‘TightLH’ lepton identification, while the loose one requires only the ‘Medium’. For muon identification,  
 1480 the ‘Medium’ selection is required for both the tight and loose selections. In terms of isolation, for both  
 1481 tight electrons and muons, the gradient working point is used, while for loose (again both  $e^\pm$  and  $\mu^\pm$ ) no  
 1482 isolation criteria are required.

Table 49: Definition of electron and muon selection criteria for ‘loose’ and ‘tight’.

		Loose		Tight	
		Definition	Isolation	Definition	Isolation
Electrons	MediumLH	None	TightLH	Gradient	
Muons	Medium	None	Medium	Gradient	

1483 The fake factor is then derived, separately for electrons and muons, in bins of  $p_T$  of the lepton associated to  
 1484 the  $W$  boson, since in almost all  $Z + \text{jets}$  events this is the lepton that is fake.

1485 **F.2 Fake-factor estimation in the 2j1b SR**1486 **F.2.1 Electron channel**

1487 The distributions of the numerator and denominator used in the fake-factor definition are shown separately  
 1488 for electrons and muons in Figs. 237 and 238.

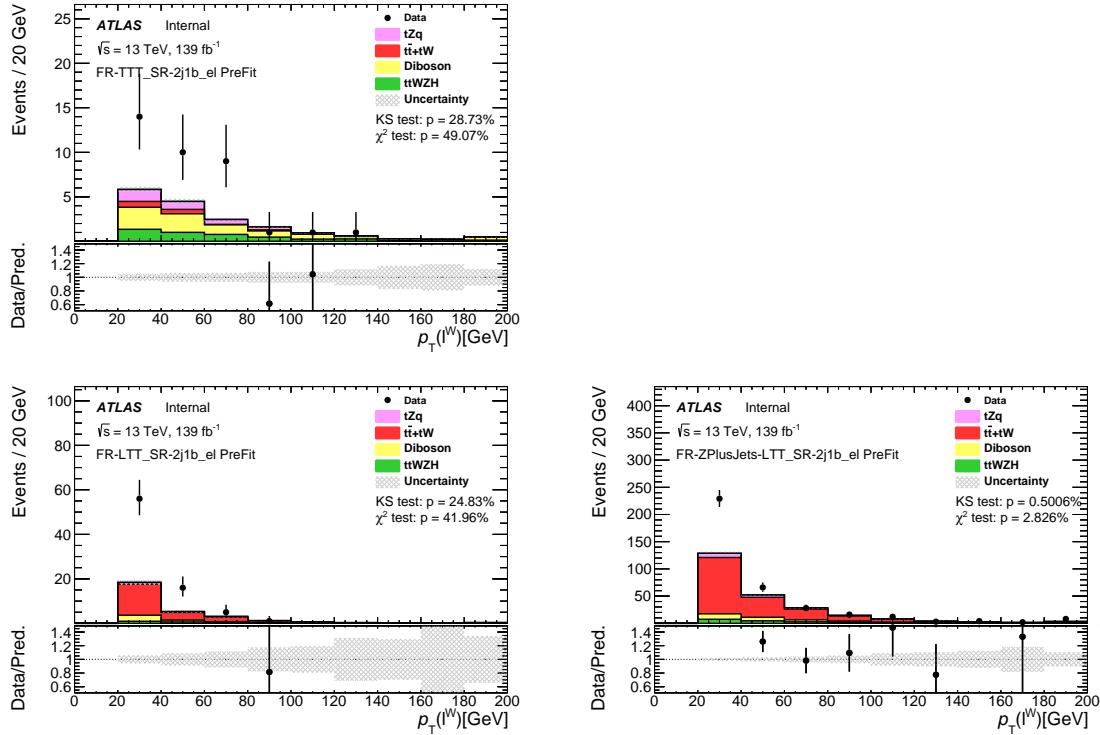


Figure 237: Control distributions for the  $Z + \text{jets}$  FF-method regions, showing the  $p_T$  of the lepton associated to the  $W$  boson for the two jet regions for the electron channel. The disposition of the plots follows the scheme in Fig. 236. On the top, the all-tight selection is shown. On the bottom, events in which one of the leptons is loose-not-tight are shown. The plot on the bottom left (right) is done in the region with the reversed (normal) selection on the transverse mass of the  $W$  boson.

1489 Table 51 shows the calculated FF for the 2j1b SR for events in which the non-prompt lepton is an electron,  
 1490 as well as the total resulting number of events, split according to the two  $p_T$  bins of the lepton associated to  
 1491 the  $W$  boson. In total, the FF method yields  $33.6 \pm 12.5$  events, with the associated error coming from the  
 1492 limited statistics in the regions used for calculating the FF.

1493 **F.2.2 Muon channel**

1494 Table 53 shows the calculated FF for the 2j1b SR for events in which the non-prompt lepton is a muon, as  
 1495 well as the total resulting number of events, split according to the two  $p_T$  bins of the lepton associated to  
 1496 the  $W$  boson. In total, the FF method yields  $9.2 \pm 4.4$  events, with the associated error coming from the  
 1497 limited statistics in the regions used for calculating the FF.

Table 50: Event yields in the  $Z + \text{jets}$  FF-method regions for the two jet regions for the electron channel. The three regions correspond to those in Fig. 237.

Process	FR-TTT	FR-LTT	CR-LTT
$t\bar{t}V + t\bar{t}H + tWZ$	$4.4 \pm 0.2$	$2.3 \pm 0.1$	$19.5 \pm 0.4$
Diboson	$7.8 \pm 0.3$	$4.6 \pm 0.5$	$26.9 \pm 0.6$
$t\bar{t} + tW$	$1.3 \pm 0.3$	$21.1 \pm 1.1$	$180.9 \pm 3.6$
$tZq$	$3.5 \pm 0.1$	$1.6 \pm 0.1$	$16.4 \pm 0.3$
Total expected	$17.0 \pm 0.5$	$29.7 \pm 1.3$	$243.7 \pm 3.6$
Data	36	78	368

Table 51

Region		$p_T(\ell_W) < 35.0 \text{ GeV}$	$p_T(\ell_W) > 35.0 \text{ GeV}$	
2j1b <sub>e</sub>	FF	$0.221 \pm$	0.106	$0.398 \pm$
	SF	$0.101 \pm$	0.048	$0.081 \pm$
	Yield	$19.727 \pm$	9.464	$13.909 \pm$
				7.968

Table 52: Event yields in the  $Z + \text{jets}$  FF-method regions for the two jet regions for the muon channel. The three regions correspond to those in Fig. 238.

Process	FR-TTT	FR-LTT	CR-LTT
$t\bar{t}V + t\bar{t}H + tWZ$	$5.3 \pm 0.2$	$2.2 \pm 0.1$	$17.3 \pm 0.4$
Diboson	$7.5 \pm 0.3$	$3.6 \pm 0.3$	$24.1 \pm 0.6$
$t\bar{t} + tW$	$1.3 \pm 0.3$	$17.4 \pm 1.2$	$132.7 \pm 3.0$
$tZq$	$3.9 \pm 0.1$	$2.0 \pm 0.1$	$16.3 \pm 0.3$
Total expected	$17.9 \pm 0.4$	$25.3 \pm 1.2$	$190.5 \pm 3.1$
Data	32	58	225

Table 53

Region		$p_T(\ell_W) < 35.0 \text{ GeV}$	$p_T(\ell_W) > 35.0 \text{ GeV}$	
2j1b <sub><math>\mu</math></sub>	FF	$0.182 \pm$	0.113	$0.629 \pm$
	SF	$0.052 \pm$	0.033	$0.033 \pm$
	Yield	$5.087 \pm$	3.165	$4.172 \pm$
				3.092

Not reviewed, for internal circulation only

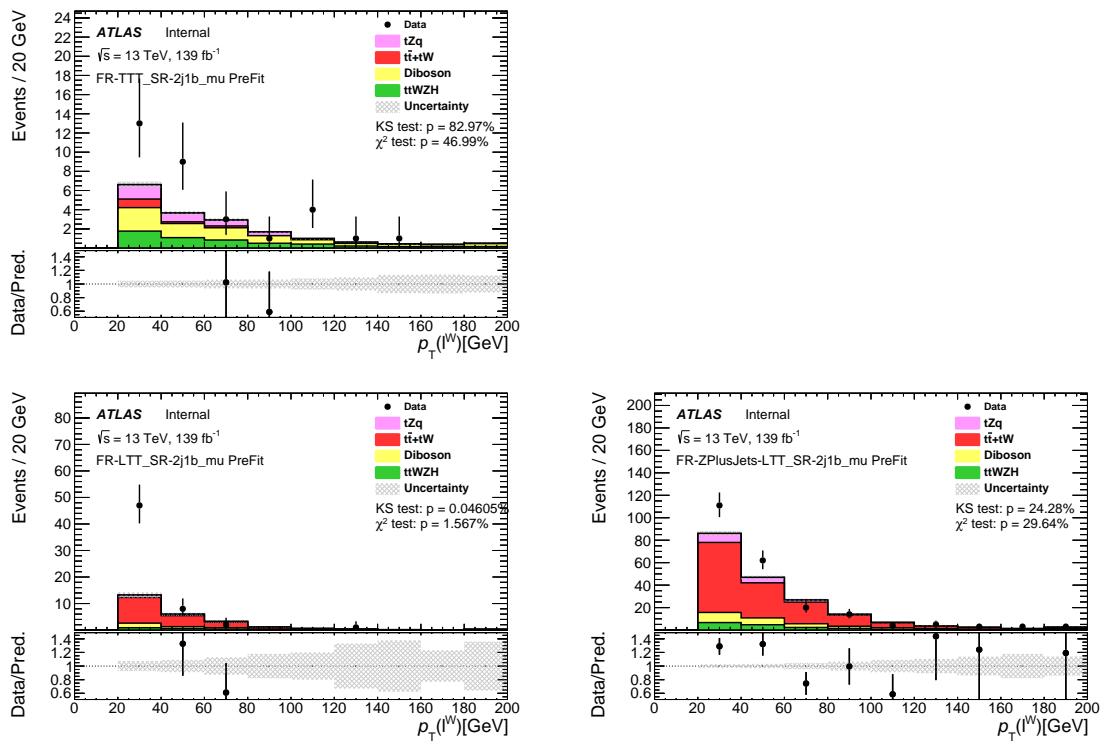


Figure 238: Control distributions for the  $Z + \text{jets}$  FF-method regions, showing the  $p_T$  of the lepton associated to the  $W$  boson for the two jet regions for the muon channel. The disposition of the plots follows the scheme in Fig. 236. On the top, the all-tight selection is shown. On the bottom, events in which one of the leptons is loose-not-tight are shown. The plot on the bottom left (right) is done in the region with the reversed (normal) selection on the transverse mass of the  $W$  boson.

1498 **F.2.3  $Z + \text{jets}$  estimation in the SR**

1499 The total number of events estimated by the FF method for the 2j1b SR is  $42.9 \pm 13.3$ , when taking into  
 1500 account the uncertainty on the FF due to limited statistics. With the BJR method, the total number of  
 1501  $Z + \text{jets}$  events is determined when performing the fit to data. Pre-fit, a  $Z + \text{jets}$  normalisation of  $7.3 \pm 0.1$ ,  
 1502 coming from MC, is considered. The fit shows that this is an underestimation and, from the Asimov fit, it  
 1503 is determined that it should be scaled by  $\mu_{Z + \text{jets}} = 2.74 \pm 1.44$ . When taking this into account, the two  
 1504 methods are compatible within the corresponding uncertainties.

1505 **F.2.4 Check in the diboson VR**

Table 54

Process	Number of events		Process	Number of events	
$t\bar{t}V + t\bar{t}H + tWZ$	$78.2 \pm$	0.8	$t\bar{t}V + t\bar{t}H + tWZ$	$78.2 \pm$	0.8
$VV + HF$	$89.8 \pm$	1.0	$VV + HF$	$89.8 \pm$	1.0
$VV + LF$	$20.2 \pm$	0.6	$VV + LF$	$20.2 \pm$	0.6
$Z + \text{jets (FF)}$	$42.9 \pm$	1.9	$Z + \text{jets (BJR)}$	$7.3 \pm$	0.1
$t\bar{t} + tW$	$23.0 \pm$	0.1	$t\bar{t} + tW$	$23.1 \pm$	0.1
$tZq$	$64.0 \pm$	0.5	$tZq$	$64.0 \pm$	0.5
Total expected	$318.0 \pm$	2.4	Total expected	$282.5 \pm$	1.5

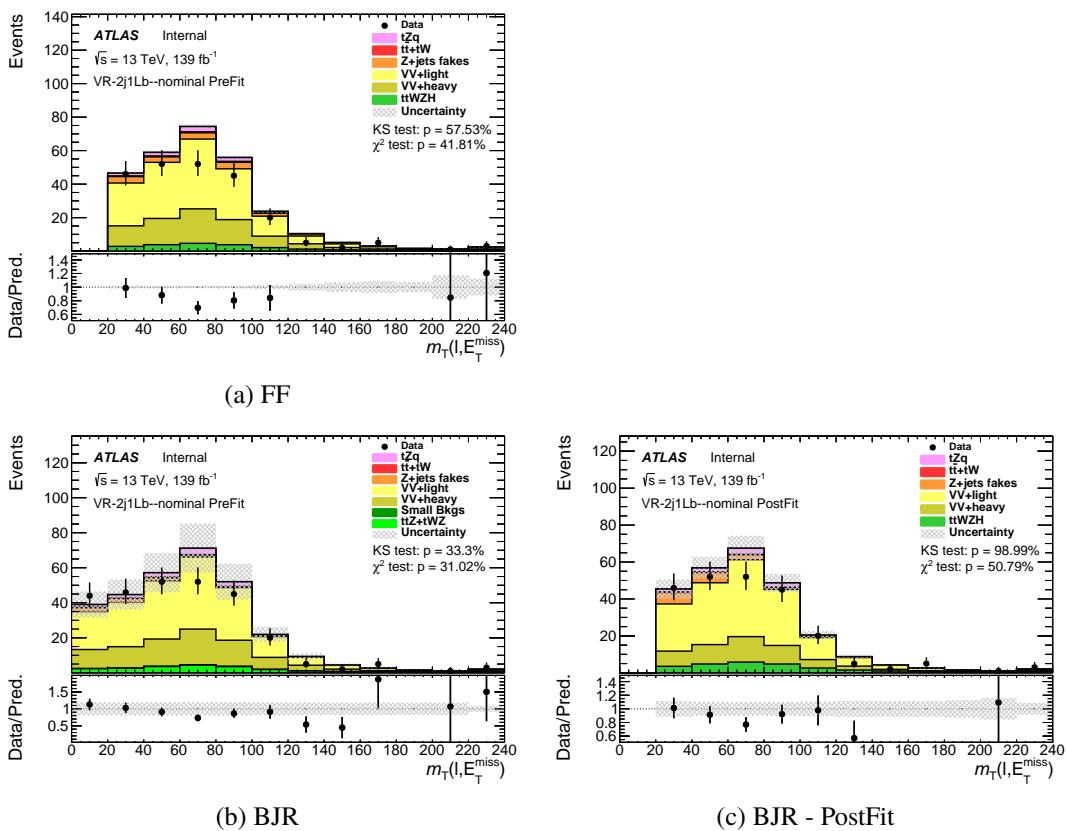


Figure 239

1506 **F.3 Fake-factor estimation in the 3j1b SR**1507 **F.3.1 Electron channel**

1508 The distributions of the numerator and denominator used in the fake-factor definition are shown separately  
 1509 for electrons and muons in Figs. 240 and 241.

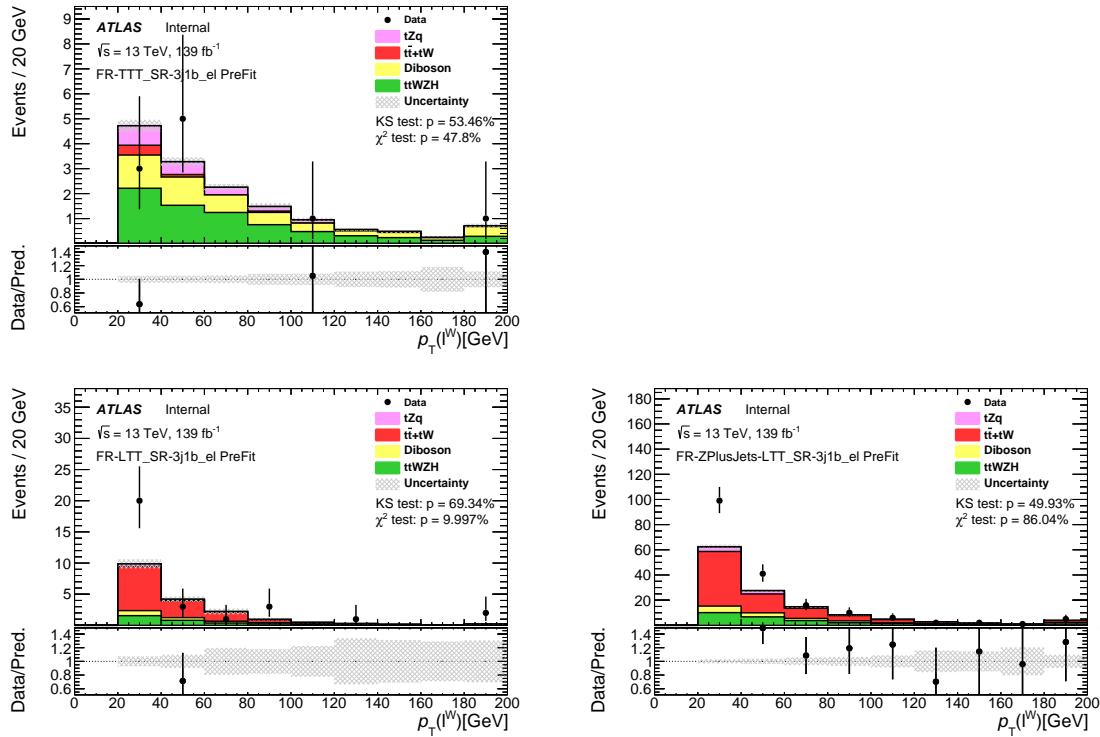


Figure 240: Control distributions for the  $Z + \text{jets}$  FF-method regions, showing the  $p_T$  of the lepton associated to the  $W$  boson for the three jet regions for the electron channel. The disposition of the plots follows the scheme in Fig. 236. On the top, the all-tight selection is shown. On the bottom, events in which one of the leptons is loose-not-tight are shown. The plot on the bottom left (right) is done in the region with the reversed (normal) selection on the transverse mass of the  $W$  boson.

1510 **F.3.2 Muon channel**1511 **F.3.3  $Z + \text{jets}$  estimation in the SR**

1512 It is already visible from Table 55 and Table 57 and the corresponding plots that no reliable estimation can  
 1513 be performed using the FF method for the 3j1b region because of the very limited statistics. This is solved  
 1514 by using the BJR method, since it increases statistics and provides a very good description of the  $Z + \text{jets}$   
 1515 shape in this region.

1516 **F.3.4 Check in the diboson VR**

Table 55: Event yields in the  $Z + \text{jets}$  FF-method regions for the three jet regions for the electron channel. The three regions correspond to those in Fig. 240.

Process	FR-TTT	FR-LTT	CR-LTT
$t\bar{t}V + t\bar{t}H + tWZ$	$7.2 \pm 0.2$	$3.4 \pm 0.2$	$26.5 \pm 0.5$
Diboson	$4.9 \pm 0.2$	$2.0 \pm 0.1$	$14.6 \pm 0.5$
$t\bar{t} + tW$	$0.5 \pm 0.2$	$12.2 \pm 0.9$	$77.6 \pm 2.3$
$tZq$	$2.1 \pm 0.1$	$0.9 \pm 0.1$	$8.9 \pm 0.2$
Total expected	$14.7 \pm 0.4$	$18.6 \pm 1.0$	$127.4 \pm 2.4$
Data	10	30	182

Table 56

Region		$p_T(\ell_W) < 35.0 \text{ GeV}$	$p_T(\ell_W) > 35.0 \text{ GeV}$	
$3j1b_e$	FF	$0.000 \pm$	0.085	$0.000 \pm$
	SF	$0.000 \pm$	0.032	$0.000 \pm$
	Yield	$0.000 \pm$	2.661	$0.000 \pm$

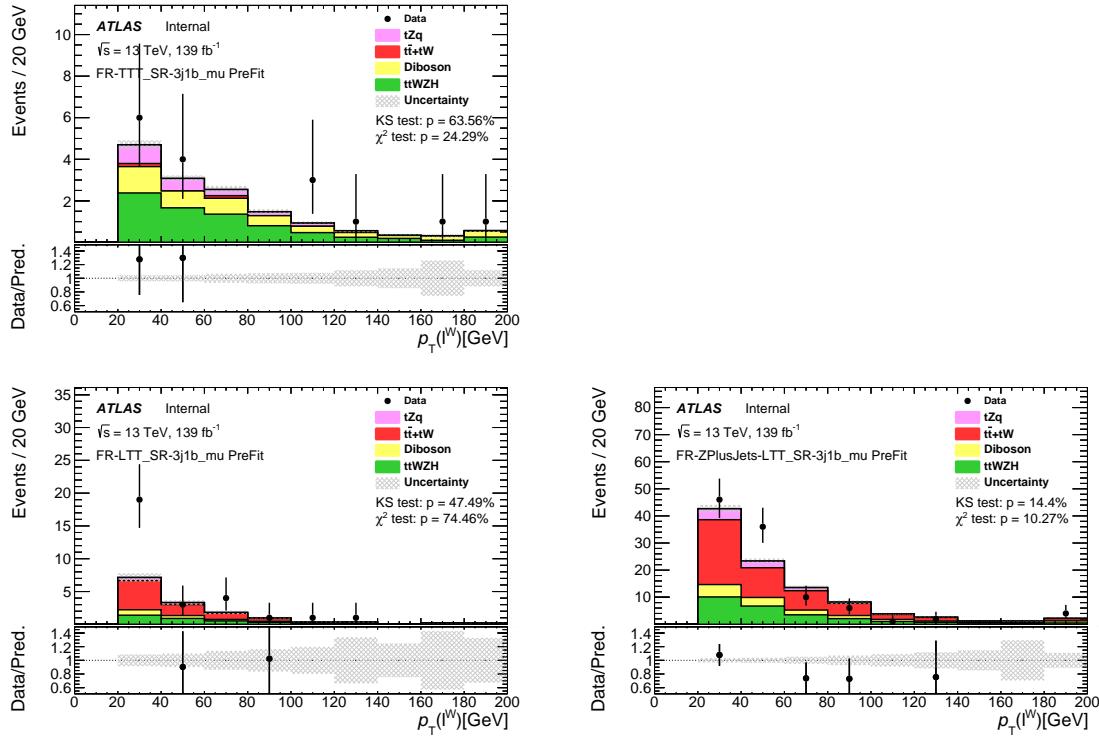


Figure 241: Control distributions for the  $Z + \text{jets}$  FF-method regions, showing the  $p_T$  of the lepton associated to the  $W$  boson for the three jet regions for the muon channel. The disposition of the plots follows the scheme in Fig. 236. On the top, the all-tight selection is shown. On the bottom, events in which one of the leptons is loose-not-tight are shown. The plot on the bottom left (right) is done in the region with the reversed (normal) selection on the transverse mass of the  $W$  boson.

Table 57: Event yields in the  $Z + \text{jets}$  FF-method regions for the three jet regions for the muon channel. The three regions correspond to those in Fig. 241.

Process	FR-TTT	FR-LTT	CR-LTT
$t\bar{t}V + t\bar{t}H + tWZ$	$7.5 \pm 0.2$	$3.5 \pm 0.2$	$25.5 \pm 0.4$
Diboson	$4.5 \pm 0.2$	$1.9 \pm 0.2$	$13.2 \pm 0.4$
$t\bar{t} + tW$	$0.3 \pm 0.1$	$8.0 \pm 0.7$	$51.7 \pm 1.8$
$tZq$	$2.3 \pm 0.1$	$1.1 \pm 0.1$	$8.8 \pm 0.2$
Total expected	$14.5 \pm 0.4$	$14.5 \pm 0.8$	$99.1 \pm 1.9$
Data	16	29	105

Table 58

Region		$p_T(\ell_W) < 35.0 \text{ GeV}$	$p_T(\ell_W) > 35.0 \text{ GeV}$		
$3j1b_\mu$	FF	$0.145 \pm$	0.188	$0.000 \pm$	0.126
	SF	$0.019 \pm$	0.025	$0.000 \pm$	0.002
	Yield	$0.721 \pm$	0.931	$0.000 \pm$	0.121

Table 59

Process	Number of events		
$t\bar{t}V + t\bar{t}H + tWZ$	$108.0 \pm$	0.9	
$VV + HF$	$52.3 \pm$	0.6	
$VV + LF$	$10.8 \pm$	0.3	
$Z + \text{jets}$ (BJR)	$3.2 \pm$	0.1	
$t\bar{t} + tW$	$10.9 \pm$	0.1	
$tZq$	$36.1 \pm$	0.5	
Total expected	$221.2 \pm$	1.3	

Not reviewed, for internal circulation only

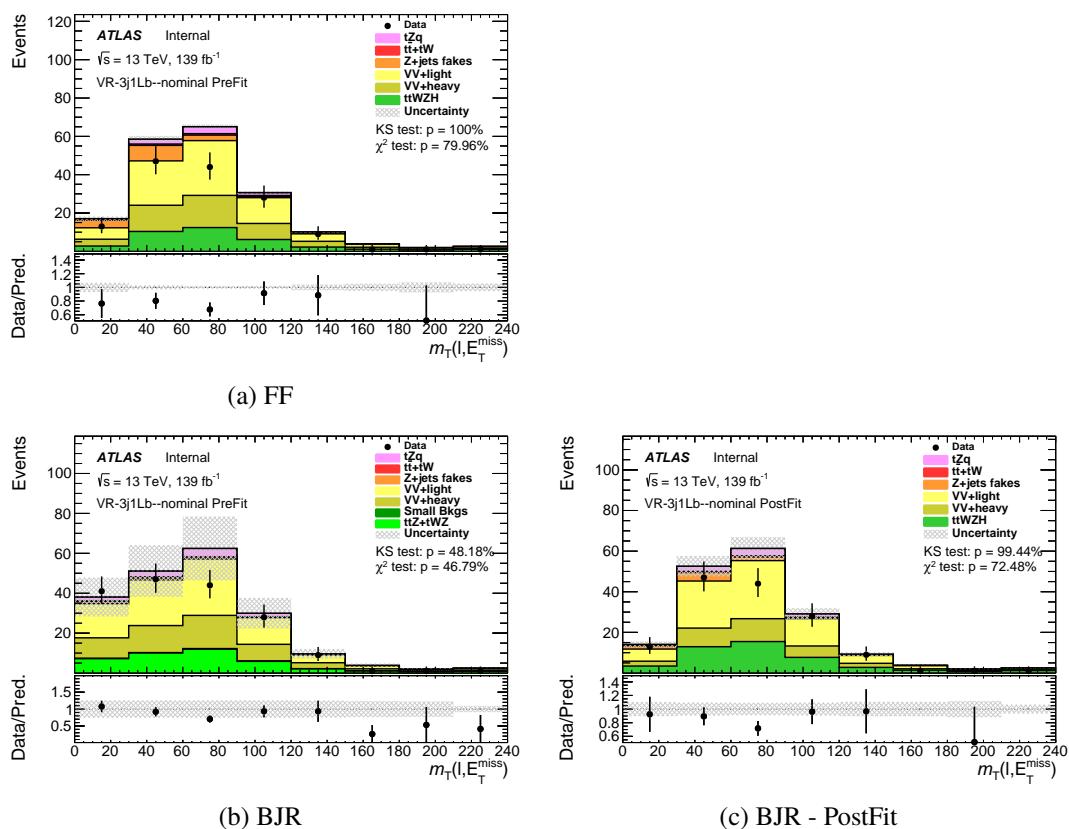


Figure 242

## 1517 G Additional fit studies

1518 In this appendix, various studies and checks for the fit strategy are presented.

### 1519 G.1 Diboson CR fitted variable

1520 Studies presented in the following were done on events with  $m_T(W) > 20$  GeV.

1521 The studies reported in the following were not repeated with the changes applied after Top Approval, i.e.:  
 1522  $tZq$  radiation uncertainty still has normalization in,  $tWZ$  DR1 vs DR2 systematic is not included and  
 1523 diboson uncertainty is 20 % for both LF and HF.

1524 Various variables and binning are tested to find a suitable variable to be fitted in the diboson CRs. These  
 1525 are shown in Fig. 243. They are:  $p_T(\ell^W)$ ,  $E_T^{\text{miss}}$  and  $m_T(\ell^W, E_T^{\text{miss}})$ .

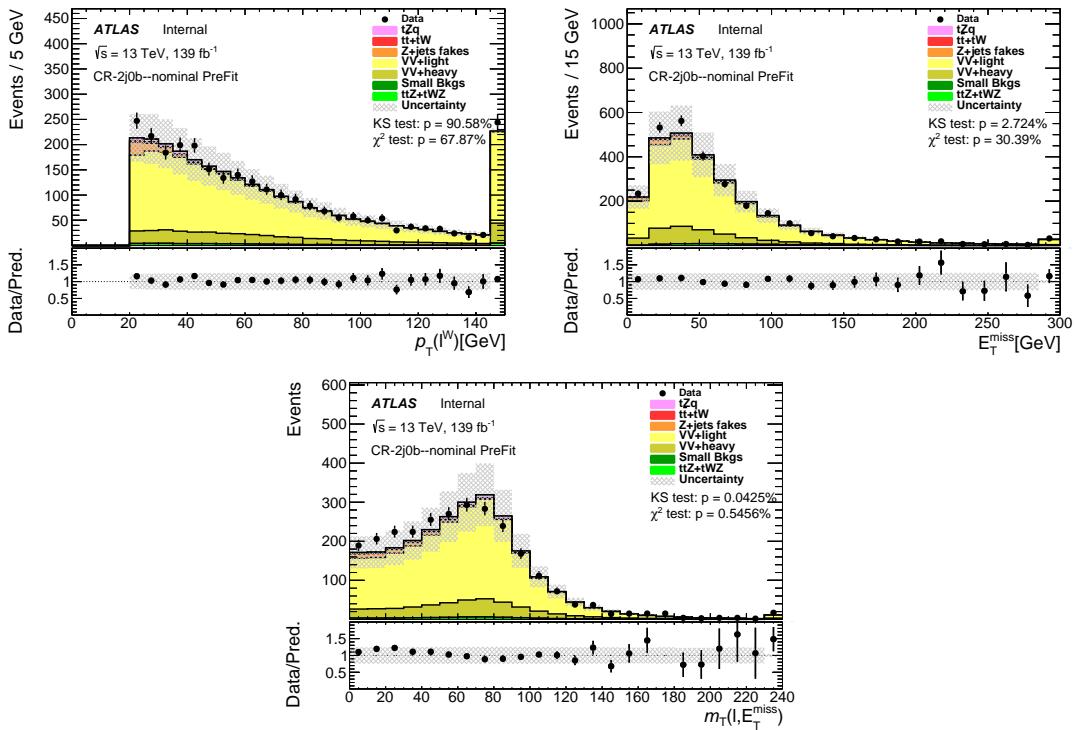


Figure 243: Various distributions for events in the diboson 2j0b CR. These distributions, with various binnings, were studied to find the most suitable variable to be fitted in the 2j0b CR. Both signal and backgrounds are normalised to the expected number of events before the fit.

1526 Particular attention is payed to the normalization of the  $Z + \text{jets}$  background that would be obtained using  
 1527 one variable or another. In general  $Z + \text{jets}$  events populate the low values of the  $p_T(\ell^W)$ ,  $E_T^{\text{miss}}$  and  
 1528  $m_T(\ell^W, E_T^{\text{miss}})$  distributions. The results of the checks on the binning and  $Z + \text{jets}$  normalization are reported  
 1529 in Table 60. The normalization values obtained using  $E_T^{\text{miss}}$  and  $m_T(\ell^W, E_T^{\text{miss}})$  are consistent with each  
 1530 other, while the ones obtained using  $p_T(\ell^W)$  are lower. This is due to a downward fluctuation of data for  
 1531 low  $p_T(\ell^W)$  values, so that  $Z + \text{jets}$  is scaled down. Between  $E_T^{\text{miss}}$  and  $m_T(\ell^W, E_T^{\text{miss}})$ , the second one is

1532 chosen for the fit.  $m_T(\ell^W, E_T^{\text{miss}})$  includes information from  $E_T^{\text{miss}}$  and it is also more important in the NN  
 1533 training. Concerning the binning, three bins are chosen.

Table 60: Variables and binning to be used in the fit for the diboson CRs. The  $Z + \text{jets}$  normalization that would be obtained from the fit is also shown.

Variable	Binning	$Z + \text{jets}$ normalization	
$p_T(\ell^W)$	[0,40,300]	$0.4 \pm$	0.6
$p_T(\ell^W)$	[0,30,40,50,100,300]	$0.7 \pm$	0.5
$E_T^{\text{miss}}$	[0,40, 300]	$2.3 \pm$	1
$E_T^{\text{miss}}$	many bins	$2.7 \pm$	1.4
$m_T(\ell^W, E_T^{\text{miss}})$	[0,60,300]	$3 \pm$	0.9
$m_T(\ell^W, E_T^{\text{miss}})$	[0,80,300]	$1.6 \pm$	1.2
$m_T(\ell^W, E_T^{\text{miss}})$	[0,40,60,80,300]	$3.0 \pm$	0.8
$m_T(\ell^W, E_T^{\text{miss}})$	[0,40,80,300]	$2.7 \pm$	0.8

1534 **G.2 Asimov fit - Additional material**1535 **G.2.1 Pre- and post-fit plots of fitted variables in fit regions**1536 Pre-fit and post-fit distributions of the fitted distributions in the various regions are shown in Figs. 244  
1537 to 247.

Not reviewed, for internal circulation only

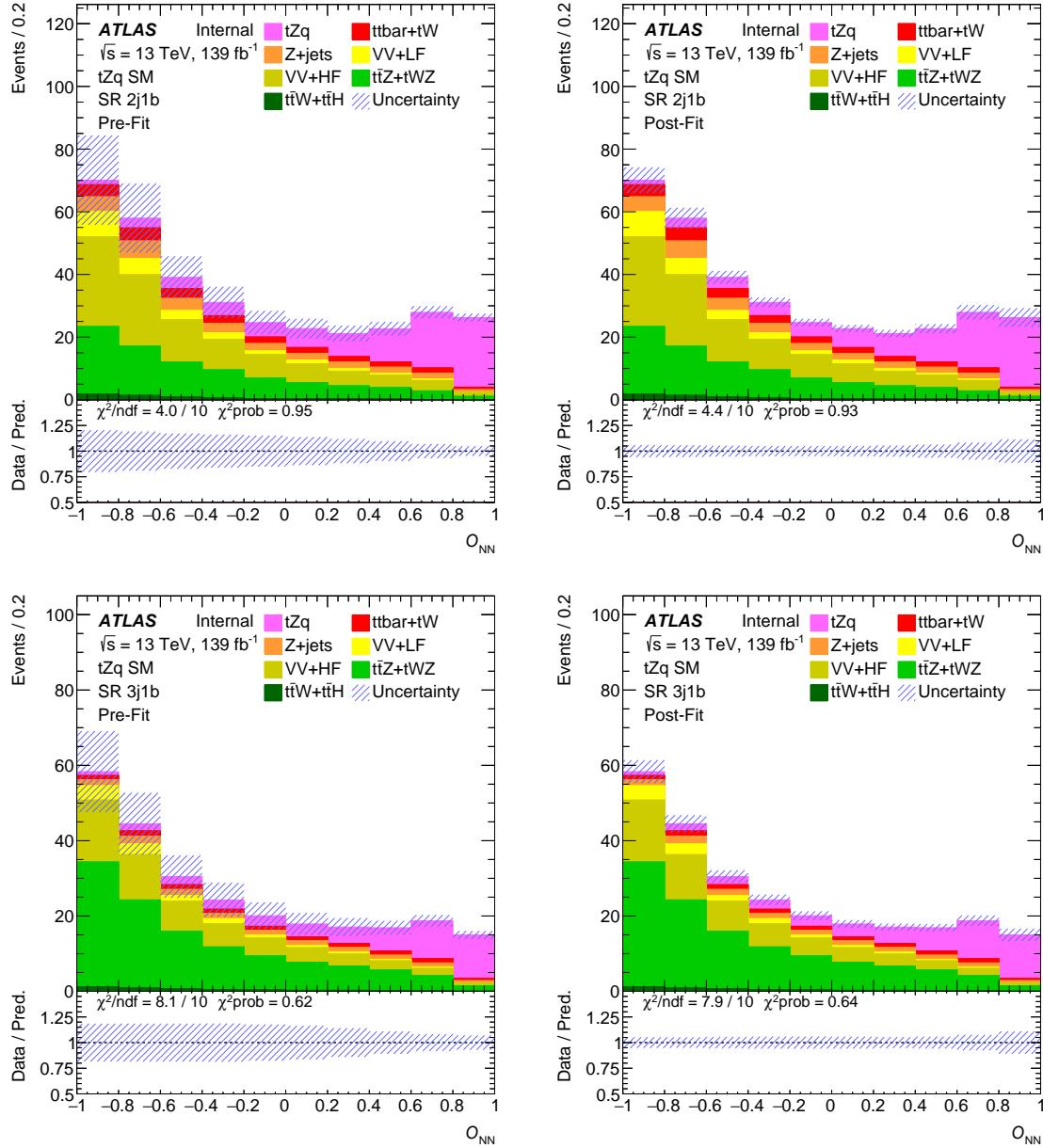


Figure 244: Pre-fit (left) and post-fit (right) NN output distributions in the signal regions. The uncertainty band includes both statistical and systematic uncertainties.

Not reviewed, for internal circulation only

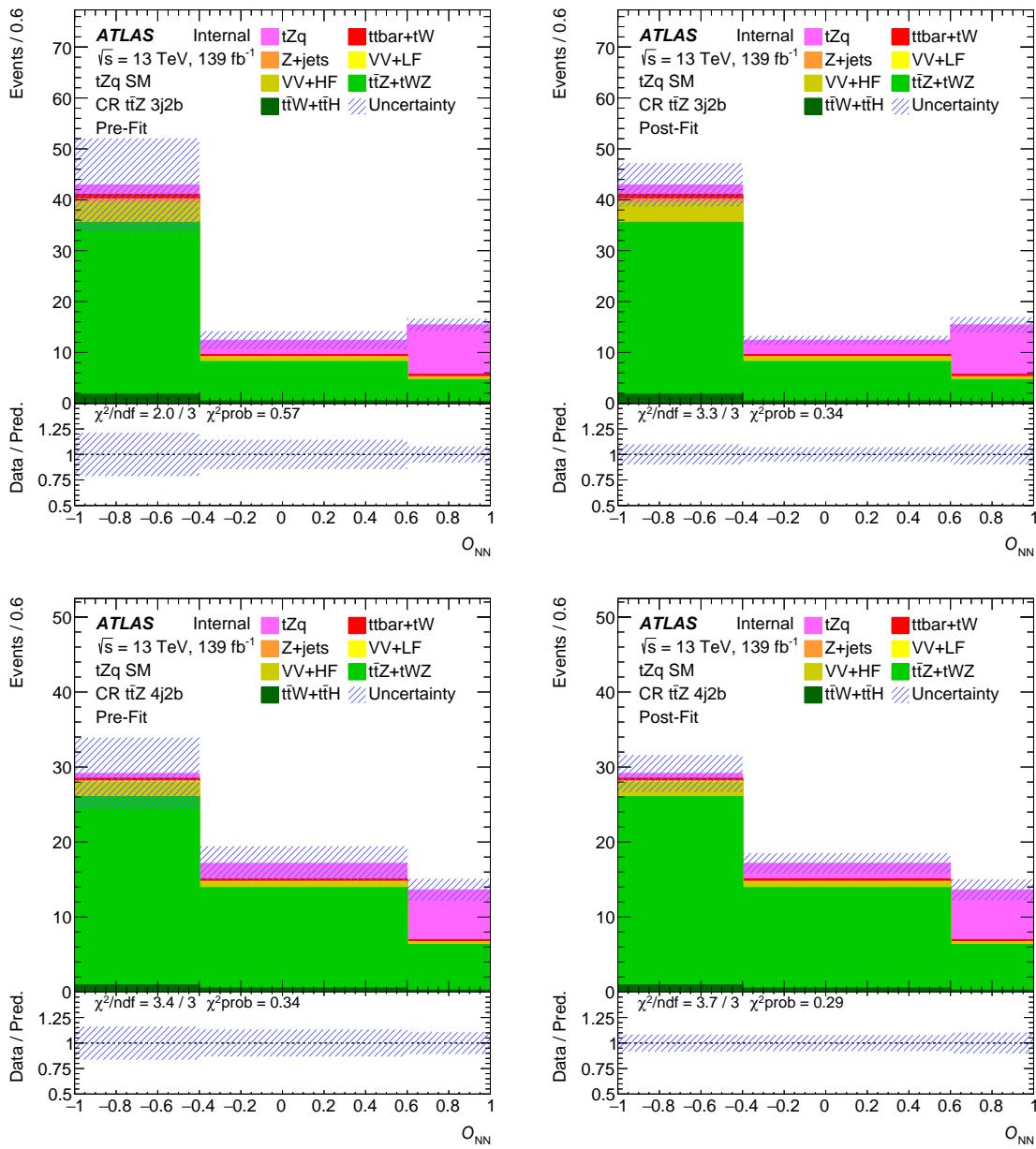


Figure 245: Pre-fit (left) and post-fit (right) NN output distributions in the  $t\bar{t}Z$  control regions. The uncertainty band includes both statistical and systematic uncertainties.

Not reviewed, for internal circulation only

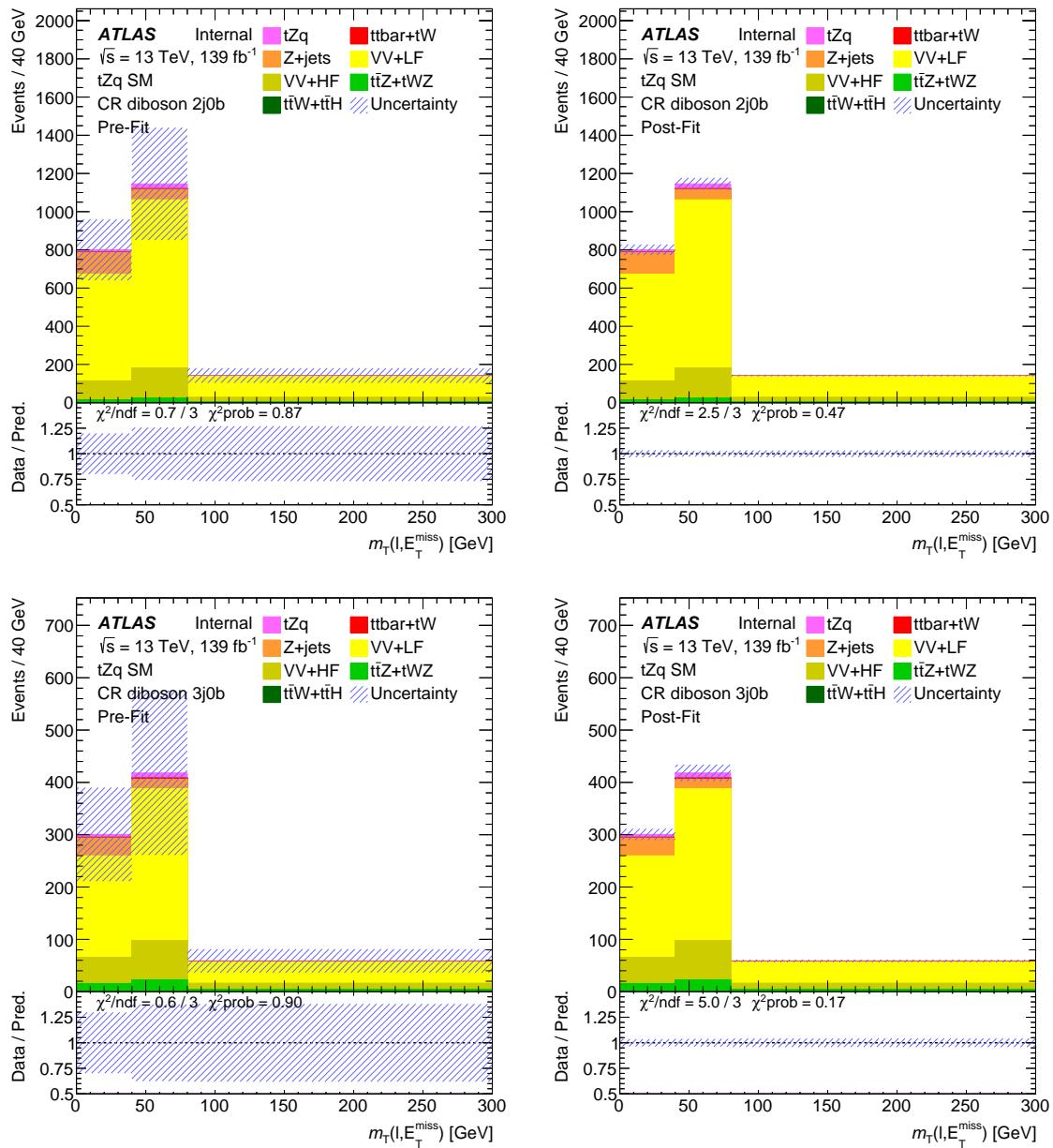


Figure 246: Pre-fit (left) and post-fit (right)  $E_T^{\text{miss}}$  distributions in the diboson control regions. The uncertainty band includes both statistical and systematic uncertainties.

Not reviewed, for internal circulation only

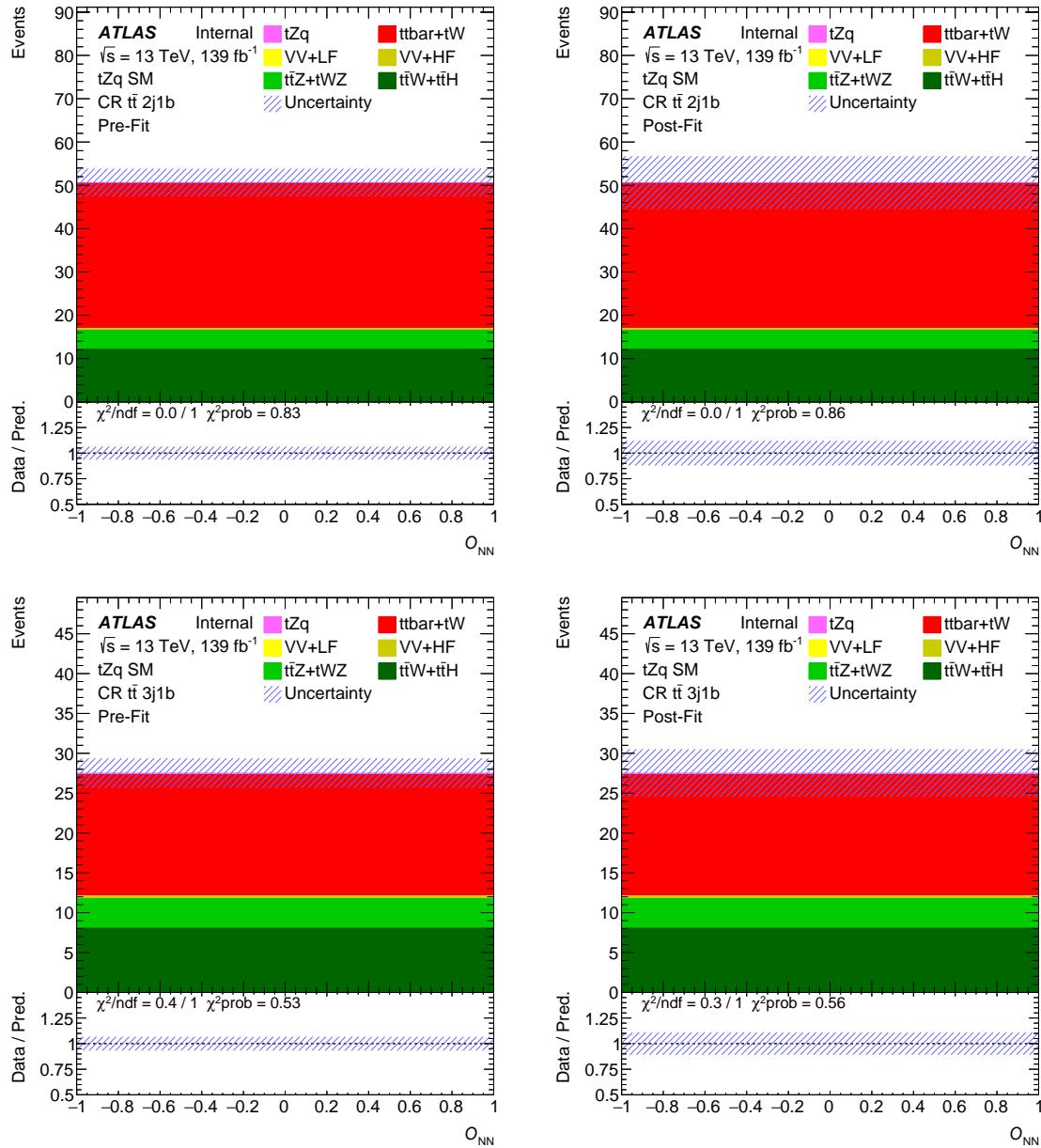


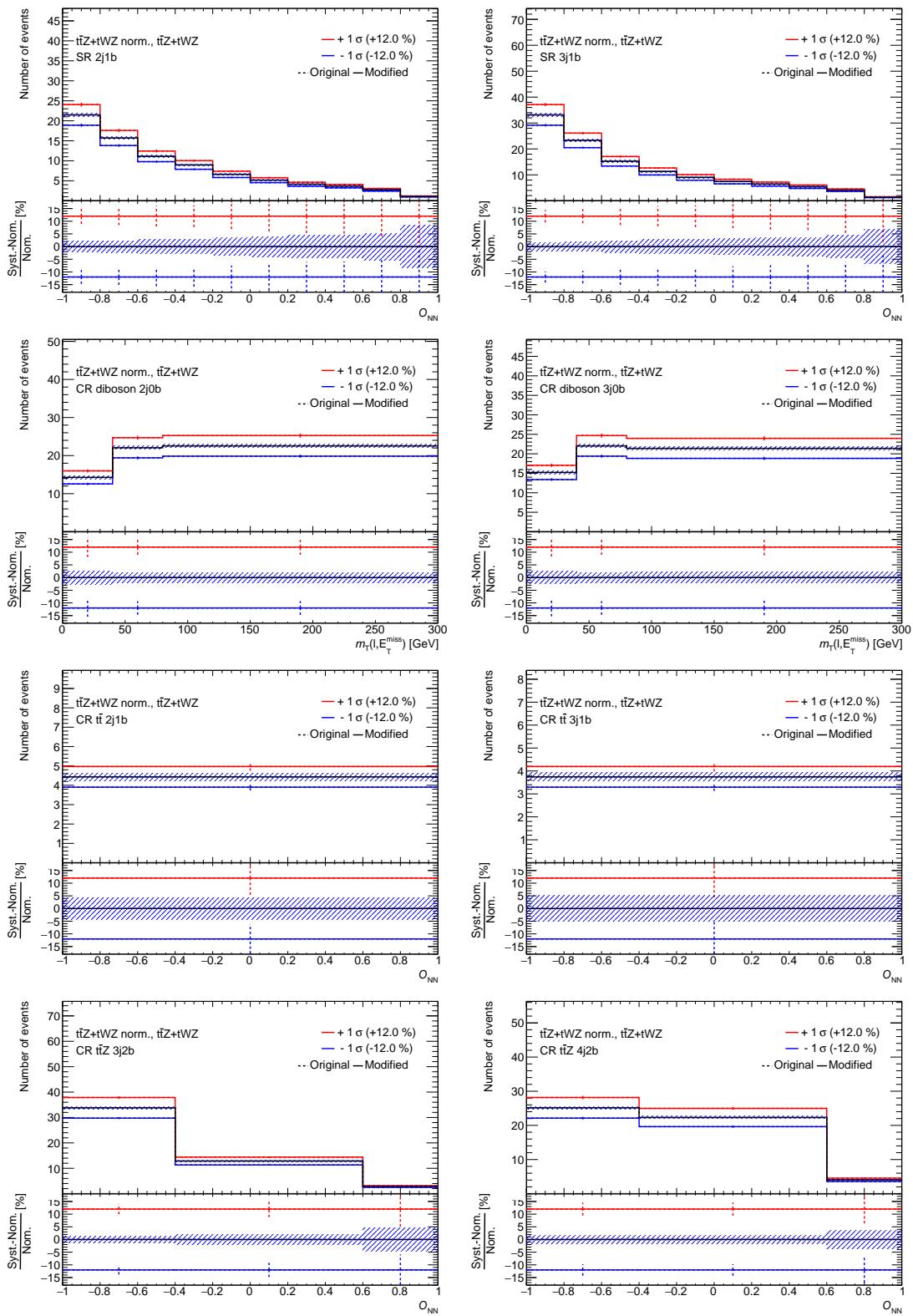
Figure 247: Pre-fit (left) and post-fit (right) NN output distributions in the  $t\bar{t}$  control regions. The uncertainty band includes both statistical and systematic uncertainties. Since the  $t\bar{t}$  background is free floating in the fit, there are no uncertainties on this background pre-fit.

1538 **G.3 Unblinded fit - Red and blue plots for pulled NPs**

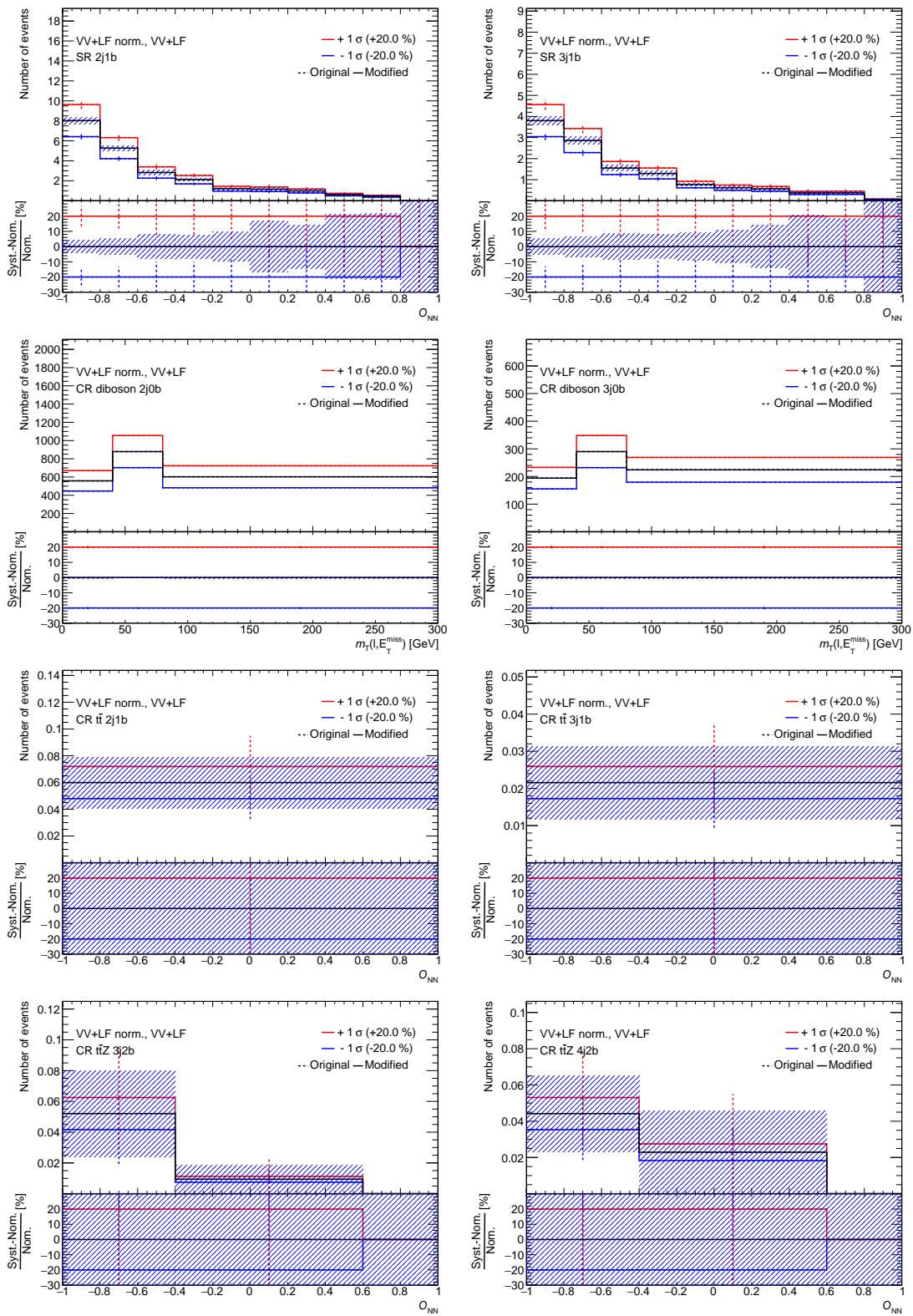
1539 **G.3.1 Normalization uncertainties**

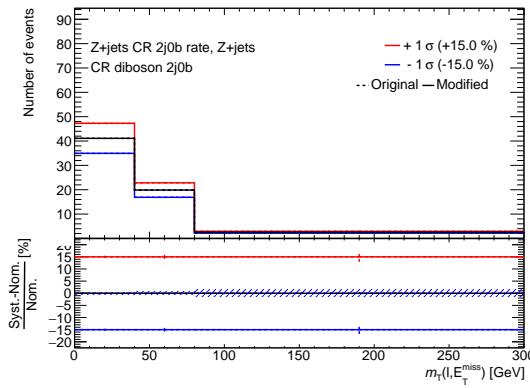
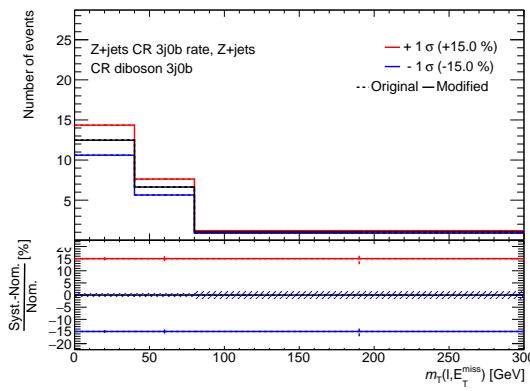
[Not reviewed, for internal circulation only]

Not reviewed, for internal circulation only

Figure 248:  $t\bar{t}Z$  normalization uncertainty.

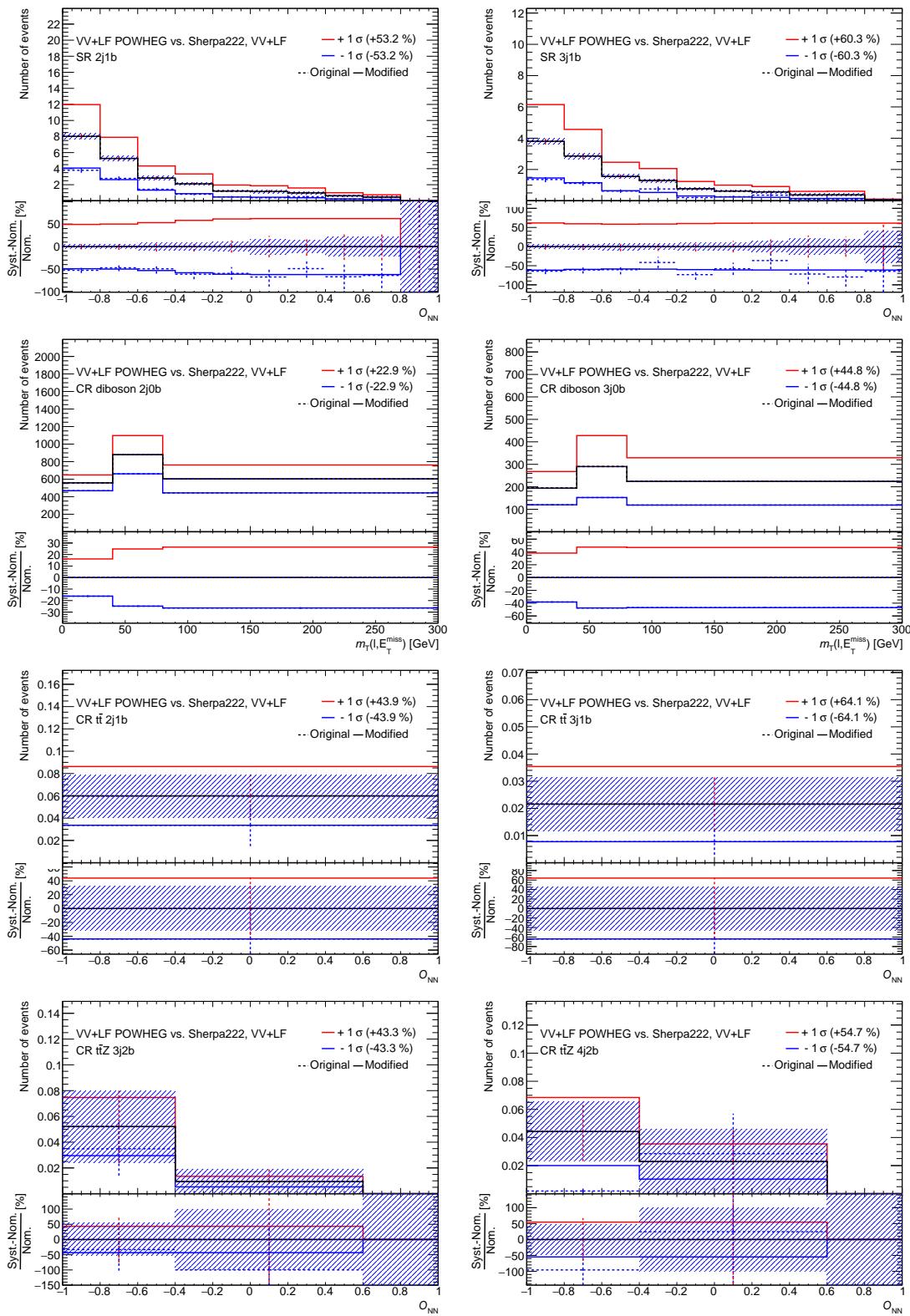
Not reviewed, for internal circulation only

Figure 249:  $VV + LF$  normalization uncertainty.

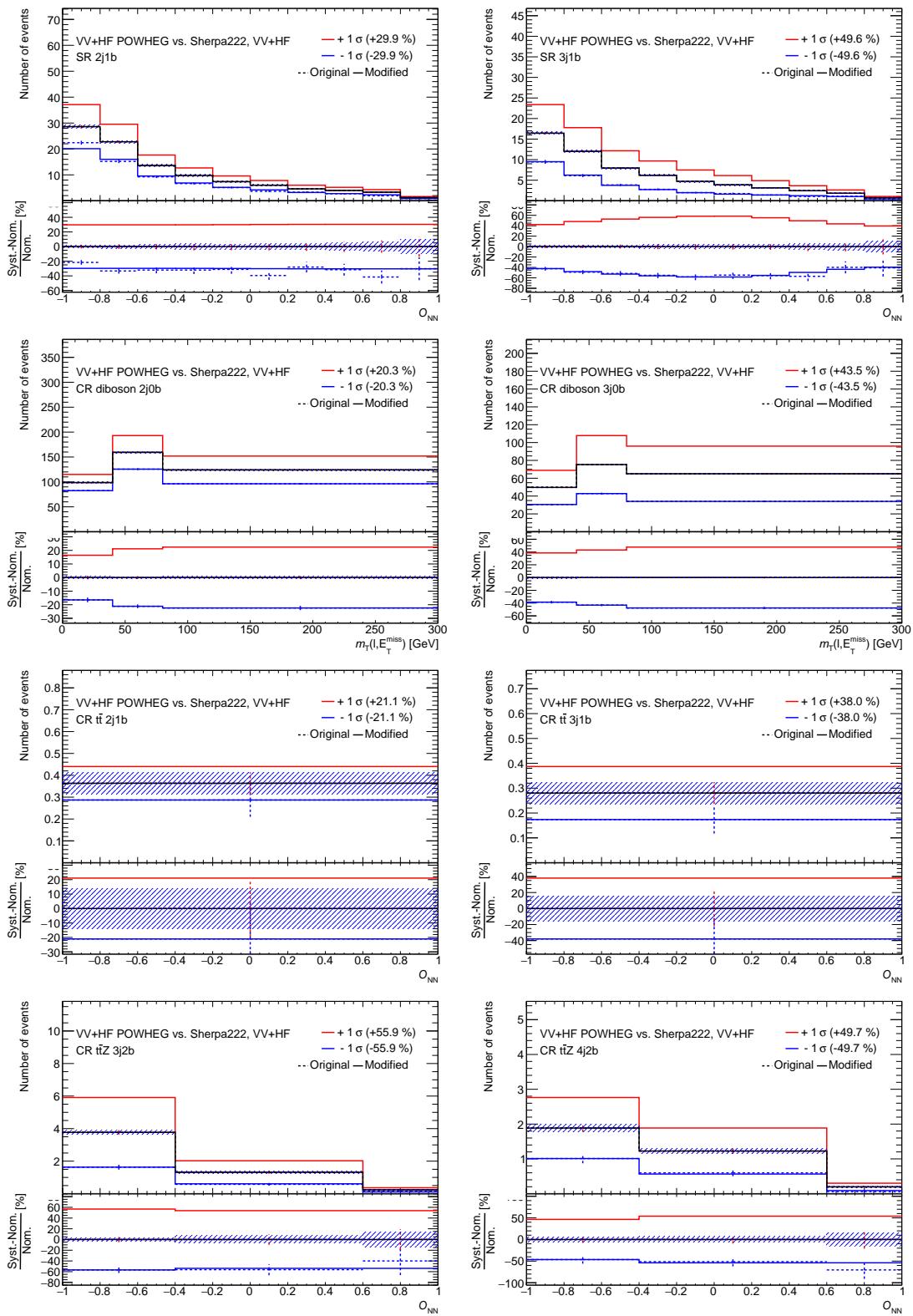
Figure 250:  $Z + \text{jets}$  in CR 2j0b normalization uncertainty.Figure 251:  $Z + \text{jets}$  in CR 3j0b normalization uncertainty.

1540 **G.3.2 Modeling uncertainties**

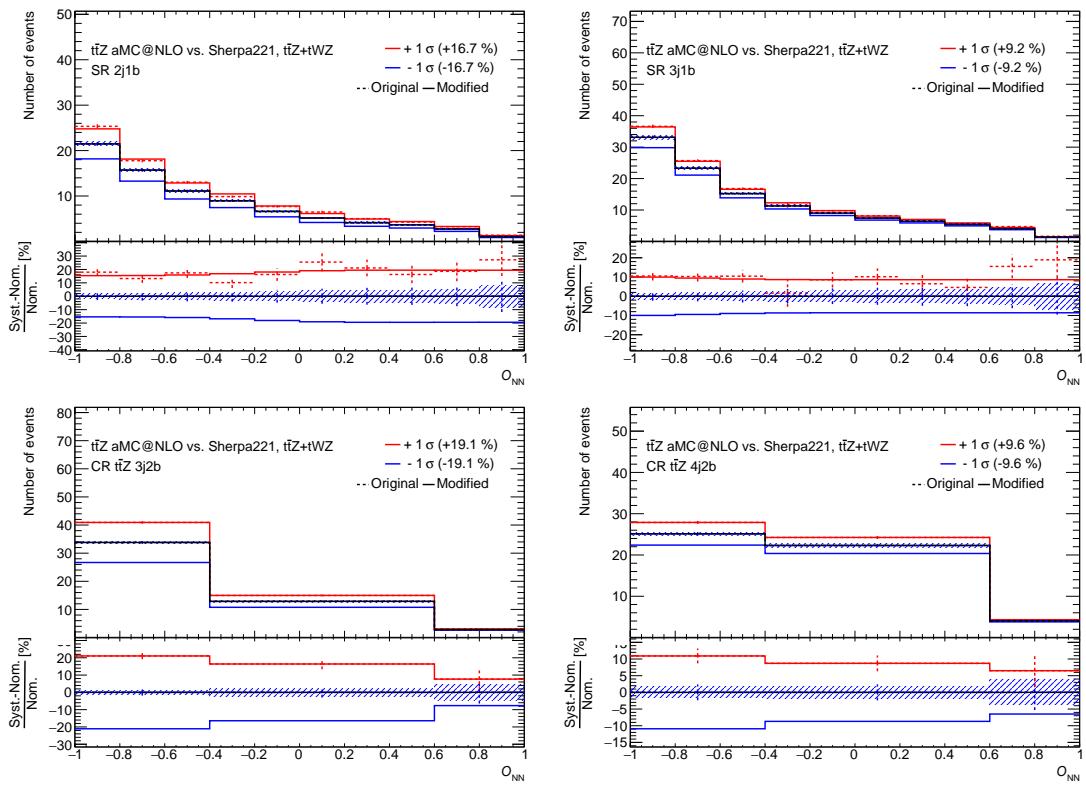
Not reviewed, for internal circulation only

Figure 252:  $VV + LF$  Powheg vs Sherpa uncertainty.

Not reviewed, for internal circulation only

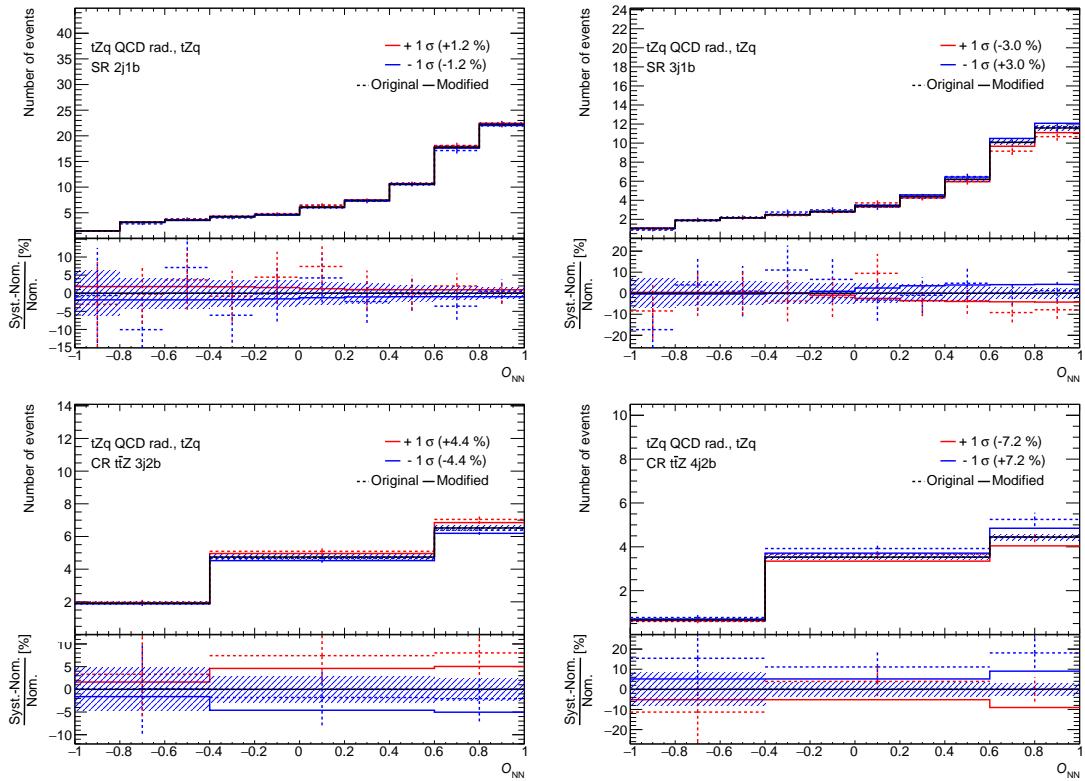
Figure 253:  $VV + HF$  Powheg vs Sherpa uncertainty.

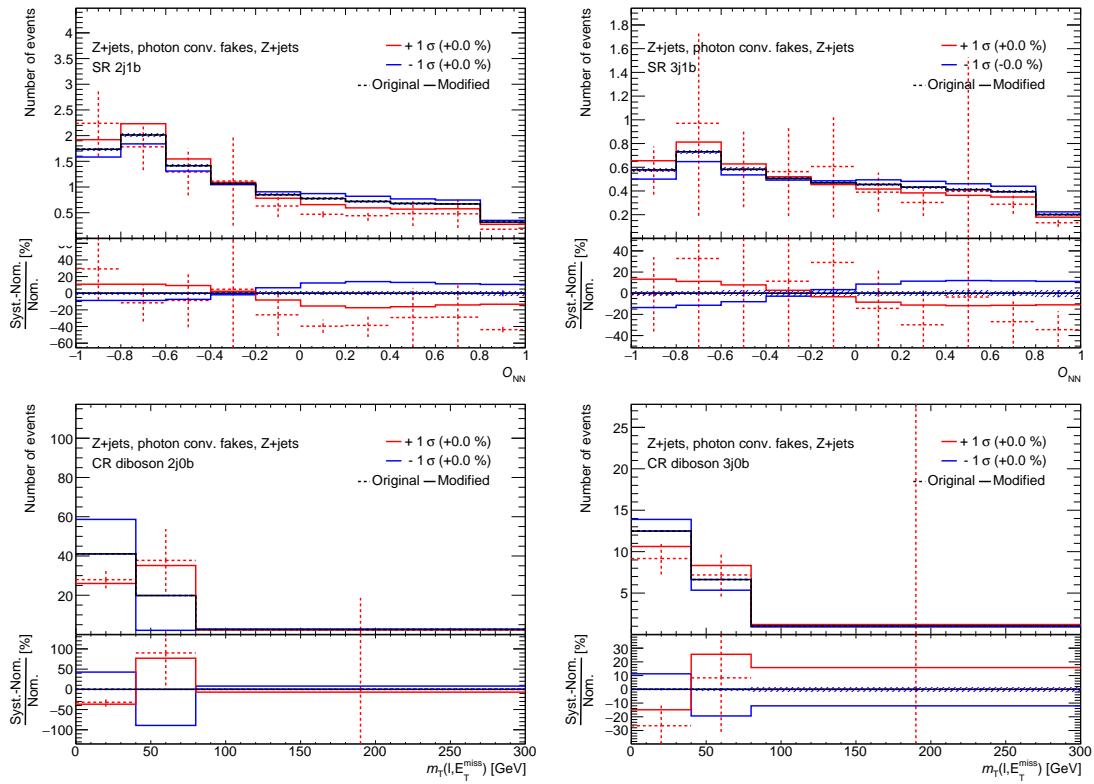
Not reviewed, for internal circulation only

Figure 254:  $t\bar{t}Z$  McAtNLO vs Sherpa uncertainty.

### 1541 G.3.3 Detector uncertainties

Not reviewed, for internal circulation only

Figure 255:  $tZq$  radiation uncertainty.

Figure 256:  $Z + \text{jets}$  BJR shape uncertainty.

Not reviewed, for internal circulation only

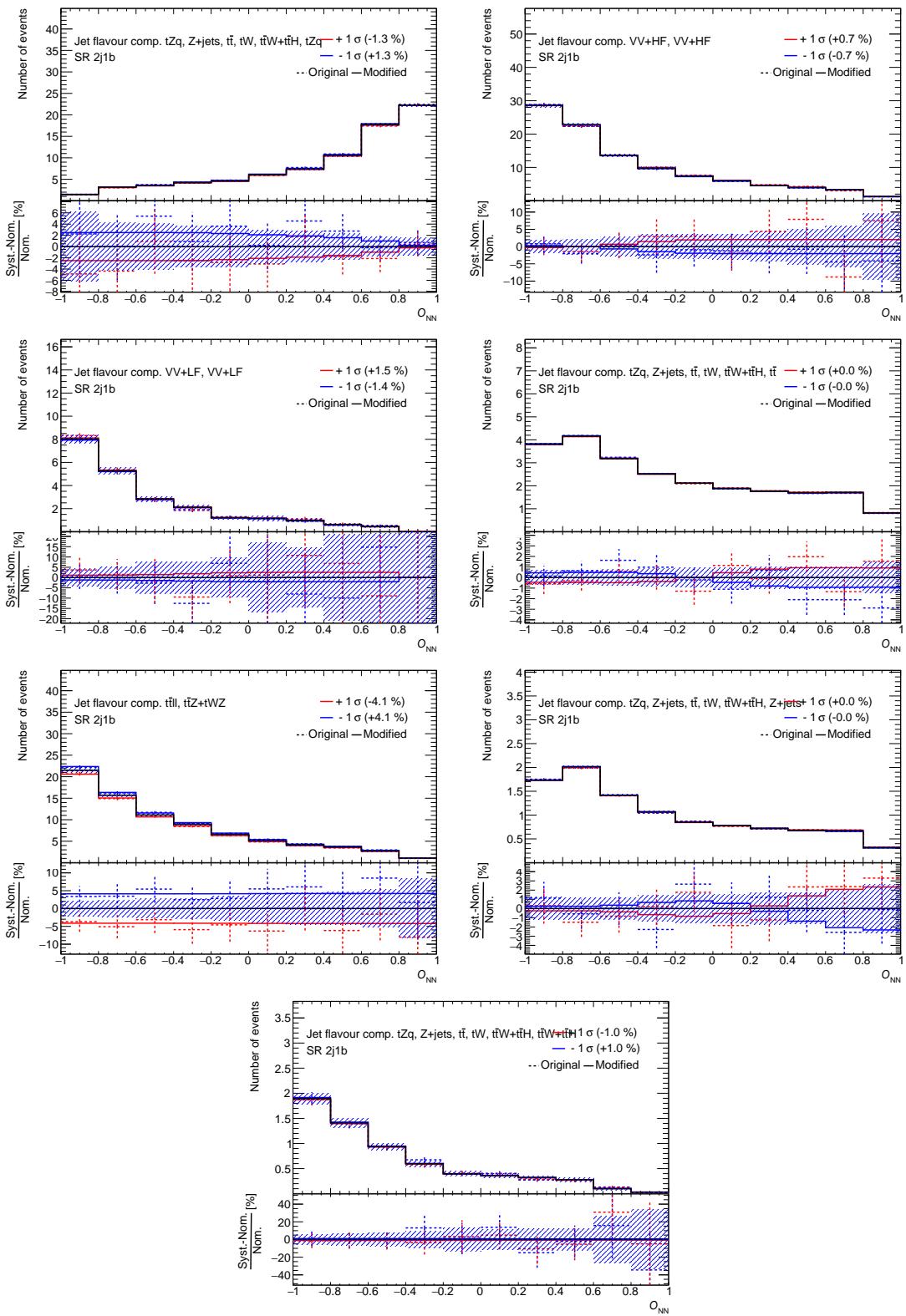


Figure 257: Jet flavour composition uncertainty in the 2j1b SR.

Not reviewed, for internal circulation only

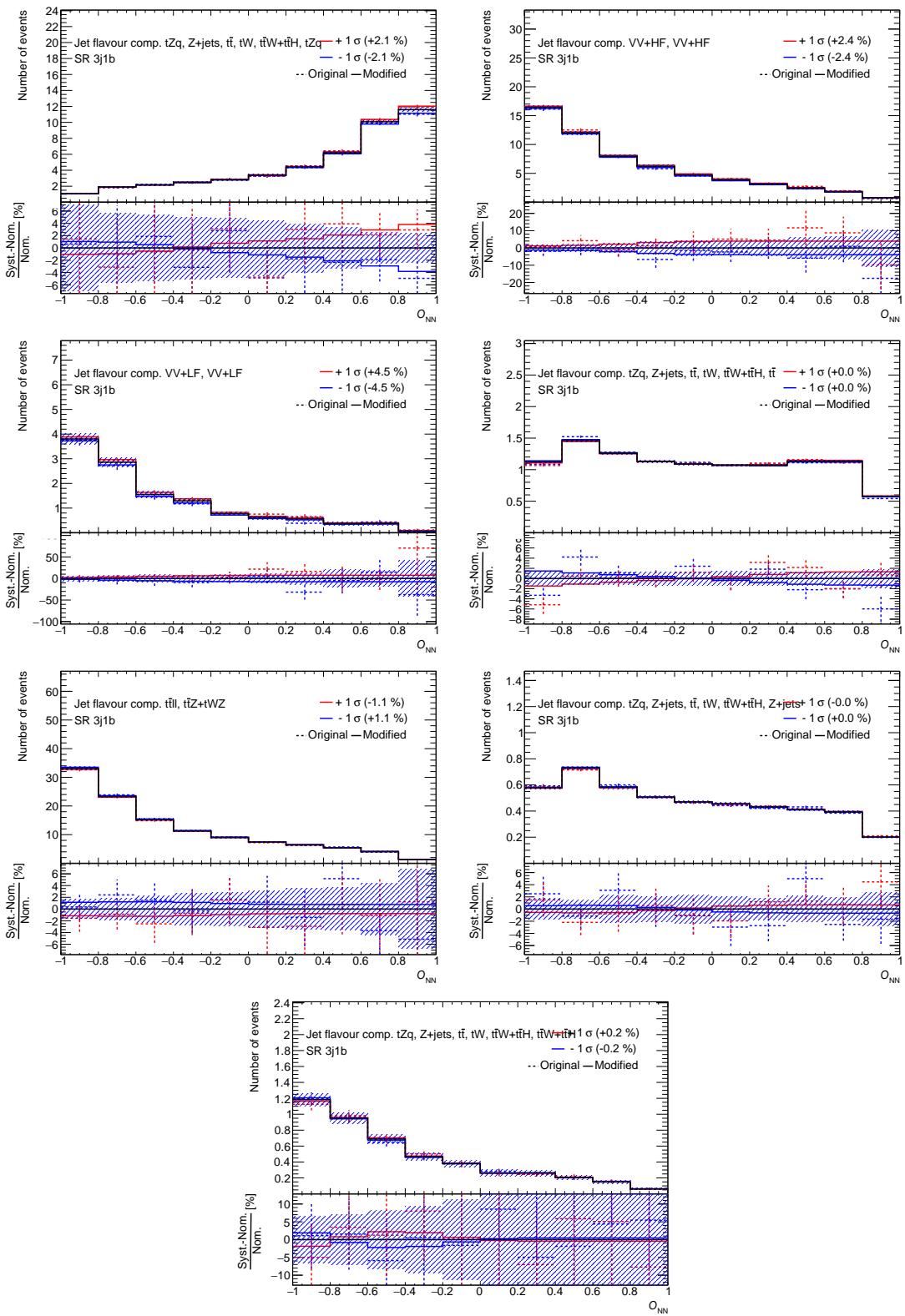


Figure 258: Jet flavour composition uncertainty in the 3j1b SR.

Not reviewed, for internal circulation only

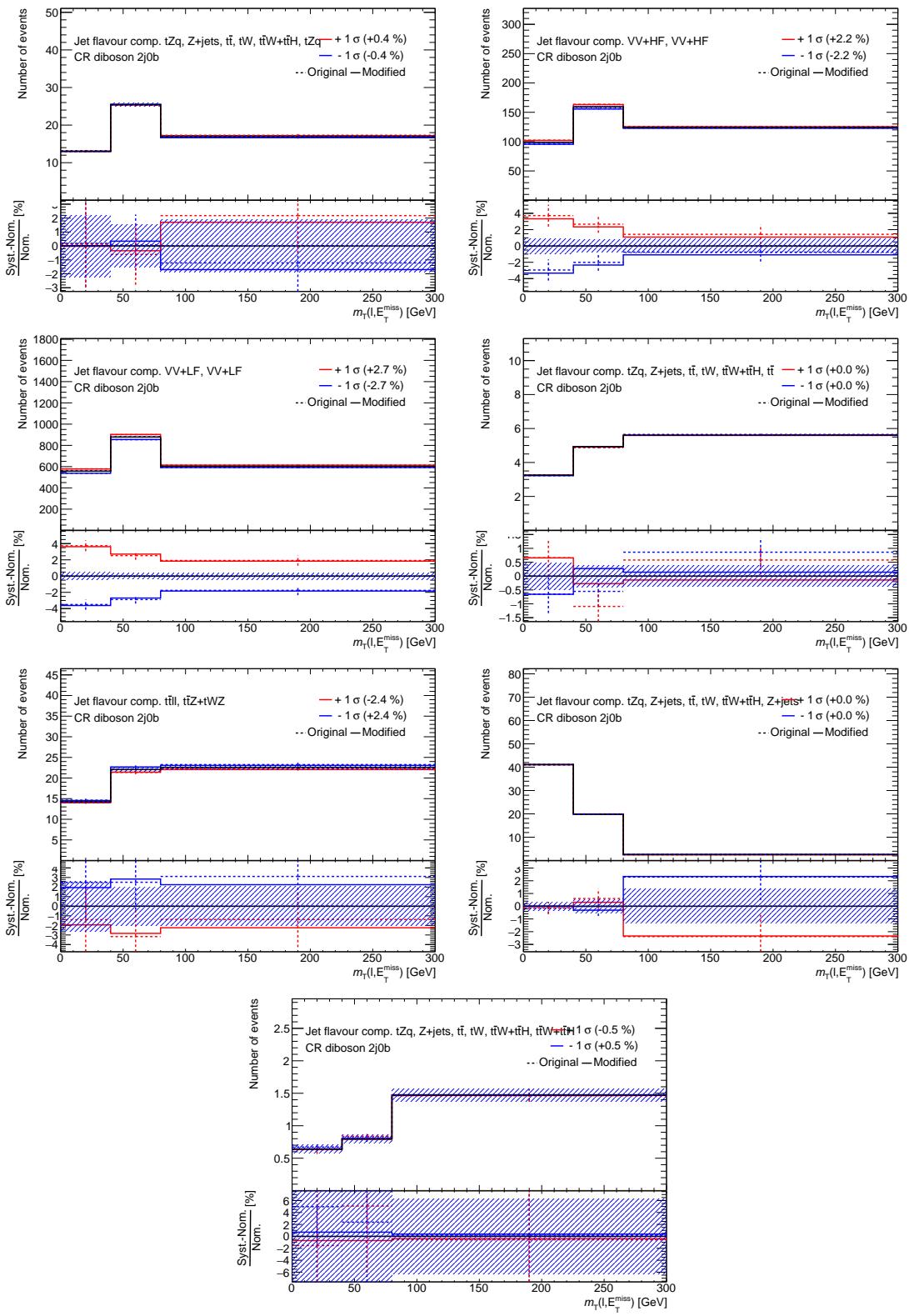


Figure 259: Jet flavour composition uncertainty in the 2j0b CR.

Not reviewed, for internal circulation only

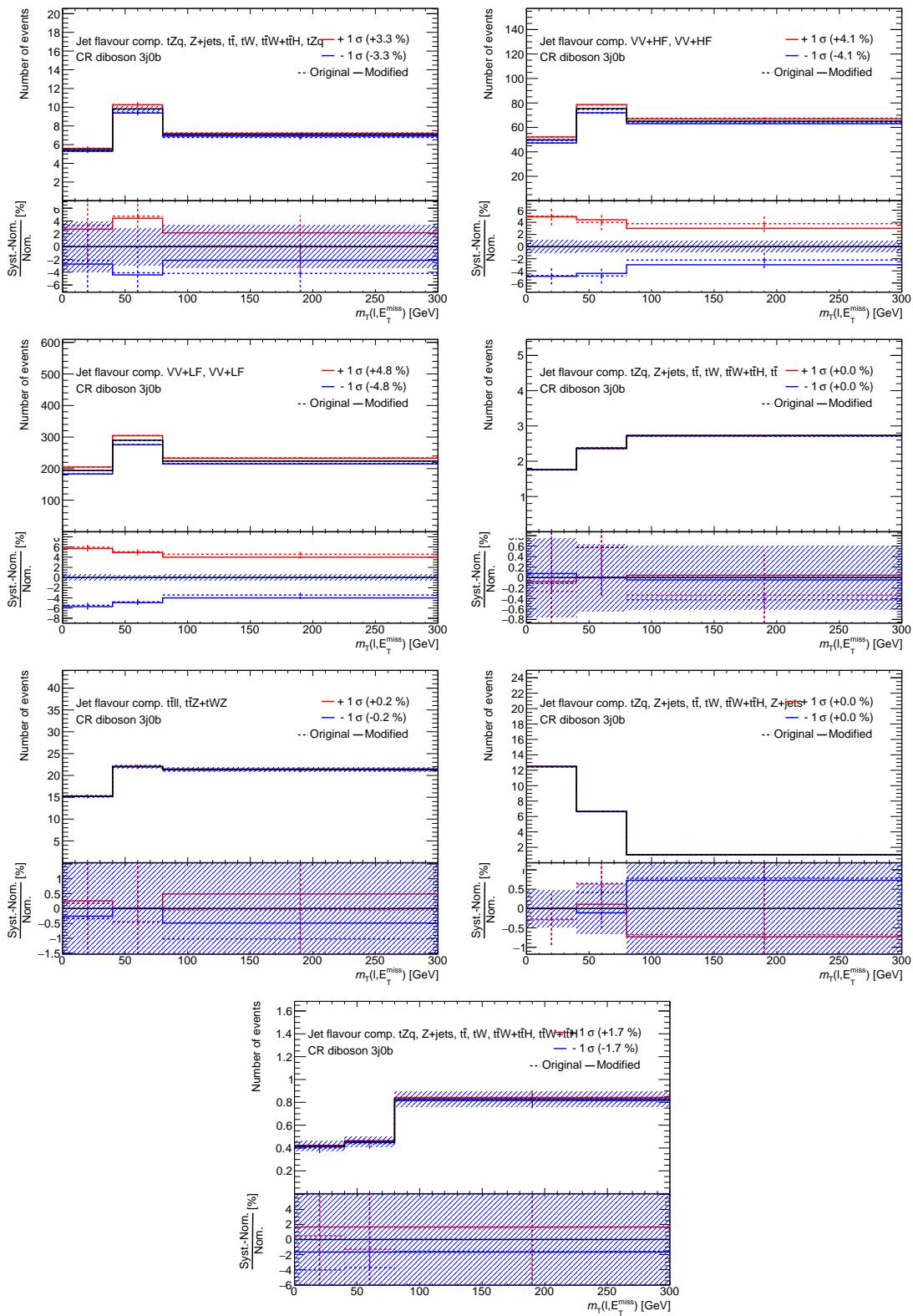


Figure 260: Jet flavour composition uncertainty in the 3j0b CR.

Not reviewed, for internal circulation only

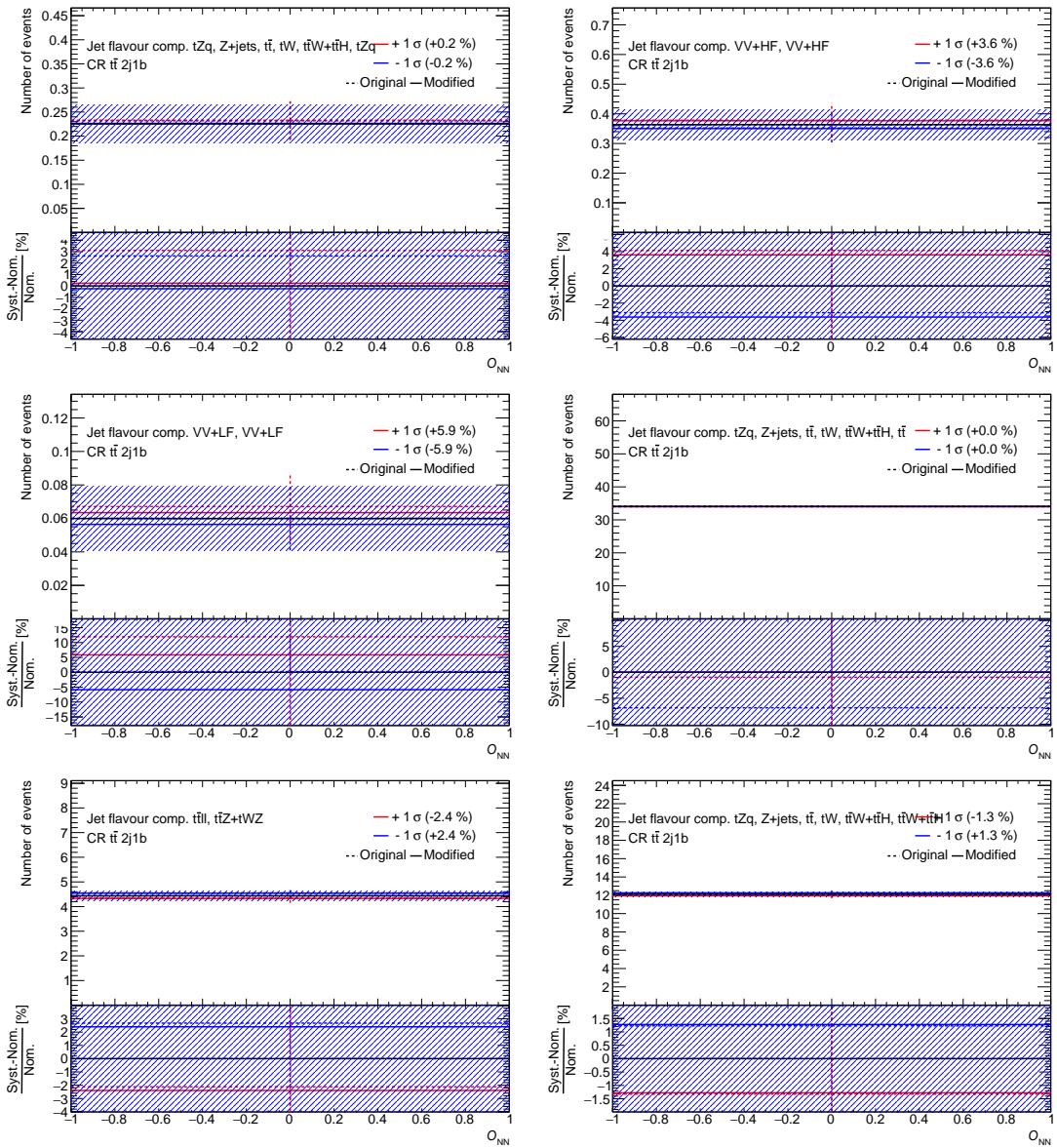


Figure 261: Jet flavour composition uncertainty in the 2j1b CR.

Not reviewed, for internal circulation only

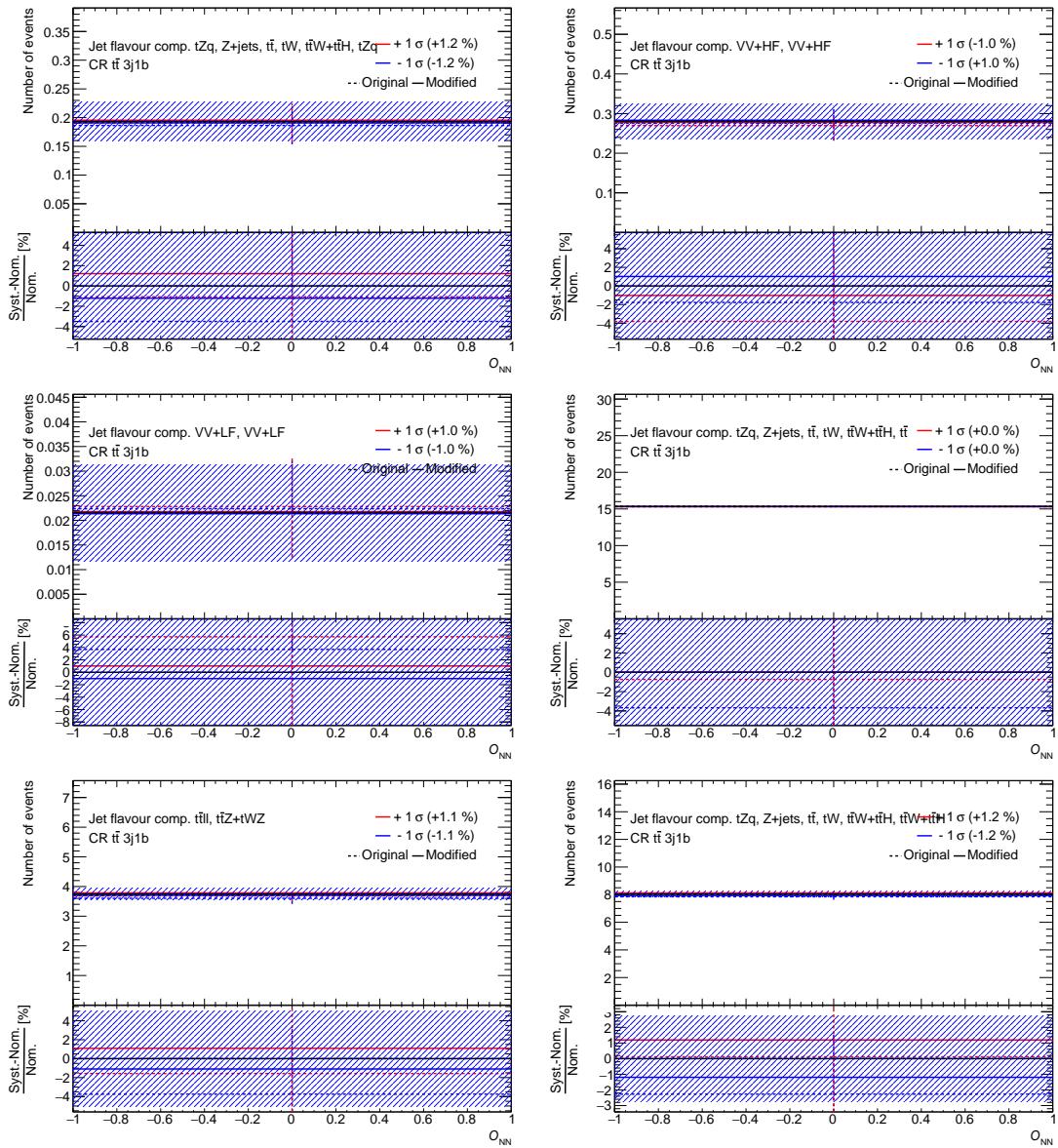


Figure 262: Jet flavour composition uncertainty in the 3j1b CR.

Not reviewed, for internal circulation only

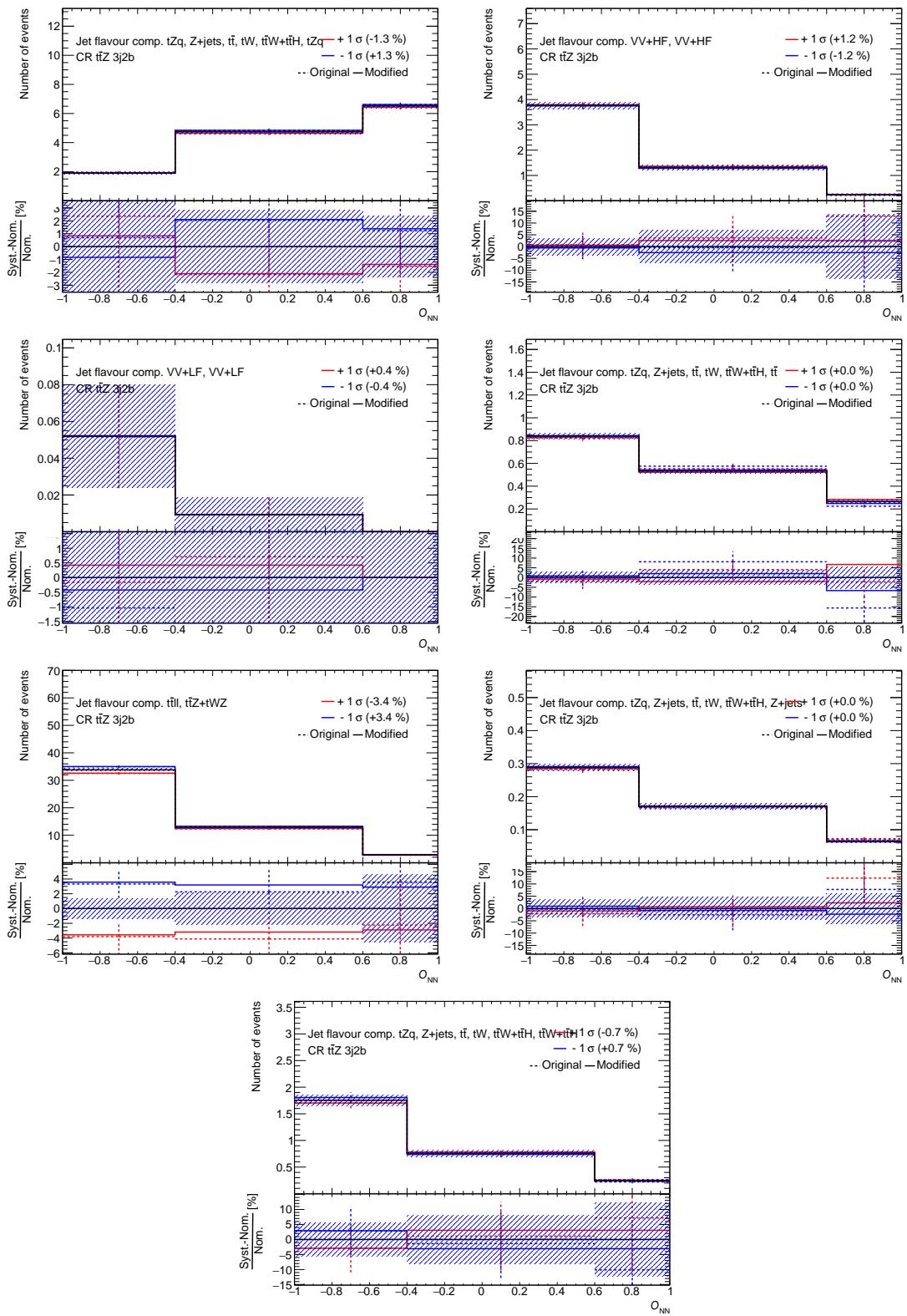


Figure 263: Jet flavour composition uncertainty in the 3j2b CR.

Not reviewed, for internal circulation only

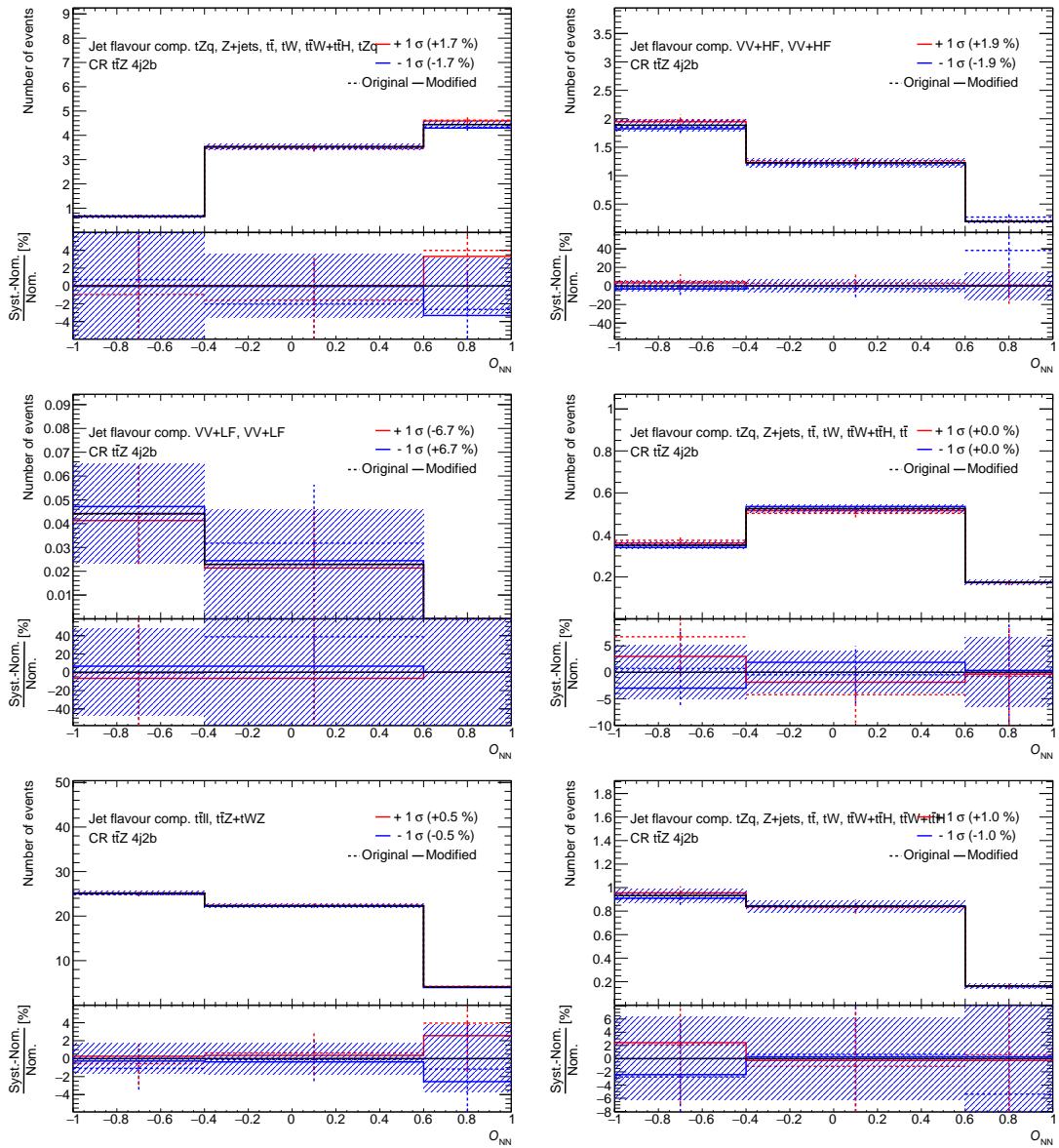


Figure 264: Jet flavour composition uncertainty in the 4j2b CR.

## 1542 G.4 Fit in signal-depleted regions

1543 To check the stability of the fit and the behaviour of the backgrounds, a fit is performed in signal-depleted  
 1544 regions, using pre-normalizations for some backgrounds.

1545 The signal-depleted-region fit is done using real data in the regions explained in Section 10.1 with the  
 1546 following differences:

1547 **signal regions** only those bins with a low  $S/B$  are used, i.e. only the low  $O_{\text{NN}}$  bins, with  $O_{\text{NN}} < -0.4$ ; the  
 1548 rest of the bins are not included;

1549 **diboson control regions** no change;

1550  **$t\bar{t}$  control regions** no change;

1551  **$t\bar{t}Z$  control regions** no change<sup>5</sup>.

1552 The  $t\bar{t}Z + tWZ$  and diboson backgrounds have a pre-normalization uncertainty defined, as described in  
 1553 Section 10.1, while  $t\bar{t}$  and  $Z + \text{jets}$  are free floating. Please note that in this fit,  $t\bar{t}V$  includes  $t\bar{t}Z$  and  $tWZ$ ,  
 1554 while  $t\bar{t}W$  and  $t\bar{t}H$  appear as *small backgrounds*.

1555 In the following the results of this fit are shown.

1556 The values of the background NPs after the fit are shown in Fig. 265. The correlation matrix of the  
 1557 parameters included in the fit is shown in Fig. 266.

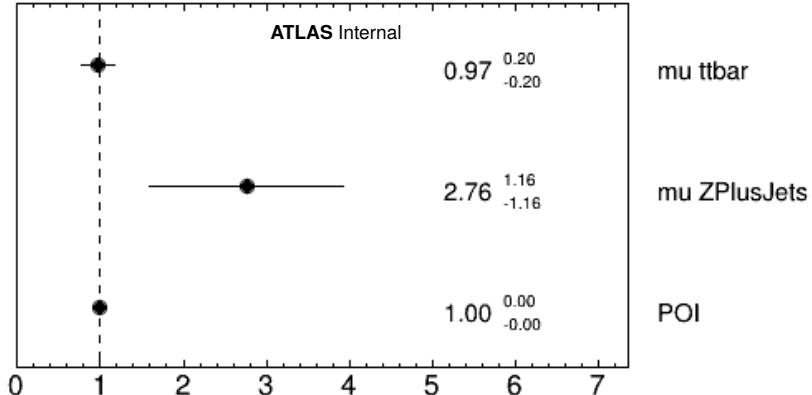


Figure 265: Normalisation factors of the signal-depleted-region fit  $\mu_{\text{SIG}} = 1$ .

1558 The  $t\bar{t}$  estimation is scaled down by 2 %, and  $\mu_{t\bar{t}}$  it is still compatible with 1 within uncertainties. The  $t\bar{t}Z$   
 1559 normalization uncertainty has been pulled upwards by 1  $\sigma$ , as shown in Fig. 268. There is also a moderate  
 1560 pull of the  $t\bar{t}Z$  generator uncertainty which contains acceptance effects. Together these contribute to the  
 1561 same general behavior as the fit with floating  $t\bar{t}Z$  normalization, approximately a 20 % increase.

1562 As already mentioned, the diboson background has two nuisance parameters with a 20 % constraint term  
 1563 in the fit: one describing the heavy-flavour component and one the light-flavour component. There are  
 1564 also generator uncertainties on each diboson processes with a rather large uncertainty between 20 %-50 %

<sup>5</sup> This is therefore different from the fit shown in Appendix G.8, where only events with  $O_{\text{NN}} < 0$  are used.

Not reviewed, for internal circulation only

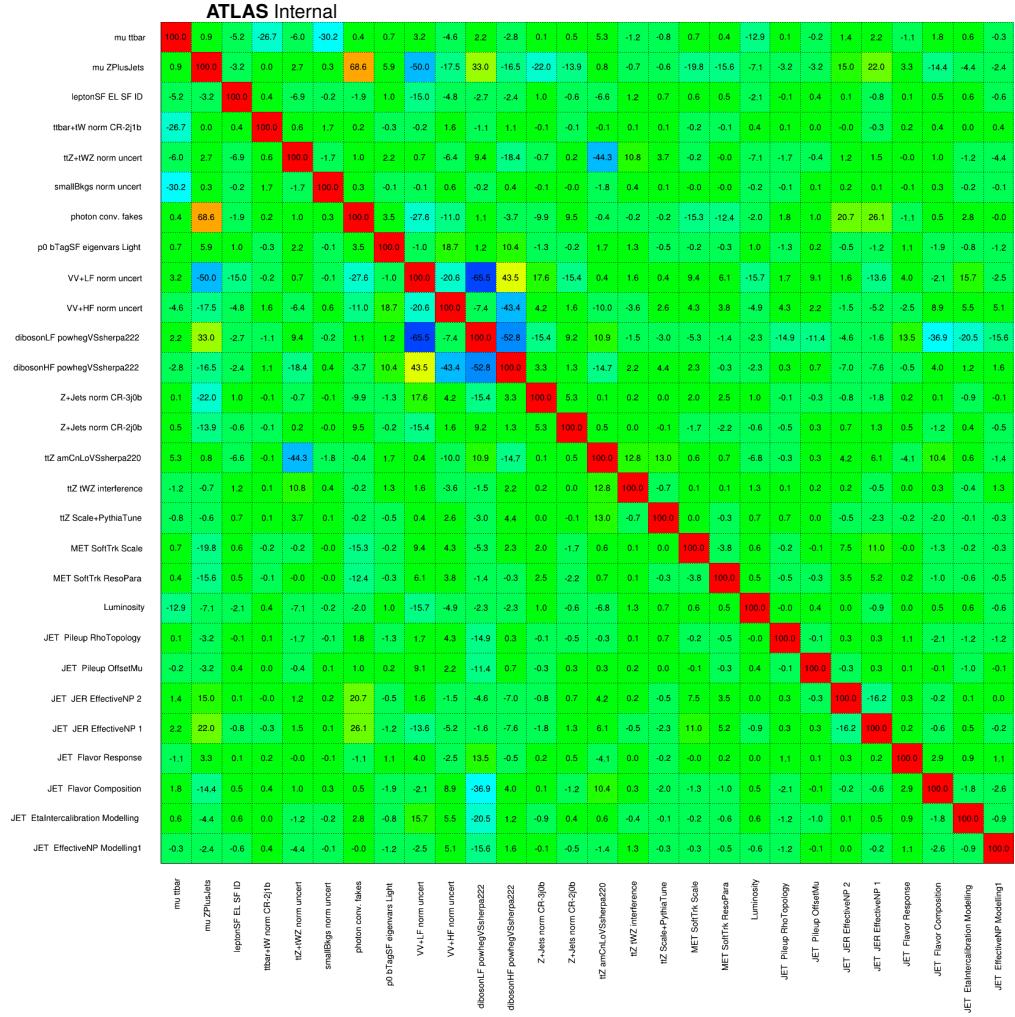


Figure 266: Correlation matrix of the signal-depleted-region fit. Only NPs with a correlation coefficient larger than 10 % with some other NP are shown.

1565 depending on the region and flavor. The combined systematics have a combined effect of scaling all  
 1566 diboson processes down by about 5 %. The amount of variation can differ from region to region due to the  
 1567 nature of the generator modeling systematic.

1568 Finally, the  $Z +$  jets background is scaled up by 280 %, with a large uncertainty. This is expected due to the  
 1569 unreliability of the nominal normalization obtained from the  $Z +$  jets MC, and the large uncertainty reflects  
 1570 the fact that there are very few  $Z +$  jets events expected in the fit regions. The extraction of  $Z +$  jets happens  
 1571 primarily through the diboson 2j0b and 3j0b CRs (Fig. 277) which explains why this background is highly  
 1572 correlated with both dibosons and  $t\bar{t}Z$ .

1573 The largest correlations are between uncertainties on background normalization and their respective  
 1574 modeling uncertainties. This is due to the large impact the modeling systematics have on acceptance.

1575 The pull distributions for the all nuisance parameters can be seen in Figs. 267 to 272 and Fig. 273. Some  
 1576 NPs are slightly pulled, still below  $1\sigma$ .

- 1577 The list of the systematic shapes that are dropped from the fit for each sample and for each region is shown  
 1578 in Figs. 274 and 275.

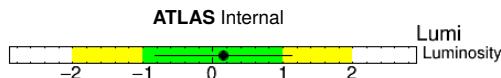


Figure 267: Pulls and constraints of the nuisance parameters of the signal-depleted-region fit  $\mu_{\text{SIG}} = 1$ : luminosity.

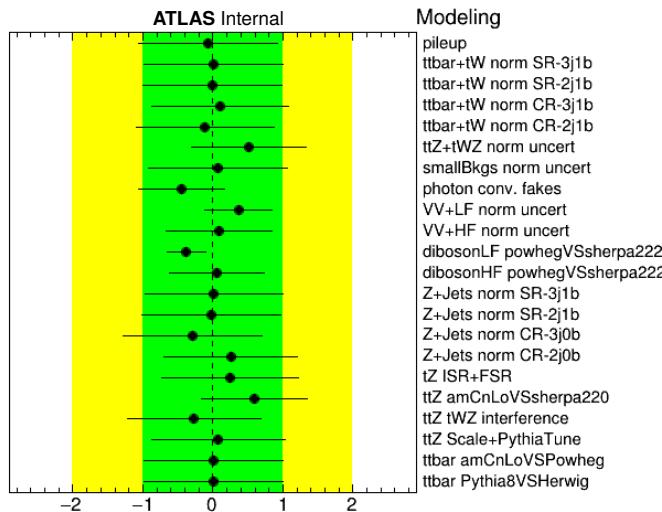


Figure 268: Pulls and constraints of the nuisance parameters of the signal-depleted-region fit  $\mu_{\text{SIG}} = 1$ : modeling systematics.

- 1579 Pre-fit and post-fit distributions of the fitted distributions are shown in Figs. 276 to 279.

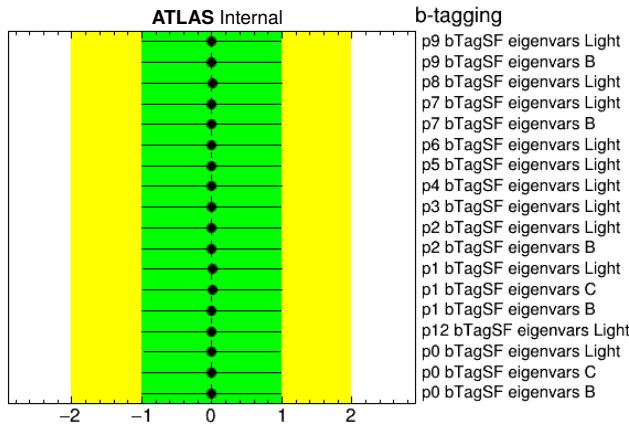


Figure 269: Pulls and constraints of the nuisance parameters of the signal-depleted-region fit  $\mu_{\text{SIG}} = 1$ : *b*-tagging systematics.

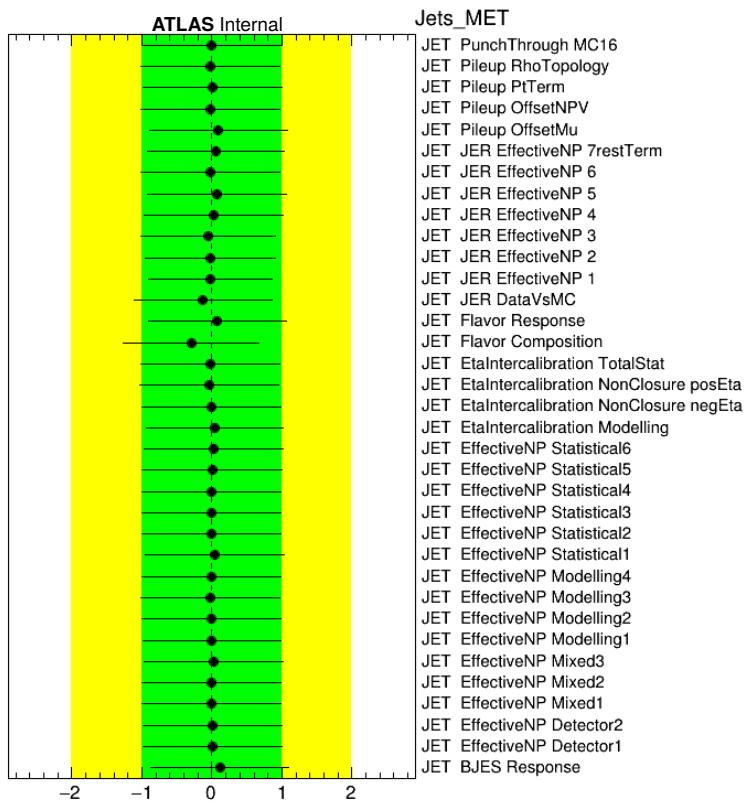


Figure 270: Pulls and constraints of the nuisance parameters of the signal-depleted-region fit  $\mu_{\text{SIG}} = 1$ : jet systematics.

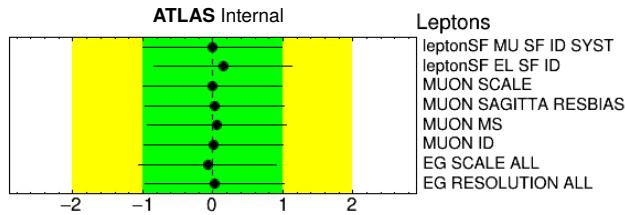


Figure 271: Pulls and constraints of the nuisance parameters of the signal-depleted-region fit  $\mu_{\text{SIG}} = 1$ : lepton systematics.

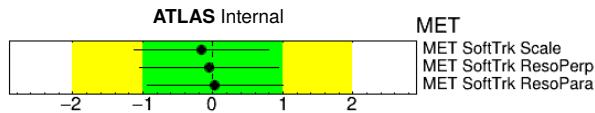


Figure 272: Pulls and constraints of the nuisance parameters of the signal-depleted-region fit  $\mu_{\text{SIG}} = 1$ :  $E_{\text{T}}^{\text{miss}}$  systematics.

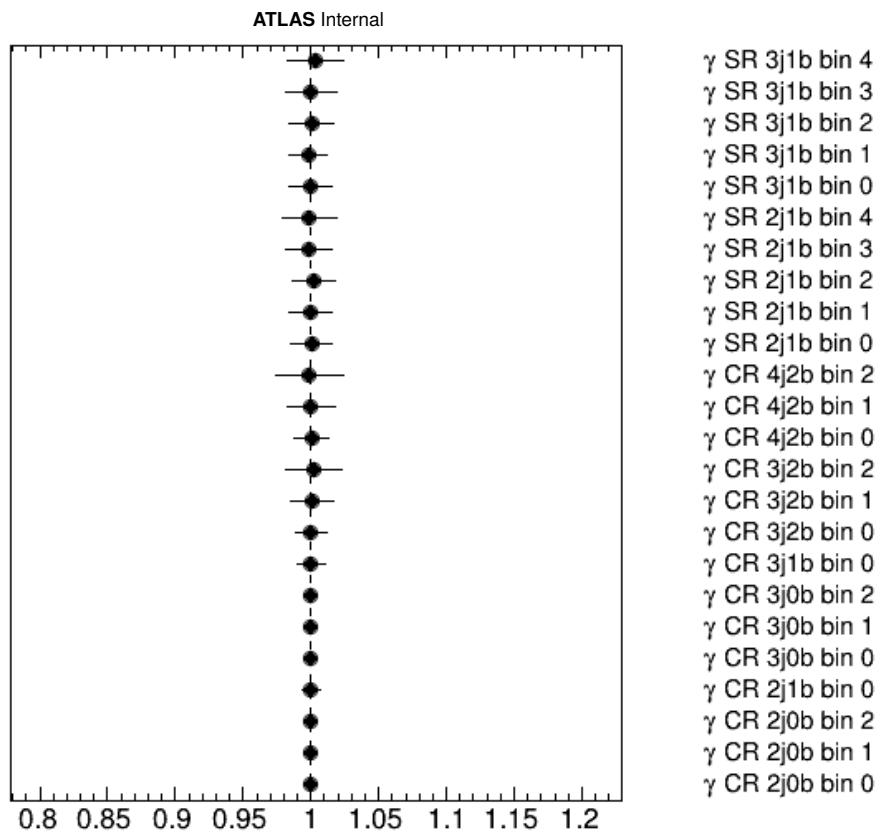


Figure 273: Gamma parameters of the signal-depleted-region fit  $\mu_{\text{SIG}} = 1$ .

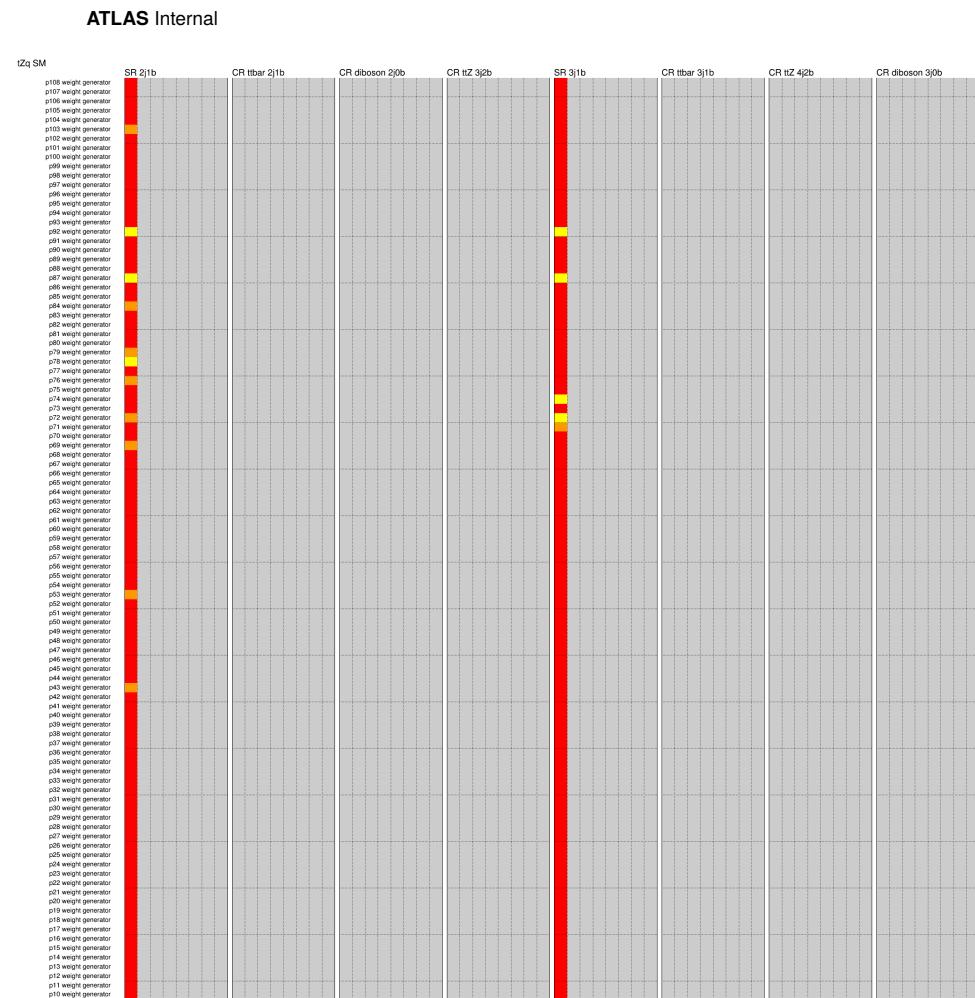


Figure 274: Pruning of the nuisance parameters of the unblinded fit.

Not reviewed, for internal circulation only

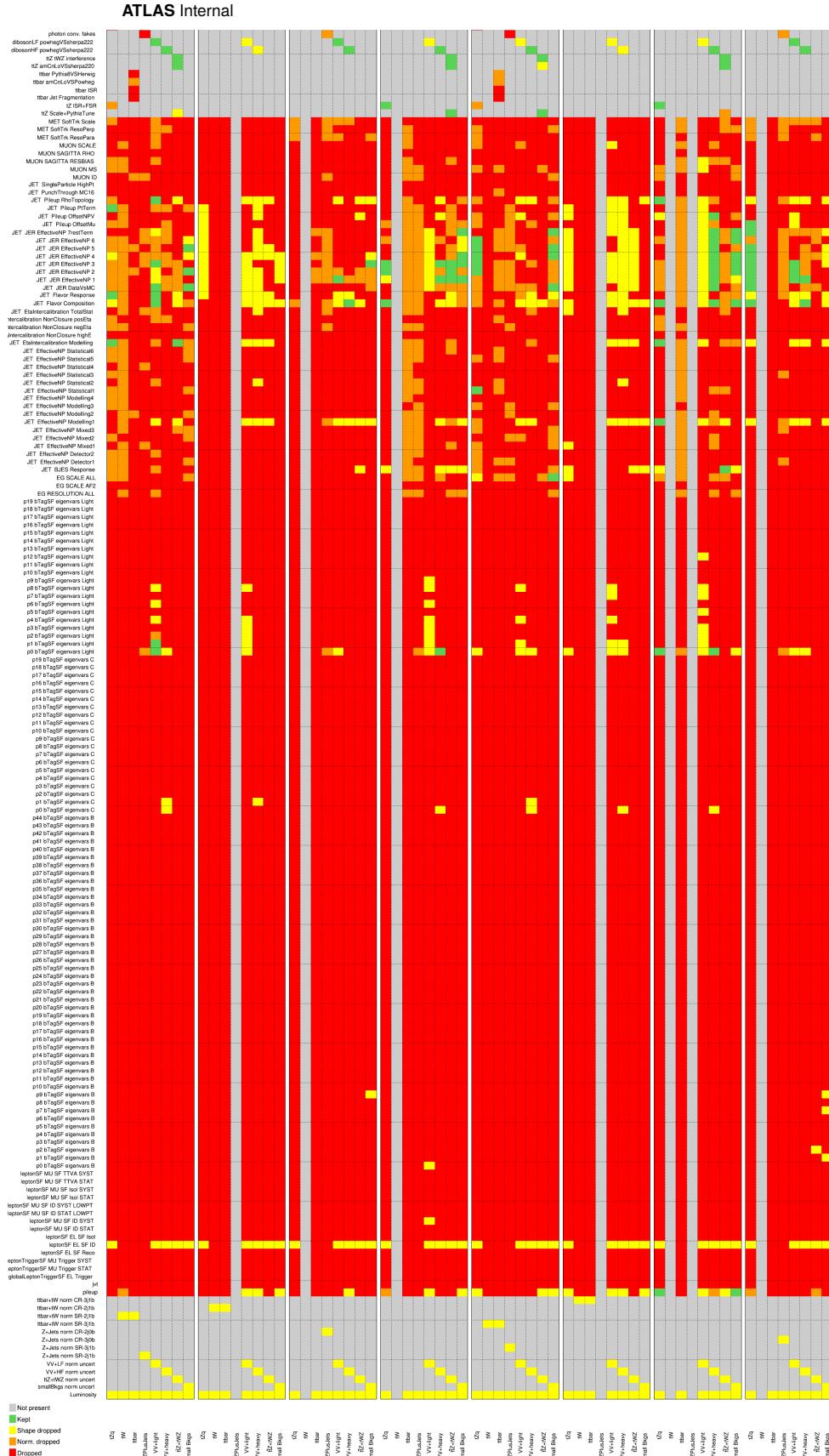


Figure 275: Pruning of the nuisance parameters of the unblinded fit.

Not reviewed, for internal circulation only

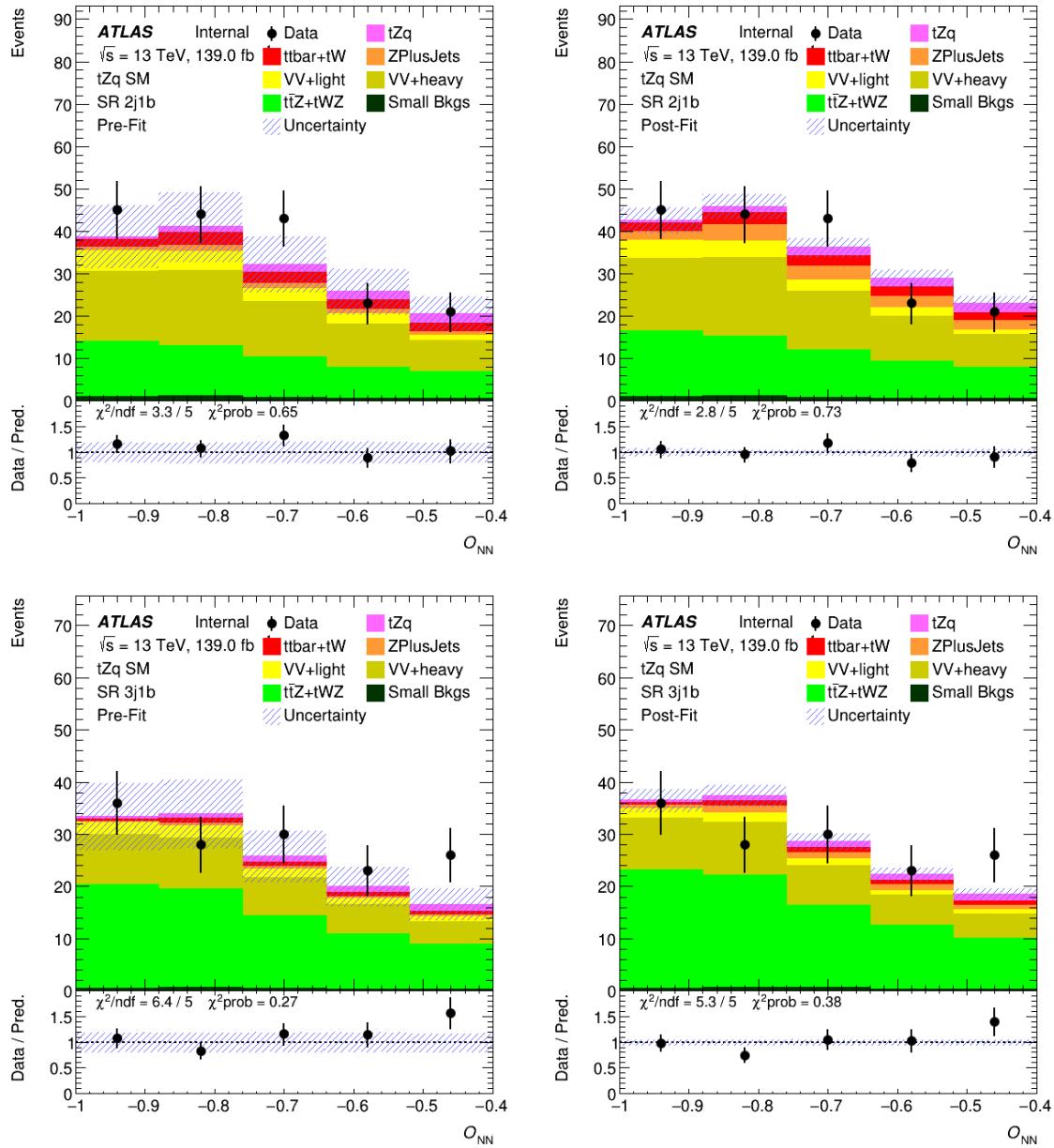


Figure 276: Pre-fit (left) and post-fit (right) NN output distributions in the signal regions with  $O_{\text{NN}} < -0.4$ . The uncertainty band includes both statistical and systematic uncertainties.

Not reviewed, for internal circulation only

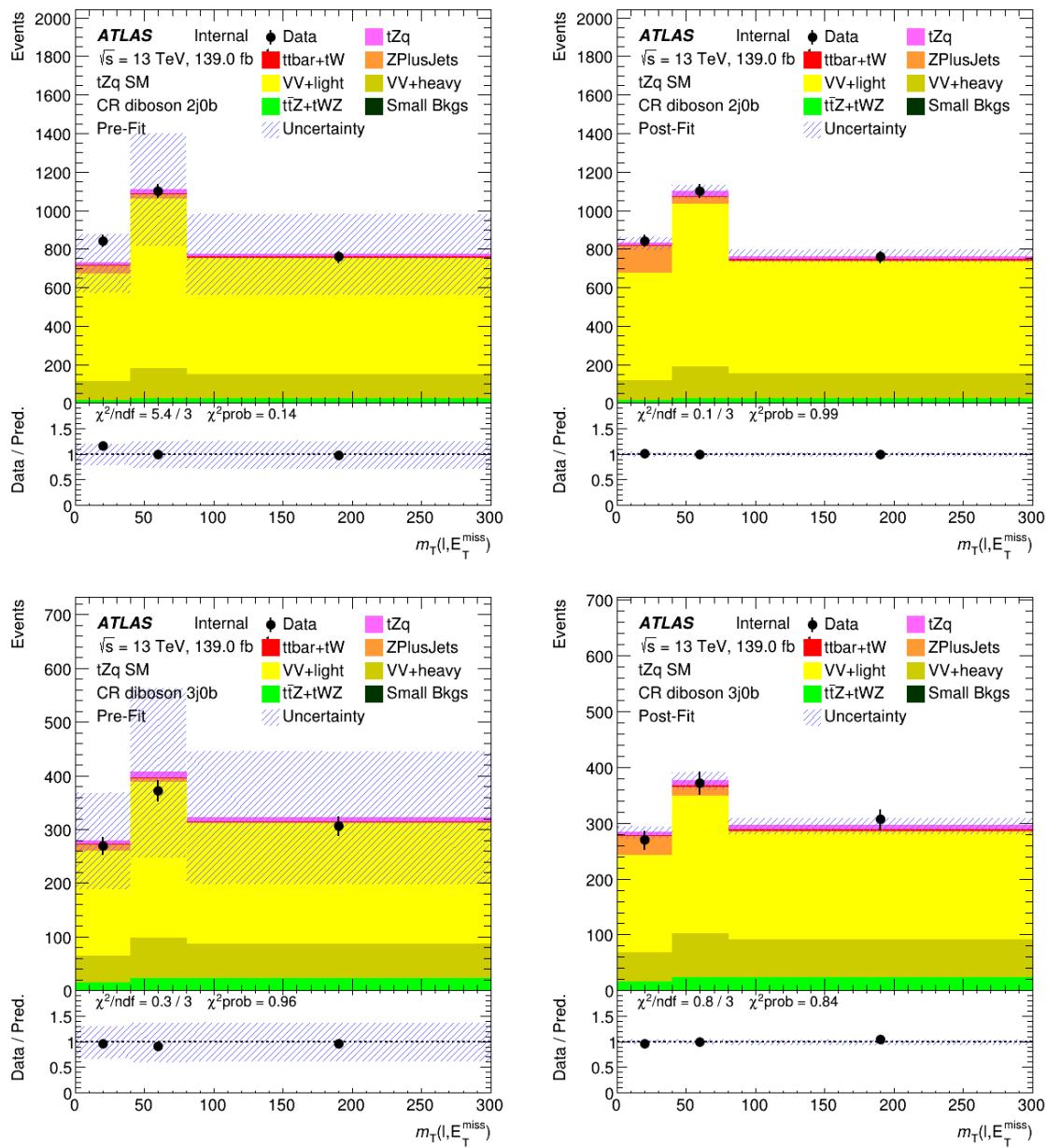


Figure 277: Pre-fit (left) and post-fit (right)  $E_T^{\text{miss}}$  distributions in the diboson control regions. The uncertainty band includes both statistical and systematic uncertainties.

Not reviewed, for internal circulation only

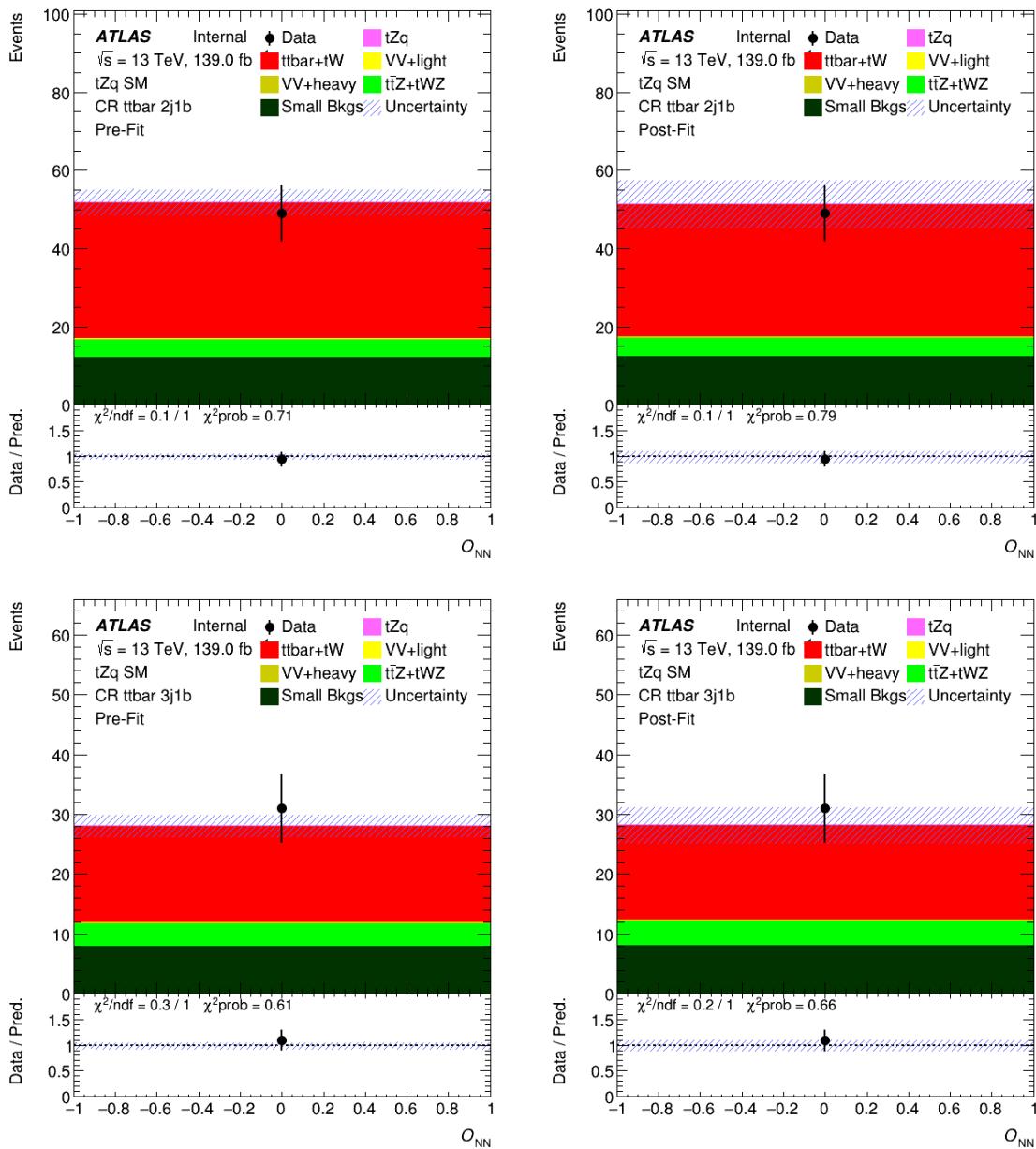


Figure 278: Pre-fit (left) and post-fit (right) NN output distributions in the  $t\bar{t}$  control regions. The uncertainty band includes both statistical and systematic uncertainties. Since the  $t\bar{t}$  background is free floating in the fit, there are no uncertainties on this background pre-fit.

Not reviewed, for internal circulation only

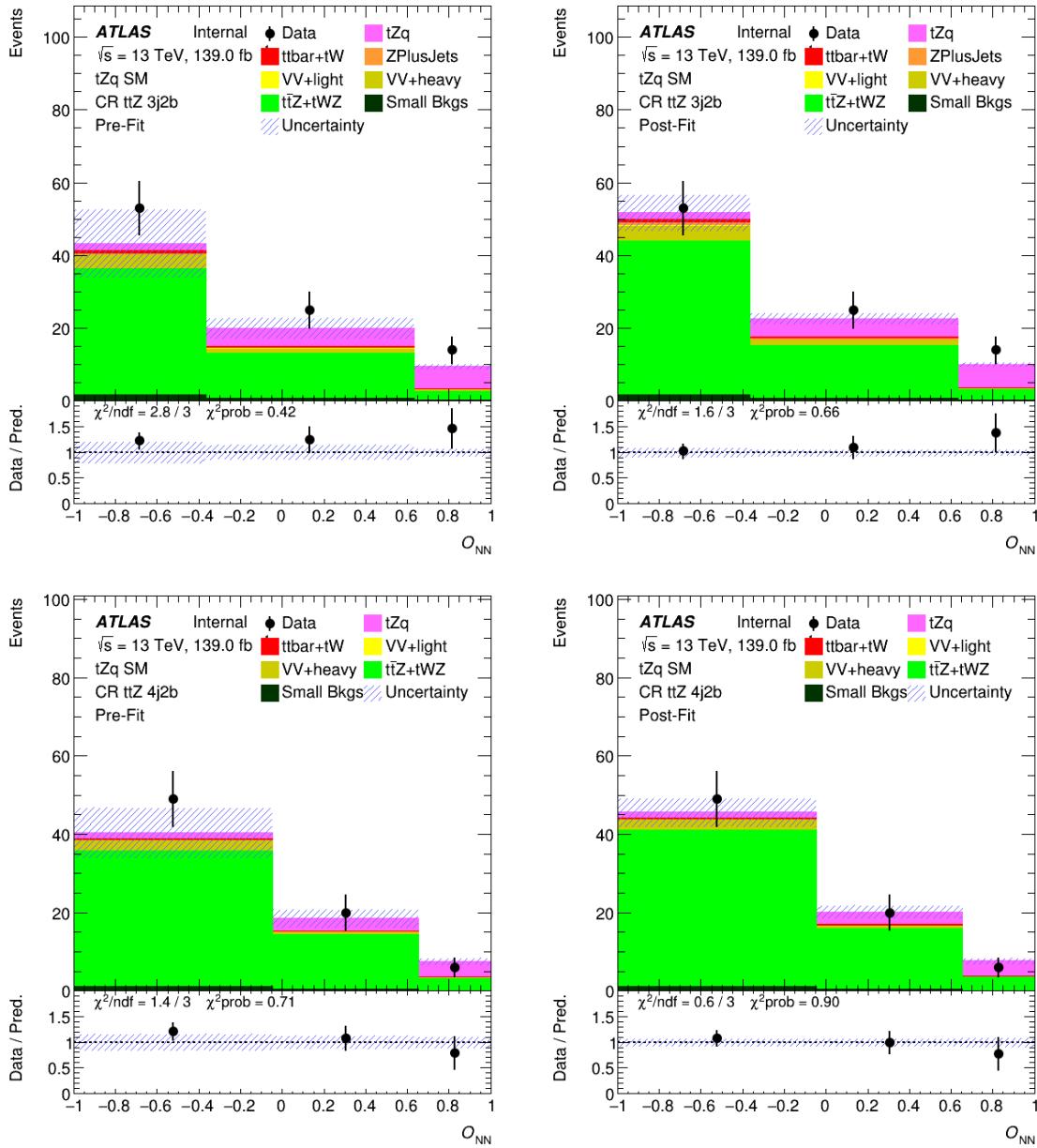


Figure 279: Pre-fit (left) and post-fit (right) NN output distributions in the  $t\bar{t}Z$  control regions with  $O_{NN} < 0$ . The uncertainty band includes both statistical and systematic uncertainties.

1580 **G.4.1 NN input variable distributions in VRs pre- and post-fit**

1581 In this section, the four highest ranked NN input variables are shown, both pre- and post-fit, in the validation  
 1582 regions.

Not reviewed, for internal circulation only

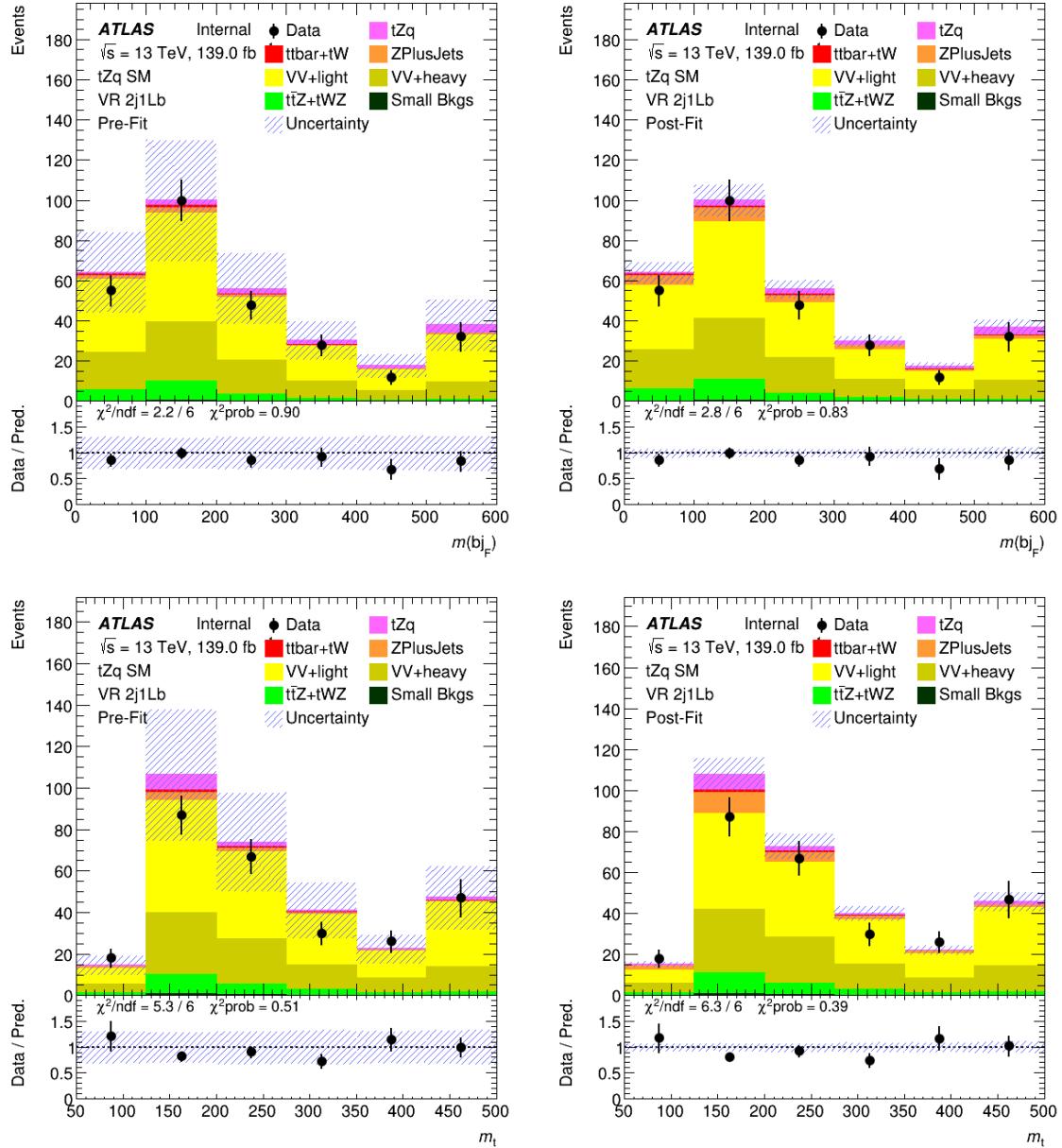


Figure 280: Pre-fit (left) and post-fit (right) NN input variable distributions in the diboson 2j1Lb validation region. The uncertainty band includes both statistical and systematic uncertainties.

Not reviewed, for internal circulation only

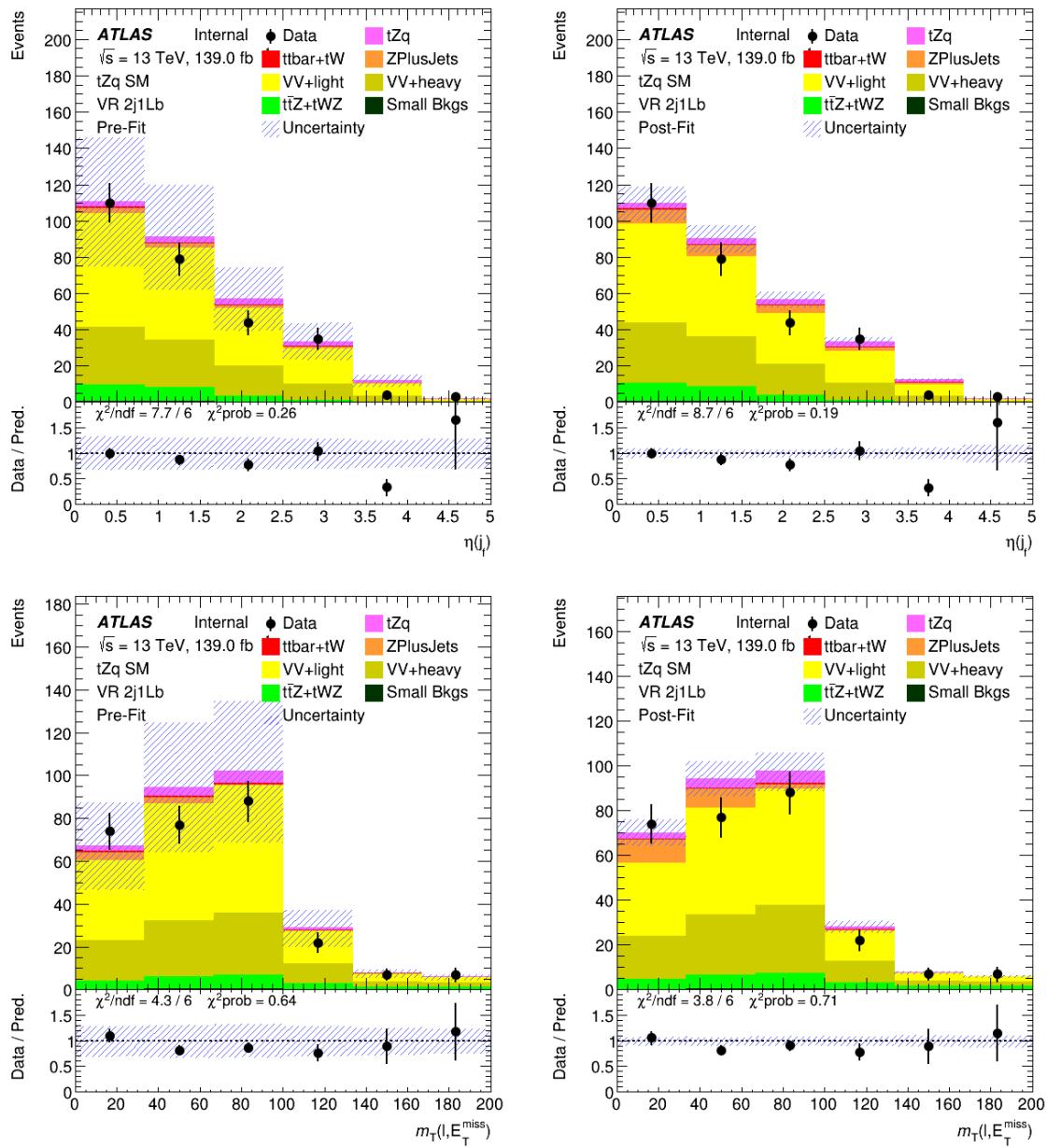


Figure 281: Pre-fit (left) and post-fit (right) NN input variable distributions in the diboson 2j1Lb validation region. The uncertainty band includes both statistical and systematic uncertainties.

Not reviewed, for internal circulation only

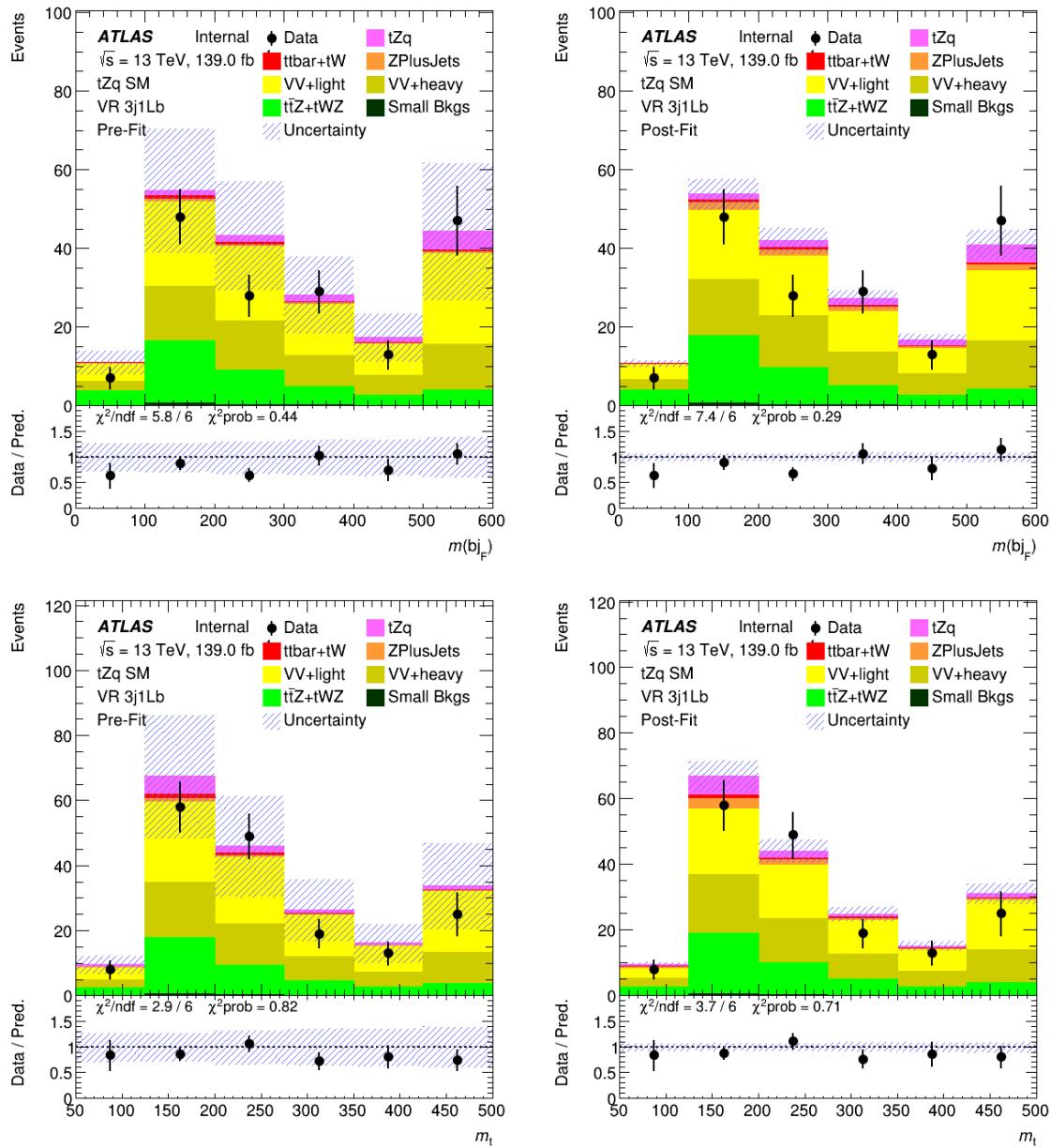


Figure 282: Pre-fit (left) and post-fit (right) NN input variable distributions in the diboson 3j1Lb validation region. The uncertainty band includes both statistical and systematic uncertainties.

Not reviewed, for internal circulation only

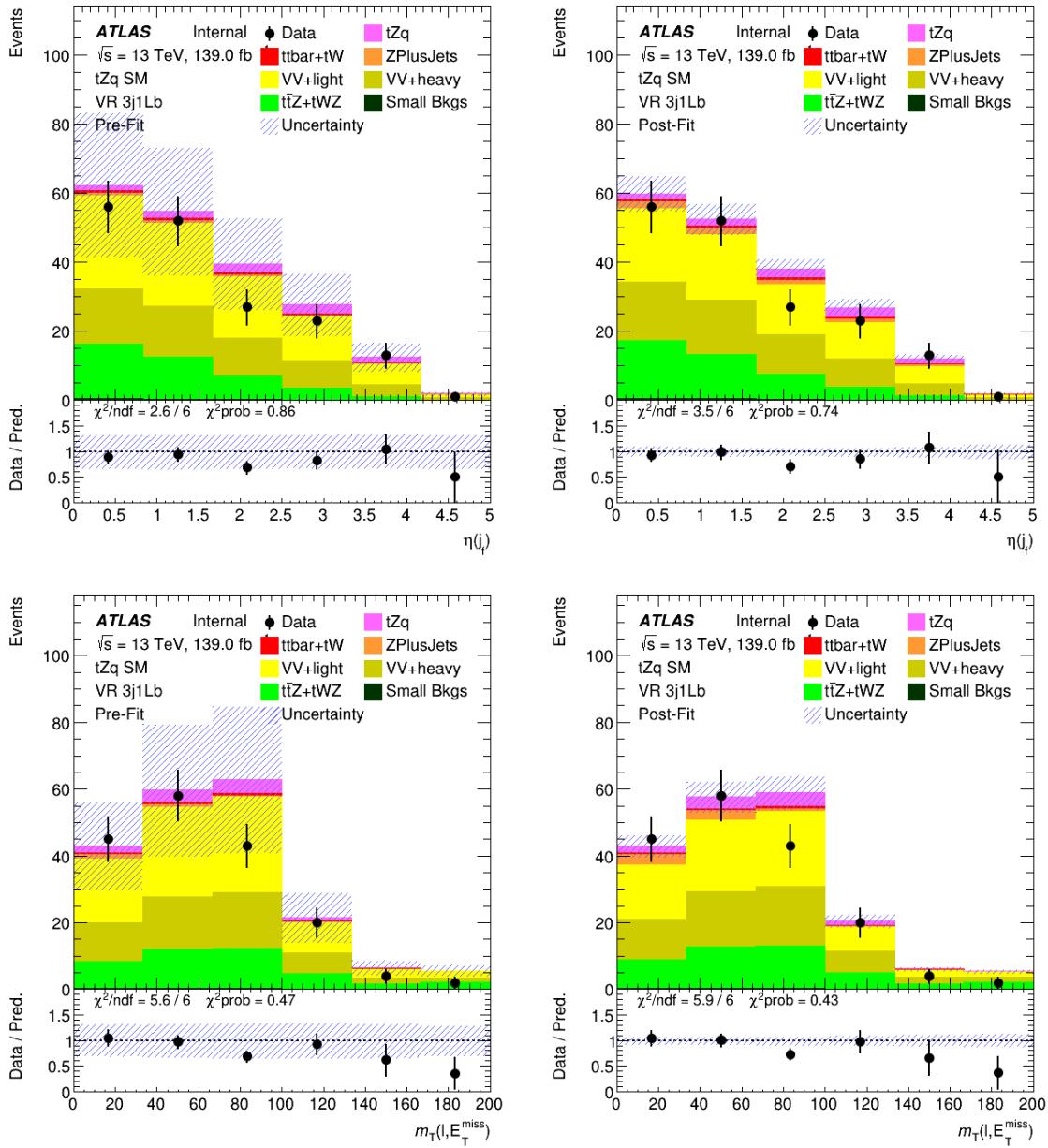


Figure 283: Pre-fit (left) and post-fit (right) NN input variable distributions in the diboson 3j1Lb validation region. The uncertainty band includes both statistical and systematic uncertainties.

Not reviewed, for internal circulation only

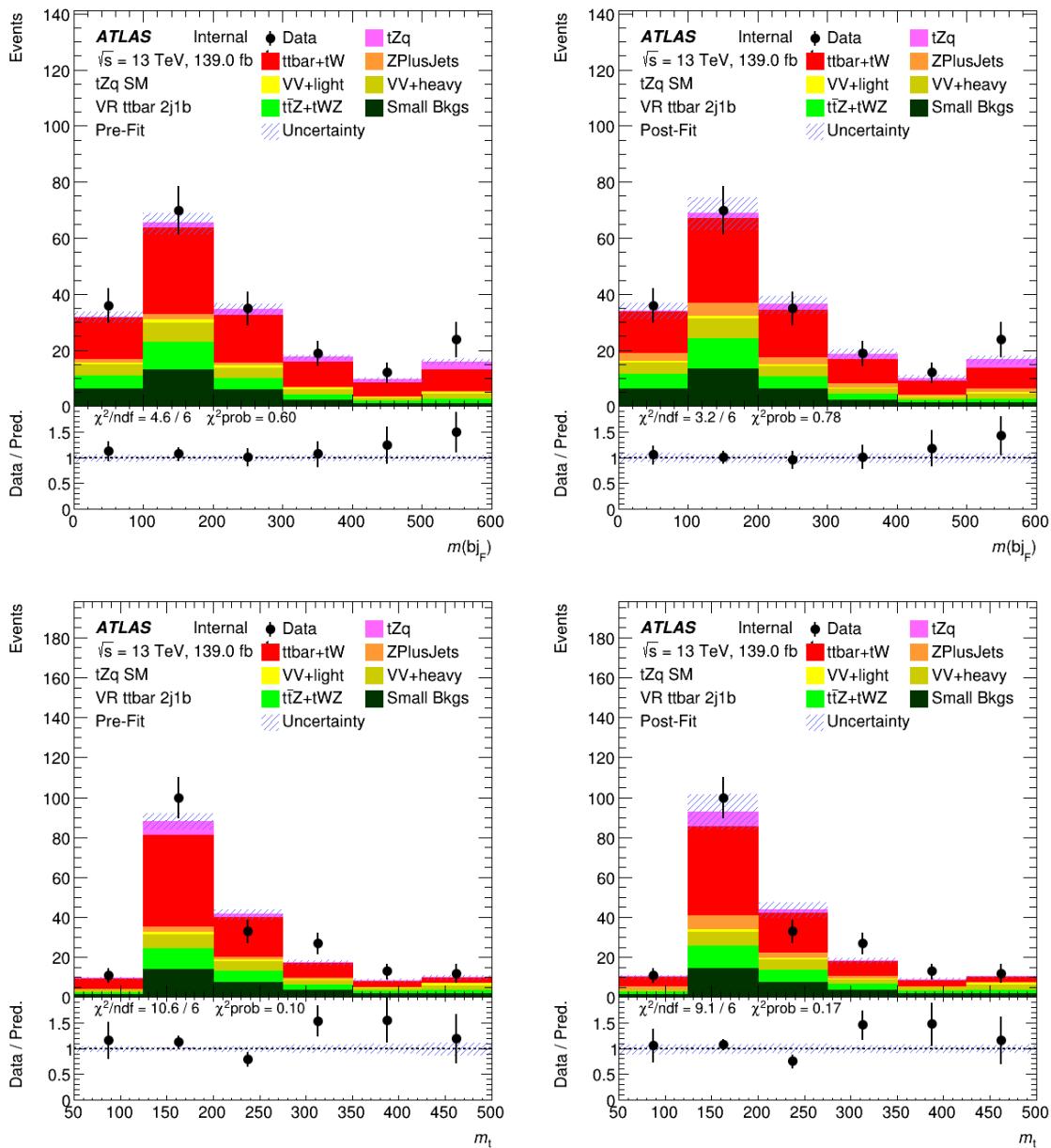


Figure 284: Pre-fit (left) and post-fit (right) NN input variable distributions in the  $t\bar{t}V + t\bar{t}2j1b$  validation region. The uncertainty band includes both statistical and systematic uncertainties. Since the  $t\bar{t}$  background is free floating in the fit, there are no uncertainties on this background pre-fit.

Not reviewed, for internal circulation only

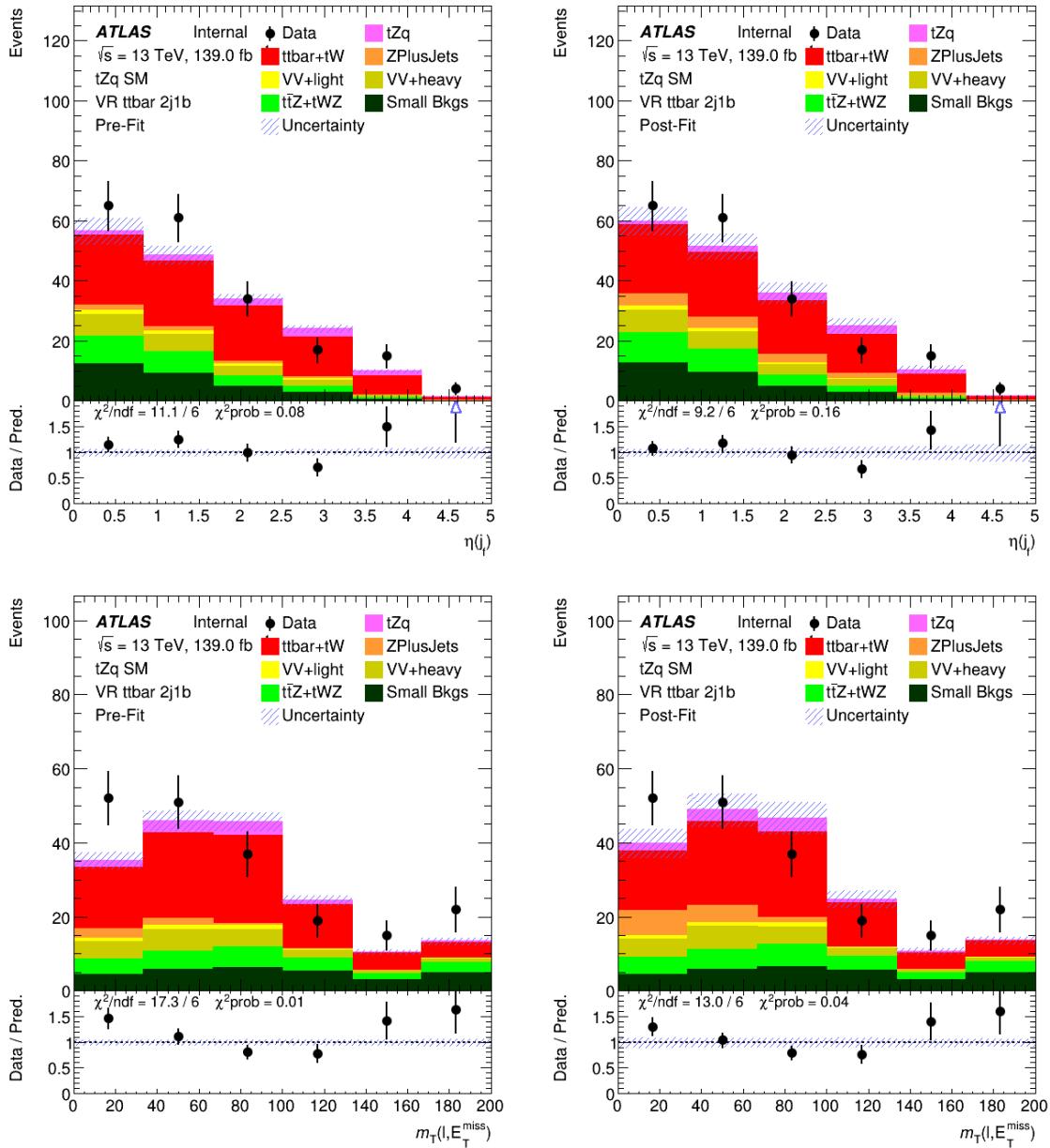


Figure 285: Pre-fit (left) and post-fit (right) NN input variable distributions in the  $t\bar{t}V + t\bar{t} 2j1b$  validation region. The uncertainty band includes both statistical and systematic uncertainties. Since the  $t\bar{t}$  background is free floating in the fit, there are no uncertainties on this background pre-fit.

Not reviewed, for internal circulation only

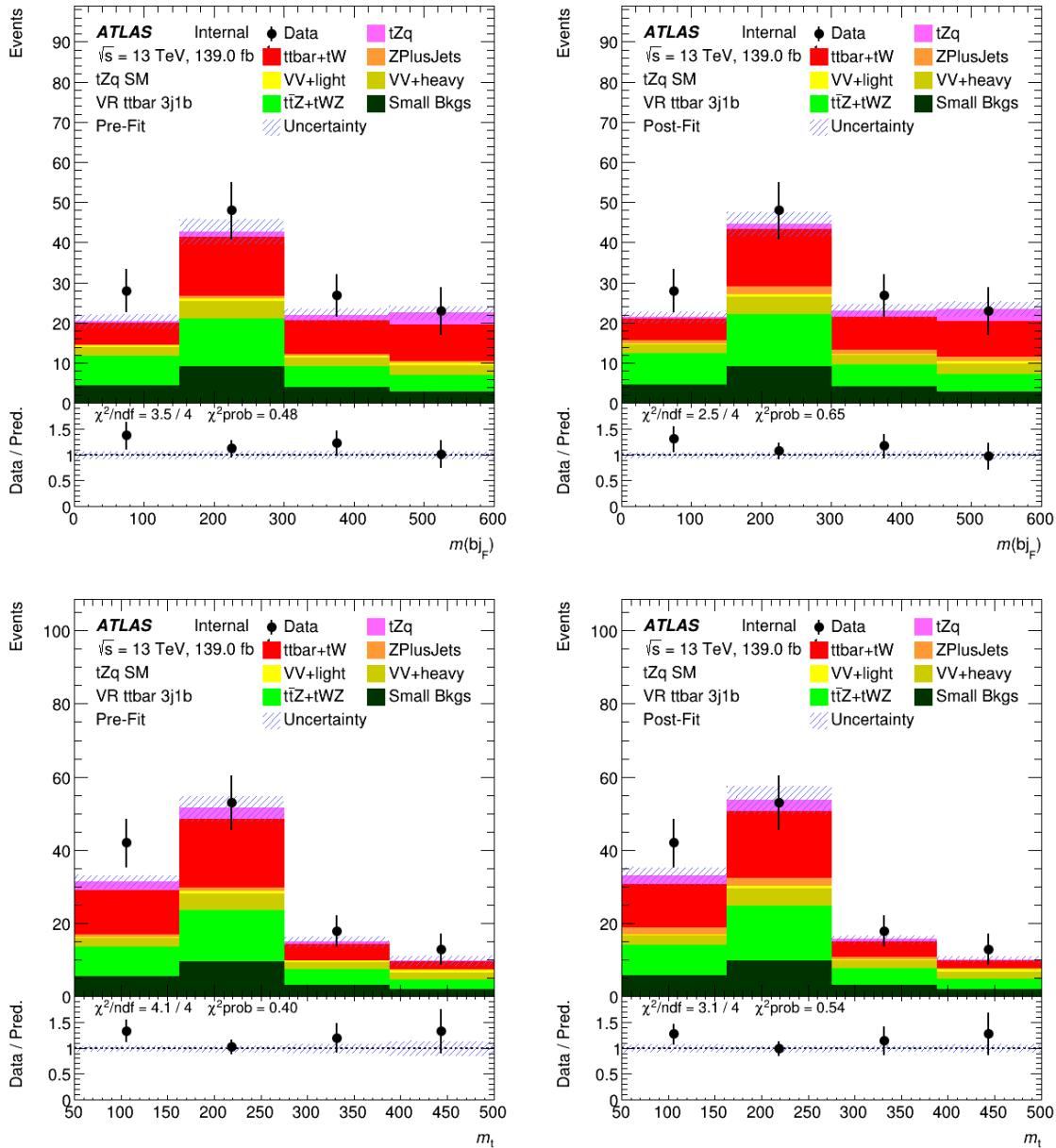


Figure 286: Pre-fit (left) and post-fit (right) NN input variable distributions in the  $t\bar{t}V + t\bar{t}$  3j1b validation regions. The uncertainty band includes both statistical and systematic uncertainties. Since the  $t\bar{t}$  background is free floating in the fit, there are no uncertainties on this background pre-fit.

Not reviewed, for internal circulation only

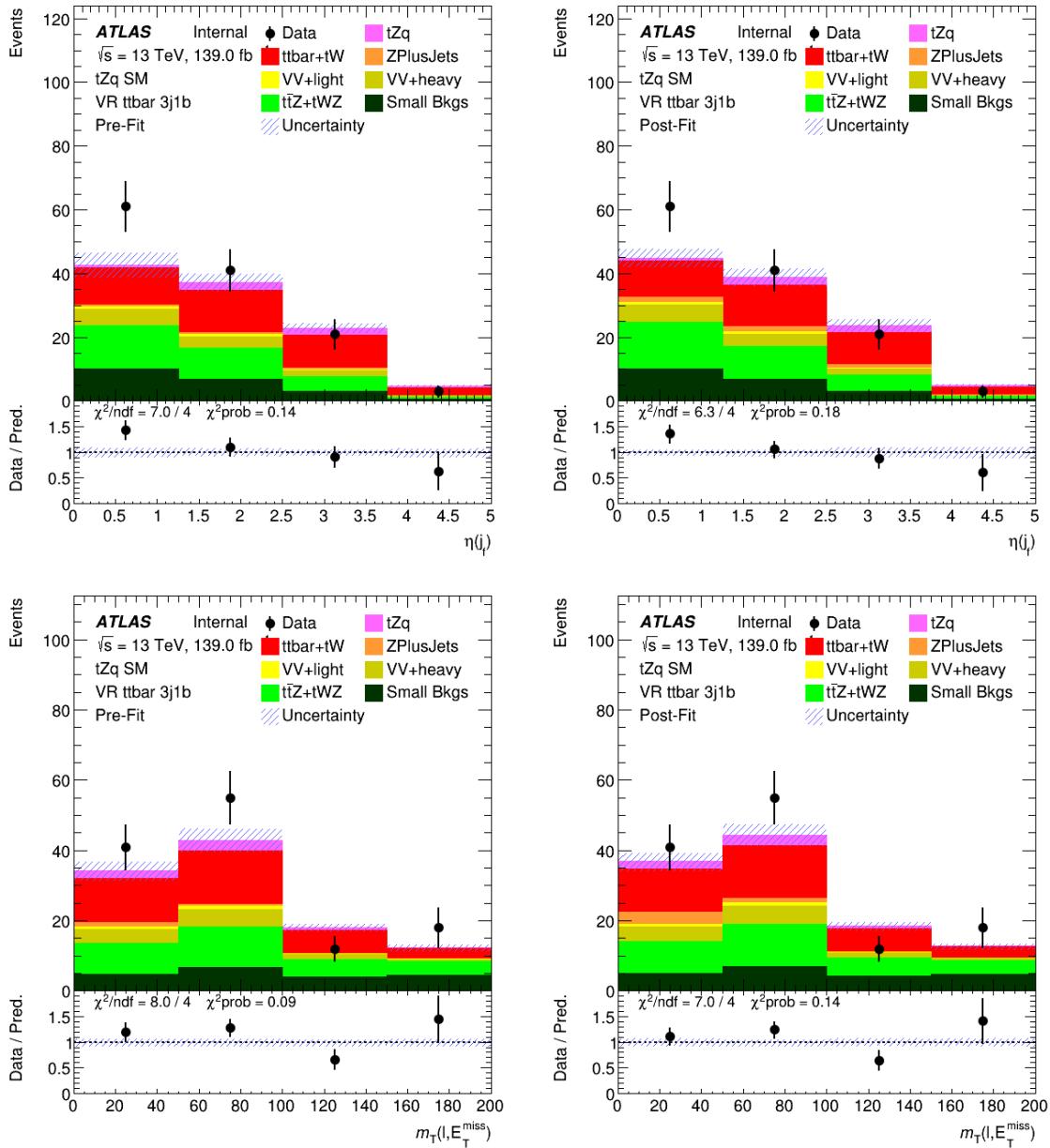


Figure 287: Pre-fit (left) and post-fit (right) NN input variable distributions in the  $t\bar{t}V + t\bar{t}$  3j1b validation regions. The uncertainty band includes both statistical and systematic uncertainties. Since the  $t\bar{t}$  background is free floating in the fit, there are no uncertainties on this background pre-fit.

1583 **G.4.2 NN input variable distributions in unblinded part of the SRs pre- and post-fit**1584 In this section, the four highest ranked NN input variables are shown, both pre- and post-fit, in the unblinded  
1585 part of the signal regions.

Not reviewed, for internal circulation only

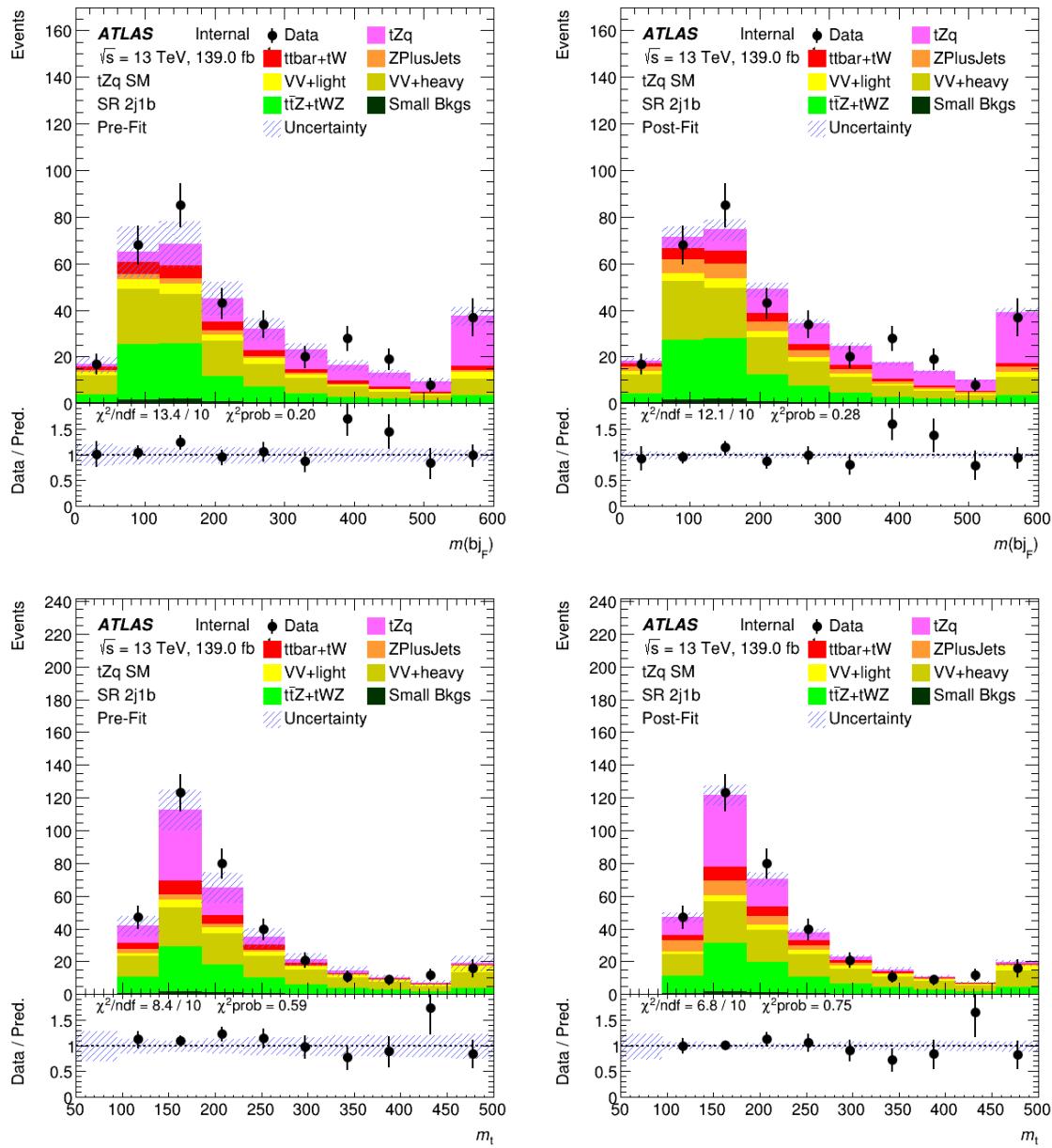


Figure 288: Pre-fit (left) and post-fit (right) NN input variable distributions in the unblinded part of the 2j1b signal region. The uncertainty band includes both statistical and systematic uncertainties.

Not reviewed, for internal circulation only

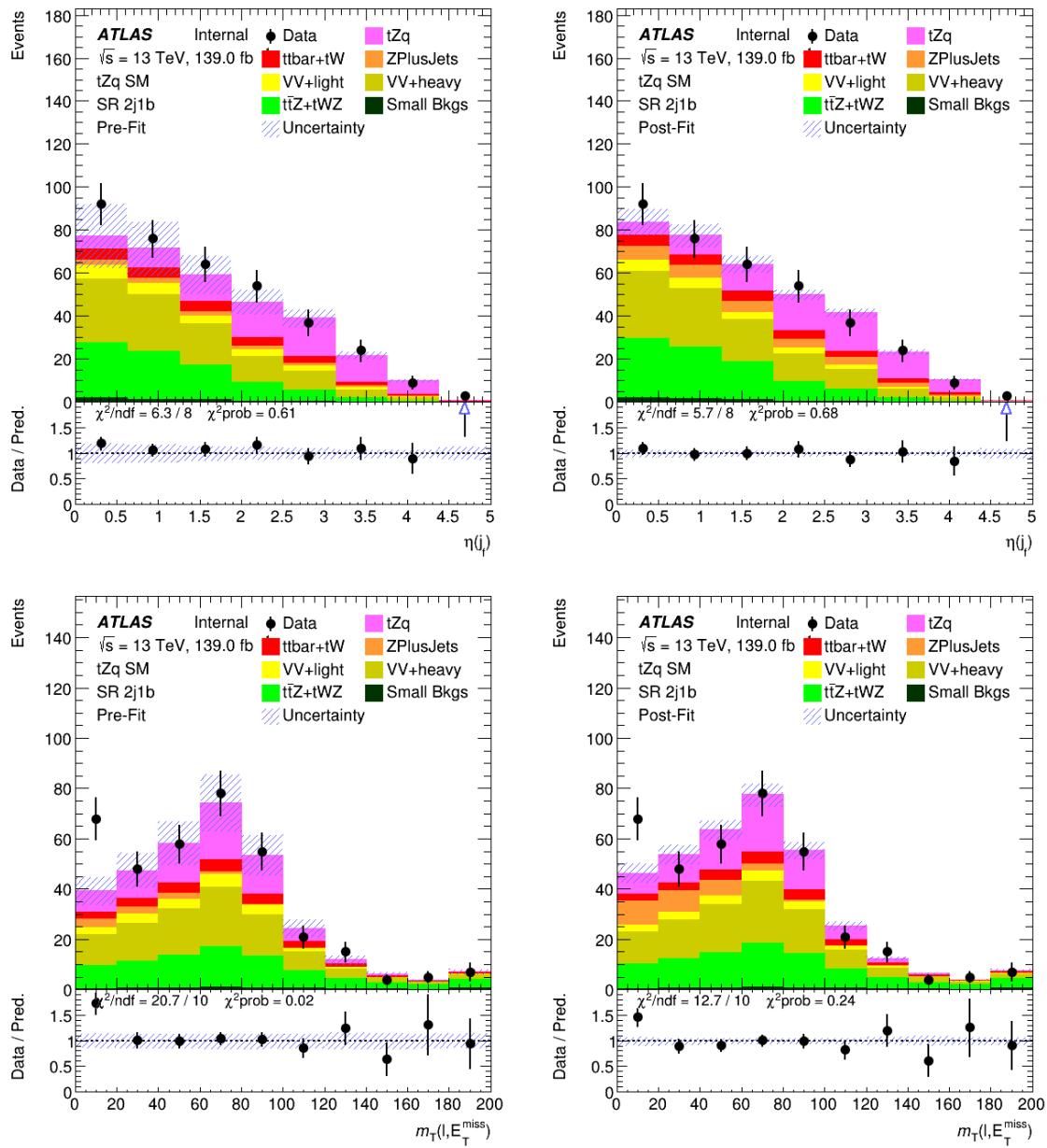


Figure 289: Pre-fit (left) and post-fit (right) NN input variable distributions in the unblinded part of the 2j1b signal region. The uncertainty band includes both statistical and systematic uncertainties.

Not reviewed, for internal circulation only

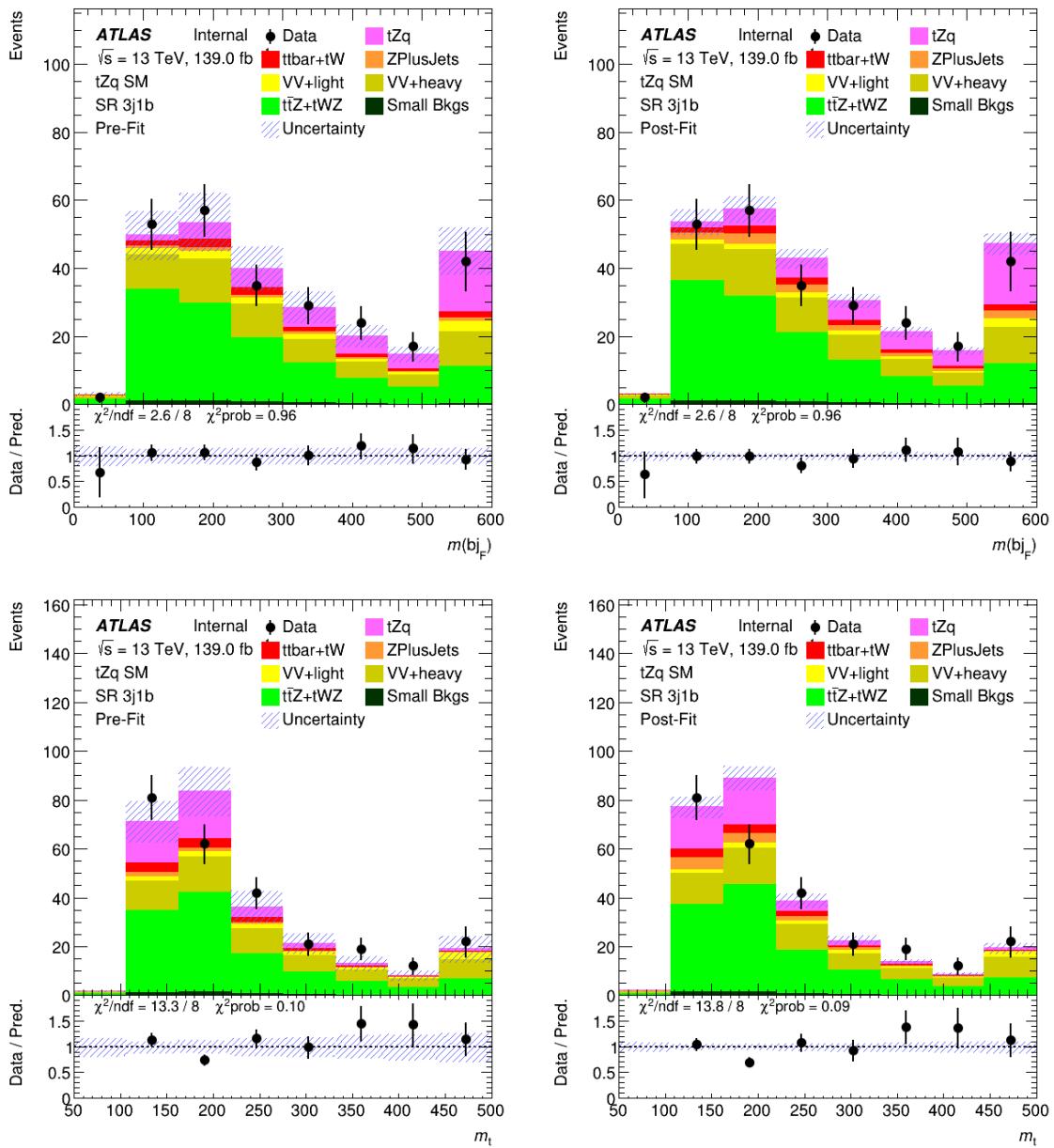


Figure 290: Pre-fit (left) and post-fit (right) NN input variable distributions in the unblinded part of the 3j1b signal region. The uncertainty band includes both statistical and systematic uncertainties.

Not reviewed, for internal circulation only

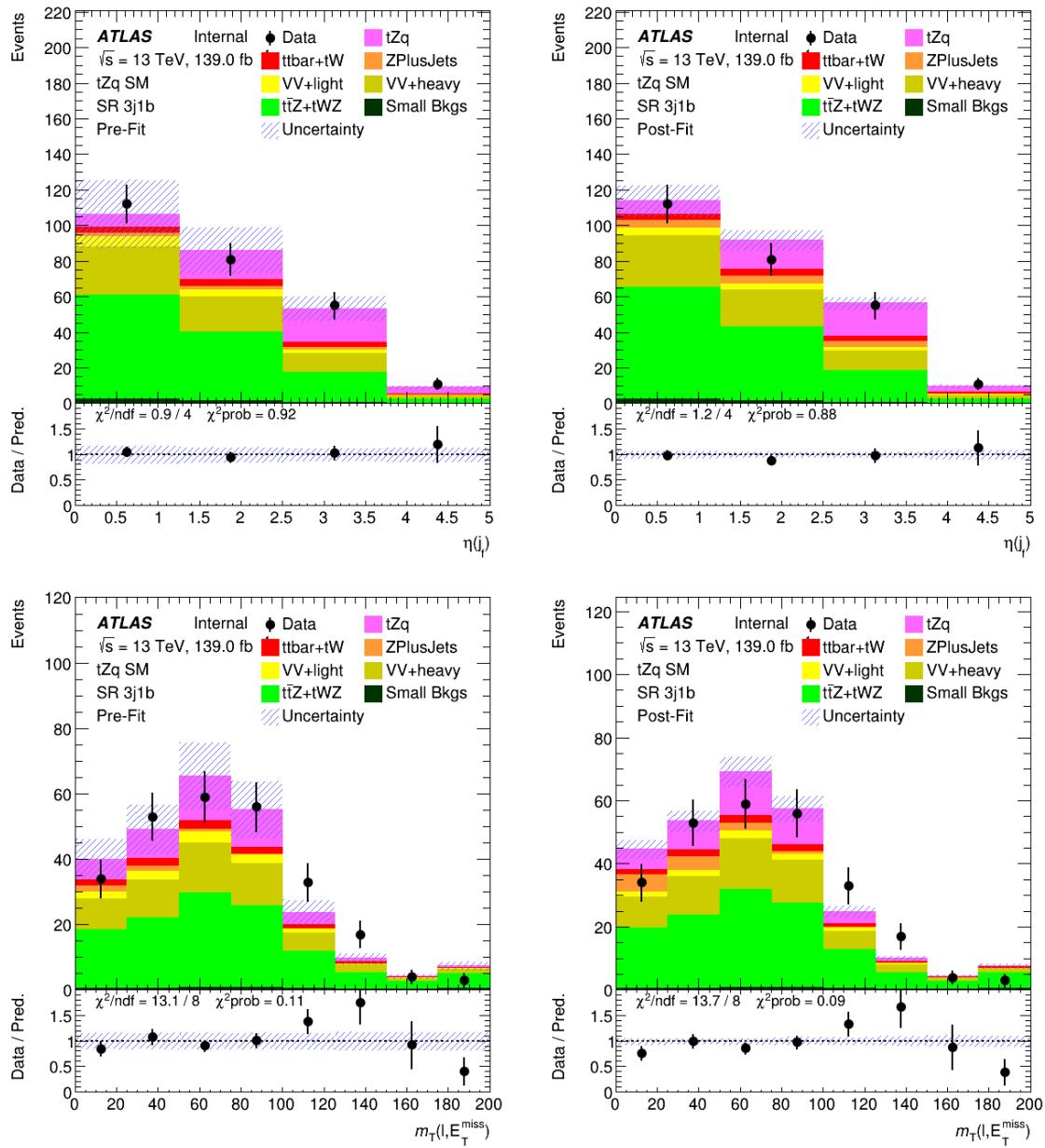


Figure 291: Pre-fit (left) and post-fit (right) NN input variable distributions in the unblinded part of the 3j1b signal region. The uncertainty band includes both statistical and systematic uncertainties.

## 1586 G.5 Unblinded fit checks - Diboson falvour split

1587 The studies reported in the following were not repeated with the changes applied after Top Approval, i.e.:  
 1588  $tZq$  radiation uncertainty still has normalization in,  $tWZ$  DR1 vs DR2 systematic is not included and  
 1589 diboson uncertainty is 20 % for both LF and HF.

1590 This section contains the results of the unblinded fit with a modified treatment of the diboson background.  
 1591 The diboson +  $b$ ,  $c$  and light components are all kept separate. For this fit, the  $\mu_{\text{SIG}}$  value is not shown.

1592 The values of the post-fit normalization parameters for the free floating backgrounds are shown in Fig. 292.  
 1593 The correlation matrix of the parameters included in the fit is shown in Fig. 293.

1594 The pull distributions for the all nuisance parameters can be seen in Figs. 294 to 301 and Fig. 302.

1595 The list of the systematic shapes that are dropped from the fit for each sample and for each region is shown  
 1596 in Fig. 303.

1597 Pre-fit and post-fit distributions of the fitted distributions in the various regions are shown in Figs. 304  
 1598 to 307.

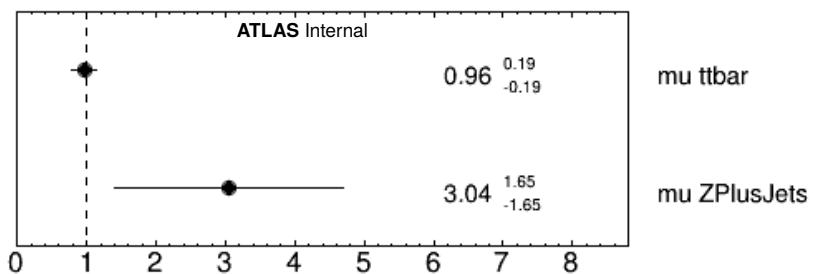


Figure 292: Normalisation factors of the unblinded fit with split diboson components.

### 1599 G.5.1 Pre- and post-fit plots of fitted variables in fit regions

Not reviewed, for internal circulation only

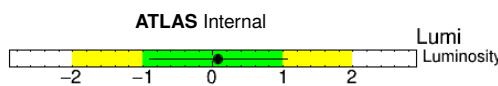
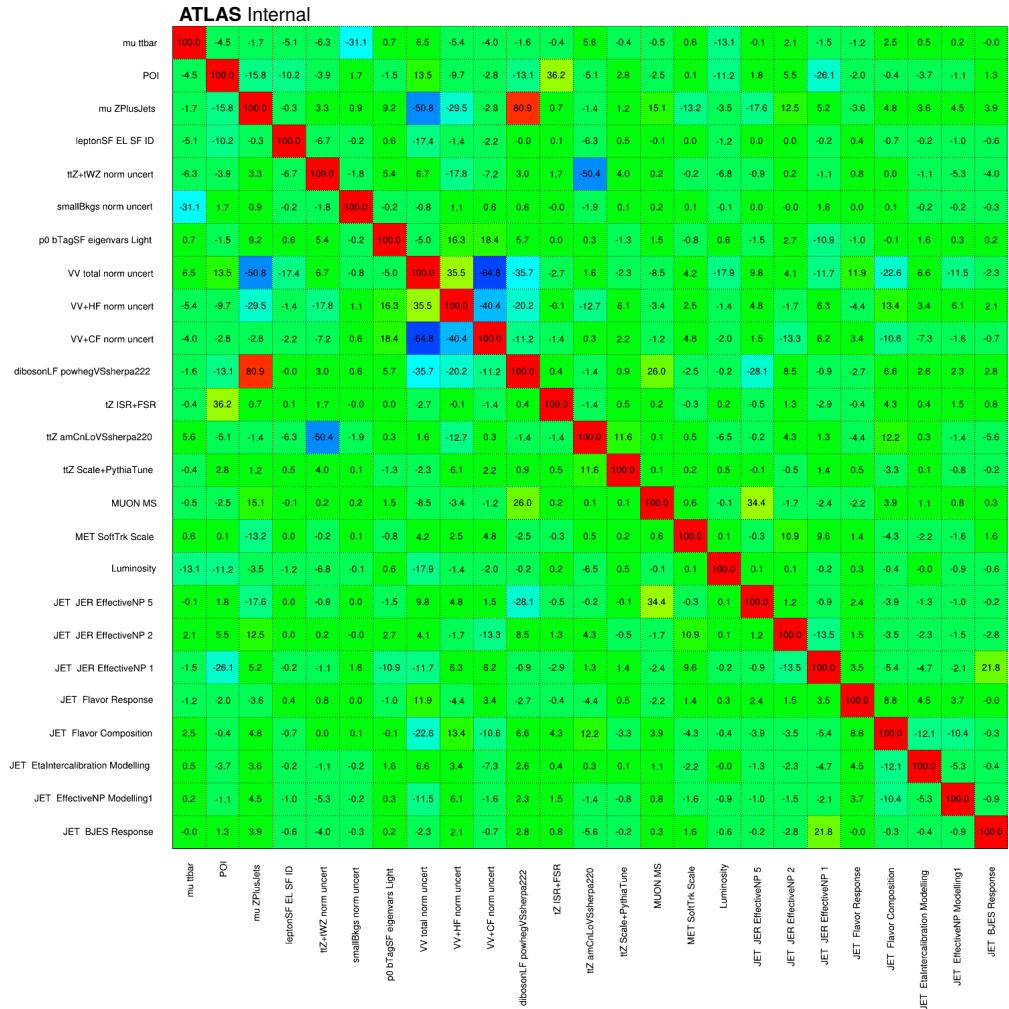


Figure 294: Pulls and constraints of the nuisance parameters of the unblinded fit: luminosity.

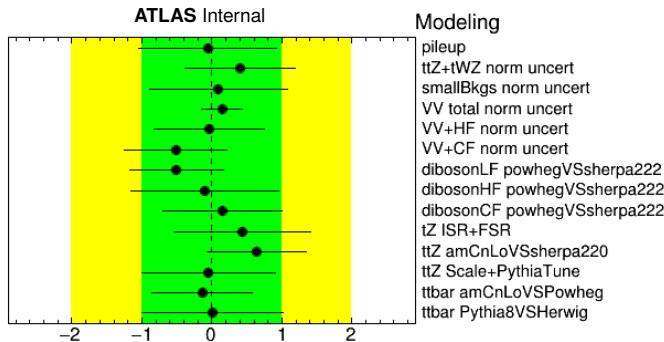


Figure 295: Pulls and constraints of the nuisance parameters of the unblinded fit: modeling systematics.

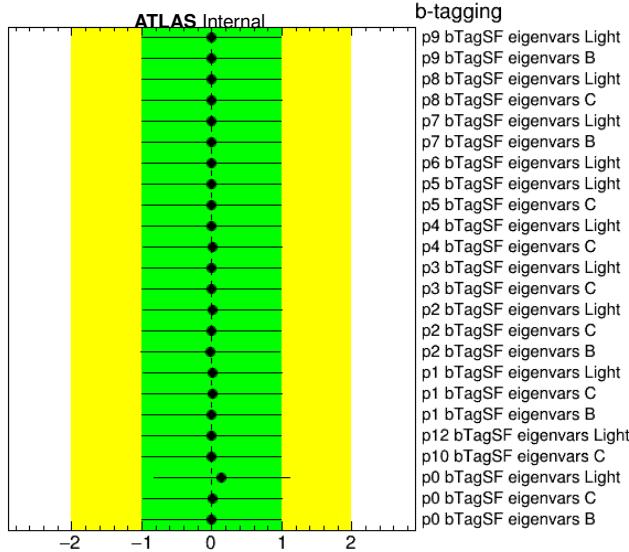


Figure 296: Pulls and constraints of the nuisance parameters of the unblinded fit:  $b$ -tagging systematics.

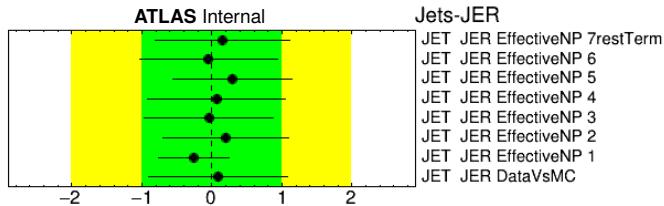


Figure 297: Pulls and constraints of the nuisance parameters of the unblinded fit: JER systematics.

Not reviewed, for internal circulation only

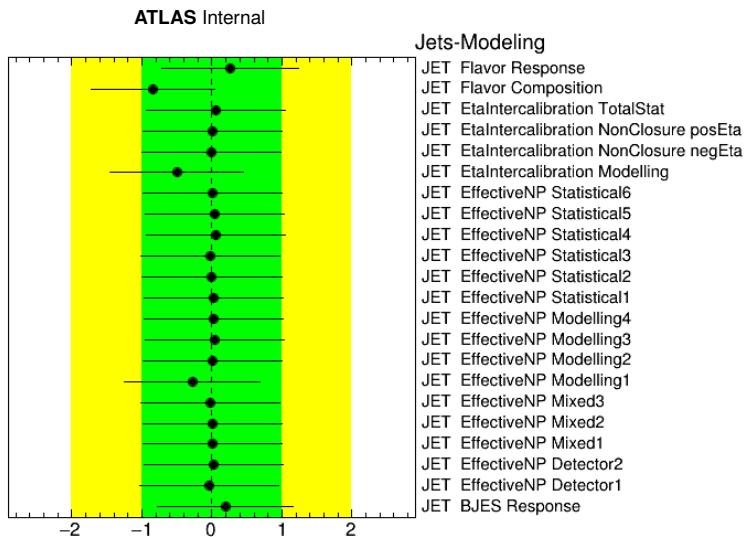


Figure 298: Pulls and constraints of the nuisance parameters of the unblinded fit: jet modeling systematics.

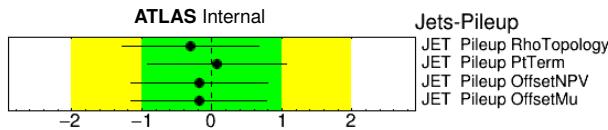


Figure 299: Pulls and constraints of the nuisance parameters of the unblinded fit: jet pile-up systematics.

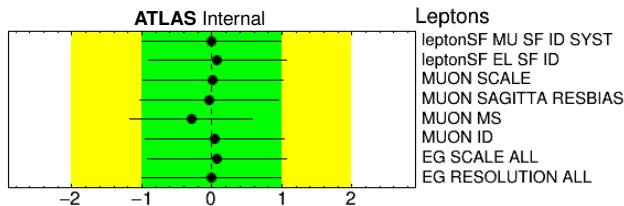


Figure 300: Pulls and constraints of the nuisance parameters of the unblinded fit: lepton systematics.

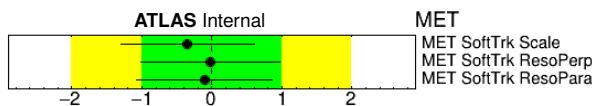


Figure 301: Pulls and constraints of the nuisance parameters of the unblinded fit:  $E_T^{\text{miss}}$  systematics.

Table 61: Pre-fit event yields in the various regions for the unblinded fit with split diboson components. The uncertainties include both statistical and systematic uncertainties.

	SR 2j1b		SR 3j1b
$tZq$	$70.6 \pm 3.7$	$tZq$	$40.1 \pm 3.6$
$tW$	$1.1 \pm 0.0$	$tW$	$0.4 \pm 0.0$
$t\bar{t}$	$23.7 \pm \text{nan}$	$t\bar{t}$	$11.1 \pm \text{nan}$
$Z + \text{jets}$	$11.1 \pm 0.5$	$Z + \text{jets}$	$4.8 \pm 0.2$
$VV + \text{LF}$	$22.7 \pm 1.3$	$VV + \text{LF}$	$12.3 \pm 6.2$
$VV + c$	$51.3 \pm 0.1$	$VV + c$	$30.6 \pm 18.0$
$VV + b$	$50.0 \pm 29.2$	$VV + b$	$28.8 \pm 16.8$
$t\bar{t}Z + tWZ$	$80.6 \pm 6.9$	$t\bar{t}Z + tWZ$	$116.7 \pm 7.4$
$t\bar{t} H + t\bar{t} W$	$6.3 \pm 1.0$	$t\bar{t} H + t\bar{t} W$	$4.6 \pm 0.7$
Total	$317.3 \pm \text{nan}$	Total	$249.3 \pm \text{nan}$
Data	359	Data	259
	CR diboson 2j0b		CR diboson 3j0b
$tZq$	$48.2 \pm 1.6$	$tZq$	$19.4 \pm 1.6$
$tW$	$0.5 \pm \text{nan}$	$tW$	$0.3 \pm 0.0$
$t\bar{t}$	$13.8 \pm 0.2$	$t\bar{t}$	$6.8 \pm 0.1$
$Z + \text{jets}$	$63.4 \pm 1.2$	$Z + \text{jets}$	$20.2 \pm 0.7$
$VV + \text{LF}$	$2039.7 \pm 619.9$	$VV + \text{LF}$	$708.0 \pm 219.5$
$VV + c$	$350.4 \pm 205.0$	$VV + c$	$172.2 \pm 101.1$
$VV + b$	$31.7 \pm 18.5$	$VV + b$	$17.8 \pm 10.5$
$t\bar{t}Z + tWZ$	$58.9 \pm 7.9$	$t\bar{t}Z + tWZ$	$58.7 \pm 7.4$
$t\bar{t} H + t\bar{t} W$	$2.9 \pm 0.5$	$t\bar{t} H + t\bar{t} W$	$1.7 \pm 0.3$
Total	$2609.5 \pm \text{nan}$	Total	$1005.1 \pm 291.5$
Data	2703	Data	949
	CR ttbar 2j1b		CR ttbar 3j1b
$tZq$	$0.2 \pm 0.1$	$tZq$	$0.2 \pm 0.0$
$tW$	$0.8 \pm 0.0$	$tW$	$0.5 \pm 0.0$
$t\bar{t}$	$34.0 \pm 0.6$	$t\bar{t}$	$15.3 \pm 0.3$
$Z + \text{jets}$	$0 \pm 0$	$Z + \text{jets}$	$0 \pm 0$
$VV + \text{LF}$	$0.1 \pm 0.0$	$VV + \text{LF}$	$0.0 \pm 0.0$
$VV + c$	$0.2 \pm 0.1$	$VV + c$	$0.2 \pm 0.1$
$VV + b$	$0.2 \pm 0.1$	$VV + b$	$0.1 \pm 0.1$
$t\bar{t}Z + tWZ$	$4.4 \pm 0.6$	$t\bar{t}Z + tWZ$	$3.7 \pm 0.6$
$t\bar{t} H + t\bar{t} W$	$12.1 \pm 1.9$	$t\bar{t} H + t\bar{t} W$	$8.0 \pm 1.3$
Total	$52.0 \pm 2.2$	Total	$28.1 \pm 1.5$
Data	49	Data	31
	CR ttV 3j2b		CR ttV 4j2b
$tZq$	$11.5 \pm 0.6$	$tZq$	$7.5 \pm 1.0$
$tW$	$0 \pm 0$	$tW$	$0 \pm 0$
$t\bar{t}$	$1.6 \pm 0.1$	$t\bar{t}$	$1.0 \pm 0.0$
$Z + \text{jets}$	$0.5 \pm 0.0$	$Z + \text{jets}$	$0 \pm 0$
$VV + \text{LF}$	$0.1 \pm 0.1$	$VV + \text{LF}$	$0.1 \pm 0.1$
$VV + c$	$1.3 \pm 0.8$	$VV + c$	$0.8 \pm 0.6$
$VV + b$	$4.0 \pm 2.4$	$VV + b$	$2.5 \pm 1.5$
$t\bar{t}Z + tWZ$	$49.5 \pm 2.2$	$t\bar{t}Z + tWZ$	$51.5 \pm 8.8$
$t\bar{t} H + t\bar{t} W$	$2.8 \pm 0.5$	$t\bar{t} H + t\bar{t} W$	$1.9 \pm 0.3$
Total	$71.3 \pm 2.7$	Total	$65.4 \pm 9.2$
Data	92	Data	75

Table 62: Post-fit event yields in the various regions for the unblinded fit with split diboson components. The uncertainties include both statistical and systematic uncertainties.

	SR 2j1b		SR 3j1b
$tZq$	$83.8 \pm 2.0$	$tZq$	$44.3 \pm 6.3$
$tW$	$1.0 \pm 0.2$	$tW$	$0.4 \pm 0.1$
$t\bar{t}$	$22.8 \pm 4.4$	$t\bar{t}$	$10.6 \pm 2.0$
$Z + \text{jets}$	$33.9 \pm 8.4$	$Z + \text{jets}$	$14.5 \pm 7.9$
$VV + \text{LF}$	$21.9 \pm 8.9$	$VV + \text{LF}$	$11.3 \pm 4.7$
$VV + c$	$37.5 \pm 6.0$	$VV + c$	$21.8 \pm 9.1$
$VV + b$	$51.1 \pm 2.5$	$VV + b$	$28.8 \pm 2.8$
$t\bar{t}Z + tWZ$	$98.3 \pm 0.2$	$t\bar{t}Z + tWZ$	$130.9 \pm 0.5$
$t\bar{t} H + t\bar{t} W$	$6.6 \pm 1.0$	$t\bar{t} H + t\bar{t} W$	$4.6 \pm 0.7$
Total	$356.8 \pm 5.6$	Total	$267.3 \pm 9.9$
Data	359	Data	259
	CR diboson 2j0b		CR diboson 3j0b
$tZq$	$56.6 \pm 8.6$	$tZq$	$21.7 \pm 3.5$
$tW$	$0.5 \pm 0.1$	$tW$	$0.3 \pm 0.1$
$t\bar{t}$	$13.2 \pm 2.6$	$t\bar{t}$	$6.6 \pm 1.3$
$Z + \text{jets}$	$193.3 \pm 104.5$	$Z + \text{jets}$	$61.4 \pm 33.2$
$VV + \text{LF}$	$2048.5 \pm 162.8$	$VV + \text{LF}$	$688.3 \pm 59.3$
$VV + c$	$253.4 \pm 106.8$	$VV + c$	$121.5 \pm 50.6$
$VV + b$	$32.2 \pm 14.3$	$VV + b$	$17.2 \pm 7.7$
$t\bar{t}Z + tWZ$	$64.5 \pm 6.7$	$t\bar{t}Z + tWZ$	$61.4 \pm 5.9$
$t\bar{t} H + t\bar{t} W$	$3.0 \pm 0.5$	$t\bar{t} H + t\bar{t} W$	$1.7 \pm 0.3$
Total	$2665.2 \pm 67.2$	Total	$980.0 \pm 28.0$
Data	2703	Data	949
	CR ttbar 2j1b		CR ttbar 3j1b
$tZq$	$0.2 \pm 0.1$	$tZq$	$0.2 \pm 0.1$
$tW$	$0.7 \pm 0.1$	$tW$	$0.5 \pm 0.1$
$t\bar{t}$	$32.7 \pm 6.3$	$t\bar{t}$	$14.7 \pm 2.8$
$Z + \text{jets}$	$0 \pm 0$	$Z + \text{jets}$	$0 \pm 0$
$VV + \text{LF}$	$0.1 \pm 0.0$	$VV + \text{LF}$	$0.0 \pm 0.0$
$VV + c$	$0.1 \pm 0.1$	$VV + c$	$0.1 \pm 0.1$
$VV + b$	$0.2 \pm 0.1$	$VV + b$	$0.1 \pm 0.1$
$t\bar{t}Z + tWZ$	$4.8 \pm 0.5$	$t\bar{t}Z + tWZ$	$3.8 \pm 0.5$
$t\bar{t} H + t\bar{t} W$	$12.6 \pm 1.9$	$t\bar{t} H + t\bar{t} W$	$8.0 \pm 1.2$
Total	$51.5 \pm 6.1$	Total	$27.6 \pm 2.8$
Data	49	Data	31
	CR ttV 3j2b		CR ttV 4j2b
$tZq$	$13.6 \pm 2.1$	$tZq$	$8.1 \pm 1.3$
$tW$	$0 \pm 0$	$tW$	$0 \pm 0$
$t\bar{t}$	$1.6 \pm 0.3$	$t\bar{t}$	$1.0 \pm 0.2$
$Z + \text{jets}$	$1.6 \pm 0.9$	$Z + \text{jets}$	$0 \pm 0$
$VV + \text{LF}$	$0.1 \pm 0.1$	$VV + \text{LF}$	$0.1 \pm 0.1$
$VV + c$	$0.9 \pm 0.4$	$VV + c$	$0.6 \pm 0.3$
$VV + b$	$4.1 \pm 1.8$	$VV + b$	$2.4 \pm 1.1$
$t\bar{t}Z + tWZ$	$61.1 \pm 7.1$	$t\bar{t}Z + tWZ$	$57.2 \pm 5.0$
$t\bar{t} H + t\bar{t} W$	$2.8 \pm 0.5$	$t\bar{t} H + t\bar{t} W$	$1.9 \pm 0.3$
Total	$85.7 \pm 6.7$	Total	$71.5 \pm 4.9$
Data	92	Data	75

Not reviewed, for internal circulation only

Not reviewed, for internal circulation only

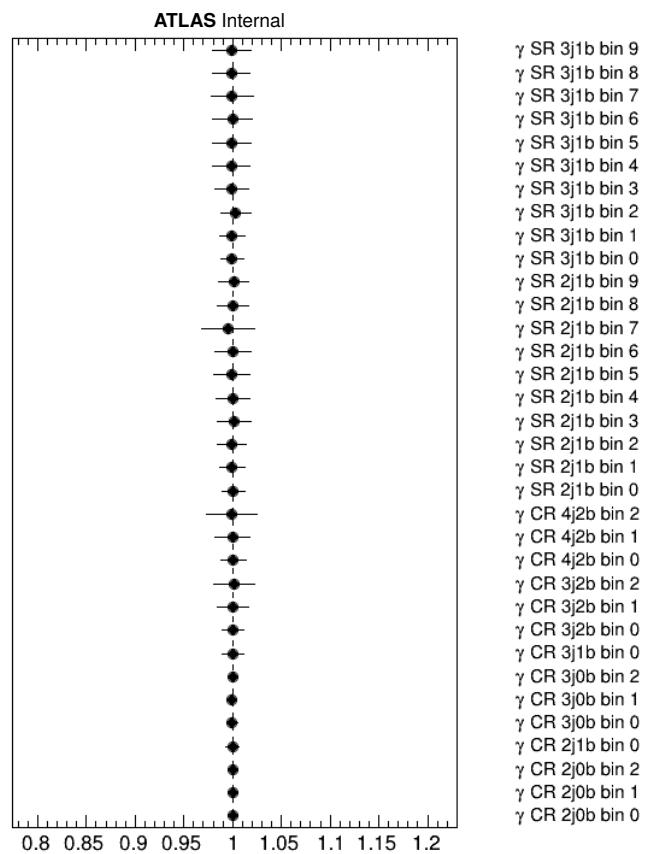


Figure 302: Gamma parameters of the unblinded fit with split diboson components.

Not reviewed, for internal circulation only

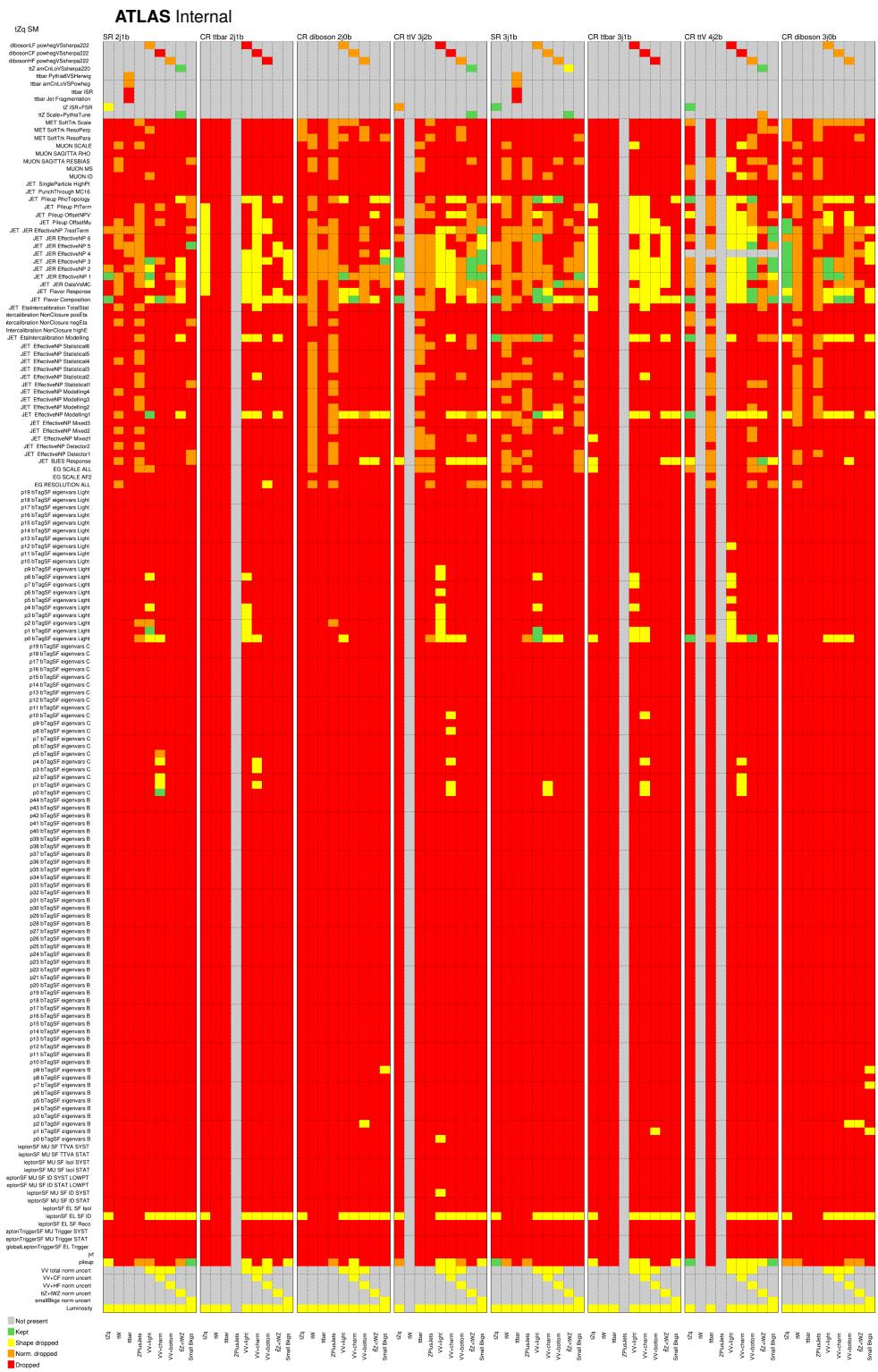


Figure 303: Pruning of the nuisance parameters of the unblinded fit with split diboson components.

Not reviewed, for internal circulation only

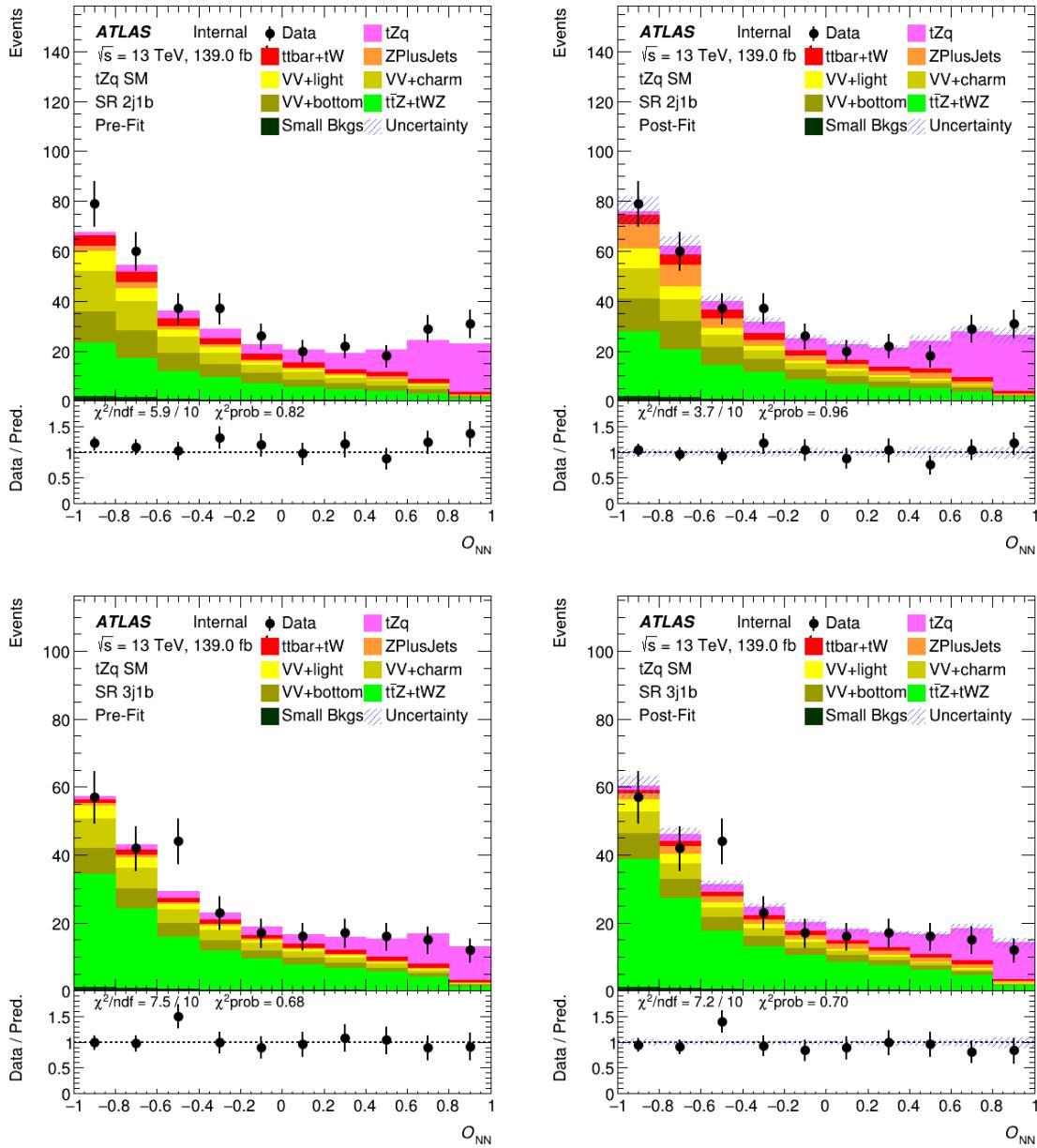


Figure 304: Pre-fit (left) and post-fit (right) NN output distributions in the signal regions. The uncertainty band includes both statistical and systematic uncertainties.

Not reviewed, for internal circulation only

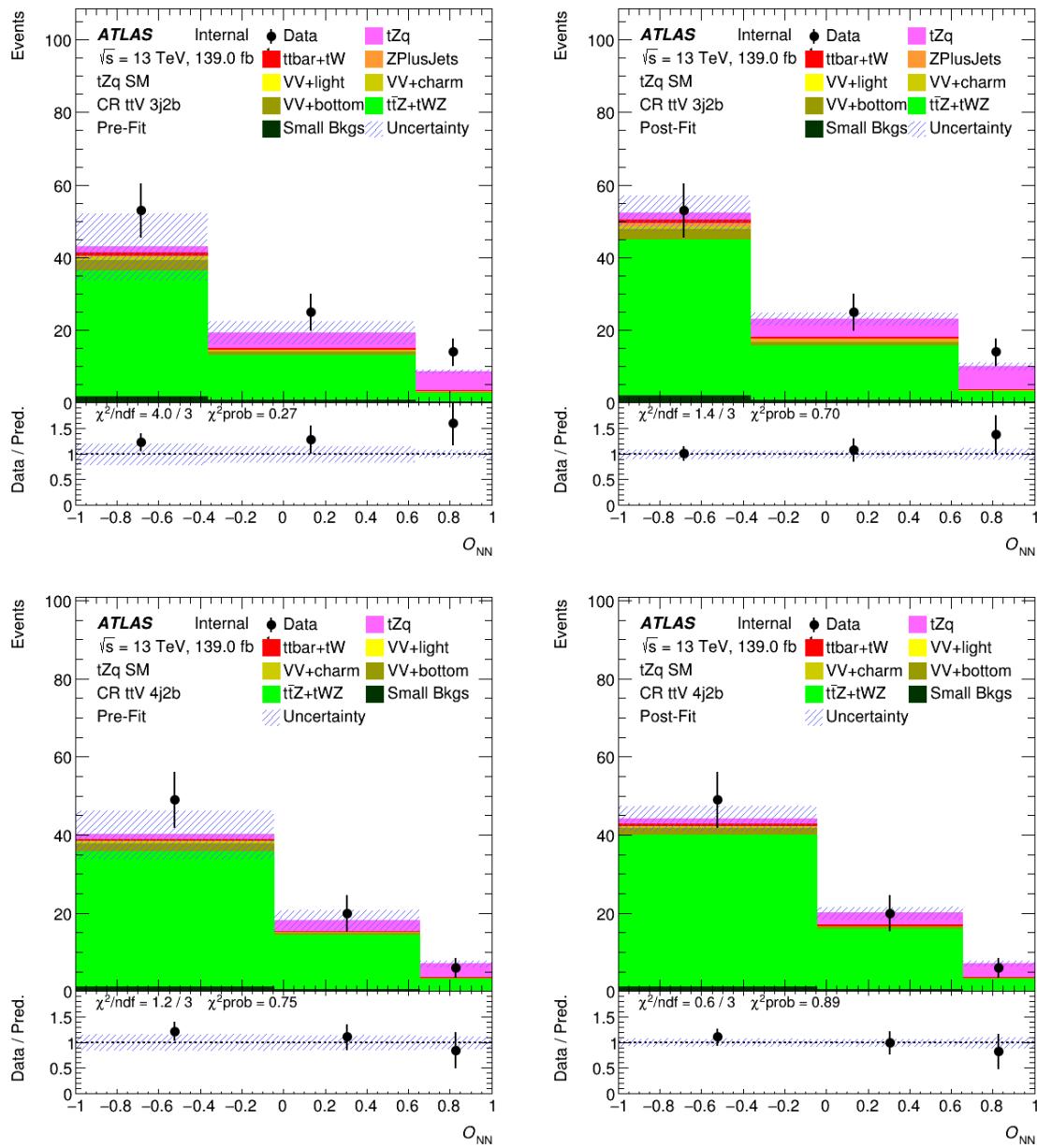


Figure 305: Pre-fit (left) and post-fit (right) NN output distributions in the  $t\bar{t}Z$  control regions. The uncertainty band includes both statistical and systematic uncertainties.

Not reviewed, for internal circulation only

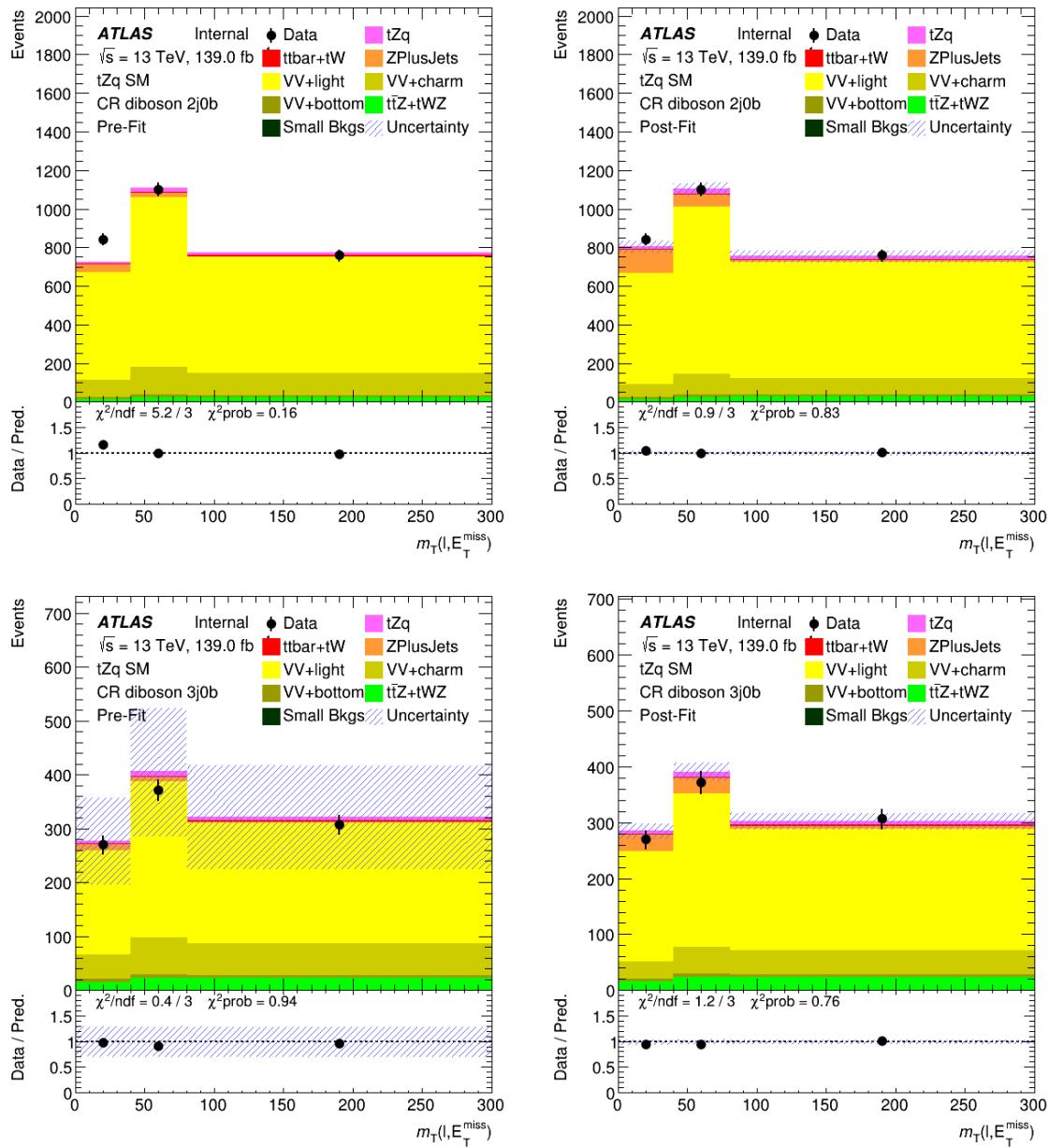


Figure 306: Pre-fit (left) and post-fit (right)  $E_T^{\text{miss}}$  distributions in the diboson control regions. The uncertainty band includes both statistical and systematic uncertainties.

Not reviewed, for internal circulation only

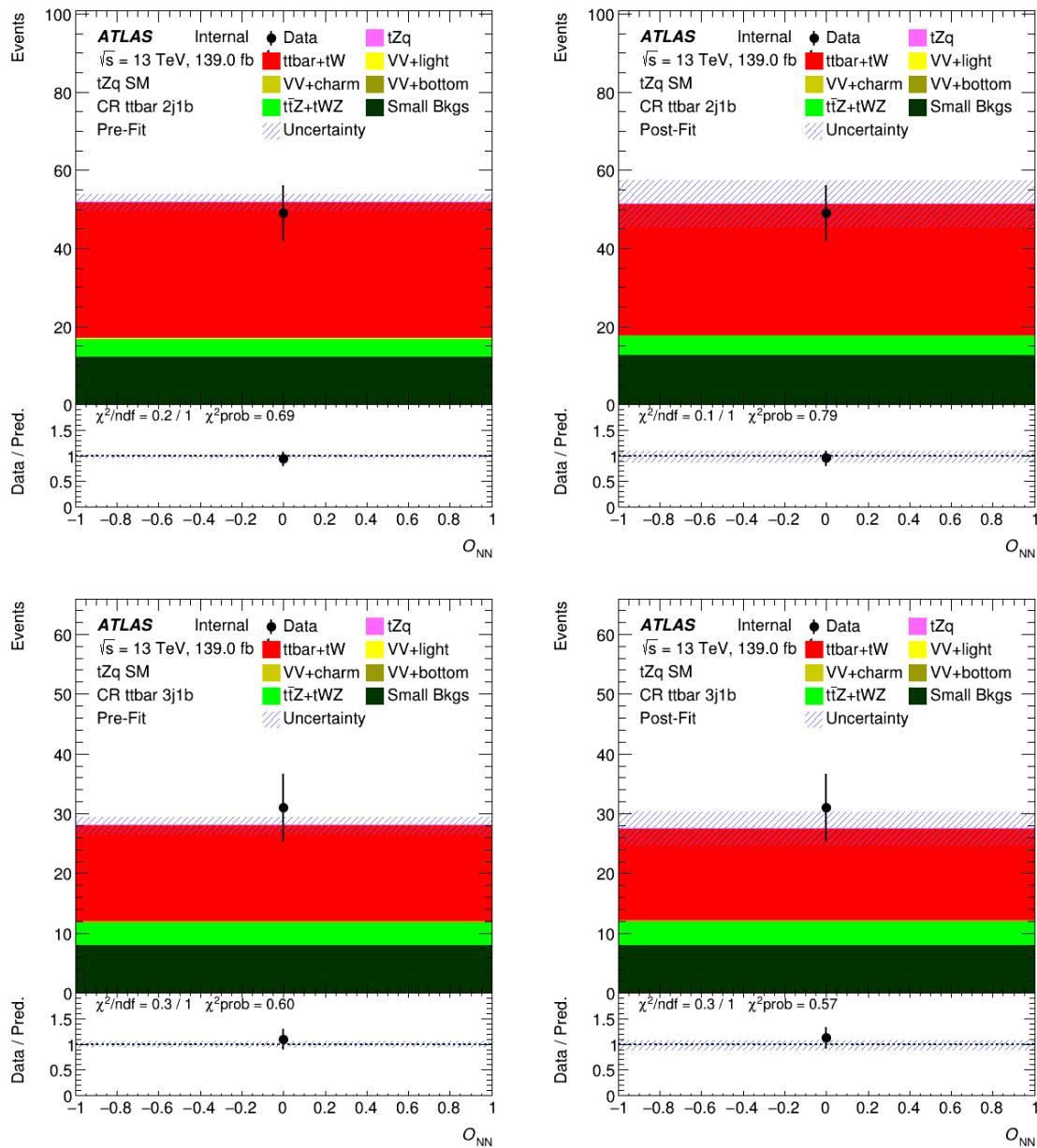


Figure 307: Pre-fit (left) and post-fit (right) NN output distributions in the  $t\bar{t}$  control regions. The uncertainty band includes both statistical and systematic uncertainties. Since the  $t\bar{t}$  background is free floating in the fit, there are no uncertainties on this background pre-fit.

## 1600 G.5.2 NN input variable distributions in SRs pre- and post-fit

Not reviewed, for internal circulation only

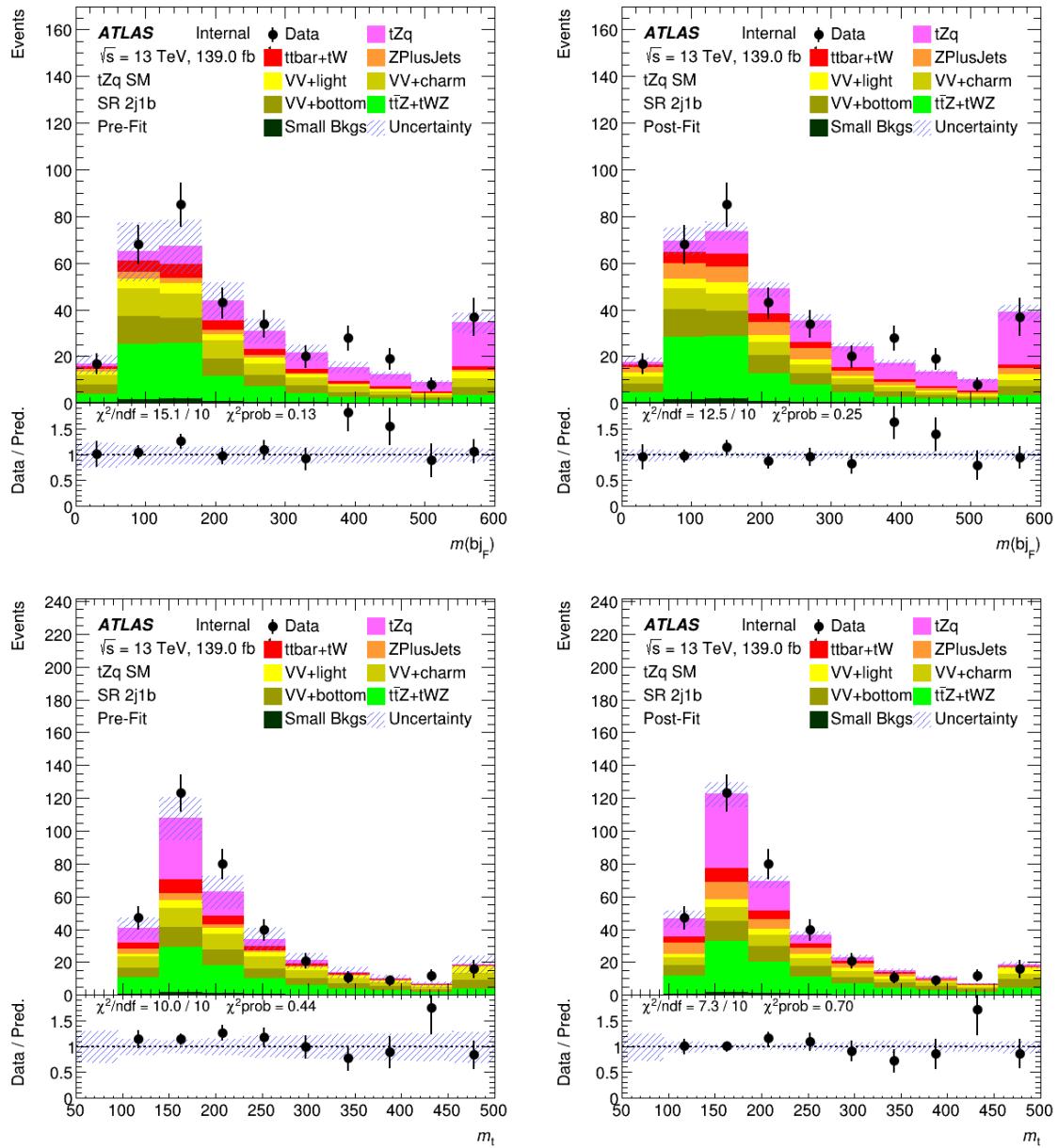


Figure 308: Pre-fit (left) and post-fit (right) NN input variable distributions in the 2j1b signal region. The uncertainty band includes both statistical and systematic uncertainties.

Not reviewed, for internal circulation only

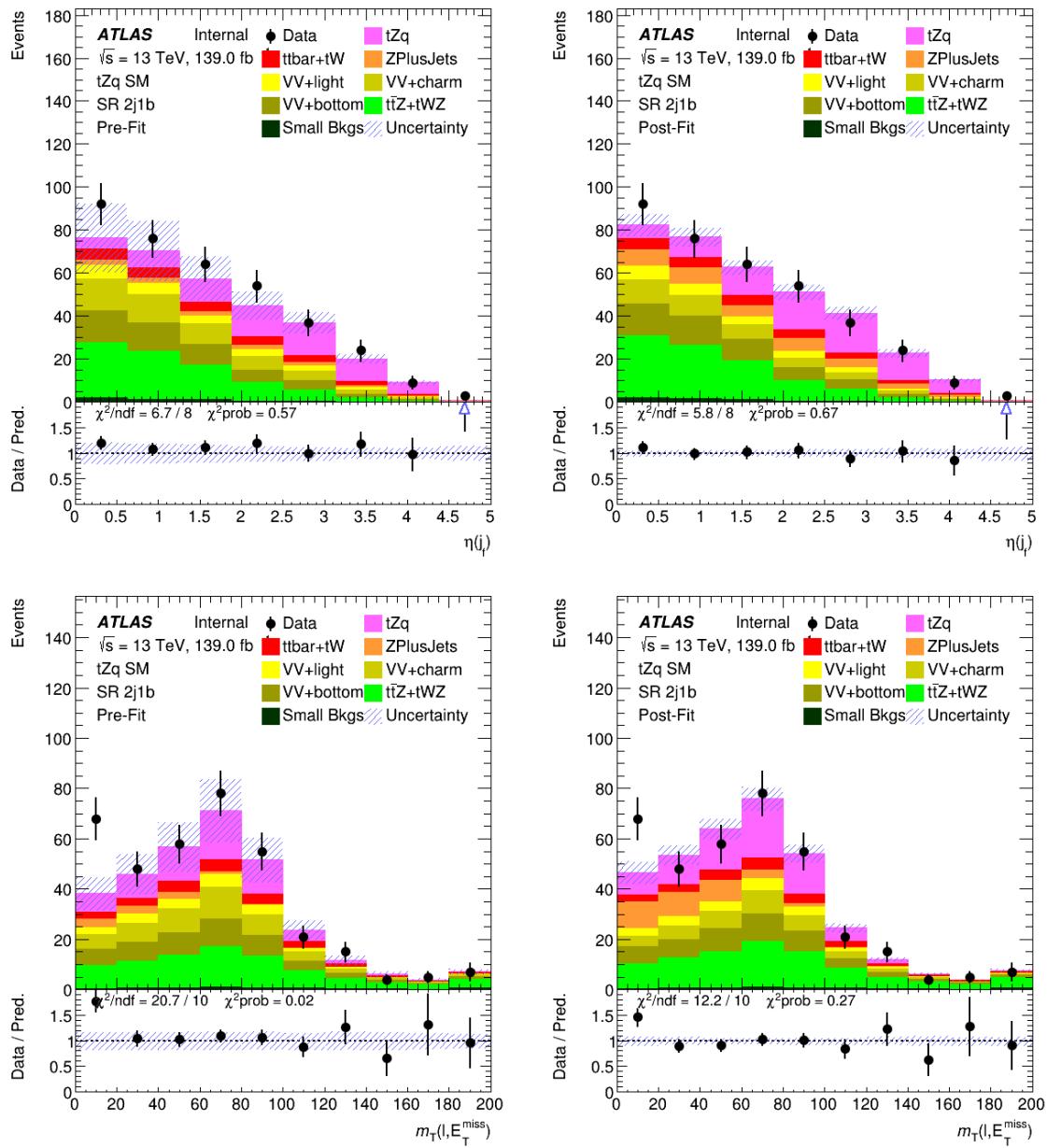


Figure 309: Pre-fit (left) and post-fit (right) NN input variable distributions in the 2j1b signal region. The uncertainty band includes both statistical and systematic uncertainties.

Not reviewed, for internal circulation only

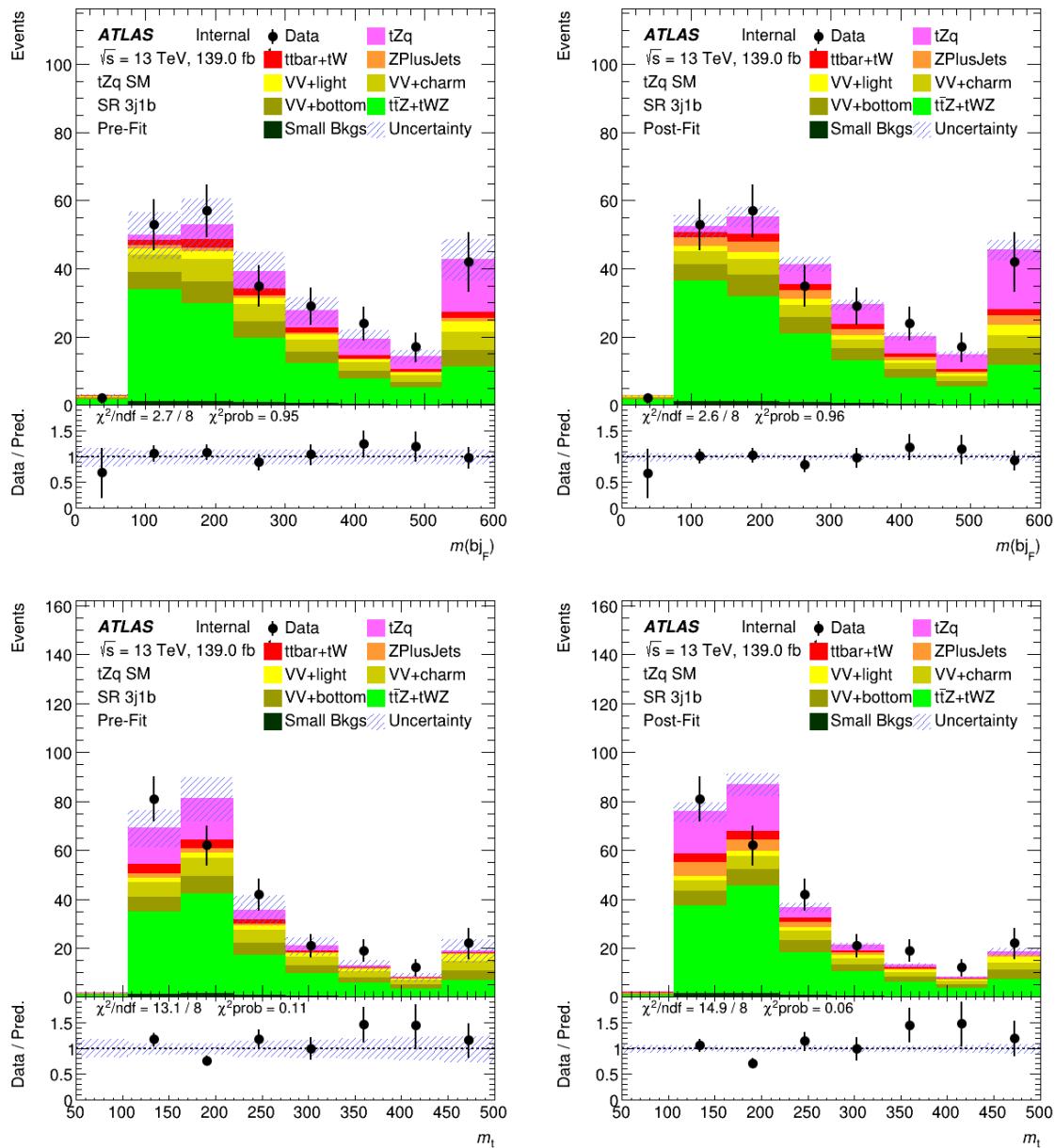


Figure 310: Pre-fit (left) and post-fit (right) NN input variable distributions in the 3j1b signal region. The uncertainty band includes both statistical and systematic uncertainties.

Not reviewed, for internal circulation only

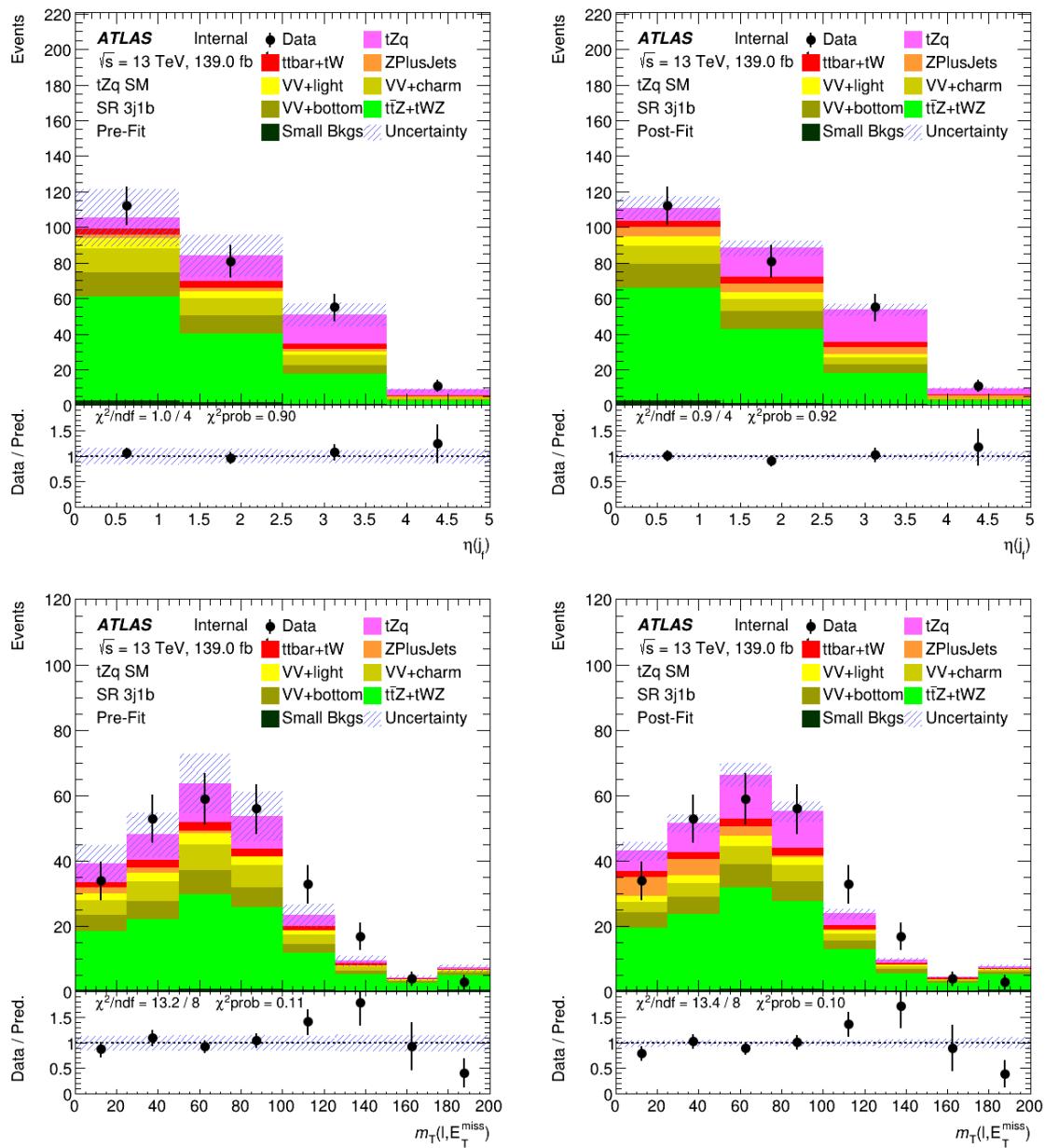


Figure 311: Pre-fit (left) and post-fit (right) NN input variable distributions in the 3j1b signal region. The uncertainty band includes both statistical and systematic uncertainties.

## 1601 G.5.3 NN input variable distributions in VRs pre- and post-fit

Not reviewed, for internal circulation only

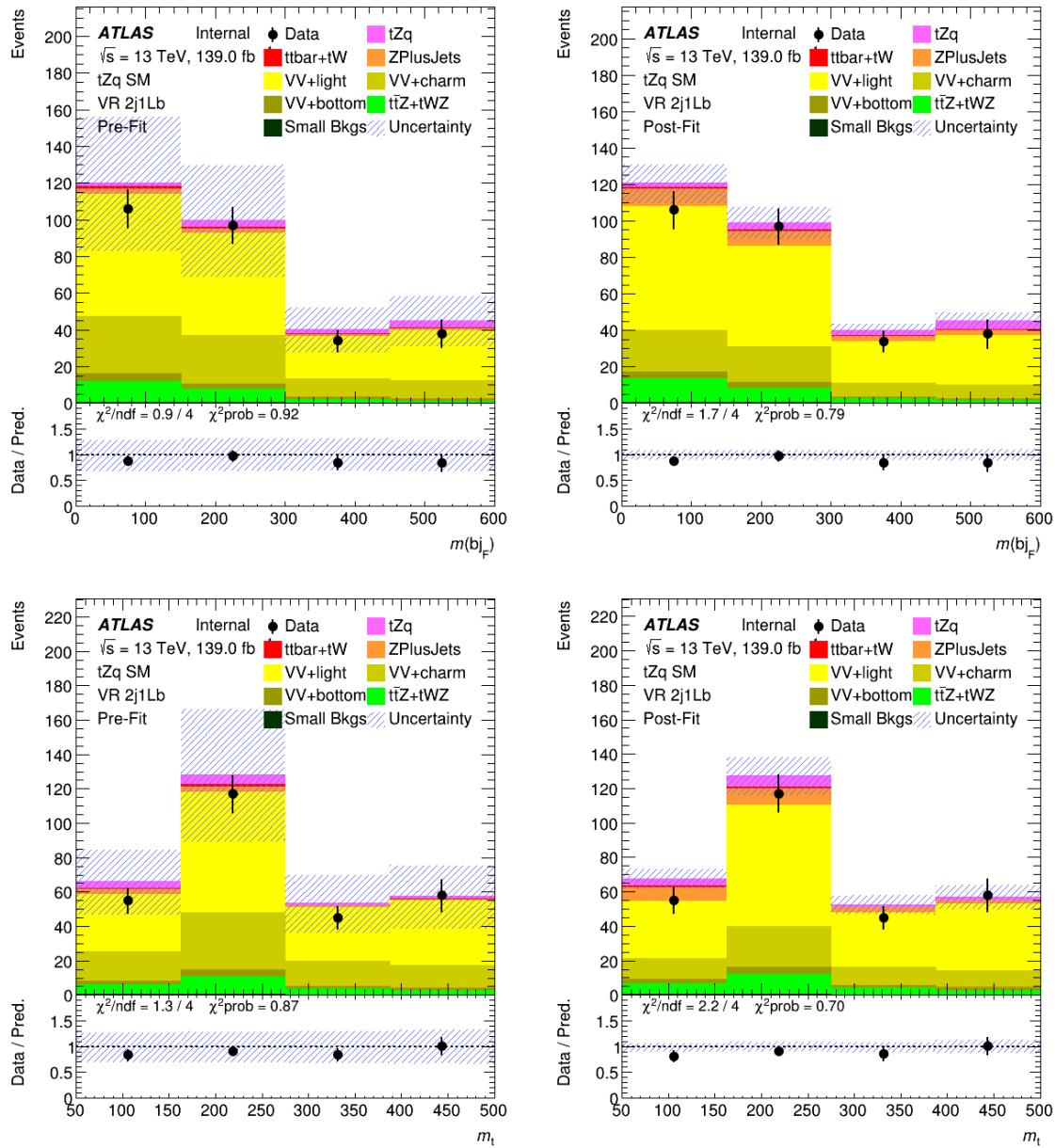


Figure 312: Pre-fit (left) and post-fit (right) NN input variable distributions in the diboson 2j1Lb validation region. The uncertainty band includes both statistical and systematic uncertainties.

Not reviewed, for internal circulation only

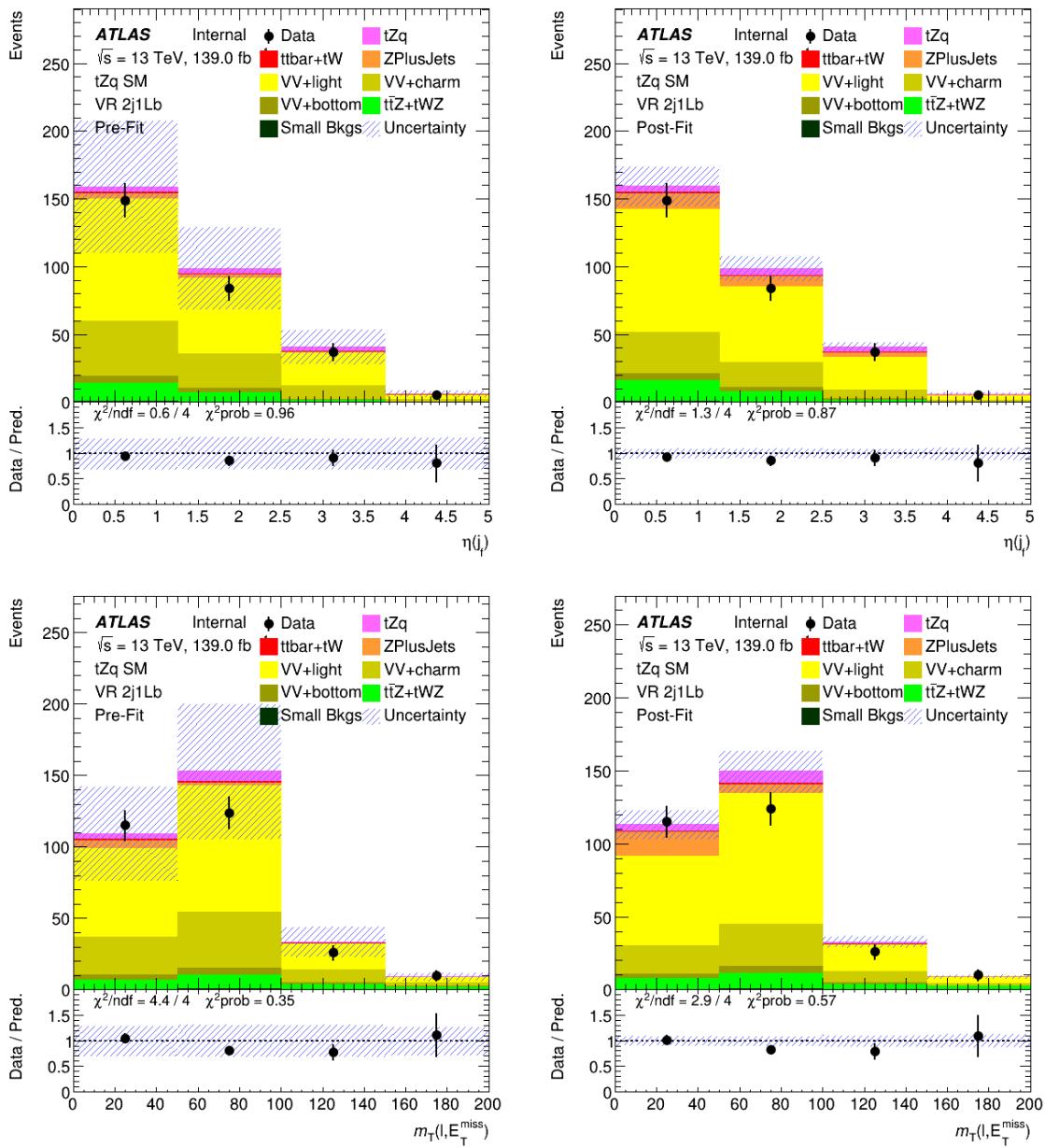


Figure 313: Pre-fit (left) and post-fit (right) NN input variable distributions in the diboson 2j1Lb validation region. The uncertainty band includes both statistical and systematic uncertainties.

Not reviewed, for internal circulation only

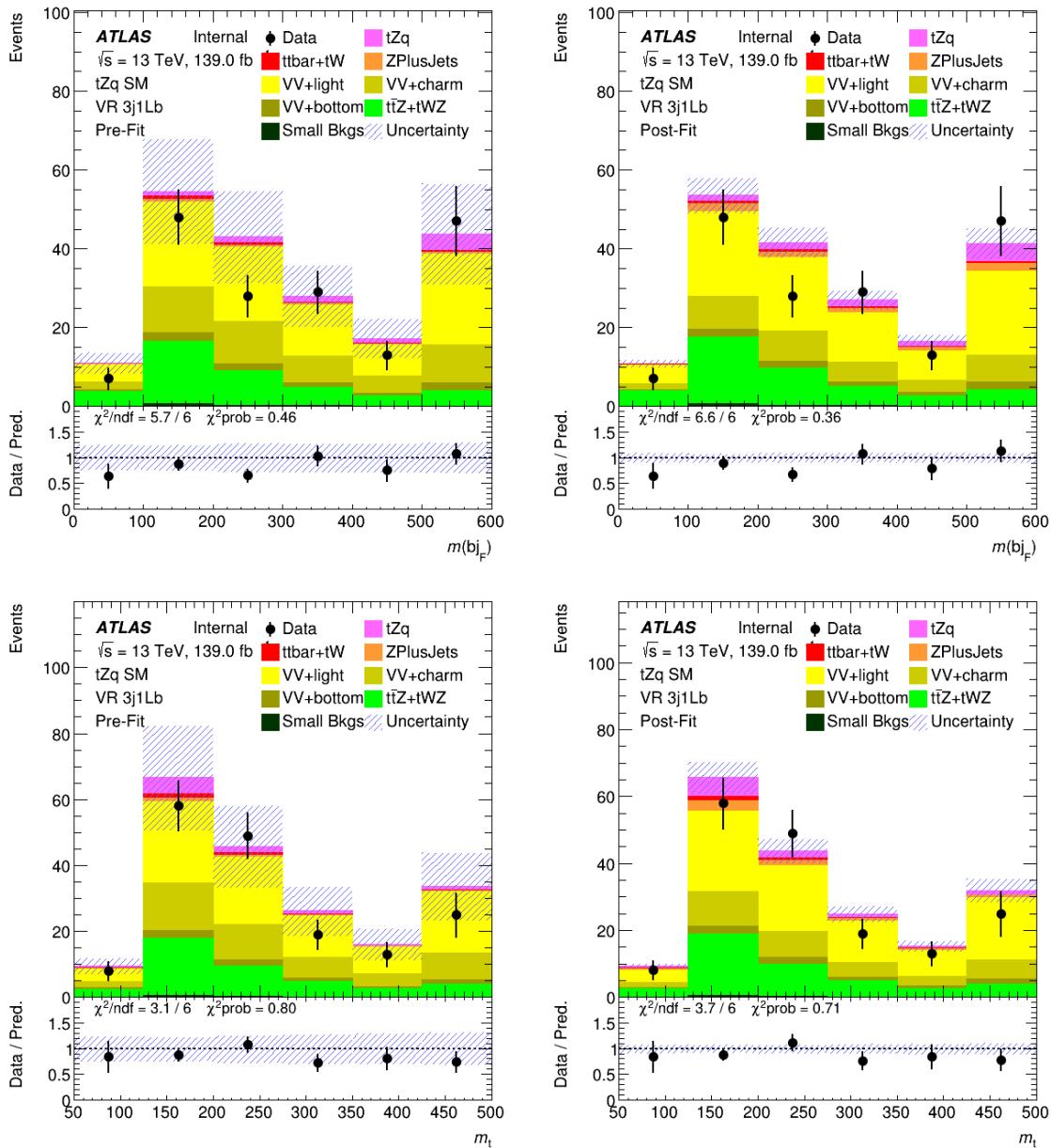


Figure 314: Pre-fit (left) and post-fit (right) NN input variable distributions in the diboson 3j1Lb validation region. The uncertainty band includes both statistical and systematic uncertainties.

Not reviewed, for internal circulation only

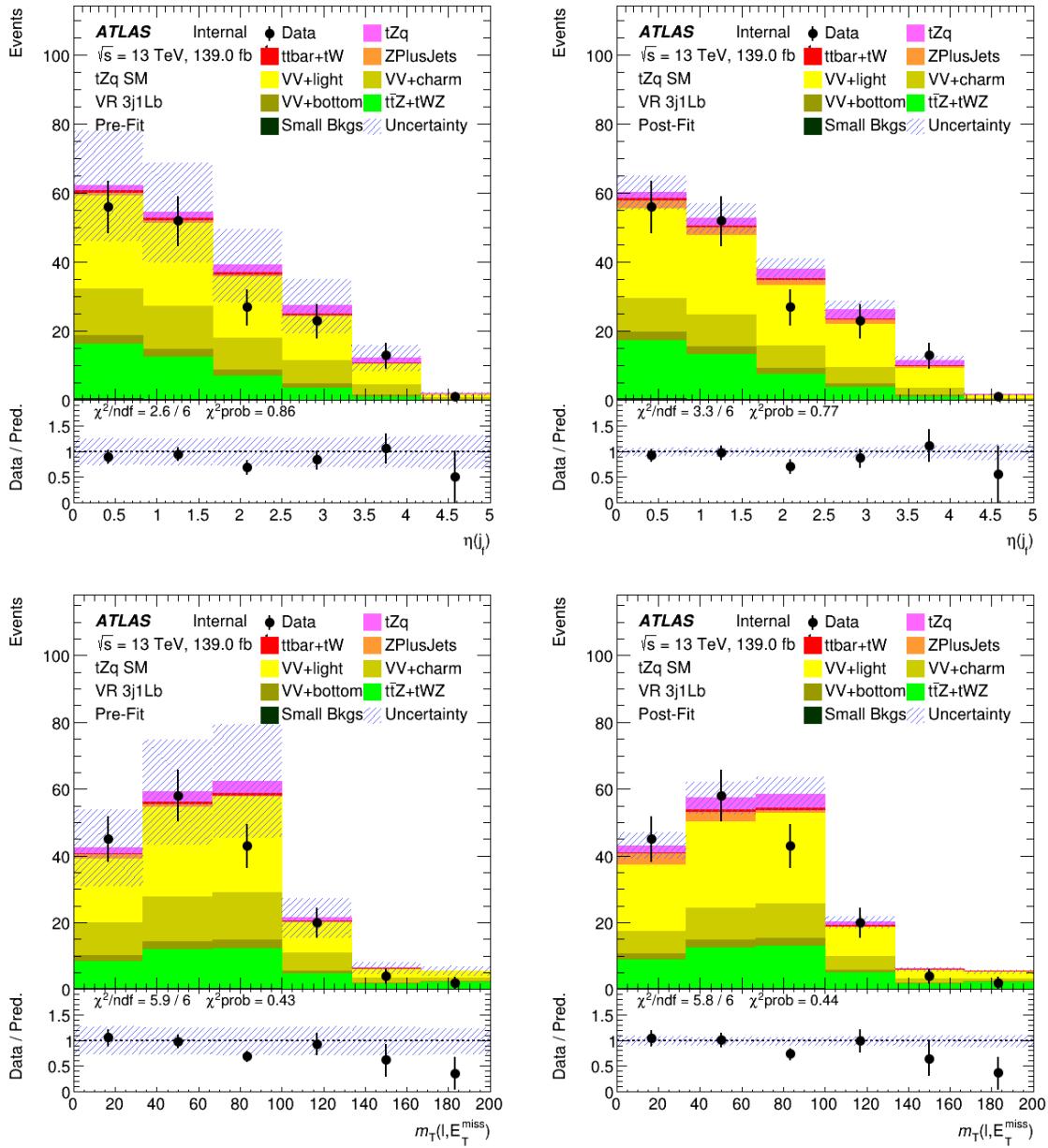


Figure 315: Pre-fit (left) and post-fit (right) NN input variable distributions in the diboson 3j1Lb validation region. The uncertainty band includes both statistical and systematic uncertainties.

Not reviewed, for internal circulation only

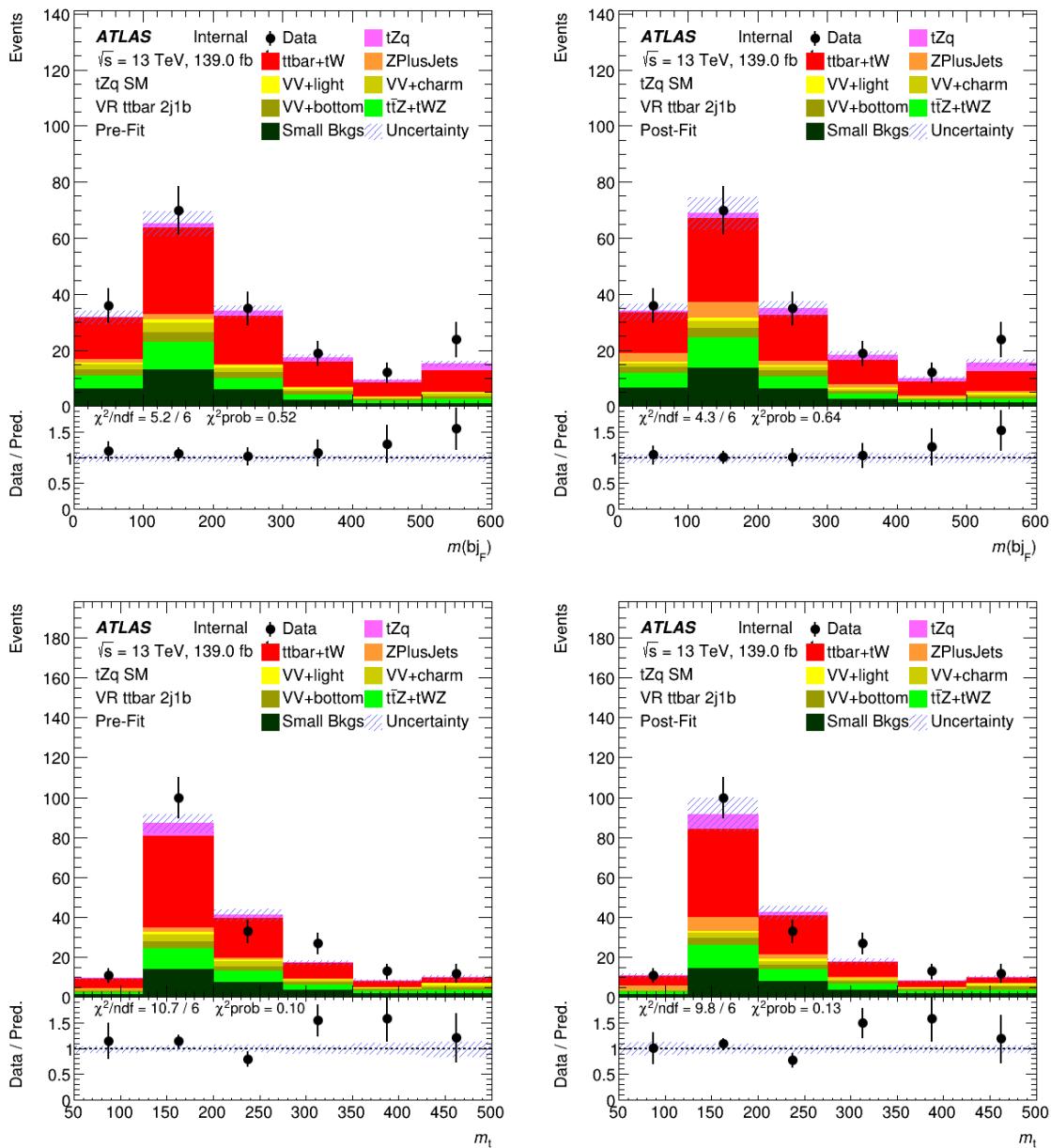


Figure 316: Pre-fit (left) and post-fit (right) NN input variable distributions in the  $t\bar{t}V + t\bar{t}2j1b$  validation region. The uncertainty band includes both statistical and systematic uncertainties. Since the  $t\bar{t}$  background is free floating in the fit, there are no uncertainties on this background pre-fit.

Not reviewed, for internal circulation only

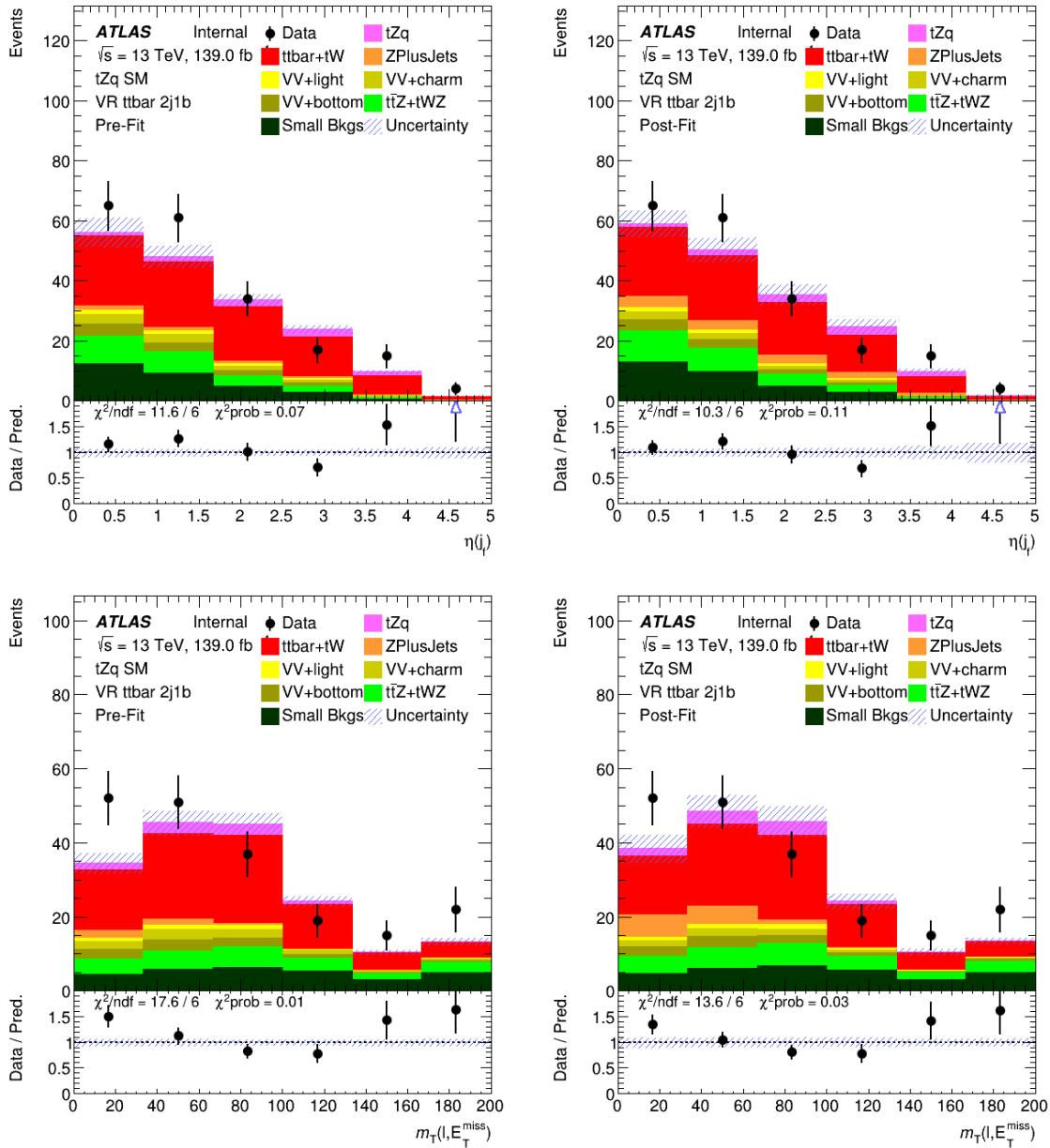


Figure 317: Pre-fit (left) and post-fit (right) NN input variable distributions in the  $t\bar{t}V + t\bar{t} 2j1b$  validation region. The uncertainty band includes both statistical and systematic uncertainties. Since the  $t\bar{t}$  background is free floating in the fit, there are no uncertainties on this background pre-fit.

Not reviewed, for internal circulation only

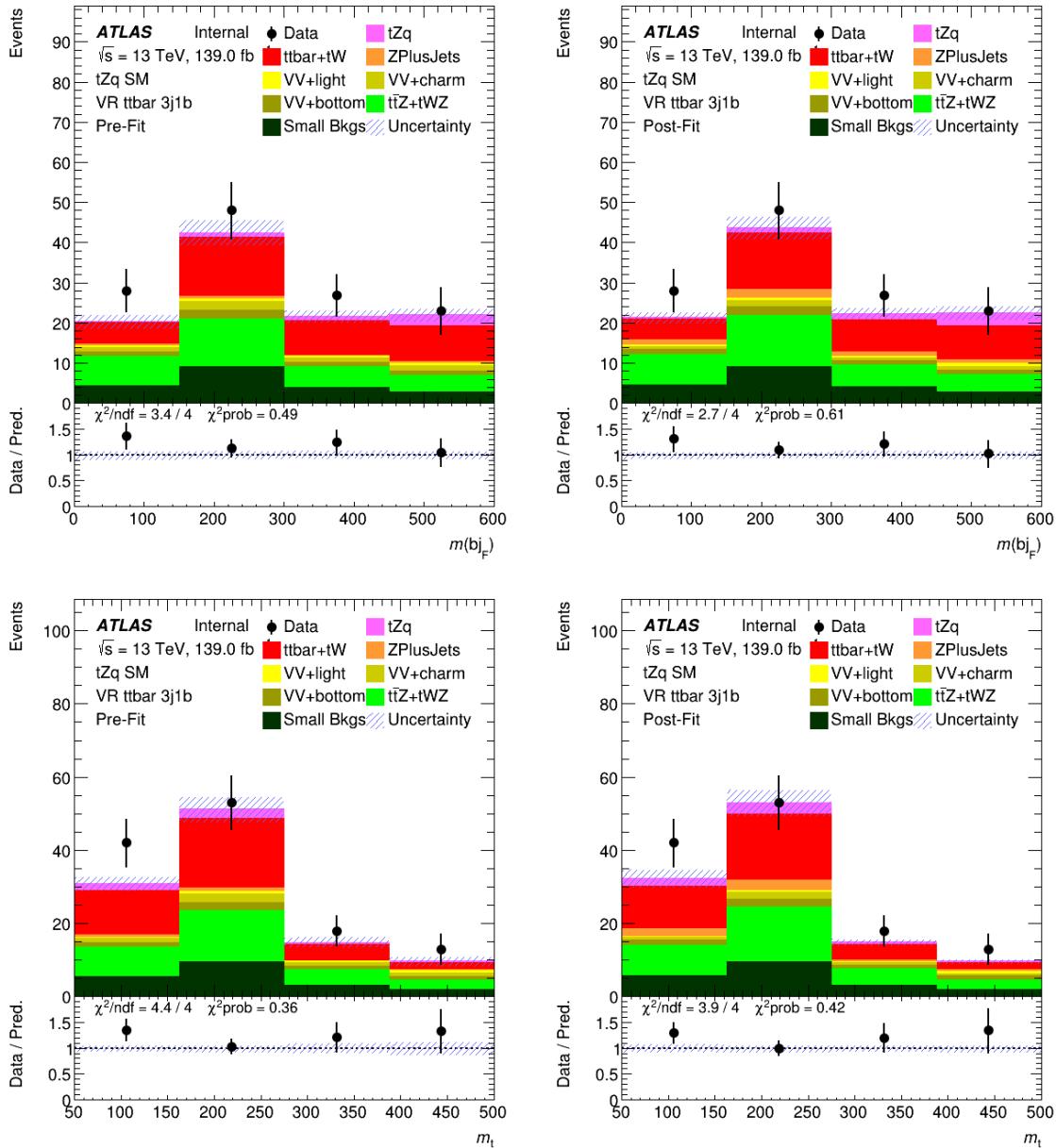


Figure 318: Pre-fit (left) and post-fit (right) NN input variable distributions in the  $t\bar{t}V + t\bar{t}$  3j1b validation regions. The uncertainty band includes both statistical and systematic uncertainties. Since the  $t\bar{t}$  background is free floating in the fit, there are no uncertainties on this background pre-fit.

Not reviewed, for internal circulation only

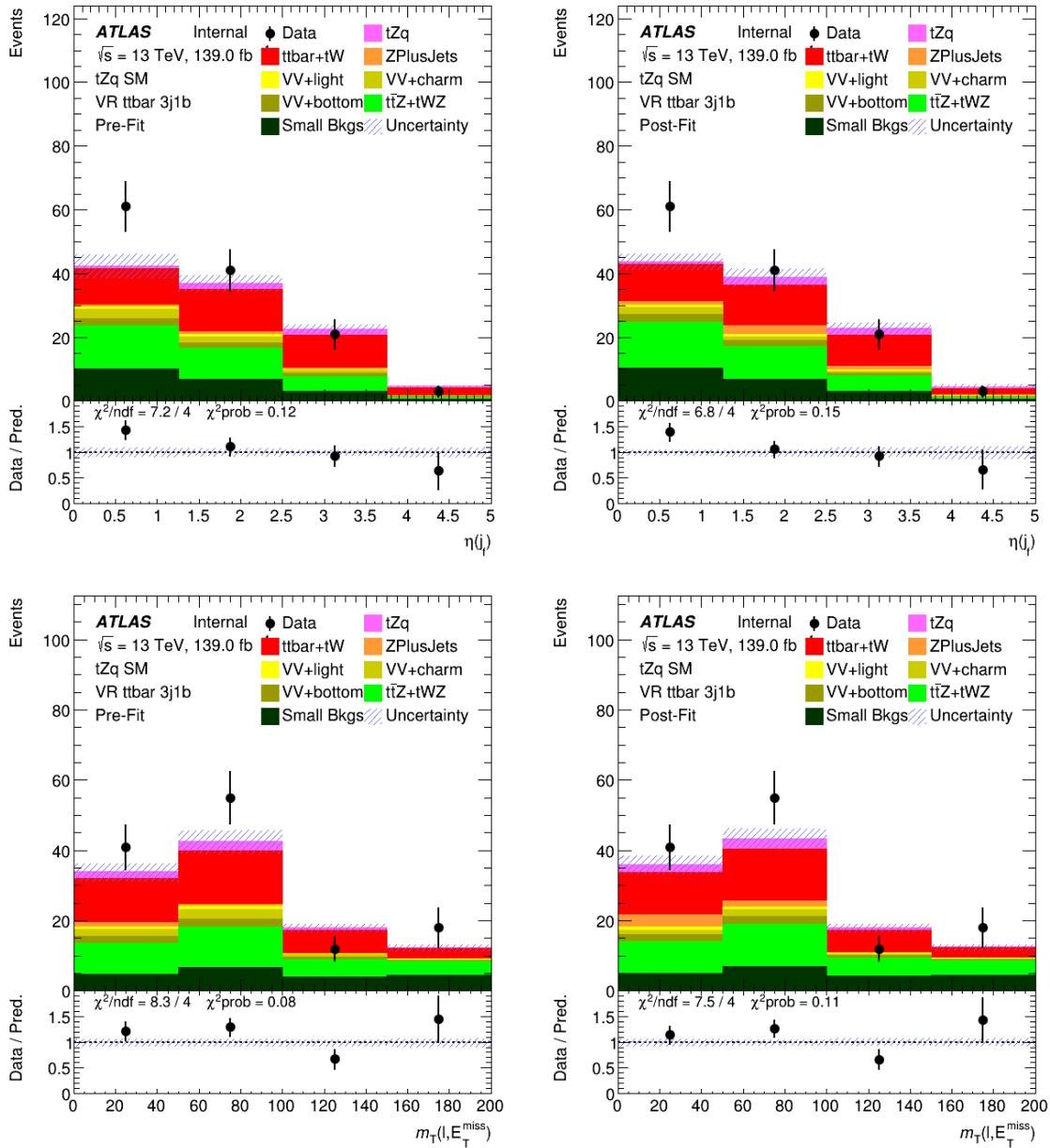


Figure 319: Pre-fit (left) and post-fit (right) NN input variable distributions in the  $t\bar{t}V + t\bar{t}$  3j1b validation regions. The uncertainty band includes both statistical and systematic uncertainties. Since the  $t\bar{t}$  background is free floating in the fit, there are no uncertainties on this background pre-fit.

Not reviewed, for internal circulation only

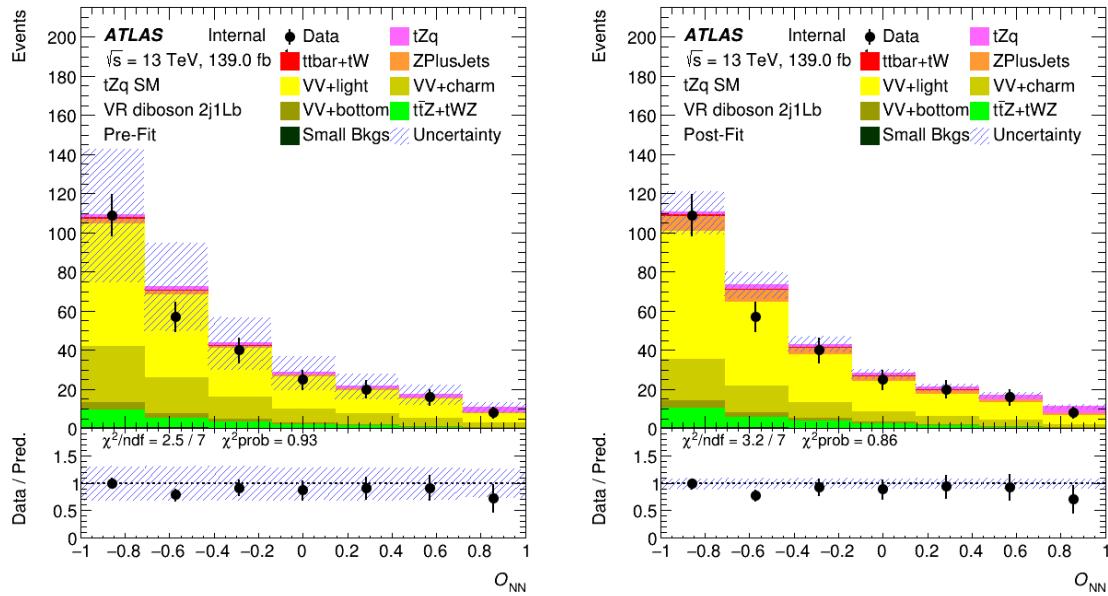


Figure 320: Pre-fit (left) and post-fit (right) NN output variable distributions in the diboson 2j1Lb validation region. The uncertainty band includes both statistical and systematic uncertainties.

Not reviewed, for internal circulation only

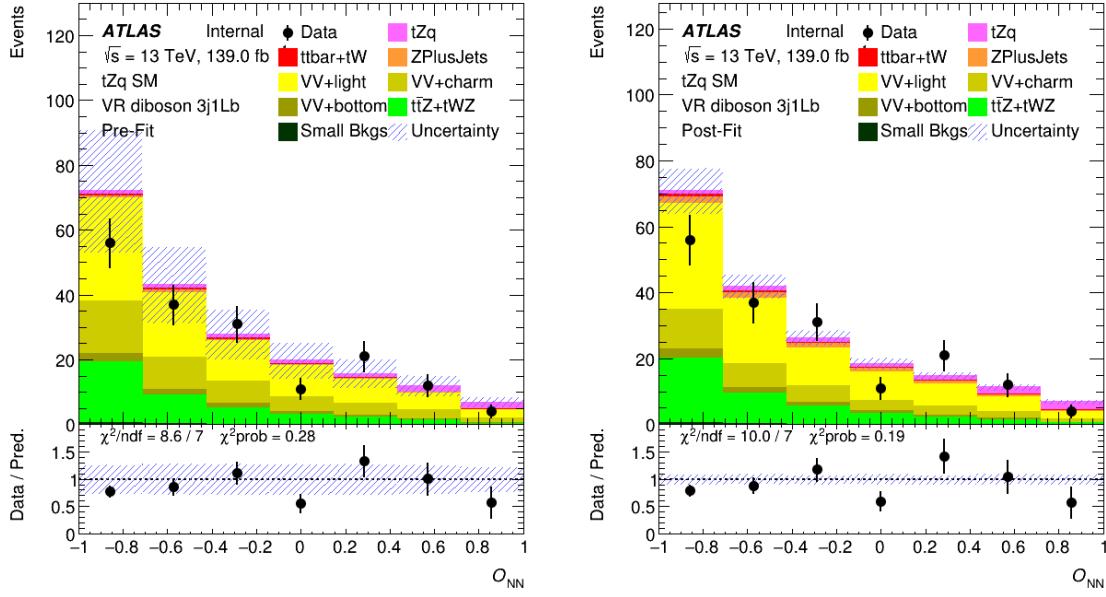


Figure 321: Pre-fit (left) and post-fit (right) NN output variable distributions in the diboson 3j1Lb validation region. The uncertainty band includes both statistical and systematic uncertainties.

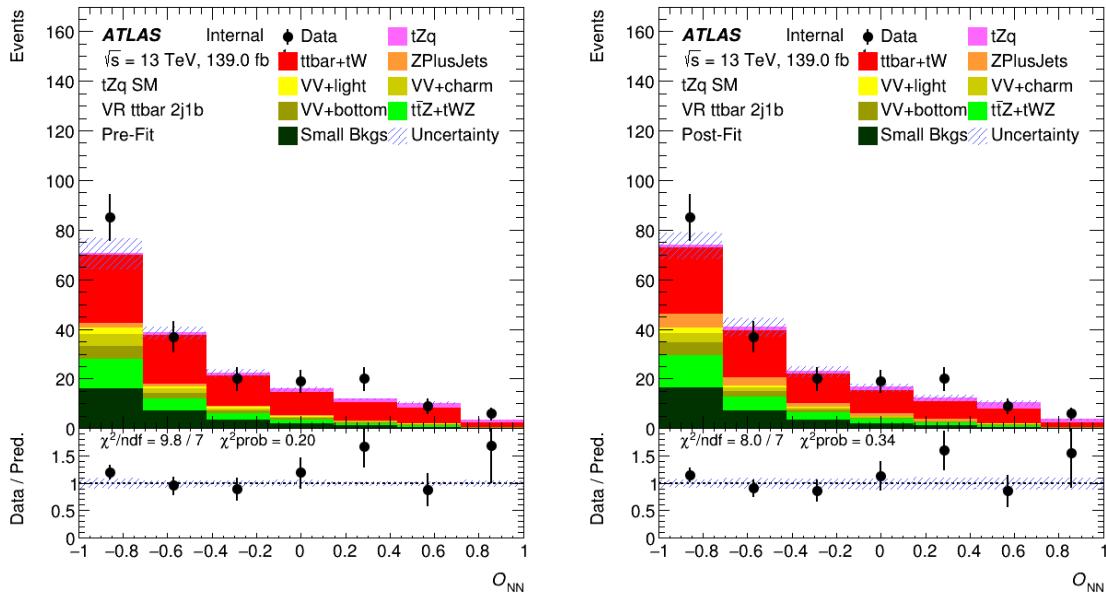


Figure 322: Pre-fit (left) and post-fit (right) NN output variable distributions in the  $t\bar{t}V + t\bar{t}$  2j1b validation region. The uncertainty band includes both statistical and systematic uncertainties. Since the  $t\bar{t}$  background is free floating in the fit, there are no uncertainties on this background pre-fit.

Not reviewed, for internal circulation only

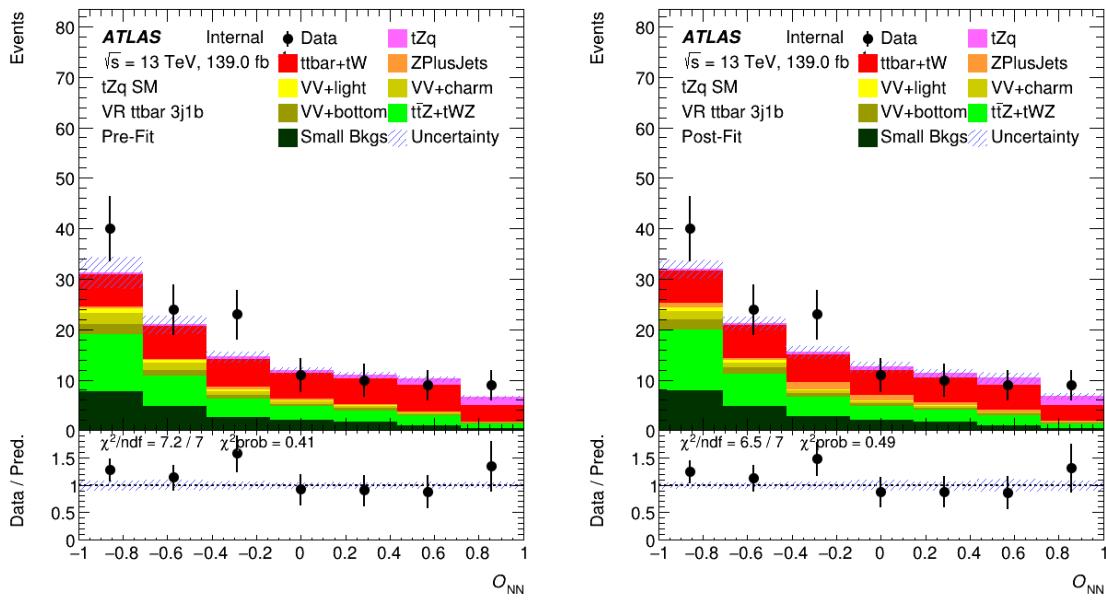


Figure 323: Pre-fit (left) and post-fit (right) NN output variable distributions in the  $t\bar{t}V + t\bar{t}$  3j1b validation regions. The uncertainty band includes both statistical and systematic uncertainties. Since the  $t\bar{t}$  background is free floating in the fit, there are no uncertainties on this background pre-fit.

1603 **G.6 Unblinded fit checks - Split into years**

1604 Studies presented in the following were done on events with  $m_T(W) > 20$  GeV.

1605 The studies reported in the following were not repeated with the changes applied after Top Approval, i.e.:  
 1606  $tZq$  radiation uncertainty still has normalization in,  $tWZ$  DR1 vs DR2 systematic is not included and  
 1607 diboson uncertainty is 20 % for both LF and HF.

1608 In the following the results of the unblinded fit (keeping  $\mu_{\text{SIG}}$  and the last two bins of the  $O_{\text{NN}}$  distributions  
 1609 blinded) are presented, split into the different data and MC campaigns: data from 2015+2016 with mc16a,  
 1610 data from 2017 with mc16d and data from 2018 with mc16e. Background normalization factors are shown  
 1611 in Fig. 324, while nuisance parameters are shown in Figs. 325 to 332. Finally, the distributions of the  
 1612 variables used in the fit in the signal and control regions, pre- and post-fit, are shown in Figs. 334 to 341.

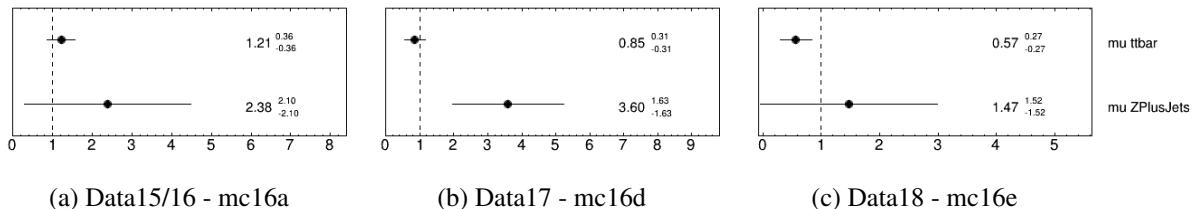


Figure 324: Normalisation factors of the unblinded fits.

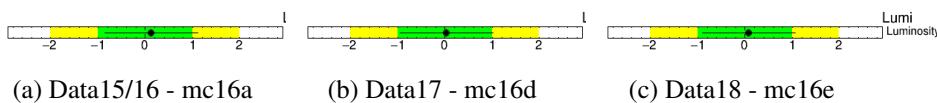


Figure 325: Pulls and constraints of the nuisance parameters of the unblinded fits: luminosity.

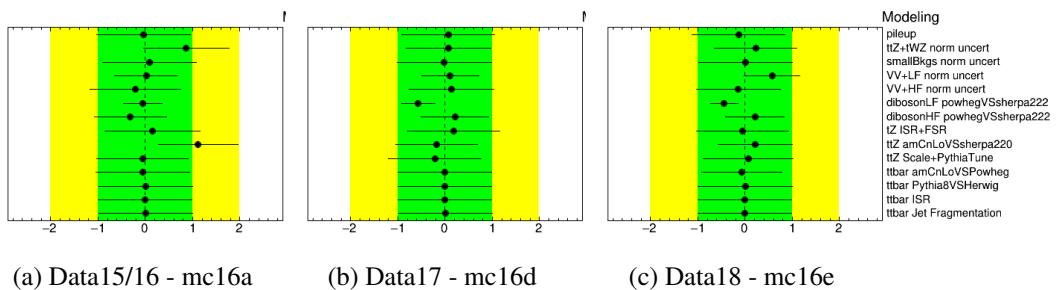


Figure 326: Pulls and constraints of the nuisance parameters of the unblinded fits: modeling systematics.

Not reviewed, for internal circulation only

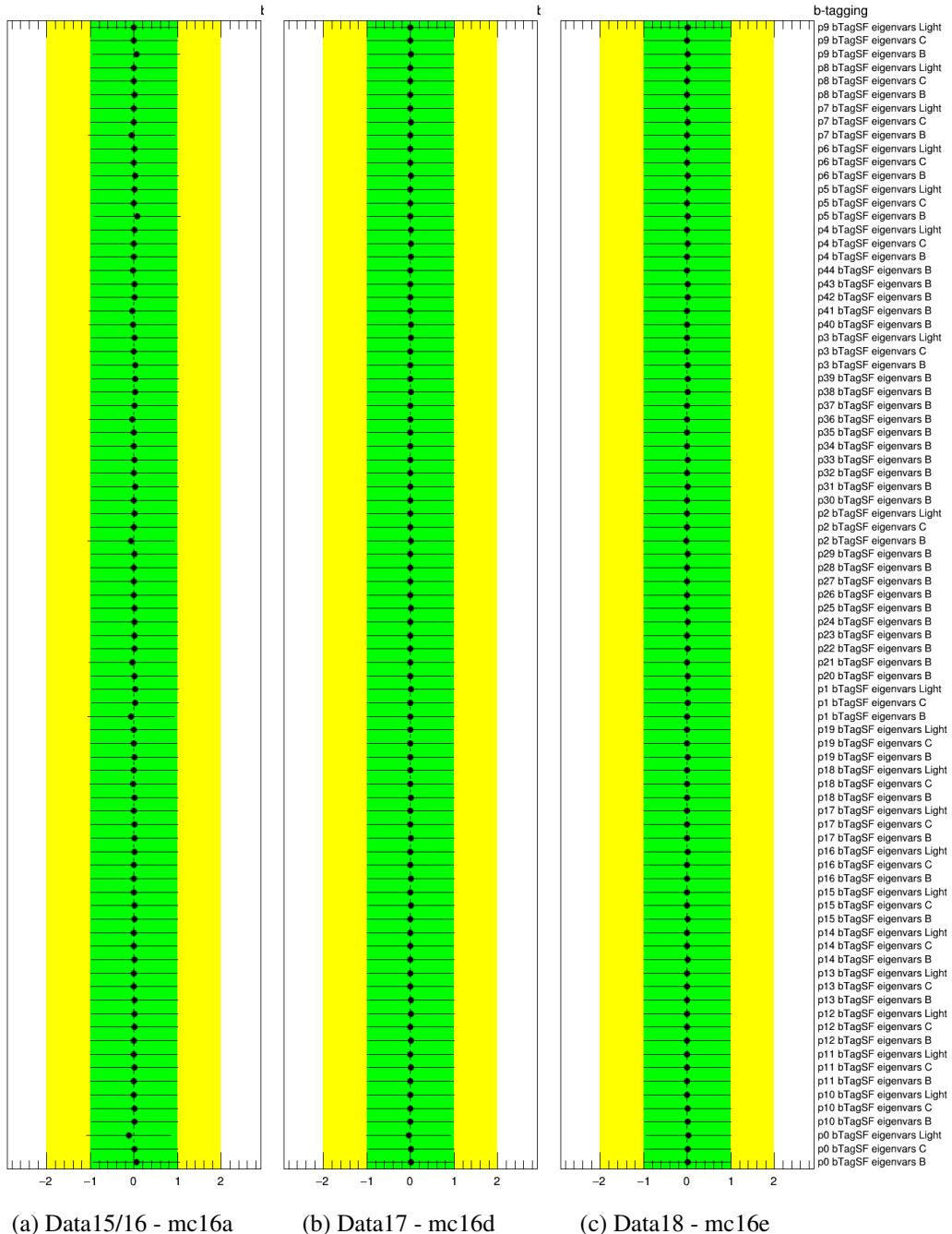


Figure 327: Pulls and constraints of the nuisance parameters of the unblinded fits:  $b$ -tagging systematics.

Not reviewed, for internal circulation only

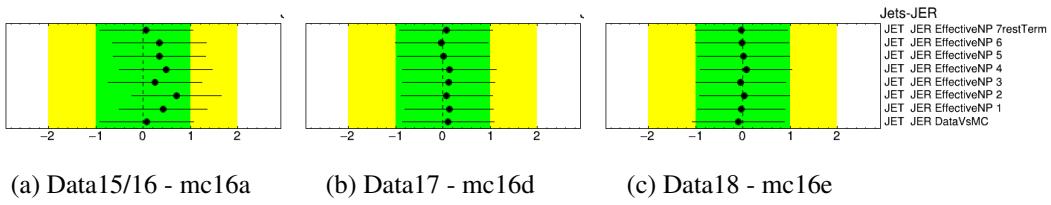


Figure 328: Pulls and constraints of the nuisance parameters of the unblinded fits: JER systematics.

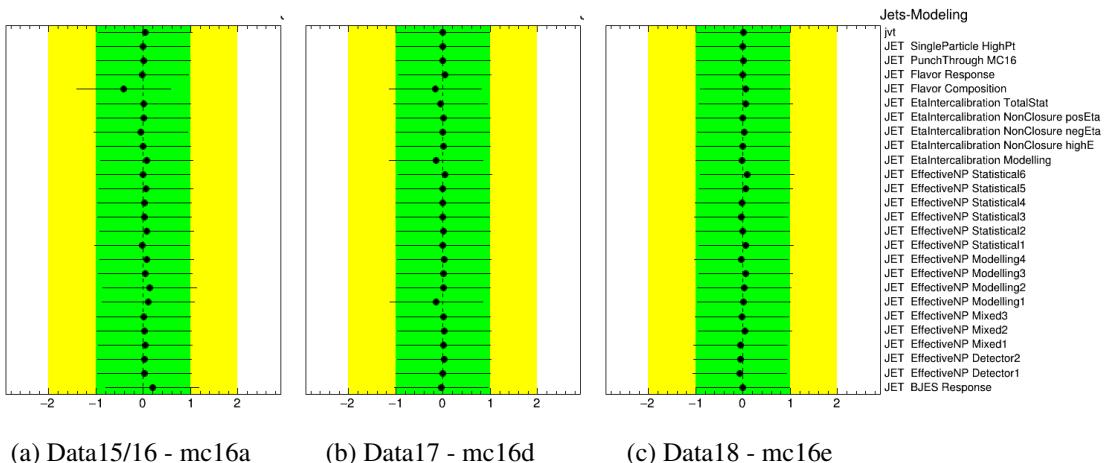


Figure 329: Pulls and constraints of the nuisance parameters of the unblinded fits: jet modeling systematics.

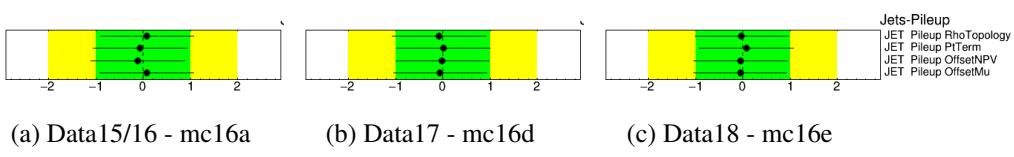


Figure 330: Pulls and constraints of the nuisance parameters of the unblinded fits: jet pile-up systematics.

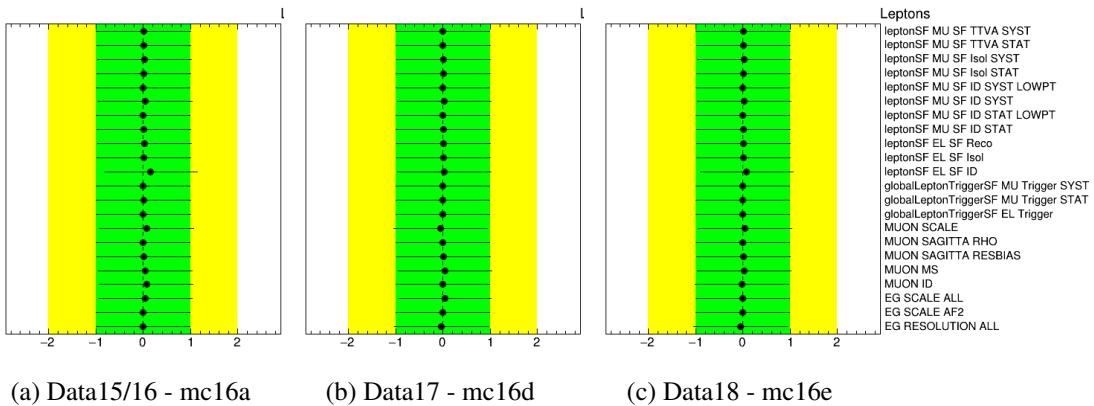


Figure 331: Pulls and constraints of the nuisance parameters of the unblinded fits: lepton systematics.

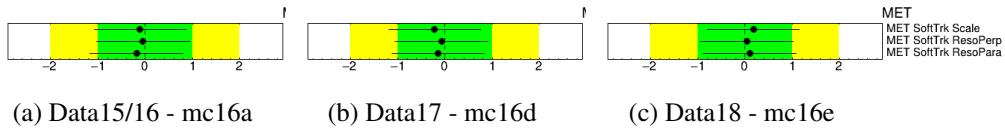


Figure 332: Pulls and constraints of the nuisance parameters of the unblinded fits:  $E_T^{\text{miss}}$  systematics.

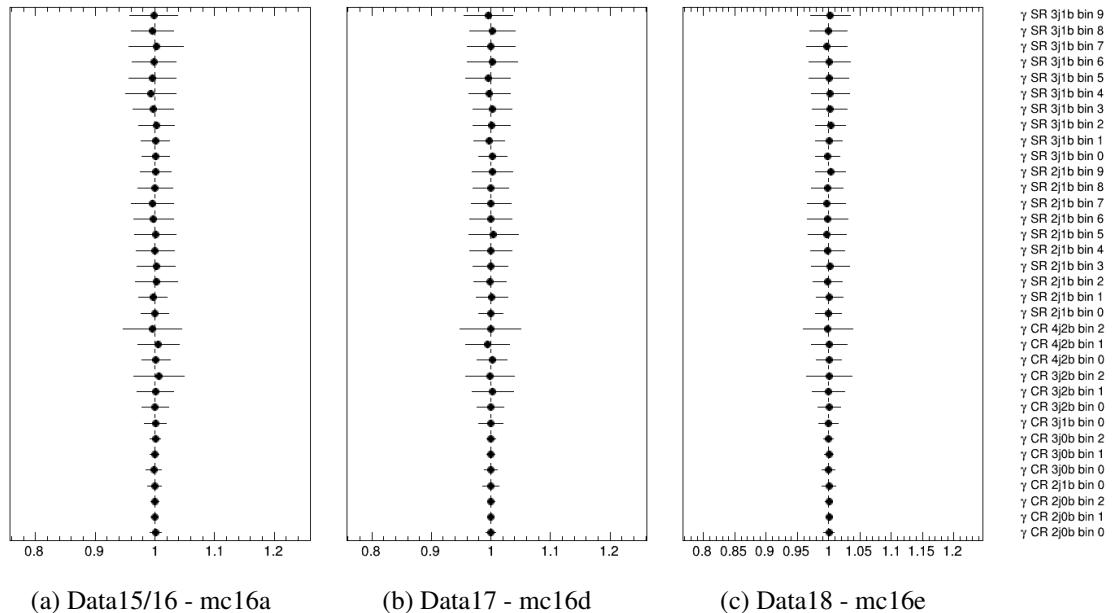


Figure 333: Gamma parameters of the unblinded fits.

Not reviewed, for internal circulation only

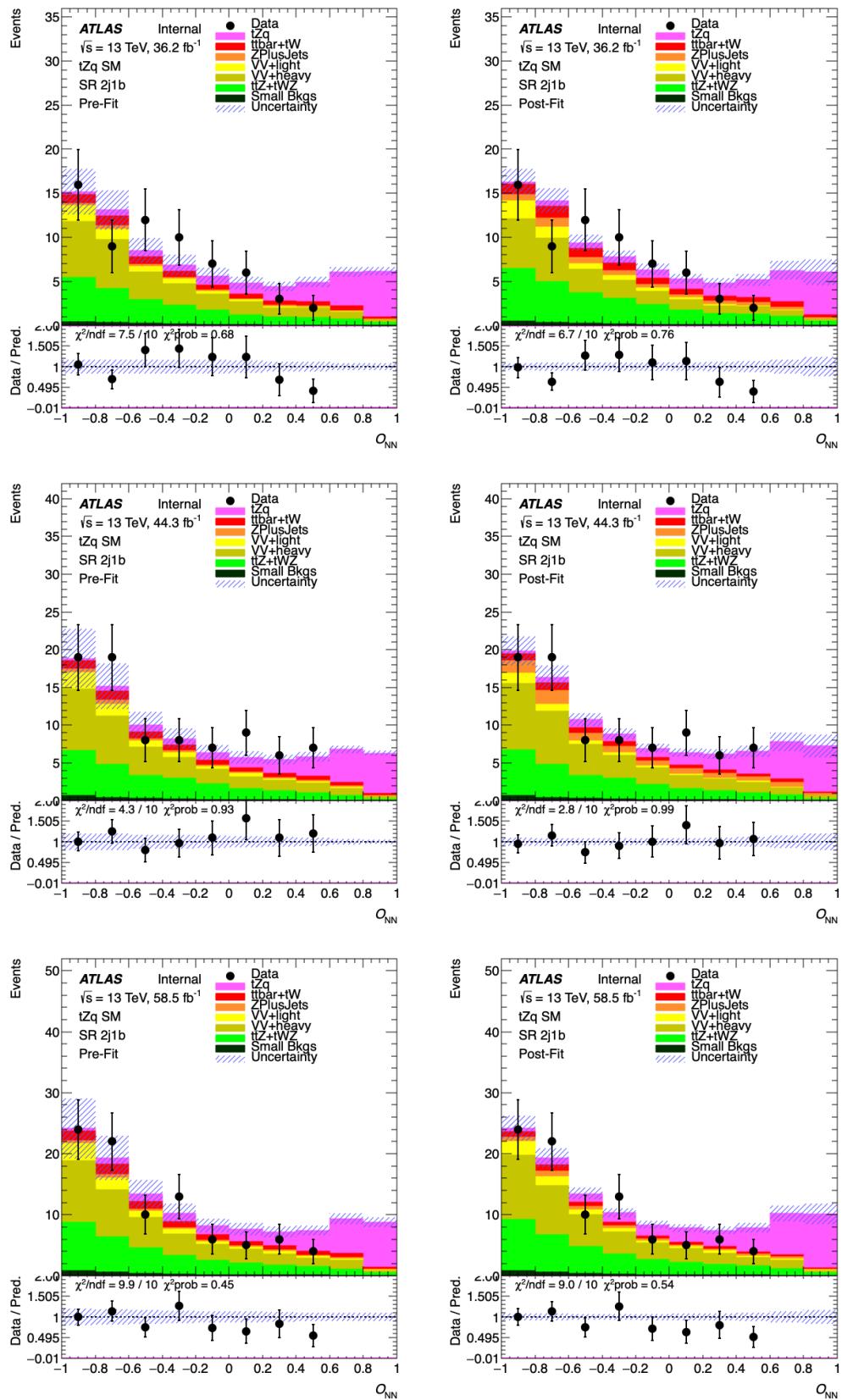


Figure 334: Pre-fit (left) and post-fit (right) NN output distributions in the signal region 2j1b in the three years. The uncertainty band includes both statistical and systematic uncertainties.

Not reviewed, for internal circulation only

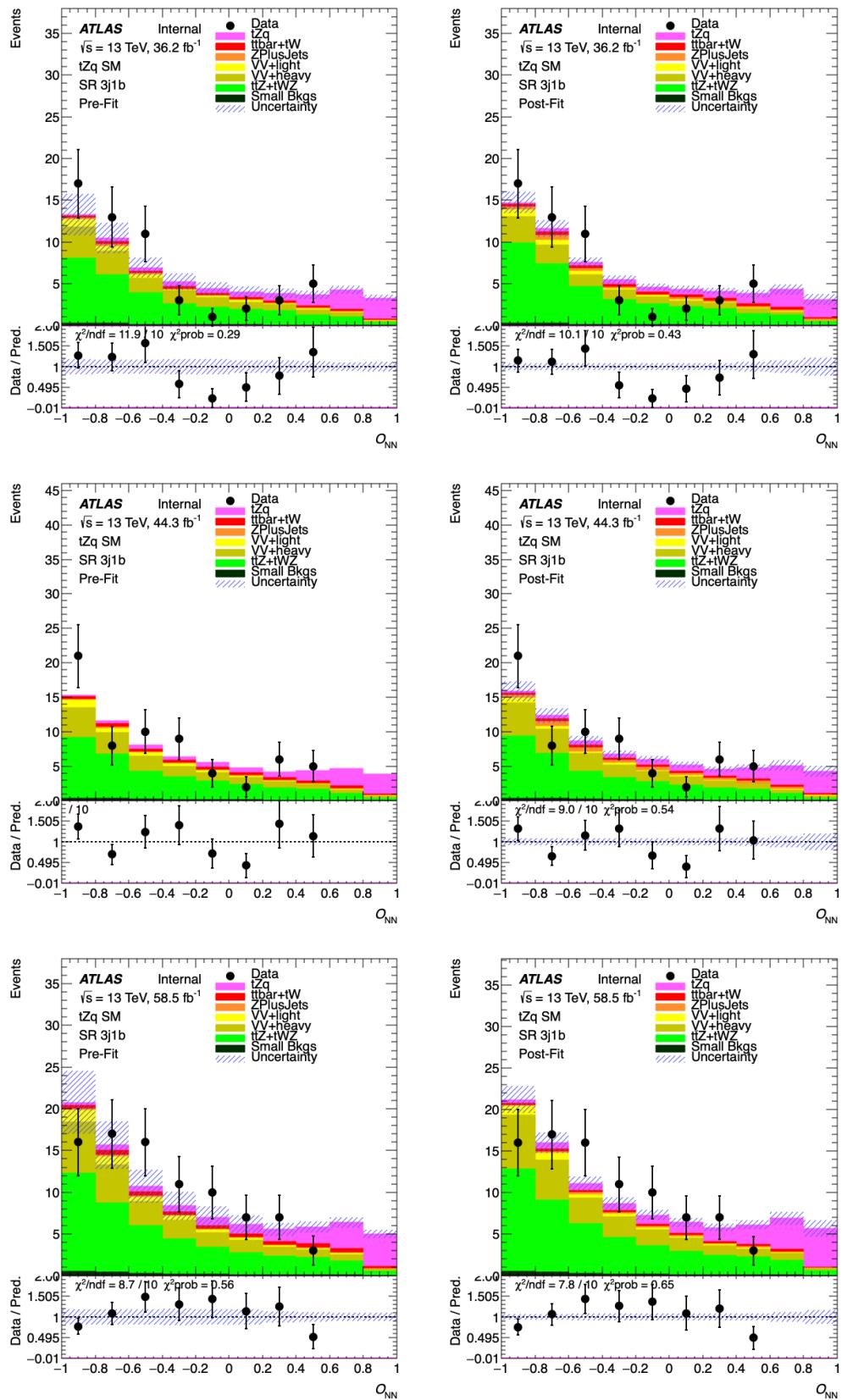


Figure 335: Pre-fit (left) and post-fit (right) NN output distributions in the signal region 3j1b in the three years. The uncertainty band includes both statistical and systematic uncertainties.

Not reviewed, for internal circulation only

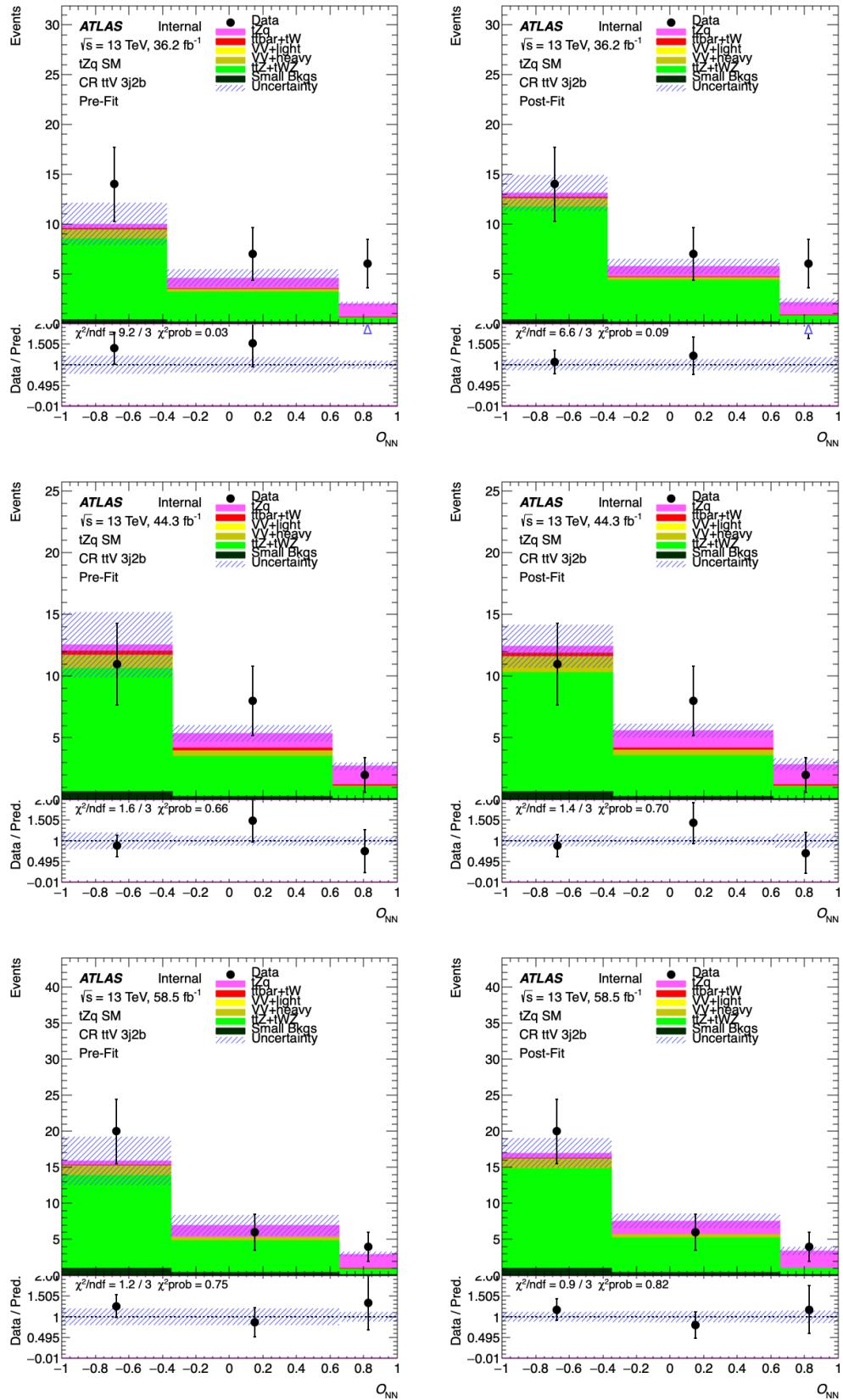


Figure 336: Pre-fit (left) and post-fit (right) NN output distributions in the  $t\bar{t}Z$  control region 3j2b in the three years. The uncertainty band includes both statistical and systematic uncertainties.

Not reviewed, for internal circulation only

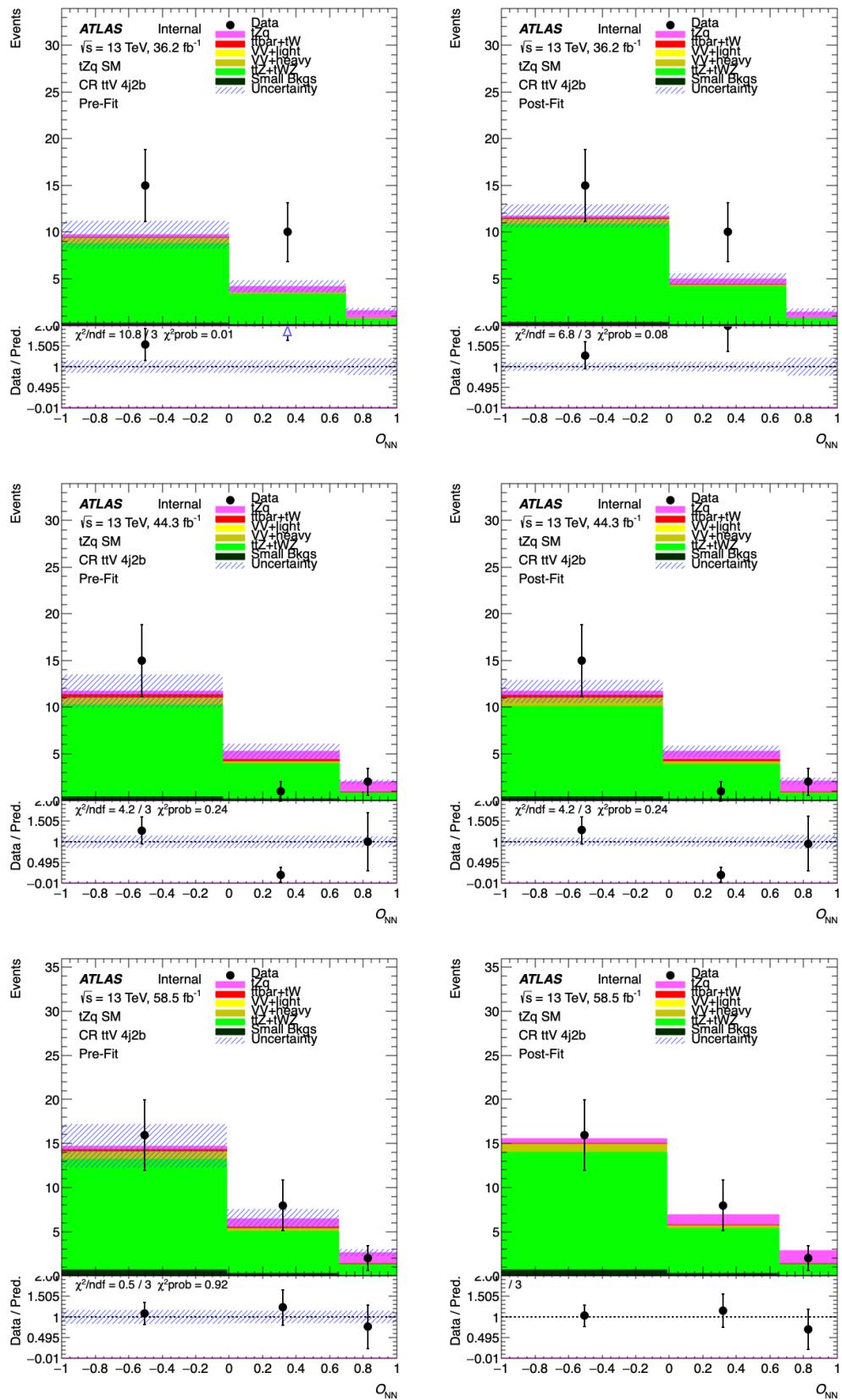


Figure 337: Pre-fit (left) and post-fit (right) NN output distributions in the  $t\bar{t}Z$  control region 4j2b in the three years. The uncertainty band includes both statistical and systematic uncertainties.

Not reviewed, for internal circulation only

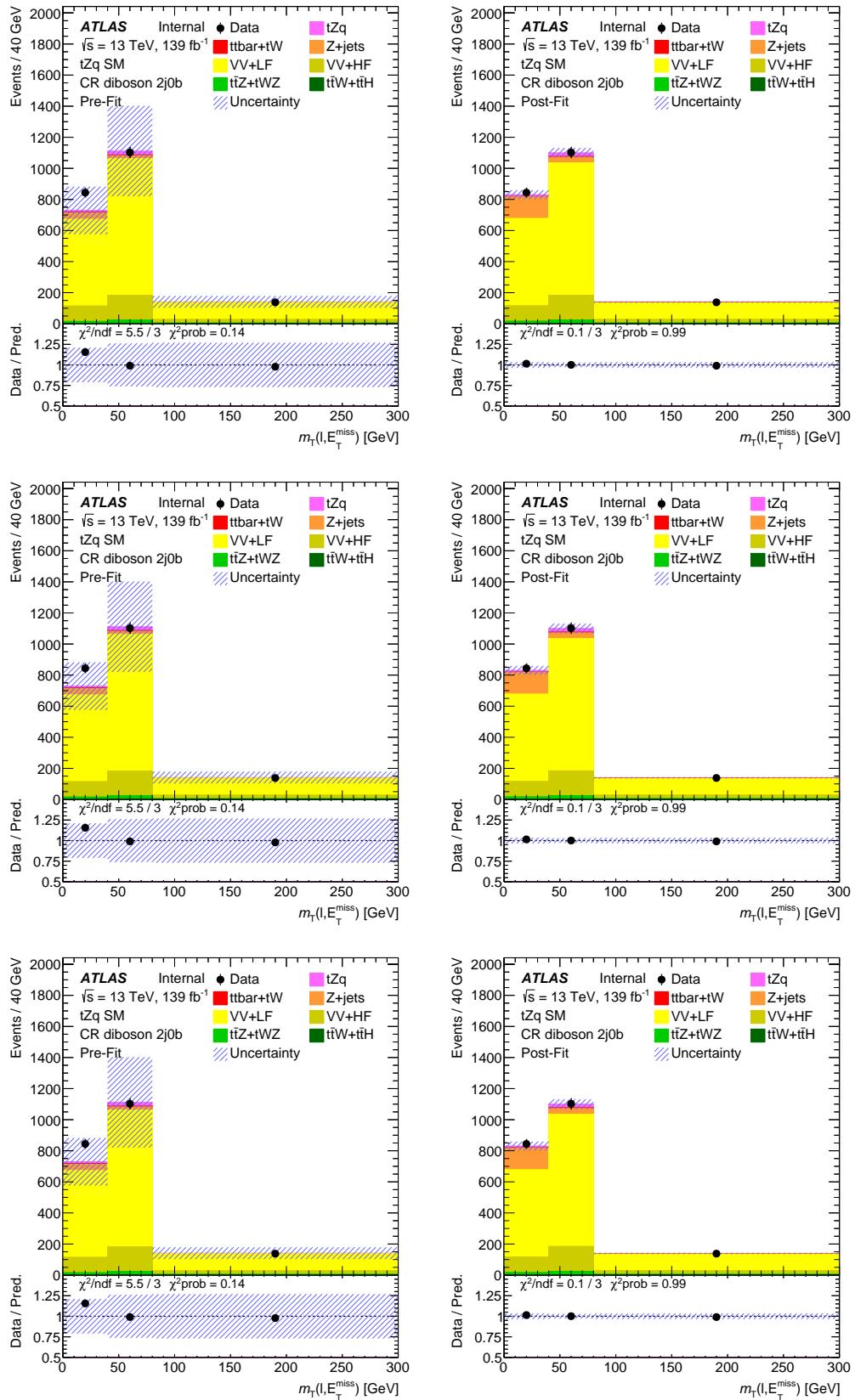


Figure 338: Pre-fit (left) and post-fit (right)  $E_T^{\text{miss}}$  distributions in the diboson control region 2j0b in the three years. The uncertainty band includes both statistical and systematic uncertainties.

Not reviewed, for internal circulation only

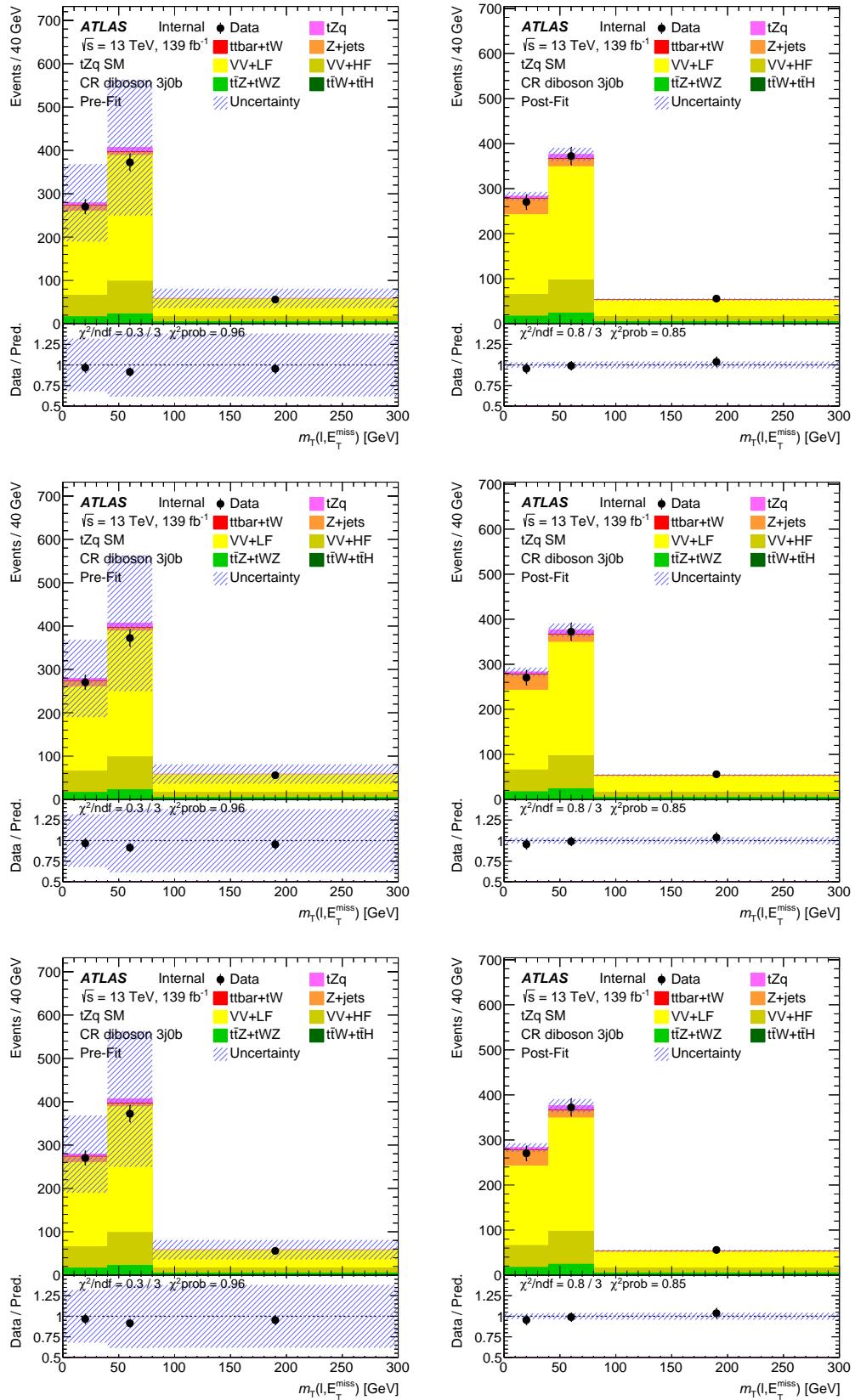


Figure 339: Pre-fit (left) and post-fit (right)  $E_T^{\text{miss}}$  distributions in the diboson control region 3j0b in the three years. The uncertainty band includes both statistical and systematic uncertainties.

Not reviewed, for internal circulation only

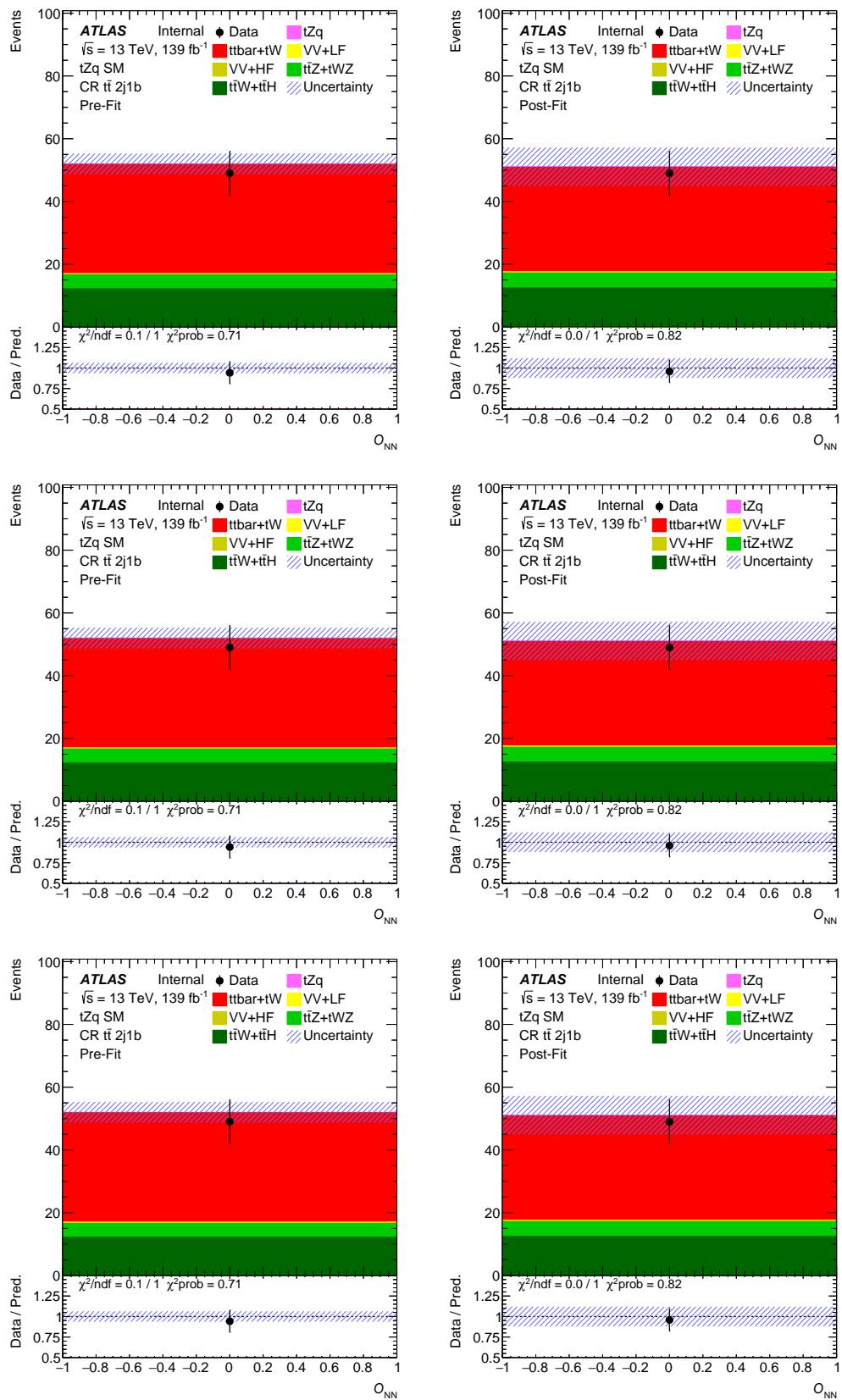


Figure 340: Pre-fit (left) and post-fit (right) NN output distributions in the  $t\bar{t}$  control region 2j1b in the three years. The uncertainty band includes both statistical and systematic uncertainties.

Not reviewed, for internal circulation only

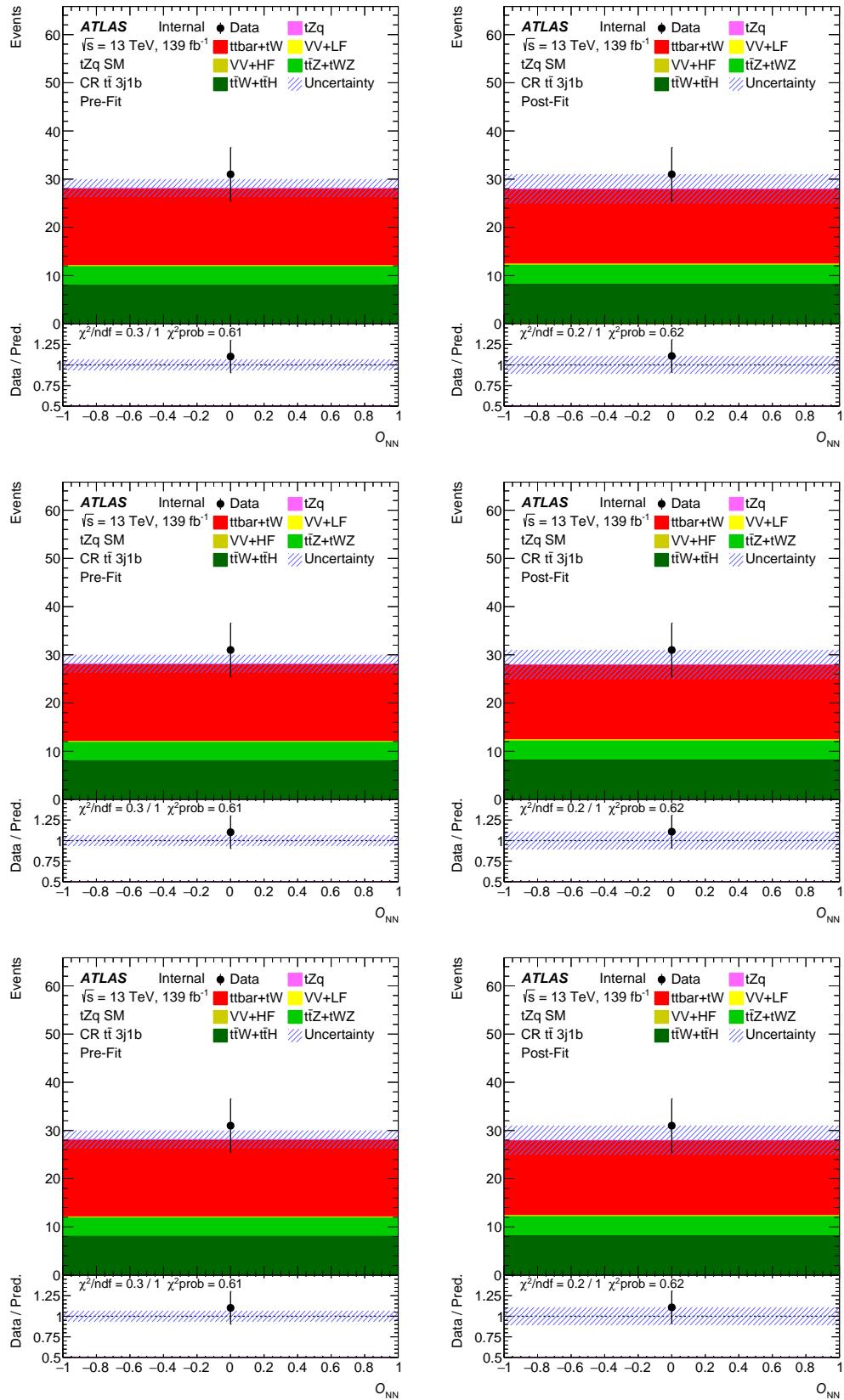


Figure 341: Pre-fit (left) and post-fit (right) NN output distributions in the  $t\bar{t}$  control region 3j1b in the three years. The uncertainty band includes both statistical and systematic uncertainties.

## 1613 G.7 Fits in signal-depleted regions with $\mu_{\text{SIG}} = 1, 0$ and floating

1614 The studies reported in the following were not repeated with the changes applied after Top Approval, i.e.:  
 1615  $t\bar{Z}$  radiation uncertainty still has normalization in,  $tWZ$  DR1 vs DR2 systematic is not included and  
 1616 diboson uncertainty is 20 % for both LF and HF.

1617 To check the stability of the fit and the behaviour of the backgrounds, several fits are performed in  
 1618 signal-depleted regions, using pre-normalizations for some backgrounds.

1619 The signal-depleted-region fits are done using real data in the regions explained in Section 10.1 with the  
 1620 following differences:

1621 **signal regions** only those bins with a low  $S/B$  are used, i.e. only the low  $O_{\text{NN}}$  bins, with  $O_{\text{NN}} < -0.4$ ; the  
 1622 rest of the bins are not included;

1623 **diboson control regions** no change;

1624  **$t\bar{t}$  control regions** no change;

1625  **$t\bar{t}Z$  control regions** no change<sup>6</sup>.

1626 The  $t\bar{t}Z + tWZ$  and diboson backgrounds have a pre-normalization uncertainty defined, as described in  
 1627 Section 10.1, while  $t\bar{t}$  and  $Z + \text{jets}$  are free floating. Please note that in this fit,  $t\bar{t}V$  includes  $t\bar{t}Z$  and  $tWZ$ ,  
 1628 while  $t\bar{t}W$  and  $t\bar{t}H$  appear as *small backgrounds*.

1629 Three fits are performed, with a different treatment of the signal:

1630  **$\mu_{\text{SIG}} = 0$**  :  $\mu_{\text{SIG}}$  is forced to be 0; the backgrounds cover the small signal contamination;

1631 **floating  $\mu_{\text{SIG}}$**  :  $\mu_{\text{SIG}}$  is free floating;

1632  **$\mu_{\text{SIG}} = 1$**  :  $\mu_{\text{SIG}}$  is forced to be 1.

1633 In the following the results of these three fits are shown. The values of the background NPs after the fit are  
 1634 shown in Fig. 342. It can be seen that the background normalisations from the three fits are compatible  
 1635 within their uncertainties.

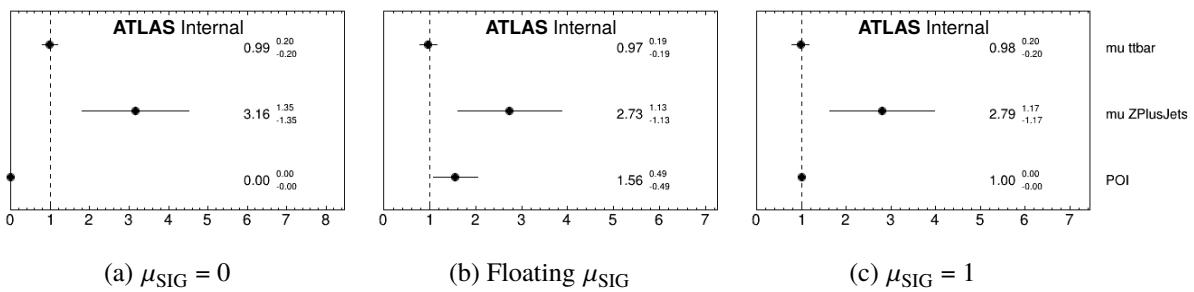


Figure 342: Normalisation factors of the signal-depleted-region fits.

1636 The pull distributions for the all nuisance parameters can be seen in Figs. 343 to 350 and Fig. 351. The  
 1637 pulls and constraints of the three fits are similar.

<sup>6</sup> This is therefore different from the fit shown in Appendix G.8, where only events with  $O_{\text{NN}} < 0$  are used.

1638 The only noticeable difference is that the normalisation of the  $t\bar{t}Z + tWZ$  backgrounds is more pulled in the  
 1639  $\mu_{\text{SIG}} = 0$  fit. This is understood as the signal contamination in the  $t\bar{t}Z$  CRs used in the fit is not negligible,  
 1640 therefore the  $t\bar{t}Z + tWZ$  need to cover that missing contribution.

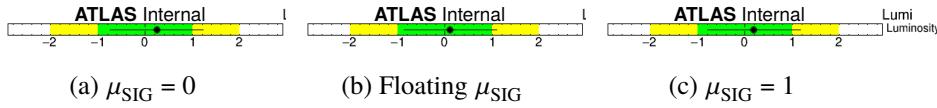


Figure 343: Pulls and constraints of the nuisance parameters of the signal-depleted-region fits: luminosity.

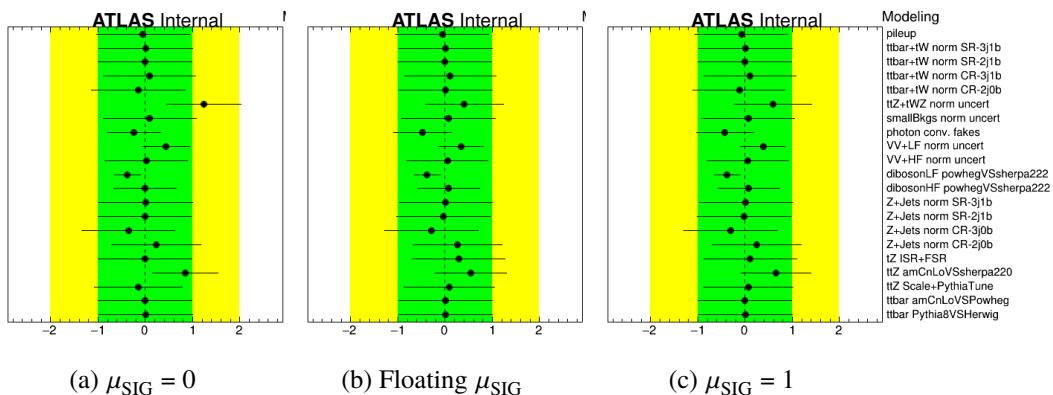


Figure 344: Pulls and constraints of the nuisance parameters of the signal-depleted-region fits: modeling systematics.

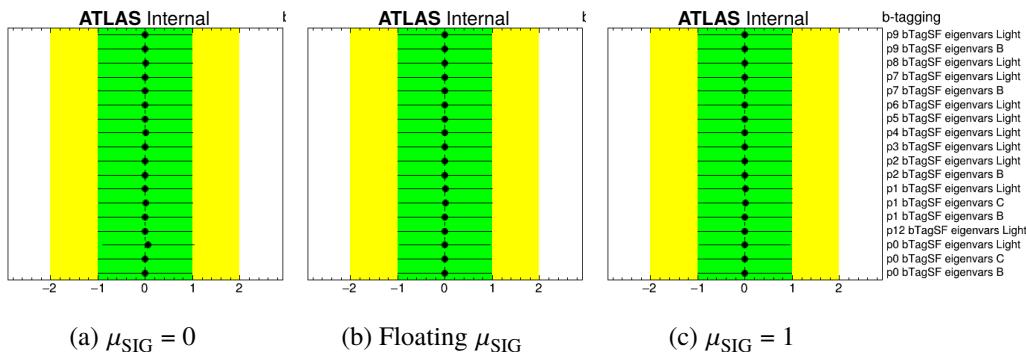


Figure 345: Pulls and constraints of the nuisance parameters of the signal-depleted-region fits: *b*-tagging systematics.

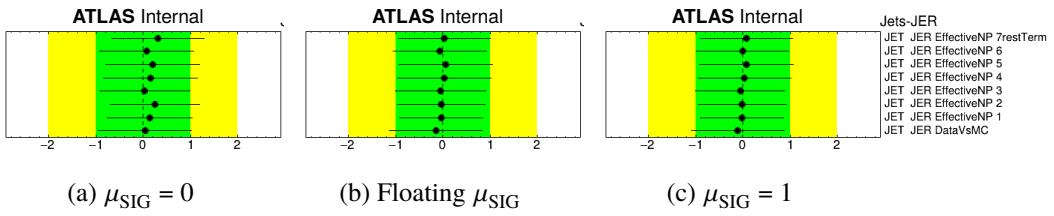


Figure 346: Pulls and constraints of the nuisance parameters of the signal-depleted-region fits: JER systematics.

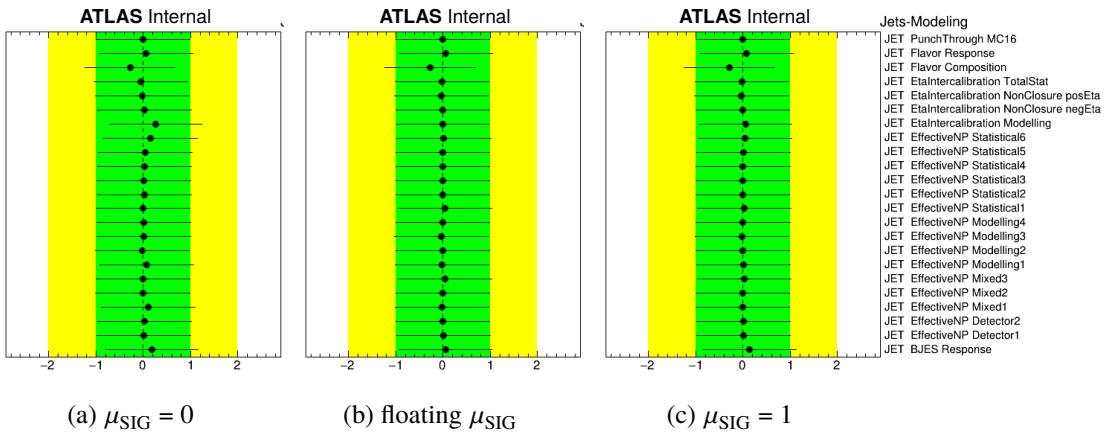


Figure 347: Pulls and constraints of the nuisance parameters of the signal-depleted-region fits: jet modeling systematics.

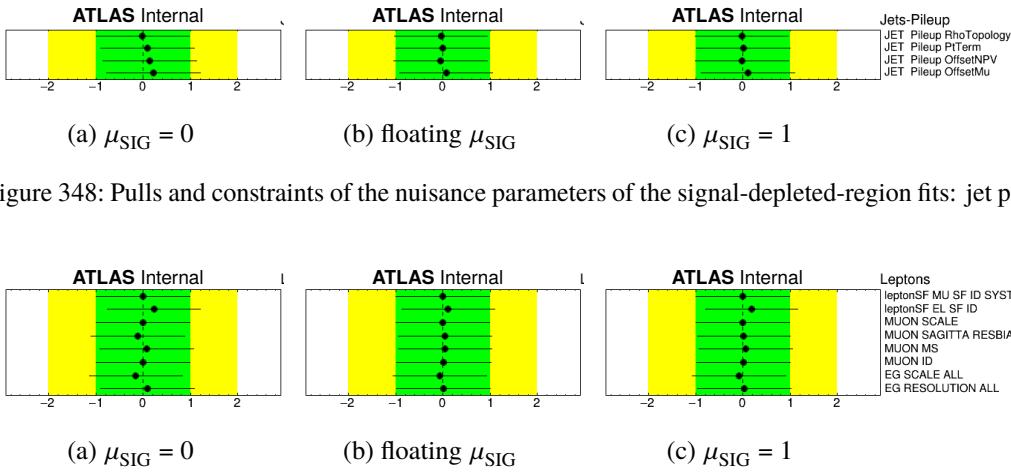


Figure 348: Pulls and constraints of the nuisance parameters of the signal-depleted-region fits: jet pile-up systematics.

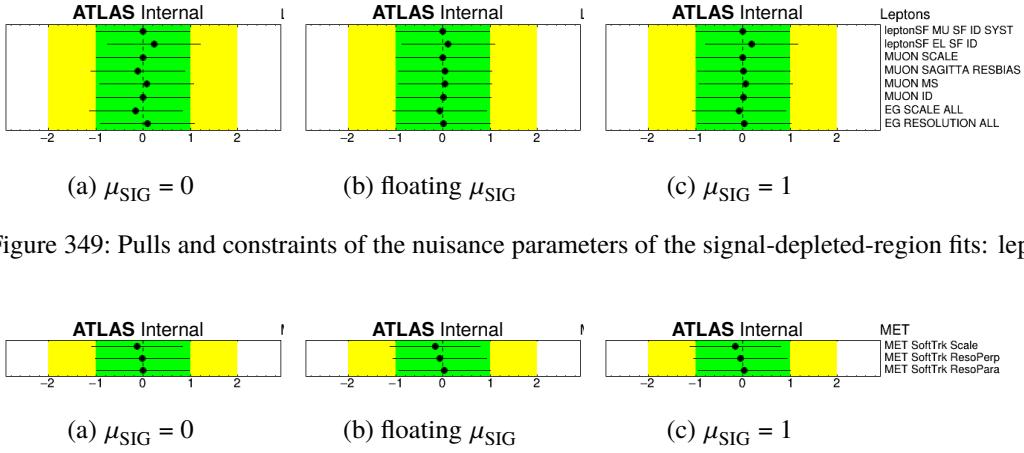
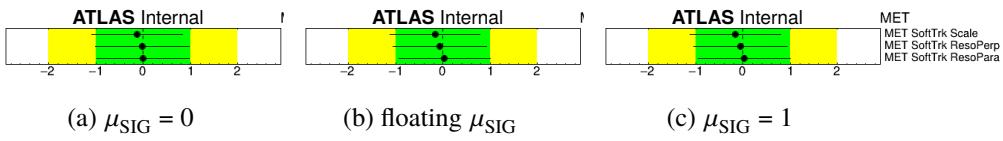


Figure 349: Pulls and constraints of the nuisance parameters of the signal-depleted-region fits: lepton systematics.

Figure 350: Pulls and constraints of the nuisance parameters of the signal-depleted-region fits:  $E_T^{\text{miss}}$  systematics.

Not reviewed, for internal circulation only

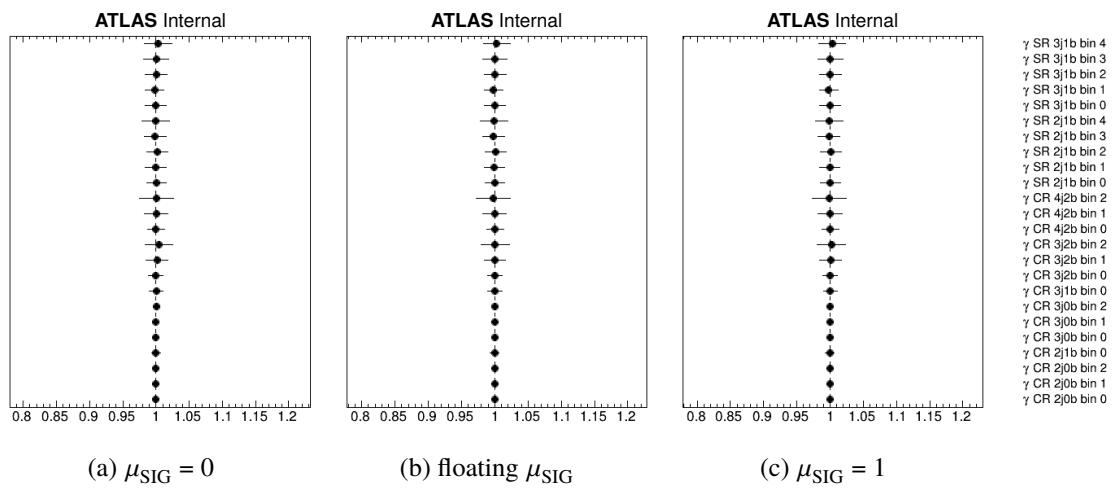


Figure 351: Gamma parameters of the signal-depleted-region fits.

1641 **G.8 Floating backgrounds - Fits in signal-depleted regions**

1642 **G.8.1 Introduction**

1643 To check the stability of the fit and the behaviour of the backgrounds, several fits are performed in  
 1644 signal-depleted regions, floating all main background sources.

1645 The signal-depleted-region fits are done using real data in the regions explained in Section 10.1 with the  
 1646 following differences:

1647 **signal regions** only those bins with a low  $S/B$  are used, i.e. only the low  $O_{NN}$  bins, with  $O_{NN} < -0.4$ ; the  
 1648 rest of the bins are not included;

1649 **diboson control regions**  $E_T^{\text{miss}}$  is fit;

1650  **$t\bar{t}$  control regions** no change;

1651  **$t\bar{t}Z$  control regions** only events with low  $O_{NN}$  are used, i.e. only events with  $O_{NN} < 0$ ; the rest of the  
 1652 events are not included; this is to reduce the signal contamination in these regions.

1653 The background normalization parameters are free floating, as explained before. Please note that in this fit,  
 1654  $t\bar{t}V$  includes  $t\bar{t}Z$ ,  $t\bar{t}W$ ,  $tWZ$  and  $t\bar{t}H$ .

1655 Three fits are performed, with a different treatment of the signal:

1656  **$\mu_{\text{SIG}} = 0$**  :  $\mu_{\text{SIG}}$  is forced to be 0; the backgrounds cover the small signal contamination;

1657 **floating  $\mu_{\text{SIG}}$**  :  $\mu_{\text{SIG}}$  is free floating;

1658  **$\mu_{\text{SIG}} = 1$**  :  $\mu_{\text{SIG}}$  is forced to be 1.

1659 In the following the results of these three fits are shown. The values of the background normalization  
 1660 parameters after the fit are shown in Fig. 352. It can be seen that the background normalisations from the  
 1661 three fits are compatible within their uncertainties.

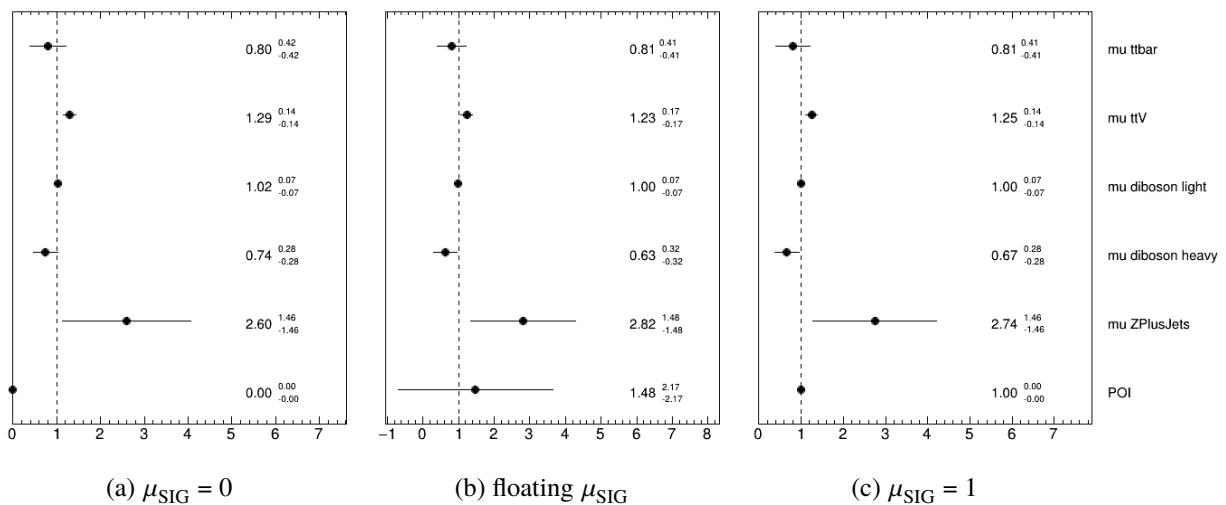


Figure 352: Normalisation factors of the signal-depleted-region fits.

- 1662 The pull distributions for the all nuisance parameters can be seen in Fig. 353 and Fig. 354. The pulls and  
 1663 constraints of the three fits are similar.

Not reviewed, for internal circulation only

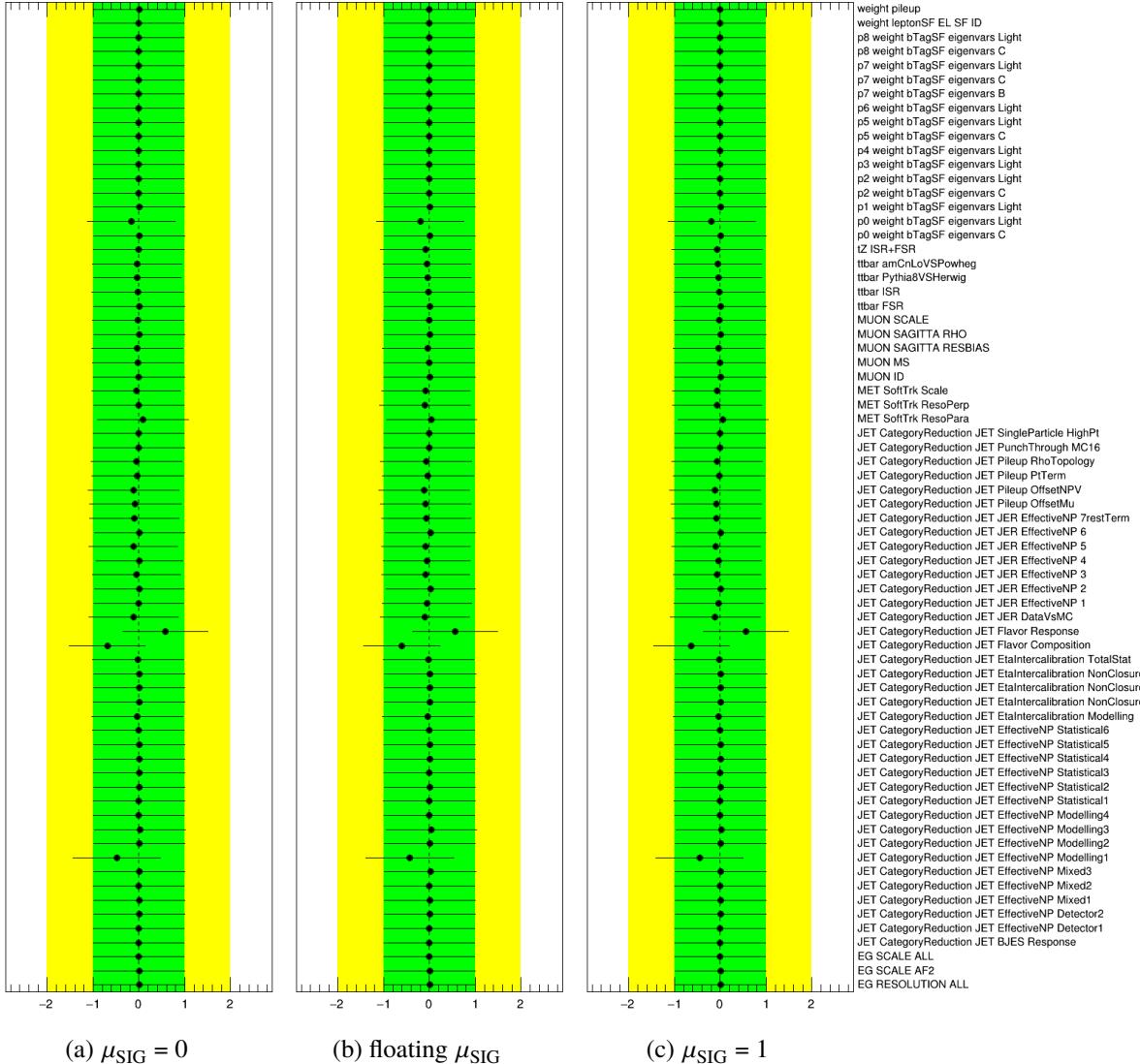


Figure 353: Pulls and constraints of the nuisance parameters of the signal-depleted-region fits.

Not reviewed, for internal circulation only

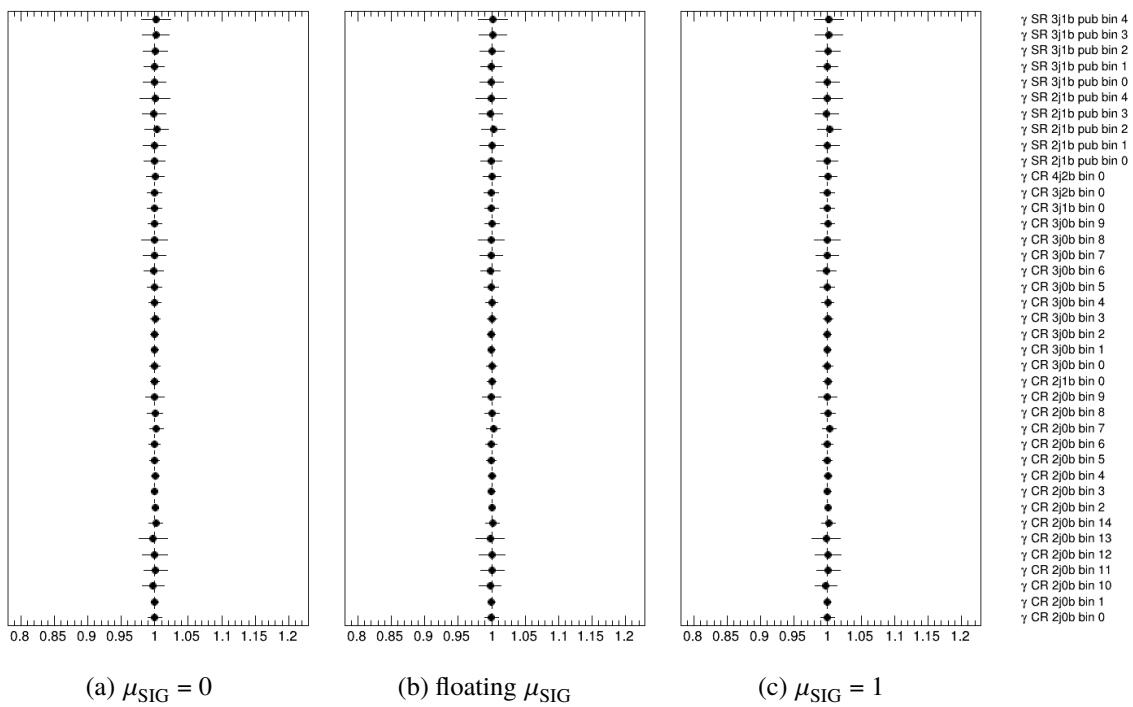


Figure 354: Gamma parameters of the signal-depleted-region fits.

### 1664 G.8.2 Fit in signal-depleted regions with $\mu_{\text{SIG}} = 1$

1665 As the three fits shown in the previous section are compatible, the complete results of the fit with  $\mu_{\text{SIG}} = 1$   
 1666 are shown in the following. This choice is connected with the fact that, in the Asimov fit used to estimate  
 1667 the expected significance,  $\mu_{\text{SIG}}$  is set to 1 and the background normalisations are set to the ones extracted  
 1668 from this fit.

1669 The values of the background normalization parameters after the fit are shown in Fig. 355. The correlation  
 1670 matrix of the parameters included in the fit is shown in Fig. 356.

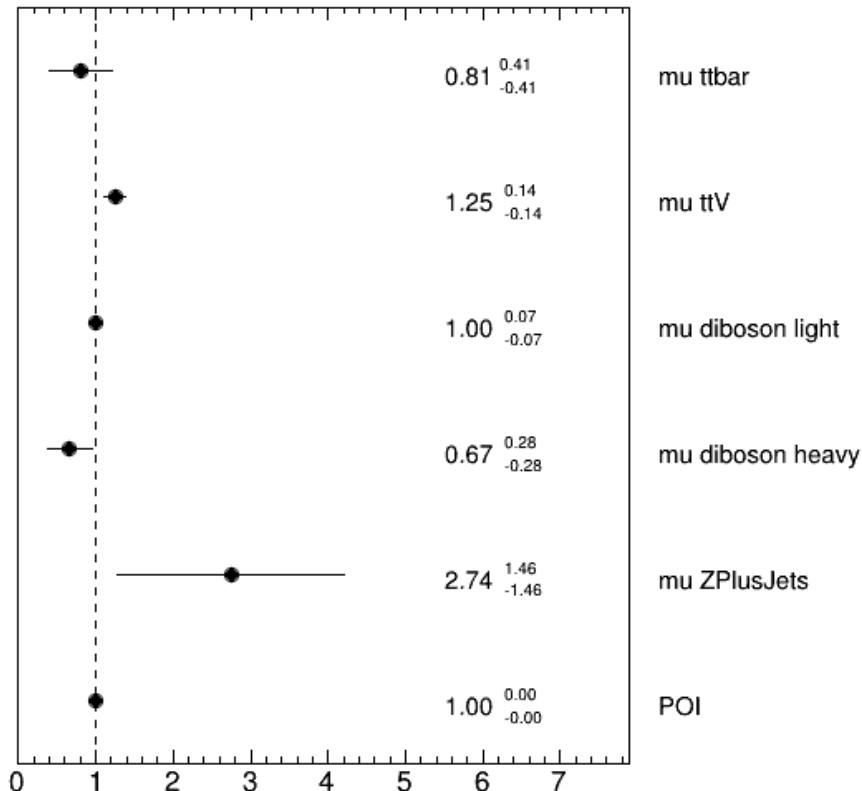


Figure 355: Normalisation factors of the signal-depleted-region fit  $\mu_{\text{SIG}} = 1$ .

1671 The  $t\bar{t}$  estimation is scaled down by 20 %, but  $\mu_{t\bar{t}}$  it is still compatible with 1 within uncertainties. The  $t\bar{t}Z$   
 1672 component is instead scaled up by 25 %. As it can be seen from Fig. 356, the  $\mu_{t\bar{t}}$  and  $\mu_{t\bar{t}Z}$  are anticorrelated.  
 1673 This can be explained by looking at the  $t\bar{t}$  2j1b and 3j1b CRs used in the fit, where the two background  
 1674 sources are estimated from (Fig. 363).

1675 As already mentioned, the diboson background has two floating parameters in the fit: one describing the  
 1676 heavy-flavour component and one the light-flavour component. While a value of  $\mu_{VV+LF}$  of 1 is extracted  
 1677 from the fit, the diboson heavy-flavour component is scaled down by 33 %. Both diboson components are  
 1678 highly correlated with  $\mu_{t\bar{t}Z}$ , with  $VV + HF$  being anticorrelated with  $t\bar{t}Z$  (as it can be seen in the  $t\bar{t}Z$  3j2b  
 1679 and 4j2b CRs in Fig. 364) and  $VV + LF$  being correlated with  $t\bar{t}Z$  through the anticorrelation with  $VV + HF$   
 1680 (as it can be seen in the diboson 2j0b and 3j0b CRs in Fig. 362).

Not reviewed, for internal circulation only

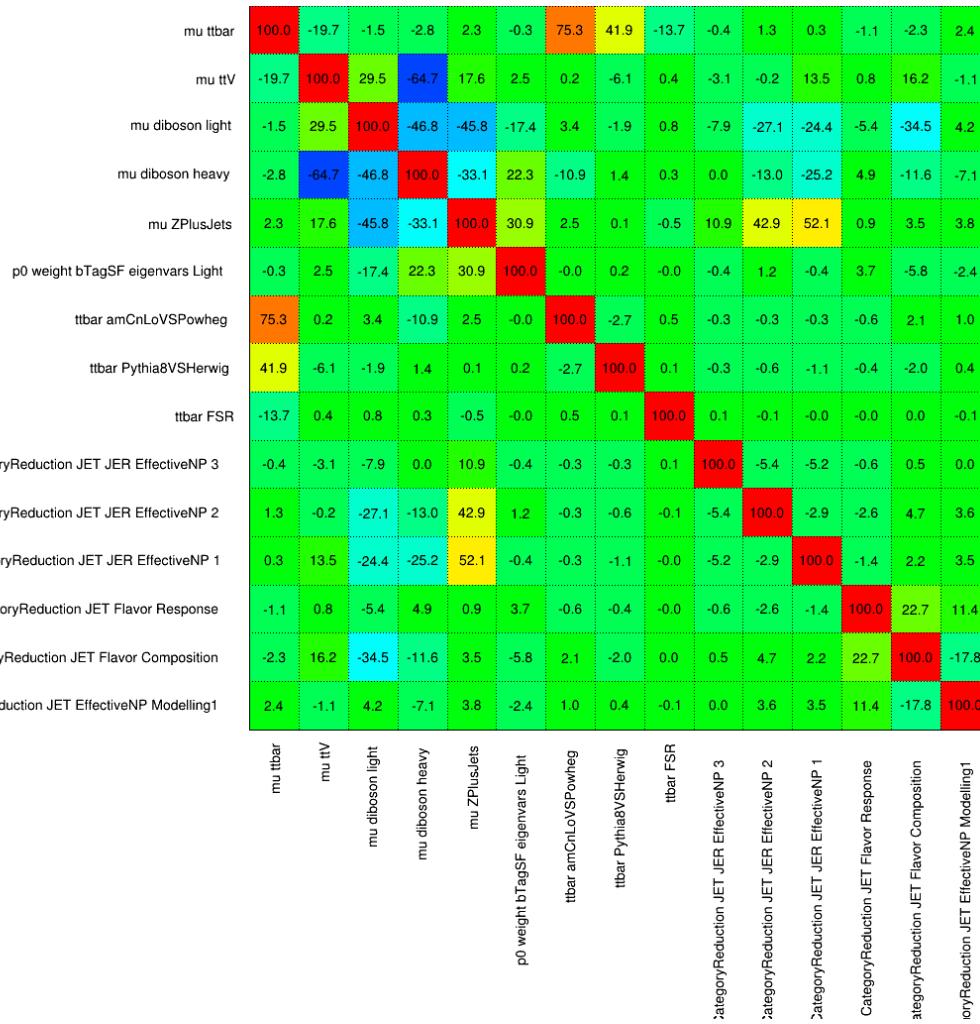


Figure 356: Correlation matrix of the signal-depleted-region fit. Only NPs with a correlation coefficient larger than 10 % with some other NP are shown.

- 1681 Finally, the  $Z + \text{jets}$  background is scaled up by 275 %, with a big uncertainty. The extraction of  $Z + \text{jets}$   
1682 happens through the diboson 2j0b and 3j0b CRs (Fig. 362). This also explains why this background is  
1683 highly correlated with both dibosons and  $t\bar{t}Z$ .
- 1684 The pull distributions for the all nuisance parameters can be seen in Fig. 357 and Fig. 358. None of the  
1685 NPs is constrained. Some NPs are slightly pulled, still below  $1\sigma$ . These are jet flavour composition  
1686 (JET\_CategoryReduction\_JET\_Flavor\_Response) and response (JET\_CategoryReduction\_JET\_Flavor\_Composition)  
1687 and one of the modeling (JET\_CategoryReduction\_JET\_EffectiveNP\_Modelling1).
- 1688 The list of the systematic shapes that are dropped from the fit for each sample and for each region is shown  
1689 in Fig. 359.
- 1690 Event yields pre- and post-fit are shown in Fig. 360. The post-fit agreement is good.
- 1691 Pre-fit and post-fit distributions of the fitted distributions are shown in Figs. 361 to 364.

Not reviewed, for internal circulation only

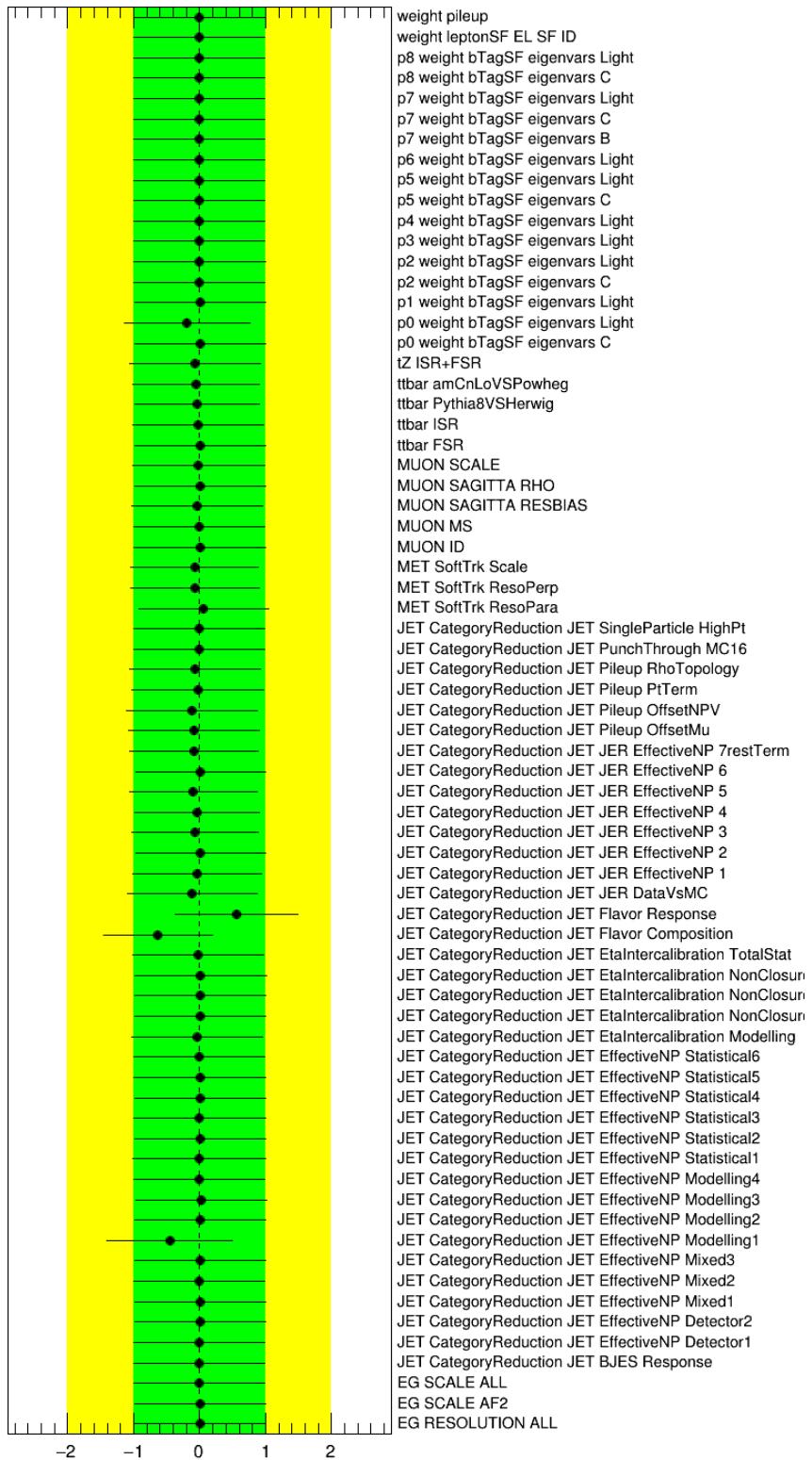
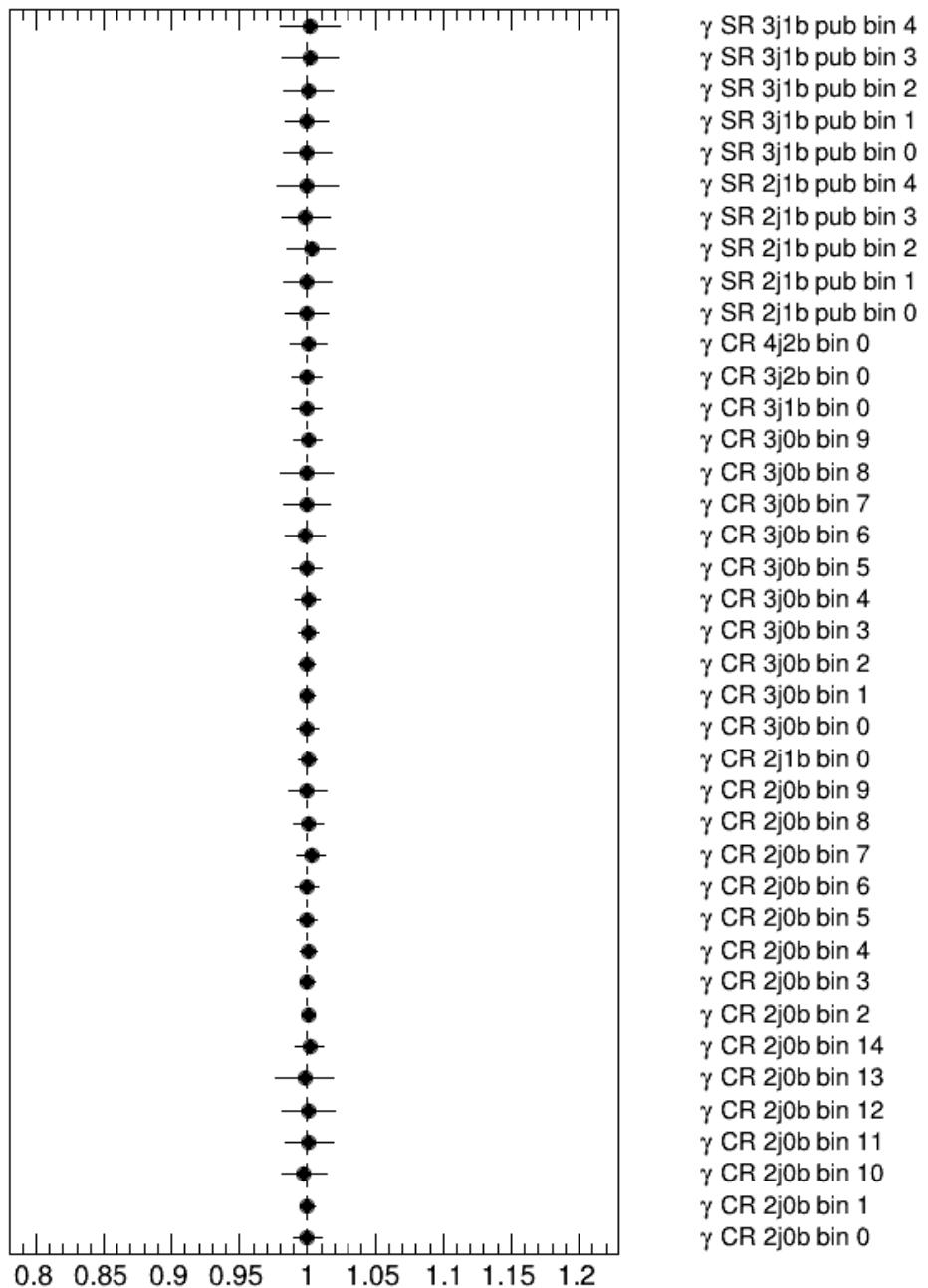


Figure 357: Pulls and constraints of the nuisance parameters of the signal-depleted-region fit  $\mu_{\text{SIG}} = 1$ .

Not reviewed, for internal circulation only

Figure 358: Gamma parameters of the signal-depleted-region fit  $\mu_{\text{SIG}} = 1$ .

Not reviewed, for internal circulation only

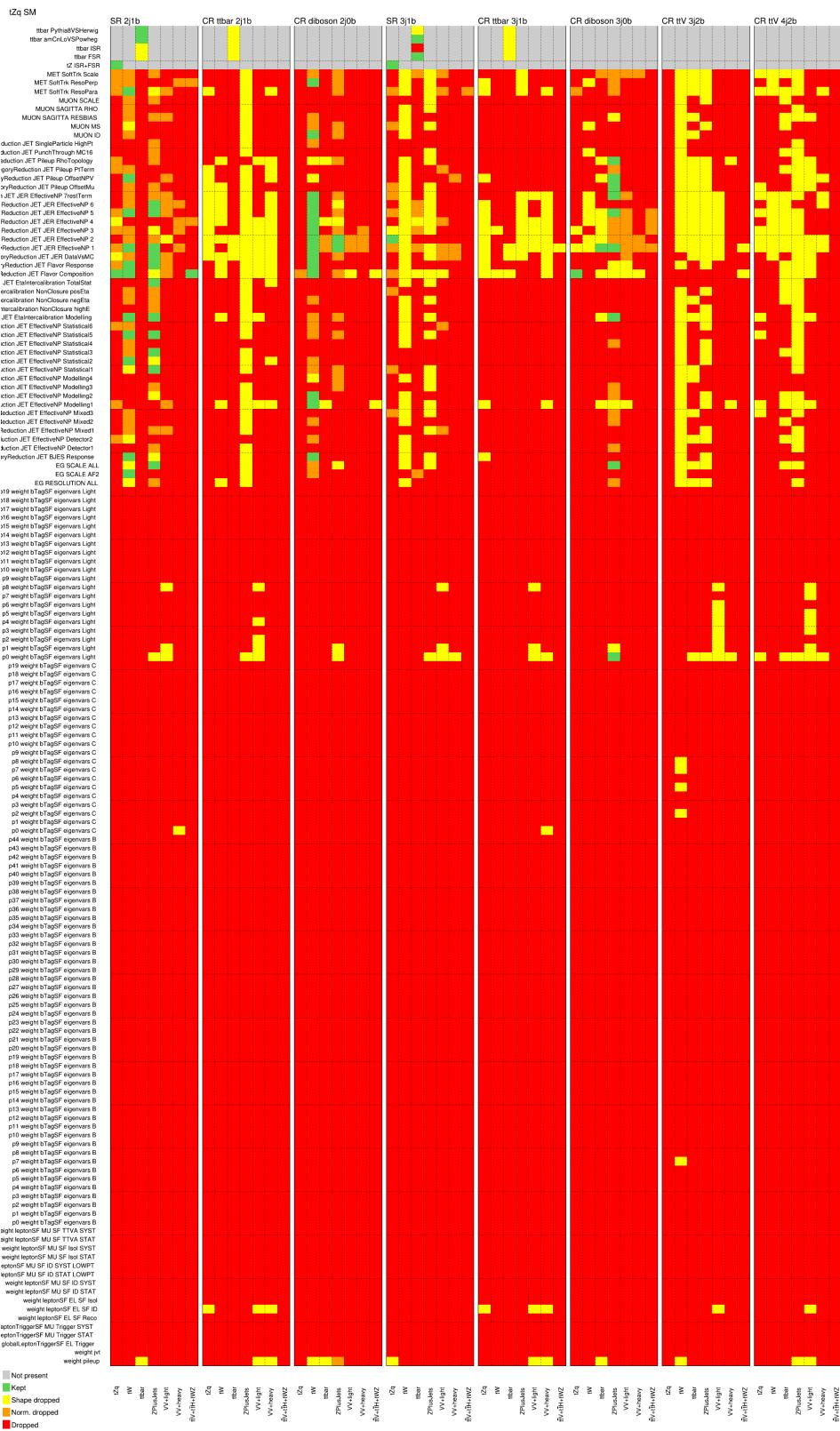


Figure 359: Pruning of the nuisance parameters of the signal-depleted-region fit  $\mu_{\text{SIG}} = 1$ .

Not reviewed, for internal circulation only

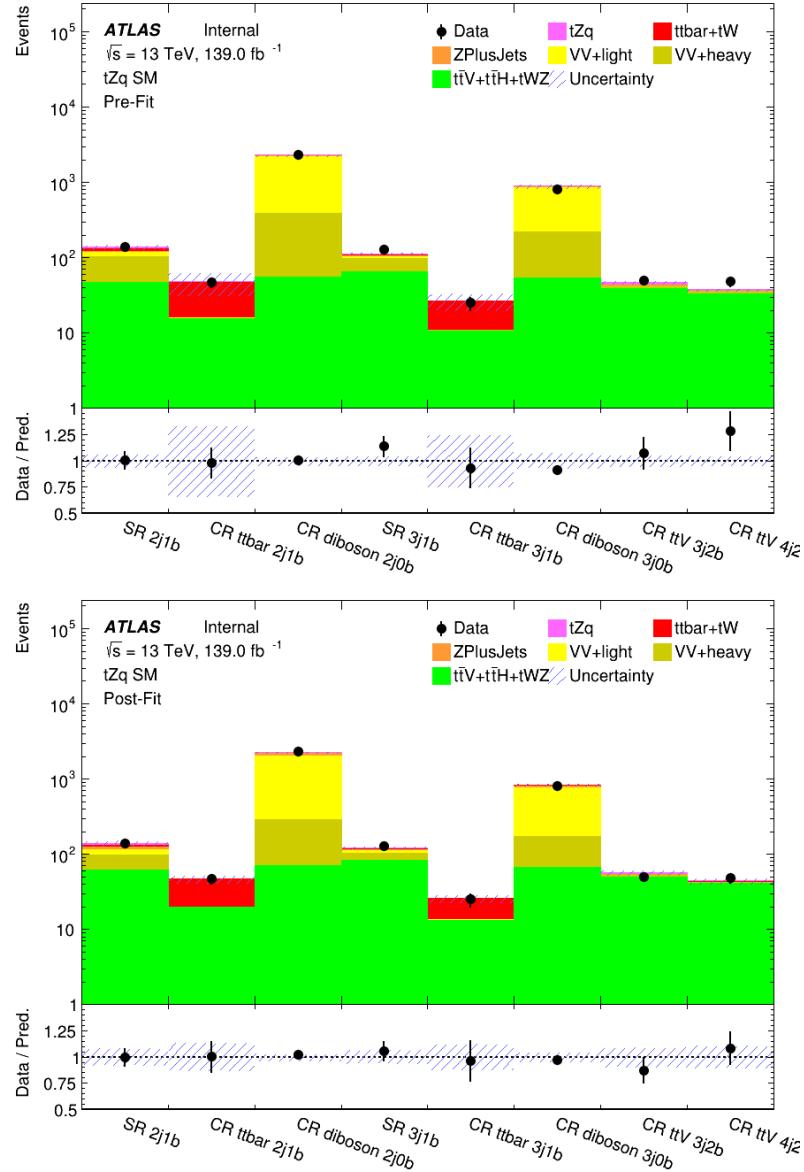


Figure 360: Pre-fit (top) and post-fit (bottom) event yields in the various regions. The uncertainty band includes both statistical and systematic uncertainties. **The big uncertainty in the pre-fit plot for the bins corresponding to the  $t\bar{t}$  CRs is due to large differences in the event yields for the generator modeling systematics.**

Not reviewed, for internal circulation only

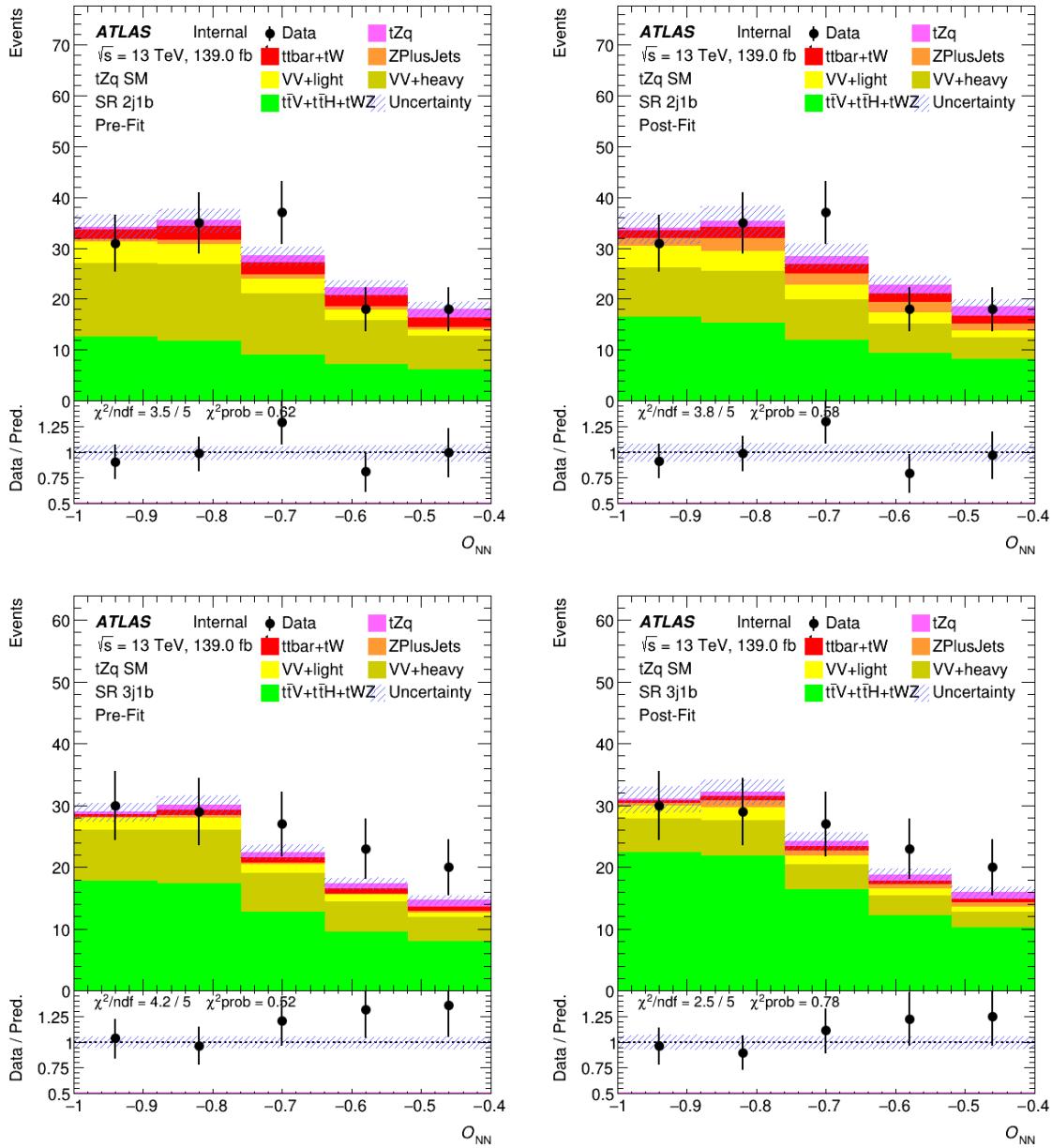


Figure 361: Pre-fit (left) and post-fit (right) NN output distributions in the signal regions with  $O_{NN} < -0.4$ . The uncertainty band includes both statistical and systematic uncertainties.

Not reviewed, for internal circulation only

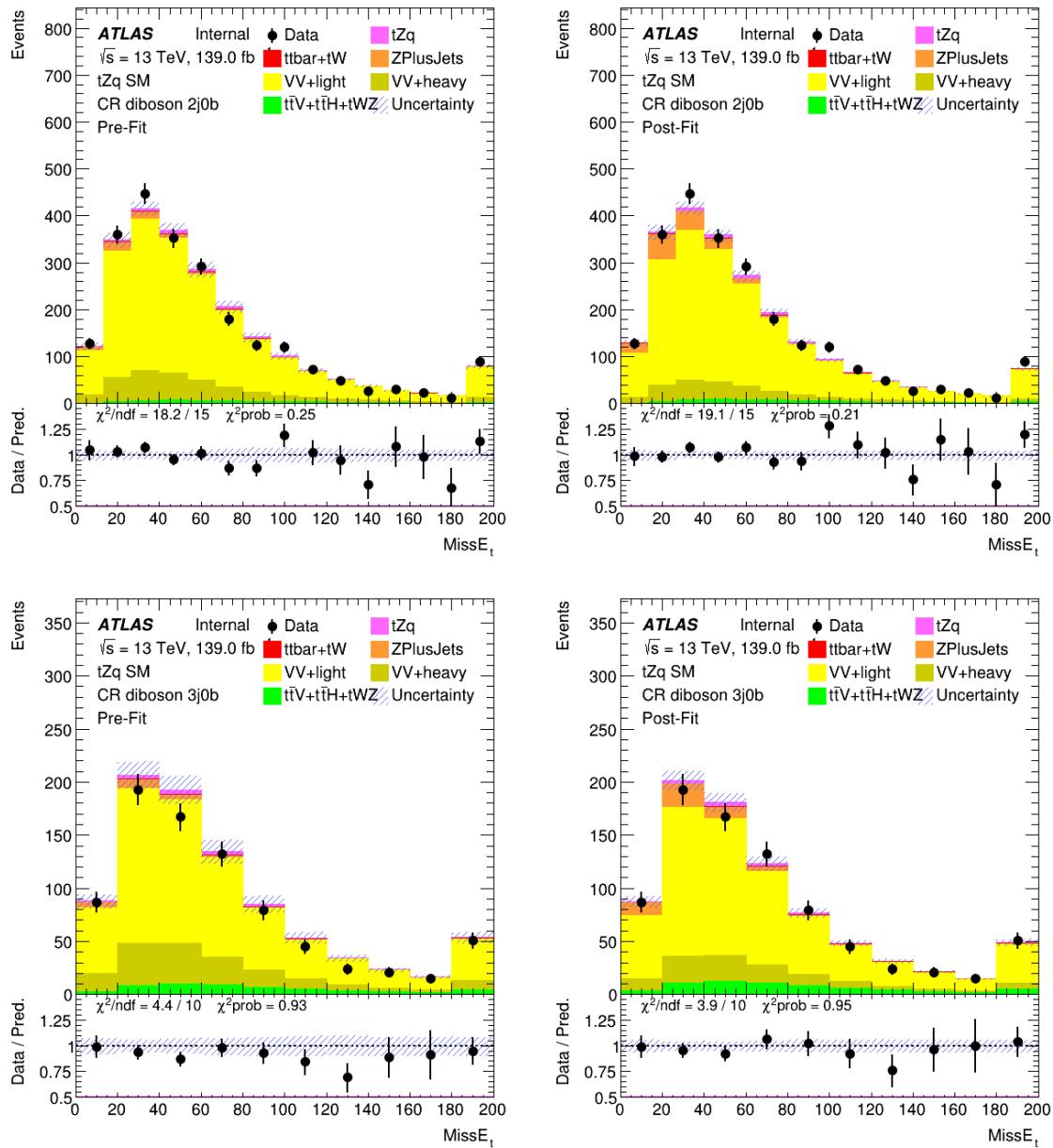


Figure 362: Pre-fit (left) and post-fit (right)  $E_T^{\text{miss}}$  distributions in the diboson control regions. The uncertainty band includes both statistical and systematic uncertainties.

Not reviewed, for internal circulation only

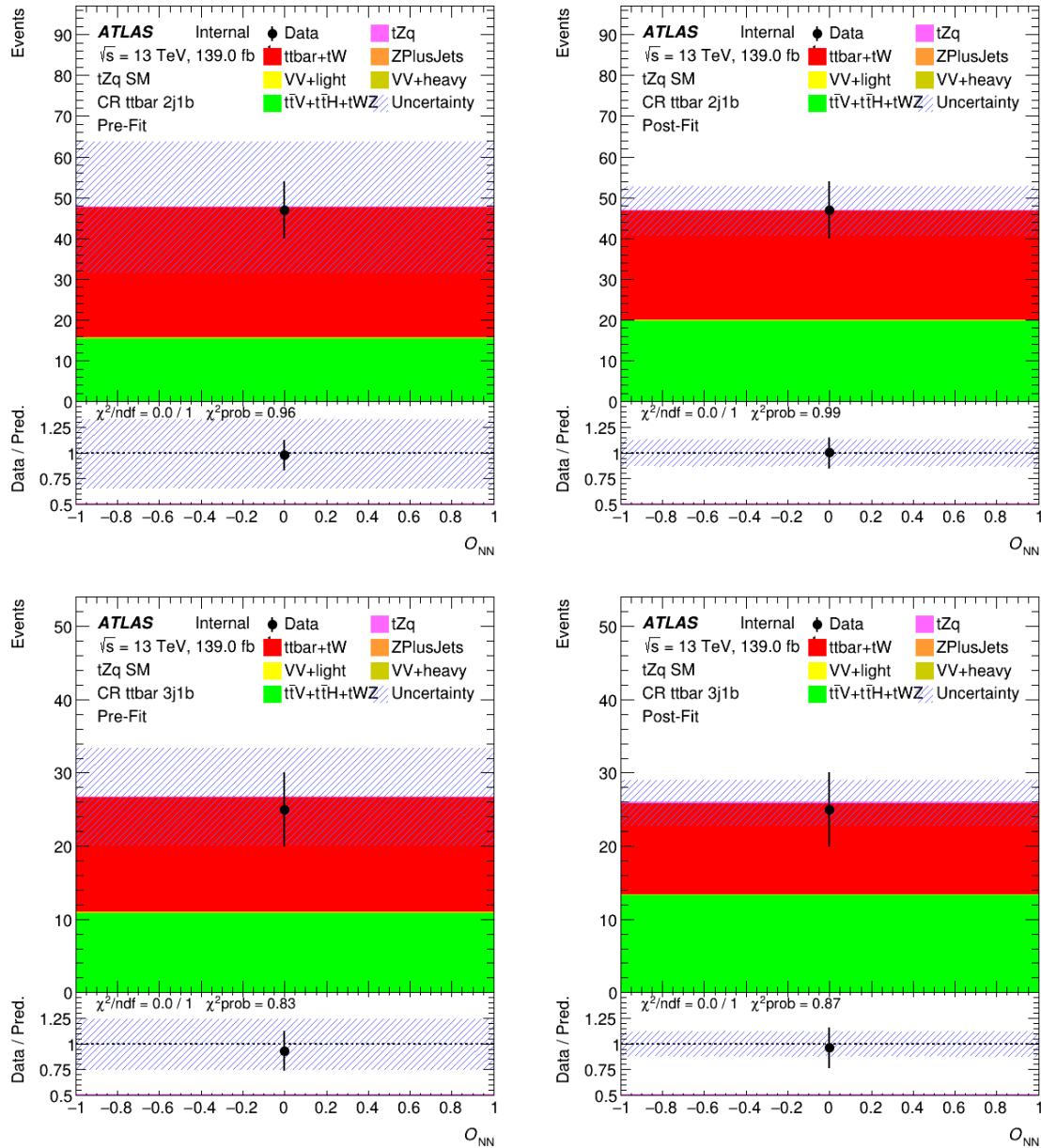


Figure 363: Pre-fit (left) and post-fit (right) NN output distributions in the  $t\bar{t}$  control regions. The uncertainty band includes both statistical and systematic uncertainties. **The big uncertainty in the pre-fit plot is due to large differences in the event yields for the generator modeling systematics.**

Not reviewed, for internal circulation only

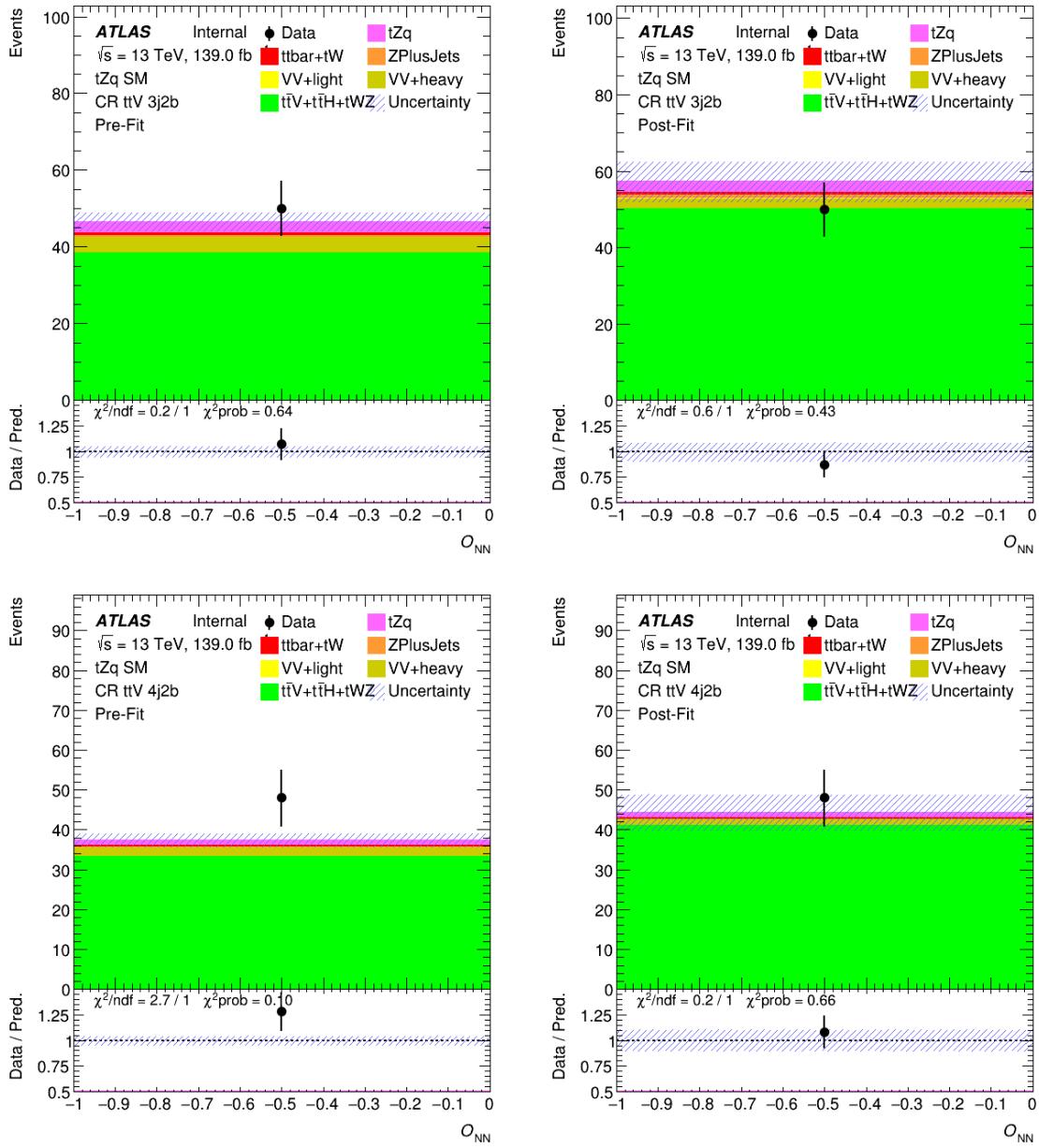


Figure 364: Pre-fit (left) and post-fit (right) NN output distributions in the  $t\bar{t}Z$  control regions with  $O_{NN} < 0$ . The uncertainty band includes both statistical and systematic uncertainties.

1692 **NN input variable distributions in VRs pre- and post-fit** In this section, the four highest ranked NN  
1693 input variables are shown, both pre- and post-fit, in the validation regions.

[Not reviewed, for internal circulation only]

Not reviewed, for internal circulation only

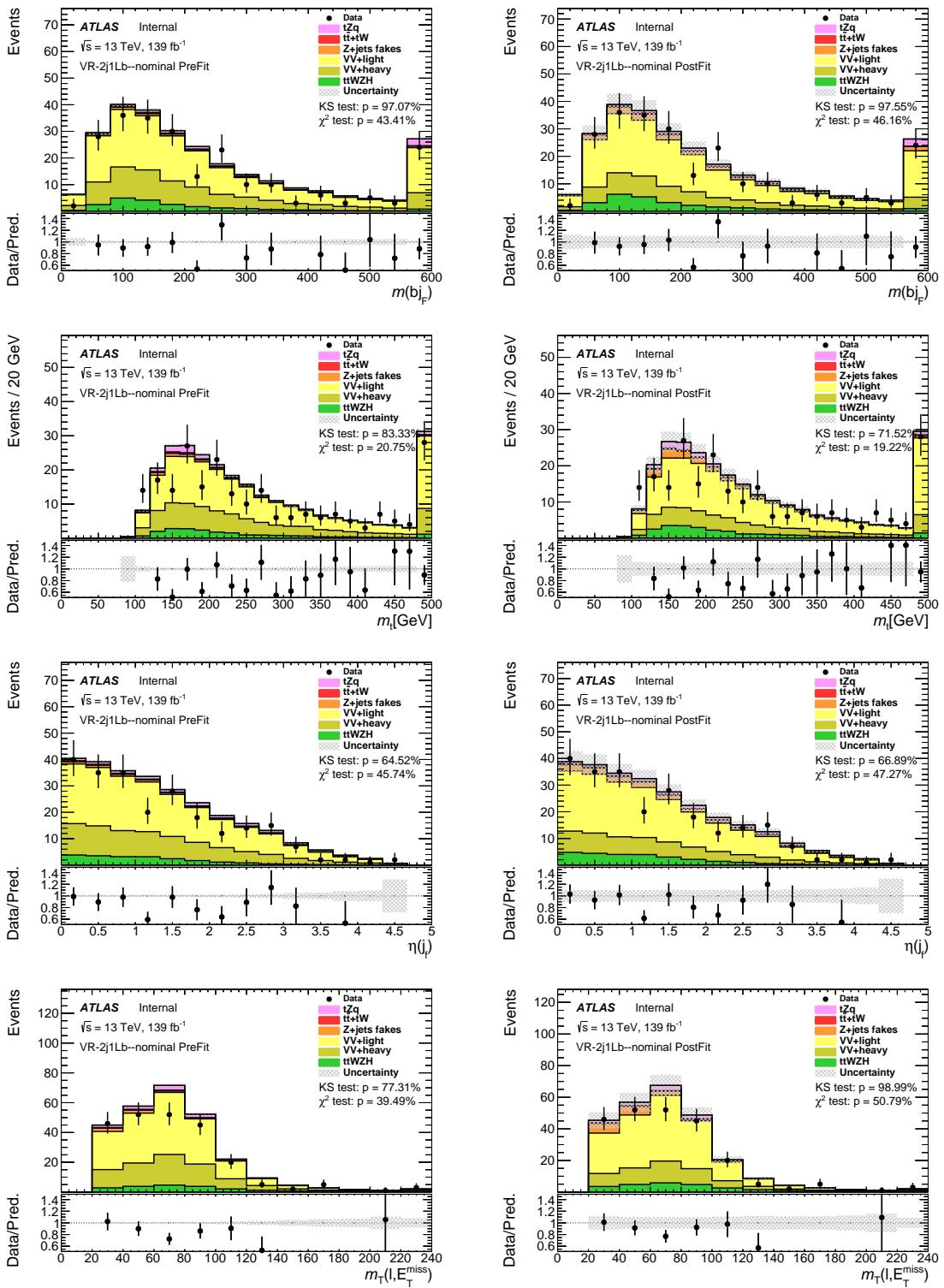


Figure 365: Pre-fit (left) and post-fit (right) NN input variable distributions in the diboson 2j1Lb validation region. For the pre-fit plots, The uncertainty band includes only statistical uncertainties. For the post-fit plots, The uncertainty band includes only the post-fit uncertainties on the background normalizations.

Not reviewed, for internal circulation only

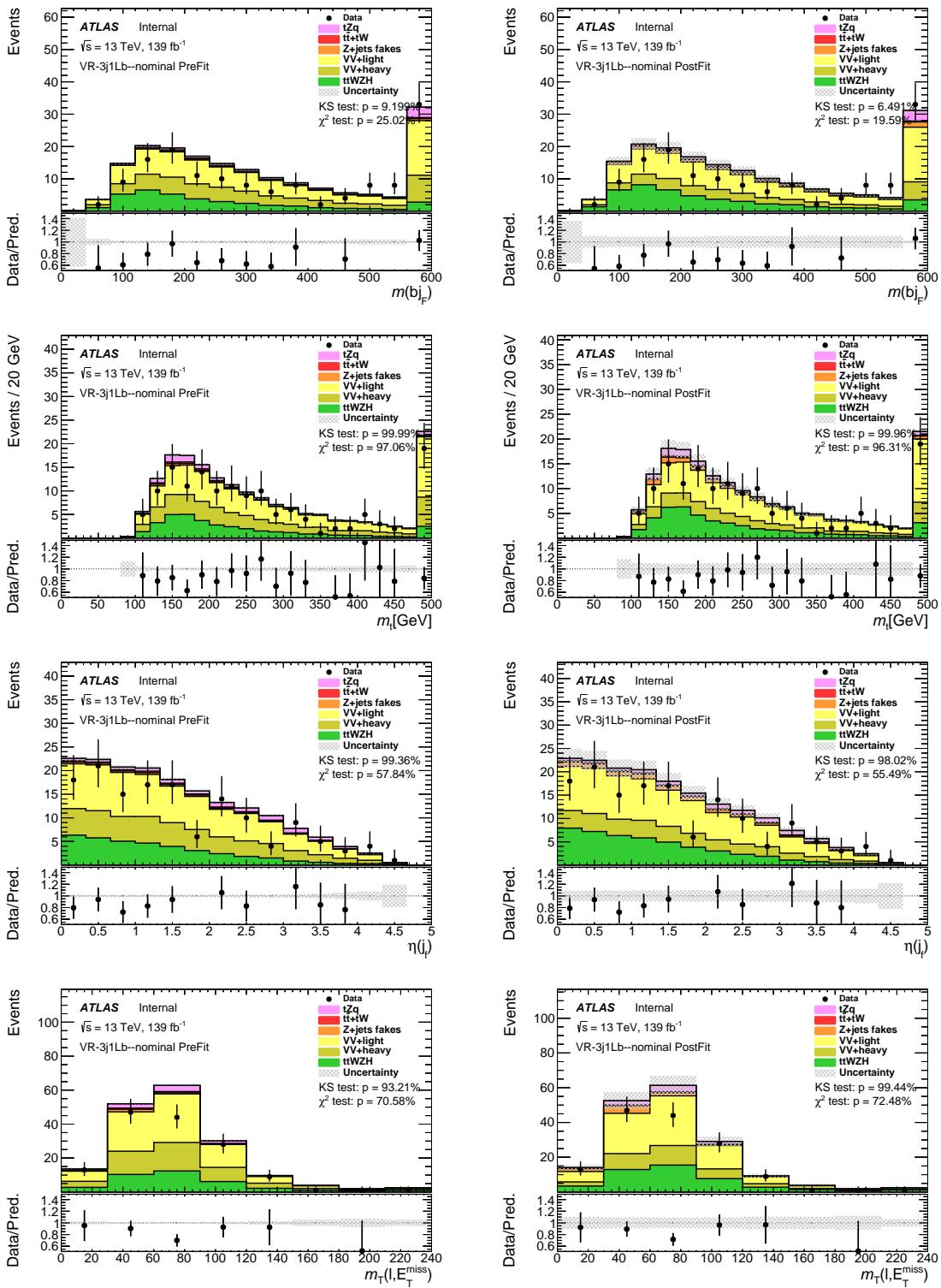


Figure 366: Pre-fit (left) and post-fit (right) NN input variable distributions in the diboson 3j1Lb validation region. For the pre-fit plots, The uncertainty band includes only statistical uncertainties. For the post-fit plots, The uncertainty band includes only the post-fit uncertainties on the background normalizations.

Not reviewed, for internal circulation only

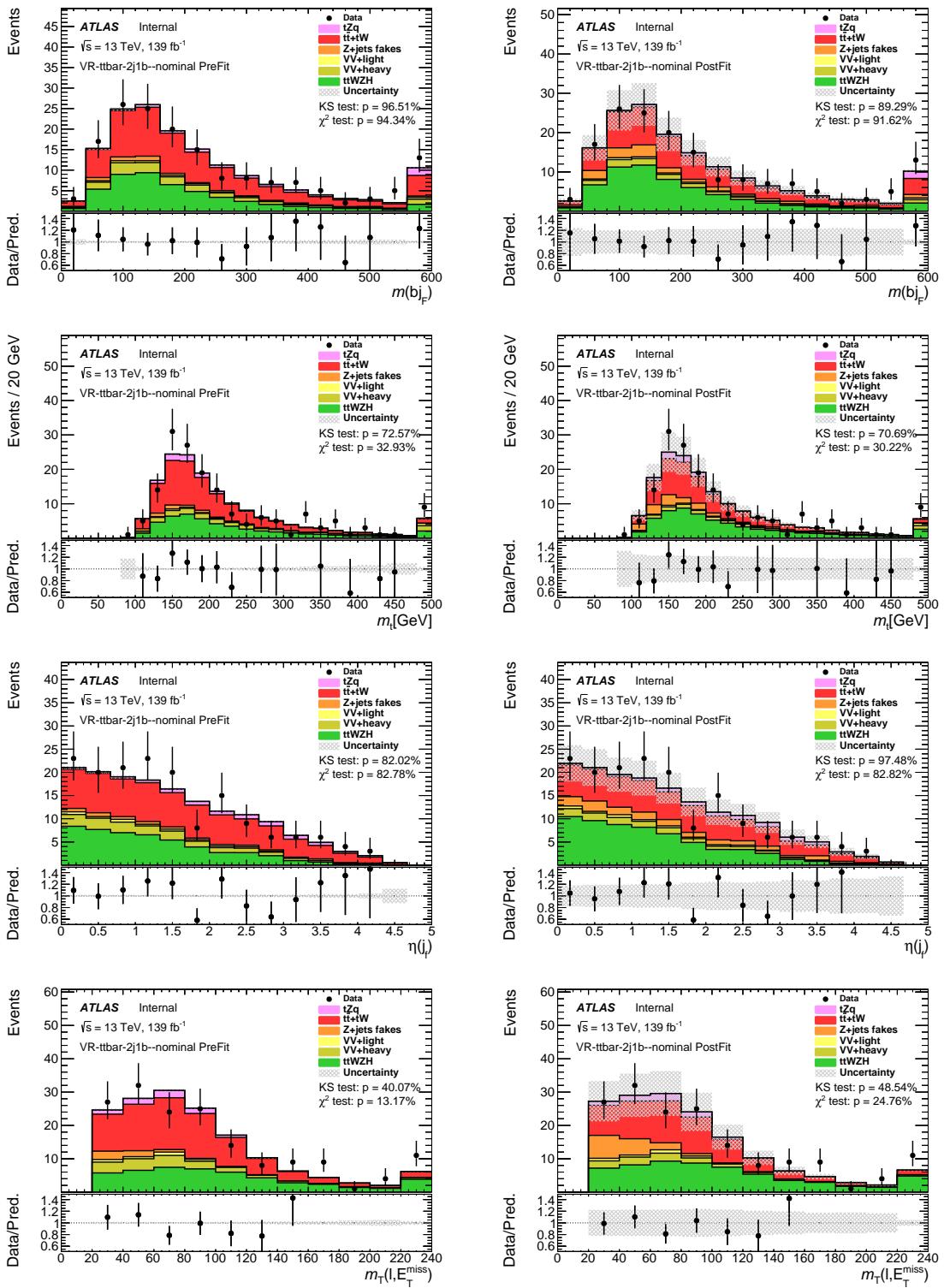


Figure 367: Pre-fit (left) and post-fit (right) NN input variable distributions in the  $t\bar{t}V + t\bar{t}$  2j1b validation region. For the pre-fit plots, The uncertainty band includes only statistical uncertainties. For the post-fit plots, The uncertainty band includes only the post-fit uncertainties on the background normalizations.

Not reviewed, for internal circulation only

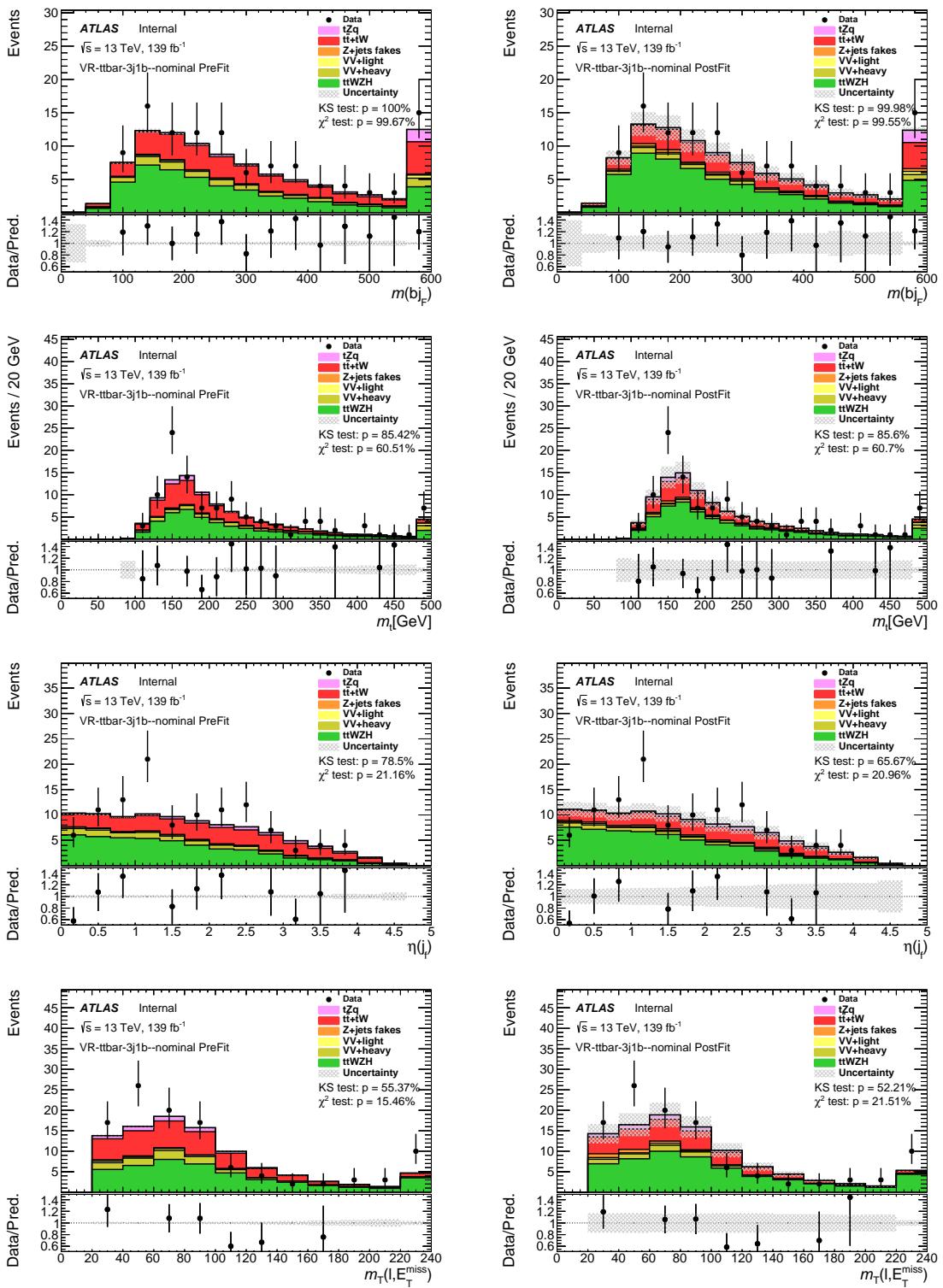


Figure 368: Pre-fit (left) and post-fit (right) NN input variable distributions in the  $t\bar{t}V + t\bar{t}$  3j1b validation regions. For the pre-fit plots, The uncertainty band includes only statistical uncertainties. For the post-fit plots, The uncertainty band includes only the post-fit uncertainties on the background normalizations.

1694 **G.9 Floating backgrounds - Asimov fit**

1695 In order to compute the expected significance, an Asimov dataset is used. The Asimov dataset is constructed  
 1696 by scaling each background to the value obtained in the signal-depleted fit described in Appendix G.8,  
 1697 with  $\mu_{\text{SIG}}$  set to 1.

1698 The values of the post-fit normalization parameters for the free floating backgrounds are shown in Fig. 369.  
 1699 The correlation matrix of the parameters included in the fit is shown in Fig. 370.

1700 The pull distributions for the all nuisance parameters can be seen in Fig. 371 and Fig. 372.

1701 The list of the systematic shapes that are dropped from the fit for each sample and for each region is shown  
 1702 in Fig. 373. The ranking of the impact of the systematic uncertainties is shown in Fig. 374.

1703 Event yields pre- and post-fit are shown in Fig. 375 and Tables 63 and 64. Pre-fit and post-fit distributions  
 1704 of the fitted distributions in the various regions are shown in Figs. 376 to 379.

1705 A fit including only the uncertainties on the normalisation of the signal and backgrounds leads to an  
 1706 uncertainty on  $\mu_{\text{SIG}}$  of 15 %. A fit including both statistical and systematical uncertainties leads to an  
 1707 uncertainty on  $\mu_{\text{SIG}}$  of 17 %. A fit to determine the expected significance yields a value of 8.9.

Not reviewed, for internal circulation only

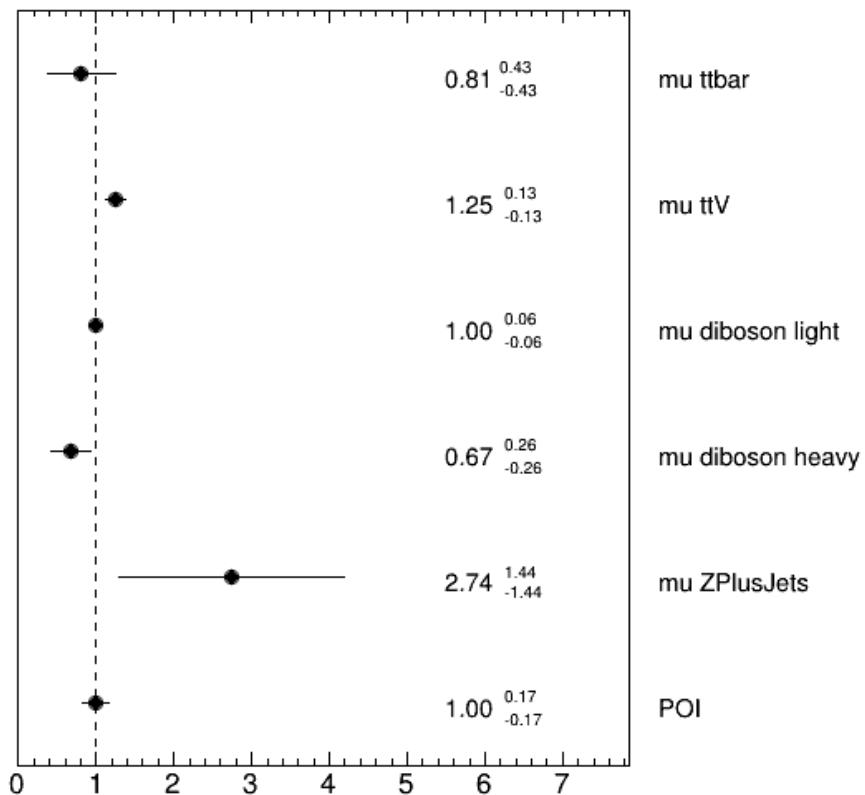


Figure 369: Normalisation factors of the Asimov fit.

Table 63: Pre-fit event yields in the various regions for the Asimov fit. The uncertainties include both statistical and systematic uncertainties.

Process	SR 2j1b	SR 3j1b	CR $t\bar{t}V$ 3j2b	CR $t\bar{t}V$ 4j2b	CR $t\bar{t}$ 2j1b	CR $t\bar{t}$ 3j1b	CR diboson 2j0b	CR diboson 3j0b
$tZq$	64.0 $\pm$ 4.6	36.1 $\pm$ 3.8	10.3 $\pm$ 0.5	6.7 $\pm$ 1.1	0.2 $\pm$ 0.1	0.2 $\pm$ 0.0	43.6 $\pm$ 1.3	17.4 $\pm$ 1.4
$tW$	0.8 $\pm$ 0.1	0.3 $\pm$ 0.3	0.1 $\pm$ 0.2	0.0 $\pm$ 0.0	0.6 $\pm$ 0.3	0.4 $\pm$ 0.1	0.1 $\pm$ 0.5	0.2 $\pm$ 0.0
$t\bar{t}$	17.8 $\pm$ 6.0	8.5 $\pm$ 2.6	0.8 $\pm$ 0.9	1.0 $\pm$ 1.2	25.2 $\pm$ 3.0	12.3 $\pm$ 5.4	10.2 $\pm$ 0.9	4.7 $\pm$ 0.6
$Z + \text{jets}$	20.1 $\pm$ 3.0	8.7 $\pm$ 1.9	1.5 $\pm$ 0.4	0.2 $\pm$ 0.4	0.1 $\pm$ 0.1	0.0 $\pm$ 0.0	153.6 $\pm$ 33.5	56.0 $\pm$ 13.7
$VV + \text{LF}$	20.2 $\pm$ 8.0	10.8 $\pm$ 4.4	0.1 $\pm$ 0.1	0.0 $\pm$ 0.1	0.1 $\pm$ 0.0	0.0 $\pm$ 0.0	1797.7 $\pm$ 78.0	623.2 $\pm$ 46.6
$VV + \text{HF}$	60.2 $\pm$ 2.3	35.0 $\pm$ 1.9	3.1 $\pm$ 0.3	2.0 $\pm$ 0.3	0.2 $\pm$ 0.1	0.1 $\pm$ 0.1	227.1 $\pm$ 9.1	112.9 $\pm$ 6.8
$t\bar{t}V$	97.7 $\pm$ 6.3	134.9 $\pm$ 4.1	58.8 $\pm$ 3.3	59.5 $\pm$ 2.7	19.2 $\pm$ 0.9	13.4 $\pm$ 0.8	69.1 $\pm$ 4.0	67.4 $\pm$ 2.7
Total	280.7 $\pm$ 5.8	234.4 $\pm$ 0.1	74.7 $\pm$ 3.8	69.4 $\pm$ 3.5	45.5 $\pm$ 3.1	26.4 $\pm$ 5.5	2301.3 $\pm$ 105.9	881.8 $\pm$ 65.5

Table 64: Post-fit event yields in the various regions for the Asimov fit. The uncertainties include both statistical and systematic uncertainties.

Process	SR 2j1b	SR 3j1b	CR $t\bar{t}V$ 3j2b	CR $t\bar{t}V$ 4j2b	CR $t\bar{t}$ 2j1b	CR $t\bar{t}$ 3j1b	CR diboson 2j0b	CR diboson 3j0b
$tZq$	64.0 $\pm$ 0.3	36.1 $\pm$ 5.7	10.3 $\pm$ 1.8	6.7 $\pm$ 1.2	0.2 $\pm$ 0.1	0.2 $\pm$ 0.1	43.6 $\pm$ 7.5	17.4 $\pm$ 3.1
$tW$	0.8 $\pm$ 0.5	0.3 $\pm$ 0.3	0.1 $\pm$ 0.2	0.0 $\pm$ 0.0	0.6 $\pm$ 0.4	0.4 $\pm$ 0.2	0.1 $\pm$ 0.4	0.2 $\pm$ 0.1
$t\bar{t}$	17.8 $\pm$ 6.0	8.5 $\pm$ 3.0	0.8 $\pm$ 1.2	1.0 $\pm$ 1.5	25.2 $\pm$ 6.0	12.3 $\pm$ 3.2	10.2 $\pm$ 5.5	4.7 $\pm$ 2.6
$Z + \text{jets}$	20.1 $\pm$ 0.9	8.7 $\pm$ 4.9	1.5 $\pm$ 1.0	0.2 $\pm$ 0.4	0.1 $\pm$ 0.1	0.0 $\pm$ 0.0	153.6 $\pm$ 83.4	56.0 $\pm$ 30.2
$VV + \text{LF}$	20.2 $\pm$ 8.1	10.8 $\pm$ 4.5	0.1 $\pm$ 0.1	0.0 $\pm$ 0.1	0.1 $\pm$ 0.0	0.0 $\pm$ 0.0	1797.7 $\pm$ 112.5	623.2 $\pm$ 45.0
$VV + \text{HF}$	60.2 $\pm$ 22.9	35.0 $\pm$ 3.1	3.1 $\pm$ 1.2	2.0 $\pm$ 0.7	0.2 $\pm$ 0.1	0.1 $\pm$ 0.1	227.1 $\pm$ 85.9	112.9 $\pm$ 42.4
$t\bar{t}V$	97.7 $\pm$ 0.9	134.9 $\pm$ 4.0	58.8 $\pm$ 6.4	59.5 $\pm$ 6.4	19.2 $\pm$ 2.1	13.4 $\pm$ 1.5	69.1 $\pm$ 7.6	67.4 $\pm$ 7.1
Total	280.7 $\pm$ 6.8	234.4 $\pm$ 1.0	74.7 $\pm$ 5.8	69.4 $\pm$ 6.0	45.5 $\pm$ 5.8	26.4 $\pm$ 3.2	2301.3 $\pm$ 78.2	881.8 $\pm$ 42.3

Not reviewed, for internal circulation only

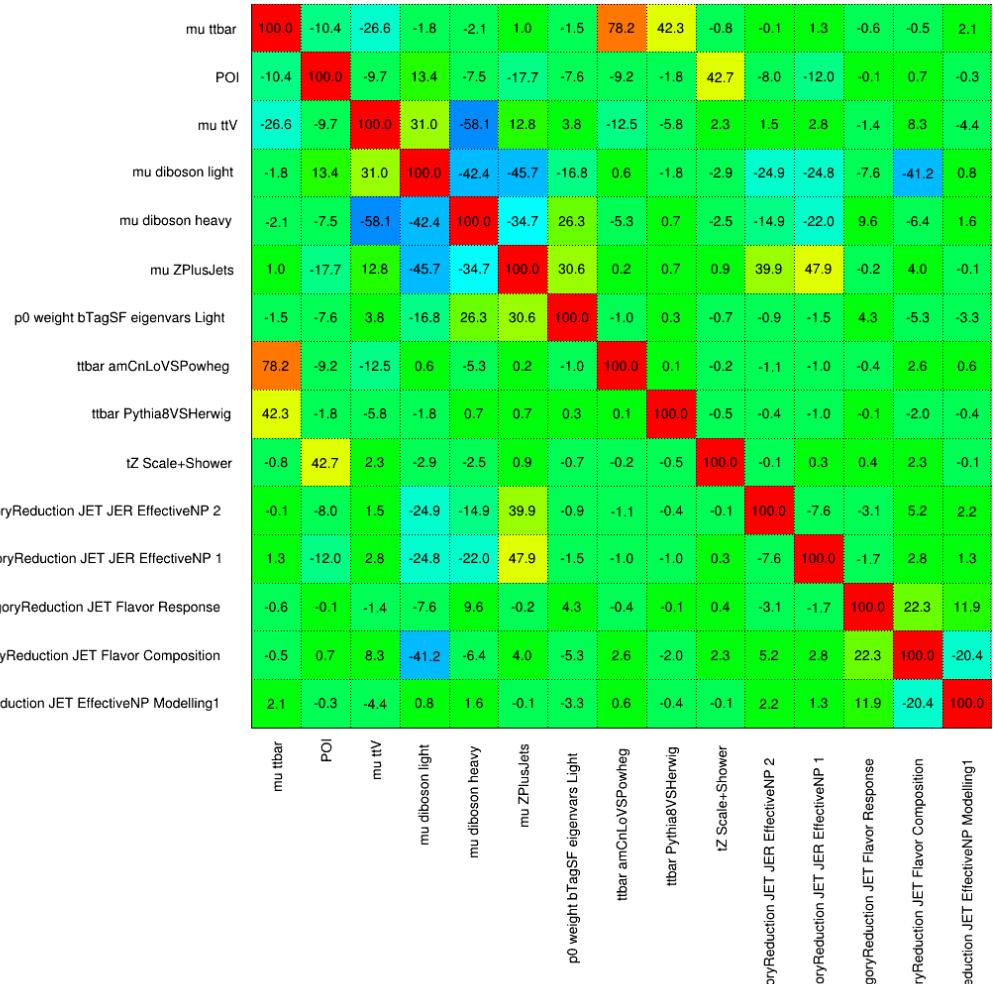


Figure 370: Correlation matrix of the Asimov fit. Only parameters with a correlation coefficient larger than 10 % with some other NP are shown.

Not reviewed, for internal circulation only

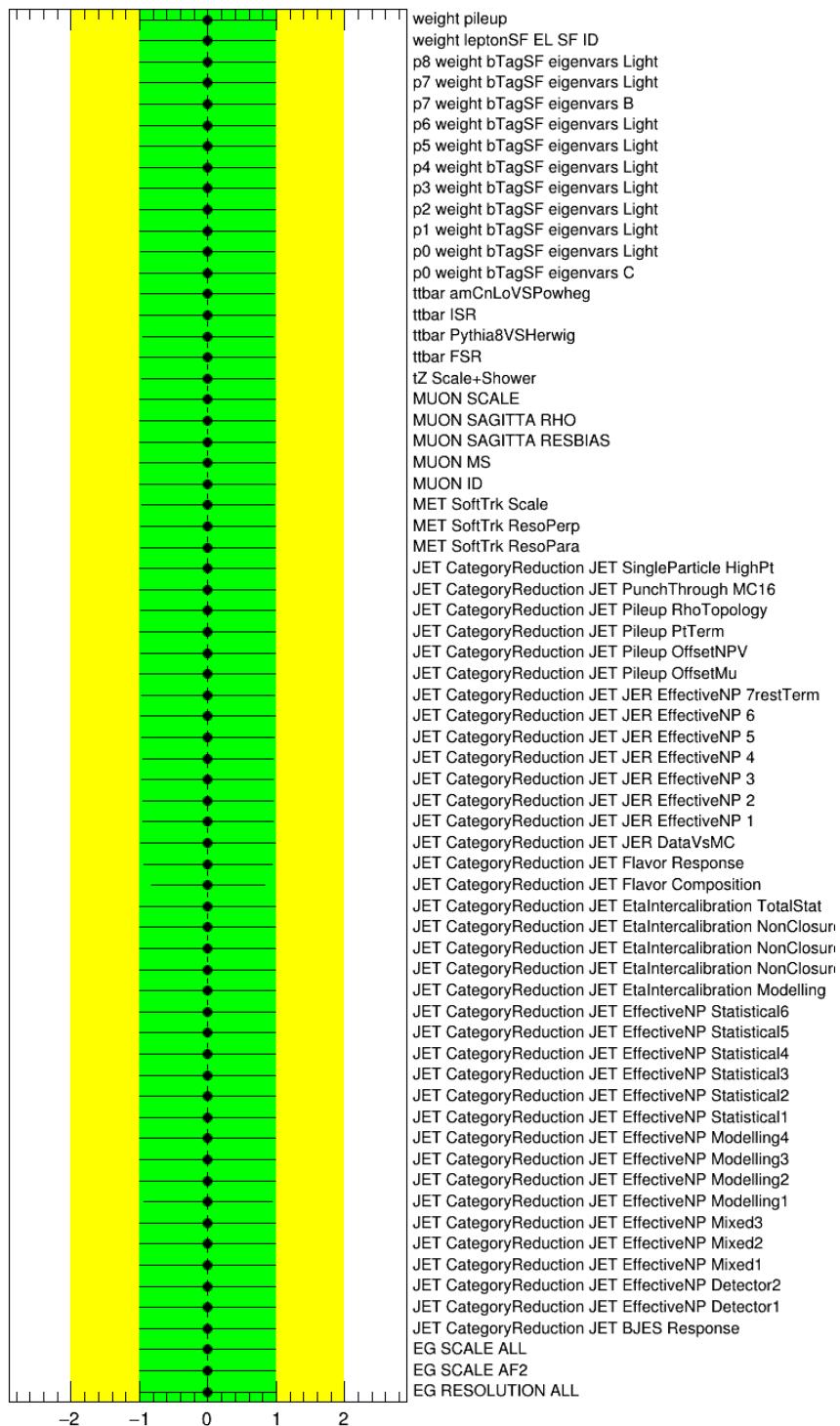


Figure 371: Pulls and constraints of the nuisance parameters of the Asimov fit.

Not reviewed, for internal circulation only

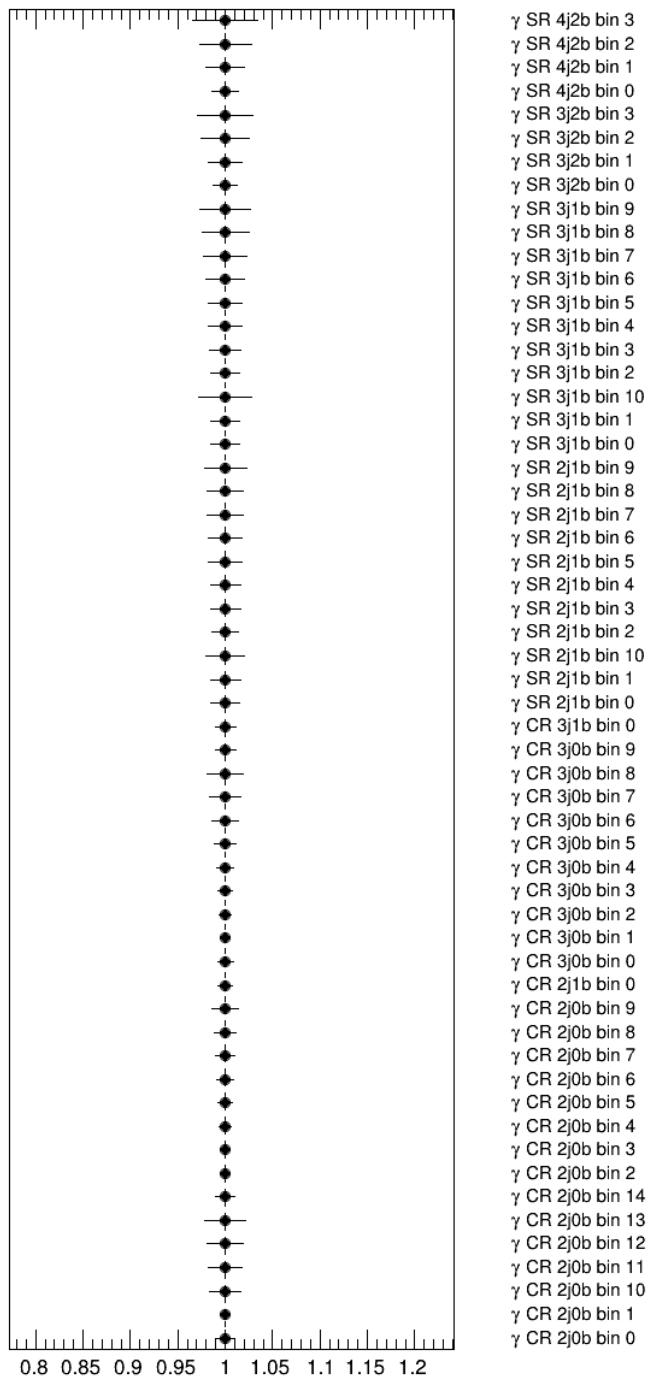


Figure 372: Gamma parameters of the Asimov fit.

Not reviewed, for internal circulation only

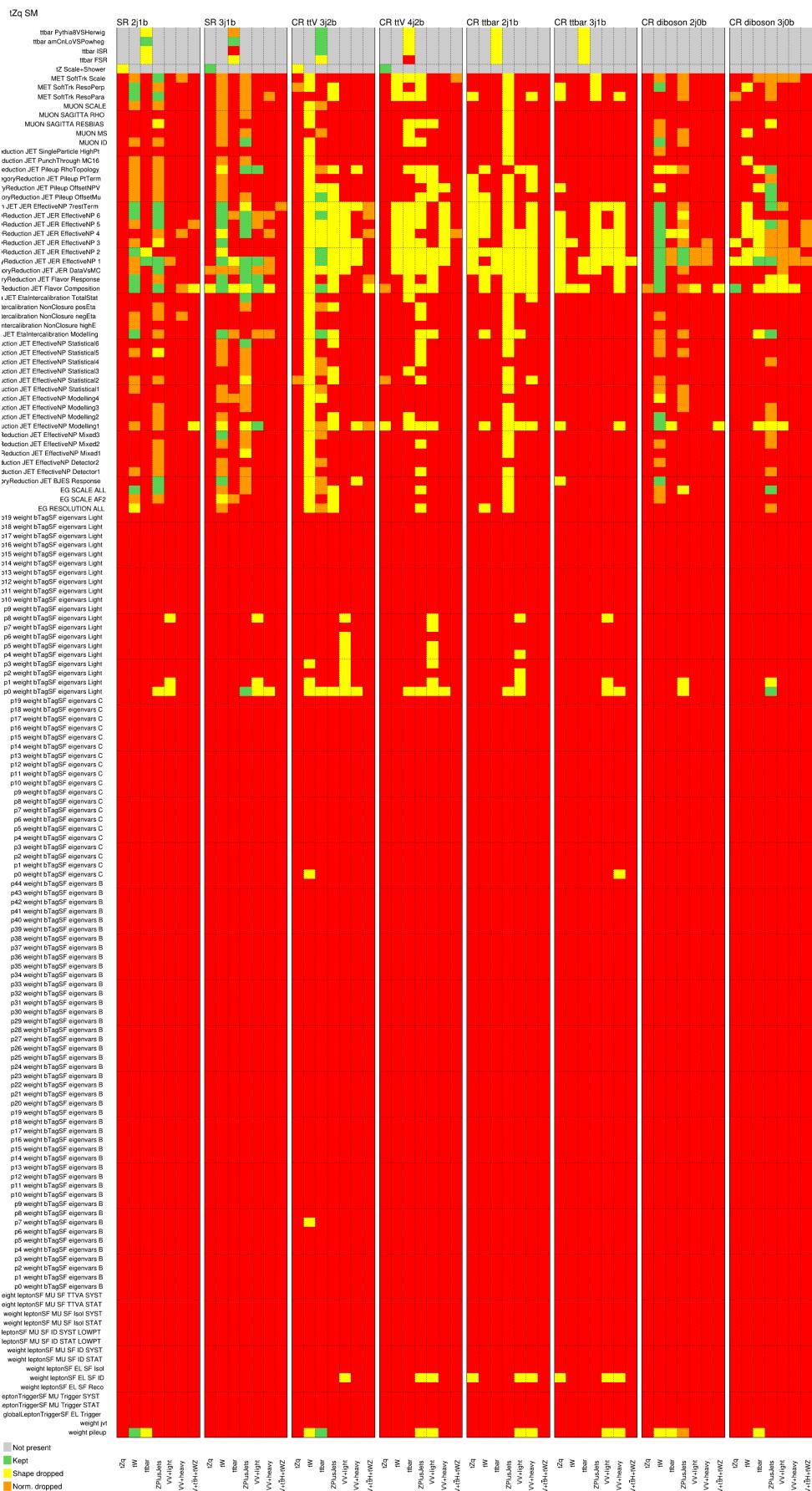


Figure 373: Pruning of the nuisance parameters of the Asimov fit.

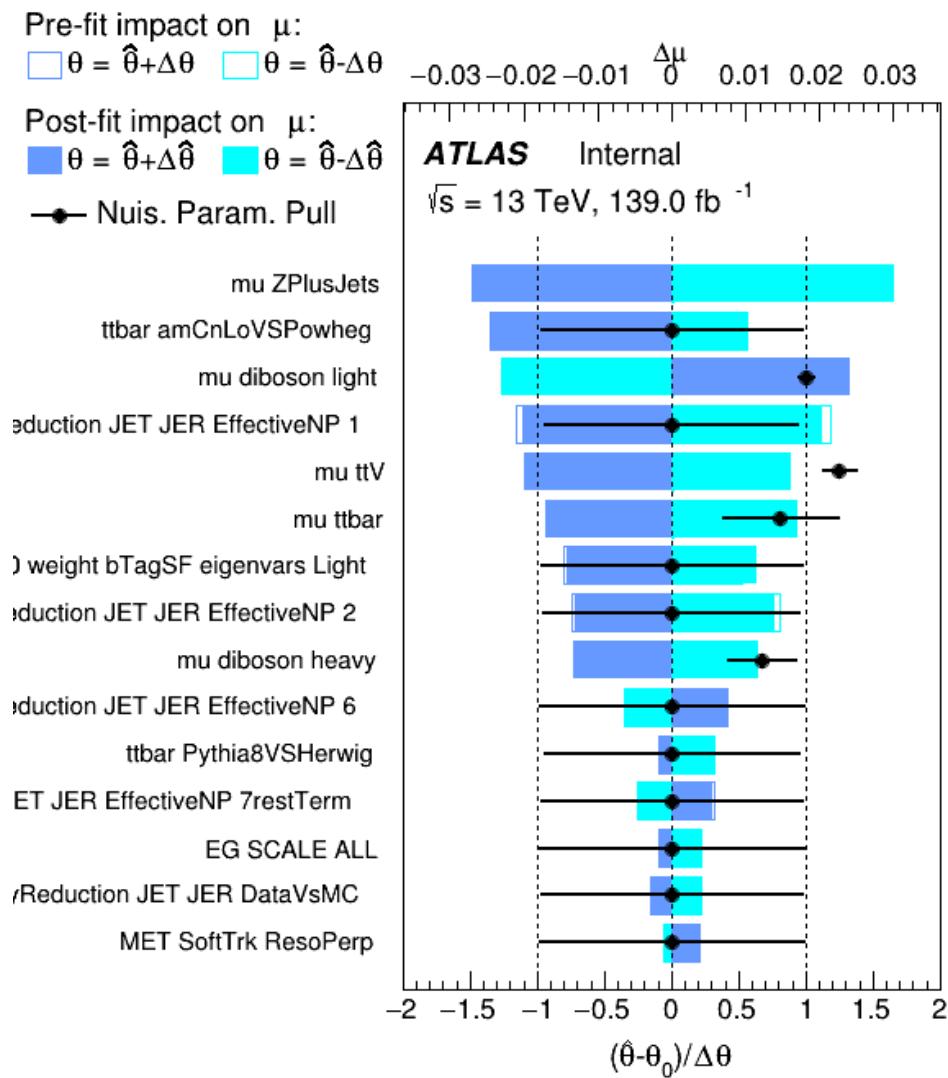


Figure 374: Ranking of the nuisance parameters of the Asimov fit. [This ranking plot is missing the  \$tZq\$  shower and scale systematic, which has an  \$\sim 5.7\%\$  impact.](#)

Not reviewed, for internal circulation only

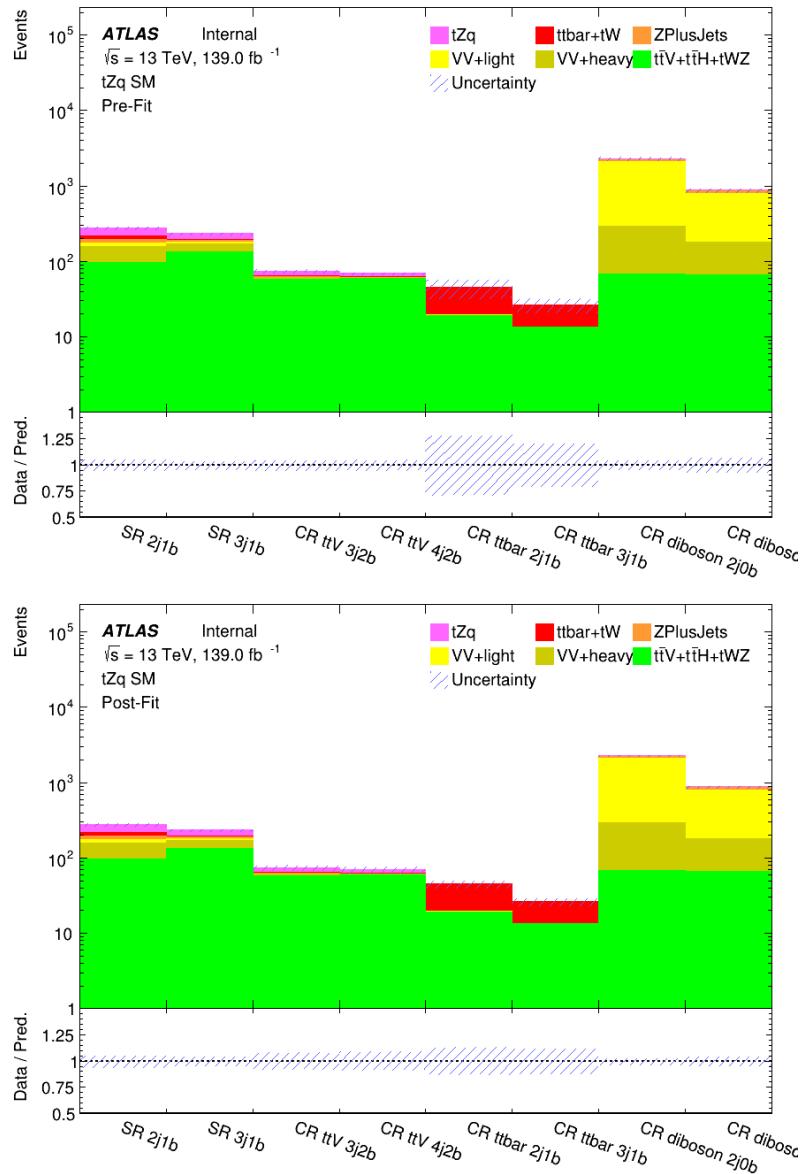


Figure 375: Pre-fit (top) and post-fit (bottom) event yields in the various regions for the Asimov fit. The uncertainty band includes both statistical and systematic uncertainties. In all regions the Asimov data points are not shown. The big uncertainty in the pre-fit plot for the bins corresponding to the  $t\bar{t}$  CRs is due to large differences in the event yields for the generator modeling systematics.

Not reviewed, for internal circulation only

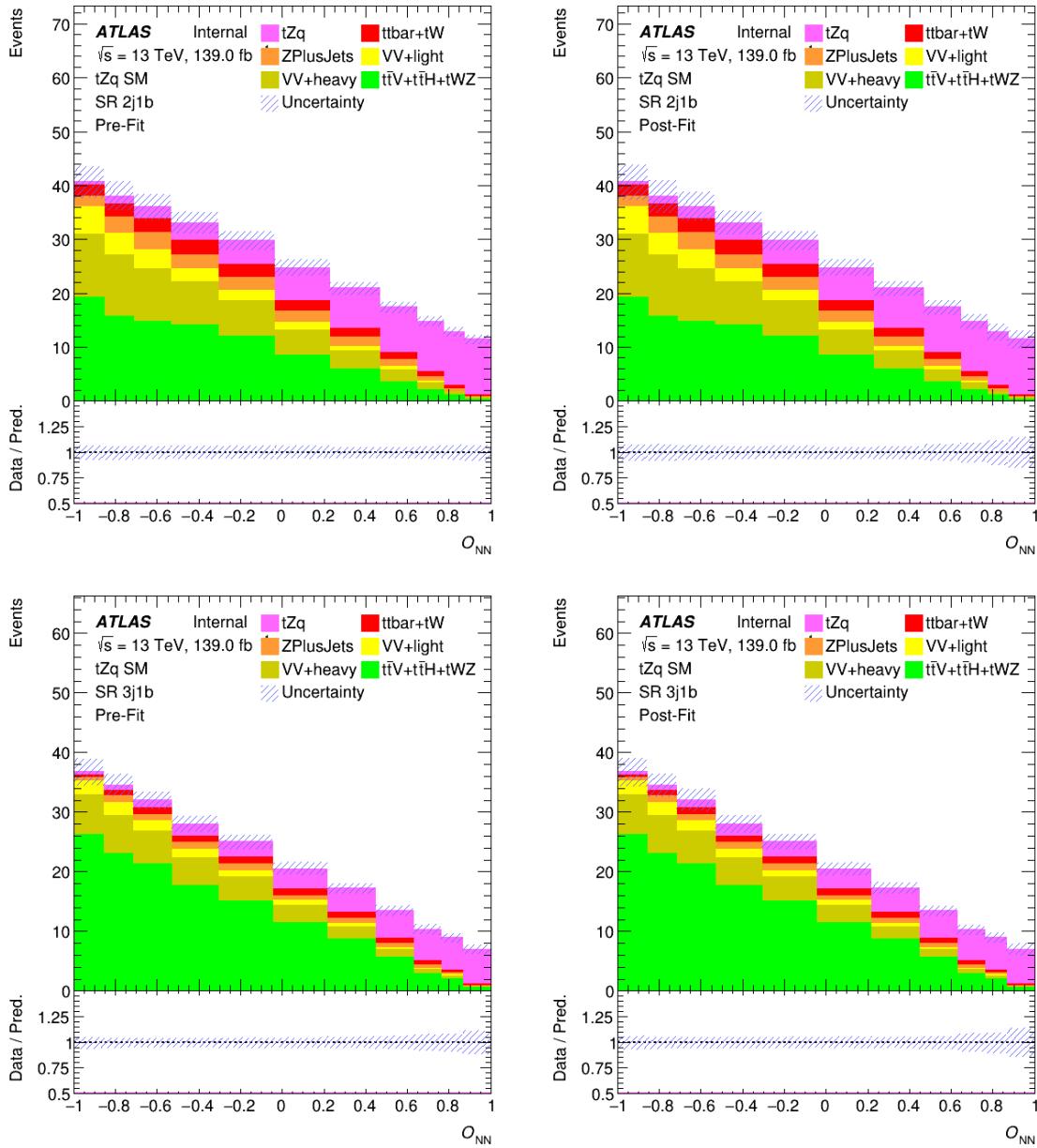


Figure 376: Pre-fit (left) and post-fit (right) NN output distributions in the signal regions. The uncertainty band includes both statistical and systematic uncertainties. [In all regions the Asimov data points are not shown.](#)

Not reviewed, for internal circulation only

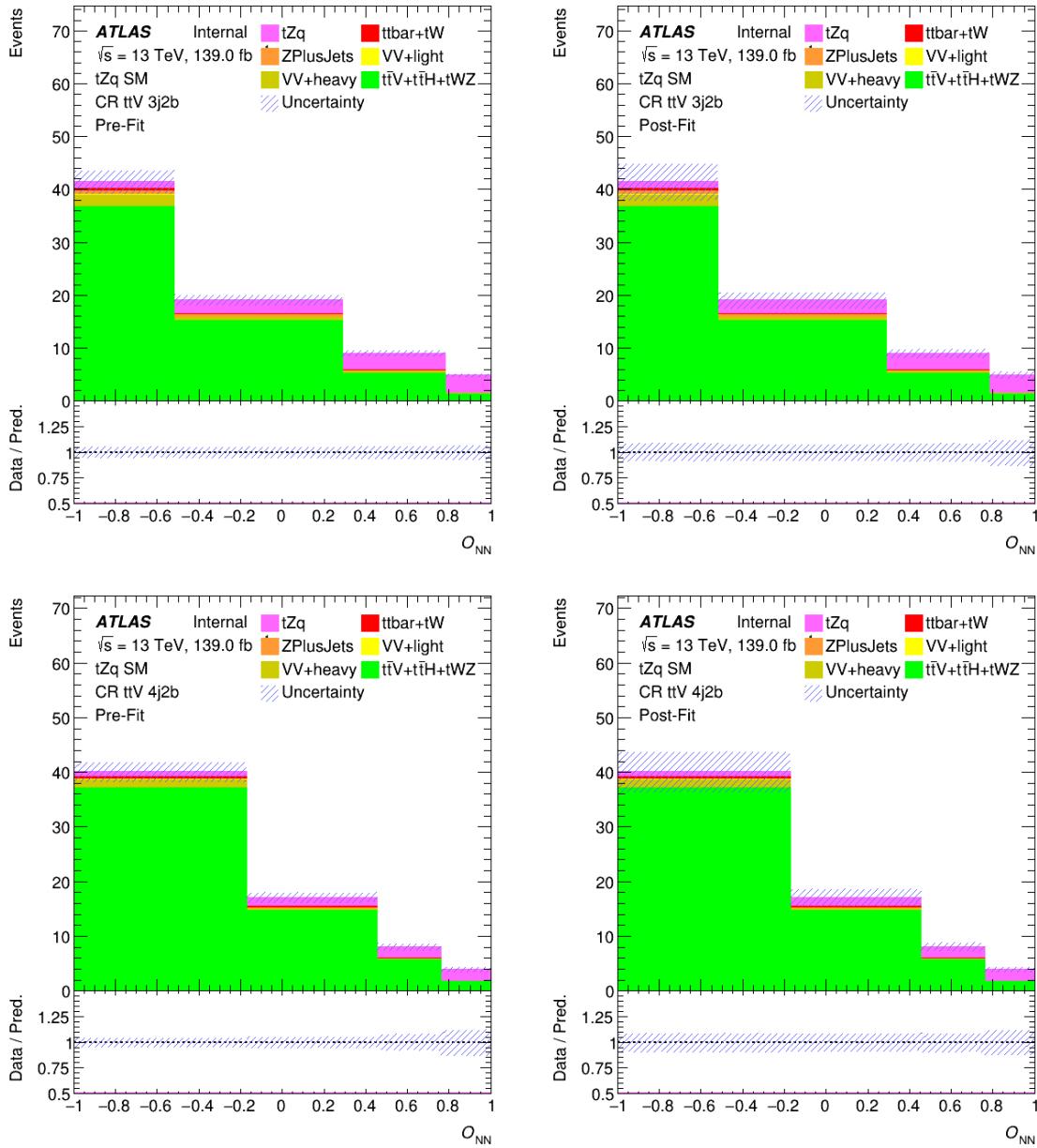


Figure 377: Pre-fit (left) and post-fit (right) NN output distributions in the  $t\bar{t}Z$  control regions. The uncertainty band includes both statistical and systematic uncertainties. [In all regions the Asimov data points are not shown.](#)

Not reviewed, for internal circulation only

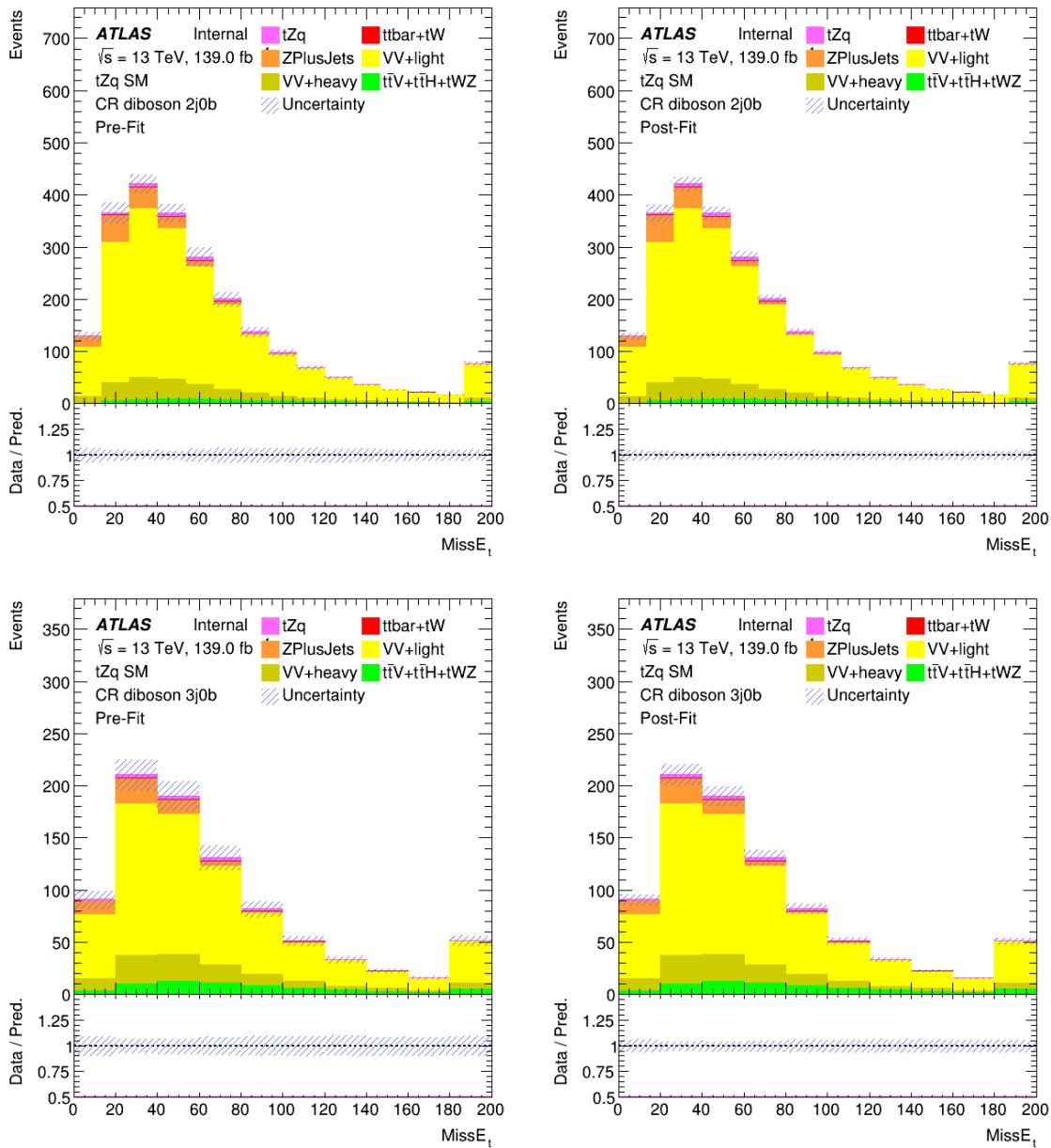


Figure 378: Pre-fit (left) and post-fit (right)  $E_T^{\text{miss}}$  distributions in the diboson control regions. The uncertainty band includes both statistical and systematic uncertainties. [In all regions the Asimov data points are not shown.](#)

Not reviewed, for internal circulation only

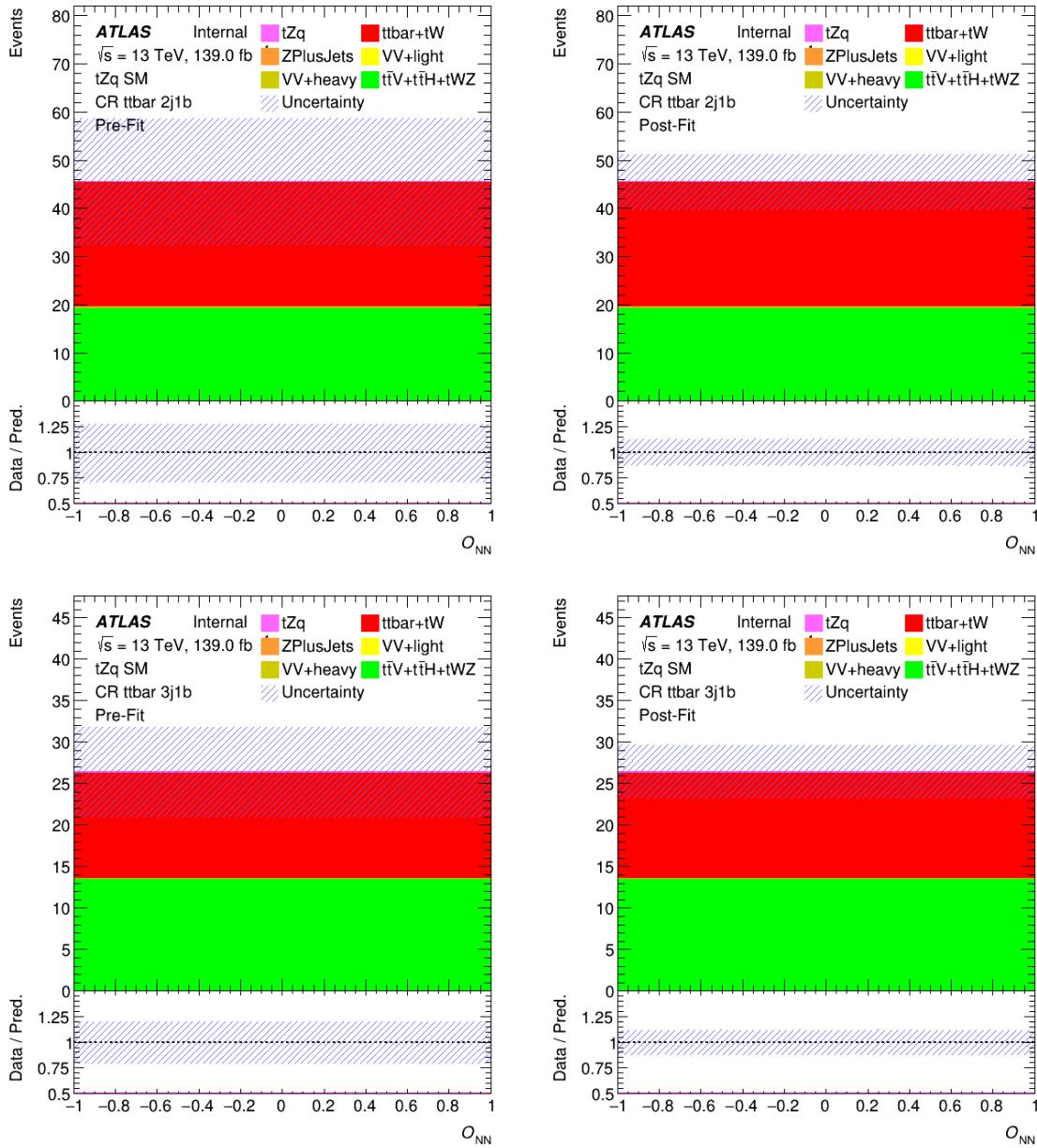


Figure 379: Pre-fit (left) and post-fit (right) NN output distributions in the  $t\bar{t}$  control regions. The uncertainty band includes both statistical and systematic uncertainties. In all regions the Asimov data points are not shown. The big uncertainty in the pre-fit plot for the  $t\bar{t}$  CRs is due to large differences in the event yields for the generator modeling systematics.

## 1708 H Comparison with CMS

1709 In this appendix, a summary of the comparison of the results of this analysis with the one published by  
 1710 CMS in [3] is presented.

1711 **Studies presented in the following were done on events with  $m_T(W) > 20 \text{ GeV}$ .**

1712 CMS uses  $77 \text{ fb}^{-1}$  of data, while ATLAS uses  $139 \text{ fb}^{-1}$ . Figure 380 shows a summary of the regions used  
 1713 in the fit by the ATLAS and CMS analyses. As it can be noticed, CMS has a more inclusive selection in  
 1714 terms of number of jets, while ATLAS adopts an exclusive jet selection to define the various regions.

Not reviewed, for internal circulation only

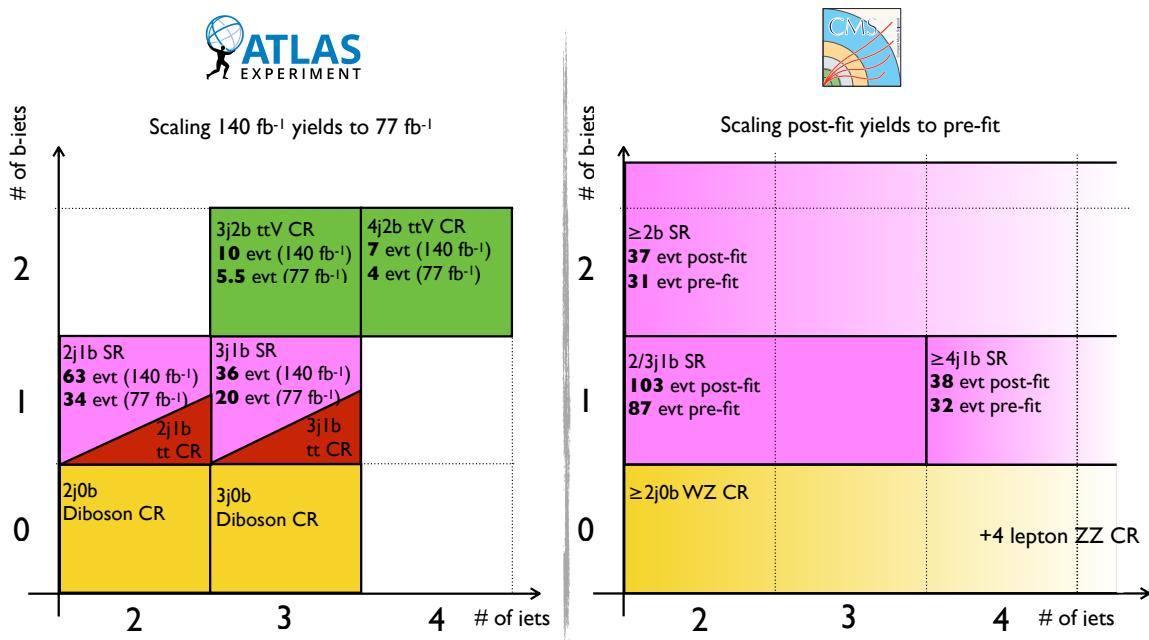


Figure 380: Summary of the regions used in the fit in the ATLAS and CMS analyses.

1715 The regions that can be directly compared are the ATLAS 2j1b and 3j1b SRs with the CMS 2/3j1b SR. In  
 1716 these two regions ATLAS expects 99 events of signal in  $139 \text{ fb}^{-1}$ , which correspond to 54 events of signal  
 1717 on an integrated luminosity of  $77 \text{ fb}^{-1}$ . CMS instead observes 103 events of signal which, scaled by the  
 1718 measured  $\mu_{\text{SIG}}$ , correspond to 87 events of signal on an integrated luminosity of  $77 \text{ fb}^{-1}$ .

1719 Table 65 summarizes the selection cuts used by ATLAS and CMS to define the signal regions. In general  
 1720 ATLAS uses much tighter cuts, both for the lepton and jet transvers momenta and for the  $m_T(\ell_W, \nu)$   
 1721 selection.

Table 65: Summary of the main differences in the event selection of the ATLAS and CMS analyses for the 2/3j1b SRs.

	ATLAS	CMS
Leptons	$p_T(\ell) > 28, 20, 20 \text{ GeV}$	$p_T(\ell) > 25, 15, 10 \text{ GeV}$
Jets	$p_T(\text{jet}) > 35 \text{ GeV}$	$p_T(\text{jet}) > 25 \text{ GeV}$ (60 GeV in crack region)
$m_T(\ell_W, \nu)$	$m_T(\ell_W, \nu) > 20 \text{ GeV}$	–
Z mass window	20 GeV	30 GeV

1722 To understand if the 54 expected signal events by ATLAS and the 87 expected events by CMS are compatible,  
 1723 we have changed the lepton transverse momenta to mimic the CMS' ones. As the trigger selection imposes  
 1724 not to change the leading lepton  $p_T$  cut, the lepton  $p_T$  selection was changed to  $p_T(\ell) > 28, 15, 10$  GeV.  
 1725 Moreover the cut on  $m_T(\ell_W, \nu)$  was removed. The event yields from this selection are shown in Tables 66  
 1726 and 67. As it can be seen, the number of expected signal events is 145, which, scaled to a luminosity of  
 1727  $77 \text{ fb}^{-1}$ , corresponds to 80 expected signal events. This value is compatible with the number of expected  
 1728 event by CMS, considering the fact that the leading lepton and jet  $p_T$  selections are still different.  
 1729 An important fact that should be noticed here is the number of fake lepton background events. In the  
 1730 nominal selection this amounts to 45 events pre-fit, considering both  $t\bar{t}$  and  $Z + \text{jets}$ . With the modified  
 1731 selection, fakes increase to 445 events pre-fit. This, scaled to a luminosity of  $77 \text{ fb}^{-1}$ , corresponds to 245  
 1732 events pre-fit. CMS instead has around 100 events from all sources of fakes with the same selection. CMS  
 1733 lepton fake rejection for low- $p_T$  objects is clearly more powerful than the ATLAS one and this allows them  
 1734 to lower the lepton  $p_T$  selection, increasing the signal acceptance.

Table 66: Numbers of expected events in the 2j1b SR with modified lepton  $p_T$  cuts. The left table shows the number of events after luminosity weighting, while the right table shows the raw number of events available. The uncertainties include only statistical uncertainties.

Process	Number of events	Process	Raw Number of Events
$t\bar{t}Z + tWZ$	$99.0 \pm 16.9$	$t\bar{t}Z + tWZ$	58 798
Small backgrounds	$8.6 \pm 1.3$	Small backgrounds	8253
$VV + \text{HF}$	$135.1 \pm 37.8$	$VV + \text{HF}$	50 378
$VV + \text{LF}$	$29.5 \pm 9.2$	$VV + \text{LF}$	6927
$Z + \text{jets}$	$199.0 \pm 2.2$	$Z + \text{jets}$	377 635
$t\bar{t} + tW$	$121.5 \pm 0.3$	$t\bar{t} + tW$	328 261
$tZq$	$91.6 \pm 0.7$	$tZq$	395 883
Total expected	$684.3 \pm 42.5$	Total expected	1 226 140

Table 67: Numbers of expected events in the 3j1b SR with modified lepton  $p_T$  cuts. The left table shows the number of events after luminosity weighting, while the right table shows the raw number of events available. The uncertainties include only statistical uncertainties.

Process	Number of events	Process	Raw Number of Events
$t\bar{t}Z + tWZ$	$145.7 \pm 24.8$	$t\bar{t}Z + tWZ$	100 149
Small backgrounds	$6.5 \pm 1.0$	Small backgrounds	7556
$VV + \text{HF}$	$79.2 \pm 38.8$	$VV + \text{HF}$	32 474
$VV + \text{LF}$	$16.2 \pm 7.8$	$VV + \text{LF}$	4220
$Z + \text{jets}$	$70.4 \pm 0.9$	$Z + \text{jets}$	164 427
$t\bar{t} + tW$	$54.1 \pm 0.2$	$t\bar{t} + tW$	143 537
$tZq$	$53.0 \pm 0.5$	$tZq$	274 173
Total expected	$425.3 \pm 46.8$	Total expected	726 536